

1 2 9 0



UNIVERSIDADE D
COIMBRA

Filip Ljubinković

CYLINDRICALLY CURVED STEEL
PANELS IN BRIDGE DESIGN

PhD thesis in Steel and Composite Construction supervised by Professor João Pedro Simões Cândido Martins and Professor Helena Maria dos Santos Gervásio and submitted to the Department of Civil Engineering, Faculty of Sciences and Technology of the University of Coimbra

December 2020



UNIVERSIDADE D
COIMBRA

Filip Ljubinković

CYLINDRICALLY CURVED STEEL PANELS IN BRIDGE DESIGN

PhD thesis in Steel and Composite Construction supervised by Professor João Pedro Simões Cândido Martins and Professor Helena Maria dos Santos Gervásio and submitted to the Department of Civil Engineering, Faculty of Sciences and Technology of the University of Coimbra

December 2020

Financial support from the Portuguese Ministry of Science, Technology and Higher Education (Ministério da Ciência, Tecnologia e Ensino Superior) under the individual contract Grant SFRH/BD/145819/2019 and project contract Grant PTDC/ ECM-EST/1494/2014 is gratefully acknowledged. The work was also financed by FEDER funds through the Competitiveness Operational Programme - COMPETE and by national funds through FCT – Foundation for Science and Technology within the scope of the project POCI-01-0145-FEDER-007633 and through the Regional Operational Programme CENTRO2020 within the scope of the project CENTRO-01-0145-FEDER-000006. Finally, funding from the European Commission's Research Fund for Coal and Steel through the research project RFCS-2015-709782 is highly acknowledged.



Preface

The work presented in this document is the result of the research developed within the research unit ISISE (Institute for Sustainability and Innovation in Structural Engineering) at the Civil Engineering Department of the University of Coimbra, under the supervision of Professor João Pedro Martins and Professor Helena Gervásio.

It is my expectation that this work provides original and relevant findings in the field of stability of cylindrically curved steel panels that may contribute to the widespread use of these elements in engineering practice.

Filip Ljubinković
Coimbra, December, 2020

Acknowledgments

I would like to express sincere gratitude to my supervisors Professor João Pedro Martins and Professor Helena Gervásio for their supervision and excellent guidance which gave this work the most significant contribution.

Very special thanks to Professor João Pedro Martins for his tireless dedication and support from day one, but also for his enthusiasm and belief in work we have developed throughout the years as pioneers in the field of curved panels. The first experimental results, numerous project meetings abroad, and journal papers written are only some particles of this long journey that I will carry in my memory for entire life.

Many thanks to Professor Luís Simões da Silva, who recognized my value and capabilities to accomplish the greatest challenge of my career thus far, and without whom this work would have been impossible. His advice and clever comments have always been a remarkable help and a huge inspiration for the successful completion of this work.

The assistance and commitment provided by Cláudio Martins, Tiago Cardoso, Miguel Queiroz, João Vidal, and eng. Ilidio Santos, the former and current technical staff of the Laboratory of Structures of the University of Coimbra were most appreciated. Thanks also to Ricardo Oliveira, Nuno Almeida, and Manuela Rodrigues, who were always there to resolve any technical and bureaucratic problems.

Thanks to all OUTBURST research project partners (University of Ljubljana, GRID International, ATKINS, MCE, University of Stuttgart and ABES) for the interesting discussions and helpful suggestions for improving my work during the project meetings, and especially to Sara Piculin and Primož Može for their hospitality during my stay at the University of Ljubljana. I am very glad, Sara, we had the opportunity to work together, but even more that I found a great friend.

A word of gratitude to all my former and current colleagues of the ISISE group, who were directly or indirectly involved in my work and, especially, to Nuno Rosa, and Tiago Manco for the good times we have shared, at and outside work. Also, working abroad alone would have been certainly more difficult if there hadn't been my Serbian co-workers and friends Nemanja Milovanović, Damjan Čekerevac, and Slobodnaka Jovašević.

Acknowledgments

A special thanks goes to my family for their unconditional support, sacrifice, and patience, but most of all for accepting my absence for four long years. I apologize for the lack of time and attention that I should have given to all of you. Хвала вам пуно!

My greatest thanks go to you, Francisca and your family, for your patience and love, for always being at my side to share my happiness and to encourage me when I was feeling down. Muito obrigado a todos! Thank you, Francisca, for accepting me the way I am and for proving my theory every day that the ‘good life’ – as Aristotle defined – consists of far more than clear thoughts and a few clever actions.

Finally, for everything that appears in this thesis after the countless stages of editing, I alone bear the responsibility.

Abstract

On one side, the topic studied in this thesis is inspired by a recent growing interest in the application of curved panels in various engineering fields, especially in the bridge design, and on the other side, by the lack of adequate and holistic design rules dealing with these structural elements. Consequently, the principal goal of the PhD research work presented herein is to develop clear, general and mechanically consistent design rules both for individual curved panels subjected to the most fundamental loading cases (*i.e.* in-plane compression and shear) and for the whole box-girder bridge cross-section integrating a curved steel panel in the bottom flange. To pursue the set goals, the work is divided into five main tasks, where experimental, numerical, and analytical research methods were implemented, accompanied by a statistical assessment of generated data.

Being the key aspect in the stability of thin-walled structures, a great part of the work is dedicated to the individual curved panels subjected to axial compression. The findings in the thesis reveal some of the substantial advantages of curved panels with respect to the flat ones, allowing for considerable savings that could be achieved. Moreover, based on the assessment of the available design methods for stiffened curved panels under compression, the method developed within the scope of the OUTBURST research project is found to be the most appropriate.

Besides, the thesis explores the buckling and post-buckling behavior of individual curved panels subjected to in-plane shear - a subject, which was only scarcely investigated in the past. The new expressions for both critical and ultimate shear load of unstiffened curved panels are developed, with a similar format to the codified ones for flat plates in EN 1993-1-5:2006.

Finally, the curved panels integrated into box-girder bridge cross-sections are also studied in the thesis, characterizing the entire spectrum of M - V interaction behavior, *i.e.* from pure bending to 'almost' pure shear. Moreover, to assess the applicability of the M - V interaction equation available in the literature, for these innovative structures, the new bending, and shear resistance models are developed.

Keywords: Curved steel panels, Box-girder bridges, Experimental tests, FEM, Compression, Shear, M-V interaction, Design rules

Resumo

Por um lado, o assunto estudado nesta tese foi inspirado pelo crescente interesse da aplicação de painéis curvos em diversos campos da engenharia, especialmente no dimensionamento de pontes. Por outro lado, não existem, até à data, regras de dimensionamento adequadas para este tipo de elementos estruturais. Assim sendo, o principal objetivo da tese de doutoramento apresentada neste documento foi o desenvolvimento de regras de dimensionamento claras e de fácil aplicação, para painéis curvos sujeitos aos casos de carga fundamentais (ex. Compressão no plano e corte) assim como para secções em caixão com painéis curvos no banzo inferior tipicamente aplicadas em pontes. De modo a conseguir alcançar os objetivos mencionados, o trabalho desenvolvido foi dividido em cinco tarefas principais que incluem trabalhos experimentais, numéricos e analíticos, acompanhados por estudos estatísticos dos resultados obtidos.

Sendo os esforços de compressão um aspeto chave na estabilidade de placas finas, uma parte significativa do trabalho apresentado foi dedicada ao estudo do comportamento de painéis curvos sujeitos a cargas axiais de compressão. Os resultados aqui apresentados ilustram as principais vantagens do uso deste tipo de painéis quando comparado com painéis planos, tendo-se observado que a sua utilização pode levar a poupanças significativas. Para além disso, foi demonstrado que o método desenvolvido ao longo do projeto de investigação OUTBURST, baseado nas metodologias já existentes para o dimensionamento de painéis curvos com reforços a esforços de compressão, é a metodologia mais apropriada para o dimensionamento das geometrias de painéis estudados nesta tese.

Adicionalmente, foi também estudado o comportamento à encurvadura e pós-encurvadura de painéis curvos sujeitos a corte no plano. É de realçar que a informação disponível na literatura referente a este tópico é, até à data, bastante escasso. Novas expressões para a determinação da carga de corte crítica e carga última de painéis curvos não reforçados foram desenvolvidas, com um formato semelhante às existentes nas normas de dimensionamento para painéis planos.

Por último, o comportamento de secções em caixão com painéis curvos no banzo inferior foi estudado, tendo-se obtido a completa caracterização da curva de interação $M-V$, *i.e.* o comportamento em flexão ‘pura’ até ao comportamento ao corte ‘puro’, para este tipo de secção.

De modo a verificar a aplicabilidade da equação da curva de interação $M-V$ correntemente utilizada na literatura, novas expressões de resistência à flexão e corte foram desenvolvidos.

Palavras-chave: Painéis curvos em aço estrutural, Secções em caixão, Testes experimentais, FEM, Compressão, Corte, Interação M-V, Regras de dimensionamento

Table of Contents

Preface	v
Acknowledgments	vii
Abstract	ix
Resumo	xi
Table of Contents	xiii
List of figures	xix
List of tables	xxv
Notations	xxvii
1. INTRODUCTION	
1.1 Research relevance and motivation.....	1
1.2 Objectives and research strategy.....	4
1.3 Organization of the thesis.....	7
2. STATE OF THE ART	
2.1 Overview	9
2.2 Geometry of a curved panel.....	10
2.3 Curved panels in bridge deck cross-sections	11
2.4 Literature review.....	15
2.4.1 Curved panels under compression.....	15
2.4.2 Curved panels under shear	32
2.5 Procedures for the computation of the ultimate resistance of curved panels.....	38
2.5.1 Design rules for panels in axial compression	39
2.5.2 Design rules for panels in shear.....	57

2.5.3	Design rules for trapezoidal box-girder bridge cross-section	62
2.6	Summary	67
3.	CYLINDRICALLY CURVED PANELS UNDER PURE COMPRESSION	
3.1	Overview.....	69
3.2	Tests setup.....	70
3.2.1	Geometry of test specimens.....	70
3.2.2	Material properties	71
3.2.3	Test layout	73
3.2.4	Instrumentation.....	74
3.3	Discussion of the experimental results	76
3.3.1	Justification for using the DIC system.....	76
3.3.2	Behavior of curved panels	78
3.3.3	Assessment of the existing design methods.....	83
3.4	Numerical analysis.....	87
3.4.1	Introduction	87
3.4.2	Model definition	88
3.4.3	Calibration of the FE model	93
3.4.4	Assessment of imperfection sensitivity.....	98
3.5	Summary	101
4.	ELASTIC BUCKLING BEHAVIOR OF CURVED PANELS UNDER SHEAR	
4.1	Overview.....	103
4.2	Numerical finite element model.....	104
4.2.1	Section overview.....	104
4.2.2	Definition of the model	104
4.2.3	Validation of the model.....	107
4.2.4	Justification of the curvature parameter as a key parameter	108
4.3	Parametric study	112
4.3.1	Section overview.....	112
4.3.2	Ranges of parameters.....	112
4.3.3	Elastic buckling behavior of curved panels.....	112
4.4	Proposal of design rules for the buckling coefficient	119
4.4.1	Section overview.....	119
4.4.2	Calibration method	119

4.4.3	Proposed formulas.....	120
4.4.4	Validation.....	121
4.5	Summary.....	121
5.	ULTIMATE SHEAR LOAD OF CURVED PANELS	
5.1	Overview.....	123
5.2	Numerical finite element model.....	124
5.2.1	Section overview.....	124
5.2.2	Definition of the model.....	124
5.2.3	Validation of the model.....	128
5.3	Parametric study.....	130
5.3.1	Goal and scope.....	130
5.3.2	Buckling behavior of the panel.....	131
5.4	Proposal of design rules for the ultimate resistance.....	144
5.4.1	General.....	144
5.4.2	Calibration methodology.....	144
5.4.3	Proposed formulas.....	146
5.4.4	Validation.....	148
5.5	Application of design rules.....	149
5.6	Summary.....	151
6.	EXPERIMENTAL STUDY ON CURVED BOTTOM FLANGES IN STEEL BOX-GIRDER BRIDGE DECKS	
6.1	Overview.....	153
6.2	Design of test specimens.....	154
6.2.1	Introduction.....	154
6.2.2	Reference case study.....	154
6.2.3	Geometry of test specimens.....	157
6.2.4	Fabrication challenges.....	158
6.2.5	Material properties.....	159
6.3	Experimental layout.....	161
6.3.1	Definition of the setup.....	161
6.3.2	Instrumentation.....	162
6.4	Experimental results.....	166
6.4.1	Loading.....	166

6.4.2	Displacements.....	167
6.4.3	Strains.....	168
6.4.4	Stresses.....	170
6.4.5	Failure mode.....	177
6.4.6	Comparison between test results and verification procedures.....	179
6.5	Summary.....	183
7.	NUMERICAL STUDY ON BOX-GIRDER BRIDGE CROSS-SECTION INTEGRATING CURVED PANELS	
7.1	Overview.....	185
7.2	Calibration of the FEM numerical model.....	186
7.2.1	Section overview.....	186
7.2.2	Definition of the model used for the calibration.....	186
7.2.3	Model validation by experimental test results.....	191
7.3	Parametric study.....	192
7.3.1	Section overview.....	192
7.3.2	Definition of the FE model for the parametric study.....	192
7.3.3	Scope of the study.....	197
7.4	Results of the parametric study.....	200
7.4.1	Section overview.....	200
7.4.2	$M-V$ interaction.....	200
7.5	Summary.....	206
8.	DESIGN PROPOSALS FOR BRIDGE CROSS-SECTIONS INTEGRATING CURVED STEEL PANELS	
8.1	Overview.....	207
8.2	Bending resistance model.....	208
8.2.1	Introduction.....	208
8.2.2	Study on the isolated bottom flange under pure compression.....	210
8.2.3	Bending resistance – FEM vs Analytical model.....	221
8.3	Shear resistance model.....	224
8.3.1	Introduction.....	224
8.3.2	Comparison of EN 1993-1-5 and FEM results.....	225
8.3.3	Study on the shear participation of the curved bottom flange.....	228
8.3.4	Proposal of a new shear resistance model.....	234

8.3.5	Shear resistance – FEM vs Analytical model	239	
8.4	Assessment of the M-V interaction	241	
8.5	Statistical evaluation of resistance models – Determination of the partial factor γ_M	245	
8.5.1	Introduction.....	245	
8.5.2	EN 1990 - methodology used for evaluation of γ_M	246	
8.5.3	Calculated γ_M factors	251	
8.6	Summary.....	255	
 9. SUMMARY AND FUTURE PROSPECTS			
9.1	Conclusions.....	257	
9.2	Outlook on future research	262	
9.3	Publications.....	263	
9.3.1	International journal papers (ISI)	263	
9.3.2	International conference proceedings	264	
9.3.3	OUTBURST Project dissemination	265	
9.3.4	Other publications and thesis-related presentations	266	
 BIBLIOGRAPHY			267
 ANNEXES			
Annex A	278	
Annex B	285	
Annex C	289	
Annex D	291	

List of figures

CHAPTER 1

Fig. 1.1: Bridge decks with variable depth: a) Dangsang Bridge (South Korea, 1999) [1]; and b) Westgate Bridge (the UK, 1974) [2]	2
Fig. 1.2: Bridges curved in plan: a) Gateshead Millennium Bridge (Newcastle, 2001) [3]; and b) Peace Bridge (Londonderry, Northern Ireland, 2011) [4]	2
Fig. 1.3: Bridges with curved bottom flange: a) “Lo Passador“ Bridge (Spain, 2011) [6]; and b) Renault bridge (France, 2009) [7]	3
Fig. 1.4: Research strategy and division of the main tasks	5

CHAPTER 2

Fig. 2.1: Geometry and notation of cylindrically curved panels: a) unstiffened; b) stiffened	10
Fig. 2.2: Cable-stayed bridges: a) “Puerta de las Rosas” Bridge; b) Bridge of Strings; c) “Serreria” Bridge; and d) PCTCAN Access Bridge (see reference in Table 2.1)	12
Fig. 2.3: Various bridge types: a) Arch bridge - “Galindo” River Bridge; b) Single girder - Charles de Gaulle Bridge; c) Bow-String arch - River Deba Bridge; and d) Suspension bridge - “Lo Passador” Bridge (see reference in Table 2.1)	12
Fig. 2.4: Bridge cross-section forms: a) Renault Bridge; b) “Serreria” Bridge; c) Footbridge ‘De Lichtenlijn’; d) Ter River Bridge (see reference in Table 2.1)	13
Fig. 2.5: Cross-section forms: a) $f < H$; and b) $f = H$	14
Fig. 2.6: Ranges of Z_{loc} of a practical interest in: bridges (see Table 2.2), aeroplanes [41] and ship hulls ([14],[16],[42]-[45])	15
Fig. 2.7: Comparison of the existing formulas for buckling coefficient $k_{\sigma,Z}$ - unstiffened curved panels	19
Fig. 2.8: Rotationally restrained curved panel model by Andico <i>et al.</i> [64]	20
Fig. 2.9: The one-bay cylindrically curved panel model used by Park <i>et al.</i> [16]	24
Fig. 2.10: Cylindrically curved panel model used by Seo <i>et al.</i> [82]	25
Fig. 2.11: Test specimens from Gall [96] (dimensions in inches)	26
Fig. 2.12: Failure mode by bending of the stiffener and sheet panel (from Gall [96])	27
Fig. 2.13: Local failure of stiffener legs (from Gall [96])	27
Fig. 2.14: Curved specimen to flat specimen strength ratio (avg.) (adapted from Gall [96])	28
Fig. 2.15: Test specimens from Ramberg <i>et al.</i> [99] (dimensions in inches)	28

Fig. 2.16: Effect of curvature on compressive strength of stiffened curved panels (adapted from Rabmerg [99]).....	29
Fig. 2.17: Test setup from Soderquist [102] (dimensions in inches).....	30
Fig. 2.18: Effect of curvature on compressive strength of stiffened curved panels (adapted from Soderquist [102]).....	30
Fig. 2.19: Test setup from Cho <i>et al.</i> [109].....	31
Fig. 2.20: NACA monographs for simply supported panels: a) $\alpha > 1$ and b) $\alpha \leq 1$ (adapted from Batdorf <i>et al.</i> [117])	33
Fig. 2.21: NACA monographs for clamped panels: a) $\alpha > 1$ and b) $\alpha \leq 1$ (adapted from Batdorf <i>et al.</i> [117]).....	34
Fig. 2.22: Effective area of a stiffened plate under uniform compression (EN 1993-1-5 [11])	41
Fig. 2.23: Column-type and plate-type interpolation.....	41
Fig. 2.24: Plates with two stiffeners in compression (EN 1993-1-5 [11]).....	43
Fig. 2.25: Definition of distances e_1 and e_2	44
Fig. 2.26: Effective area of a stiffened curved panel under uniform compression	51
Fig. 2.27: Effective cross-section of stiffeners	59
Fig. 2.28: Geometry and notations of a stiffened web plate in bending.....	64

CHAPTER 3

Fig. 3.1: Four groups of specimens based on radius R – R20, R10, R5 and R2.5	70
Fig. 3.2: Division of specimens based on the stiffener configuration.....	70
Fig. 3.3: Tensile coupon test: a) optical extensometer; b) specimen geometry.....	72
Fig. 3.4: Summarized true stress – true strain curves for three considered angles.....	72
Fig. 3.5: Test layout.....	73
Fig. 3.6: Boundary conditions	74
Fig. 3.7: DIC system: a) tripod with two cameras, b) speckle pattern on the outer surface.....	74
Fig. 3.8: Position of horizontal LVDTs	75
Fig. 3.9: Position of strain gauges.....	75
Fig. 3.10: Out-of-plane displacements - DIC vs LVDT (R20-S0-1).....	76
Fig. 3.11: Strain measurements - DIC vs LVDT (R20-S1-1).....	77
Fig. 3.12: Force-displacement curves for: a) R20; b) R10; c) R5 and d) R2.5	78
Fig. 3.13: Effect of curvature on compressive strength of stiffened curved panels.....	80
Fig. 3.14: Failure mode of curved panels without stiffeners S0 (in mm)	81
Fig. 3.15: Failure mode of curved panels with 1 stiffener S1 (in mm).....	81
Fig. 3.16: Failure mode of curved panels with 2 stiffeners S2 (in mm).....	81
Fig. 3.17: Failure mode of curved panels with 3 stiffeners S3 (in mm).....	82
Fig. 3.18: Local buckling of a shallow panel R20-S2-1 recorded by the DIC system	82
Fig. 3.19: Comparison of results with respect to radius R : a) S0; b) S1; c) S2; d) S3	85
Fig. 3.20: Comparison of the available procedures for stiffened curved panels.....	86
Fig. 3.21: Material model used in FEM analyses	89
Fig. 3.22: Numerical model	90
Fig. 3.23: Mesh convergence study using finite element S4R.....	91
Fig. 3.24: Types of imperfections: a) global; b) local-subpanel; c) local-stiffener.....	92
Fig. 3.25: Local initial imperfection pattern: a) DIC; b) FEM.....	94
Fig. 3.26: Collapse shape-front side: a) DIC; b) FEM	94
Fig. 3.27: Force-radial displacement curves for R10-S2-1 and R10-S2-2	94

Fig. 3.28: Comparison of experimental and FEM results (front view).....	96
Fig. 3.29: Behavior of panel R5-S2 assuming various imperfection shapes.....	99
Fig. 3.30: Comparison of results with respect to radius R : a) S0; b) S1; c) S2; d) S3.....	100
Fig. 3.31: Comparison of results: a) Frequency of imperfection leading to the lowest strength; b) CoV (%) of different imperfections around the experimental results	101

CHAPTER 4

Fig. 4.1: Boundary conditions: a) coordinate system, b) BC1; c) BC2 and d) BC3.....	105
Fig. 4.2: Different buckling behavior of a panel with $Z = 100$	109
Fig. 4.3: Minimum values of b/t ratio for a suitable Z parameter.....	111
Fig. 4.4: Ranges of the b/t ratio and the Z_{loc} parameter of practical interest (see Fig. 2.6)	111
Fig. 4.5: Influence of α on the shear buckling coefficient for: a) BC1; b) BC2; c) BC3	113
Fig. 4.6: Influence of α on the buckling mode for various boundary conditions ($Z = 100$).....	114
Fig. 4.7: Influence of curvature on the shear buckling coefficient: a) $\alpha \leq 1.0$; b) $\alpha > 1.0$	115
Fig. 4.8: Influence of curvature on the shear buckling mode.....	116
Fig. 4.9: Influence of boundary conditions - FEM vs theoretical results (NACA curves).....	117
Fig. 4.10: Influence of boundary conditions on the eigenmode form ($\alpha = 1.0$).....	119
Fig. 4.11: Shear buckling coefficient as a function of the curvature and aspect ratio	120
Fig. 4.12: Correlation between $k\tau$, prop and $k\tau$, num	121

CHAPTER 5

Fig. 5.1: Types of instability: a) bifurcation and b) snap-through.....	125
Fig. 5.2: Material behavior applied in GMNIA.....	127
Fig. 5.3: Comparison between FEM results and various methods: a) $\alpha = 1.0$ and b) $\alpha = 2.0$	129
Fig. 5.4: Comparison between numerical results: FEM (solid) and Amani <i>et al.</i> (dashed).....	130
Fig. 5.5: Post-buckling behavior of a curved panel subjected to shear loading.....	131
Fig. 5.6: Influence of geometry on the ultimate shear resistance for a) $Z = 0$ and b) $Z = 40$	132
Fig. 5.7: Influence of curvature on the ultimate shear resistance for $\alpha = 1.0$ and $b/t = 300$	133
Fig. 5.8: Influence of the boundary conditions on the panels with a low slenderness.....	134
Fig. 5.9: Deformed shapes of the panels with boundary condition BC1	135
Fig. 5.10: Basler's model (adapted from [125]) – boundary condition BC2.....	135
Fig. 5.11: Comparison of the deformed shapes for BC2 (left) and BC3 (right): a) $\alpha = 1.0$ and b) $\alpha = 2.0$	136
Fig. 5.12: Influence of BC on the ultimate shear resistance: a) $Z = 0$ and b) $Z = 50$	137
Fig. 5.13: Influence of α on the ultimate shear resistance for a) $Z = 10$ and b) $Z = 50$	138
Fig. 5.14: Influence of the imperfection shape: a) $\alpha = 1.0$ and b) $\alpha = 2.0$	140
Fig. 5.15: Comparison between two imperfection amplitudes – $b/200$ and $b/420$	142
Fig. 5.16: imperfection sign: a) positive and b) negative.....	143
Fig. 5.17: Comparison between two imperfection signs – <i>positive</i> and <i>negative</i>	143
Fig. 5.18: Buckling curves for boundary condition BC1	145
Fig. 5.19: Buckling curves for boundary condition BC2 ($Z = 50$).....	145
Fig. 5.20: Buckling curves for boundary condition BC3 ($Z = 50$).....	146
Fig. 5.21: Correlation between $\bar{\chi}_{w,prop}$ and $\bar{\chi}_{w,num}$	149
Fig. 5.22: Flowchart for determination of the ultimate shear resistance of curved panels.....	149
Fig. 5.23: Corresponding buckling curve for the considered study cases ($Z = 20$, $\alpha > 3.0$)	151

CHAPTER 6

Fig. 6.1: Span layout of the reference case study - bridge elevation [147].....	155
Fig. 6.2: Alternative cross-section with the curved panel at a) span and b) pier [5].....	155
Fig. 6.3: Curved steel plate in the bottom flange (adapted from [5]).....	156
Fig. 6.4: Structural steel distribution [5].....	156
Fig. 6.5: Length of bridge deck close to an intermediate pier.....	157
Fig. 6.6: Cross-section of the tested prototypes.....	157
Fig. 6.7: Fabrication of test specimens by MCE GmbH.....	158
Fig. 6.8: Geometry and orientation of the tensile test specimens	160
Fig. 6.9: Engineering stress-strain curves: a) S460; b) S690	160
Fig. 6.10: Global view of the test setup	161
Fig. 6.11: Test setup: a) load application; b) end support - 2 back-to-back U260 beams (white) and 2 HEB300 beams (blue)	162
Fig. 6.12: Lateral constraints.....	162
Fig. 6.13: The position of LVDTs.....	163
Fig. 6.14: LVDTs to measure vertical displacements: a) V-1, V-2, and V-3; b) V-4 and V-5.....	163
Fig. 6.15: LVDTs to measure: a) longitudinal (L-2) and b) horizontal (H-1) displacements	163
Fig. 6.16: Position of SGs close to the intermediate support.....	164
Fig. 6.17: a) Application of SGs (L and T); b) SGs on curved part (C and N); c) SGs on flat webs (F)	164
Fig. 6.18: Position of SGs in cross-sections 1-1, 2-2 and 3-3	165
Fig. 6.19: Measurements of applied load (F) and reactions (R1-R4).....	166
Fig. 6.20: Load (F)-displacement (V-1) curves.....	166
Fig. 6.21: Reactions at the end-support: a) specimen S460 and b) specimen S690	167
Fig. 6.22: Vertical displacement of the bridge: a) before and b) after the test	167
Fig. 6.23: Vertical displacements measured at the ultimate load in [mm].....	168
Fig. 6.24: Strains in curved (C) and flat (F) parts of cross-section 1-1 – S460.....	169
Fig. 6.25: Strains in curved (C) and flat (F) parts of cross-section 1-1 – S690.....	169
Fig. 6.26: Comparison of the experimental and analytical (LBT) results at point 2F/5F	171
Fig. 6.27: Axial stresses in specimen S460 in cross-section: a) 1-1 and b) 2-2.....	172
Fig. 6.28: Axial stresses in specimen S690 in cross-section: a) 1-1 and b) 2-2.....	172
Fig. 6.29: a) Elastic bending moment M_{el} ; b) Plastic bending moment M_{pl}	173
Fig. 6.30: Moment-rotation curves.....	174
Fig. 6.31: Neutral axis shifting after yielding at section 1-1 for a) S460 and b) S690.....	174
Fig. 6.32: Shear lag effect in the prototype: a) S460 and b) S690 – σ_1 [MPa]	175
Fig. 6.33: Position and notation of SGs on the longitudinal stiffeners.....	176
Fig. 6.34: Axial stresses in longitudinal stiffeners - prototype S690 (cross-section 2-2).....	176
Fig. 6.35: Failure mode of the bottom curved panel: a) specimen S460; b) specimen S690	177
Fig. 6.36: Failure mode of the bottom curved panel inside the box-girder – specimen S460.....	177
Fig. 6.37: Local buckling of the stiffened bottom curved panel.....	178
Fig. 6.38: Deformed shape of prototype S460 (cross-section 1-1) for: a) $F = 0.7F_{max}$; b) $F = 0.9F_{max}$; c) $F = 0.95F_{max}$; and d) $F = F_{max}$	179
Fig. 6.39: Equivalent flat panel approach.....	180
Fig. 6.40: Effective cross-section of specimen S690 according to equivalent panel approach	181
Fig. 6.41: Effective cross-section of specimen S690 according to curved panel approach.....	181

CHAPTER 7

Fig. 7.1: Stress-strain relations applied in FEM: a) S460 and b) S690	187
Fig. 7.2: Applied loading and support condition	188
Fig. 7.3: a) FE mesh configuration used for the model calibration; b) supporting beams; c) segment between two cross-frames; d) supporting foot; e) loading beam	190
Fig. 7.4: Eigenmodes used for the calibration of the model: a) 1 st mode and b) 14 th mode	190
Fig. 7.5: a) Failure mode obtained by FEM; b) outside; c) inside	191
Fig. 7.6: Comparison of force-displacement curves: a) specimen S460; b) specimen S690	192
Fig. 7.7: Simplified FE model: a) Step 1; b) Step 2	193
Fig. 7.8: Simplified FE model vs experimental results - comparison of results	193
Fig. 7.9: Static scheme: a) experimental test; b) numerical parametric study	194
Fig. 7.10: Example of a numerical model used for the parametric study	195
Fig. 7.11: Imperfection sensitivity analysis – shear failure: a) force-displacement curves; b) peak region of force-displacement curves	196
Fig. 7.12: Imperfection sensitivity analysis – bending failure: a) force-displacement curves; b) peak region of force displacement curves	196
Fig. 7.13: Stiffener typologies: a) flat; b) trapezoidal– Type 1 and c) trapezoidal – Type 2	197
Fig. 7.14: Stiffener configurations: a) $Z = 0$; b) $Z = 300$	198
Fig. 7.15: Cross-section with: a) constant height; b) variable height H	198
Fig. 7.16: Position of the longitudinal stiffeners on webs: a) $H = \text{const.}$ ($n_{\text{st,web}} = 1$); b) $H = \text{var.}$ ($n_{\text{st,web}} = 2$)	200
Fig. 7.17: a) Force-deflection curves and b) M - V interaction diagram for box-girder ($H = \text{const.}$; $Z = 300$; $\alpha = 0.5$; $n_{\text{st}} = 3$; $t = 25$ mm; $t_w = 25$ mm)	201
Fig. 7.18: Bending (M), mixed ($M+V$) and shear dominant (V) failure modes and Mises stress distributions	202
Fig. 7.19: M - V interaction diagrams for $H = \text{const.}$ and various Z parameters	203
Fig. 7.20: M - V interaction diagrams for $H = \text{var.}$ and various Z parameters	204

CHAPTER 8

Fig. 8.1: Graphical interpretation of the M - V interaction formula by Jáger <i>et al.</i> [136]	208
Fig. 8.2: Typical bending failure modes - FEM: a) yielding of bottom flange; b) local buckling; c) global buckling	209
Fig. 8.3: Comparison between FEM and analytical results for panels with flat stiffeners	214
Fig. 8.4: Comparison between FEM and analytical results for panels with trapezoidal stiffeners ...	214
Fig. 8.5: Numerical results vs EN 1993-1-5 [11] – comparison of the ultimate resistances for various curvatures Z (avg.)	216
Fig. 8.6: Comparison of the ultimate resistances for various curvatures (avg.): a) FEM vs Tran <i>et al.</i> [59] and b) FEM vs OUTBURST [83]	218
Fig. 8.7: Comparison of methods by Tran <i>et al.</i> [59] and OUTBURST [83]	218
Fig. 8.8: FEM vs Tran <i>et al.</i> [59] in a function of a) Z parameter and b) aspect ratio	219
Fig. 8.9: FEM vs OUTBURST [83] in a function of a) Z parameter; b) aspect ratio	220
Fig. 8.10: Definition of the ‘bottom flange’ (in black) in box-girders with curved bottom flange for various Z parameters	222

Fig. 8.11: Comparison of FEM results with the analytical model: a) for various Z parameters and b) various aspect ratios.....	223
Fig. 8.12: Typical shear failure modes - FEM: a) global buckling and b) local buckling.....	225
Fig. 8.13: Definition of the ‘flat web’ (in black) in box-girders with a curved bottom flange.....	226
Fig. 8.14: Comparison of the shear resistances calculated by FEM and EC3 considering: a) $I_{sl}/3$ and b) I_{sl} - full.....	227
Fig. 8.15: Shear stress distribution in cross-sections with $H=\text{const.}$ (FEM).....	229
Fig. 8.16: Shear stress distribution in cross-sections with $H=\text{var.}$ (FEM).....	229
Fig. 8.17: The ratio between the area participating in shear resistance in a cross-section with curved bottom flange ($Z > 0$) and cross-section with flat bottom flange ($Z = 0$) for: a) $H=\text{const}$ and b) $H=\text{variable}$	229
Fig. 8.18: Notations and the shear area A_w for a) circular and b) half-circular cross-section.....	230
Fig. 8.19: Shear stress distribution at reaching the plastic resistance (V_{pl}).....	231
Fig. 8.20: Definition of relevant geometric parameters for the study on the shear participation of the curved bottom flange ξ_s	232
Fig. 8.21: Shear stress distribution in the bottom flange at reaching the plastic resistance (V_{pl}) for $H=\text{var.}$ and curvatures: a) $Z = 0$; b) $Z = 100$; c) $Z = 200$ and d) $Z = Z_{\text{max}} = 352$	233
Fig. 8.22: Bottom flange shear participation as a function of α and β angles.....	233
Fig. 8.23: Verification of the FEM results against the EC3-based method with respect to the $\lambda_w - \chi_w$ correlation.....	235
Fig. 8.24: Proposed shear resistance model: a) real web geometry; b) extended flat web.....	236
Fig. 8.25: Verification of the FEM results against the EC3-based extended web method with respect to the $\lambda_w - \chi_w$ correlation.....	238
Fig. 8.26: Comparison of the shear resistances calculated by FEM and by new analytical method considering: a) $I_{sl}/3$ and b) I_{sl} - full.....	239
Fig. 8.27: Comparison of the EC3-method and the proposed method against the FEM results considering: a) $I_{sl}/3$ and b) I_{sl} - full.....	240
Fig. 8.28: Comparison of the proposed method against the FEM results considering full (I_{sl}) and reduced ($I_{sl}/3$) longitudinal stiffener inertia.....	241
Fig. 8.29: Comparison of the proposed method against the FEM results considering full (I_{sl}).....	242
Fig. 8.30: Comparison between the FEM results and M-V interaction formula Eq.(8.13) for both I_{sl} (red) and $I_{sl}/3$ (black): a) front view; b) back view.....	243
Fig. 8.31: FEM results vs M-V interaction formula for various $M_{f,Rk}/M_{eff,Rk}$ ratios.....	243
Fig. 8.32: FEM results vs M-V interaction formula for various $M_{f,Rk}/M_{eff,Rk}$ ratios: a) $I_{sl}/3$ and b) I_{sl} - full.....	245
Fig. 8.33: Schematic illustration of $r_t - r_e$ diagram.....	248
Fig. 8.34: All results organized by curvature parameter for four different distributions of the basic variables ($V_{r,t,1} = 0$, $V_{r,t,2} = 0.05$, $V_{r,t,3} = 0.056$ and $V_{r,t,4} = 0.07$).....	251
Fig. 8.35: All results organized by four different distributions of the basic variables – for reduced ($I_{sl}/3$) and full (I_{sl} - full) stiffener inertia.....	253
Fig. 8.36: All results organized by curvature parameter for four different distributions of the basic variables, considering reduced stiffener inertia $I_{sl}/3$	253
Fig. 8.37: All results organized by curvature parameter for four different distributions of the basic variables, considering full stiffener inertia I_{sl} -full.....	254

List of tables

Table 2.1: Bridge decks integrating cylindrically curved steel panels.....	13
Table 2.2: Ranges of geometrical parameters of curved panels used in bridges	14
Table 2.3: Ranges of geometrical parameters from the available literature.....	35
Table 2.4: Available design procedures for unstiffened curved panels under compression	45
Table 2.5: Definition of α_Z (Tran <i>et al.</i> [75]).....	46
Table 2.6: Definition of α_Z , c_Z and S_Z (Martins <i>et al.</i> [78]).....	47
Table 2.7: Available design procedures for stiffened curved panels under compression	50
Table 2.8: Definition of parameters X_i	53
Table 2.9: Available design procedures for unstiffened curved panels under shear.....	59
Table 2.10: Definition of the longitudinal stiffeners – gross and effective area.....	64
Table 3.1: Geometry of the specimens.....	71
Table 3.2: Mechanical properties of steel S355	72
Table 3.3: Comparison of the ultimate resistance – unstiffened panels (S0).....	84
Table 3.4: Comparison of the ultimate resistance – 1-stiffened panels (S1).....	84
Table 3.5: Comparison of the ultimate resistance – 2-stiffened panels (S2).....	84
Table 3.6: Comparison of the ultimate resistance – 3-stiffened panels (S3).....	85
Table 3.7: Equivalent imperfections used for the calibration of numerical models.....	97
Table 3.8: Imperfections considered in the study	98
Table 3.9: Imperfection and corresponding collapse shapes for panel R5-S2	99
Table 4.1: Geometry of the curved panels considered in this study.....	104
Table 4.2: In-plane edge constraints applied in the model for BC2 and BC3.....	106
Table 4.3: Mesh convergence study (shear buckling coefficient - k_z)	107
Table 4.4: Validation of numerical models – flat panel.....	108
Table 4.5: Ranges of parameters for a study on the Z parameter justification.....	108
Table 4.6: Justification for the use of Z as a key parameter - $k_z/k_{z,ref}$ (%)	109
Table 4.7: Minimum R/t ratio for a suitable Z parameter	110
Table 4.8: Buckling coefficient k_z for panels with $\alpha \geq 3.0$	115
Table 4.9: Influence of boundary conditions on shear buckling coefficient k_z	118
Table 4.10: A_k and B_k parameters for computation of the shear buckling coefficient - $k_z^{1,2}$	120
Table 4.11: Statistical assessment based on the ratio $\bar{k}_{z,prop}/\bar{k}_{z,num}$	121
Table 5.1: Material properties of steel S355 ($t = 10$ mm).....	127
Table 5.2: Mesh convergence study (shear reduction factor - χ_w).....	128

Table 5.3: Scope of the parametric study.....	130
Table 5.4: Influence of imperfection shape on the shear reduction factor χ_w ($\alpha = 1.0$).....	139
Table 5.5: Influence of imperfection shape on the shear reduction factor χ_w ($\alpha = 2.0$).....	139
Table 5.6: Influence of imperfection shape on the shear reduction factor χ_w (BC2 and BC3).....	141
Table 5.7: A_χ and B_χ parameters ($1.1 \leq \bar{\lambda}_w < 3.0$).....	147
Table 5.8: A_χ , B_χ and C_χ parameters ($\bar{\lambda}_w < 1.1$).....	147
Table 5.9: Simplified expressions for A_χ , B_χ and C_χ parameters (BC2).....	148
Table 5.10: Simplified expressions for A_χ , B_χ and C_χ parameters (BC3).....	148
Table 5.11: Statistical assessment based on the ratio $\bar{\chi}_{w,prop}/\bar{\chi}_{w,num}$	148
Table 5.12: Definition of example.....	150
Table 6.1: Geometrical parameters of the adopted cross-section at support.....	157
Table 6.2: Adopted geometry of the tested prototype in [mm].....	158
Table 6.3: Measured mechanical properties for two steels – engineering stresses.....	160
Table 6.4: Longitudinal and horizontal displacements measured at the ultimate load.....	168
Table 6.5: Elastic, plastic and measured bending moments.....	173
Table 6.6: Comparison of bending moment capacity.....	181
Table 6.7: Comparison of two design approaches – bottom flange effective width factors.....	182
Table 6.8: Comparison of shear force capacity.....	182
Table 7.1: Mechanical properties of steels in the top flange (by MCE GmbH [18]).....	187
Table 7.2: Stiffness of springs adopted in the FEM model – specimen S460.....	188
Table 7.3: Stiffness of springs adopted in the FEM model – specimen S690.....	189
Table 7.4: Characteristic values of considered material properties – steel S355 [144].....	195
Table 8.1: Validation of the numerical models with results from Tran [8] and Manco [10] for ‘rigid’ boundary conditions – ultimate resistance (MN).....	213
Table 8.2: Numerical results vs EN 1993-1-5 [11] – comparison of the ultimate resistances for ‘free’ boundary condition (avg.).....	216
Table 8.3: Numerical results vs EN 1993-1-5 [11] – comparison of the ultimate resistances for ‘rigid’ boundary condition (avg.).....	216
Table 8.4: Comparison between methods by Tran <i>et al.</i> [59] and OUTBURST [83] with respect to the FEM results.....	220
Table 8.5: Statistical assessment of the V_{num}/V_{EC3} ratio for various Z parameters.....	227
Table 8.6: Statistical assessment of the V_{num}/V_{analy} ratio for various Z parameters.....	240
Table 8.7: Statistical assessment of the numerical results with respect to the M-V interaction formula Eq.(8.13) for both I_{sl} and $I_{sl}/3$ and various Z parameters.....	244
Table 8.8: Recommended values for γ_M – EN 1993-1-5.....	245
Table 8.9: Scenarios for the statistical assessment based on the choice of the basic variables.....	247
Table 8.10: Recommended distributions for material and geometrical variables [162].....	248
Table 8.11: Partial factors γ_M for bending resistance model.....	252
Table 8.12: Equivalent partial factors γ_M for M-V resistance model – $I_{sl}/3$	254
Table 8.13: Equivalent partial factors γ_M for M-V resistance model – I_{sl} full.....	254

Notations

Greek uppercase letters

Δu_r	Imperfection in the radial direction
Φ_R	Strength increment factor

Greek lowercase letters

α	Aspect ratio
α_{loc}	Local aspect ratio
α_e	Equivalent imperfection factor
α_z	Elastic imperfection reduction factor
β	Sectorial angle; Interaction coefficient; Web inclination angle
β_z	Plastic range factor
γ_M	Partial factor for a material property
$\gamma_{M,0}$	Partial factor for resistance associated with cross-section checks
$\gamma_{M,1}$	Partial factor for resistance associated with instability problems
δ	Vertical displacement
δ_0	Imperfection amplitude
δ_i	Error term
ε	Strain
ε_u	Yield strain
η	Parameter attributed to strain hardening
η_1, η_3	Bending and shear utilization factors

λ	Slenderness parameter
λ_β	Double slenderness ratio
λ_F, λ_M	Force and bending moment load amplifiers
$\bar{\lambda}$	Normalized slenderness parameter
$\bar{\lambda}_0$	Squash limit relative slenderness (initial plateau length)
$\bar{\lambda}_p$	Slenderness limiting elastic-plastic domain of the response
$\bar{\lambda}_w$	Slenderness parameter related to plates in shear
μ	Mean value
ν	Poisson's coefficient
ξ	Interpolation parameter between the plate and column-type buckling
ξ_s	Shear participation of bottom flange
ρ	Reduction factor
ρ_c	Reduction factor for global buckling
ρ_{loc}	Reduction factor for local buckling
σ	Axial stress
σ_{cr}	Elastic critical stress
$\sigma_{cr,c}$	Elastic critical column buckling stress
$\sigma_{cr,p}$	Elastic critical plate buckling stress
$\sigma_{cr,s}$	Elastic critical shell buckling stress
$\sigma_{cr,sl}$	Elastic critical stress of a stiffener
σ_E	Euler's elastic critical stress
τ	Shear stress (load)
τ_{cr}	Critical shear stress
τ_u	Yield shear stress (load)
φ	Inclination angle of the tension field
χ^c	Reduction factor for column buckling
χ^w	Reduction factor for shear buckling
ψ	Axial stress ratio

Roman uppercase letters

A	Cross-section area
-----	--------------------

A_{eff}	Effective cross-section area
A_p	Cross-section area of a sheet plate alone
$A_{sl}, A_{sl,\text{eff}}$	Gross and effective cross-section area of a stiffener
A_k, B_k	Parameters for computation of the shear buckling coefficient
A_χ, B_χ, C_χ	Parameters for computation of the shear reduction factor
D	Flexural stiffness of a plate
E	Young's modulus
F	Applied force
G	Shear modulus
H_w	Total height of a box-girder cross-section
I_y	Second moment of area around y-axis
I_p	Second moment of area of a sheet plate alone
$I_{sl}, I_{sl,\text{eff}}$	Gross and effective second moment of area of a stiffener
L	Member length
L_w	Length of curved bottom flange participating in shear resistance
M_{Ed}	Design bending moment
$M_{eff,Rd}$	Effective moment of resistance for a class 4 cross-section
$M_{el,Rd}$	Elastic moment of resistance
$M_{f,Rd}$	Bending resistance considering only the effective flanges
M_{num}	Bending resistance obtained in FEM simulations
$M_{pl,Rd}$	Plastic moment of resistance
M_{Rd}	Resistant bending moment
N_{pl}	Plastic compressive resistance
N_{Rd}, N_{Rk}	Design and characteristic compressive resistance
Q	Log-normal variation coefficients
R	Radius of curvature of the curved panel
$R_{p0.2}$	Yield strength corresponds to the proof strength
V	Shear force
$V_{b,Rd}$	Shear resistance
$V_{bf,Rd}$	Shear resistance – flange contribution
$V_{bw,Rd}$	Shear resistance – web contribution

V_{Ed}	Design shear force
V_{num}	Shear resistance obtained in FEM simulations
V_{pl}	Plastic shear resistance
W_{eff}	Effective section modulus
W_{el}	Elastic section modulus
W_{pl}	Plastic section modulus
X_j	Basic independent variable
Z	Curvature parameter
Z_a	Curvature parameter in the transverse direction
Z_b	Batdorf curvature parameter
Z_{loc}	Local curvature parameter

Roman lowercase letters

a	Panel length
a_{loc}	Subpanel length
b	Panel width
b_{eff}	Effective width
b_f	Top flange width
b_{loc}	Subpanel width
f	Curved panel depth
f_u	Ultimate strength of the steel
f_y	Yield stress
f_{yw}	Yield shear stress
h_{st}	Stiffener height
h_w	Web height
k_σ	Elastic buckling coefficient
$k_{\sigma,pl}$	Elastic buckling coefficient for flat plates
$k_{\sigma,Z}$	Elastic buckling coefficient for curved panels
k_τ	Shear buckling coefficient
n_{st}	Number of stiffeners
q_c	Applied in-plane axial load

r_k, r_k	Characteristic and design value of the strength
r_t	Resistance function
t	Panel thickness
t_f	Top flange thickness
t_{st}	Stiffener thickness
t_w	Web thickness
u_z, u_φ, u_r	Displacement in longitudinal, circumferential and radial directions

ABBREVIATIONS AND ACRONYMS

ABS	American Bureau of Shipping
BC	Boundary Condition
C/UC	Constrained/Unconstrained
CCD	Charged-Coupled Device
CoV	Coefficient of Variation
DIC	Digital Image Correlation
DNV	Det Norske Veritas
DOF	Degree of Freedom
ECCS	European Convention for Constructional Steelwork
FCT	Portuguese Foundation for Science and Technology
FE	Finite Element
FEM	Finite Element Method
GBT	Generalised Beam Theory
GMNIA	Geometrically and Materially Nonlinear Analysis with Imperfections
HSS	High Strength Steel
IMP	Imperfection
ISISE	Institute for Sustainability and Innovation in Structural Engineering
LBA	Linear Buckling Analysis
LBT	Linear Beam Theory
LVDT	Linear Displacement Transducers
NACA	National Advisory Committee for Aeronautics

OUTBURST	Optimization of Steel Plated Bridges in Shape and Strength
RD	Rolling Direction
RFCS	Research Fund for Coal and Steel
RP	Reference Point
SG	Strain Gauge
SHS	Steel Hollow Section
ULS	Ultimate Limit State

1. Introduction

1.1 Research relevance and motivation

Owing to tremendous technological progress in recent years, there is a growing need for more challenging architectural and structural solutions in bridge design. To encounter these demands, the use of curved steel panels has become a very attractive trend, both for aesthetic and structural reasons.

Such non-conventional bridge designs may be generally divided into three categories: *i*) bridges with longitudinally curved webs (*i.e.* girders with variable depth along the span), *ii*) bridges with horizontally curved panels (*i.e.* girders curved in the plan), and *iii*) bridges with transversally curved panes.

The girders with variable depth along the span are commonly used in bridges, for their remarkable structural efficiency in large spans and/or aesthetical reasons. Another possible advantage of these bridges may be utilized in urban areas, where not rarely due to major clearance constraints, it is required to use profiles with a lower depth. These bridges are characterized by the girder webs that change from a rectangular to a tapered shape, which may be achieved either by the addition of haunches near the supports or by means of webs that gradually vary their depth, thus having a parabolic shape. Among many examples, the railway twin box-girder Dangsang bridge in South Korea ([Fig. 1.1a](#)) and the roadway multi-girder Westgate bridge in the UK ([Fig. 1.1b](#)) are highlighted.



Fig. 1.1: Bridge decks with variable depth: a) Dangsang Bridge (South Korea, 1999) [1]; and b) Westgate Bridge (the UK, 1974) [2]

The need for bridges curved in plan appears predominantly in urban areas, where the surrounding buildings present an obstacle in the longitudinal layout of the bridge. Moreover, horizontally curved bridges, when carefully integrated with the surrounding context may offer various aesthetical benefits. These bridges have been extensively built in Great Britain, two of which are presented in Fig. 1.2.

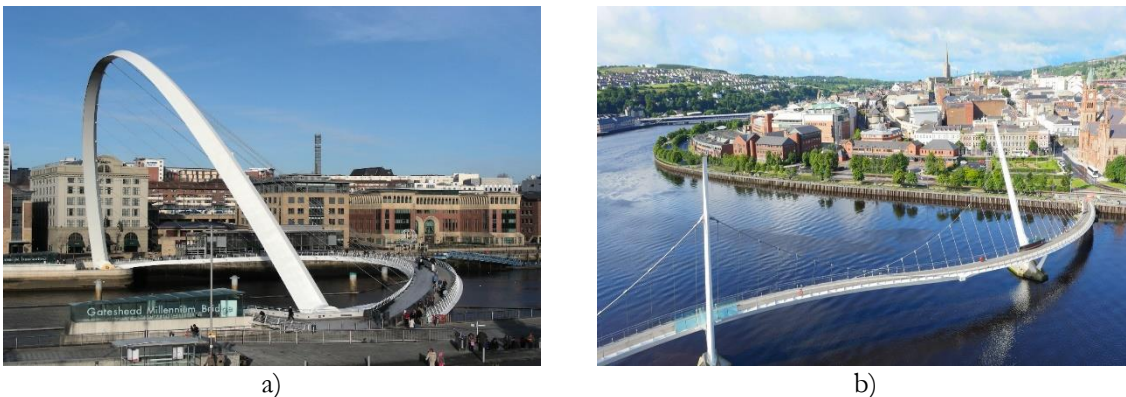


Fig. 1.2: Bridges curved in plan: a) Gateshead Millennium Bridge (Newcastle, 2001) [3]; and b) Peace Bridge (Londonderry, Northern Ireland, 2011) [4]

While there is a significant number of bridge decks with variable depth along the span, as well as the bridge girders curved in plan, there is only a handful of bridge decks with cylindrically curved panels in the bottom flange. In fact, according to a comprehensive survey carried out in 2017 by Reis *et al.* [5], 18 bridges with curved cross-sectional parts have been recently built, most of them in urban environments where again aesthetics play an important role. Two of them are highlighted in Fig. 1.3, whereas all the others are addressed later in the document, being relevant (and the only) source for the identification of possible cross-section forms and the characterization of key parameters of curved bridge decks.

As it may be noticed, the major difference between these bridge decks and conventional trapezoidal box-girder decks is the presence of a transversely curved panel in the bottom flange. One might say that the main motive for such solutions is exclusively to enhance its aesthetical performance. However, the adoption of a box-girder cross-section integrating a cylindrically curved bottom flange proffers an aerodynamic shape that may significantly improve response to

undesired dynamic effects caused by wind load, which is particularly convenient in the case of the cable-stayed and suspension bridges. Finally, yet importantly, using curved panels in bridge decks instead of classical flat ones, considerable gains in resistance may be achieved. Namely, with the introduction of curvature, which is the main characteristic of curved panels that differentiates substantially their behavior from flat plates, vast gains in resistance can be achieved when subject to compression, as shown in recent research and PhD theses dealing with this topic (*e.g.* Tran [8], Martins [9] and Manco [10]).

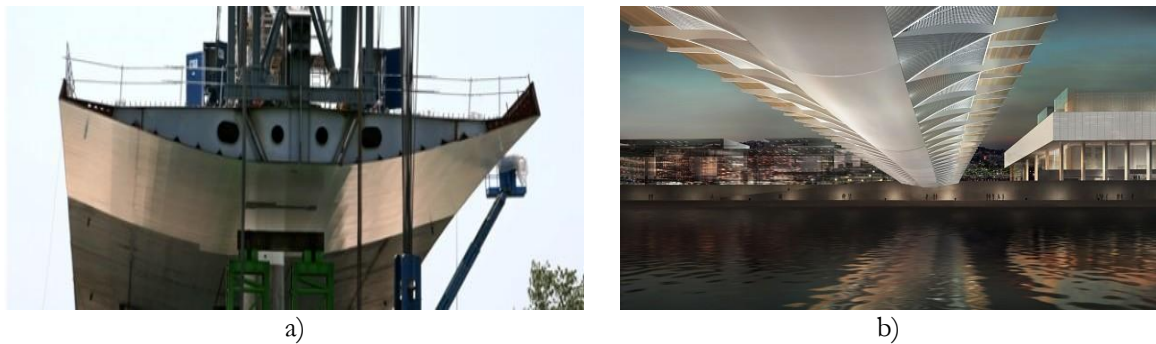


Fig. 1.3: Bridges with curved bottom flange: a) “Lo Passador“ Bridge (Spain, 2011) [6]; and b) Renault bridge (France, 2009) [7]

One of the main difficulties for the widespread use of curved steel panels in engineering practice is the lack of adequate and holistic design standards that are able to assess the buckling strength for the entire range of parameters relevant to curved panels, in the same way as it was long established for the flat plates. Namely, the scope of the actual design code for plated elements EN 1993-1-5 [11] is restricted to flat or nearly flat plates (*i.e.* $Z = b^2/(Rt) \leq 1$, where b is the width, R is the radius, and t is the thickness of the panel), whereas EN 1993-1-6 [12] is not applicable since its scope is limited to cylinder sheets, not covering the design of structures such as bridge decks with a cylindrically curved bottom flange.

Furthermore, in other engineering fields, in which thin curved steel panels have been used in the past few decades (*e.g.* aeronautics, offshore and the naval industry) only recently some new design recommendations for shells and curved panels were published, such as DNVGL-RP-C202 [13], DNVGL-CG-0128 [14] and ABS – Guide for Buckling and Ultimate Strength Assessment for Offshore Structures [15]. Nevertheless, these standards provide semi-empirical formulae obtained from estimations made using full cylinder models and not necessarily isolated curved panels, which may lead to unsafe results, as recently shown by Park *et al.* [16]. Moreover, in these design guidelines, the buckling of a cylindrically curved panel is regarded only as a possible failure mode of an orthogonally stiffened cylinder that keeps the boundary conditions of a panel within very specific bounds, thus preventing the use of these standards in other engineering applications, such as bridges.

The evident lack of design rules coerces designers to rely on their experience and on the use of advanced Finite Element Methods (FEM), which in many cases results in a time-consuming design process. Hence, the main motivation for this PhD dissertation is to contribute to the development of the first design methodology able to assess the safety level of bridge deck cross-

sections integrating a cylindrically curved steel panel in the bottom flange and thus to promote and encourage the design of these attractive and innovative design solutions.

Due to the appearance of new application of curved panels over the past years, especially in the bridge design, the study of curved panels seems to have gained a new momentum in the research community worldwide, as presented in an extensive literature review by Martins *et al.* [17], summarizing the previous studies dealing with this topic. However, none of these works provides a robust and physically consistent design method able to deal with different aspects of cylindrically curved panels. Principally, most of the studies tackled the problem of curved panels subjected only to uniform compression, whereas the other fundamental load arrangements, such as shear load, seem to be unreasonably ignored. In addition, despite a great number of numerical investigations, only a few experimental programs were reported, mainly focusing on full cylinders and aluminum-alloy sheets for monocoque constructions used in aeronautics and ship industry, which are different from those encountered in civil engineering (*i.e.* bridges).

Confronting and correcting, at last, these deficiencies should be an absolute priority. Within the context of overcoming the mentioned void in knowledge, the curved panels are studied in this PhD dissertation also as an individual structural element, subjected to loads that may be relevant in case of bridge design, such as axial compression, shear load and the combination of these two load cases. In addition, it is necessary to take a step forward and to propose accurate but also simple and universal design rules that should enable the use of curved panels not only in bridge design but also, in other engineering fields.

The work presented in the thesis is developed within the OUTBURST research project [18], a European RFCS project, as well as the national research project ULTIMATEPANEL [19], both completely oriented to cylindrically curved steel panels. Therefore, it was possible to perform much needed experimental campaigns and to generate new data in a comprehensive way, which may be considered as a major contribution of the thesis, distinguishing it from the previous studies available in the literature.

1.2 Objectives and research strategy

The PhD dissertation portrays the major contributions of the author, who actively participated in two research projects. The first, “Curved thin panels for structural application”, with the acronym ULTIMATEPANEL, focused mainly on the cylindrically curved steel panels as an individual element, whereas the latter with the acronym OUTBURST derived from “OpTimization of steel plated BRidges in shape and STrength”, dealt with the curved steel panels used for optimized applications in steel and composite bridges.

Inspired by the mutual goal of both projects, the paramount objective of the PhD research work presented herein is to develop a clear design approach both for individual curved panels subjected to the most fundamental loading cases (*i.e.* compression and shear), and for the whole box-girder bridge cross-section integrating a curved steel panel in the bottom flange.

To pursue the set goals, the research strategy is to perform a thorough experimental, numerical and analytical study, accompanied by a statistical assessment of generated data. The work is divided into five main tasks, completed according to the scheme illustrated in Fig. 1.4:

i) Task 1: Literature review

The main objectives of the first task are:

- Critical assessment of the up-to-date literature regarding the design of cylindrically curved panels;
- Characterization of the most relevant parameters (*i.e.* geometry, material, geometric imperfections, boundary and load cases, etc.) and their influence on the behavior of panels;
- To define limits of application of curved panels in bridges and other engineering fields.

The findings from Task 1 are crucial for all subsequent tasks since they serve as a benchmark to prepare experimental tests and subsequently the framework of the numerical investigation.

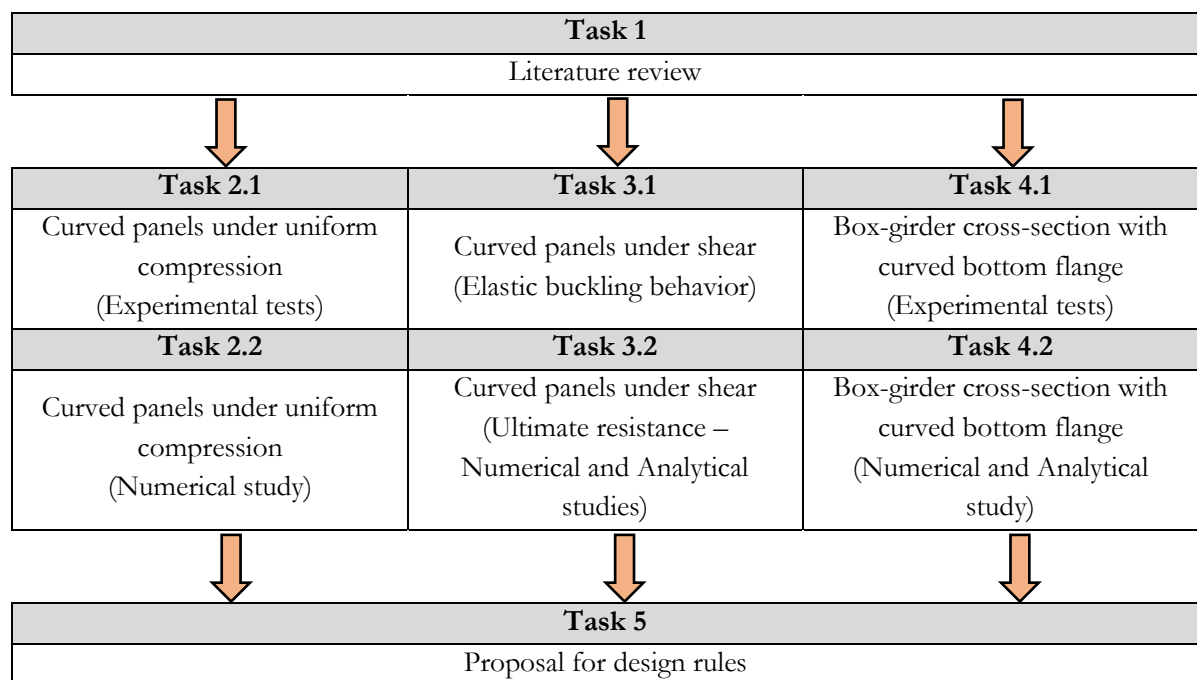


Fig. 1.4: Research strategy and division of the main tasks

ii) Task 2: Curved panels under uniform compression

The objective of this task is not to perform another exhaustive numerical study on the cylindrically curved panels under compression since that has already been done and reported multiple times in the literature. On the contrary, the objective is to generate an adequate database of the experimental results, thus overcoming the present deficiencies discovered in Task 1. The task is divided into two sub-tasks, Task 2.1 and Task 2.2, where the first is completely dedicated to the experimental program, whereas in Task 2.2, some further numerical investigations are performed using the model validated against the experimental results.

Hence, in Task 2.1, as a part of the ULTIMATEPANEL research project, an experimental campaign is carried out, in which 32 simply-supported square panels (stiffened and unstiffened) are tested under in-plane compression. All the experimental tests are performed at the Civil

Engineering Department of the University of Coimbra. In specific, using the recorded test data it is aimed:

- To get insight into the complex buckling behavior of curved steel panels under compression, within the applicable geometrical ranges defined in Task 1;
- To assess the influence of radius (R) and the number of stiffeners (n_{st}) on the ultimate resistance and failure mode;
- To generate the initial imperfections (shapes and amplitudes) measured by Digital Image Correlation (DIC), specifying their dependence on the radius of curvature and/or number of stiffeners;
- To critically assess the numerically derived empirical expressions for computation of the ultimate resistance of unstiffened and stiffened curved panels available in the literature;

The objective of Task 2.2 is to build a reliable finite element (FE) model, validated against the experimental results, acquired in Task 2.1. The goal is to use this model to perform an imperfection sensitivity analysis, in which the effect of the imperfection amplitude and shape is studied in an attempt to identify a critical imperfection shape (*i.e.* that in most cases returns the lowest ultimate resistance of curved panels), suitable when no information on ‘real’ imperfections is available.

iii) Task 3: *Curved panels under shear*

The third task investigates the behavior of unstiffened simply supported cylindrically curved steel panels subjected to a pure shear load. Moreover, the goal is to develop for the first time a simple and reliable methodology for the prediction of the ultimate shear resistance of curved panels. In particular, the goal is to expand the existing rules for flat plates to a wide range of the curvature parameter and aspect ratios, with various boundary conditions, therefore addressing most practical cases of bridge, offshore and aeronautical applications.

Since the proposed methodology is conceptually similar to the existing one for flat plates, it is required first to calculate the shear buckling coefficient k_τ for a curved panel. Therefore, the task is divided into two subtasks:

- Task 3.1 – Studies the elastic buckling behavior of curved panels and ultimately gives a simple expression to calculate k_τ
- Task 3.2 – Investigates the post-buckling behavior and proposes a method to calculate ultimate shear resistance

iv) Task 4: *Box-girder bridge cross-section integrating curved bottom flange*

Within this task, the behavior of the entire box-girder bridge cross-section integrating the bottom curved panels is investigated. The task is completed according to the following research strategy:

- Task 4.1 – An experimental research program is planned and performed at the Civil Engineering Department of the University of Coimbra, in which two bridge deck

prototypes are tested as three-point bending tests simulating the bridge behavior near the internal support. Such an experimental program was not reported in the literature, least of all with the scale that is tested within the OUTBURST research project. The experimental tests aim to get insight into the behavior of box-girder bridge deck with curved panel in the bottom flange loaded in compression; where near the internal support besides bending moment significant shear force develops. Test results serve as the benchmark for the forthcoming numerical study in Task 4.2.

- **Task 4.2** – The objective of this sub-task is first to develop a reliable finite element model able to predict experimental tests on prototype bridge segments (Task 4.1). Subsequently, using the validated model, a numerical investigation is performed, in which the influence of various geometrical parameters on the complex M - V interaction behavior of a box girder bridge deck near the intermediate support is assessed.

v) **Task 5: Proposal of design rules**

Its main ambition is to present proposals and corresponding commentary for design rules developed for stiffened and unstiffened curved steel panels integrated into steel bridge cross-sections. In specific, based on the results generated in Task 2 and Task 3, and following a narrow relation to EN 1993-1-5, new bending and shear resisting models are proposed, adapted for box-girder cross-section with curved bottom flange. Finally, slightly modified M - V interaction equation for cross-section safety verification is proposed and statistically assessed against the numerical results. In addition, numerical examples are prepared on the level of individual curved panels, but also on the level of the whole cross-section, illustrating the proper use of design rules developed within the thesis.

1.3 Organization of the thesis

The thesis is divided into 9 chapters, organized as follows:

Chapter 1, Introduction - a general introduction is made, highlighting the relevance of the topic and specifying the main objectives of the thesis, as well as the research strategy used for their accomplishment.

Chapter 2, State of the art - the geometry of cylindrically curved panels is first introduced, focusing on the dimension ranges commonly encountered in real bridge deck applications. Subsequently, a brief recapitulation of the background studies on the cylindrically curved panels subjected to uniform compression and/or shear is presented, emphasizing the historical references closely related to the work presented in this thesis. Finally, this chapter gives an overview of design methodologies available in the literature for the assessment of the resistance of curved panels subjected to compression and shear, highlighting their limitations.

Chapter 3, Cylindrically curved panels under pure compression - an experimental study on cylindrically curved steel panels under uniform axial compression is reported and the most relevant test results are discussed. In addition, the available procedures for determination of the ultimate compressive resistance, described in Chapter 2 are critically assessed against the test results. Finally, using the

numerical model validated against the test results, the sensitivity to initial geometric imperfections of curved panels is studied.

Chapter 4, *Elastic buckling behavior of curved panels under shear* - the influence of several parameters on the elastic buckling behavior of simply supported cylindrically curved panels subjected to pure shear is numerically investigated. Based on the results of an extensive numerical study shown in this chapter, a new formula is proposed for the estimation of the critical shear stress.

Chapter 5, *Ultimate shear load of curved panels* – the influence of various geometrical parameters, imperfections, and boundary conditions on the post-buckling behavior of unstiffened simply supported curved steel panels under shear load is numerically investigated, hence presenting a logical continuation of Chapter 4. Moreover, a new set of formulas for the prediction of the ultimate shear strength is developed and statistically validated. Finally, the use of the proposed methodology is illustrated in two worked examples.

Chapter 6, *Experimental behavior of curved bottom flanges in steel box-girder bridge decks* – another experimental campaign is reported, however, in this chapter, the study comprises two prototype box-girder bridge segments, in scale 1:3 with respect to a real study case. The segments are tested as three-point bending tests, with the aim to assess the moment-shear ($M - V$) interaction near the intermediate support. A detailed description of the most relevant data is provided, and the main observations (load measurements, displacements, strains, stresses, failure modes) are discussed.

Chapter 7, *Numerical simulations on box-girder bridge cross-section integrating curved panels* – the $M - V$ interaction behavior of a box girder bridge deck, with a curved bottom flange is analyzed, using a FEM model built and verified against the experimental results reported in Chapter 6. A comprehensive numerical study covers multiple geometrical parameters, varied within the common ranges found in bridge applications in Chapter 2. For each geometry, an $M-V$ interaction diagram is generated, being the main output used in the following Chapter 8 for the statistical evaluation of the existing $M-V$ interaction criterion.

Chapter 8, *Design proposals for bridge cross-sections integrating curved steel panels* – the design rules for the prediction of the bending and the shear resistance are first developed and validated against the results from the previous chapter. Subsequently, both resistance models are implemented in the $M-V$ interaction equation, proposed by Jäger *et al.* [139], whose validity and safety is checked against FEM-generated $M-V$ interaction diagrams. Finally, all three design rules, for bending, shear, and $M-V$ interaction resistance verification, are statistically assessed against the numerical results by calculating the partial factor (γ_M).

Chapter 9, *Summary and future prospects* – finally, the main findings and contributions of this work are summarized and some suggestions for future research are indicated.

2. State of the art

2.1 Overview

The interest for the cylindrically curved steel panels has particularly grown in recent years with the appearance of innovative applications in bridge design, which explains the fact that the number of studies dealing with the curved panels enthusiastically increased. However, given that the use of curved panels started first in the area of the aeronautical and aerospace industry as early as in the 1930s and 1940s, and somewhat later in the naval industry, the evolution of the fundamental theoretical knowledge on the buckling behavior of thin cylindrically curved panels has a very long history. Hence, the goal of this chapter is to make a brief recapitulation of the studies on the cylindrically curved panels carried out by the scientific community thus far, giving more emphasis to the historical references narrowly related to the work presented in this thesis.

In [section 2.2](#), an introduction is made, in which the most relevant geometrical parameters commonly used in the literature for the characterization of cylindrically curved panels are defined. Furthermore, in [section 2.3](#), the dimension ranges of curved panels that are potentially used in bridge deck applications are identified and compared with the ranges usually encountered in some other engineering fields.

Since the main focus of this dissertation is the use of curved panels in bridge deck cross-sections, predominantly loaded in compression and shear, the literature revision in [section 2.4](#), where the most representative historical references are addressed, is divided into two groups, based on the load arrangement – curved panels under uniform compression and curved panels

under shear. It is important to stress out the fact that in the case of panels subjected to compression, more attention is given to the experimental references, being useful for the experimental work presented in the thesis. In addition, some numerical and a few analytical references deserve to be mentioned, especially the ones in which a methodology for the calculation of the buckling and/or ultimate load is proposed. On the other hand, owing to the scarcity of experimental studies on curved panels subjected to shear, the focus is given to the most relevant numerical investigations known to the research community.

Finally, in [section 2.5](#), design methodologies available in the literature for the assessment of the resistance of curved panels subjected to compression and shear are presented. Moreover, an outlook on the design standards applicable to the design of curved panels are addressed and their applicability and limitations are discussed. Ultimately, as there are currently no rules to assess the safety level of bridge cross-sections integrating cylindrically curved panels in the lower flange, the design rules from EN 1993-1-5 [11] for the conventional trapezoidal box-girders with a flat bottom flange are presented, being essential to the methodology developed in the thesis.

2.2 Geometry of a curved panel

In order to discuss the structural behavior of a cylindrically curved panel, it is necessary first to identify the most relevant geometrical parameters that are used throughout the entire research work. Hence, the main geometrical parameters are presented in [Fig. 2.1](#), both for unstiffened and stiffened panels.

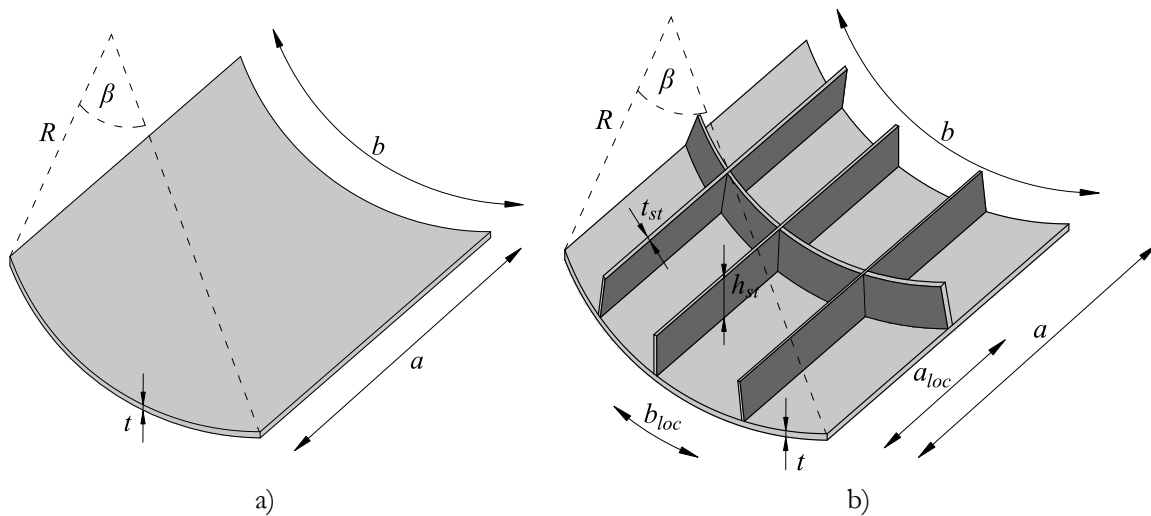


Fig. 2.1: Geometry and notation of cylindrically curved panels: a) unstiffened; b) stiffened

Based on the figure, t and R are the thickness and the radius of the panel, a and b are the length and width of the panel, β is the sectorial angle defined as the ratio between the width and the radius of the panel. In addition, in the case of a stiffened panel, a_{loc} is the length of the subpanel that corresponds to the distance between transverse stiffeners, b_{loc} is the width of the subpanel that corresponds to the distance between longitudinal stiffeners, whereas t_{st} and h_{st} are the thickness and the height of the longitudinal stiffeners, respectively. The thesis is mainly focused on the flat stiffeners, however, the trapezoidal stiffeners are also addressed, in an attempt to compare these two stiffener typologies commonly encountered in box-girder bridge decks.

To define the geometry of a curved panel, it is common to use two non-dimensional parameters, the aspect ratio, and the curvature parameter. The aspect ratio α is defined as the ratio between the length and width of the panel, according to Eq.(2.1):

$$\alpha = \frac{a}{b} \quad (2.1)$$

Additionally, using the notation of Fig. 2.1, the non-dimensional curvature parameter Z of a curved panel is defined by Eq.(2.2):

$$Z = \frac{b^2}{Rt} \quad (2.2)$$

Curvature parameter, which was introduced by Batdorf [20], had initially a slightly different form that includes the Poisson's coefficient ν , given by Eq.(2.3), which still may be found in the literature.

$$Z_b = \frac{b^2}{Rt} \sqrt{1-\nu^2} \quad (2.3)$$

However, numerous authors proved that the parameter given by Eq.(2.2) is a suitable parameter to define the mechanical behavior of cylindrically curved panels under axial compression, whereas the suitability of this parameter in the case of the shear load is discussed in this thesis in chapter 4.

In the case of steel bridge decks, it is common to have stiffened curved panels in the bottom flange (see Fig. 2.1b). Hence, besides the global aspect ratio (α) and the curvature parameter (Z), given by Eq.(2.1) and Eq.(2.2), it is necessary to define the local aspect ratio (α_{loc}) and curvature parameter (Z_{loc}), given by Eq.(2.4) and Eq.(2.5), respectively, using the width and length of the corresponding sub-panel, whereas n_{st} is the number of the longitudinal stiffener.

$$\alpha_{loc} = \frac{a_{loc}}{b_{loc}} = \alpha(n_{st} + 1) \quad (2.4)$$

$$Z_{loc} = \frac{b_{loc}^2}{Rt} = \frac{Z}{(n_{st} + 1)^2} \quad (2.5)$$

2.3 Curved panels in bridge deck cross-sections

In this section, an overview of the existing bridges integrating curved bottom flanges is presented. The majority of the cases (*i.e.* 18 to be precise) were referred in a survey carried out in 2017 by Reis *et al.* [5], while four more cases built in the meantime were subsequently added. Based on the gathered data, it is aimed to identify the possible cross-section forms and usual structural systems, but also to define, whenever possible, the ranges of geometrical parameters (presented in section 2.2) relevant for curved panels used in steel bridges.

The aforementioned 22 bridges are listed in Table 2.1. Regarding the bridge type, it may be noticed that most were built as cable-stayed bridges, but also as arch, bowstring arch, single girder, or suspension bridges, as shown in Fig. 2.2 and Fig. 2.3.

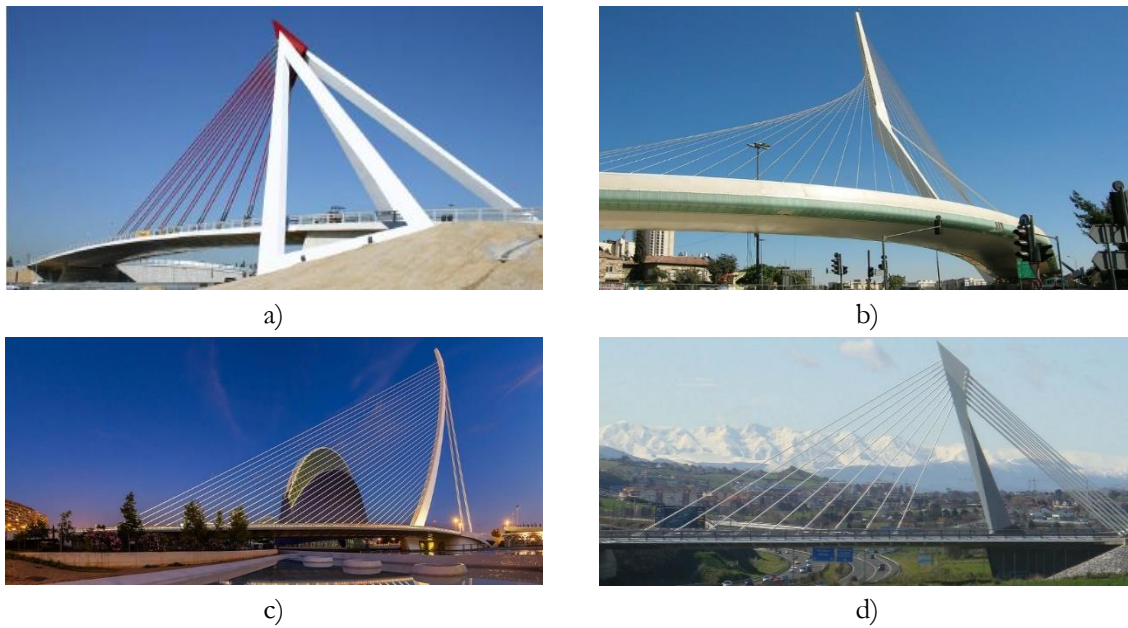


Fig. 2.2: Cable-stayed bridges: a) “Puerta de las Rosas” Bridge; b) Bridge of Strings; c) “Serreria” Bridge; and d) PCICAN Access Bridge (see reference in [Table 2.1](#))

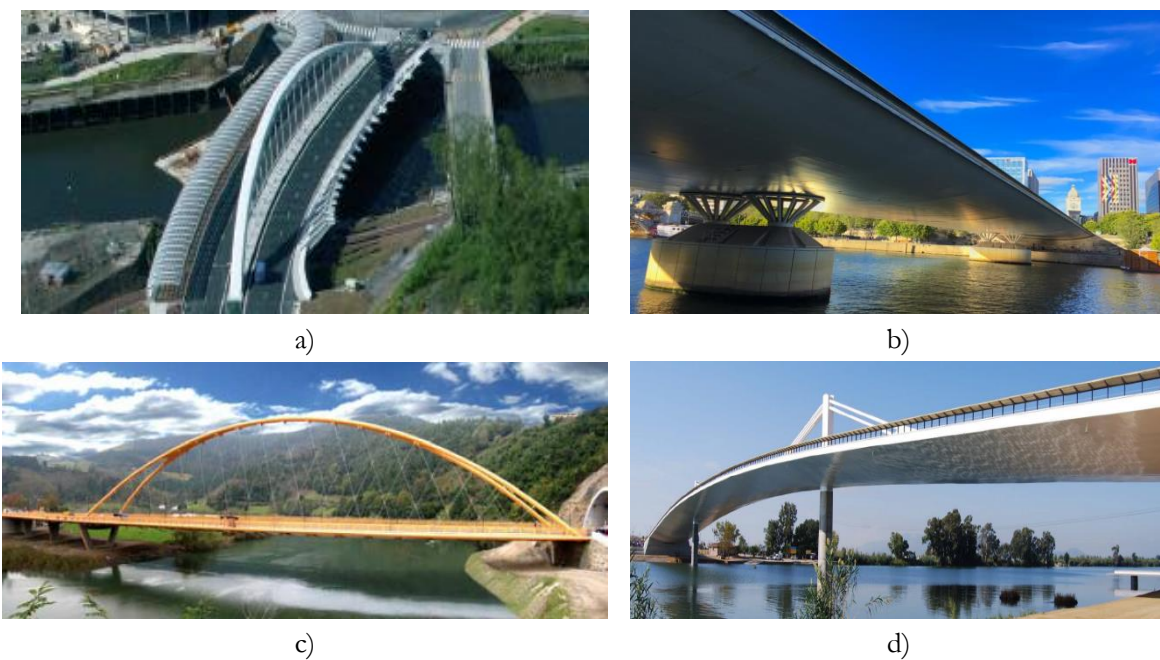


Fig. 2.3: Various bridge types: a) Arch bridge - “Galindo” River Bridge; b) Single girder - Charles de Gaulle Bridge; c) Bow-String arch - River Deba Bridge; and d) Suspension bridge - “Lo Passador” Bridge (see reference in [Table 2.1](#))

This deck has been widely used in urban environments mainly as roadway, railway, and pedestrian bridges, demonstrating the diversity of such deck solutions.

Table 2.1: Bridge decks integrating cylindrically curved steel panels

Name	Country	Bridge Type	Service year	Ref.
<i>Charles de Gaulle Bridge</i>	France	Single Girder	1996	[21]
<i>Chaves' Pedestrian Bridge</i>	Portugal	Cable-Stayed	1997	[22]
<i>'Escaleritas' Viaduct</i>	Spain	Cable-Stayed	2006	[23]
<i>'Puerta de las Rosas' Bridge</i>	Spain	Cable-Stayed	2007	[24]
<i>Twins Bridge</i>	Italy	Cable-Stayed	2007	[25]
<i>PCTCAN Access Bridge</i>	Spain	Cable-Stayed	2007	[26]
<i>River Deba Bridge</i>	Spain	Bow-String	2007	[27]
<i>"Galindo" River Bridge</i>	Spain	Arch	2007	[28]
<i>Ebro River Pedestrian Bridge</i>	Spain	Cable-Stayed	2008	[29]
<i>'Serreteria' Bridge</i>	Spain	Cable-Stayed	2008	[30]
<i>Bridge of Strings</i>	Israel	Cable-Stayed	2008	[31]
<i>Footbridge 'De Lichtenlijn'</i>	Belgium	Single Girder	2008	[32]
<i>Stonecutters Bridge</i>	China	Cable-Stayed	2009	[33]
<i>Renault Bridge</i>	France	Single Girder	2009	[7]
<i>Confluences Bridge</i>	France	Arch	2010	[34]
<i>"Lo Passador" Bridge</i>	Spain	Suspension	2011	[6]
<i>Ter River Bridge</i>	Spain	King-post Truss	2015	[35]
<i>Norgessporten</i>	Norway	Cable-Stayed	2017	[36]
<i>New Wear Crossing</i>	England	Cable-Stayed	2018	[37]
<i>Mainland – Čiovo Island Bridge</i>	Croatia	Single Girder	2018	[38]
<i>"Boekelose" Bridge</i>	Holland	Single Girder	2019	[39]
<i>New Genoa Bridge</i>	Italy	Single Girder	2020	[40]

As for the cross-section forms, multiple solutions may be encountered: *i*) with the curved bottom flange welded to vertical (Fig. 2.4a) or slightly inclined webs (Fig. 2.4b); *ii*) with the straight and inclined webs following the flange curvature (Fig. 2.4c); and *iii*) with the curved panel acting both as web and flange (Fig. 2.4d).

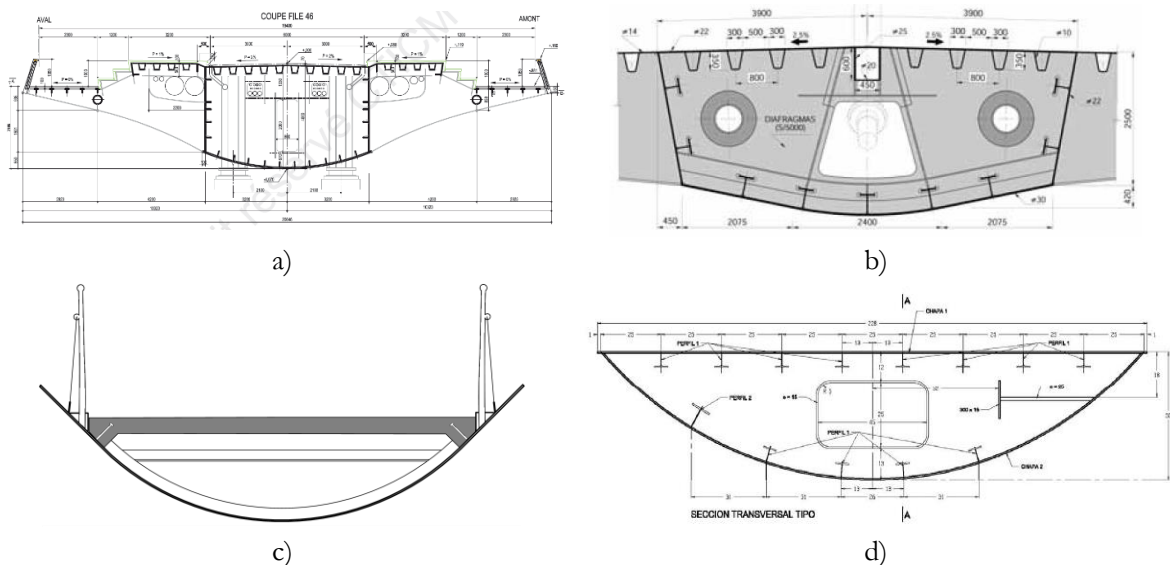


Fig. 2.4: Bridge cross-section forms: a) Renault Bridge; b) "Serreteria" Bridge; c) Footbridge 'De Lichtenlijn'; d) Ter River Bridge (see reference in Table 2.1)

Based on the cross-section shape, another division can be made, indispensable for the design rules proposed in the thesis. Namely, the division is made based on the ratio between the depth f of the curved part of the cross-section and the total height of the cross-section H , as illustrated in Fig. 2.5. In other words, in the first case, the distinction between the bottom flange and the webs can be clearly made, whereas in the second case the curved panel act simultaneously as both web and flange.

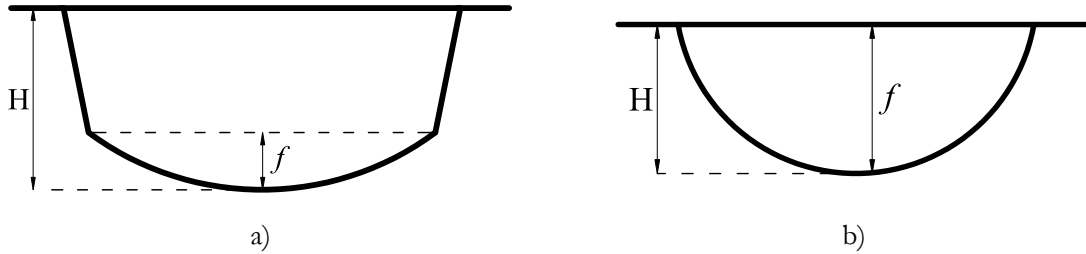


Fig. 2.5: Cross-section forms: a) $f < H$; and b) $f = H$

The ranges of the most relevant geometrical parameters in the surveyed 22 bridges are summarized in Table 2.2.

Table 2.2: Ranges of geometrical parameters of curved panels used in bridges

Bridge	Z	Z_{loc}	α	α_{loc}	b/t
<i>Charles de Gaulle Bridge</i>	30 - 60	0.6 - 1.2	1.0	7.14	23 - 47
<i>Chaves' Pedestrian Bridge</i>	-	-	-	-	-
<i>Escaleritas' Viaduct</i>	21 - 50	0.4 - 1.0	0.73	5.0	23 - 50
<i>Twins Bridge</i>	82 - 121	9.1 - 13.4	0.95	2.85	56 - 82
<i>PCTCAN Access Bridge</i>	28 - 56	1.8 - 3.5	0.67	2.67	37.5 - 75
<i>River Deba Bridge</i>	67 - 134	2.7 - 5.4	1.0	5.0	33 - 66
<i>Puerta de las Rosas' Bridge</i>	24 - 48	1.5 - 3.0	0.67	2.88	35 - 70
<i>'Galindo' River Bridge</i>	128 - 257	3.1 - 6.3	0.83	5.3	28 - 56
<i>'Serreria' Bridge</i>	95 - 159	3.2 - 5.3	0.76	4.17	24 - 40
<i>Bridge of Strings</i>	-	-	-	-	-
<i>Ebro River Pedestrian Bridge</i>	286 - 571	5.8 - 11.7	0.58	4.03	24 - 48
<i>Footbridge 'De Lichtlijn'</i>	134 - 336	-	0.5	0.5	95 - 237
<i>Stonecutters Bridge</i>	46 - 85	0.2 - 0.5	0.65	10.0	12.5 - 32
<i>Renault Bridge</i>	20 - 88	0.8 - 3.2	0.69	7.5	10 - 42
<i>Confluences Bridge</i>	16 - 26	0.4 - 0.6	1.0	6.67	37.5 - 62.5
<i>"Lo Passador" Bridge</i>	34 - 69	0.3 - 0.7	0.49	5.0	20 - 40
<i>Ter River Bridge</i>	70 - 140	0.8 - 1.0	0.54	5.0	27 - 32
<i>Norgessporten</i>	389 - 580	2.5 - 5.0	0.4	5.0	20 - 30
<i>New Wear Crossing</i>	70 - 123	6.3 - 11.1	1.35	4.5	34 - 60
<i>Mainland - Ciovo Island Bridge</i>	88 - 220	2.1 - 5.2	1.03	6.66	20 - 50
<i>'Boekelose' Bridge</i>	-	-	-	-	-
<i>New Genoa Bridge</i>	-	-	-	-	-

It may be observed that the global curvature parameter reaches a value of almost $Z = 600$, while the global aspect ratio is commonly between $\alpha = 0.5$ and $\alpha = 1.0$. Furthermore, owing to the variation of the curved panel thickness along the bridge length, the local curvature parameter

varies between $Z_{loc} = 0$ and $Z_{loc} = 15$. Finally, the local aspect ratio varies in a wide range between $\alpha_{loc} = 0.5$ and $\alpha_{loc} = 10$.

In order to compare the local curvature parameter Z_{loc} found in bridges with the other engineering fields where the curved panels are used, a similar investigation on the real examples in the aerospace and naval industry is carried out. The results are summarized in Fig. 2.6, where the Z_{loc} is plotted against the slenderness b/t ratio.

It may be concluded from the graph that the local curvature parameter rarely exceeds the value of $Z_{loc} \leq 40$, except for panels used in ship hulls, where it may go up to $Z_{loc} = 60 - 70$ due to smaller radii of curvature R . In the case of bridge decks, relatively thick panels and high radii lead to lower values of local curvature parameter.

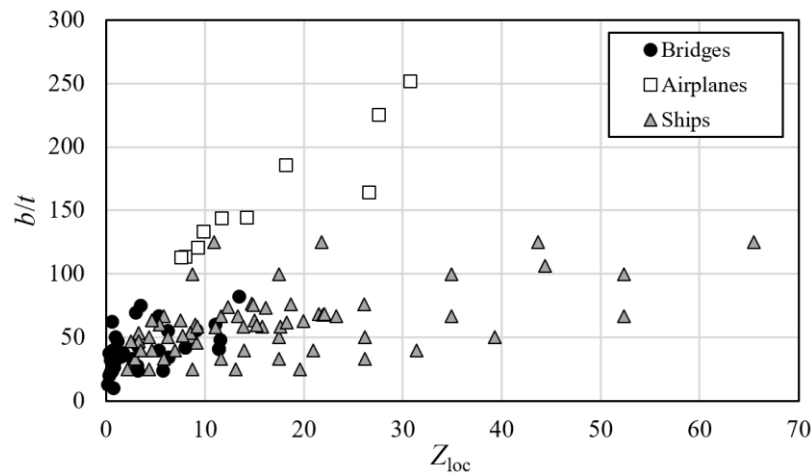


Fig. 2.6: Ranges of Z_{loc} of a practical interest in: bridges (see Table 2.2), aeroplanes [41] and ship hulls ([14],[16],[42]-[45])

2.4 Literature review

2.4.1 Curved panels under compression

2.4.1.1 General

An overview of the existing studies is presented, in which the current knowledge on the behavior of curved panels subjected to uniform compression is discussed. In 2018, Martins *et al.* [17] rigorously reviewed the studies on the stability and design of isolated cylindrically curved panels under generalized in-plane loading available in the literature. Hence, the objective is not to replicate the documented work, but to emphasize the useful findings that are strictly related to the topic presented in the thesis. Consequently, the section is divided into three sub-sections: *i*) elastic buckling behavior of curved panels, in which several available expressions for the critical load are presented; *ii*) ultimate resistance of curved panels, where the most relevant numerical and analytical studies dealing with the ultimate load of curved panels are summarized; and *iii*) experimental behavior of curved panels that provides an outlook on the experimental results, essential for the experimental work performed in this thesis.

2.4.1.2 Elastic buckling behavior of curved panels

The main reason for the substantial use of thin curved steel panels that initiated in the 1930s laid in numerous benefits these structural elements proffered, such as efficiency of load-carrying performance, high strength to weight ratio, high value from an aesthetic point of view, etc. However, due to much lower out-of-plane than in-plane stiffness, curved panels, similar to flat plates, showed remarkable susceptibility to local and global instabilities, which seems to have gained great attention among the researchers. Although the evolution of theoretical knowledge on the buckling behavior of curved panels under pure compression started parallel with the flat plates, with Redshaw [46] in 1934, Timoshenko [47] in 1936, and Marguerre [48] in 1937, owing to the complexity of the problem, the progress was never as fast as it was in the case of flat plates. Namely, only after the elastic critical behavior of flat plates had been completely understood, the expression for the calculation of the elastic critical stress of curved panels (σ_{cr}) was proposed, and it was agreed to have the same base form as the one for the flat plates, given by Eq.(2.6) as follows:

$$\sigma_{cr} = k_{\sigma} \sigma_E = k_{\sigma} \frac{\pi^2 E}{12(1-\nu^2)} \left(\frac{t}{b} \right)^2 \quad (2.6)$$

where b and t are respectively the width and the thickness of the panel, ν is the Poisson's ratio, E is the modulus of elasticity of the material, and k_{σ} is the elastic buckling coefficient. In the case of curved panels, Eq.(2.6) is slightly altered by adjusting the elastic buckling coefficient to account for the effect of the curvature Z . To prevent any further confusion, in this document, the elastic buckling coefficient of curved panels subjected to compression is labelled as $k_{\sigma,Z}$, whereas in the case of flat plates, the symbol $k_{\sigma,pl}$ is assigned.

For a long time, it was believed that cylindrically curved panels are an intermediate case, between two extreme cases - flat plates on one side, and full cylinders on the other. Namely, according to Gerard & Becker [49], who in 1957 made an review of the up-to-date studies on this topic, the behavior of a curved panel subjected to uniaxial compression corresponds to the one of a flat plate for small curvature parameters (*i.e.* $Z \rightarrow 0$), and to cylinders for very large curvatures (*i.e.* $Z \rightarrow \infty$). Inspired by this theory, several authors, using analytical and semi-analytical methods, proposed expressions to determine the elastic buckling coefficient ($k_{\sigma,Z}$) for unstiffened simply supported cylindrically curved panels. Firstly, Redshaw [46] proposed a method using the Rayleigh-Ritz method, which is given by Eq.(2.7) as follows:

$$k_{\sigma,Z} = 2 + \sqrt{4 + \frac{48(1-\nu^2)}{\pi^4} Z^2} \quad (2.7)$$

Soon afterward, Timoshenko [47] proposed another expression, given by Eq.(2.8) that was derived using the approximated expressions for the out-of-plane displacement of the panel. Later, in 1963, Volmir [50] derived the expression for the elastic buckling coefficient of a simply supported curved square panel with all edges constrained using the Galerkin method, which completely coincides with the first branch of Eq.(2.8).

$$k_{\sigma,Z} = \begin{cases} 4 + \frac{3(1-\nu^2)}{\pi^4} Z^2 & \text{if } Z \leq \frac{4\pi^2}{\sqrt{12(1-\nu^2)}} \\ \frac{4\sqrt{3(1-\nu^2)}}{\pi^2} Z & \text{if } Z > \frac{4\pi^2}{\sqrt{12(1-\nu^2)}} \end{cases} \quad (2.8)$$

However, the most known expression and generally most commonly used nowadays is the one from Stowell [51], given by Eq.(2.9), which may be understood as a modified Redshaw's formula, yet extended to account for the higher values of curvatures.

$$k_{\sigma,Z} = \frac{k_{\sigma,pl}}{2} \left(1 + \sqrt{1 + \frac{48(1-\nu^2)}{\pi^4 k_{\sigma,pl}^2} Z^2} \right) \quad (2.9)$$

In addition, it is worth mentioning the solution derived by Batdorf [20] in the form of Fourier series for both simply supported and clamped perfect cylindrically curved panels. Namely, the author used an equivalent Donnell's equation to fit theoretical curves to experimental data previously obtained, approximating the displacements by trigonometric functions. Besides the studies on unstiffened curved panels, Batdorf was among the first authors who studied stiffened panels. Namely, Batdorf & Schildrout [52] obtained the theoretical critical stress of a simply supported curved rectangular panel with one middle transverse stiffener, whereas Schildrout & Stein [53], later on, conducted the first studies on curved panels with one longitudinal stiffener.

Analysing the proposed formulas, it may be noticed that for $Z = 0$, the buckling coefficient converges to the minimum elastic buckling coefficient for simply supported flat plates (*i.e.* $k_{\sigma,Z} = k_{\sigma,pl,min} = 4.0$), whereas for high curvatures Z , the formulae from Redshaw and Timoshenko tend to the elastic critical stress of cylinders of revolution. However, many years later, with the appearance of numerical tools, a large number of studies have been carried out, assessing the validity of the proposed solutions. In 2001, using finite element analyses, Domb & Leigh [54] proved that buckling behavior of curved panels is unique and different from both flat plates and cylinders. In addition, the authors proposed an improved solution for the buckling coefficient of unstiffened panels, given by Eq.(2.10), as follows:

$$k_{\sigma,Z} = \begin{cases} 10^{\sum_{i=0}^3 c_i [\log(Z(1-\nu^2))]^i} & \text{if } 1 \leq Z(1-\nu^2) \leq 23.15 \\ c [Z(1-\nu^2)]^d & \text{if } 23.15 \leq Z(1-\nu^2) \leq 200 \end{cases} \quad (2.10)$$

where the required coefficients are: $c_0 = 0.6021$, $c_1 = 0.005377$, $c_2 = 0.192495$, $c_3 = -0.002670$, $c = 0.4323$, and $d = 0.9748$.

The proposed expression returns result quite similar to the Stowell's solution (see Eq.(2.9)), confirming that the critical stress of curved panels loaded in compression actually tends to reach half of the elastic critical stress of cylinders of revolution. In 2012, Tran [8] reached the same conclusion.

Nevertheless, in 2013, Martins *et al.* [55] demonstrated that even the expressions from Stowell and Domb & Leigh might lead to significant errors. The authors derived numerically a new set of formulas for the buckling coefficient of unstiffened curved panels subjected to various in-plane loading (*i.e.* from pure compression to pure in-plane bending). The expression for pure compression, relevant for this thesis, is based on the formula from EN 1993-1-5 for the flat plates, written in a general format by Eq.(2.11) as:

$$k_{\sigma,Z} = \frac{a_1 + a_2 Z + a_3 Z^2}{b_1 + b_2 Z + b_3 Z^2 + 1} \quad (2.11)$$

where for $0 < Z \leq 23$, the required coefficient are: $a_1 = 8.2$, $a_2 = 0.074$, $a_3 = 0.0163$, $b_1 = 1.05$, $b_2 = -0.0002$, and $b_3 = 0.0003$, whereas for $23 < Z \leq 100$, the coefficients are: $a_1 = 3.214$, $a_2 = 0.5976$, $a_3 = 0.0028$, $b_1 = 0.961$, $b_2 = 0.0104$, and $b_3 = 0$.

However, the proposed expression, although independent from the aspect ratio α , was proven to be suitable only for the short panels with the aspect ratio $0.2 < \alpha \leq 1.0$. Moreover, the formula is obtained solely through the calibration of numerical results, without real mechanical meaning. To overcome these deficiencies, Martins *et al.* [56] carried out another study in 2016, in which energy-based analytical formulations were used to derive a closed-form solution for buckling coefficient of unstiffened curved panels under uniaxial compression, given by Eq.(2.12) as:

$$k_{\sigma,Z} = 2 \left[1 + \frac{\sqrt{\pi^6 + \alpha_{BC}(\pi^2 - 8)Z^2}}{\pi^3} \right] \quad (2.12)$$

Besides the physical meaning, the new formula was expanded to a wide spectrum of aspect ratio ($0.2 < \alpha \leq 4.0$). Regarding the coefficient α_{BC} , it may have two values depending on the boundary conditions. Namely, although the majority of the referred studies have dealt with the simply supported curved panels, it is important to stress that the definition of the simply supported boundary conditions is not entirely the same for all the authors. For instance, Stowell in his work considered that all the edges of a panel are constrained (*i.e.* forced to remain straight). On the other hand, the first expression by Martins *et al.*, Eq.(2.11), was derived assuming that only the curved edges were constrained, whereas the unloaded edges were unconstrained (*i.e.* free-to-wave). Finally, expression (2.12) by Martins *et al.* allows for both types of simply supported boundary conditions: *i)* the same as Stowell's, with $\alpha_{BC} = 12$, and *ii)* the same as the first expression from Martins, with $\alpha_{BC} = 9.6$.

In Fig. 2.7, a comparison between the presented expressions is made, where the elastic buckling coefficient $k_{\sigma,Z}$ for unstiffened simply supported curved panels under uniform compression is plotted against the curvature parameter Z . The comparison is made for the curvature parameter up to $Z < 100$, being the upper limit in both proposed expressions by Martins. Moreover, in order to make the comparison valid in terms of the boundary conditions, in Eq.(2.12), the value $\alpha_{BC} = 9.6$ is adopted.

As expected, the expressions by Redshaw and Timoshenko indeed lead to a significant overestimation (*i.e.* around 50%) of the buckling strength for higher values of the curvature

parameter. However, even the formulas from Stowell and Domb & Leigh seem to give optimistic results (*i.e.* around 15%) when compared with the expressions from Martins.

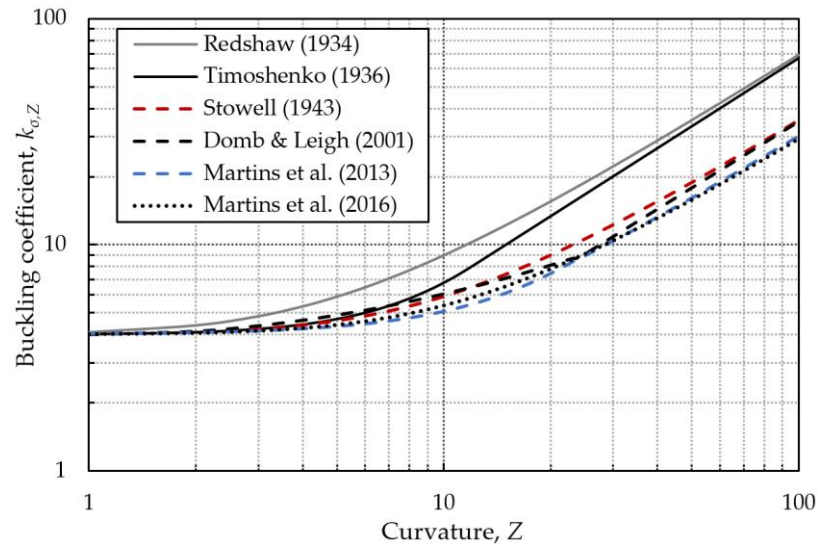


Fig. 2.7: Comparison of the existing formulas for buckling coefficient $k_{\sigma,Z}$ - unstiffened curved panels

Regarding the elastic buckling behavior of stiffened simply supported curved panels, the number of published works is considerably lower than for the unstiffened panels. Namely, besides the aforementioned studies from Batdorf & Schildrout [52] and Schildrout & Stein [53], in which the curved panels with a single stiffener in the middle of the panel were studied, only recently a few numerical parametric studies were carried out, among which those from Park *et al.* [57] in 2008, and from Khedmati & Edalat [58] in 2010, are highlighted. Using the FE analyses, the authors investigated the influence of several parameters on the buckling behavior of curved stiffened panels; however, no practical method was proposed to determine the critical buckling stress.

More recently, in 2014, Tran *et al.* [59] performed a comprehensive numerical study, in which, among many aspects, the linear buckling of stiffened curved panels under uniform longitudinal compression was also addressed. The authors concluded that the increased curvature might have a significant influence on the global shape of the buckling mode, increasing the number of half-waves in the circumferential direction. In addition, it was shown that the main benefit of the stiffeners is to prevent the global buckling of the panel, whereas the shape of the stiffeners has only a minor effect. The authors proposed design rules for assessing the ultimate resistance of curved panels, which is based on the methodology for stiffened flat plates provided in EN 1993-1-5, hence, requires first the calculation of the elastic buckling stress for stiffened curved panel. According to the proposed methodology, the curved stiffened panel should be considered as a corresponding flat one, where the critical stress, $\sigma_{cr,s}$, is evaluated using a standard column-type buckling procedure from EN 1993-1-5, whereas the plate-type buckling is neglected. Based on this methodology, another similar procedure for the determination of the ultimate resistance of stiffened panels was recently proposed within the OUTBURST research project [60]. However, in this procedure, besides the elastic critical column buckling stress ($\sigma_{cr,s}$), the critical shell buckling stress is also accounted for ($\sigma_{cr,i}$). Both procedures (from Tran *et al.* and from the OUTBURST

research project) for the ultimate resistance of curved panels are addressed in the subsequent [section 2.5](#), where additionally, the expressions for the critical column and the critical shell stresses are provided.

Although not necessarily related to the work presented in the thesis, it is important to highlight that several authors recently studied curved panels with boundary conditions other than simply supported in all four edges. For instance, Magnucki & Mackiewicz [61], using the Galerkin method to solve Donnell's equation, proposed in 2006 an analytical model to predict the elastic buckling stress for curved panel with three simply supported and one free edge. One year later, in 2007, Wilde *et al.* [62] addressed the same problem proposing a similar analytical solution, which gave a good agreement with the solution from the former author, but also with the numerical results. In 2011, Eipakchi & Shariati [63] studied the elastic buckling behavior of cylindrically curved panels subjected to axial stress with the two opposite sides simply supported and the other two edges free. The authors also proposed an analytical solution to find the critical stress, based on the perturbation methods. Finally, it is worth mentioning another recent study, carried out in 2018 by Andico *et al.* [64], in which the authors investigated the buckling behavior of partially restrained curved panels, stiffened longitudinally by trapezoidal stiffeners, under compression, as presented in [Fig. 2.8](#).

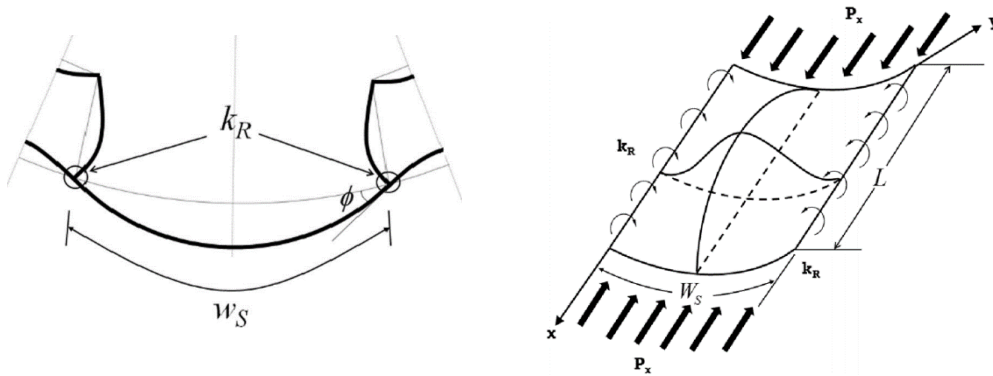


Fig. 2.8: Rotationally restrained curved panel model by Andico *et al.* [64]

The authors proposed an approximate method to assess the buckling behavior of partially restrained curved panels, accounting not only for the curvature effect but also for a reinforcing effect due to the rotational stiffness of rigid trapezoidal stiffeners, given by Eq.(2.13) as:

$$\sigma_{cr} = \Phi_R k_{\sigma,Z} \sigma_E = \Phi_R k_{\sigma,Z} \frac{\pi^2 E}{12(1-\nu^2)} \left(\frac{t}{b} \right)^2 \quad (2.13)$$

where $k_{\sigma,Z}$ is the elastic buckling coefficient of simply-supported curved panel obtained using the expression by Timoshenko & Gere (see Eq.(2.8)), whereas Φ_R is the strength increment factor that accounts for the reinforcing effect due to the rotational stiffness. The authors proposed three possible methods to calculate Φ_R : *i)* the first one derived by using a 4th order polynomial function as a shape function; *ii)* assuming a harmonic function as a shape function; *iii)* a simplified form through regression analysis. The authors compared all three methods against the results of a parametric study, where several geometrical parameters were varied, and

concluded that the third method returns the results closest to the numerical ones ($\Delta < 8\%$). The expression for Φ_R according to this method is given by Eq.(2.14) as:

$$\Phi_R = 1.15 \left(\frac{3.2D + \kappa}{7.2D + \kappa} \right) + 0.5 \quad (2.14)$$

where D is the flexural stiffness of a plate given by $D = E t^3 / 12(1 - \nu^2)$, whereas κ is obtained as $\kappa = W_s k_R$, where W_s is the sub-panel width, and k_R is the rotational restraint stiffness (see Fig. 2.8). However, as authors claim, further study on a wider range of panel curvature is required until a more efficient design formula is obtained. Moreover, the authors used the elastic buckling coefficient proposed by Timoshenko & Gere, which was several times proven to be overly conservative.

In conclusion, it should be highlighted that although it was long discovered that the theoretical elastic critical stress is not sufficient to predict the ultimate resistance of curved panels, and thus has only limited practical importance, it still has a fundamental role in the available design methodologies. Namely, in most of the design standards (*e.g.* EN 1993-1-5, DNV-RP-C202, DNVGL-CG-0128, ABS, etc.), in order to calculate the ultimate resistance, it is necessary first to calculate the elastic critical stress and subsequently the slenderness of the element. Therefore, the study on the elastic buckling behavior of cylindrically curved panels is still essential and gains tremendous attention from the research community. The design rules from the previously mentioned standards are presented in section 2.5, where all the required steps for the evaluation of the ultimate resistance are provided, including the first step – determination of the critical stress.

2.4.1.3 Ultimate compressive resistance of curved panels

A significant discrepancy between the theoretical critical load and experimental data that was identified in the 1940's and 1950's, led to the conclusion that in case of cylindrically curved steel panels, the theoretical critical buckling load could not be reached and that the concept of initial imperfections should be introduced in order to attain the ultimate resistance of the structural element. It was soon discovered that an increased imperfection sensitivity characterizes the behavior of curved panels due to an unstable post-buckling path, which is not the case with flat plates that have a stable one.

In order to solve the noticed inconsistencies, extensive use of large deflection theory was initiated. In 2018, Martins *et al.* [17] carried out a thorough literature review, summarizing the previous studies dealing with the post-buckling behavior of perfect and imperfect curved panels under uniform compression. Some of the most relevant and thriving studies (*e.g.* Levy [65], Volmir [66], Tamate & Sekine [67], Chia [68], Breivik [69], and Magnucka-Blandzi & Magnucki [70]), were discussed in detail in the most recent work by Manco [10], where their main contributions but also their evident limitations were pointed out. In addition, in 2018, Manco *et al.* [71]-[72] proposed a semi-analytical procedure for the prediction of the post-buckling behavior of unstiffened and stiffened cylindrically curved steel panels under uniaxial compression, based on large deflection theory and calibrated with an extensive parametric study using advanced FE models. The authors further proposed closed-form analytical equations based on a single degree-

of-freedom approximation. Subsequently, the same authors [73] developed an analytical solution for the ultimate resistance of uniformly compressed unstiffened curved panels valid for constrained in-plane boundary conditions. Due to the complexity of the problem, there are still no methodologies that predict the ultimate strength of curved panels based on analytical or semi-analytical approach, except for the aforementioned study by Manco *et al.*, however, no experimental evidence was provided to validate these computational models.

Hence, most of the studies available in the literature dealing with the ultimate load of curved panels are based solely on FEM that started to gain force in the 2000s. Several rigorous parametric studies were performed by Maeno *et al.* [44] in 2004, Park *et al.* [74] in 2007, and Andico *et al.* [64] in 2018, in which the authors assessed the influence of various parameters on the behavior of curved stiffened plates, revealing a strong sensitivity on the shape and amplitude of the initial imperfections. Finally, several authors proposed empirical expressions to assess the ultimate resistance of unstiffened and stiffened simply supported curved panels subject to compression, which is briefly addressed in the following paragraphs.

In 2012, Tran [8] studied both unstiffened and stiffened curved panels under uniform compression, exclusively based on FE analyses, making one of the most remarkable contributions in this field. A series of numerical simulations were carried out to characterize the elastic-plastic behavior of curved panels, where in specific, the influence of curvature parameter, initial imperfections, and stiffeners were identified. Tran proposed two methodologies to determine the ultimate resistance of unstiffened simply supported curved panels, one based on the procedure given in EN 1993-1-5 (*i.e.* Ayrton-Perry methodology) and the other based on the procedure provided in EN 1993-1-6. The first methodology would be later recalibrated and a slightly modified version was presented in Tran *et al.* [75]. In all the proposed methodologies, curvatures were varied between $Z = 0$ and $Z = 100$, whereas the aspect ratio was kept constant and equal to $\alpha = 1$, with the width b and the length a equal to 3 m, which might be one of the shortcomings of the approach. Regarding the boundary conditions, only simply supported edges, with the constrained loaded edges (*i.e.* forced to remain straight) were considered. Furthermore, the shape of the equivalent geometric imperfections was adopted to be affine to the 1st buckling mode, obtained from the linear buckling analysis (LBA). The author claims that although not necessarily the most unfavorable shape, a 1st buckling mode leads to safe results. Finally, it should be pointed out that Tran's method uses Stowell's formula (Eq.(2.9)) to obtain the elastic critical stress, which may lead to erroneous results as shown later on by Martins *et al.* [56].

Besides the design approaches for the unstiffened panel, Tran [8] was the first author to propose the methodology for the stiffened curved panels under uniform compression, which is based on the procedure available in EN 1993-1-5 for longitudinally stiffened flat plates, presented in section 2.5. Namely, the ultimate resistance is obtained by interpolation of two distinct behaviors: a column-type and plate-type behavior. To determine the reduction factor due to plate-type buckling, the author suggests the same procedure proposed for the unstiffened panels, substituting the global curvature Z with corresponding local curvature Z_{loc} (see Eq.(2.5)). On the other hand, the reduction factor due to column-type behavior is obtained according to EN 1993-1-1 [76], assuming the buckling curve C ($\alpha = 0.49$), whereas the geometrical properties (*i.e.* the

area and inertia) required to obtain critical column stress are evaluated on the gross cross-section of the panel (shell and stiffeners) and not on a single strut model.

In 2014, Tran *et al.* [59] carried out another study on the linear buckling and the ultimate strength of stiffened curved panels, assessing the influence of the coupled effects of curvature and stiffening. The authors proposed another simplified design methodology to assess the ultimate resistance similar to the previous one, however, neglecting the plate-type behavior. The methodology is simple, but it was verified against a relatively narrow range of parameters. Namely, the width and the thickness are constant and equal to $b = 4.8$ m and $t = 0.012$ m, respectively, the number of stiffeners is fixed to be $n_{st} = 8$, whereas the maximum aspect ratio considered in the study is equal to $\alpha = 1.25$.

In the same year, using the design of the experiment method, Tran *et al.* [77] proposed another design formula, applicable for both unstiffened and stiffened panels. The approach is based on the quasi-Monte Carlo statistical calibration of the variables used as the input data for the considered problem. Although the scope of this method is somewhat extended by adding the possibility to explicitly account for the aspect ratio, there are still several limitations in this approach. First, the formula is valid for a very narrow range of parameters, for instance, $0.01 \leq t/b \leq 0.04$, $0.6 \leq \alpha \leq 1.6$, $0 \leq b/R \leq 1$, and $0 \leq Z \leq 26$ for unstiffened panels, and $0.67 \leq \alpha \leq 1.5$, $0 \leq t/R \leq 0.1$, and $5 \leq n_{st} \leq 20$ for stiffened panels. Second, the formula is validated solely against the numerical results obtained in the previous study, thus encountering the same shortcomings already addressed. Finally, the formula is conceptually different from the usual standard-like formulism, which may obstruct its applicability in conventional design.

Martins *et al.* [78] performed an extensive numerical study in 2014, attempting to overcome the limitations discovered in the methods proposed by Tran. Based on the effective width concept and on a modification of the reduction curves given in EN 1993–1-5, the author proposed a new design formula to assess the ultimate strength of unstiffened short curved panels ($\alpha \leq 1.0$) under pure compression, but also under pure in-plane bending. The extension of these rules to long panels ($\alpha > 1.0$) was proposed in Martins [9], where the reduction factor for short panels should be multiplied by a numerically generated correction factor.

In 2015, Martins *et al.* [79] carried out a series of FE analyses, studying the effect of geometric imperfection on the ultimate strength of curved panels. In specific, the study comprises ten different shapes of geometric imperfections (corresponding to the first ten buckling modes) and various imperfection amplitudes. The authors concluded that the first buckling mode might lead to unsafe results and that panels with larger curvature are more sensitive to initial geometric imperfections. However, the main shortcoming of this study is that the authors considered only imperfections affine to the eigenmodes. As it would be concluded later by Manco [10], a perfect semi-wave in each direction might result in the ultimate resistance much lower than those given by eigenmodes.

Kim *et al.* [80] studied in 2014 the unstiffened cylindrically curved panels subject to axial compression and lateral load, thus addressing the panels used mainly in ships and offshore structures, such as wind towers, bilge circle parts in ship vessels, etc. Using the FE analyses, a series of elastic and elastic-plastic large deflection analyses were performed and the effects of

curvature, the aspect ratio, the slenderness and the initial imperfections on the buckling and ultimate load were identified. In addition, an empirical design formula is proposed to determine both the critical load and the ultimate resistance of a panel under a variety of loading conditions (*i.e.* longitudinal and transverse compressive loads, combined biaxial compression, and lateral pressure). The expression for the critical load is based on the plasticity correction by Johnson-Ostenfeld, while the formula for the ultimate resistance has the same general format as the one developed in 1975 by Faulkner [81], with the modified coefficients. The proposed approach is valid within certain geometrical ranges, namely, for the sectorial angle between $5^\circ \leq \beta \leq 30^\circ$ (see Fig. 2.1). Moreover, the formula is proposed based on the analyses of stiffened curved panels, where an unstiffened panels is actually a subpanel framed by longitudinal stiffeners, with very specific boundary conditions. However, no clear specification on the level of the constraint of the loaded and specifically unloaded edges is provided.

Most recently, in 2018, Park *et al.* [16] performed a similar study like the one from Kim *et al.*, and another improved closed-form expression was proposed to calculate the ultimate strength through double-beta forms, widely used in prediction of the ultimate resistance of unstiffened flat plates. The authors identified the difficulty in modeling of the boundary conditions of an unstiffened panel surrounded by stiffeners, stating that the degree of rotational restraint at the plate boundary is neither zero nor infinite, which largely depends on the torsional rigidity of its supporting members. Nevertheless, a more conservative *one bay* model with all four edges simply supported was adopted, as presented in Fig. 2.9.

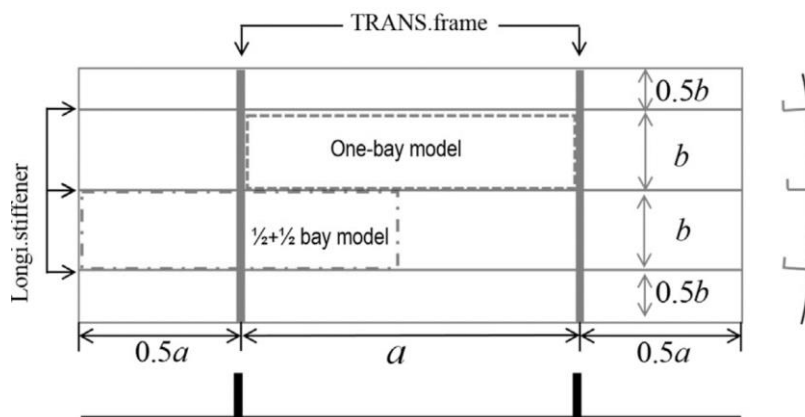


Fig. 2.9: The one-bay cylindrically curved panel model used by Park *et al.* [16]

The proposed formula is valid for a wide range of the aspect ratio ($1.0 \leq \alpha \leq 5.0$), and thicknesses ($8 \text{ mm} \leq t \leq 40 \text{ mm}$), whereas the width is kept fixed and equal $b = 1000 \text{ mm}$. The authors compared the formula with the available standard DNV [13] and concluded that the existing design rules are excessively conservative, which was confirmed by Martins *et al.* [9].

Unlike the unstiffened panels, there have been only a few studies in which a proposal for the assessment of the ultimate resistance of stiffened curved panels is provided. Namely, besides those aforementioned approaches by Tran, the study by Seo *et al.* [82] deserves to be mentioned. Namely, relying solely on FE analysis, the influence of various parameters on buckling and the ultimate load was characterized, such as curvature, slenderness b/t ratio, as well as three different

stiffeners shape. For all the analyses, a double-span & double-bay model was used as shown in Fig. 2.10.

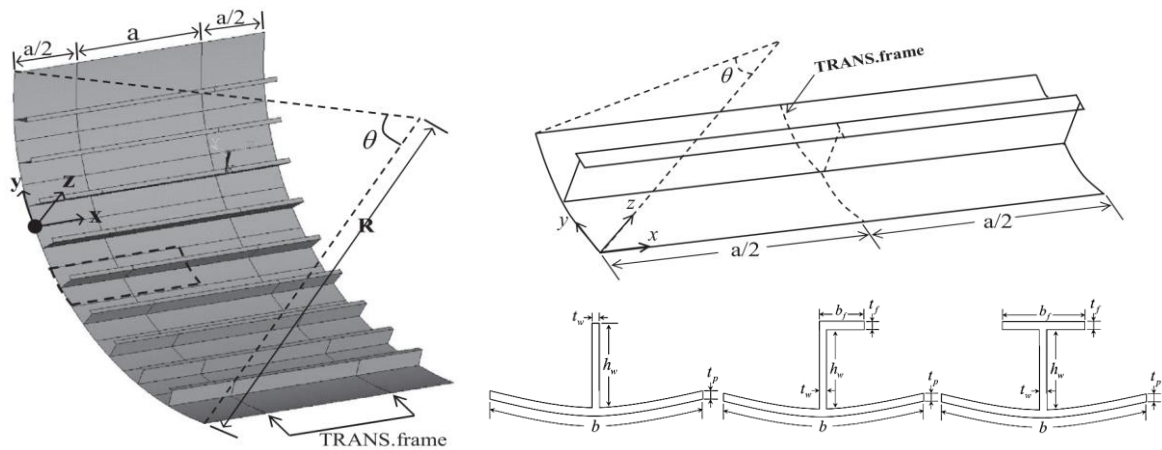


Fig. 2.10: Cylindrically curved panel model used by Seo *et al.* [82]

Based on 400 FE analyses, the author claims that the shape of the stiffener affects only the buckling pattern, whereas its influence on the ultimate strength is negligible, adding that flat stiffeners commonly result in a collapse induced by stiffeners, whereas T-shaped stiffeners and angles lead to local failure of stiffener and global buckling of panel, respectively. In addition, a design empirical formula was derived using the least-squares method based on FE analysis results obtained for 150 different cases. However, the main drawback of this approach is the fact that it could be applied only for the panels with T-shaped longitudinal stiffeners. Moreover, in all 150 cases, the aspect ratio was kept constant and equal to $\alpha = 3.0$. Finally, to calculate the ultimate resistance, it is required to determine the elastic buckling strength of the curved panel and of the corresponding flat plate; however, the expression proposed by Kim *et al.* [80] for the unstiffened curved panels was adopted, without consideration of the stiffener type and/or size on the buckling load.

In two consecutive works published in 2019 by Silvestre *et al.* [83] and Silvestre&Martins [84], the authors applied a semi-analytical technique - Generalised Beam Theory (GBT) to classify (*i.e.* decompose) the buckling modes of curved panels under axial compression, based on well defined mechanical behavioral features. In the first study, the authors assessed the influence of different deformation modes (global, distortional, local, warping shear, transverse extension) on the buckling load of unstiffened and stiffened panel. In the latter, a numerical study was carried out, in which post-buckling behaviour of curved panels was investigated. The authors assessed the sensitivity to different initial geometrical imperfection shapes, previously determined by GBT, providing the equilibrium paths of relevant modal displacement profiles, modal participation diagrams and deformed configurations.

Finally, in 2019, stiffened curved panels were thoroughly studied within the OUTBURST research project [60],[85], [86]. One of the most relevant contributions of this work is the use of a numerical model calibrated against experimental test results, reported in 2020 by Piculin & Može [85]. An extensive parametric study was subsequently carried out using the model of stiffened panels with unconstrained longitudinal edges and constrained loaded edges, varying

the curvature ($0 \leq Z \leq 500$), the aspect ratio ($0.5 \leq \alpha \leq 2.0$), the size and the type (flat and trapezoidal) of stiffeners. The authors stressed the importance of the initial imperfections and emphasized the difficulty to identify the most critical mode of geometric imperfection without an exhaustive analysis of all eigenmodes. Furthermore, the design method for longitudinally stiffened curved plates subjected to axial compression was proposed, using the formalism of EN 1993-1-5 for flat plated structures. The ultimate resistances obtained using the proposed method showed good agreement with the FEM-based results for a wide range of geometrical parameters.

In conclusion, each of the proposed design methodologies for the prediction of the ultimate strength of cylindrically curved panels that are discussed in this section is in detail presented in [section 2.5](#), where the design rules from the design standards (*i.e.* DNV-RP-C202, DNVGL-CG-0128, ABS) are gathered as well.

2.4.1.4 Experimental behavior of curved panels loaded in compression

As indicated in [2.4.1.3](#), there has been an increased interest for curved panels as of late; however, as general impression, experimental evidence is still missing to validate the presented analytically and numerically built computational models.

The early experimental works on curved panels under compression were comprehensively summarized first by Gerard [87] in 1958 and later discussed by Thomas [88] in 1974. Namely, the majority of the experimental investigations, carried out on both unstiffened [89]-[99] and stiffened [100]-[107] curved panels, were reported back in the 1930s and 1940s, where the corresponding authors actually intended to compare the experimental results with the most recent theoretical findings developed at the time. Some of the most relevant studies are discussed in this section.

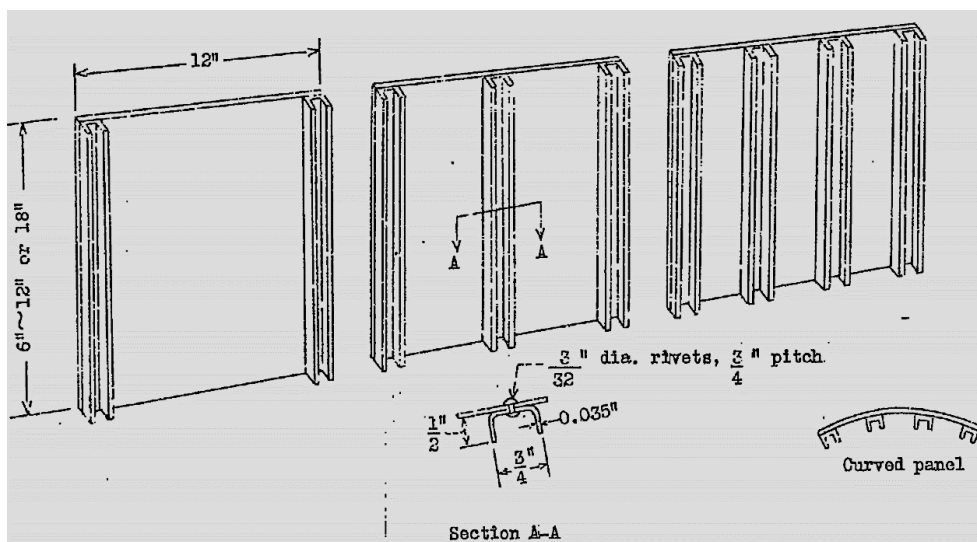


Fig. 2.11: Test specimens from Gall [100] (dimensions in inches)

In 1930, Gall [100] in his PhD thesis carried out 42 axial compression tests on the stiffened aluminum curved panels. The geometry of the panels was varied within the practical ranges in the field of aeronautics, where the width of all the panels was kept constant

($b = 12$ in. ≈ 152 mm), whereas three sheet thicknesses (*i.e.* 0.48 mm, 0.84 mm, 1.32 mm), three aspect ratios (*i.e.* 0.5, 1.0, 1.5) and four radii of curvature (including flat plates) were examined. In addition, two types of U-shaped stiffeners were considered, attached to the plate using rivets (see Fig. 2.11). The author concluded that, in general, two failure modes might occur, in a manner similar to flat plates. In the first, failure by bending of the stiffener and sheet panel normal to the plane of the panel occurs, similar to primary failure in columns, characterized by noticeable buckling of the sheet between stiffeners (see Fig. 2.12). In the second, local wrinkling of the outstanding legs of the stiffener takes place (see Fig. 2.13).

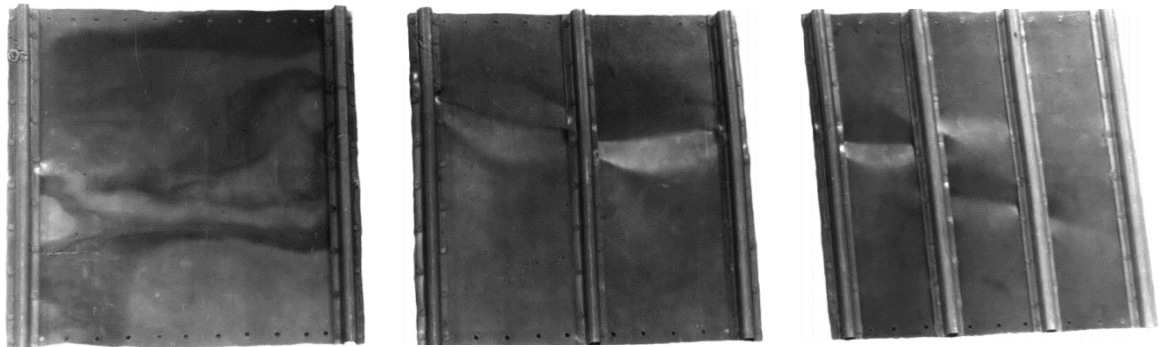


Fig. 2.12: Failure mode by bending of the stiffener and sheet panel (from Gall [100])

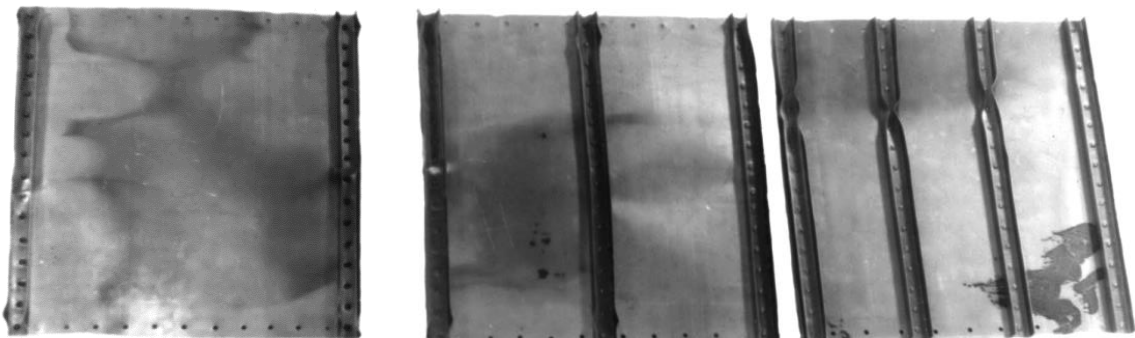


Fig. 2.13: Local failure of stiffener legs (from Gall [100])

Finally, Gall concluded that a lower R/t ratio (*i.e.* more curved panel) leads to increased resistance of a panel, regardless of the number of stiffeners, as presented in Fig. 2.14. In the figure, ratio of average curved specimen strength (σ_z) to average flat specimen strength (σ_p) is plotted against the level of stiffening expressed in percentage (%).

It may be seen that for low curved panels (*i.e.* $R/t > 935$), the resistance tends to be up to 15% lower than the resistance of corresponding flat plates. As the author later explained, this unexpected strength reduction was caused by a non-uniform curvature along the panels' length, thus introducing significant load eccentricities and non-uniform load distribution.

In 1933, using the experimental data from Gall, Lundquist [101] studied three simplified procedures available at the time for calculation of the compressive strength of stiffened flat plates and verified their applicability for low curvature aluminium panels. The author concluded that for curved panels that fail by bending of the stiffener and sheet panel (see Fig. 2.12), which is based on a mutual action of panel and stiffener, the *effective width method* proposed by Theodore

von Kármán [108] for flat plates may be used. Namely, according to this method, it is assumed that the stiffener together with the adjacent effective width of the panel sheet behaves as a column that fails by bending normal to the panel plane. Therefore, the second moment of area, as well as the slenderness ratio of combined stiffener and effective panel should be calculated and the effective area multiplied by the stress for a considered column. This method was adopted in EN 1993-1-5 and it is presented in section 2.5, being a relevant base for the design of stiffened curved panels. Moreover, similar to Gall, Lundquist also recommended the use of the design rules for flat plates in case of very shallow panels, setting a slightly more rigorous lower limit to $R/t > 1200$.

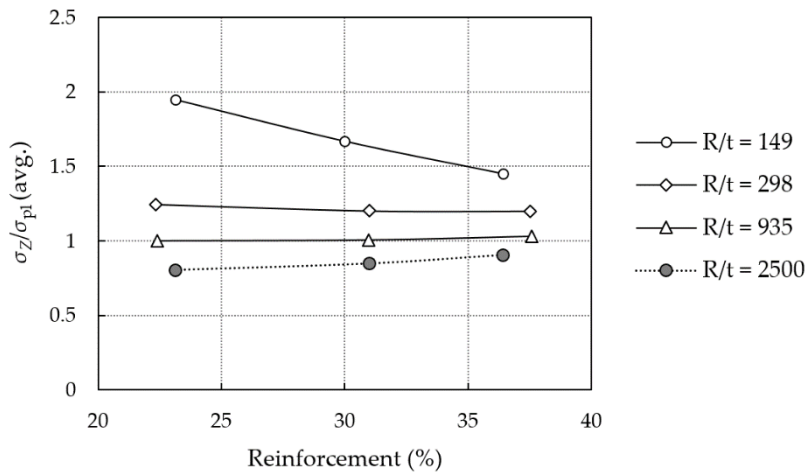


Fig. 2.14: Curved specimen to flat specimen strength ratio (avg.) (adapted from Gall [100])

Ramberg *et al.* [103] in 1944 carried out another experimental campaign, in which 21 aluminum curved panels, reinforced by four Z-shaped stiffeners attached by rivets (see Fig. 2.15), were tested under pure compression. All tested panels have the same aspect ratio $\alpha = 0.75$ (with $a = 304.8$ mm and $b = 406.4$ mm), whereas the radii of curvature R and the sheet thickness t were varied so that the local curvature (see Eq.(2.5)) covers a range of values up to $Z_{loc} = 32.5$.

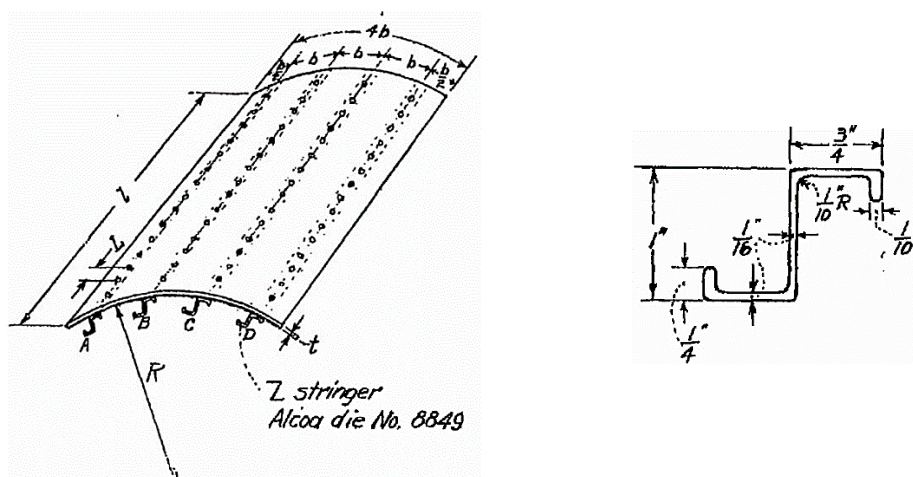


Fig. 2.15: Test specimens from Ramberg *et al.* [103] (dimensions in inches)

Several failure modes were identified in the tests by visual inspection: *i*) local buckling of the stiffener (in 15 out of 21 tests); *ii*) local buckling of sub-panels (two by separation of rivets and

one between the stiffeners); *iii*) global buckling of both stiffeners and sheet panels as one unit (in three tests with a thick sheet plate).

The results of the tests are summarized in Fig. 2.16, where, similar to Fig. 2.14, ratio of average curved specimen strength (σ_z) to average flat specimen strength (σ_{pl}) is plotted against the local curvature parameter Z_{loc} . The results show that for shallow panels ($Z_{loc} < 10$), the effect of curvature is more pronounced, leading to a gain in resistance of up to 15% (*i.e.* 6% in average value), whereas, for the higher values of curvature, the ultimate load appears to show descending trend with curvature. Becker [87] later emphasized that the higher curvature necessarily induces a higher imperfection sensitivity of panels, which to some extent might explain the reduction of the ultimate strength, insisting that more tests should be performed before any firm conclusion could be drawn.

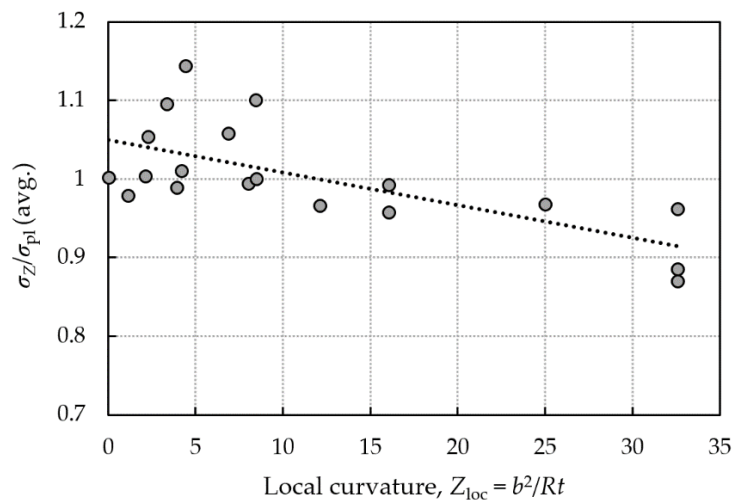


Fig. 2.16: Effect of curvature on compressive strength of stiffened curved panels (adapted from Rabmerg [103])

Some years later, in 1960, Soderquist [106] tested another series of 19 aluminium alloy flat and curved stiffened panels under pure compression, with the ranges of geometric parameters encountered in the aircraft industry. The principal objective of the study was to investigate the curvature effect on the ultimate strength of panels and to reveal the reason for a descending trend with increasing curvature reported by Ramberg (see Fig. 2.16), contrary to expectations. The test setup is similar to the one by Ramberg; however, several changes were introduced to eliminate undesired complications found by the previous author, such as the local instability of stiffeners and failure due to rivet separation (see Fig. 2.17).

Therefore, instead of Z-shaped and U-shaped stiffeners, rather stiff rectangular stiffeners were used, whereas the attachment of the stiffeners to the panel was done by means of bolting with screws and not by rivets. Finally, in order to secure simple support at the two unloaded edges, two stiff angle sections were fitted around it, allowing the edge to slide up and down, as shown in Fig. 2.17. Prior to each test, the initial imperfections were measured and recorded for the first time, and it was noticed that the differences of the local curvature radii might be significant (up to 20%), especially in the zones close to the stiffeners.

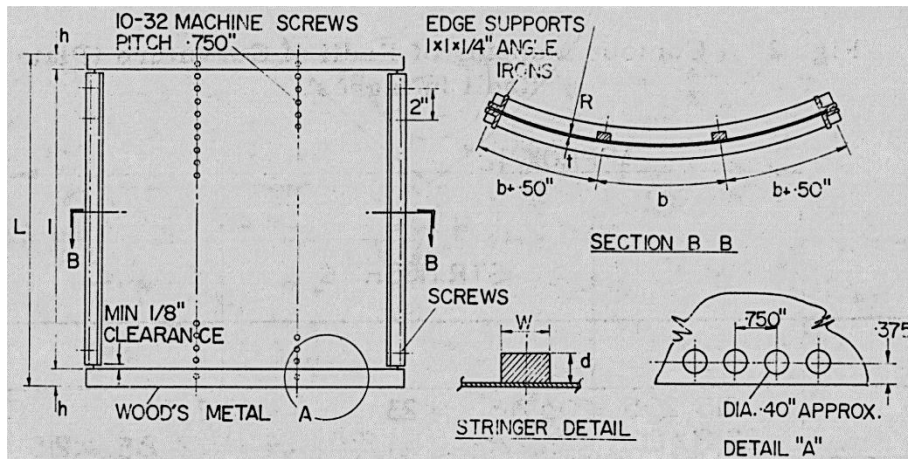


Fig. 2.17: Test setup from Soderquist [106] (dimensions in inches)

One of the major conclusions of this work is that the ultimate strength cannot be observed only as a function of the curvature parameter Z as it was believed before, but also the slenderness b/t ratio has to be accounted for. The results of the tests are presented in Fig. 2.18, where again average ultimate strength ratio σ_z/σ_{pl} is plotted against the local curvature parameter Z_{loc} , however, the results are sorted according to the b/t ratio.

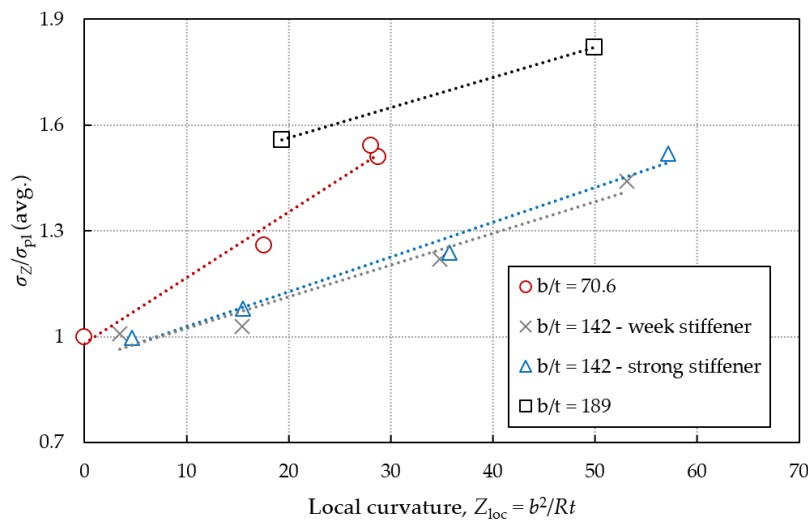


Fig. 2.18: Effect of curvature on compressive strength of stiffened curved panels (adapted from Soderquist [106])

The results show a strong dependence on both the curvature parameter and b/t ratio. Namely, the higher the curvature the higher is the gain in the ultimate resistance, regardless of the b/t ratio. On the other side, for a constant value of curvature, the ultimate resistance ratio (σ_z/σ_{pl}) increases with decreasing b/t ratio (e.g. for $Z_{loc} = 30$ and $b/t = 142$, the ultimate load ratio is $\sigma_z/\sigma_{pl} = 1.18$, whereas, for $b/t = 70.6$, the value is $\sigma_z/\sigma_{pl} = 1.57$). In conclusion, in contrast to the results from Ramberg, it may be observed that for a certain b/t ratio, the ultimate strength shows always a rising trend with increasing curvature. The rate of increase depends on the b/t ratio.

Despite a significant deviation of experimental results from the expected theoretical results and apparent contradiction in results obtained by different authors, only a few experimental programs have been reported ever since.

In 1998, Featherston & Ruiz [109] carried out a series of tests on unstiffened thin engine fan blades made of aluminium. All the tested specimens have a constant thickness and width (*i.e.* $t = 0.55$ mm and $b = 100$ mm), whereas three different aspect ratios were considered (*i.e.* $\alpha = 1.0$, $\alpha = 1.5$ and $\alpha = 2.0$) and only two different curvatures (*i.e.* $Z = 56$ and $Z = 103$). Featherston [110] extended the scope of the study in 2001, adding another curvature of $Z = 181$. Although the work contains much needed experimental results, all tests were carried out only on unstiffened panels subject to the combined action of compression and shear, with very specific boundary conditions. Namely, the unloaded straight edges remained unsupported, one curved edge was clamped, whereas the opposite curved edge was simply supported.

Two European research projects, POSICOSS [111] and COCOMAT [112], carried out in 2006 an experimental study on composite curved panels, with geometry selected to correspond to typical dimensions encountered in the aeronautics. Similar to the aforementioned first experimental references, the stiffeners were attached to the panel sheets by riveting, leading often to failure modes governed by the separation of the composite components or by the failure of the rivets. Hence, the experimentally based design rules proposed in these projects have a very limited field of practical application, disabling their use in welded structural steel applications.

In 2007, Cho *et al.* [113] conducted six compressive tests on longitudinally stiffened curved panels with the geometry that corresponds to curved panels used in bilge strakes of container ships. Each specimen contains seven (or more) angle bars stiffeners (see Fig. 2.19) that are welded to the panel. The radius of curvature R , the thickness t and the width b are varied so that the global curvatures ranges from $Z = 620$ to $Z = 1150$ and the local curvature from $Z_{loc} = 9.0$ to $Z_{loc} = 19$. The main drawback of this study is the fact that the geometry of the panels was adapted from the marine industry, where mainly short ($\alpha = 0.3 - 0.5$) and heavily stiffened panels are used. The authors compared the experimental results with the numerical ones and a significant inconsistency was perceived in both the initial stiffness and the ultimate resistance of the panels (10% on average). In conclusion, the authors insist that additional experimental tests are required before any conclusion could be drawn.

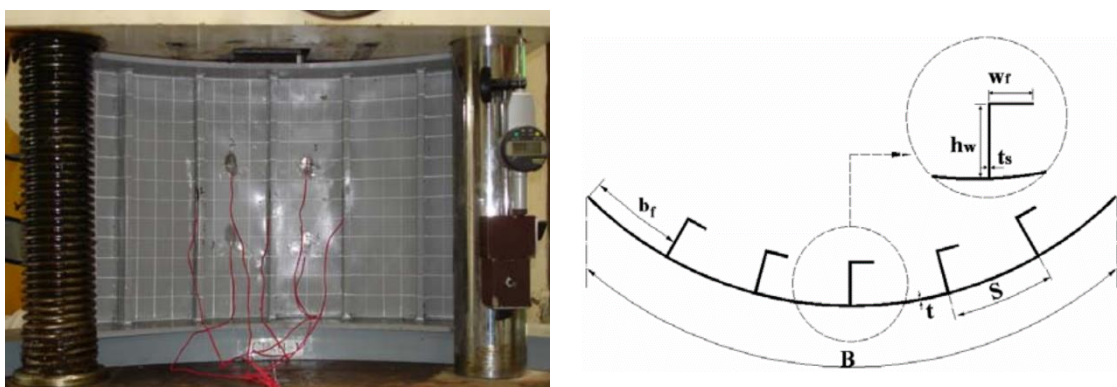


Fig. 2.19: Test setup from Cho *et al.* [113]

Finally, in 2020, Piculin & Može [85] carried out an experimental study within the aforementioned OUTBURST research project, in which five stiffened curved plates with different geometry and steel grades (S460 and S690) were tested under pure axial compression.

The authors investigated the influence of various parameters on the ultimate strength of the panels, concluding that the use of higher steel grade negligibly increases the ultimate strength, whereas no difference was noticed among the plates with different aspect ratios. In addition, the importance of the initial imperfections is highlighted, directly affecting the failure mode of the tested specimens, which is, according to the authors, associated with a combination of buckling and yield of the material. Although the tests data (*i.e.* initial geometric imperfection, displacement field, strains, failure modes, etc.) were reported in a very comprehensive way, the main drawback of the study is relatively small number of tests performed (*i.e.* 1 per geometry), thus limiting the ranges of the studied parameters. Namely, only two curvature parameters ($Z_{loc} = 12$ and $Z_{loc} = 18$) and two aspect ratios ($\alpha = 2.3$ and $\alpha = 4.6$) were accounted for, keeping the number of flat stiffeners constant in all tests (*i.e.* $n_{st} = 2$).

Based on this overview of the experimental references, it may be understood that there are insufficient experimental results to enhance the validity of the above-mentioned empirical design methods. Besides, the majority of the available studies have focused on full cylinders, aluminium alloy sheets for monocoque constructions and composite curved panels used in aircraft and marine industry, which differ from those encountered in civil engineering (*i.e.* bridges). Hence, in an attempt to get insight into the complex buckling behavior of curved steel panels under compression, with geometry that may be encountered in offshore, aeronautics and bridge applications, an experimental program was undertaken within the research project ULTIMATEPANEL that is described in detail in [chapter 3](#).

2.4.2 Curved panels under shear

2.4.2.1 General

Unlike the curved steel panels under uniform compression, the panels under pure shear have been considerably less studied and there are still no practical design rules to estimate the ultimate shear resistance. Martins *et al.* [17] thoroughly reviewed up-to-date studies found in the literature, dealing with the stability and design of isolated cylindrically curved panels under shear loading. Thus, this section addresses only the most relevant historical references in this field, useful for the work presented in the thesis, discussing the scope of their application and emphasizing the main limitations.

Similar to curved panels under compression, discussed in 2.4.1, this section is divided into two sub-sections: *i*) elastic buckling behavior of curved panels under shear, where available methods for the computation of the critical shear load are demonstrated; *ii*) ultimate shear resistance of curved panels, summarizing the most relevant numerical studies dealing with the ultimate load of curved panels. To the best of the author's knowledge, there are no references in which the isolated curved panels under shear are experimentally tested.

2.4.2.2 Elastic buckling behavior of curved panels

The first attempts to obtain the critical load of curved panels under shear were reported back in the 1930s by Leggett [114] and Kromm [115], who studied shallow long simply supported panels, proposing the first analytical solution by solving the Dean's differential equation [116]. In

the subsequent studies by Batdorf [117] in 1947 and Schildcrout & Stein [118] in 1949, significant progress was made in the critical behavior of curved panels under shear, extending the scope of the study to various boundary and loading conditions, for the whole range of curvatures Z . Moreover, using Donnell's equations, the authors proposed the expression for the critical shear load, similar to the one for the curved panels under compression (see Eq.(2.6)) that has been in use in an unchanged form ever since, given by Eq.(2.15) as:

$$\tau_{cr} = k_{\tau} \sigma_E = k_{\tau} \frac{\pi^2 E}{12(1-\nu^2)} \left(\frac{t}{b} \right)^2 \quad (2.15)$$

where k_{τ} is the shear buckling coefficient that, depending on the panel geometry and boundary conditions, may be obtained using NACA design curves (monographs) published by the National Advisory Committee for Aeronautics (NACA) [119]-[120]. The monographs provide design information in the form of empirical knockdown factors, obtained as lower bounds of experimental results available at the time, carried out on the full cylinders subject to torsional moment. The monographs for unstiffened curved panels with simply supported and clamped edges are presented in Fig. 2.20 and Fig. 2.21, respectively. As it may be observed, the monographs give the shear buckling coefficient (k_{τ}) to be used with Eq.(2.15), as a function of the curvature parameter Z (defined by Eq.(2.2)), for various aspect ratios (defined by Eq.(2.1)).

Although the curves have been widely used in aeronautics, there are several limitations that hindrance their use in other civil engineering applications. First, the curves cover aspect ratios up to $\alpha = 3.0$, whereas those with a higher aspect ratio are considered as *infinitely long* (see Fig. 2.20a and Fig. 2.21a). On the other hand, only two curves for the so-called *wide panels* are provided (*i.e.* $\alpha = 0.66$ and $\alpha = 0.5$), which in case of simply supported panels are valid for curvatures up to $Z = 100$ and $Z = 10$, respectively, whereas panels with aspect ratio lower than $\alpha = 0.5$ are considered as *cylinders* (see Fig. 2.20b and Fig. 2.21b). Finally, it is necessary to emphasize that the NACA curves cover simply supported and clamped panels, without a clear specification of the in-plane boundary conditions (*i.e.* in-plane edge constraints).

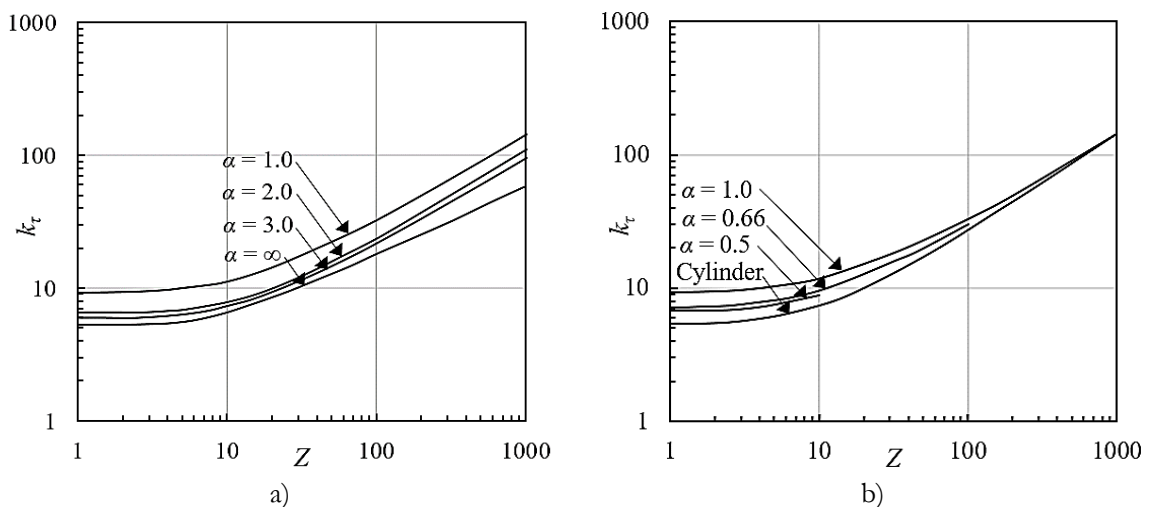


Fig. 2.20: NACA monographs for simply supported panels: a) $\alpha > 1$ and b) $\alpha \leq 1$
(adapted from Batdorf *et al.* [120])

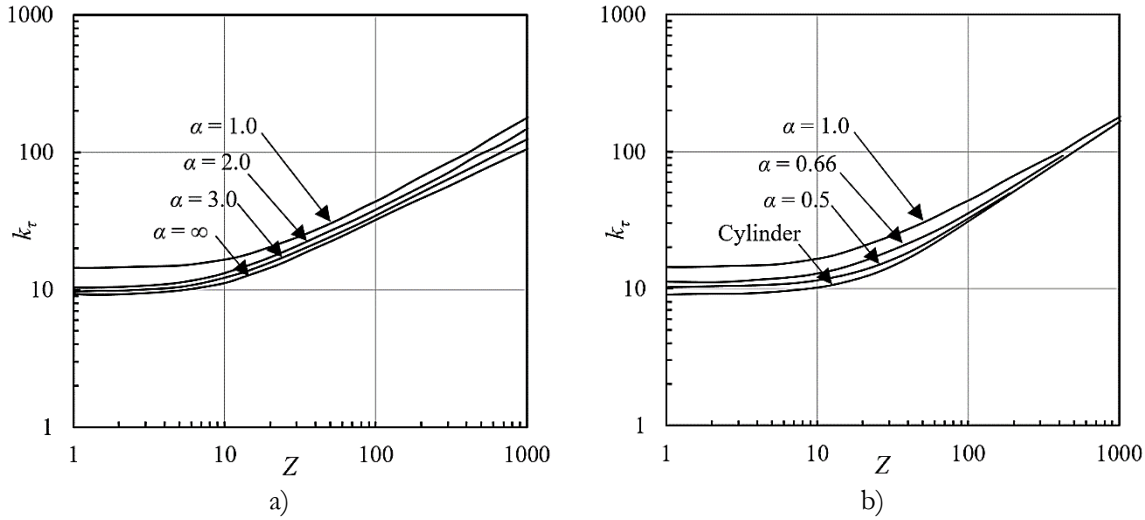


Fig. 2.21: NACA monographs for clamped panels: a) $\alpha > 1$ and b) $\alpha \leq 1$
 (adapted from Batdorf *et al.* [120])

In 1963, Timoshenko & Gere [121] studied long and perfect curved panels without stiffeners under various load arrangements. The authors proposed a simple expression for the shear buckling coefficient as a function of the curvature parameter Z , given by Eq.(2.16); however, it is valid for long curved panels only (*i.e.* $a \gg b$).

$$k_{\tau} = 5.34 \sqrt[4]{1 + 0.0145Z^2} \quad (2.16)$$

Later, in the 1970s–1990s, several authors summarized the latest studies on isotropic curved panels (*e.g.* Baker *et al.* [122] and Bismarck-Nasr [123]); however, no significant changes were introduced with respect to the NACA curves. In 1998, Nemeth & Starnes [124] revised the NACA curves and concluded that the curves are outdated, providing overly conservative results.

Most recently, with the appearance of FE software packages, the number of studies on the buckling behavior of the curved panels under shear seems to have increased. In 2002, Domb & Leigh carried out two numerical studies on curved panels, under pure shear [41] and under combined action of compression and shear [125], assessing the validity of the available analytical techniques, *i.e.* NACA curves. The authors agreed with Nemeth & Starnes that the curves were outdated and proposed a single design curve (see Eq.(2.17)) representing the shear buckling coefficient as a function of curvature for panels with aspect ratio greater than $\alpha > 4.0$, thus extending the scope of NACA curves.

$$k_{\tau} = \begin{cases} 10^{\sum_{i=0}^3 c_i [\log(Z(1-\nu^2))]^i} & \text{if } 1 \leq Z(1-\nu^2) \leq 15 \\ c [Z(1-\nu^2)]^d & \text{if } 15 \leq Z(1-\nu^2) \leq 200 \end{cases} \quad (2.17)$$

where the required coefficients are: $c_0 = 0.7782$, $c_1 = -0.1088$, $c_2 = 0.2025$, $c_3 = -0.0037$, $c = 1.4805$, and $d = 0.6401$.

In 2010, Machaly *et al.* [126], investigated horizontally curved I-girder web panels and proposed a method to predict the shear buckling coefficient, given by Eq.(2.18).

$$k_{\tau} = 1.04\eta \left[k_{ss} + 0.8(k_{sf} - k_{ss}) \right] \quad (2.18)$$

In this expression, the coefficient k_{ss} , given by Eq.(2.19), is the theoretical buckling coefficient of flat plate assuming simply supported boundary condition at flanges; k_{sf} is a coefficient given by Eq.(2.20); η is an amplification factor given by Eq.(2.21), where the constants c_1 and c_2 are equal to 0.18 and 0.09, respectively.

$$k_{ss} = 5.34 + 4 / (b / a)^2 \quad (2.19)$$

$$k_{sf} = \frac{5.61}{(b / a)^2} - \frac{1.99}{(b / a)^3} + 8.98 \quad (2.20)$$

$$\eta = 1 + \frac{Z}{8} \left[c_1 - c_2 \left(\frac{b}{a} \right) \right] \geq 1.0 \quad (2.21)$$

However, this method is derived by calibration of a relatively small number of numerical results (*i.e.* 100), where the curvature parameter and the aspect ratio were kept within a narrow range (*i.e.* $Z = 2-10$ and $\alpha = 0.5-1$).

Finally, in 2011, Amani *et al.* [127] carried out a comprehensive numerical study in which the theoretical values of buckling coefficient from the NACA curves were compared with the numerical results for a very wide range of curvatures ($Z = 0-1000$) and aspect ratios up to $\alpha = 2.5$. Good agreement with the numerical results was achieved for lower values of curvatures, *i.e.* up to $Z = 10$. However, in the intermediate range of curvatures (*i.e.* $Z = 10-100$) a sudden alteration of the buckling modes occurs (*i.e.* from the symmetric to antisymmetric), which eventually leads to a higher deviation from the theoretical results since this phenomenon was not accounted for in the original NACA curves.

Although several authors revised and criticized the NACA monographs, they remained practically the only valid method for the prediction of the critical shear load for the unstiffened simply supported curved panels. In fact, none of the authors proposed a simple design formula to replace the outdated and impractical NACA monographs, at least not for various curvatures and aspect ratios, as it may be seen in Table 2.3, where the ranges of the most relevant parameters from the aforementioned studies are summarized.

Table 2.3: Ranges of geometrical parameters from the available literature

Author	Year	Aspect ratio, α	Curvature, Z	b/t
NACA [119]-[120]	1947	0.5	0 - 10	-
		0.66	0 - 100	
		1.0 / 1.5 / 2.0 / 3.0	0 - 1000	
Domb & Leigh [41]	2001	≥ 4.0	0 - 200	46 - 460
Machaly <i>et al.</i> [126]	2010	0.5 - 1.0	2 - 10	100 - 200
Amani <i>et al.</i> [127]	2011	0.4 - 2.5	5 / 15 / 50 / 150	333

Nevertheless, the contribution from these studies is essential since the elastic critical load is needed to obtain the ultimate shear resistance, which is the principal goal in the design process.

The most relevant studies on the ultimate resistance of the curved panels subject to a shear load are addressed in [2.4.2.3](#).

Finally, similar to curved panels under uniform compression, the calculation of the shear buckling coefficient and subsequently critical shear stress according to the available standards (*e.g.* EN 1993-1-5, DNV-RP-C202, and DNVGL-CG-0128) is presented in [section 2.5](#), being the initial step in the determination of the ultimate shear resistance of curved panels.

2.4.2.3 Ultimate shear resistance of curved panels

An overview of the references is presented, in which the post-buckling behavior of unstiffened curved panels under shear was investigated. Prior to this, it is necessary to make a brief introduction to the behavior of flat panels under pure shear, being a reference case, essential for the understanding of the main concepts of the post-buckling behavior of curved panels.

Many studies have dealt with the post-buckling behavior of flat plates under pure shear, and the main findings were well documented and summarized in 1986 by Dubas & Gehri [128]. Generally, the response of an isolated plate under shear may be separated into two phases: *i*) pre-buckling; *ii*) post-critical phase. First, before the buckling occurs, the state of pure shear develops, in which the uniformly distributed shear stresses in the plate may be decomposed into the principal tensile stresses and destabilizing compressive stresses that eventually lead to the buckling of the panel. However, owing to this dual stress system and the presence of the tensile component, the critical stresses are slightly higher than in the case of pure compression. Once the buckling occurs, the main compression stress remains constant, whereas the tensile one increases, leading to a stable post-buckling behavior, which is the main characteristic of flat plates. Due to this favorable stabilizing mechanism, in the literature known as *tension field*, significant post-buckling reserves can be utilized until the ultimate load is reached. According to Dubas & Gehri, the extent of this gain in resistance depends on multiple factors, such as the initial geometric and material imperfections, the effect of plasticity, the effect of post-buckling stability, etc.

In contrast to flat plates, the knowledge on the post-critical response of the unstiffened cylindrically curved panels subjected to pure shear is still inexcusably scarce. Only recently, with the appearance of FE based software packages, several studies have been reported, among which the aforementioned studies by Domb & Leigh [41], Featherston [129], Machaly *et al.* [126], and Amani *et al.* [127] are the most representative.

Besides the study on the critical shear load (see in [2.4.2.2](#)), Domb & Leigh [41] analysed the non-linear post-buckling behavior of curved panels. In specific, the authors assessed the imperfection sensitivity of curved panels, stating that ultimate shear load highly depends on the shape and amplitude of the initial imperfections. However, no specific design rules were proposed for the calculation of the ultimate shear load. In fact, the curvature parameter Z is taken into account only for the prediction of the shear buckling coefficient k_s , see Eq.(2.17), whereas the subsequent steps for the calculation of the ultimate resistance remain the same as for flat plates, provided by EN 1993-1-5.

In 2003, Featherston [129] examined the post-critical behavior of a curved panel subjected to a combined action of shear and compression, thus expanding the scope of the previous two studies from the author (*i.e.* Featherston & Ruiz [109] and Featherston [110]). In addition to the previous two studies, the influence of the initial geometric imperfections on the ultimate load was investigated. Namely, the initial imperfections detected by means of Digital Image Correlation (DIC) were explicitly included in the numerical models, which led to an acceptably good agreement between the numerical and the experimental results. Nevertheless, the authors discovered a large portion of uncertainty in FE analysis, emphasizing the importance of an adequate modeling of geometric imperfection shape and amplitude. Finally, based on the results of an extensive parametric study, the authors concluded that for any combination of curvature Z and aspect ratio α modeling of the initial geometric imperfection in the form of the 1st or 2nd eigenmode leads to the minimum collapse load in 85% of the studied cases. However, no design rules were proposed for the prediction of the ultimate shear load.

In the same work in which the expression for the shear buckling coefficient was proposed (see Eq.(2.18)), Machaly *et al.* [126] proposed a simplified method for the calculation of the ultimate shear load of unstiffened curved panels under shear, which is presented in section 2.5 with the other available procedures. However, as it was already highlighted, the empirical formula is verified using a small sample of numerical results, and it is valid for a very specific geometries that are encountered in horizontally curved I-girders (*i.e.* $Z = 2-10$ and $\alpha = 0.5-1$), without a clear specification of the in-plane boundary conditions.

Finally, in the aforementioned study by Amani *et al.* [127], besides the pre-buckling phase, the authors made a step forward and studied the post-critical behavior of unstiffened curved panels under shear, within the same ranges of parameters. In particular, two principal objectives of the study were: *i*) to investigate the influence of the key parameters (*i.e.* curvature parameter Z and aspect ratio α) on the post-buckling behavior of a perfect curved panel; *ii*) to assess the effect of the shapes and the amplitudes of the initial imperfections in case of imperfect panels. Therefore, a series of geometrical and material nonlinear analysis with imperfection included (GMNIA) were carried out, which led to some advances in the knowledge on the behavior of curved panels under shear. Namely, moderately curved panels, similar to flat plates, are characterized by a rather stable post-critical response and considerable post-buckling capacities. On the other hand, the increased curvature leads to a dominant shell-like behavior, with a highly unstable and imperfection sensitive post-buckling response. Regarding the imperfection shape, similar to findings from Featherston, the authors state that it is sufficient to consider the first eigenmode shape for lower and intermediate curvatures, whereas for the higher curvatures, the authors recommend to combine the first two or first four modes in order to obtain the lowest resistance. In what concerns the imperfection amplitudes, the authors claim that only the initial post-buckling response is affected, whereas the ultimate load remains practically unchanged.

To sum up, although these studies contributed to increased knowledge on the post-critical behavior of unstiffened curved panels under pure shear, no clear design rules for the assessment of the ultimate shear load were developed, at least not for any desired aspect ratio and curvature parameter. Instead, the authors propose two possible methods for the design of cylindrically curved panels under shear. In the first (simplified) method, it is necessary to calculate the elastic

critical load (analytically or numerically), where the ultimate load is, then, obtained by applying empirical reduction factors that account for the imperfections and plasticity. Most of the design standards comply with this method; however, as Featherston stated, the main drawback is the definition of the reduction factors for various boundary and load conditions. In the second method, the ultimate load is directly obtained from a numerical non-linear analysis (GMNIA), in which imperfections and plasticity are explicitly introduced in the models. However, owing to the lack of standardized geometric imperfection shapes and amplitudes in the way it exists for flat plates, an imperfection sensitivity study needs to be carried out each time, which is the main restriction of this method. This iterative process of guessing the *critical* imperfection shape might be time-consuming and thus impractical for design purposes.

Hence, the only available design guidance for the prediction of the ultimate shear resistance of shells and curved panels are recently published standards for oil & gas industry structures (DNV-RP-202), as well as for marine industry structures (DNVGL-CG-0128) presented in [section 2.5](#) with the other available procedures. Nevertheless, in 2018, Martins *et al.* [17] revised and compared these two standards with the numerical results for a wide range of curvature parameters and a significant deviation in results was noticed, especially for the lower and intermediate values of curvatures. This discrepancy is justified by a lack of data on geometric imperfections that were used in the semi-empirical expressions provided in the standards. In addition, the standard DNVGLCG-0128 is mainly applicable for ship hull structures with higher curvature parameters ($R/t \leq 2500$); while for the lower curvatures, the standard unjustifiably suggests the use of the design methodology for flat plates, which is a very conservative approach.

Based on the literature review, there is apparently plenty of space for improvements in this field. Thus, one of the principal goals of this thesis is to propose a formulae-wise methodology, allowing the computation of the ultimate shear resistance of unstiffened simply supported curved panels with various edge in-plane constraints, applicable for curvatures and aspect ratios within the ranges that may be of the practical use in offshore, aeronautics and bridge applications. This problem is addressed in [chapter 4](#) and [chapter 5](#), where the expressions for the critical shear load and ultimate shear load are proposed, respectively.

2.5 Procedures for the computation of the ultimate resistance of curved panels

In contrast to flat plates, robust and physically consistent design formulations able to deal with all the specific features inherent to curved panels are generally not available. Thus, the objective of this section is to summarize all design procedures available in the literature to assess the ultimate resistance of curved panels. The section is divided into three parts, each of them providing the available design rules, relevant for the work covered in this thesis: *i*) design rules for the isolated panels under compression; *ii*) design rules for the isolated panels under shear loading; and *iii*) design rules for the box-girder bridge cross-section.

The standard procedures available in EN 1993-1-5 for the determination of the ultimate compression and ultimate shear resistance for flat plates are also demonstrated, being an extreme case of curved panels (*i.e.* $Z = 0$). Regarding the rules for the box-girder cross-section, only the

procedure for the trapezoidal box-girder available in EN 1993-1-5 is presented since no proposal for the cross-section containing curved bottom flange is still available.

2.5.1 Design rules for panels in axial compression

2.5.1.1 Flat plates – EN 1993-1-5:2006

The design rules for unstiffened and stiffened flat plates, based on the *effective width method*, are provided in section 4 of EN 1993-1-5. In section 10, the standard provides alternatively the reduced stress method; however, this procedure is not presented in this thesis.

The effective width method, which was introduced by von Kármán *et al.* [108] in 1932, is a simplified method for the determination of the ultimate load of a plated element. According to this method, after the buckling occurs, the central portion of the plate loses its stiffness, which causes a stress redistribution towards the stiffer outstand parts, located along the unloaded longitudinal edges. Therefore, after the buckling occurs, the load is carried only by these two strips of equal width that together compose so-called effective width, until the ultimate load is reached. Although the stress distribution, in reality, is non-linear, von Kármán adopted a linear (*i.e.* uniform) distribution acting only on the *effective* parts of the cross-section, whereas the contribution of the buckled central parts is completely neglected in the cross-section resistance. Finally, assuming that the stresses along the effective parts of the plate (b_{eff}) at the ultimate limit state are equal to the yielding stress (f_y), the characteristic compressive resistance of a flat plate, N_{Rk} , may be derived using Eq.(2.22):

$$N_{Rk} = A_{eff} f_y = b_{eff} t f_y = \rho b t f_y = \frac{1}{\bar{\lambda}} b t f_y \quad (2.22)$$

where A_{eff} is cross-section's effective area, ρ is the reduction factor and $\bar{\lambda}$ is the relative slenderness parameter, calculated as a function of the elastic critical stress (σ_{cr}) by Eq.(2.23) as:

$$\bar{\lambda} = \sqrt{\frac{f_y}{\sigma_{cr}}} \quad (2.23)$$

Although the concept of the effective width method remained the same, the expressions for the reduction factor used in the standard have been somewhat modified and updated in time, accounting for a wider range of slenderness parameter, and for the influence of the initial imperfections. The design rules from EN 1993-1-5 for flat plates are divided into two groups: *i*) unstiffened plate elements (section 4.4 of EN 1993-1-5); and *ii*) stiffened plate elements (section 4.5 of EN 1993-1-5). The most relevant steps of these two design procedures are summarized in this section.

i) Unstiffened plate elements:

In the case of unstiffened plates, characterized by a plate-type buckling (column-type buckling might be relevant only for very small values of aspect ratio) the total cross-section effective width is obtained as a sum of effective widths of each sub-panel that builds the cross-section. Depending on the position of a sub-panel in the cross-section, the effective width formulae (*i.e.*

reduction factor formulae) are defined either by Eq.(2.24) for internal compressed elements or by Eq.(2.25) for outstand compressed elements.

$$\rho = \begin{cases} 1.0 & \text{if } \bar{\lambda} < 0.5 + \sqrt{0.085 - 0.055\psi} \\ \frac{\bar{\lambda} - 0.055(3 + \psi)}{\bar{\lambda}^2} & \text{if } \bar{\lambda} \geq 0.5 + \sqrt{0.085 - 0.055\psi} \end{cases} \quad (2.24)$$

$$\rho = \begin{cases} 1.0 & \text{if } \bar{\lambda} < 0.748 \\ \frac{\bar{\lambda} - 0.188}{\bar{\lambda}^2} & \text{if } \bar{\lambda} \geq 0.748 \end{cases} \quad (2.25)$$

In these expressions, ψ is the stress ratio ($\psi = 1.0$ for pure compression), whereas $\bar{\lambda}$ is the relative slenderness parameter, calculated in general by Eq.(2.23), or simplified by Eq.(2.26) as:

$$\bar{\lambda} = \frac{b_i/t}{28.4\varepsilon\sqrt{k_{\sigma,pl}}} \quad \text{with} \quad \varepsilon = \sqrt{\frac{235}{f_y}} \quad (2.26)$$

where $k_{\sigma,pl}$ is the elastic buckling coefficient for flat plates (for uniform compression, $k_{\sigma,pl} = 4.0$ for internal elements and $k_{\sigma,pl} = 0.43$ for outstand elements, *i.e.* stiffeners), whereas b_i is the corresponding width of each subpanel.

ii) Stiffened plate elements:

In the case of stiffened plates, the calculation of the ultimate compressive resistance is far more complex. The process may be divided into three major steps:

I. Determination of the *local buckling* reduction factor ρ_{loc} for each subpanel of width b_{loc} (see Fig. 2.1b), using the design rules for unstiffened plate elements (Eq.(2.24) and Eq.(2.25)).

II. Determination of the *global buckling* of the entire stiffened element, which requires the calculation of three reduction factors:

- Reduction factor ρ for plate-type buckling
- Reduction factor χ_c for column-type buckling
- Final global reduction factor ρ_c

III. Determination of the effective area of the stiffened plate, using Eq.(2.27) as:

$$A_{c,eff} = \rho_c A_{c,eff,loc} + \sum b_{i,edge,eff} t \quad (2.27)$$

where ρ_c is previously addressed global reduction factor, and $A_{c,eff,loc}$ presents the effective section areas of all the subpanels and stiffeners that are fully or partially in the compression zone, excluding the effective parts supported by an adjacent plate element with the width $b_{edge,eff}$ (see Fig. 2.22), calculated using Eq.(2.28).

$$A_{c,eff,loc} = A_{st,eff} + \sum_c \rho_{loc} b_{c,loc} t \quad (2.28)$$

In this expression, $A_{st,eff}$ presents the sum of the effective sections of all longitudinal stiffeners with gross area A_{sl} located in the compression zone, obtained using the rules for the unstiffened

plate elements. Finally, $b_{c,loc}$ and ρ_{oc} are the local width and the corresponding reduction factor, calculated for each subpanel in compression using the rules for unstiffened elements, except the parts $b_{edge,eff}$ (see Fig. 2.22).

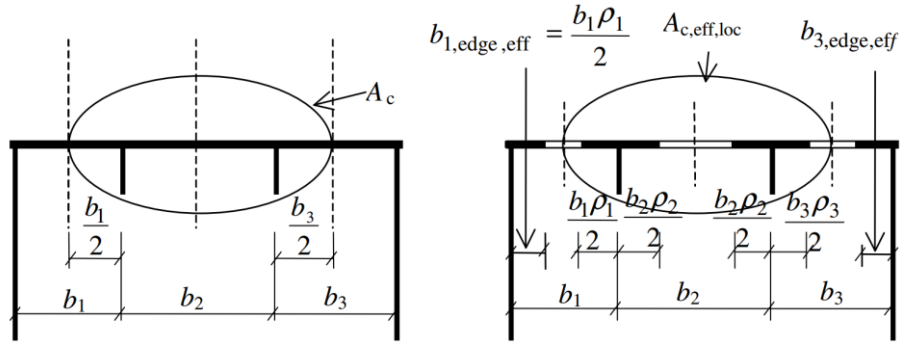


Fig. 2.22: Effective area of a stiffened plate under uniform compression (EN 1993-1-5 [11])

In Eq.(2.27), in order to determine the effective area, it is necessary to calculate the final reduction factor ρ_c by interpolation between χ_c and ρ , using Eq.(2.29), where the interpolation parameter ξ is a function of the elastic critical plate buckling stress ($\sigma_{cr,p}$) and the elastic critical column buckling stress ($\sigma_{cr,c}$) determined by Eq.(2.30) as:

$$\rho_c = (\rho - \chi_c)\xi(2 - \xi) + \chi_c \tag{2.29}$$

$$\xi = \frac{\sigma_{cr,p}}{\sigma_{cr,c}} - 1 \quad \text{but} \quad 0 \leq \xi \leq 1 \tag{2.30}$$

A typical ($\chi_c - \rho$) interpolation diagram is presented in Fig. 2.23. It is important to emphasize that the plate-type behavior prevails only in the case of unstiffened plates, or lightly stiffened plates with larger aspect ratios. Therefore, for the aspect ratios that are commonly encountered in the engineering applications (*i.e.* bridges), it is to expect that the column-type buckling is the governing instability mode ($\xi \rightarrow 0$), regardless of the level of stiffening, meaning that the plate-type buckling verification may be completely ignored. Finally, it is necessary to determine the critical stress and the reduction factor, both for plate-type and column-type behavior.

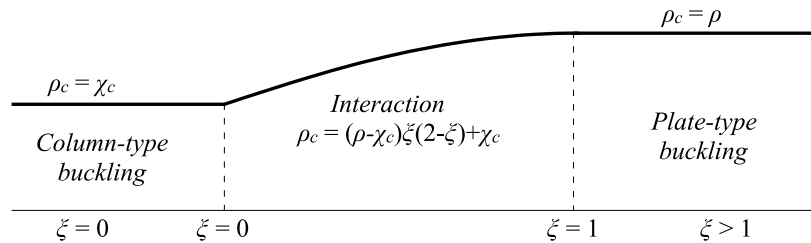


Fig. 2.23: Column-type and plate-type interpolation

- Plate-type buckling:

The reduction factor ρ for the equivalent orthotropic plate is obtained using the expression for the unstiffened plates (see Eq.(2.24) and Eq.(2.25)), where the relative slenderness parameter $\bar{\lambda}_p$ is obtained by Eq.(2.31) as:

$$\bar{\lambda}_p = \sqrt{\frac{\beta_{A,c} f_y}{\sigma_{cr,p}}} \quad \text{with} \quad \beta_{A,c} = \frac{A_{c,eff,loc}}{A_c} \quad (2.31)$$

where $A_{c,eff,loc}$ is defined by Eq.(2.28), A_c is the gross area of the compression zone of the stiffened plate, without the parts $b_{edge,eff}$ (see Fig. 2.22) and $\sigma_{cr,p}$ is the elastic critical plate buckling stress, determined in accordance with Annex A of EN 1993-1-5. Namely, depending on the number of longitudinal stiffeners (*i.e.* one, two or more), the standard correspondingly provides rules for the critical load.

In the case of a plate with a single longitudinal stiffener in the compression zone, a simplified expression for the critical stress is provided, given by Eq.(2.32) as:

$$\sigma_{cr,p} = \frac{1.05E}{A_{sl,1}} \frac{\sqrt{I_{sl,1} t^3 b}}{b_1 b_2} \quad \text{if} \quad a \geq a_c \quad (2.32)$$

$$\sigma_{cr,p} = \frac{\pi^2 E I_{sl,1}}{A_{sl,1} a^2} + \frac{E t^3 b a^2}{4\pi^2 (1-\nu^2) A_{sl,1} b_1^2 b_2^2} \quad \text{if} \quad a \leq a_c$$

where $A_{sl,1}$ is the gross area of the stiffener, $I_{sl,1}$ is the second moment of area of the stiffener about the axis parallel to the plane of plate, a and b are the length and the width of the plate, b_1 and b_2 are the distances from the longitudinal (unloaded) edges to the stiffener, so that $b = b_1 + b_2$, whereas a_c is calculated using Eq.(2.33) as:

$$a_c = 4.33 \sqrt{\frac{I_{sl,1} b_1^2 b_2^2}{t^3 b}} \quad (2.33)$$

For calculation of $A_{sl,1}$ and $I_{sl,1}$, the *stiffener* should be considered as the gross area not only of the stiffener itself, but also of the adjacent parts of the plate, with a portion $(3 - \psi)/(5 - \psi)$ of its width b_1 and $2/(5 - \psi)$ of its width b_2 , which lays at the edge with the highest stress. Subsequently, in the case of a plate that is fully in compression ($\psi = 1.0$), the adjacent parts of the plate are equal to $0.5b_1$ and $0.5b_2$, respectively.

If the stiffened plate has two longitudinal stiffeners in the compression zone, the same procedure for one stiffener may be applied (see Eq.(2.32)), where the elastic critical plate buckling stress should be taken as the lowest of the three possible cases, *i.e.* with $b_1 = b_1^*$, $b_1 = b_2^*$, and $b_1 = B^*$ (see Fig. 2.24).

First, it is assumed that one of the stiffeners is a rigid support, while the other buckles, which corresponds to the first two cases: case 1 (see Fig. 2.24a) with $A_{sl,I}$ and $I_{sl,I}$ and case 2 (see Fig. 2.24b) with $A_{sl,II}$ and $I_{sl,II}$. Subsequently, a simultaneous buckling of the two stiffeners is accounted for by considering a single lumped stiffener (case 3, see Fig. 2.24c). The substitution of two stiffeners into a lumped one is done in two steps. First, its area and its second moment of area should be replaced by the sum of that for the individual stiffeners (*i.e.* $A_{sl,III} = A_{sl,I} + A_{sl,II}$ and $I_{sl,III} = I_{sl,I} + I_{sl,II}$). Second, the position of the lumped stiffener needs to be determined as the resultant of the respective forces in the individual stiffeners. In the case of a uniform axial compression, the position of the lumped stiffener lays in the middle between two stiffeners.

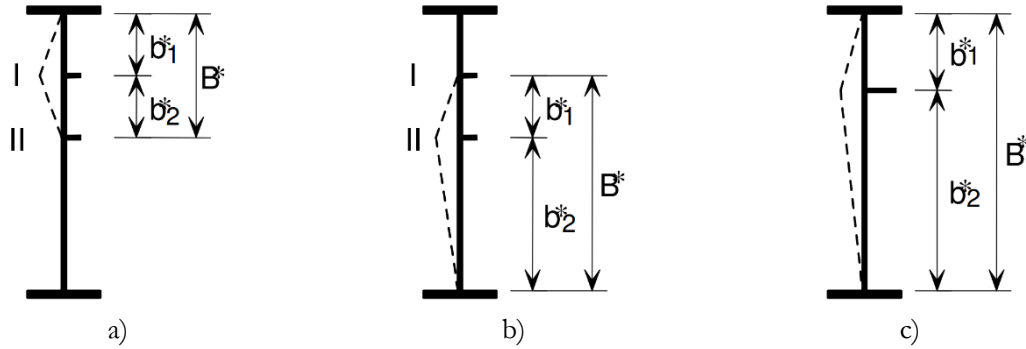


Fig. 2.24: Plates with two stiffeners in compression (EN 1993-1-5 [11])

Finally, for plates with three or more stiffeners, which standard treats as *equivalent orthotropic plates*, the elastic critical plate buckling stress is calculated by Eq.(2.6), where the elastic buckling coefficient $k_{\sigma,p}$ is obtained using Eq.(2.34).

$$k_{\sigma,p} = \frac{2 \left[(1 + \alpha^2)^2 + \gamma - 1 \right]}{\alpha^2 (1 + \psi)(1 + \delta)} \quad \text{if} \quad \alpha \leq \sqrt[4]{\gamma} \quad (2.34)$$

$$k_{\sigma,p} = \frac{4(1 + \sqrt{\gamma})}{(1 + \psi)(1 + \delta)} \quad \text{if} \quad \alpha > \sqrt[4]{\gamma}$$

Therefore, the coefficient $k_{\sigma,p}$ depends on:

- the aspect ratio α : see Eq.(2.1);
- the ratio between the flexural stiffness of the entire stiffened plate and that of sheet plate alone: $\gamma = I_{st}/I_p$, ($I_p = bt^3/12(1-\nu^2)$);
- the ratio between the gross area of the stiffeners (*i.e.* the sum of all stiffeners, without adjacent plates) and that of the sheet plate alone: $\delta = \Sigma A_{st}/A_p$, ($A_p = bt$);
- and the ratio between the larger and the smaller edge stress: $\psi = \sigma_2/\sigma_1$, ($\psi = 1.0$ for uniform compression).

▪ Column-type buckling:

The column-type behavior is based on a simple assumption that the longitudinal (unloaded) edges are not supported so that the critical stress of a plate corresponds to the buckling stress of a column. Since the stiffeners are commonly equivalent in practice, the determination of the critical stress can be carried out on a representative part, consisting of the stiffener alone and an adjacent width of the plate closest to the most compressed edge. The considered *column* is assumed to be compressed on both edges, thus having the buckling length equal to the plate length a .

The reduction factor χ_c for this instability mode is determined by Eq.(2.35), using the buckling curves, provided in clause 6.3.1.2 (1) of EN 1993-1-1 [76] that present the reduction factor as a function of the relative slenderness parameter, defined by Eq.(2.36) as:

$$\chi_c = \frac{1}{\phi + \sqrt{\phi^2 - \bar{\lambda}_c^2}} \quad \text{with} \quad \phi = 0.5 \left[1 + \alpha_e (\bar{\lambda}_c - 0.2) + \bar{\lambda}_c^2 \right] \quad (2.35)$$

$$\bar{\lambda}_c = \sqrt{\frac{\beta_{A,c} f_y}{\sigma_{cr,c}}} \quad \text{with} \quad \beta_{A,c} = \frac{A_{sl,1,eff}}{A_{sl,1}} \quad (2.36)$$

where $A_{sl,1,eff}$ and $A_{sl,1}$ are respectively the effective and the gross cross-sectional area of the stiffener with the adjacent parts of the plate sheet, determined in accordance with Fig. 2.22 for the plate-type buckling, whereas $\sigma_{cr,c}$ is the elastic critical column buckling stress, determined by Eq.(2.37) as the critical stress of the stiffener ($\sigma_{cr,sl}$) closest to the panel edge with the highest compressive stress:

$$\sigma_{cr,c} = \sigma_{cr,sl} = \frac{\pi^2 EI_{sl,1}}{A_{sl,1} a^2} \quad (2.37)$$

where $A_{sl,1}$ and $I_{sl,1}$ are respectively the gross area and the second moment of area of the stiffener about the axis parallel to the plane of the adjacent plating.

Finally, in Eq.(2.35), α_e presents the equivalent imperfection factor that is obtained by Eq.(2.38) as:

$$\alpha_e = \alpha + \frac{0.09}{i/e} \quad \text{with} \quad i = \sqrt{\frac{I_{sl,1}}{A_{sl,1}}} \quad (2.38)$$

where α is the imperfection factor (adopted as $\alpha = 0.34$ for closed cross-section stiffeners and $\alpha = 0.49$ for open cross-section stiffeners), and e is the larger of distances e_1 (between the centre of gravity of the stiffener alone G_{st} and the entire stiffener with the adjacent plate G_{sl}) and e_2 (between the adjacent plating alone G_p and the entire stiffener with the adjacent plate G_{sl}), according to Fig. 2.25.

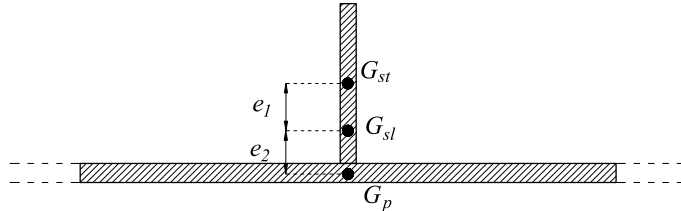


Fig. 2.25: Definition of distances e_1 and e_2

Finally, once the effective area A_{eff} is determined, the design compressive resistance, N_{Rd} , is calculated according to Eq.(2.39), where γ_{M0} is the partial factor for cross-section checks defined by standard (recommended value is $\gamma_{M0} = 1.0$).

$$N_{Rd} = \frac{A_{eff} f_y}{\gamma_{M0}} \quad (2.39)$$

2.5.1.2 Unstiffened curved panels

As discussed in 2.4.1, several authors proposed the design rules for the assessment of the ultimate resistance for the unstiffened curved panels under axial compression. In Table 2.4, the design procedures available in the literature are summarized, including the rules prescribed by the design standards.

Table 2.4: Available design procedures for unstiffened curved panels under compression

Author	Ref.	Year	Range of validity
Tran	[8]	2012	$Z \leq 100$; $\alpha = 1$, simply-supported
Tran <i>et al.</i>	[75]	2012	$Z \leq 100$; $\alpha = 1$, simply-supported
Tran <i>et al.</i>	[77]	2014b	$0.01 \leq t/b \leq 0.04$; $0.6 \leq \alpha \leq 1.6$; $0 \leq Z \leq 26$
Martins <i>et al.</i>	[78]	2014	$Z \leq 100$; simply-supported
Kim <i>et al.</i>	[80]	2014	$5^\circ \leq \beta \leq 30^\circ$, simply-supported
Park <i>et al.</i>	[16]	2018	$1.0 \leq \alpha \leq 5.0$, $5^\circ \leq \beta \leq 45^\circ$ simply-supported
DNV-RP-C202	[13]	2017	simply-supported
DNVGL-0128	[14]	2018	$R/t \leq 2500$; simply-supported
ABS	[15]	2018	$E/9f_y \leq R/t \leq 500$; simply-supported

- **Tran (2012):**

The approach provides an expression, Eq.(2.40), for the reduction factor ρ , in a similar format as the procedure given in EN 1993-1-6, which is then multiplied by the plastic resistance of the panel ($N_{pl} = btf_f$), giving its ultimate strength.

$$\rho = \begin{cases} 1.0 & \text{if } \bar{\lambda} \leq \bar{\lambda}_0 \\ 1 - \beta_Z \left(\frac{\bar{\lambda} - \bar{\lambda}_0}{\bar{\lambda}_p - \bar{\lambda}_0} \right)^\eta & \text{if } \bar{\lambda}_0 \leq \bar{\lambda} \leq \bar{\lambda}_p \\ \frac{\alpha_Z}{\bar{\lambda}^2} & \text{if } \bar{\lambda}_p \leq \bar{\lambda} \end{cases} \quad (2.40)$$

with

$$\bar{\lambda}_0 = 0.2 + 0.473 e^{-\frac{Z}{20}} \quad (2.41)$$

$$\bar{\lambda}_p = 0.673 + 0.54 e^{-\frac{4}{Z}} \quad (2.42)$$

$$\beta_Z = 0.54 e^{-\frac{2.7}{Z}} \quad (2.43)$$

$$\alpha_Z = A_Z \bar{\lambda} + B_Z \quad (2.44)$$

$$A_Z = \frac{1 + e^{-\frac{Z}{33}}}{2} \quad (2.45)$$

$$B_Z = (1 - \beta_Z) \bar{\lambda}_p^2 - A_Z \bar{\lambda}_p \quad (2.46)$$

where $\bar{\lambda}_0$ is the squash limit relative slenderness (*i.e.* the initial plateau length), α_Z is the elastic imperfection reduction, β_Z is the plastic range factor, η is an interaction exponent ($\eta = 1.0$), and $\bar{\lambda}_p$ is the slenderness limiting the elastic-plastic domain of the response of cylindrically curved panels. The relative slenderness parameter $\bar{\lambda}$ is obtained using the same general expression as for the flat plates (see Eq.(2.23)), where the critical stress σ_{cr} is determined by Eq.(2.6), with the elastic buckling coefficient, $k_{\sigma,Z}$, calculated using Stowell's expression (see Eq.(2.9)).

▪ **Tran *et al.* (2012):**

This design approach is based on the procedure given in EN 1993-1-5 (*i.e.* Ayrton-Perry methodology), and similar to the previous method, the expression (2.47) defines the reduction factor ρ applied to the plastic resistance N_{pl} .

$$\rho = \begin{cases} 1.0 & \text{if } \bar{\lambda} \leq \bar{\lambda}_0 \\ \frac{2\beta_Z}{\beta_Z + \bar{\lambda} + \sqrt{(\beta_Z + \bar{\lambda})^2 - 4\beta_Z(\bar{\lambda} - \alpha_Z(\bar{\lambda} - \bar{\lambda}_0))}} & \text{if } \bar{\lambda} > \bar{\lambda}_0 \end{cases} \quad (2.47)$$

with

$$\bar{\lambda}_0 = 0.2 + 0.473(0.95^Z) \quad (2.48)$$

$$\beta_Z = \frac{1 + 0.97^Z}{2} \quad (2.49)$$

where α_Z is the elastic imperfection reduction factor, obtained as a function of curvature Z according to Table 2.5.

Table 2.5: Definition of α_Z (Tran *et al.* [75])

Z	0	10	20	30	≥ 40
α_Z	0.28	0.38	0.33	0.21	0.13

The relative slenderness parameter $\bar{\lambda}$ is obtained using respectively Eq.(2.23), Eq.(2.6) and Eq.(2.9), as explained in the previous method by the same author.

▪ **Tran *et al.* (2014b):**

This methodology provides Eq.(2.50) for the reduction factor ρ that is applied to the plastic resistance N_{pl} .

$$\rho = (-0.09 + 0.326\alpha - 0.148\alpha^2) + (40.6 + 0.314Z)\left(\frac{t}{b}\right) - (444 + 8.4Z)\left(\frac{t}{b}\right)^2 \quad (2.50)$$

where the aspect ratio and the curvature are defined by Eq.(2.1) and Eq.(2.2), respectively.

▪ **Martins *et al.* (2014):**

The design rules are divided into two groups since the authors initially derived expressions for short curved panels only ($\alpha \leq 1.0$), which was subsequently extended to account for long panels ($\alpha > 1.0$). Although the proposed rules allow also for pure in-plane bending ($\psi = -1$), here are presented only those for the uniform axial compression ($\psi = 1$), relevant for this thesis.

i) Short curved panels ($\alpha \leq 1.0$):

The methodology is based on EN 1993–1-5 (*i.e.* effective width concept) and it requires determination of the reduction factor ρ , by Eq.(2.51), which is multiplied by the plastic resistance N_{pl} to define the ultimate resistance.

$$\rho = \begin{cases} 1.0 & \text{if } \bar{\lambda} \leq \bar{\lambda}_{0,Z} \\ \frac{\bar{\lambda}_{0,p} - \bar{\lambda} - \rho_{0,Z} (\bar{\lambda} - \bar{\lambda}_{0,Z})}{\bar{\lambda}_{0,p} - \bar{\lambda}_{0,Z}} & \text{if } \bar{\lambda}_{0,Z} \leq \bar{\lambda} \leq \bar{\lambda}_{0,p} \\ \frac{\bar{\lambda} - 0.22\alpha_Z}{c_Z \bar{\lambda}^2} + S_Z & \text{if } \bar{\lambda}_{0,p} \leq \bar{\lambda} \end{cases} \quad (2.51)$$

with

$$\bar{\lambda}_{0,Z} = 0.2 + 0.473(0.95^Z) \quad (2.52)$$

$$\bar{\lambda}_{0,p} = 0.5 + \sqrt{0.085 - 0.055\psi} = 0.673 \quad (2.53)$$

$$\rho_{0,Z} = \frac{\bar{\lambda}_{0,p} - 0.22\alpha_Z}{c_Z \bar{\lambda}_{0,p}^2} + S_Z \quad (2.54)$$

where α_Z , c_Z and S_Z are numerically calibrated parameters, defined in Table 2.6, where intermediate values are obtained by linear interpolation.

Table 2.6: Definition of α_Z , c_Z and S_Z (Martins *et al.* [78])

	α_Z	c_Z	S_Z
$Z = 0$	1	1	0
$Z = 10$	1	1.29	0.06
$Z = 23$	1	1.15	-0.04
$Z = 100$	0.545	1.7	-0.04

The relative slenderness parameter $\bar{\lambda}$ is obtained using Eq.(2.23), with the critical stress σ_r determined by Eq.(2.6), where the elastic buckling coefficient, $k_{\sigma,Z}$, is calculated using one of two proposals from the author, Eq.(2.11) or Eq.(2.12).

ii) Long curved panels ($\alpha > 1.0$):

The reduction factor ρ for long panels ($\alpha > 1.0$) is obtained by Eq.(2.55), where ρ is the reduction factor for short panels (see Eq.(2.51)), and C_{long} is a numerically generated correction factor in function of Z , with the values equal to 1.0, 0.782 and 0.912, for curvatures $Z = 1$, $Z = 30$ and $Z = 70 - 100$, respectively (intermediate values are obtained by linear interpolation).

$$\rho_{long} = C_{long} \rho \quad (2.55)$$

▪ **Kim *et al.* (2014):**

The reduction factor ρ , which is multiplied by the plastic resistance N_{pl} to obtain the ultimate resistance, is given by Eq.(2.56) as:

$$\rho = C_F \left(\frac{2.25}{\lambda_\beta} - \frac{1.25}{\lambda_\beta^2} \right) \quad (2.56)$$

with

$$C_F = \frac{C_a}{\lambda_\beta^2} + \frac{C_b}{\lambda_\beta} + C_c \quad (2.57)$$

$$C_a = 3.434 \left(\frac{b}{R} \right)^2 - 1.989 \left(\frac{b}{R} \right) + 0.646 \quad (2.58)$$

$$C_b = -4.138 \left(\frac{b}{R} \right)^2 + 1.934 \left(\frac{b}{R} \right) - 1.023 \quad (2.59)$$

$$C_c = 1.001 \left(\frac{b}{R} \right)^2 - 0.181 \left(\frac{b}{R} \right) + 1.382 \quad (2.60)$$

where λ_β is double slenderness ratio, which in contrast to the previously presented methods, may be obtained independently from the critical stress, using Eq.(2.61) as:

$$\lambda_\beta = \frac{b}{t} \sqrt{\frac{f_y}{E}} \quad (2.61)$$

▪ **Park et al. (2018):**

The ultimate resistance is again obtained by multiplying the reduction factor and the plastic resistance, $N_{Rk} = \rho(Af_f)$, where the expression for the reduction factor ρ , is given by Eq.(2.62) as:

$$\rho = \begin{cases} 1.0 & \text{if } \lambda_{\beta,Z} < 1.0 \\ \frac{2}{\lambda_{\beta,Z}} - \frac{1}{\lambda_{\beta,Z}^2} & \text{if } \lambda_{\beta,Z} > 1.0 \end{cases} \quad (2.62)$$

with a modified slenderness parameter $\lambda_{\beta,Z}$ that accounts for the ratio of the buckling load of a flat plate, and that of a curved plate, given by Eq.(2.63) as:

$$\lambda_{\beta,Z} = \frac{b}{t} \sqrt{\frac{f_y}{E}} \sqrt{\frac{k_{\sigma,pl}}{k_{\sigma,Z}}} \quad (2.63)$$

where $k_{\sigma,pl}$ is the elastic buckling coefficient of a flat plate ($k_{\sigma,pl} = 4.0$ for uniform compression), and $k_{\sigma,Z}$ is the elastic buckling coefficient of a curved plate. It is important to stress that authors suggest the use of linear buckling analysis (LBA) for the determination of $k_{\sigma,Z}$, not providing any specific expression. Therefore, in this thesis, the expression by Martins (see Eq.(2.11)) is to be considered.

▪ **DNV-RP-C202 (2017):**

According to this standard, the reduction factor ρ is obtained using Eq.(2.64), which is multiplied by the plastic resistance N_{pl} to obtain the ultimate resistance of simply-supported curved panels.

$$\rho = \frac{1}{\sqrt{1 + \bar{\lambda}^4}} \quad (2.64)$$

The relative slenderness parameter $\bar{\lambda}$ is obtained using Eq.(2.23), with the critical stress σ_{cr} determined by Eq.(2.6), where the elastic buckling coefficient, $k_{\sigma,Z}$, is calculated according to Eq.(2.65) as:

$$k_{\sigma,Z} = 4 \sqrt{1 + \left(\frac{0.702 Z_b \cdot 0.5 \left(1 + \frac{R}{150t} \right)^{-0.5}}{4} \right)^2} \quad (2.65)$$

where Z_b is Batdorf's curvature parameter, defined by Eq.(2.3).

▪ **DNVGL-CG-0128 (2018):**

The standard provides specifications to assess the reduction factor ρ , defined by Eq.(2.66), which is multiplied by the plastic resistance N_{pl} to obtain the ultimate resistance of simply-supported curved panels.

$$\rho = \begin{cases} 1 & \text{if } \bar{\lambda} \leq 0.25 \\ 1.233 - 0.933\bar{\lambda} & \text{if } 0.25 \leq \bar{\lambda} \leq 1 \\ \frac{0.3}{\bar{\lambda}^3} & \text{if } 1 \leq \bar{\lambda} \leq 1.5 \\ \frac{0.2}{\bar{\lambda}^2} & \text{if } \bar{\lambda} > 1.5 \end{cases} \quad (2.66)$$

The relative slenderness parameter $\bar{\lambda}$ is obtained by Eq.(2.23), with the critical stress σ_{cr} determined from Eq.(2.6), where the elastic buckling coefficient, $k_{\sigma,Z}$, is calculated according to Eq.(2.67) as:

$$k_{\sigma,Z} = \begin{cases} 1 + \frac{2}{3} \frac{a^2}{Rt} & \text{if } \frac{a}{R} \leq 0.5 \sqrt{\frac{R}{t}} \\ 0.267 \frac{a^2}{Rt} \left[3 - \frac{a}{R} \sqrt{\frac{t}{R}} \right] \geq 0.4 \frac{a^2}{Rt} & \text{if } \frac{a}{R} > 0.5 \sqrt{\frac{R}{t}} \end{cases} \quad (2.67)$$

▪ **ABS (2018):**

According to this standard, the ultimate load is obtained by multiplication of the *reduced* critical stress, $\sigma_{cr,R}$, by the corresponding area of the cross-section, $N_{Rk} = \sigma_{cr,R}bt$. Namely, the critical load of a perfect curved panel, defined by Eq.(2.6), is reduced by means of knockdown factors to account for the influence of the initial imperfection, leading to Eq.(2.68) as:

$$\sigma_{cr,R} = \begin{cases} \sigma_{cr,R,0} & \text{if } \sigma_{cr,R,0} \leq 0.6 f_y \\ f_y \left[1 - 0.24 \frac{f_y}{\sigma_{cr,R,0}} \right] & \text{if } \sigma_{cr,R,0} > 0.6 f_y \end{cases} \quad (2.68)$$

with

$$\sigma_{cr,R,0} = \rho_\lambda \rho_Z \sigma_{cr} \quad (2.69)$$

$$\rho_\lambda = \begin{cases} 1.15 & \text{if } \lambda_n > 1 \\ 1 + 0.15\lambda_n & \text{if } \lambda_n \leq 1 \end{cases} \quad (2.70)$$

$$\rho_Z = \begin{cases} 1 - 0.019Z_b^{1.25} + 0.0024Z_b \left(1 - \frac{R}{300t}\right) & \text{if } Z_b \leq 11.4 \\ 0.27 - \frac{1.5}{Z_b} + \frac{27}{Z_b^2} + 0.008\sqrt{Z_b} \left(1 - \frac{R}{300t}\right) & \text{if } Z_b > 11.4 \end{cases} \quad (2.71)$$

$$\lambda_n = \sqrt{\frac{f_y}{\rho_Z \sigma_{cr}}} \quad (2.72)$$

The critical load of a perfect curved panel, σ_{cr} , is defined by Eq.(2.6), where the elastic buckling coefficient $k_{\sigma,Z}$, is obtained by Eq.(2.73) as:

$$k_{\sigma,Z} = \begin{cases} 4 + \frac{3Z_b^2}{\pi^4} & \text{if } Z_b \leq 11.4 \\ 0.702Z_b & \text{if } Z_b > 11.4 \end{cases} \quad (2.73)$$

2.5.1.3 Stiffened curved panels

The design rules for the assessment of the ultimate resistance for the stiffened curved panels under axial compression are discussed in 2.4.1 and summarized in Table 2.7, where additionally the rules prescribed by the design standards are presented.

Table 2.7: Available design procedures for stiffened curved panels under compression

Author	Ref.	Year	Range of validity
Tran	[8]	2012	$Z_{loc} \leq 100$; simply-supported
Tran <i>et al.</i>	[59]	2014a	$\alpha \leq 1.25$; simply-supported
Tran <i>et al.</i>	[77]	2014b	$0.67 \leq \alpha \leq 1.5$; $0 \leq 1/R \leq 0.1$; $5 \leq n_s \leq 20$
Seo <i>et al.</i>	[82]	2016	$0^\circ \leq \beta \leq 45^\circ$, simply-supported; T-stiffeners
OUTBURST	[85]	2019	$Z_{loc} \leq 100$; simply-supported
DNV-RP-C202	[13]	2017	simply-supported
ABS	[15]	2018	$E/9f_y \leq R/t \leq 500$; simply-supported

▪ **Tran (2012):**

The proposed methodology is based on the procedure available in EN 1993-1-5 for longitudinally stiffened flat plates, presented in 2.5.1.1. Hence, the ultimate resistance is obtained by multiplying the effective area with the yield strength (*i.e.* $N_{Rk} = A_{eff}f_y$). To obtain the effective area, the same three steps as for the flat plates have to be undertaken:

I. Determination of the *local buckling* reduction factor ρ_{oc} for each curved subpanel of width b_{loc} , in order to obtain $A_{e,eff,loc}$ (Eq.(2.28)), using the design rules for unstiffened curved panels

developed by the same author (Eq.(2.40) or Eq.(2.47)). Fig. 2.26 illustrates the effective area $A_{c,eff,loc}$ accounting for local buckling.

II. Determination of the *global buckling* of the entire stiffened element, which requires the calculation of three reduction factors: *i)* ρ for plate-type buckling; *ii)* χ_c for column-type buckling and *iii)* ρ_c global reduction factor obtained by interpolation of a column-type and plate-type buckling.

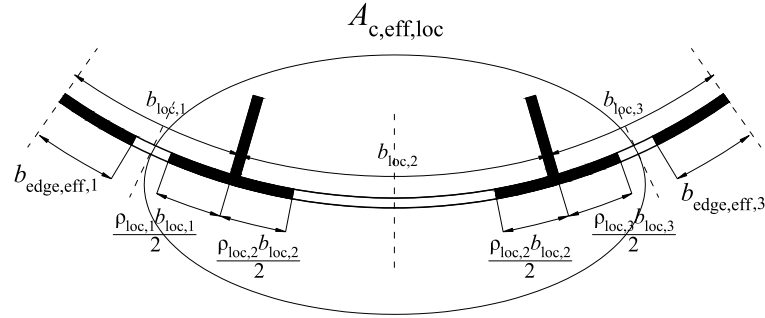


Fig. 2.26: Effective area of a stiffened curved panel under uniform compression

- Plate-type buckling:

To determine the reduction factor ρ due to plate-type buckling, the author combined the rules for the plate-type behavior of a flat stiffened plate, prescribed by EN 1993-1-5, with the ones for unstiffened curved panels, presented in 2.5.1.2. Namely, the relative slenderness $\bar{\lambda}$ is obtained as a function of elastic critical stress for plate-type behavior, by Eq.(2.31) calculated using the Stowell's expression (Eq.(2.9)), where Z corresponds to the global curvature, and $k_{\sigma,p}$ is calculated for a corresponding flat plate, assuming the same width b and the distances between the stiffeners, b_{loc} . Subsequently, the reduction factor ρ is determined using one of two procedures, proposed by the authors for the unstiffened panels, Eq.(2.40) or Eq.(2.47), substituting the global curvature Z with the corresponding local curvature Z_{loc} in each intermediate step.

- Column-type buckling:

The reduction factor due to column-type behavior χ_c is obtained according to the rules for flat plates presented, assuming the buckling curve C ($\alpha = 0.49$), whereas the geometrical properties (*i.e.* the area and inertia) required to obtain critical column stress are evaluated for the entire gross cross-section of the panel (shell and stiffeners) and not on a single strut model. This means that in equations Eq.(2.36) - Eq.(2.38), the values $A_{sl,1}$ and $I_{sl,1}$ should be substituted by A_{sl} and I_{sl} , respectively.

- Interpolation between plate-type and column-type buckling:

To determine the final reduction factor ρ_c that accounts for the interaction between two instability phenomena, the authors proposed a new expression, given by Eq.(2.74) as:

$$\rho_c = \chi_c + (\rho - \chi_c) \frac{1}{0.95 + \frac{0.04}{\xi} + \frac{0.01}{\xi^2}} \quad (2.74)$$

where the interpolation parameter ξ may be determined using the same expression (2.30), prescribed by EN 1993-1-5; however, ξ may be lower than 0.

III. Determination of the effective area of the stiffened curved plate, $A_{e,eff}$, is done according to EN 1993-1-5, using Eq.(2.27).

▪ **Tran et al. (2014a):**

In this simplified design methodology, the authors neglected the plate-type buckling of a stiffened panel, which automatically excludes also the interpolation between the two buckling phenomena. Thus, for the assessment of the ultimate resistance, the following steps need to be undertaken (similar to the procedure from EN 1993-1-5):

I. Determination of the *local buckling* reduction factor ρ_{oc} for each curved subpanel of width b_{oc} , in order to obtain $A_{e,eff,loc}$ (Eq.(2.28)), using the design rules prescribed by EN 1993-1-5, neglecting the local curvature (see Eq.(2.24) - Eq.(2.26)).

II. Determination of the reduction factor χ_c for column-type buckling according to Eq.(2.35)-Eq.(2.38), substituting the geometrical properties of a single strut model ($A_{st,1}$ and $I_{st,1}$) by gross cross-section of the entire panel (A_{st} and I_{st}), and assuming the buckling curve C ($\alpha = 0.49$). It is necessary to stress that for determination of ℓ in Eq.(2.38), the distances ℓ_1 is the distance between the centre of gravity of all stiffeners alone G_{st} (without panel sheet) and the entire stiffened panel G_{st} , whereas the distance ℓ_2 is the distance between the curved panel sheet alone G_p and the entire stiffened panel G_{st} .

III. Determination of the ultimate (characteristic) resistance N_{Rk} by Eq.(2.22), where the effective area of the curved stiffened panels is obtained by Eq.(2.27), with $\rho_c = \chi_c$.

▪ **Tran et al. (2014b):**

The authors proposed a simplified expression (2.75), which directly returns the ultimate resistance N_{Rk} [in MN], valid within the ranges defined in Table 2.7.

$$\begin{aligned} N_{Rk} = & 17.09 - 0.47X_1 + 3.58X_2 + 4.24X_3 + 7.32X_4 - 3.87X_5 + 4.83X_6 \\ & + 2.33X_7 + 1.65X_2X_4 - 1.72X_2X_5 + 1.71X_2X_6 + 0.89X_2X_7 + 1.33X_3X_4 \\ & - 0.76X_3X_5 - 1.73X_4X_5 + 0.81X_4X_6 - 1.18X_5X_6 + 0.94X_6X_7 \end{aligned} \quad (2.75)$$

where the required parameters X_i are given in Table 2.8, with the corresponding ranges of validity of geometric parameters defined in Fig. 2.1.

Table 2.8: Definition of parameters X_i

Parameter X_i	Range of validity [m]
$X_1 = a - 5$	$4 \leq a \leq 6$
$X_2 = b - 5$	$4 \leq b \leq 6$
$X_3 = 200t - 3$	$0.01 \leq t \leq 0.02$
$X_4 = 20/R - 1$	$0 \leq 1/R \leq 0.1$
$X_5 = 4b_{loc} - 2.2$	$0.3 \leq b_{loc} \leq 0.8$
$X_6 = 20h_{st} - 3$	$0.1 \leq h_{st} \leq 0.2$
$X_7 = 200t_{st} - 3$	$0.01 \leq t_{st} \leq 0.02$

▪ **Seo *et al.* (2016):**

The ultimate resistance is obtained by multiplying the reduction factor and the plastic resistance, $N_{Rk} = \rho(A_f f)$, where the expression for the reduction factor ρ , is given by Eq.(2.76) as:

$$\rho = \begin{cases} \frac{1}{\sqrt{0.0683 + 0.994\lambda_{\beta,Z} + 0.0065\lambda_{\beta,Z}^2}} & \text{if } \beta \leq 5^\circ \\ \frac{1}{\sqrt{1.1339 - 0.1291\lambda_{\beta,Z} + 0.0392\lambda_{\beta,Z}^2}} & \text{if } \beta > 5^\circ \end{cases} \quad (2.76)$$

with a modified relative slenderness parameter $\lambda_{\beta,Z}$ that accounts for the ratio of the buckling load of a flat plate, and that of a curved plate, given by Eq.(2.77) as:

$$\lambda_{\beta,Z} = \frac{b}{t} \sqrt{\frac{f_y}{E}} \sqrt{\frac{1}{C_B}} \quad (2.77)$$

where coefficient C_B is adopted from the study on elastic buckling behavior of unstiffened curved panels by Kim *et al.* [80], defined by Eq.(2.78) as:

$$C_B = 0.0323C_J Z_b \left(\frac{R}{t}\right)^{-0.751} \quad (2.78)$$

with

$$C_J = \begin{cases} 1.0 & \text{if } \lambda_\beta < 2.0 \\ 0.88 & \text{if } \lambda_\beta \geq 2.0 \text{ and } 0^\circ \leq \beta \leq 10^\circ \\ 1.1 & \text{if } \lambda_\beta \geq 2.0 \text{ and } 10^\circ \leq \beta \leq 30^\circ \end{cases} \quad (2.79)$$

The double slenderness ratio λ_β is defined by Eq.(2.61).

▪ **OUTBURST (2019):**

The proposed methodology is based on a combination of two design procedures [85]: *i*) the one provided by EN 1993-1-5 for longitudinally stiffened flat plates, presented in 2.5.1.1; and *ii*) the one prescribed in DNV-RP-C202 for stiffened panels, addressed in the following paragraphs. In fact, the main three steps (*i.e.* local buckling, global buckling, and effective area calculation)

are adopted from EN 1993-1-5, whereas the procedure for the elastic critical plate-type buckling is taken from DNV-RP-C202. Hence, to obtain the ultimate resistance, it is necessary to determine the effective area with the yield strength (*i.e.* $N_{Re} = A_{eff}f_y$), using the same three steps as for the flat plates:

I. Determination of the *local buckling* reduction factor ρ_{oc} for each curved subpanel of width b_{loc} , in order to obtain $A_{e,eff,loc}$ (see Eq.(2.28) and Fig. 2.26), using the design rules for unstiffened curved panels developed by Martins *et al.* [78] (see Eq.(2.51)).

II. Determination of the *global buckling* of the entire stiffened element, by calculation of three reduction factors: *i)* ρ for *shell-type* buckling; *ii)* χ_c for column-type buckling and *iii)* ρ_c global reduction factor obtained by interpolation of a column-type and shell-type buckling.

▪ Shell-type buckling:

To determine the reduction factor ρ due to shell-type buckling, the author combined the rules for the plate-type behavior of a flat stiffened plate, given by EN 1993-1-5, with the ones for unstiffened curved panels, proposed by Martins *et al.* [78].

The relative slenderness parameter $\bar{\lambda}$ is obtained using Eq.(2.23) provided that the critical stress σ_{cr} is equal to the critical shell stress $\sigma_{cr,s}$, defined for the equivalent orthotropic curved plate by Eq.(2.80) in accordance with the expression prescribed in the design standard DNV-RP-C202:

$$\sigma_{cr,s} = k_{\sigma,Za} \frac{\pi^2 E}{12(1-\nu^2)} \left(\frac{t}{a} \right)^2 \quad (2.80)$$

where the elastic buckling coefficient, $k_{\sigma,Za}$, is calculated by Eq.(2.81)

$$k_{\sigma,Za} = \gamma \sqrt{1 + \left(\frac{4\sqrt{3}Z_a}{\pi^2 \gamma} \right)^2} \quad (2.81)$$

with

$$Z_a = \frac{a^2}{Rt} \sqrt{1-\nu^2} \quad (2.82)$$

$$\gamma = \frac{1 + \frac{I_{sl,1}}{I_p}}{1 + \frac{A_{st}}{A_p}} \quad (2.83)$$

In Eq.(2.83), $I_{sl,1}/I_p$ is the ratio between the second moment of area of the gross cross-section of one longitudinal stiffener with the adjacent parts of the plate and that of the plate between stiffeners, disregarding curvature (*i.e.* $I_p = b_{loc}^3/12(1-\nu^2)$), while A_{st}/A_p is the ratio between the gross area of one stiffeners (*i.e.* $A_{st} = b_{st}t_{st}$) and that of the sheet plate between the stiffener alone (*i.e.* $A_p = b_{loc}t$).

Subsequently, the reduction factor ρ is determined from equations for the unstiffened panels proposed by Martins *et al.* [78] (see Eq.(2.51)), with the global curvature Z , defined by Eq.(2.2).

- Column-type buckling:

The reduction factor due to column-type behavior χ_c is obtained according to the proposal by Tran [8]. Namely, in Eq.(2.36) - Eq.(2.38), the values $A_{sl,1}$ and $I_{sl,1}$ (*i.e.* the geometrical properties of a single column-strut) should be respectively substituted by A_{sl} and I_{sl} (*i.e.* the gross properties of the whole cross-section).

In specific, in Eq.(2.36), $A_{c,eff,loc}$ is the effective cross-sectional area of the whole cross-section with due allowance for local curved plate buckling (see Fig. 2.26), whereas, in Eq.(2.38), e is the largest distance from the respective centroids of the plating and the stiffeners to the neutral axis of the whole cross-section.

- Interpolation between shell-type and column-type buckling:

The final reduction factor ρ_c for $Z < 100$ is obtained by interpolation between χ_c and ρ , according to expressions given by EN 1993-1-5 (see Eq.(2.29) and Eq.(2.30)), whereas for curved panels with $Z > 100$, the shell-type buckling is conservatively neglected (*i.e.* $\rho_c = \chi_c$).

III. Determination of the effective area of the stiffened curved plate, $A_{c,eff}$, is done according to EN 1993-1-5, using Eq.(2.27).

- DNV-RP-C202 (2017):

To obtain the ultimate resistance of a simply supported stiffened curved panel, the standard prescribes design rules similar to the ones for the unstiffened curved panel. Therefore, the reduction factor ρ , which is a function of the relative slenderness parameter $\bar{\lambda}$, is obtained using the same Eq.(2.64), which is applied to the plastic resistance.

The relative slenderness parameter $\bar{\lambda}$ is obtained using Eq.(2.23), provided that the critical stress σ_{cr} is defined by Eq.(2.84), as:

$$\sigma_{cr} = k_{\sigma,Za} \frac{\pi^2 E}{12(1-\nu^2)} \left(\frac{t}{a} \right)^2 \quad (2.84)$$

where the elastic buckling coefficient, $k_{\sigma,Za}$, is calculated by Eq.(2.85)

$$k_{\sigma,Za} = \gamma_{eff} \sqrt{1 + \left(\frac{2\sqrt{3}Z_a}{\pi^2 \gamma_{eff}} \right)^2} \quad (2.85)$$

with Z_a defined by Eq.(2.82) and γ_{eff} obtained by Eq.(2.86).

$$\gamma_{eff} = \frac{1 + \frac{I_{sl,1,eff}}{I_p}}{1 + \frac{A_{st}}{A_{p,eff}}} \quad (2.86)$$

In Eq.(2.86), $I_{sl,1,eff}$ is the second moment of area of longitudinal stiffener including effective shell width $b_{loc,eff}$; I_p is the second moment of area of the plate between stiffeners (*i.e.* $I_p = b_{loc}^3 / 12(1-$

v^2); A_{st} is the gross area of one stiffener (i.e. $A_{st} = b_{st}t_{st}$), and $A_{p,eff}$ is the effective area of sheet plate between the stiffener alone (i.e. $A_{p,eff} = b_{loc,eff}t$).

To obtain the effective shell width ($b_{loc,eff}$), it is necessary to calculate first the reduction factor ρ_{loc} that accounts for the local buckling of subpanels (see Fig. 2.26), using expressions (2.64) and (2.65), presented among the rules for the unstiffened panels.

▪ **ABS (2018):**

The ultimate (characteristic) load N_{Rk} for a stiffened panel is obtained by Eq.(2.87).

$$N_{Rk} = \sigma_{cr,Rs} \left(\frac{A_{sl,1,eff,m}}{A_{sl,1}} \right) A \quad (2.87)$$

Therefore, the ultimate load depends on:

- the gross cross-section area: $A = bt + n_{st}b_{st}t_{st}$ (see Fig. 2.1);
- the gross area of one stiffener including shell width b_{loc} : $A_{sl,1} = b_{loc}t + b_{st}t_{st}$;
- the area of longitudinal stiffener including modified effective shell width $b_{loc,eff,m}$: $A_{sl,1,eff,m} = b_{loc,eff,m}t + b_{st}t_{st}$;
- the *reduced* critical stress for the stiffened curved panel: $\sigma_{cr,Rs}$

The modified effective shell width, $b_{loc,eff,m}$, is obtained by Eq.(2.88) as:

$$b_{loc,eff,m} = \begin{cases} \left(\frac{1.05}{\lambda_{s,m}} - \frac{0.28}{\lambda_{s,m}^2} \right) b_{loc} & \text{if } \lambda_{s,m} > 0.53 \\ b_{loc} & \text{if } \lambda_{s,m} \leq 0.53 \end{cases} \quad (2.88)$$

where $\lambda_{s,m}$ is the modified relative slenderness parameter, defined by Eq.(2.89).

$$\lambda_{s,m} = \sqrt{\frac{\sigma_{cr,Rs}}{\sigma_{cr,R,0}}} \quad (2.89)$$

In this equation, $\sigma_{cr,R,0}$ is the elastic buckling stress for imperfect curved panel between adjacent stringer stiffeners, defined by Eq.(2.69)-Eq.(2.72), whereas the *reduced* critical stress for the stiffened curved panel, $\sigma_{cr,Rs}$, defined by Eq.(2.90) as:

$$\sigma_{cr,Rs} = \begin{cases} \sigma_{cr,Rs,0} & \text{if } \sigma_{cr,Rs,0} \leq 0.6f_y \\ f_y \left[1 - 0.24 \frac{f_y}{\sigma_{cr,Rs,0}} \right] & \text{if } \sigma_{cr,Rs,0} > 0.6f_y \end{cases} \quad (2.90)$$

with elastic compressive buckling stress of imperfect stiffened shell, $\sigma_{cr,Rs,0}$, obtained as a sum of the elastic critical stress of column ($\sigma_{cr,c}$) and the elastic critical stress of shell ($\sigma_{cr,s}$).

$$\sigma_{cr,Rs,0} = \sigma_{cr,c} + \sigma_{cr,s} \quad (2.91)$$

$$\sigma_{cr,s} = 0.75 \frac{0.605E \left(\frac{t}{R} \right)}{1 + \frac{A_{st}}{A_p}} \quad (2.92)$$

$$\sigma_{cr,c} = \frac{\pi^2 EI_{sl,1,eff}}{a^2 A_{sl,1,eff}} \quad (2.93)$$

In these equations, A_{st}/A_p is the ratio between the gross area of one stiffeners (*i.e.* $A_{st} = b_{st}t_{st}$) and that of the sheet plate between the stiffener alone (*i.e.* $A_p = b_{loc}t$), whereas $A_{sl,1,eff}$ and $I_{sl,1,eff}$ are respectively the area and the second moment of area of stiffener including associated *reduced* effective shell plate width $b_{loc,eff}$, obtained by Eq.(2.94) as:

$$b_{loc,eff} = \begin{cases} \frac{0.53}{\lambda_s} b_{loc} & \text{if } \lambda_s > 0.53 \\ b_{loc} & \text{if } \lambda_s \leq 0.53 \end{cases} \quad (2.94)$$

where λ_s is the *reduced* relative slenderness parameter, defined by Eq.(2.95).

$$\lambda_s = \sqrt{\frac{f_y}{\sigma_{cr,R,0}}} \quad (2.95)$$

with $\sigma_{cr,R,0}$ being the elastic buckling stress for imperfect curved panel between adjacent stringer stiffeners, defined by Eq.(2.69)-Eq.(2.72).

2.5.2 Design rules for panels in shear

2.5.2.1 Flat plates – EN 1993-1-5:2006

Numerous design models for the prediction of the ultimate shear resistance of a flat plate (*i.e.* a plate as a web of a girder) are thoroughly summarized by Dubas & Gehri [128]. Owing to the lack of a consistent method, applicable for both unstiffened and longitudinally stiffened webs and for any aspect ratio, Höglund [130] in 1981 proposed the *rotated stress field* model, which was in this form integrated into the European standard EN 1993-1-5. The model is adapted mainly to assess the shear resistance of I-girders, thus, the ultimate shear resistance, $V_{b,Rd}$, consists of two components: *i)* contribution from the web ($V_{bw,Rd}$) and *ii)* contribution from flanges ($V_{bf,Rd}$). However, as the objective is to present a more general solution for the assessment of the shear resistance of an isolated simply supported flat plate, which may be compared with the shear resistance of an isolated simply supported curved panel studied in this thesis, the contribution from the flanges is not considered. Therefore, the ultimate resistance of a flat plate is determined according to Eq.(2.96).

$$V_{b,Rd} = V_{bw,Rd} = \frac{\chi_w b t f_y}{\sqrt{3} \gamma_{M1}} \quad (2.96)$$

where b and t correspond respectively to the width (*i.e.* web height in I-girders) and thickness of a flat plate, γ_{M1} is the partial factor for stability checks, whereas χ_w is the reduction factor for

shear buckling. Depending on the axial and flexural stiffness of the surrounding stiffeners, the standard distinguishes *non-rigid* and *rigid* end posts, thus offering two distinct solutions for the determination of the reduction factor, given by Eq.(2.97) and Eq.(2.98), respectively.

$$\chi_w = \begin{cases} \eta & \text{if } \bar{\lambda}_w < \frac{0.83}{\eta} \\ \frac{0.83}{\bar{\lambda}_w} & \text{if } \bar{\lambda}_w \geq \frac{0.83}{\eta} \end{cases} \quad (2.97)$$

$$\chi_w = \begin{cases} \eta & \text{if } \bar{\lambda}_w < \frac{0.83}{\eta} \\ \frac{0.83}{\bar{\lambda}_w} & \text{if } \frac{0.83}{\eta} \leq \bar{\lambda}_w < 1.08 \\ \frac{1.37}{0.7 + \bar{\lambda}_w} & \text{if } \bar{\lambda}_w \geq 1.08 \end{cases} \quad (2.98)$$

In these expressions, η is a parameter attributed to strain hardening, defined by the National Annexes depending on steel grade and the field of application ($\eta = 1.0 - 1.2$), and $\bar{\lambda}_w$ is the relative slenderness parameter, defined by Eq.(2.99) as:

$$\bar{\lambda}_w = \sqrt{\frac{f_y / \sqrt{3}}{\tau_{cr}}} = 0.76 \sqrt{\frac{f_y}{\tau_{cr}}} = \frac{b/t}{37.4 \cdot \varepsilon \cdot \sqrt{k_\tau}} \quad \text{with } \varepsilon = \sqrt{\frac{235}{f_y}} \quad (2.99)$$

In the case of the longitudinally stiffened plates, the slenderness has to be calculated for the entire stiffened plate, with corresponding elastic buckling coefficient k_τ and for the entire width b , but should not be lower than the slenderness of each subpanel, considered as an unstiffened panel with the appropriated $k_{\tau,i}$ and local width $b_{loc,i}$, see Eq.(2.100).

$$\bar{\lambda}_w = \max \left(\frac{b/t}{37.4 \cdot \varepsilon \cdot \sqrt{k_\tau}}; \frac{b_{loc,i}/t}{37.4 \cdot \varepsilon \cdot \sqrt{k_{\tau,i}}} \right) \quad (2.100)$$

Finally, in Annex A.3 of EN 1993-1-5, the expressions for the hand calculation of the shear buckling coefficient k_τ are provided, as follows:

i) Unstiffened plate elements:

$$k_\tau = \begin{cases} 4.0 + 5.34 \left(\frac{1}{\alpha} \right)^2 & \text{if } \alpha < 1.0 \\ 5.34 + 4.0 \left(\frac{1}{\alpha} \right)^2 & \text{if } \alpha \geq 1.0 \end{cases} \quad (2.101)$$

ii) Stiffened plate elements:

- Panels with 1 or 2 longitudinal stiffeners and $\alpha < 3.0$:

$$k_\tau = 4.1 + \frac{6.3 + 0.18 \frac{I_{st}}{t^3 b}}{\alpha^2} + 2.2 \sqrt[3]{\frac{I_{st}}{t^3 b}} \quad (2.102)$$

- Panels with 1 or 2 longitudinal stiffeners and $\alpha \geq 3.0$, as well as the panels with more than two longitudinal stiffeners:

$$k_{\tau} = \begin{cases} 4.0 + 5.34 \left(\frac{1}{\alpha}\right)^2 + k_{\tau sl} & \text{if } \alpha < 1.0 \\ 5.34 + 4.0 \left(\frac{1}{\alpha}\right)^2 + k_{\tau sl} & \text{if } \alpha \geq 1.0 \end{cases} \quad (2.103)$$

with

$$k_{\tau sl} = 9 \left(\frac{1}{\alpha}\right)^2 \sqrt[4]{\left(\frac{I_{sl}}{t^3 b}\right)^3} > \frac{2.1}{t} \sqrt[3]{\frac{I_{sl}}{b}} \quad (2.104)$$

Where I_{sl} is the second moment of area of the longitudinal stiffener determined around the z-z axis with an effective plate width equal to $15\epsilon t$ on each side of the stiffener but not larger than a half of the corresponding width b_{loc} between two stiffeners (see Fig. 2.27). For plates with two or more longitudinal stiffeners, I_{sl} is obtained simply as the sum of all individual stiffeners regardless of being equally spaced or not.

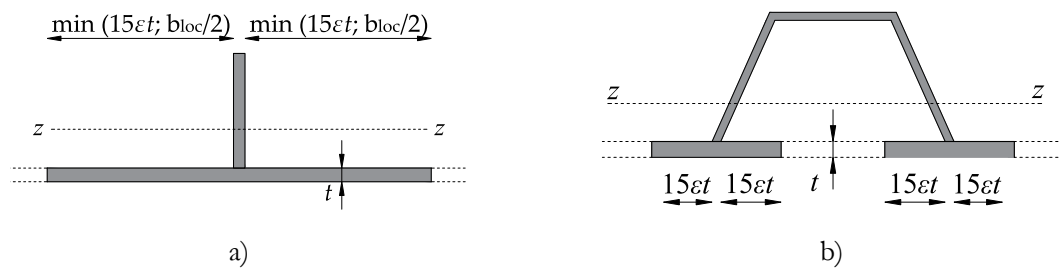


Fig. 2.27: Effective cross-section of stiffeners

2.5.2.2 Unstiffened curved panels

The design rules for the assessment of the ultimate resistance of the unstiffened curved panels under shear are discussed in 2.4.2. In Table 2.9, the design procedures available in the literature are summarized, including the rules provided by the design standards.

Table 2.9: Available design procedures for unstiffened curved panels under shear

Author	Ref.	Year	Range of validity
Domb & Leigh	[41]	2002	$Z \leq 200$; $\alpha \geq 4$, simply-supported
Machaly <i>et al.</i>	[126]	2010	$0.5 \leq \alpha \leq 1.0$; $2 \leq Z \leq 10$, simply-supported
DNV-RP-C202	[13]	2017	simply-supported
DNVGL-0128	[14]	2018	$R/t \leq 2500$; simply-supported

- **Domb & Leigh (2002):**

To assess the ultimate resistance of a curved panel, the methodology from EN 1993-1-5 should be applied (*i.e.* Eq.(2.97) and Eq.(2.99)), where for the determination of the shear buckling

coefficient k_τ , the expression (2.17) is to be used, developed by the authors to account for the curvature Z and initial imperfections.

▪ **Machaly et al. (2010):**

The authors proposed a formula that returns the ultimate shear load for a horizontally curved I-girder web panel, given by Eq.(2.105) as:

$$V_R = 0.58at(0.7C + 0.3) \frac{f_y}{\sqrt{3}} \quad (2.105)$$

where the coefficient C is the ratio between the ultimate shear load and the shear yield strength, and depending on the a/t ratio may be obtained respectively by one of three branches in Eq.(2.106) that represent one of three governing failure mechanisms (*i.e.* yielding, inelastic buckling or elastic buckling), where the shear buckling coefficient k_τ is determined by Eq.(2.18) proposed by the authors.

$$C = \begin{cases} 1.0 & \text{if } \frac{a}{t} \leq 1.10 \sqrt{\frac{Ek_\tau}{f_y / \sqrt{3}}} \\ 1.10 \left(\frac{t}{a}\right) \sqrt{\frac{Ek_\tau}{f_y / \sqrt{3}}} & \text{if } 1.10 \sqrt{\frac{Ek_\tau}{f_y / \sqrt{3}}} < \frac{a}{t} \leq 1.39 \sqrt{\frac{Ek_\tau}{f_y / \sqrt{3}}} \\ 1.51 \left(\frac{t}{a}\right)^2 \frac{Ek_\tau}{f_y / \sqrt{3}} & \text{if } \frac{a}{t} > 1.39 \sqrt{\frac{Ek_\tau}{f_y / \sqrt{3}}} \end{cases} \quad (2.106)$$

▪ **DNV-RP-C202 (2017):**

Similar to the design methodology used in EN 1993-1-5, to obtain the ultimate shear resistance of a simply supported curved panel it is necessary to multiply the shear reduction factor χ_w with the plastic shear resistance, according to Eq.(2.96). The reduction factor χ_w is obtained using Eq.(2.107) as:

$$\chi_w = \frac{1}{\sqrt{1 + \bar{\lambda}_w^4}} \quad (2.107)$$

The relative slenderness parameter $\bar{\lambda}_w$ is obtained using Eq.(2.99), with the critical stress τ_{cr} determined by Eq.(2.15), where the buckling coefficient, k_τ , is calculated from Eq.(2.108) as:

$$k_\tau = \left[5.34 + 4 \left(\frac{1}{\alpha} \right)^2 \right] \sqrt{1 + \frac{\left(0.856 Z_b^{3/4} \cdot 0.6 \sqrt{\frac{1}{\alpha}} \right)^2}{\left[5.34 + 4 \left(\frac{1}{\alpha} \right)^2 \right]}} \quad (2.108)$$

where Z_b is Batdorf's curvature parameter, defined by Eq.(2.3).

▪ **DNVGL-CG-0128 (2018):**

The standard provides specifications to assess the shear reduction factor χ_w , defined by Eq.(2.109), which is applied to the plastic shear resistance to obtain the ultimate resistance of simply supported curved panels.

$$\chi_w = \begin{cases} 1.0 & \text{if } \bar{\lambda}_w \leq 0.4 \\ 1.274 - 0.686\bar{\lambda}_w & \text{if } 0.4 < \bar{\lambda}_w \leq 1.2 \\ \frac{0.2}{\bar{\lambda}_w^2} & \text{if } \bar{\lambda}_w > 1.2 \end{cases} \quad (2.109)$$

The relative slenderness parameter $\bar{\lambda}_w$ is obtained by Eq.(2.99), with the critical stress τ_{cr} determined from Eq.(2.15), where the elastic buckling coefficient, k_τ , is calculated according to Eq.(2.110) as:

$$k_\tau = \begin{cases} \sqrt{3} \sqrt{28.3 + \frac{0.67a^3}{R^{1.5}t^{1.5}}} & \text{if } \frac{a}{R} \leq 8.7 \sqrt{\frac{R}{t}} \\ \sqrt{3} \frac{0.28a^2}{R\sqrt{Rt}} & \text{if } \frac{a}{R} > 8.7 \sqrt{\frac{R}{t}} \end{cases} \quad (2.110)$$

2.5.2.3 Stiffened curved panels

To the best of author's knowledge, the only available design rules for the assessment of the ultimate shear resistance for the longitudinally stiffened curved panels under shear are reported in the design standard DNV-RP-C202 [13].

▪ **DNV-RP-C202 (2017):**

According to the standard, if a stiffened curved panel satisfies the criterion given by Eq.(2.111), it may be considered as *lightly stiffened*, which means that the influence of the stiffeners may be neglected and the design rules presented in 2.5.2.2 for the unstiffened panels should be used.

$$\frac{b}{t} > 3\sqrt{\frac{R}{t}} \quad (2.111)$$

If this condition is not satisfied, the panel may be considered as stiffened, and the following set of rules needs to be applied. Namely, to determine the ultimate resistance of a simply supported stiffened curved panel, the standard prescribes an expression to assess the shear reduction factor χ_w , given by Eq.(2.107), which is applied to the plastic resistance.

The reduction factor χ_w is a function of the relative slenderness parameter $\bar{\lambda}_w$, obtained by Eq.(2.99), provided that the critical stress τ_{cr} is defined by Eq.(2.112), as:

$$\tau_{cr} = k_{\tau a} \frac{\pi^2 E}{12(1-\nu^2)} \left(\frac{t}{a} \right)^2 \quad (2.112)$$

where the elastic buckling coefficient, $k_{\tau a}$, is calculated by Eq.(2.113)

$$k_{\tau a} = \gamma_{w,eff} \sqrt{1 + \left(0.6 \frac{0.856 Z_a^{3/4}}{\gamma_{w,eff}} \right)^2} \quad (2.113)$$

with Z_a defined by Eq.(2.82) and $\gamma_{w,eff}$ obtained by Eq.(2.114)

$$\gamma_{w,eff} = 5.34 + 1.82 \alpha^{4/3} \sqrt[3]{\frac{I_{sl,1,eff}}{I_p}} \quad (2.114)$$

where, $I_{sl,1,eff}$ is the second moment of area of longitudinal stiffener including effective shell width $b_{loc,eff}$, I_p is the second moment of area of the plate between stiffeners (*i.e.* $I_p = b_{loc}^3 / 12(1-\nu^2)$).

Finally, to determine the effective shell width ($b_{loc,eff}$), it is necessary to calculate first the reduction factor $\chi_{w,loc}$ that accounts for the local shear buckling of subpanels, using Eq.(2.107) and Eq.(2.108) from the previous section, among the rules for the unstiffened panels.

2.5.3 Design rules for trapezoidal box-girder bridge cross-section

As stated before, one of the main objectives of this PhD thesis is to develop a moment-shear (M - V) interaction resistance model for cross-section safety verification of a box-girder bridge deck near the intermediate support, with a cylindrically curved panel located in the lower flange. Since such model is still not available in the literature for these relatively new bridge decks, the strategy is to extend the existing (M - V) interaction resistance model prescribed by EN 1993-1-5, applicable for cross-section safety checks of trapezoidal box-girder bridge decks, with a flat bottom flange. Therefore, it is necessary first, to introduce the design rules for the M - V safety verification of a trapezoidal box-girder, which is briefly presented in this section.

In general, when subjected to bending moment M_{Ed} and shear V_{Ed} , the following cross-section verifications need to be carried out:

- I. Cross-section bending resistance – $M_{b,Rd}$
- II. Cross-section shear resistance – $V_{bw,Rd}$
- III. Cross-section M - V interaction resistance (if necessary)

It is necessary to emphasize that besides these safety checks, in the case of a real bridge design, several additional verifications need to be performed depending on the load case and considered design situation (*e.g.* patch load verification, interaction between patch loading and bending moment, torsion, etc.). However, the scope of this work is strictly dedicated only to ultimate limit state (ULS) M - V interaction verification under permanent design situation, *i.e.* normal use under traffic load.

2.5.3.1 Bending resistance design model

According to EN 1993-1-1 [76], a box-girders cross-section subjected to bending moment has sufficient bending capacity in the ultimate limit state if the criterion given by Eq.(2.115) is satisfied:

$$\eta_1 = \frac{M_{Ed}}{M_{c,Rd}} \leq 1.0 \quad (2.115)$$

where M_{Ed} is the design bending moment acting on the cross-section, and $M_{c,Rd}$ is the design bending moment resistance, which depending on the cross-section class may be obtained by Eq.(2.116).

$$M_{c,Rd} = \begin{cases} M_{pl,Rd} = \frac{W_{pl} f_y}{\gamma_{M0}} & \text{for class 1 and 2 cross-section} \\ M_{el,Rd} = \frac{W_{el} f_y}{\gamma_{M0}} & \text{for class 3 cross-section} \\ M_{eff,Rd} = \frac{W_{el,eff} f_y}{\gamma_{M0}} & \text{for class 4 cross-section} \end{cases} \quad (2.116)$$

where W_{pl} and W_{el} , are respectively the plastic and elastic sectional modulus, and $W_{el,eff}$ is the section modulus considering the effective area of the section, f_y is the yield strength, and γ_{M0} is the partial factor for cross-section checks defined by standard (recommended value is $\gamma_{M0} = 1.0$).

Since the box-girder bridge decks are commonly class 4 cross-sections, being built up from very slender stiffened plates, it is required to determine effective section modulus $W_{el,eff}$ based on the effective width method that is applied to all parts of the cross-section subject to compressive stresses. Hence, the determination of the effective cross-section properties is divided into two main steps: *i*) effective cross-section of the stiffened bottom flange and *ii*) effective cross-section of the stiffened web.

i) Effective cross-section of the stiffened bottom flange:

Since the stiffened bottom flange is under pure compression at the intermediate support, the design rules for a simply supported internal plate element are used, presented in 2.5.1.1. It is important to remind that prior to the application of these rules; the thickness should be reduced to account for the shear lag effect. In this work, the reduction due to shear lag is neglected, however, for a more complete description of this procedure, the reader is invited to further investigate clause 4.4(3) in EN 1993-1-5.

ii) Effective cross-section of the stiffened web:

In contrast to the stiffened bottom flange, the web of the box-girder cross-section is under bending, with a linear distribution of the axial stresses along the height (upper part in tension), meaning that buckling may occur only in its compressed bottom part.

Therefore, the first step is to determine the stress distribution in the web, which depends on the location of the centre of gravity of the cross-section consisting of: *i*) gross area of the top flanges (in tension); *ii*) gross area of the web and *iii*) effective area of the bottom (compressed) flange calculated in the previous step.

Once the stress distribution, the web depth and the position of the stiffeners are defined, the stress parameter ψ may be determined, which presents the ratio of stresses at both edges of the plate (or sub-plate) with the maximum compression stress being in the denominator (*i.e.* $\psi = \sigma / \sigma_{c,max}$). Fig. 2.28 illustrates the most relevant notations in an example of 2-stiffened web plate, whereas Table 2.10 summarizes the expressions required for the determination of the effective properties.

Based on Fig. 2.28 and Table 2.10, it becomes possible to carry on with the calculation of the effective properties of the main web, A_{eff} , using Eq.(2.27), based on the same two steps that were required for the bottom stiffened panel: *i*) local buckling and *ii*) global buckling.

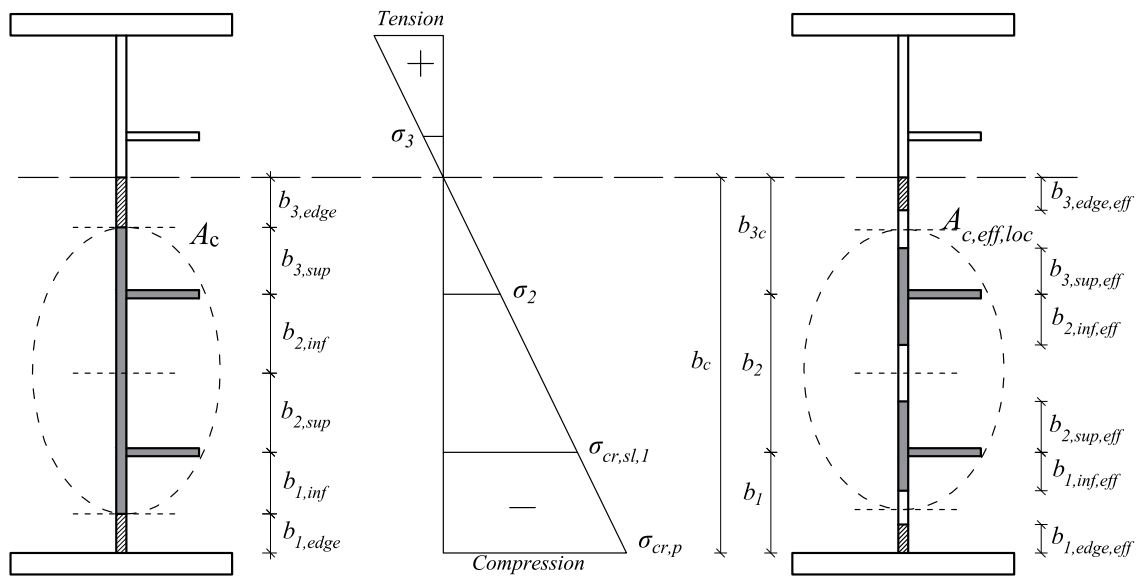


Fig. 2.28: Geometry and notations of a stiffened web plate in bending

Table 2.10: Definition of the longitudinal stiffeners – gross and effective area

	Gross area width	Effective area width	Condition for ψ_i
$b_{1,edge}$	$\frac{2}{5-\psi_1} b_1$	$\frac{2}{5-\psi_1} b_{1,eff}$	$\psi_1 = \frac{\sigma_{cr,sl,1}}{\sigma_{cr,p}} > 0$
$b_{1,inf}$	$\frac{3-\psi_1}{5-\psi_1} b_1$	$\frac{3-\psi_1}{5-\psi_1} b_{1,eff}$	$\psi_1 > 0$
$b_{2,sup}$	$\frac{2}{5-\psi_2} b_2$	$\frac{2}{5-\psi_2} b_{2,eff}$	$\psi_2 = \frac{\sigma_2}{\sigma_{cr,sl,1}} > 0$
$b_{2,inf}$	$\frac{3-\psi_2}{5-\psi_2} b_2$	$\frac{3-\psi_2}{5-\psi_2} b_{2,eff}$	$\psi_2 > 0$
$b_{3,sup}$	$0.4 b_{3c}$	$0.4 b_{3c,eff}$	$\psi_3 = \frac{\sigma_3}{\sigma_2} < 0$
$b_{3,edge}$	$0.6 b_{3c}$	$0.6 b_{3c,eff}$	$\psi_3 < 0$

I. Determination of the *local buckling* reduction factor ρ_{loc} for each subpanel, using the design rules for unstiffened plate elements (Eq.(2.24) and Eq.(2.25)), based on the relative slenderness parameter given by Eq.(2.26). However, due to a stress gradient (*i.e.* $\psi \neq 1.0$), the elastic buckling coefficient is no longer equal to $k_{\sigma,pl} = 4.0$ as it was the case with the uniformly compressed bottom flange. Depending on the previously calculated stress ratio ψ in Table 2.10, the elastic buckling coefficient for internal compressed elements is determined by Eq.(2.117) as:

$$k_{\sigma,pl} = \begin{cases} 4.0 & \text{for } \psi = 1 \\ 8.2 / (1.05 + \psi) & \text{for } 1 > \psi > 0 \\ 7.8 & \text{for } \psi = 0 \\ 7.81 - 6.29\psi + 9.78\psi^2 & \text{for } 0 > \psi > -1 \\ 23.9 & \text{for } \psi = -1 \\ 5.98(1 - \psi)^2 & \text{for } -1 > \psi > -3 \end{cases} \quad (2.117)$$

For the stiffeners, being the outstand elements in uniform compression ($\psi = 1.0$), the elastic buckling coefficient is equal to $k_{\sigma,pl} = 0.43$.

II. Determination of the *global buckling* of the entire stiffened web, which requires the calculation of three reduction factors:

- Reduction factor ρ for plate-type buckling
- Reduction factor χ_c for column-type buckling
- Final global reduction factor ρ_c

All three steps are in detail presented in 2.5.1.1. It is necessary to highlight that the elastic critical stress for column-type buckling $\sigma_{cr,c}$ is determined only for the stiffener closest to the panel edge with the highest compressive stress, using Eq.(2.37). In addition, all the required gross geometrical properties of stiffeners ($A_{sl,1}$ and $I_{sl,1}$), as well as the effective properties ($A_{sl,1,eff}$), are determined based on Fig. 2.28 and Table 2.10.

Finally, the effective section modulus $W_{el,eff}$ is calculated based on the gross area of the top flange (in tension) and the effective area of the bottom flange and webs.

2.5.3.2 Shear resistance design model

According to EN 1993-1-5, a box-girders cross-section subjected to shear force has sufficient shear capacity at ULS if the criterion given by Eq.(2.118) is satisfied:

$$\eta_3 = \frac{V_{Ed}}{V_{b,Rd}} \leq 1.0 \quad (2.118)$$

where V_{Ed} is the design shear force (including shear from torque) acting on the cross-section, and $V_{b,Rd}$ is the design shear resistance, which generally may be determined as the sum of the dominant web contribution ($V_{bw,Rd}$) and flange contribution ($V_{bf,Rd}$), given by Eq.(2.119).

$$V_{b,Rd} = V_{bw,Rd} + V_{bf,Rd} \leq \frac{\eta h_w t_w f_y}{\sqrt{3} \gamma_{M1}} \quad (2.119)$$

where b_w and t_w , are the total height and the thickness of the web, respectively, γ_{M1} is the partial factor for stability checks, and η is modification factor defined by the National Annexes depending on steel grade and the field of application ($\eta = 1.0 - 1.2$). The design model for the determination of the web contribution $V_{bw,Rd}$ is presented in 2.5.2.1, where b_w and t_w correspond to b and t , respectively. The flange contribution model ($V_{bf,Rd}$) is given in clause 5.4(1) in EN 1993-1-5, however, it is not considered in this study for the box-girder cross-sections.

Finally, for the shear resistance verification in the case of box-girders with inclined webs, it is necessary to recalculate the vertical shear force V_{Ed} to a shear force in the inclined plane of one main web (*i.e.* $V_{Ed,1} = V_{Ed}/2\sin\beta$, with β being the angle of the inclination).

2.5.3.3 M-V interaction resistance design model

The theoretical background of the M - V interaction equation is established on the assumption that the shear force acting on a girder is carried only by the web as long as the bending moment is less than the bending capacity of flanges alone. However, for larger bending moments, *e.g.* at ULS, a part of the bending moment should be also carried by the web, which consequently reduces the shear resistance of the girder. In 2017, Jáger *et al.* [131] carried out a thorough literature review on the existing M-V interaction proposals available in the literature. The majority of the studies, among which the most representative ones are those by Gerard & Becker [49] in 1957, by Rockey [132] in 1971 and by Alina & Moosavi [133] in 2009, dealt with the M-V interaction behavior of stiffened webs in I-girders.

In 1961, Basler [134] proposed the first force-based formulation of the M - V interaction equation for unstiffened girder web, given by Eq.(2.120) as:

$$\frac{M_{Ed}}{M_{pl,Rd}} + \left[1 - \frac{M_{f,Rd}}{M_{pl,Rd}} \right] \left(\frac{V_{Ed}}{V_{bw,Rd}} \right)^\beta \leq 1.0 \quad \text{if} \quad M_{Ed} \leq M_{f,Rd} \quad (2.120)$$

where $M_{f,Rd}$ is the bending resistance of the cross-section considering the effective area of the flanges alone, $M_{pl,Rd}$ is the plastic moment of resistance of the cross-section regardless of its class, $V_{bw,Rd}$ is the shear buckling resistance of the web panel alone, M_{Ed} and V_{Ed} are the applied design bending moment and shear force. The interaction coefficient is equal to $\beta = 2$.

The model proposed by Basler underwent minor alteration before it was eventually adopted by several design standards, such as EN 1993-1-5, the Swedish code K18 [135] and EN 1999-1-1 [136]. Namely, according to these standards, if the shear utilization ratio of webs is exceeded by more than 50% (*i.e.* $V_{Ed}/V_{bw,Rd} > 0.5$), the combined effects of bending and shear in the web of an I or box girder should satisfy Eq. (2.121)

$$\frac{M_{Ed}}{M_{pl,Rd}} + \left[1 - \frac{M_{f,Rd}}{M_{pl,Rd}} \right] \left(2 \frac{V_{Ed}}{V_{bw,Rd}} - 1 \right)^\beta \leq 1.0 \quad \text{if} \quad M_{Ed} \leq M_{f,Rd} \quad (2.121)$$

with the interaction coefficient equal to $\beta = 2$ in EN 1993-1-5, while in the Swedish code K18 and EN 1999-1-1 the value of $\beta = 1$ was adopted.

A slightly modified M - V interaction equation may be found in the Slovak standard STN 73 1401 [137] and the Czech standard ČSN 73 1401 [138], given by Eq.(2.122)

$$\frac{M_{Ed}}{M_{el,eff,Rd}} + \left[1 - \frac{M_{f,Rd}}{M_{el,eff,Rd}} \right] \left(2 \frac{V_{Ed}}{V_{bw,Rd}} - 1 \right)^\beta \leq 1.0 \quad \text{if} \quad M_{Ed} \leq M_{f,Rd} \quad (2.122)$$

where the main difference is that the equation uses the design effective bending moment resistance ($M_{el,eff,Rd}$) of the cross-section, instead of the plastic moment capacity ($M_{pl,Rd}$) while keeping the interaction coefficient equal to $\beta = 2$.

Finally, in the aforementioned study by Jäger *et al.* [131], a comprehensive parametric study was carried out to investigate the M - V interaction behavior of unstiffened girder webs and to assess the suitability of the proposed expressions for a wide range of geometrical parameters. It was found that the interaction coefficient in Eq.(2.122) leads to conservative results for girders with the geometry encountered in bridge applications, and thus the authors proposed a new interaction coefficient given by Eq.(2.123) as:

$$\beta = \left(\frac{M_{f,Rd}}{M_{el,eff,Rd}} + 0.2 \right)^{15} + 1 \quad (2.123)$$

In 2018, Jäger *et al.* [139] carried another numerical study, this time on the M - V interaction behavior of the stiffened girder webs, and showed that Eq.(2.122) with the interaction coefficient given by Eq.(2.123) may be also applied for the stiffened webs of I-girders in the entire range of analyzed parameters ($M_{f,Rd}/M_{el,eff,Rd} = 0.6$ – 1.0). Finally, the proposal from Jäger *et al.* [139] is adopted in prEN 1993-1-5 [140].

2.6 Summary

In this chapter, an introduction to the cylindrically curved steel panels was made and the most relevant geometrical parameters that differentiate these elements from flat plates (*e.g.* curvature Z), were identified.

Moreover, a comprehensive literature review on cylindrically curved panels was presented, highlighting some of the most significant experimental, numerical and analytical works related to this topic. Particular attention was given to the studies dealing with the curved panels loaded in compression and shear, being dominant loads in case of curved panels used as flanges in bridge deck cross-sections, as one of the main objectives of this thesis.

Due to the lack of adequate design standards, the widespread use of cylindrically curved steel panels in innovative bridge applications is hindered, which has recently inspired the research community to deepen the knowledge on these structural elements. Numerous authors proved that with the introduction of curvature the behavior of curved panels starts to differentiate positively from flat plates, providing substantial gains in resistance. Several authors even proposed numerically based empirical and semi-empirical expressions for determination of the ultimate resistance of isolated curved panels, mainly under uniform compression, which are gathered in this chapter, highlighting their limitations and ranges of validity.

Despite an increased number of numerical studies, the experimental studies on the curved panels under compression are still rather scarce, as identified in this chapter. In addition, the tests were carried out merely to show qualitatively the influence of curvature, whereas no analytical expression for the assessment of the resistance was provided. Hence, an urgent need for more experimental results was emphasized, and, in this regard, one of the main objectives of this thesis is to make a major contribution in this area, grasping a more solid insight into the experimental behavior of curved panels.

On the other hand, very few studies on the curved panels under shear have been reported in the literature and no clear design method for the assessment of the ultimate shear load was developed, at least not for any desired aspect ratio and curvature parameter. Thus, the thesis aims to propose a methodology, allowing the computation of the ultimate shear resistance of unstiffened simply supported curved panels under shear.

Finally, in this chapter, the procedures available in EN 1993-1-5 for the determination of the ultimate compression and shear resistance for flat plates were also demonstrated, being an extreme case of curved panels (*i.e.* $Z = 0$) and an important basis for the work developed in the thesis. Regarding the rules for the box-girder cross-section, only the procedure for the trapezoidal box-girder available in EN 1993-1-5 was presented since no proposal for the cross-section containing curved bottom flange is still available. The ultimate objective of this thesis, thus, is to fill the main gaps identified in the state-of-the-art and more specifically, to contribute to the extension of the existing design standards.

3. Cylindrically curved panels under pure compression

3.1 Overview

In this chapter, an experimental study on cylindrically curved steel panels is reported, carried out within the research project ULTIMATEPANEL. The study comprises 32 compression tests on both stiffened and unstiffened simply supported curved panels, with geometry that may be encountered in offshore, aeronautics and bridge applications. The aim of the test results is principally to get insight into the buckling behavior of cylindrically curved steel panels under compression, being one of the dominant loading conditions in box-girder bridge decks close to the intermediate support, where the curved panel is integrated into the lower flange of the cross-section. Thus, this chapter is fully dedicated to the research targets set in Task 2 of the thesis (see [section 1.2](#)).

The experimental program is thematically divided into three sections. In [section 3.2](#), a full description of the test setup is provided, specifying the geometry and the material properties of the specimens measured prior to the tests, but also the instrumentation used for data acquisition during the tests. The most relevant test results are described in detail and discussed in [section 3.3](#) and based on them, an assessment of the available procedures for determination of the ultimate resistance (see [section 2.5](#)) is made. Subsequently, using the experimental data, a numerical model

is built in [section 3.4](#), which is used to investigate the sensitivity to initial geometric imperfections of curved panels.

3.2 Tests setup

3.2.1 Geometry of test specimens

In total, 32 full-scale isolated curved panels are tested under axial compression. The specimens are square ($\alpha = a/b = 1$), with the length and the width equal to $a = b = 1500$ mm and a constant thickness equal to $t = 4$ mm. Four different radii are considered ($R = 2.5$ m, $R = 5.0$ m, $R = 10.0$ m and $R = 20.0$ m), comprising four groups of panels, R2.5, R5, R10, and R20, as shown in [Fig. 3.1](#).

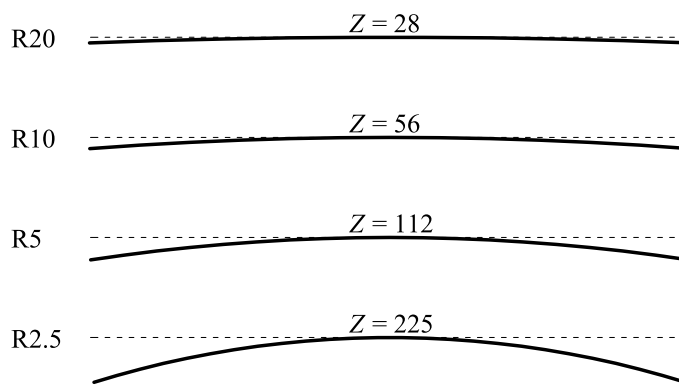


Fig. 3.1: Four groups of specimens based on radius R – R20, R10, R5 and R2.5

Based on the number of the longitudinal stiffeners (n_{st}), the specimens are divided into four sub-groups: unstiffened (S0), with one (S1), two (S2), and three (S3) stiffeners. [Fig. 3.2](#) illustrates the cross-section of these four sub-groups.

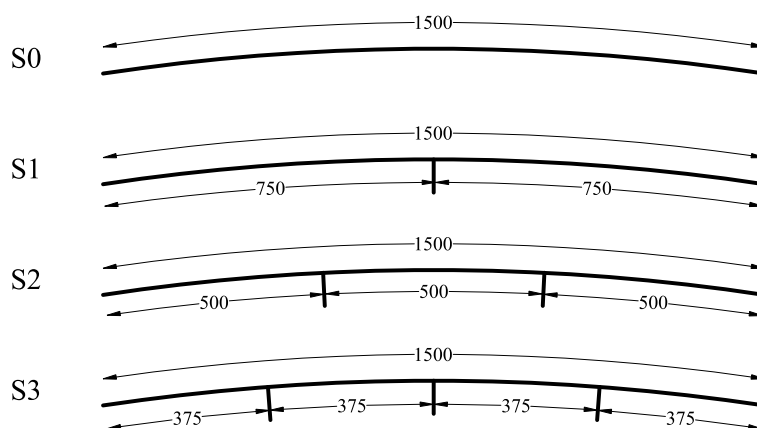


Fig. 3.2: Division of specimens based on the stiffener configuration

As it may be noticed, the stiffeners, which are welded to the curved panel by means of continuous fillet welds, are oriented radially, parallel to the generator of the cylindrical panel so

that the width of the subpanels (b_{loc}) remains equal. The stiffeners are flat, with the height and the thickness constant and equal to $h_{st} = 50$ mm and $t_{st} = 4$ mm, respectively.

[Table 3.1](#) summarizes the geometry of all tested specimens. From this table, it may be noticed that there are 16 different geometries, however, two experimental tests ($n = 2$) are performed for each panel, comprising 32 tests in total. The aspect ratios and the curvature parameters (both global and local) are obtained using expressions given in [section 2.2](#). The global curvature varies between $Z = 28$ and $Z = 225$, whereas the local curvature does not exceed the value of $Z_{loc} = 56$, which falls within the common ranges encountered in real applications (see [Fig. 2.6](#)).

Table 3.1: Geometry of the specimens

Specimen	n	R [mm]	t [mm]	a [m]	b [mm]	α	Z	n_{st}	h_{st}/t_{st} [mm]	α_{loc}	Z_{loc}
R2.5-S0	2	2500	4	1500	1500	1.0	225	0	-	-	-
R2.5-S1	2	2500	4	1500	1500	1.0	225	1	50/4	2.0	56
R2.5-S2	2	2500	4	1500	1500	1.0	225	2	50/4	3.0	25
R2.5-S3	2	2500	4	1500	1500	1.0	225	3	50/4	4.0	14
R5-S0	2	5000	4	1500	1500	1.0	112	0	-	-	-
R5-S1	2	5000	4	1500	1500	1.0	112	1	50/4	2.0	28
R5-S2	2	5000	4	1500	1500	1.0	112	2	50/4	3.0	12
R5-S3	2	5000	4	1500	1500	1.0	112	3	50/4	4.0	7
R10-S0	2	10000	4	1500	1500	1.0	56	0	-	-	-
R10-S1	2	10000	4	1500	1500	1.0	56	1	50/4	2.0	14
R10-S2	2	10000	4	1500	1500	1.0	56	2	50/4	3.0	6
R10-S3	2	10000	4	1500	1500	1.0	56	3	50/4	4.0	4
R20-S0	2	20000	4	1500	1500	1.0	28	0	-	-	-
R20-S1	2	20000	4	1500	1500	1.0	28	1	50/4	2.0	7
R20-S2	2	20000	4	1500	1500	1.0	28	2	50/4	3.0	3
R20-S3	2	20000	4	1500	1500	1.0	28	3	50/4	4.0	2

3.2.2 Material properties

All specimens are made of steel grade S355. The mechanical properties of the S355 steel are obtained by standard tensile tests according to recommendations prescribed by ASTM E8M [141] standard. The tensile coupon tests are carried out at room temperature, at a controlled speed of 5 mm/min, using an INSTRON 4026 testing machine for the load application, with 100 kN load capacity. Strain acquisition is done by an optical extensometer, GOM ARAMIS 5M, presented in [Fig. 3.3a](#). The use of such an extensometer requires careful sample preparation. Firstly, an opaque white mask is applied at samples' surface, and then, a uniform splash of black paint is added to produce a speckle pattern, which is essential for a high-quality strain measurement by digital image correlation (DIC). [Fig. 3.3b](#) shows the geometry of a specimen.

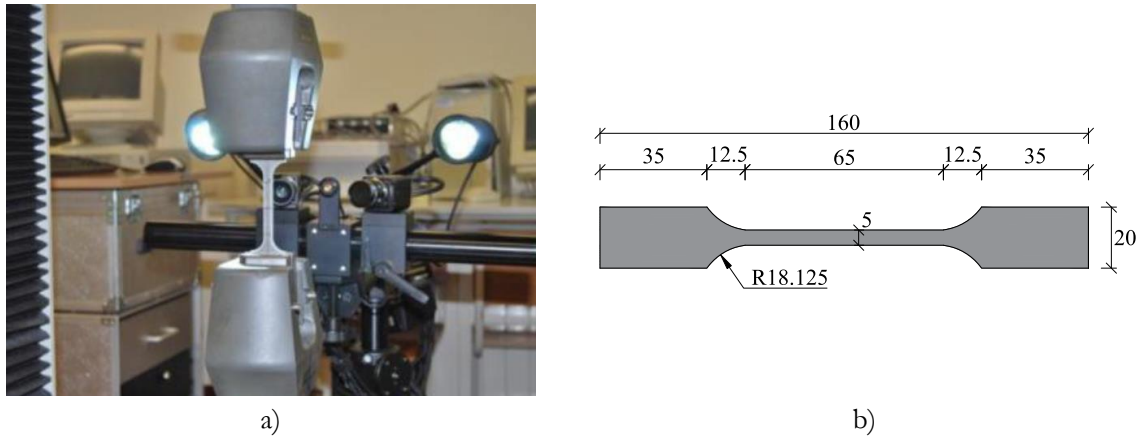


Fig. 3.3: Tensile coupon test: a) optical extensometer; b) specimen geometry

To assess the level of anisotropy of steel material, the test samples are taken in three different angles with the rolling direction RD (*i.e.* 0° , 45° , and 90°). Three coupon tests are performed for each direction (*i.e.* 9 in total) to assure the results reliability. In Fig. 3.4, true stress (σ) – true strain (ϵ) curves for three different angles with the RD are plotted.

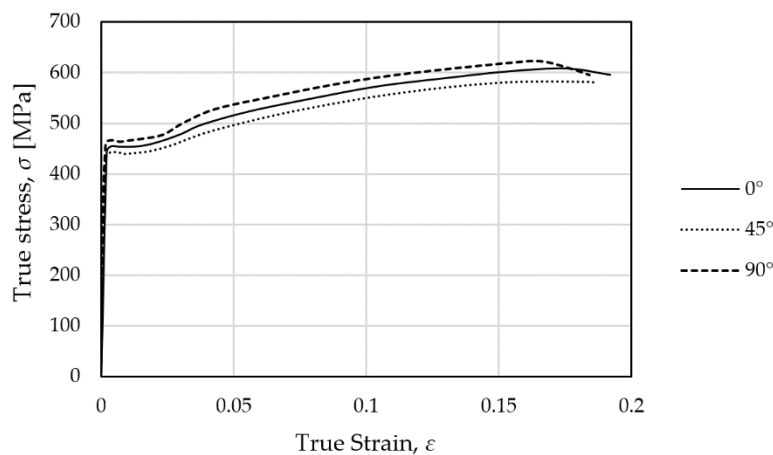


Fig. 3.4: Summarized true stress – true strain curves for three considered angles

Based on the results, it is possible to verify the excellent concordance between the curves, independently of the direction, confirming the isotropy of the S355 steel. Table 3.2 summarizes some of the most relevant mechanical properties, such as the yield strength (f_y), the tensile strength (f_u) and the ultimate strain (ϵ_u).

Table 3.2: Mechanical properties of steel S355

Angle	f_y [MPa]	f_u [MPa]	ϵ_u
0°	444	619	0.17
45°	433	581	0.175
90°	438	606	0.18

For the numerical study carried out in section 3.4, the average values of the yield and the tensile strength are considered, *i.e.* $f_y = 438$ MPa and $f_u = 602$ MPa.

3.2.3 Test layout

The test layout is presented in Fig. 3.5. It may be seen that the panels are tested in the vertical position, where the axial load is applied by a 90-ton hydraulic jack RCS-1002, placed in the middle of a rigid loading beam on the top of the specimen.

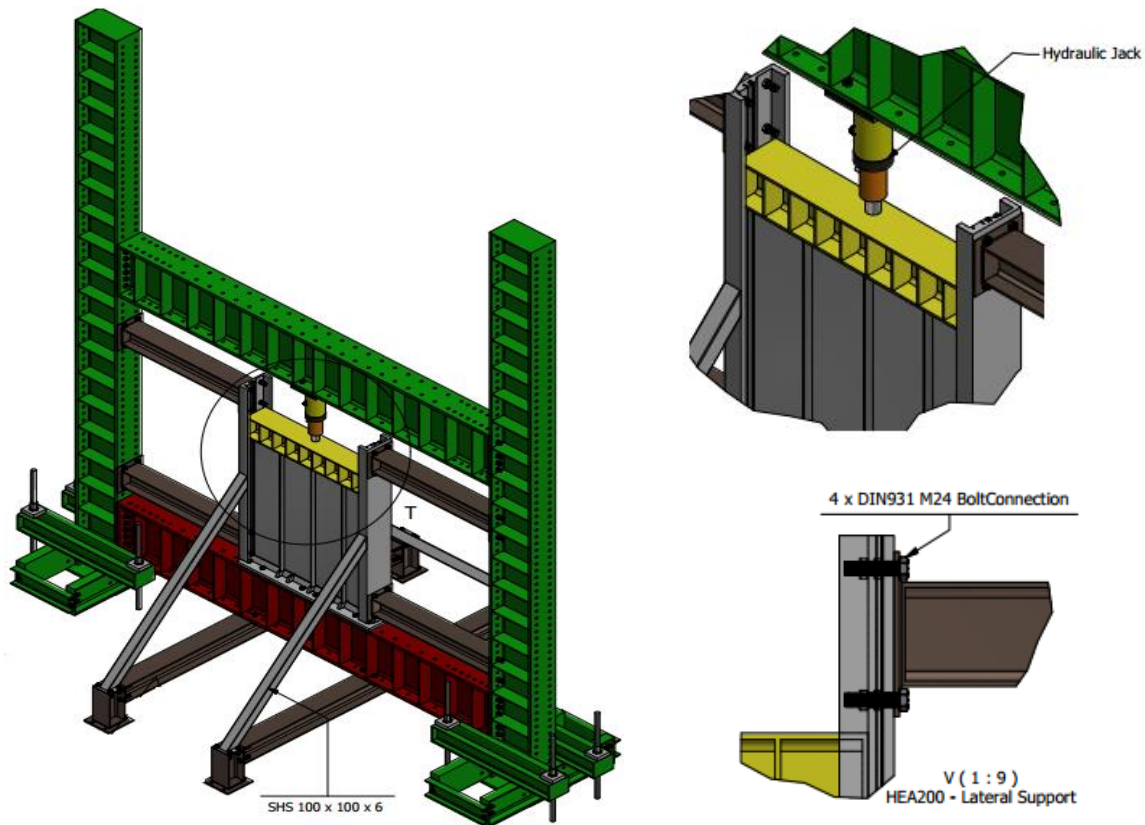


Fig. 3.5: Test layout

The panels are simply supported on all four edges. On the top and the bottom edges of a panel, these boundary conditions are ensured by two steel bars ($\text{Ø } 20 \text{ mm}$) welded to the bottom plate and the loading beam (see Fig. 3.6), thus preventing the out-of-plane displacements, but allowing rotation of a panel placed in-between two bars. The bars are fabricated to have the same radius as a corresponding panel. In addition, narrow cuts ($\approx 10 \text{ mm}$) are prepared in the bars at the position of the longitudinal stiffeners, as shown in Fig. 3.6.

Regarding the lateral edges, the simply supported boundary conditions are provided by two back-to-back L 50 x 50 x 5 angles (see Fig. 3.6) that allow for the circumferential displacements and the rotation around the vertical axis, but prevent the out-of-plane displacement of a panel. These angles are continuously connected to the flanges of two vertical UPN 280 profiles by means of bolts that enable manual adjustment of the position of the angles, required for the various radii of curvature. The width of the loading beam is chosen so it may freely slide during the load application in the vertical direction, between the flanges of UPN 280 profiles. The stability of UPN 280 profiles in-plane is achieved by two horizontal HEA 200 beams, whereas the out-of-plane movements are prevented by two inclined SHS 100 x 100 x 6 bracings, as shown in Fig. 3.5.



Fig. 3.6: Boundary conditions

3.2.4 Instrumentation

The tests are displacement controlled, with monotonously increased displacement (0.01 mm/s) up to collapse. To assess the structural response of the curved panels, the following data are recorded during the tests:

- Applied axial force
- Vertical and out-of-plane displacements
- Strains in panel

The axial force applied during the test is recorded by load cell HBM – C6A, with the capacity of 2 MN, located below the hydraulic jack, as presented in Fig. 3.7a. Since the maximum stroke of the hydraulic jack is 57 mm, several steel plates had to be added below the load cell to ensure the required vertical displacement of the specimens.

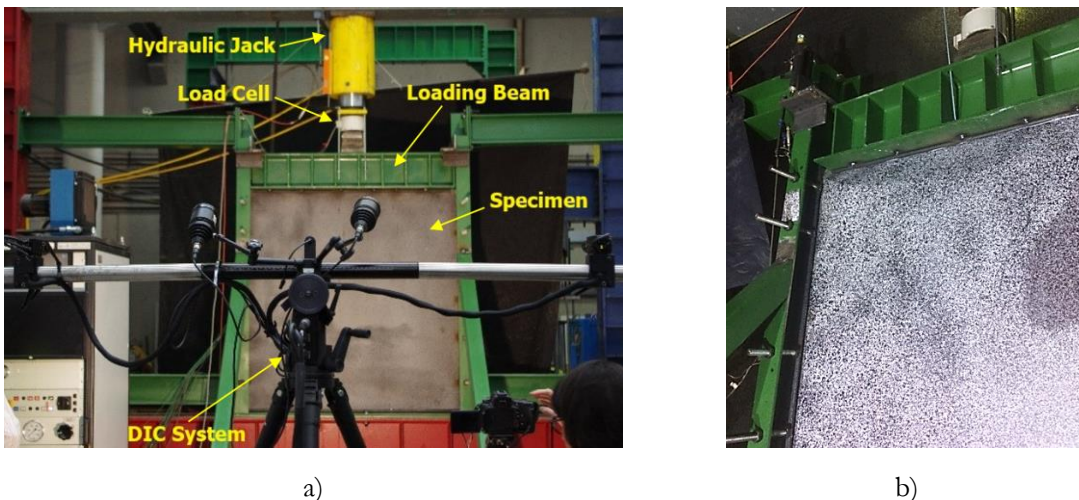


Fig. 3.7: DIC system: a) tripod with two cameras, b) speckle pattern on the outer surface

The displacements and strains during the load application are measured by an optical (non-contact) ARAMIS Digital Image Correlation (DIC) system (see Fig. 3.7a). To detect the deformation and strains of a specimen, ARAMIS uses the triangular algorithm on digital images, recorded at user-defined time intervals (*e.g.* 5 s here) during a deformation event. However, in order to obtain high image quality and full-field 3D results, it is necessary, prior to each test, to

ensure adequate conditions on the specimens' surface. Therefore, a non-repetitive isotropic pattern of black speckles, with the size of 0.5 - 3 mm, is applied on the white convex surface of the panel by canned spray paint method, as shown in Fig. 3.7b. The tripod with two CCD cameras is positioned at around 5 m distance from the panel.

In order to have more confidence in results obtained by the DIC system, for each test, 1 linear displacement transducers LVDT (V-1) is used to measure vertical (axial) displacement and another 5 LVDTs are used to measure horizontal (out-of-plane) displacements, according to the scheme in Fig. 3.8. Furthermore, in the first test of each geometry shown in Table 3.1, 16 TML FLA-6-11 strain gauges SG, positioned according to Fig. 3.9 are used to measure the strain (ε_z) in the axial z-direction (*i.e.* a direction parallel to the load application).

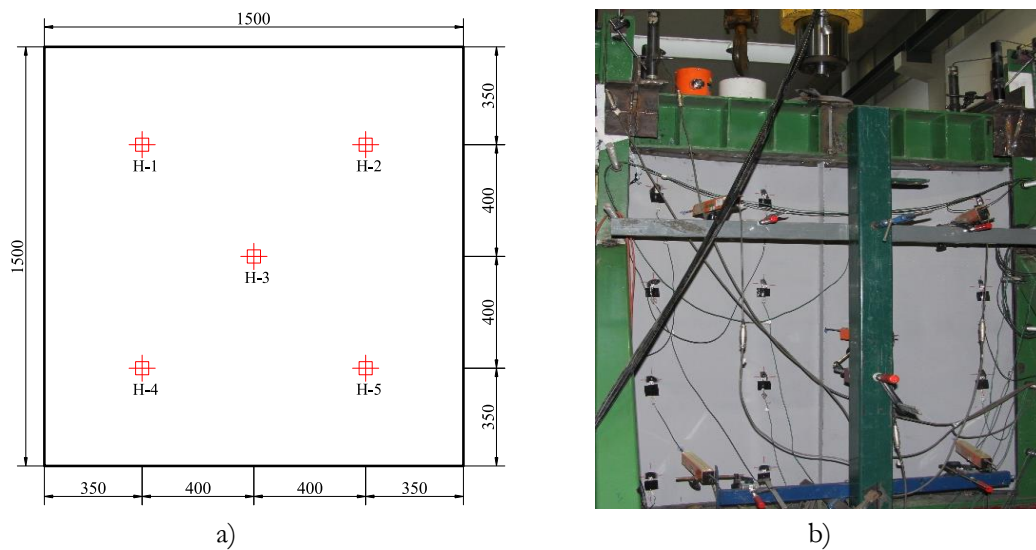


Fig. 3.8: Position of horizontal LVDTs

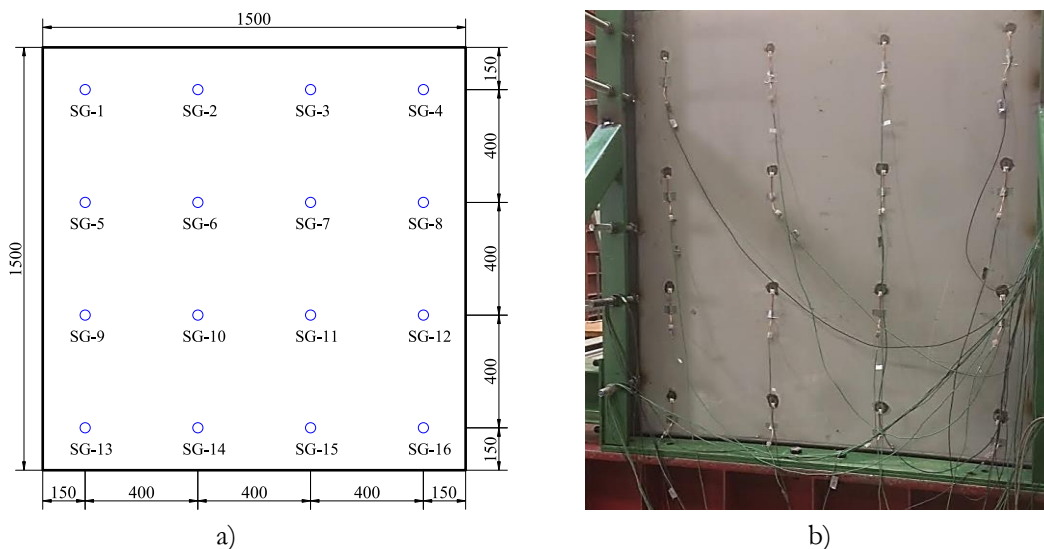


Fig. 3.9: Position of strain gauges

Both LVDTs and SGs are positioned on the inner concave surface of specimens (the side with stiffeners), whereas the measurements with the DIC system are made from the front (outer) side.

3.3 Discussion of the experimental results

3.3.1 Justification for using the DIC system

The principal objective of the experimental program is to measure the ultimate compressive strength of the curved panels, but also to assess the influence of the geometry on the buckling behavior (*i.e.* failure mode). The displacements and failure modes are recorded using the DIC system, whose validity had to be first checked. Therefore, the results of displacements and strains recorded by the DIC system are compared against those obtained by other techniques, *i.e.* LVDTs and SGs.

The comparison of two techniques based on the measured displacement field is presented in Fig. 3.10, through an example, in which the applied force F is plotted against the radial (out-of-plane) displacements u_r for specimen R20-S0-1, measured by LVDTs at points H-1, H-2, H-4, and H-5, specified in Fig. 3.8. From the figure, it may be observed that a very good correspondence between two techniques is obtained, with the maximum difference less than 1.0% between two measurements, noticed at point H-2.

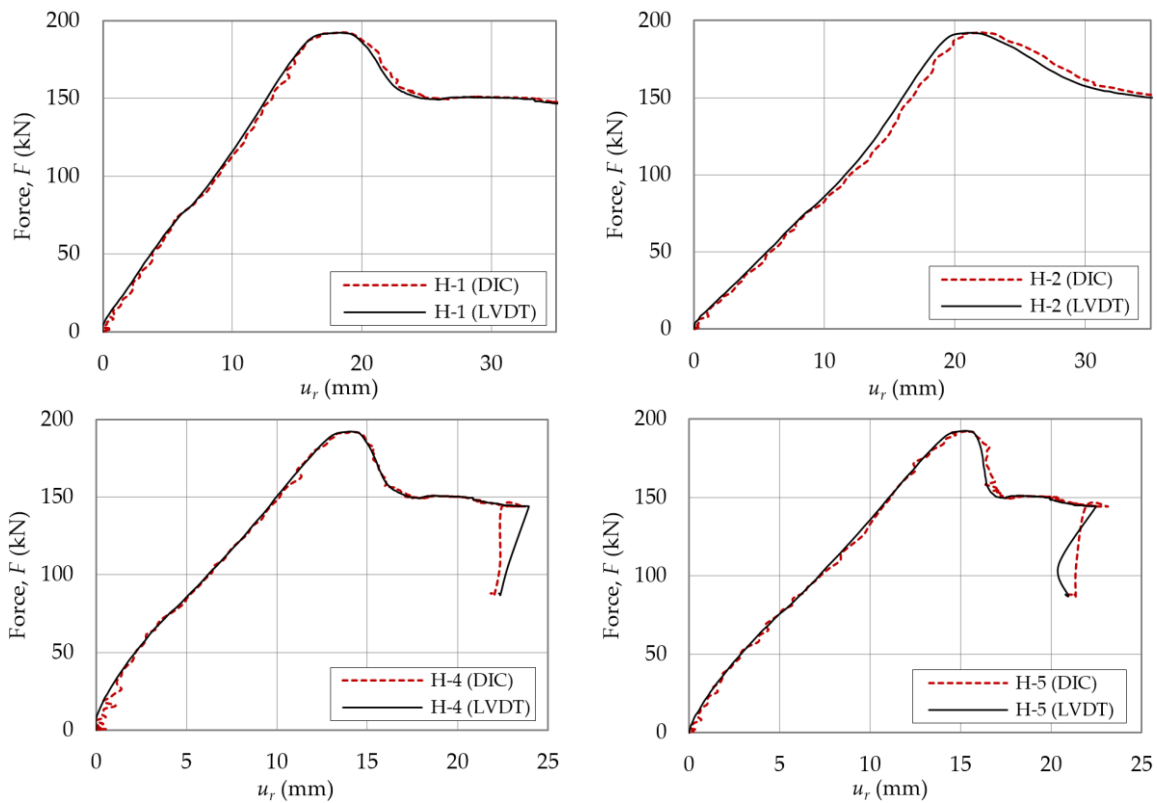


Fig. 3.10: Out-of-plane displacements - DIC vs LVDT (R20-S0-1)

In Fig. 3.11, the comparison between the results of strains recorded by two techniques (*i.e.* DIC and SGs) is presented, in which the development of strains with the increase of the applied force F is plotted for specimen R20-S1-1 at several points (*i.e.* SG-1, SG-4, SG-15, and SG-16, see Fig. 3.9), where slightly higher strain values are noticed. From the figure, it may be observed that a very good agreement is achieved also between the DIC and SGs (*i.e.* $\Delta_{\max} = 4.6\%$ at SG-

4), which gives confidence in the validity of the experimental results and justifies the use of the simpler DIC technique.

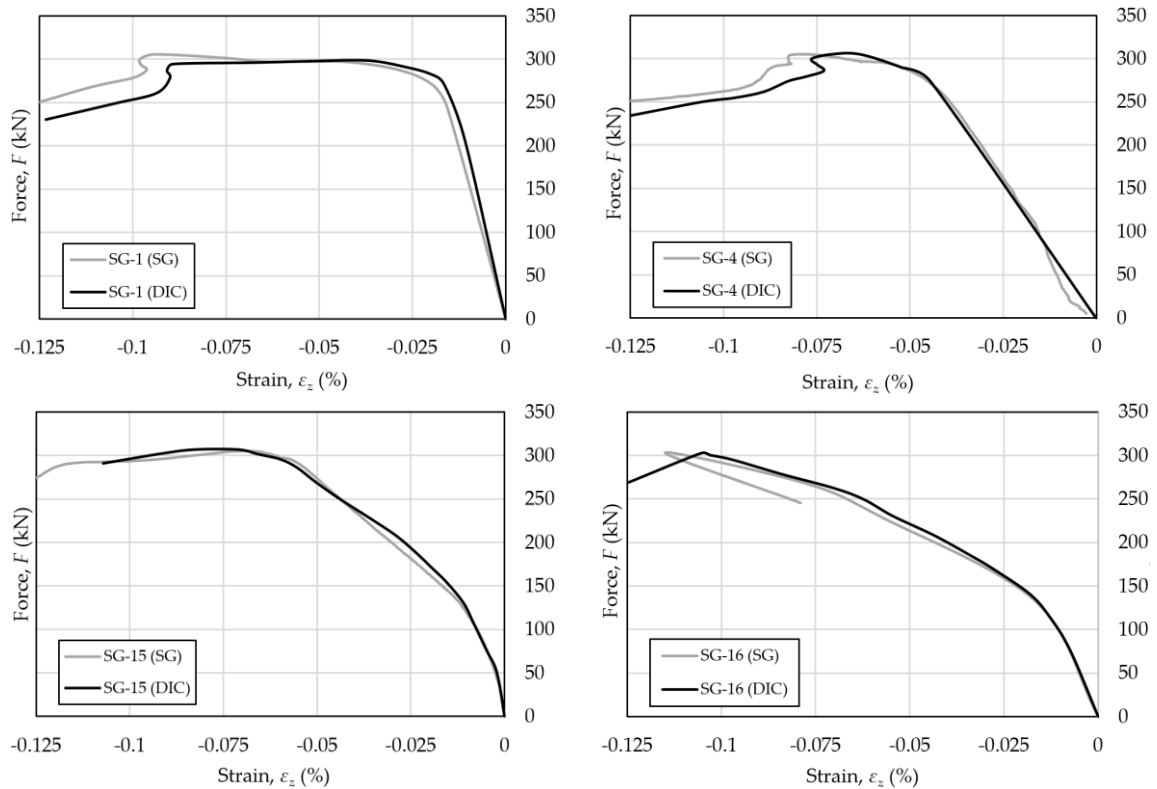


Fig. 3.11: Strain measurements - DIC vs LVDT (R20-S1-1)

Moreover, Fig. 3.11 shows that the value of strains is lower than the yield strain ($\epsilon_u \approx 0.2\%$) for all measured points, meaning that failure is related to geometric nonlinearity, with the response highly affected by the initial imperfections. The same results are obtained in other tested specimens, as it may be seen in Annex A (A.1), where the development of strains measured by SGs, are presented for 16 tested panels, sorted into four groups based on the radius. Namely, before buckling occurs, the strains linearly increase with the force, having an almost constant value in all measured points. With a further increase of force, a non-linear response and stiffness reduction is noticed in many cases, mainly in case of stiffened panels, which may be associated with local buckling of subpanels, with or without the torsional buckling of adjacent longitudinal stiffeners. In the post-buckling phase, with a further increase of force until the ultimate force is reached (*i.e.* force at which failure occurs), the strains remained in the elastic region, rarely exceeding the value of $\epsilon_z < 0.1\%$, for all tested panels, which confirms that failure is related to geometric nonlinearity.

3.3.2 Behavior of curved panels

3.3.2.1 Force-displacement curves

The force-displacement curves for all 32 tests are presented in Fig. 3.12, divided into four groups based on the radius, aiming to emphasize the influence of curvature and the number of stiffeners on the panels' response. The displacement is measured in the radial direction at the middle point H-3 (see Fig. 3.8a).

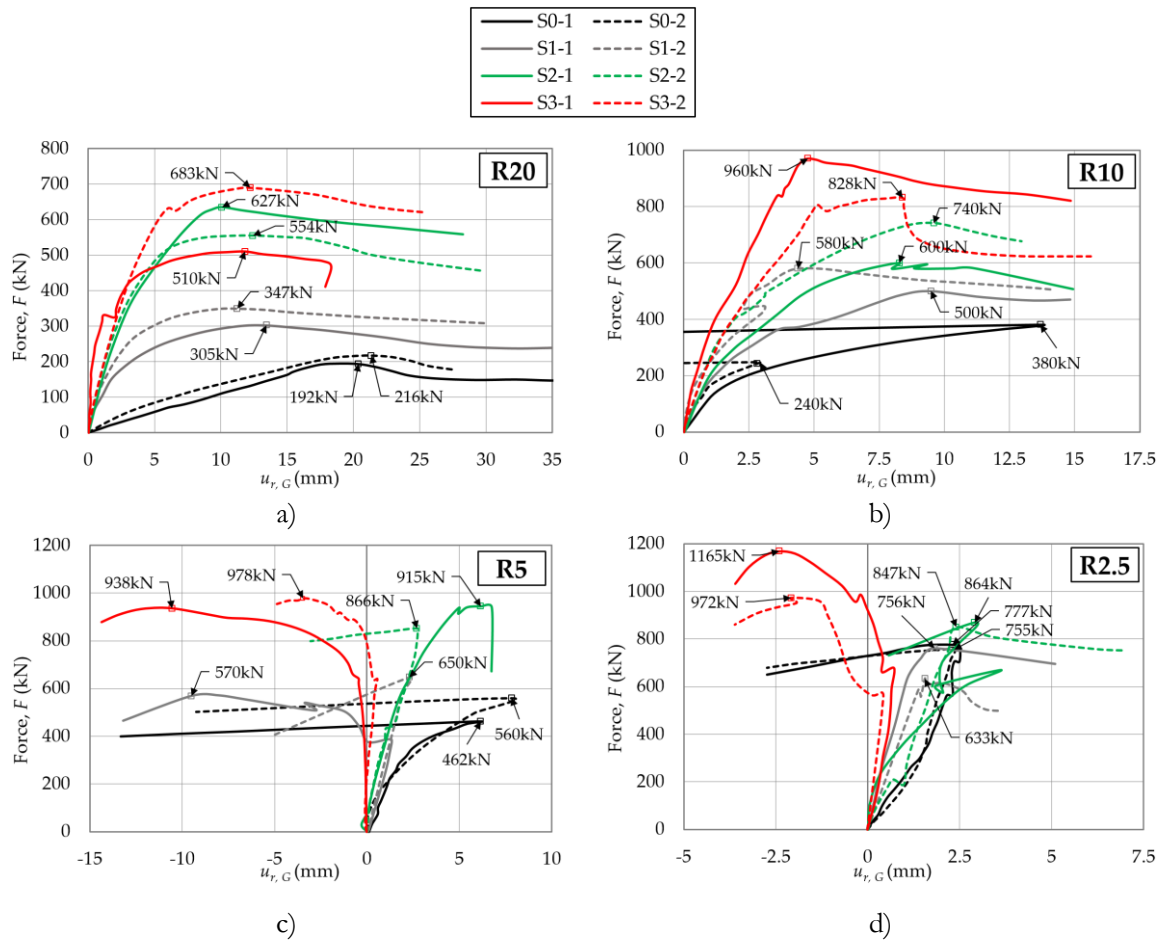


Fig. 3.12: Force-displacement curves for: a) R20; b) R10; c) R5 and d) R2.5

It is necessary to highlight that it is initially intended to plot force against the axial shortening, as it would be a more appropriate comparator for panel stiffness. However, when compared later with the numerical results, the vertical displacements, measured by the only LVDT placed next to the hydraulic jack, are significantly higher for all the tested 32 panels. The reason for this is that the recorded vertical displacements account not only for the axial shortening of the panel itself but also for the displacement of the whole test layout (*i.e.* loading beam, loading plates between load cell and loading beam, testing frame beam below the curved panel, etc.). On the other hand, the radial (out-of-plane) displacements are measured by the horizontal LVDT, placed independently from the test layout. Hence, the results of the radial displacements at the middle point are adopted, being the most accurate and unaffected by any external factor. This way any

biased conclusion (*i.e.* underestimation or overestimation of the stiffness) on the behavior of the panel is avoided, enabling far more realistic comparison with the FEM results, which is at the same time one of the main purposes of the experimental campaign. Consequently, due to the lack of reliable end shortening data, the explicit comparison of the *axial stiffness* of the panels is not possible; however, it is also not necessarily the primal goal of the tests.

Based on Fig. 3.12, several important conclusions may be drawn regarding the behavior of curved panels. As expected, the smaller the radius of curvature, while keeping the same cross-sectional area, the higher is the ultimate resistance. In addition, the decrease in radius increases the second moment of area of the cross-section, resulting in a stiffer system with considerably reduced radial displacements. However, in the case of panels with higher curvature, *i.e.* with the radii R5 and R2.5 (see Fig. 3.12c and Fig. 3.12d), a significant variation in the behavior of panels is noticed. This might be explained by the fact that panels with higher curvatures tend to behave like thin shells rather than flat plates, which consequently leads to a significant sensitivity to initial imperfections. Therefore, even in the case of two panels with the same geometry, the panels' response may be substantially different, resulting also in a different ultimate resistance. The imperfection sensitivity of panels is discussed in sections 3.4.

Regarding the influence of stiffeners, the higher the number of stiffeners the higher the ultimate resistance, due to the increased effective area of the adjacent panel acting alongside the stiffener, thus increasing its column strength. However, the addition of such small flat stiffeners has only a minor effect on the initial stiffness of curved panels. Namely, the presence of stiffeners is observable only in the case of *almost flat* panels with a radius R20 (see Fig. 3.12a), where the stiffeners notably increase the cross-section second moment of area. For smaller radii, it may be noticed that the difference in the initial stiffness is almost negligible regardless of the number of stiffeners.

To have a better understanding of the curvature effect on the ultimate strength of panels, ratio of average curved specimen strength (σ_z) to average flat specimen strength (σ_{pl}), calculated according to EN 1993-1-5 (see 2.5.1), is plotted against the local curvature parameter Z_{loc} in Fig. 3.13, sorted based on the b_{loc}/t ratio.

The figure shows that considerable gains in the ultimate resistance might be achieved with increasing curvature (*e.g.* up to 2.0 - 2.5 times higher than corresponding flat plate), whereas the rate of increase depends on the b_{loc}/t ratio. On the other hand, the ultimate resistance ratio (σ_z/σ_{pl}) shows a rising trend with decreasing b_{loc}/t ratio, which coincides with the findings reported by Soderquist [106]. For instance, for $Z_{loc} = 28$ and $b_{loc}/t = 375$, the ultimate load ratio is equal to $\sigma_z/\sigma_{pl} = 0.69$, whereas, for $b_{loc}/t = 187.5$ and $b_{loc}/t = 125$, the values are respectively $\sigma_z/\sigma_{pl} = 1.59$ and $\sigma_z/\sigma_{pl} = 1.79$. Therefore, it may be stated that the higher the curvature and the higher the number of longitudinal stiffeners, the use of design rules for flat plates deems to give results that are more conservative. The only exception is noticed for unstiffened and 1-stiffened shallow panels (*i.e.* R20-S0 and R20-S1), where the ultimate load ratio is equal to $\sigma_z/\sigma_{pl} = 0.69$ and $\sigma_z/\sigma_{pl} = 0.85$, respectively, which might have been caused by a non-uniform curvature along the panels' length, thus introducing significant load eccentricities.

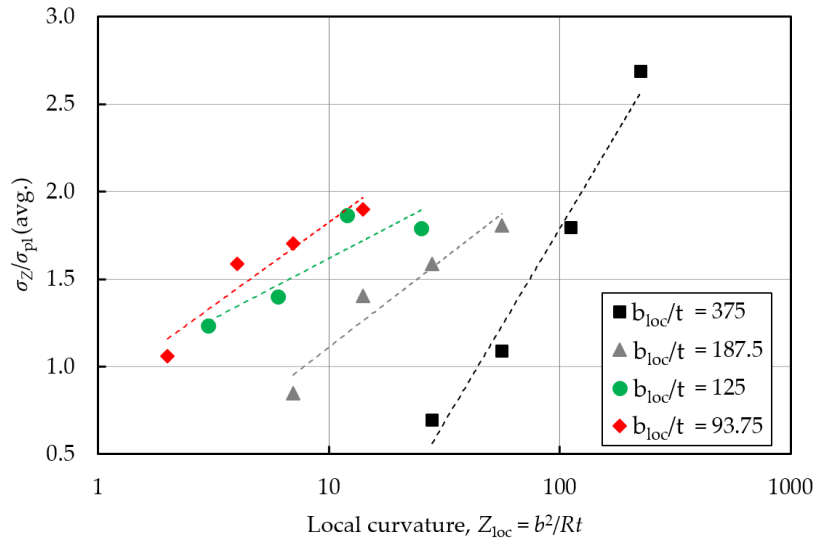


Fig. 3.13: Effect of curvature on compressive strength of stiffened curved panels

3.3.2.2 Failure modes

The failure modes of the tested panels are presented in Fig. 3.14 – Fig. 3.17. The out-of-plane displacements (in mm) are recorded using the DIC system, with the negative values corresponding to the displacements oriented radially inwards, *i.e.* towards the generator of the cylindrical panel. For stiffened panels, the photos taken from the backside of the panels are added to show the location of the failure of stiffeners.

Analysing the failure modes presented in Fig. 3.14 – Fig. 3.17, it may be noticed that the behavior of curved panels is quite complex, characterized by an unstable post-buckling path and in most cases by a sudden loss of stability (see Fig. 3.12). This type of behavior corresponds to the behavior of thin shells, with the response governed by geometrical nonlinearities, which was discussed earlier in this section.

Although no clear trend in failure modes could be observed, some regularities in response are noticed, based merely on the visual observation and qualitative assessment of panels' deformed shapes. Namely, in the case of unstiffened panels (see Fig. 3.14), regardless of the radius of curvature, the global plate-type buckling is noticed to occur before any localized buckling is detected. On the other hand, in the case of stiffened panels, the response showed a high dependence on both the radius of curvature and the number of stiffeners. Therefore, it is necessary to observe the back (concave) side of the panel for a better characterization of the instability modes, in the same manner as it is defined in EN 1993-1-5 for flat stiffened plates (see 2.5.1).

For more curved panels (*i.e.* R5 and R2.5), the dominant global buckling is noticed, however, the number of stiffeners determines whether a column-type or plate-type mode prevails. For instance, for 3-stiffened panels R5-S3 and R2.5-S3 (see photos in Fig. 3.17), the global column-type buckling may be observed, characterized by the buckling of the stiffeners with the effective adjacent curved panel, acting as three individual compressed columns (*i.e.* struts).

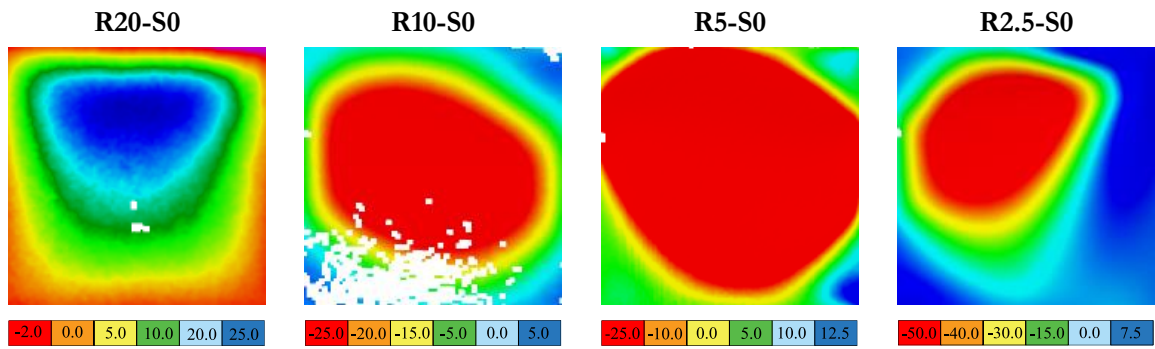


Fig. 3.14: Failure mode of curved panels without stiffeners S0 (in mm)

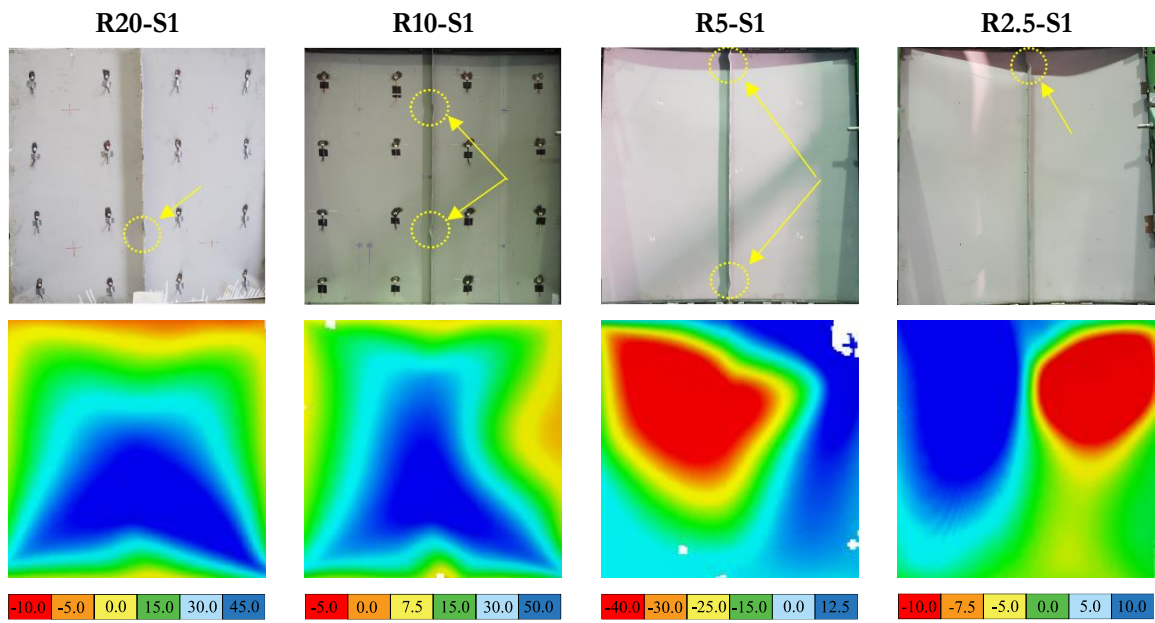


Fig. 3.15: Failure mode of curved panels with 1 stiffener S1 (in mm)

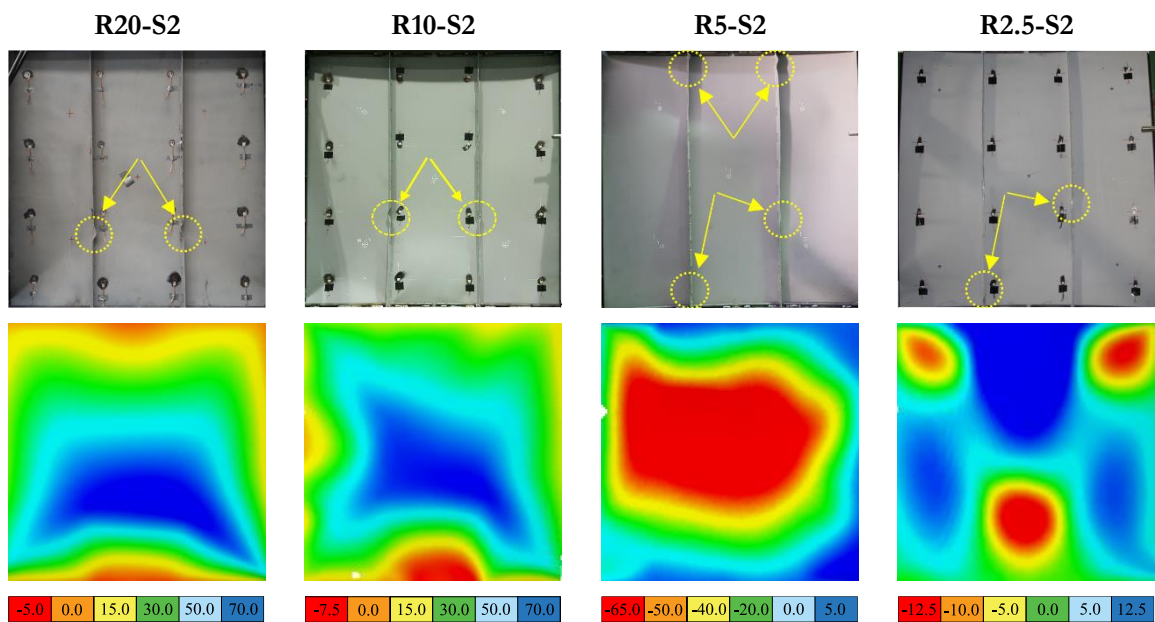


Fig. 3.16: Failure mode of curved panels with 2 stiffeners S2 (in mm)

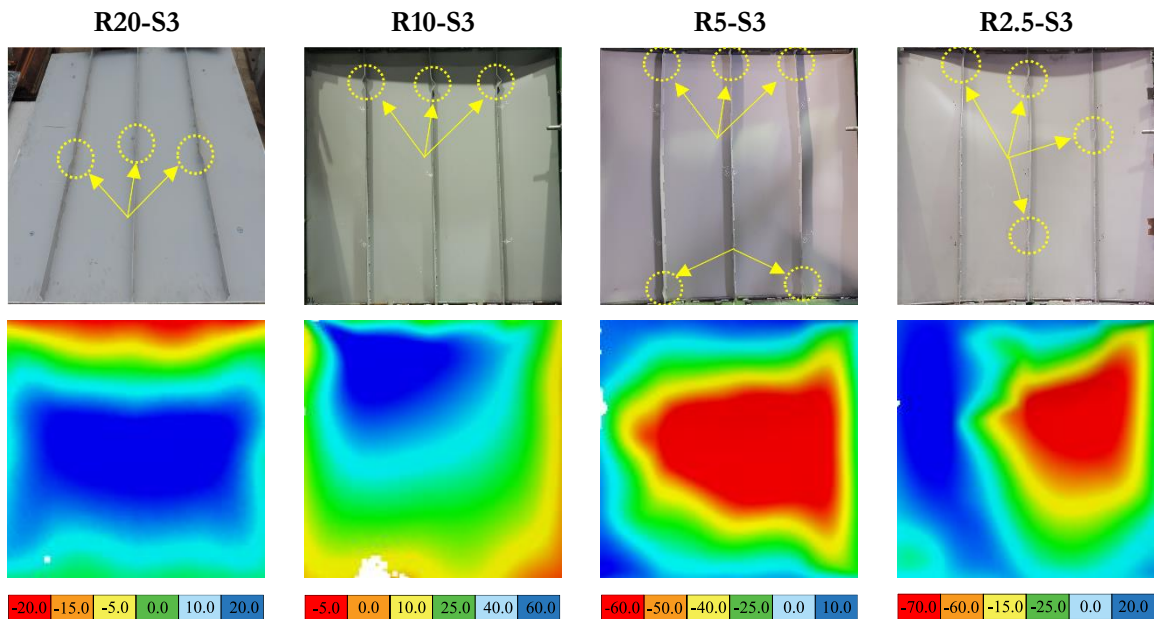


Fig. 3.17: Failure mode of curved panels with 3 stiffeners S3 (in mm)

No membrane effects took place that would lead to the global buckling of the entire curved plate together with the stiffeners, which resulted in a low post-buckling reserve and quite a brittle failure, as it may be noticed also in Fig. 3.12. On the other hand, in the case of the lightly stiffened panel, it is more difficult to distinguish whether global plate-type or global column-type behavior prevailed. Most likely, an interaction between these two modes took place.

Regarding the behavior of shallow panels (*i.e.* R20 and R10), the local instability modes of both sub-panels and stiffeners seem to have become dominant, as it may be observed in Fig. 3.18, where an example of a panel that underwent a local buckling phenomenon is illustrated. The figure shows the radial displacements of panel R20-S2-1, recorded at different values of applied force F .

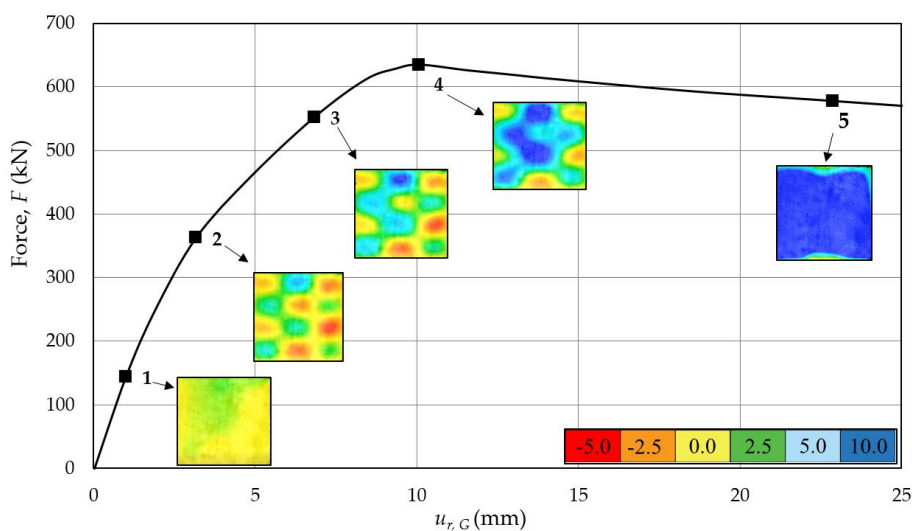


Fig. 3.18: Local buckling of a shallow panel R20-S2-1 recorded by the DIC system

It may be noticed from the figure, that the local buckling of sub-panels between the stiffeners first takes place, characterized by a chessboard pattern (see point 2). With a further increase of force (phase 2-4), the panel starts to behave nonlinearly until the ultimate load is reached, caused by the local tripping of stiffeners due to a low torsional stiffness of the flat stiffeners (see Fig. 3.16). Subsequently, after the ultimate load is reached (at point 4), an immediate global buckling mode occurs due to the loss of effective stiffening (point 5).

Finally, based on the presented failure modes, it may be concluded that the curvature significantly affects the buckling behavior of the curved panels. Namely, an increase in curvature increases the arch effect of curved panels, resulting in a stronger column buckling mechanism that differs significantly from that of a stiffened flat plate, which explains also the gains in resistance that may be attained. In addition, it is noticed that a higher curvature (*e.g.* R2.5) in general increases the number of half-waves in the circumferential direction, which coincides with the observations found in historical experimental reports by Schildrout & Stein [53], and in a recent study by Tran *et al.* [59].

The experimental results presented in this section (*i.e.* the ultimate strength, the radial displacement curves, and the failure modes) are essential comparators for the calibration of the numerical models, presented later in this chapter.

3.3.3 Assessment of the existing design methods

In 2.5.1, the design procedures available in the literature for the assessment of the ultimate resistance of unstiffened and stiffened curved panels under axial compression are summarized. Most of the proposed expressions are of the empirical nature, derived from extensive numerical studies; however, for an adequate validation of these design methods, it is necessary first to compare them against the experimental results, which according to 2.4.1 still seem to be insufficiently reported in the literature.

Therefore, the objective of this section and one of the main objectives of this thesis is not to repeat another extensive numerical study and to propose a new empirical expression that would reproduce the results obtained by the former authors, but on the contrary, to use the presented experimental results for a critical assessment of the available design methods. Ultimately, the goal of this comparative analysis is to identify the most appropriate method (or methods) that may be used for the assessment of the ultimate resistance of curved steel panels as an isolated element, but also, for the determination of effective properties of compressed bottom flange in box-girder bridge decks, addressed in chapter 7.

In Table 3.3 - Table 3.6 the ultimate resistances of the 32 experimental tests are summarized and compared with the values obtained using existing empirical methods for unstiffened and stiffened panels presented in 2.5.1.

Table 3.3: Comparison of the ultimate resistance – unstiffened panels (S0)

Experimental tests: F_{max} (kN)	R20	R10	R5	R2.5
Test 1	192	380	462	777
Test 2	216	240	560	755
Test avg.	204	310	511	766
Authors: N_{Rk} (kN)	R20	R10	R5	R2.5
Tran (2012) [8]	341	391	N/A	N/A
Tran <i>et al.</i> (2012) [75]	343	386	N/A	N/A
Tran <i>et al.</i> (2014b) [77]	N/A	N/A	N/A	N/A
Martins <i>et al.</i> (2014) [78]	267	322	N/A	N/A
Kim <i>et al.</i> (2014) [80]	442	445	458	520
Park <i>et al.</i> (2018) [16]	460	610	817	1091
Design standards: N_{Rk} (kN)	R20	R10	R5	R2.5
EN 1993-1-5 [11]	285	285	285	285
DNV-RP-C202 (2017) [13]	35	49	105	269
DNVGL-0128 (2018) [14]	322	203	400	795
ABS (2018) [15]	N/A	N/A	N/A	N/A

Table 3.4: Comparison of the ultimate resistance – 1-stiffened panels (S1)

Experimental tests: F_{max} (kN)	R20	R10	R5	R2.5
Test 1	305	500	570	756
Test 2	347	580	650	633
Test avg.	326	540	610	695
Authors: N_{Rk} (kN)	R20	R10	R5	R2.5
Tran (2012) [8]	457	481	N/A	N/A
Tran <i>et al.</i> (2014a) [59]	378	431	546	616
Seo <i>et al.</i> (2016) [82]	105	110	220	409
OUTBURST (2019) [85]	392	472	588	748
Design standards: N_{Rk} (kN)	R20	R10	R5	R2.5
EN 1993-1-5 [11]	384	384	384	384
DNV-RP-C202 (2017) [13]	118	181	330	633

Table 3.5: Comparison of the ultimate resistance – 2-stiffened panels (S2)

Experimental tests: F_{max} (kN)	R20	R10	R5	R2.5
Test 1	627	600	915	864
Test 2	554	740	866	847
Test avg.	591	670	891	856
Authors: N_{Rk} (kN)	R20	R10	R5	R2.5
Tran (2012) [8]	608	624	N/A	N/A
Tran <i>et al.</i> (2014a) [59]	449	536	737	945
Seo <i>et al.</i> (2016) [82]	155	165	344	639
OUTBURST (2019) [85]	448	544	776	959
Design standards: N_{Rk} (kN)	R20	R10	R5	R2.5
EN 1993-1-5 [11]	478	478	478	478
DNV-RP-C202 (2017) [13]	204	248	376	671

Table 3.6: Comparison of the ultimate resistance – 3-stiffened panels (S3)

Experimental tests: F_{max} (kN)	R20	R10	R5	R2.5
Test 1	510	960	938	1165
Test 2	683	828	978	972
Test avg.	597	894	958	1069
Authors: N_{Rk} (kN)	R20	R10	R5	R2.5
Tran (2012) [8]	527	786	N/A	N/A
Tran <i>et al.</i> (2014a) [59]	539	635	895	1183
Seo <i>et al.</i> (2016) [82]	198	228	476	882
OUTBURST (2019) [85]	534	628	897	1196
Design standards: N_{Rk} (kN)	R20	R10	R5	R2.5
EN 1993-1-5 [11]	563	563	563	563
DNV-RP-C202 (2017) [13]	322	353	455	726

The geometrical properties of the stiffened curved panels required for the calculation of the ultimate resistance according to procedure by Tran (2012) [8], Tran *et al.* (2014a) [59] and OUTBURST (2019) [85], as well as the properties required for the method given by DNV-RP-C202 (2017) [13] are summarized in Annex A (A.2). The proposal by Tran *et al.* [77], as well as the standard ABS [15], are not applicable for neither unstiffened nor stiffened panels since the geometry of tested panels exceeds the ranges of validity given in Table 2.4 and Table 2.7.

To better assess results shown in the tables, in Fig. 3.19, the calculated ultimate resistances (N_{Rk}) are normalized to average experimental results ($F_{max,avg}$), with respect to radius R .

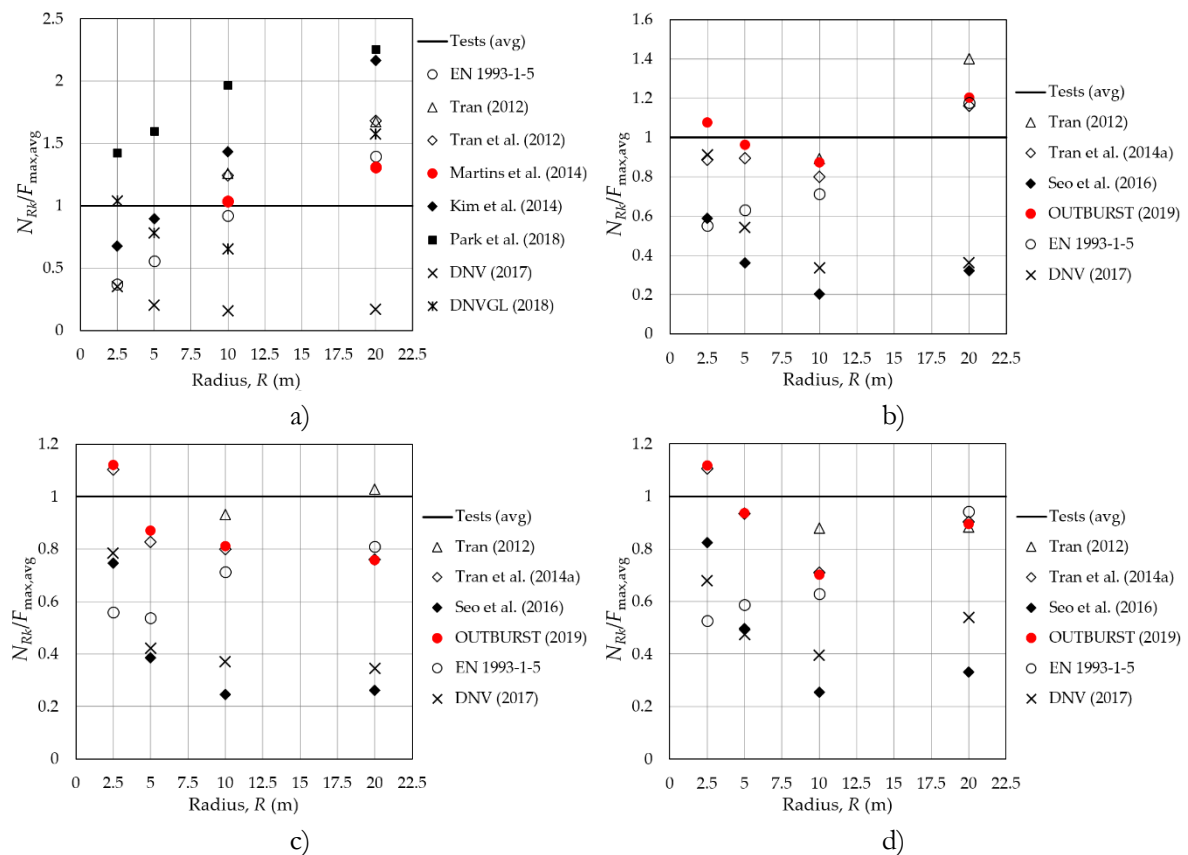


Fig. 3.19: Comparison of results with respect to radius R : a) S0; b) S1; c) S2; d) S3

Regarding the unstiffened panels (Fig. 3.19a), a large scatter of the results is noticed that can be partly explained by the differences in the software and modeling assumptions made by the authors when deriving the various expressions. Moreover, none of the methodologies provide satisfactory results for the whole range of curvatures. The results obtained using the design standard DNVGL are comparable to the experimental ones for more curved panels (e.g. $\Delta_{\max} = 3.6\%$ for R2.5), whereas for the shallow panels ($R/t > 2500$) the standard recommends the rules for flat plates, which leads to considerably conservative results (e.g. $\Delta_{\max} \approx 60\%$ for R20). Finally, the expressions from and Martins *et al.* [78] give acceptably good results for shallow panels (e.g. $\Delta_{\max} = 3.5\%$ for R10), however, these expressions are limited to the curvatures up to $Z < 100$, thus cannot be applied to all considered panels. These restrictions are encountered also in the expressions from Tran [8] and Tran *et al.* [75].

As for the stiffened panels, in Fig. 3.20, the available design procedures are statistically assessed and compared using the coefficient of variation CoV (%), which is calculated for each methodology based on the normalized values $N_{Rk}/F_{\max,avg}$ (see Fig. 3.19b - Fig. 3.19d). Namely, the coefficient of variation, which is defined as the ratio of the standard deviation to the mean value, is a suitable non-dimensional statistical parameter that shows to what extent the data varies around mean value. In principle, the lower the CoV the smaller is the difference between the two data series, which in this case means that the proposed methodology gives the ultimate resistance of stiffened curved panels closer to the ones obtained experimentally.

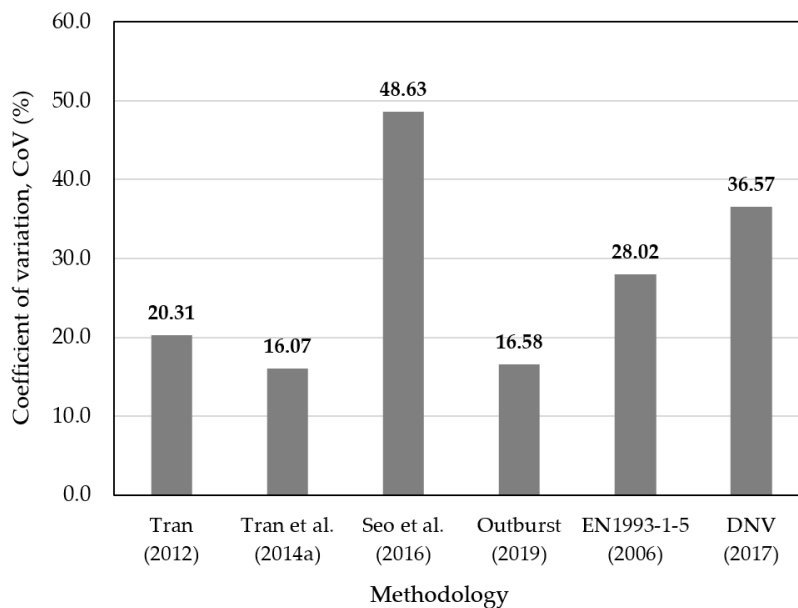


Fig. 3.20: Comparison of the available procedures for stiffened curved panels

Based on this figure, it may be concluded that both the methodology from Tran *et al.* [59] and the one proposed in the OUTBURST project [85] give results comparable with the experimental ones, with $\text{CoV} \approx 16\%$ in both cases. On the other hand, the methodology proposed by Seo *et al.* [82] gives considerably conservative results in comparison to the experimental results, with $\text{CoV} \approx 49\%$.

Finally, regarding the available design standards, the use of EN 1993-1-5 almost in all cases leads to an underestimation of the ultimate resistance ($\text{CoV} \approx 28\%$), with the exception of the shallow unstiffened and lightly stiffened panels, where an overestimation is noticed. A significant deviation from the experimental results is also noticed ($\text{CoV} \approx 37\%$) when the methodology prescribed by DNV-RP-C202 is used. This might be explained by the fact that the semi-empirical formulae proposed in the standard were derived based on the analyses made on full cylinders and not on the individual curved panels. Consequently, the expressions fail to give a good estimate of the structural behavior of curved panels, which seems to be particularly noticeable for very shallow panels (see Fig. 3.19).

To summarize, the most adequate methodology cannot be claimed with a high certainty based merely on the comparison of results against 32 tested panels since the geometry of panels covers only a narrow range of parameters. Therefore, in order to have more reliable conclusions on the ultimate resistance of the curved panels, the scope of the experimental study needs to be enlarged, by varying not only the curvature parameter but also the slenderness of the panels b/t and the aspect ratio α .

Nevertheless, based on the comparative analysis presented in this section, it may be concluded that the expressions proposed by Tran *et al.* [59] and in the OUTBURST research project [85] seem to be the most adequate for the estimation of the ultimate resistance of the stiffened curved panels, having conceptually the same format used in the European standard EN 1993-1-5.

The substantial difference between the two methodologies, however, is in the determination of the local buckling of the subpanels between the stiffeners. Namely, in Tran's proposal, the local buckling is determined for a corresponding flat plate, neglecting the local curvature, whereas the method proposed in the OUTBURST research project accounts for the local curvature, suggesting the use of the expressions developed by Martins *et al.* [78] for unstiffened curved panels. In the case of panels with a low local curvature (*i.e.* $Z_{\text{loc}} < 30$ in almost all tested stiffened panels, see Table 3.1) the influence of the local curvature parameter seems to be less relevant, which explains almost identical results obtained by these two methodologies. Therefore, in case of bridges, where the local curvature parameter of bottom curved flange rarely exceeds $Z_{\text{loc}} < 20$ (see Fig. 2.6), technically, both methods may be used. However, for the sake of complicity, the expression proposed in the OUTBURST research project is used further in the thesis since it allows for higher local curvatures, *i.e.* up to $Z_{\text{loc}} = 100$, thus may be applied to engineering structures other than bridges (*e.g.* airplanes and ships hulls), where local curvatures may reach values up to $Z_{\text{loc}} < 70$. In chapter 8, these two methodologies are to be compared again, however, for panels with geometry encountered in bridges.

3.4 Numerical analysis

3.4.1 Introduction

In this section, using as a reference previously presented experimental results, a numerical study is carried out in order to further investigate one of the most relevant characteristics of thin curved steel panels – significant sensitivity to initial geometric imperfections.

As discussed in 2.4.1, multiple authors performed extensive numerical studies, analysing mainly the influence of the amplitudes and shapes of the initial imperfections on buckling behavior of curved panels and their ultimate compressive resistance. In those studies, among which the most relevant are those from Martins *et al.* [79] and Manco [10], the authors expressed an increased difficulty in defining the critical imperfection shape, *i.e.* the shape that yields the lowest resistance of curved panel. Namely, according to Martins, the critical imperfection shape may vary significantly depending on the geometry of the panel (curvature and aspect ratio), and it is not only the shape or the amplitude that dictates the lowest ultimate resistance, but most commonly a certain combination of two, which additionally increases the level of uncertainty.

Therefore, owing to the lack of adequate recommendations in a standard format, a simplified engineering approach is generally accepted, in which the imperfection shapes and amplitudes are defined using the prescriptions given by the design standard for flat plates – EN 1993-1-5. Hence, the objective of the numerical study presented in this section is to assess the validity of such an approach, using the experimental results as the comparator, something that was not done in any of the aforementioned numerical studies.

The numerical analyses are carried out using the FEM software ABAQUS [142], which is suitable for the application of the studied approach since it allows a simple implementation of the initial imperfections. The most relevant considerations required for the definition of the numerical model (*e.g.* type of analysis, geometry, boundary and loading conditions, material properties, finite element (FE) type and size, imperfections, etc.) are described in 3.4.2. Subsequently, the model is validated against the experimental results in 3.4.3, whereas the results of the study are discussed in 3.4.4.

3.4.2 Model definition

3.4.2.1 Type of analyses

For this study, specifically, two types of analyses are performed: *i)* Linear elastic bifurcation (or eigenvalue) analysis (LBA) and *ii)* Geometrically and materially nonlinear analysis with imperfections included (GMNIA).

First, to generate the eigenmodes, the LBA is performed for each model, using the Subspace algorithm available in ABAQUS. Subsequently, the extracted eigenmodes are used as the shapes of the initial geometrical imperfections in a GMNIA, in which the ultimate load of the panels is obtained. For that purpose, the arc-length Riks method [143] from the software's library is used, which gives non-linear static equilibrium solutions for unstable structures, where the load level and/or the displacement decrease along the loading path, causing energy loss (*i.e.* negative stiffness).

When GMNIA is performed, it is necessary to define carefully the arc-length parameters in order to avoid numerical issues, such as missing bifurcation points, and thus an overestimation of the ultimate load. This is particularly important in the case of panels with a higher curvature parameter, where the shell-like behavior occurs with a highly unstable post-buckling equilibrium path, manifested by a sudden drop in the bearing capacity (*i.e.* snap-through buckling). To

overcome this problem, a constrained small arc-length is defined, with an adequate size of the initial and the maximum increment.

Finally, according to EN 1993-1-5, the ultimate resistance of a panel is obtained as the maximum load factor on the load-deformation curve. However, it is necessary to observe carefully the load-displacement curves since the arc-length routine may, in some cases, decide to follow the primary loading path as the post-buckling path instead of opting for the new secondary path at the bifurcation point, thus, missing the true bifurcation load. For more details regarding the problems that may be encountered in arc-length procedures of unstable structures, the reader is invited to see also the book by Crisfield [144], published in 1997.

3.4.2.2 Geometry

In total, 16 different numerical models are built, with the geometry that corresponds to 16 tested panels, defined in 3.2.1.

3.4.2.3 Applied material model

The material properties of steel S355 assigned to the curved panels in the numerical simulations are based on the simplified true stress-strain relations determined by tensile coupon tests in 3.2.2. The simplified elastic-plastic material model, with a modulus of elasticity equal to $E = 210$ GPa, a Poisson's coefficient equal to $\nu = 0.3$, and linear strain hardening is presented in Fig. 3.21, together with the true stress-strain relation obtained as an average of tensile test results for three rolling directions (see Fig. 3.4). These two models are compared and a negligible difference in panels response is noticed ($\Delta < 0.5\%$).

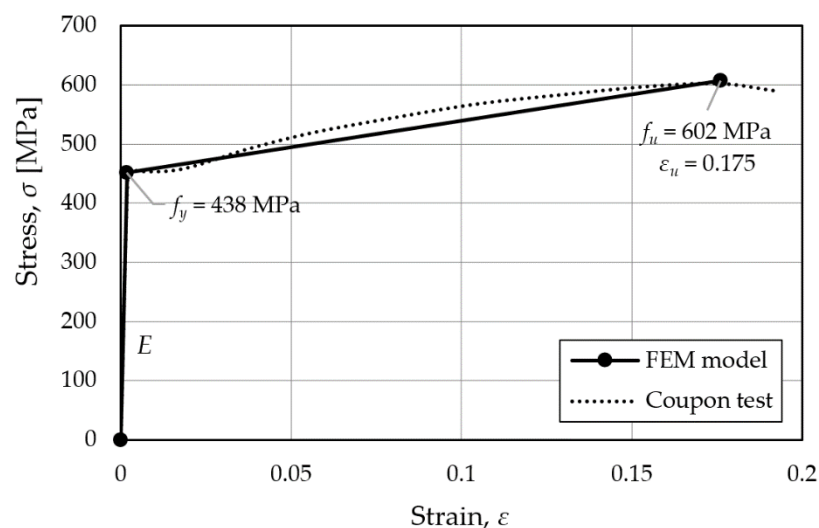


Fig. 3.21: Material model used in FEM analyses

3.4.2.4 Load and boundary conditions

To define the load and the boundary conditions, a cylindrical coordinate system is adopted with the origin at point O, as indicated in Fig. 3.22. The displacement field is defined by u_z , u_φ and u_r that correspond to longitudinal, circumferential and radial directions, respectively.

To achieve the boundary conditions that correspond to the experimental tests, the radial displacements are prevented along all four edges (*i.e.* $u_r = 0$), except for the stiffeners. In addition, the longitudinal displacements are prevented at the bottom edge of panels (CD), including stiffeners (*i.e.* $u_z = 0$). Finally, to obtain simply supported boundary conditions, the circumferential displacements are prevented at points E and F (*i.e.* $u_\varphi = 0$).

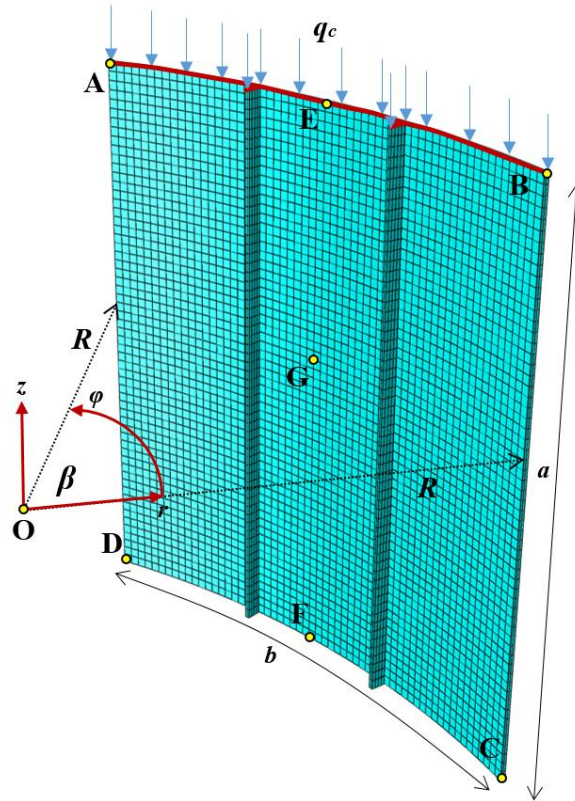


Fig. 3.22: Numerical model

The in-plane compressive load, q_c , is uniformly distributed along the top edge (see AB in Fig. 3.22), including the edges of stiffeners, thus simulating the contact between the loading beam and the specimen realized in the experimental tests.

3.4.2.5 Finite element type and size

Numerical models are discretized by four-node shell elements (S4R) with the reduced integration and 6 DOF per node, as a finite element commonly used for the discretization of thin plates and shell structures (*e.g.* Cho *et al.* [113], Seo *et al.* [82], Manco [10], etc.).

Since all modeled panels have aspect ratio equal to $\alpha = 1.0$, it is opted for squared FE, *i.e.* with approximately equal dimensions in both directions. Moreover, it is aimed to have an integer number of FE between stiffeners, to match the node of the stiffeners with the node of the panel. Finally, the size of an element of $25 \times 25 \text{ mm}^2$ (*i.e.* 3600 FE in total) is adopted based on the results from a mesh convergence study, performed for two unstiffened panels with a different radius of curvature (R20-S0 and R2.5-S0), as indicated in Fig. 3.23. The ultimate resistance (F_{\max}) is obtained using the Riks' method, where for the sake of this mesh convergence study only, the

shape of the imperfection affine to the first buckling mode with an amplitude equal to $b/200$ is considered.

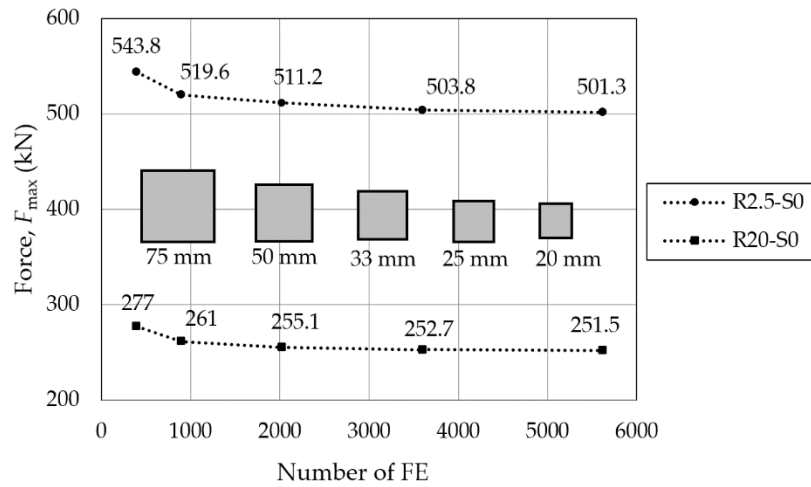


Fig. 3.23: Mesh convergence study using finite element S4R

Since several authors (*e.g.* [75], [109]) used S8R finite element in their studies, a comparison between S4R and S8R is made, using as an example the same two panels with the adopted mesh size of $25 \times 25 \text{ mm}^2$. In the case of R20-S0, the ultimate resistance with S8R finite elements is 1.14% lower (*i.e.* 249.8 kN), whereas the computation time is 2.5 times higher. In the case of a more curved panel, R2.5-S0, the difference in ultimate resistance is 1.06% (496 kN), whereas the difference in the computation time is even higher (3.5 times). Hence, the finite element S4R is adopted in this study as it gives accurate results and reduces considerably the CPU time.

Finally, in the case of stiffened panels, 5 finite elements along the web are adopted, in total 300 FE per stiffener.

3.4.2.6 Applied initial imperfections

It has been long acknowledged that the structural response of curved steel panels is directly influenced by the presence of the initial imperfections, being thin elements with increased susceptibility to instability phenomena. Therefore, the modeling of imperfections requires particular attention, which is the main topic of this study.

Since the information on the *real* material and geometrical imperfections is generally not available, numerous studies in the field of stability analysis of shells have attempted to propose a simple alternative approach, applicable for design purposes. One of the most widely accepted approach, implemented later in the European standard, is the one introduced by Koiter [145], according to which the imperfections are assumed as a pattern of fictive initial deflections (*i.e.* equivalent imperfections) applied perpendicularly to the middle surface of the shell. One of the main advantages of this approach is that the equivalent imperfections account for geometric imperfections but also structural ones (*i.e.* residual stresses, load eccentricity, etc.), which are often difficult to be measured.

Therefore, for this study, the concept of equivalent imperfections is also adopted, using the well-established recommendations from Annex C.5 of EN 1993-1-5 for the modeling of

imperfections in the case of flat plates. This assumption is justified to some extent by the fact that the fabrication of curved and flat panels is quite similar, leading to approximately similar fabrication tolerances.

According to Annex C.5 of EN 1993-1-5, for the stiffened panels, it is recommended to use the shape of the initial imperfections affine to the critical buckling shape, *i.e.* the one leading to the lowest resistance. Based on the possible eigenmodes, the standard recognizes three distinct imperfections – local, global and stiffener imperfection, presented in Fig. 3.24, with corresponding amplitudes δ_0 .

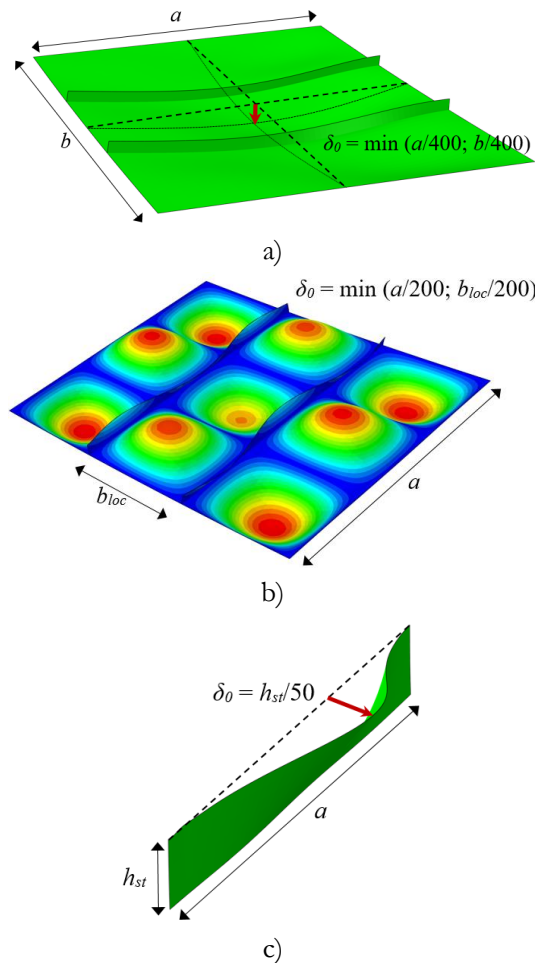


Fig. 3.24: Types of imperfections: a) global; b) local-subpanel; c) local-stiffener

In ABAQUS, the imperfections are implemented using the keyword **IMPERFECTION*, referring it to the corresponding LBA results and attributing the desired amplitude. Namely, the shape of the imperfections is obtained from a linear combination of the relevant buckling modes of each panel, using linear eigenvalue analysis (LBA), performed on a *perfect* structure. The imperfections (Δu_r) are introduced in a piecewise manner through a perturbation of radial translational DOF for each node (N), given in a general form by Eq.(3.1) as:

$$\Delta u_r^N = \sum_i \delta_{0,i} \phi_i^N \quad (3.1)$$

where ϕ_i is the shape of the i^{th} buckling mode and $\delta_{0,i}$ is the corresponding scale factor (*i.e.* imperfection amplitude), which according to Annex C.5 of EN 1993-1-5 should be adopted in accordance with the Fig. 3.24 for a leading imperfection, whereas the remaining ones may have their values reduced to 70 %.

Finally, it is necessary to highlight that the presented equivalent imperfections are used for the assessment of the imperfection sensitivity in 3.4.4, which is the paramount objective of this numerical study. However, in order to calibrate a numerical model that accurately reproduces the experimental results, and thus to validate its geometry, material properties, boundary conditions, loads, size and type of FE, it is necessary in 3.4.3 to model the imperfections as realistic as possible and not the fictive simplified imperfections prescribed by standard.

Since the DIC system used in the experimental tests is found to be impractical for the detection of the local imperfections, as it registers only the relative movements of the surface point with respect to a user-defined reference plane, an assumption is made. Namely, soon after the axial load is applied, due to the eccentricity of the load in the zones where the out-of-plane imperfections are present, an additional bending moment appears, tending to increase further this deformation. Only now, using the DIC system, it is possible in some cases to detect the location and the pattern of the imperfections on the panel surface, as it corresponds to an 'initial' deformed shape. Subsequently, in ABAQUS, an adequate buckling mode (or a linear combination of several modes) is chosen to correspond to this 'initial' deformed shape of a panel measured by the DIC.

Regarding the amplitudes, the values defined by standard (see Fig. 3.24) correspond to design values that were established to lead to safe estimates of the design resistance [146]. Therefore, once the imperfection shape is defined, the amplitudes are then varied within a lower bound and an upper bound (*e.g.* $b/150 - b/750$ for the global imperfections, and $b_{\text{loc}}/150 - b_{\text{loc}}/750$ for the local imperfections), until good convergence is achieved, *i.e.* until results matched with the experimental ones. Since the measurements with the DIC system are made from the front (radially outer) side of specimens, it is not possible to detect the initial stiffener imperfections (see Fig. 3.24c), thus these local imperfections are not considered for the calibration.

3.4.3 Calibration of the FE model

The numerical models are calibrated against the experimental results shown in section 3.3, based on three main comparators: *i)* the ultimate strength (F_{max}); *ii)* the radial displacement curve at the middle of the panel (point G, in Fig. 3.22); *iii)* the collapse shape (Fig. 3.14 – Fig. 3.17).

The calibration is done for each of 16 models, where the biggest challenge is modeling of the initial imperfections that correspond to the real ones (see in 3.4.2.6). To understand better how the results of the DIC are used for the modeling of imperfections, an example is presented for panel R10-S2-2.

The initial deformed shape recorded at low values of applied force (in this case $F/F_{\text{max}} \approx 0.3$), as well as the collapse mode are presented in Fig. 3.25 and Fig. 3.26, respectively.

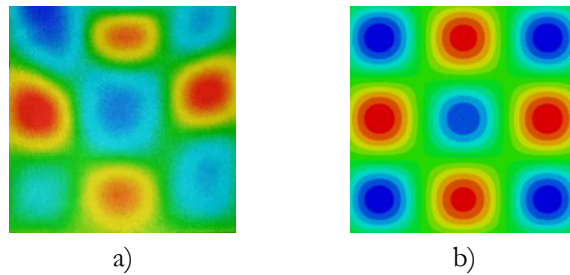


Fig. 3.25: Local initial imperfection pattern: a) DIC; b) FEM

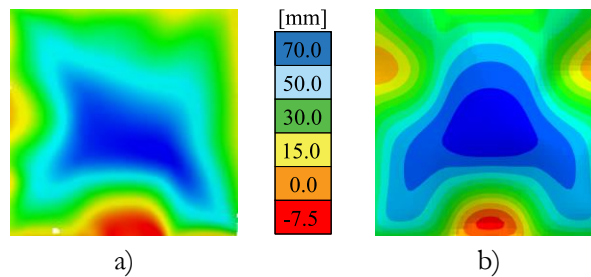


Fig. 3.26: Collapse shape-front side: a) DIC; b) FEM

From these figures, it may be noticed that the panel initially deforms locally, with a chessboard pattern, whereas the collapse of the panel corresponds to a radially outward deflection. Hence, in the numerical model, the global buckling mode, oriented radially outward (30th buckling mode in this case) is assumed to be the governing one, accompanied by the local buckling mode with a similar chessboard pattern (1st in this case, see Fig. 3.25b). Additionally, in order to have the failure mode as close as the one captured by the DIC system, it is necessary in this case to combine the first mode with the local 3rd mode. The collapse shapes are compared in Fig. 3.26, and it may be noticed that good agreement is achieved. In Fig. 3.27, the force-radial displacement curves for both R10-S2-1 and R10-S2-2 are presented.

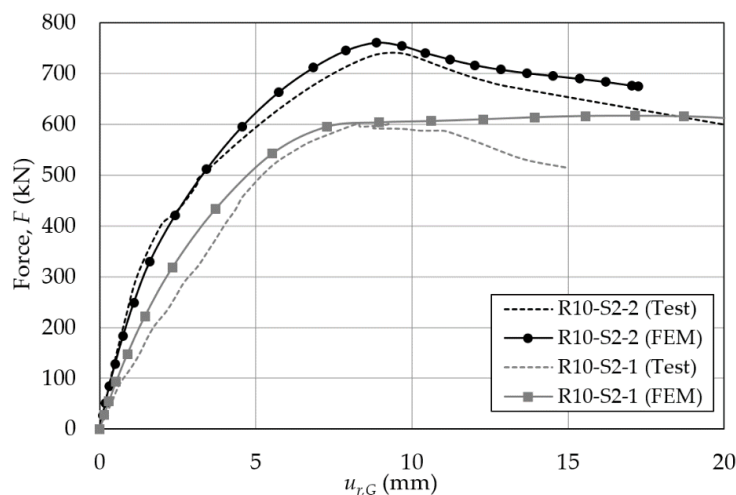
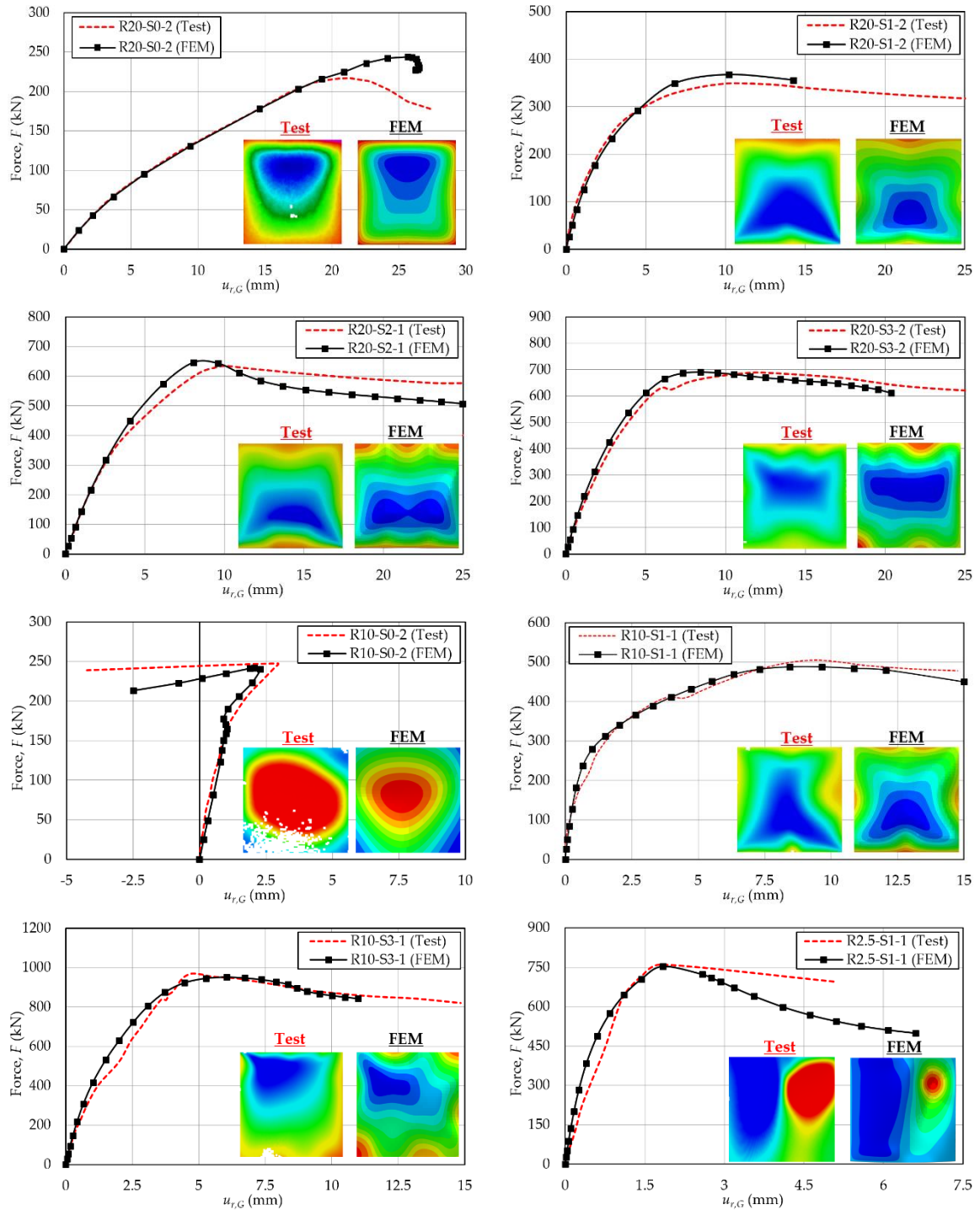


Fig. 3.27: Force-radial displacement curves for R10-S2-1 and R10-S2-2

As it may be noticed, a quite good correspondence is obtained, with the maximum difference in the ultimate strength of $\Delta_{\max} \approx 2.7\%$. For both cases, the same imperfection shapes are considered, however, in the case of R10-S2-1, slightly higher imperfection amplitudes are used (see Table 3.7), which explains also the major difference between two experimental tests,

performed on two panels with an identical geometry, with the same material and under the same load and boundary conditions.

The same calibration procedure is repeated for all panels. In Fig. 3.28, some of the most relevant results are summarized for several examples, in which both the collapse shapes and the force-displacement curves obtained numerically are compared with the experimental results for various radii of curvature and number of stiffeners.



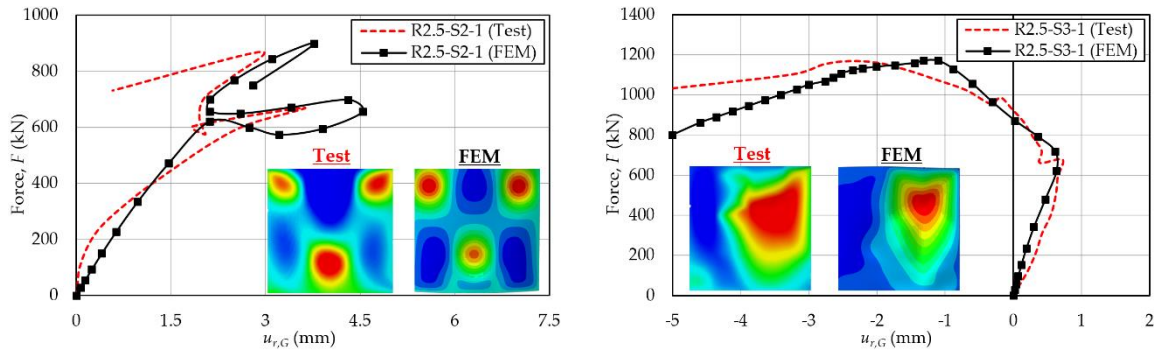


Fig. 3.28: Comparison of experimental and FEM results (front view)

Finally, since comparison against the results obtained by the DIC system is possible only from the front side, for some cases of stiffened panels, a better comparison is achieved using the photos, taken from the backside of the specimen after the collapse occurred, as presented in Annex A (A.3).

The same procedure is repeated for each panel, and in most cases, it is proven very accurate and simple to apply. However, in a few cases, it is not quite possible to detect any local deformation by the DIC at the lower values of force (*i.e.* $F/F_{\max} < 0.5$), which is found to be the biggest limitation of this methodology. Furthermore, in several cases, it is a huge challenge to replicate the desired imperfection pattern by combining different eigenmodes. In particular, in the case of stiffened panels, the global eigenmode seems to be difficult to attain by LBA, as in some cases it appears only after tens of eigenmodes.

Based on the presented calibration process, several important preliminary conclusions are drawn:

- The shape of imperfections highly influences both the collapse shape and the ultimate resistance of curved panels, which is particularly emphasized in the case of panels with higher curvatures. Therefore, a sensitivity analysis is conducted in 3.4.4, where several models of imperfections are considered;
- In most cases, the leading global imperfection accompanied by local imperfections (one or more) lead to the results that correspond to the real behavior obtained experimentally;
- In the case of unstiffened panels, it is sufficient to model only a global panel imperfection, whereas, in the case of stiffened panels, the leading global mode had to be combined with the accompanying local imperfections;
- Regarding the global modes, it is relatively easy to find them in the case of unstiffened panels, being affine to the 1st buckling mode. However, in the case of stiffened panels, the global modes are commonly higher-order buckling modes (*e.g.* 30th in the case of R10-S2-2);
- As for the local imperfections, in those cases where it is possible to determine a buckling mode that corresponds to an ‘initial’ deformed shape recorded by DIC, as shown in Fig. 3.25, the numerical results are in excellent agreement with the experimental ones ($\Delta_{\max} < 5\%$). However, in those cases where it is not possible, the local imperfections are

modeled iteratively as one (or as a combination of several local buckling modes) until satisfactory results are achieved;

- The imperfections used for the calibration are summarized in [Table 3.7](#), where for each case the buckling mode(s) and the corresponding amplitudes are provided. In some cases, where a huge difference between the two tests is noticed (*e.g.* R20-S2-1 and R20-S2-2), the calibration is done separately for each case.

Table 3.7: Equivalent imperfections used for the calibration of numerical models

Panel	Imperfection: Eigenmode (amplitude)
R20-S0	1st (7.5mm) + 2nd (2mm) + 4th (2mm)
R20-S1	10th (7.5mm) + 1st (0.5mm) + 4th (5mm)
R20-S2-1	27th (7.5mm) + 1st (5mm)
R20-S2-2	17th (7.5mm)
R20-S3-1	22nd (10mm) + 27th (7.5mm) + 1st (1.5mm)
R20-S3-2	22nd (4.5mm) + 27th (4.5mm) + 1st (0.2mm)
R10-S0	13th (4mm)
R10-S1-1	12th (3mm)
R10-S1-2	12th (1mm) + 3rd (1mm)
R10-S2-1	30th (12.5mm) + 1st (12.5mm) + 3rd (12.5mm)
R10-S2-2	30th (3.75mm) + 1st (1.75mm) + 3rd (1.75mm)
R10-S3-1	31st (3.75mm) + 1st (1.3125mm) + 4th (1.3125mm)
R10-S3-2	31nd (5mm) + 1st (5mm) + 2nd (5mm)
R5-S0	1st (1mm) + 2nd (1mm)
R5-S1-1	4th (3.75mm)
R5-S1-2	44th (10mm)
R5-S2-1	8th (7.5mm)
R5-S2-2	8th (3.75mm)
R5-S3-1	2nd (6mm) + 19th (3.5mm)
R5-S3-2	19th (3.75mm)
R2.5-S0	1st (2mm)
R2.5-S1-1	2nd (3.75mm)
R2.5-S1-2	1st (3mm) + 2nd (3.75mm)
R2.5-S2-1	5th (10mm) + 1st (2.5mm)
R2.5-S2-2	5th (7.5mm)
R2.5-S3-1	14th (4mm) + 1st (4mm) + 2nd (4mm)

In conclusion, a good agreement is obtained between the experimental and numerical results in all cases, in terms of both the failure mode and ultimate resistance, with a maximum difference of $\Delta_{\max} = 12.5\%$. This may be partly attributed to non-uniform curvature along the panels' length, thus inevitable load eccentricities, uneven contacts between specimens and the loading beam and/or bottom plate that are not accounted for in the numerical models. On the other hand, it should be reminded that various simplifications are made in the numerical model, such as the adoption of the buckling modes as the shapes of the imperfections.

Nevertheless, it may be stated that geometry, material properties, boundary conditions, loads, size and type of FE are modeled correctly, thus these numerical models may be used with conformity for the imperfection sensitivity analysis.

3.4.4 Assessment of imperfection sensitivity

The influence of various imperfection shapes on the ultimate strength is assessed, using the same 16 numerical models previously calibrated against the experimental results. [Table 3.8](#) summarizes the imperfections considered in the study, all of them determined by LBA.

Table 3.8: Imperfections considered in the study

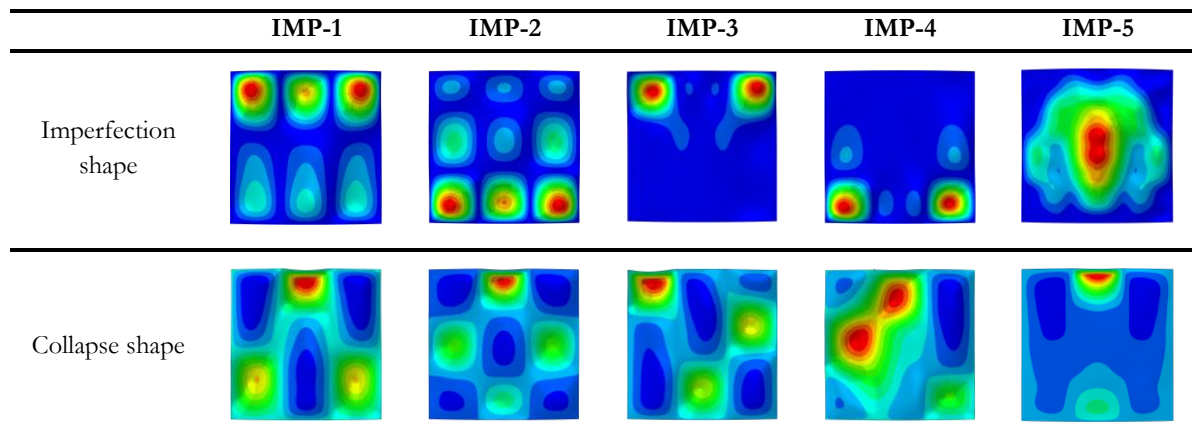
<i>IMP-1</i>	1 st buckling mode
<i>IMP-2</i>	2 nd buckling mode
<i>IMP-3</i>	3 rd buckling mode
<i>IMP-4</i>	4 th buckling mode
<i>IMP-5</i>	global mode
<i>IMP-6</i>	IMP-5 + 0.7*IMP-1
<i>IMP-7</i>	IMP-5 + 0.7*IMP-1 + 0.7*IMP-2
<i>IMP-8</i>	IMP-5 + 0.7*IMP-1 + 0.7*IMP-3
<i>IMP-9</i>	IMP-5 + 0.7*IMP-1 + 0.7*IMP-4

The modeling of imperfections is based on equivalent geometric imperfections recommended by EN 1993-1-5, as explained in [3.4.2](#). Therefore, the amplitudes are adopted in accordance with [Fig. 3.24](#), bearing in mind that for the imperfections IMP-1 to IMP-4 the amplitude depends on the type of the buckling mode (global or local). In the case of unstiffened panels, where the 1st mode is a global mode, imperfections IMP-5 and IMP-6 are not relevant, while imperfections IMP-7 to IMP-9 are combined so that the leading imperfection is IMP-1 and the imperfections IMP-2, IMP-3, and IMP-4 are the accompanying, with reduced values of amplitudes (*i.e.* 70% of the nominal value).

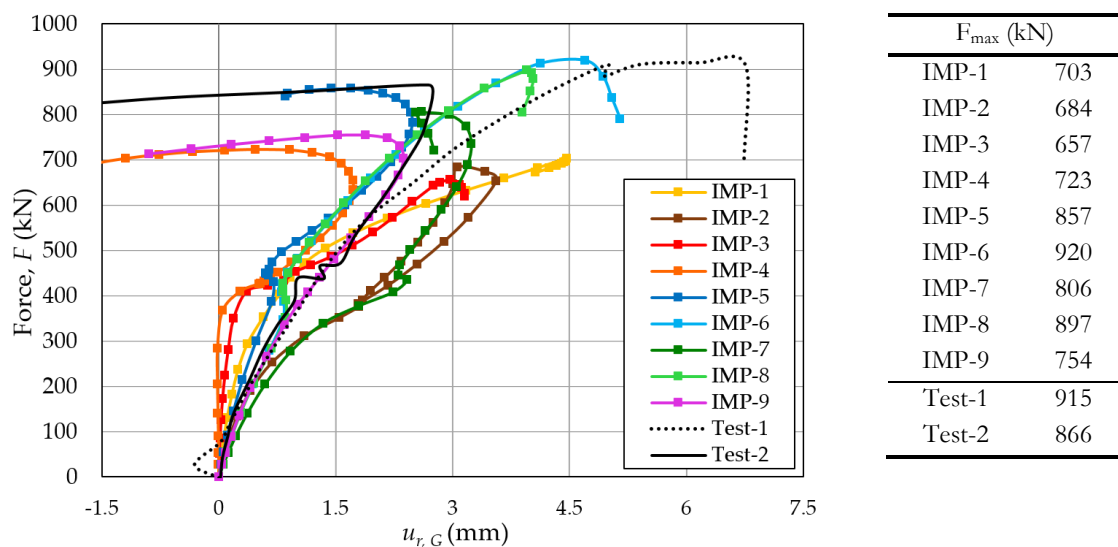
For the sake of simplicity, many authors suggest an imperfection shape affine to the 1st buckling mode (or combination of the first four modes), which has become the common practice often found in the literature (*e.g.* [\[16\]](#), [\[75\]](#), [\[78\]](#), [\[80\]](#), [\[82\]](#), to name a few). Hence, one of the objectives of the present study is also to assess this assumption since, in [3.4.3](#), it is concluded that the leading global imperfection (with or without accompanying local imperfections) is the one that leads to the most realistic behavior of curved panels, observed in experimental results.

To demonstrate to what extent the imperfection shape may affect the response of curved panels, an example is presented hereby, using the geometry of a 2-stiffened panel, with the radius equal to $R = 5.0$ m (*i.e.* R5-S2). The shapes of the first 4 buckling modes that correspond to different local imperfections, as well as the global mode (57th in this case), are presented in [Table 3.9](#). These eigenmodes, when used as initial imperfections, lead to very different failure modes, as presented also in [Table 3.9](#).

In [Fig. 3.29](#), the force-radial displacement curves are plotted and the ultimate resistances are summarized for each of the considered cases, including the two experimental results.

Table 3.9: Imperfection and corresponding collapse shapes for panel R5-S2

From Fig. 3.29, it may be observed that the imperfection shape significantly affects the behavior of the panels, leading to a wide scatter of results, with the largest difference between the maximum and the minimum value of the ultimate resistance of 40% in this case. The results for all 16 geometries, sorted based on the number of stiffeners, are summarized in Fig. 3.30, where the values of the ultimate compressive strength obtained numerically (F_{num}) are normalized to the experimental results F_{exp} (*i.e.* an average of two tests).

**Fig. 3.29:** Behavior of panel R5-S2 assuming various imperfection shapes

Based on these graphs, it may be concluded that the panels' sensitivity to imperfections, in general, decreases with the number of stiffeners, which is manifested by a reduced difference between the studied 9 imperfections, regardless of the radius of curvature (see Fig. 3.30c and Fig. 3.30d). This means that the importance of the adopted imperfection shape decreases and thus, the results are closer to the ones obtained experimentally, with the coefficient of variation of $\text{CoV} = 18\%$, which is significantly lower than in the case of unstiffened panels ($\text{CoV} = 36\%$). Moreover, in the case of unstiffened and lightly stiffened panels, an increased imperfection sensitivity is noticed for the increased curvatures, where the difference between the maximum and the minimum value between the analyzed 9 imperfections exceeds 60%.

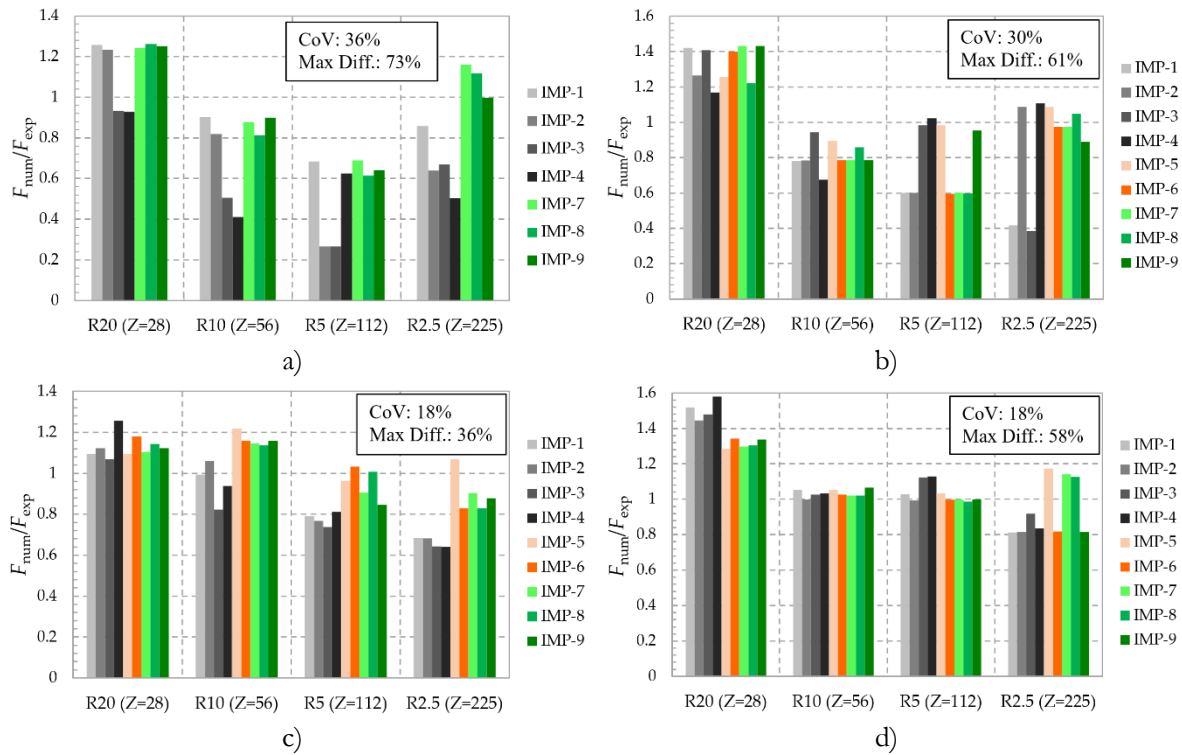


Fig. 3.30: Comparison of results with respect to radius R: a) S0; b) S1; c) S2; d) S3

Furthermore, in all four graphs, a declining trend may be noticed with the increase of the curvature parameter, extending the gap between the numerical and experimental results. This leads to the conclusion that the adoption of the equivalent geometric imperfections from Annex C.5 of EN 1993-1-5 for flat plates leads to conservative results and thus, are not appropriate for highly curved panels that are known to be more susceptible to imperfections.

In Fig. 3.31a and Fig. 3.31b, the results of the study are statistically processed, in order to identify: *i*) the critical imperfection shape that most frequently gives the lowest ultimate resistance out of 9 studied imperfection patterns; *ii*) the imperfection pattern that gives the result closest to *reality* (*i.e.* experimental results).

Based on the results presented in Fig. 3.31, it may be stated that for the prediction of the ultimate strength of curved panels, the adoption of one of the first four buckling modes as the imperfection shape is not necessarily a good assumption, as commonly believed. In fact, the imperfection shape affine to the global eigenmode leads to the most accurate results (*i.e.* CoV = 11%, see Fig. 3.31b, with the mean error of 7%), which coincides with the conclusions found by Tran *et al.* [59]. On the other hand, another widespread assumption that the 1st buckling mode is the critical imperfection shape is proven to be wrong. Namely, in this study, imperfection with the shape of the 1st buckling mode leads to the lowest ultimate resistance only in 6.25% of cases, according to Fig. 3.31a. However, it may be seen that for any given combination of radius of curvature and number of stiffeners, in more than 80% of cases the minimum collapse load is found by introducing an imperfection in the form of one of the first four modes. Therefore, for the design practice, where the safest solution is sought for, it is not sufficient to consider only

the first buckling mode, but the first four buckling modes should be verified as possible critical imperfection shapes.

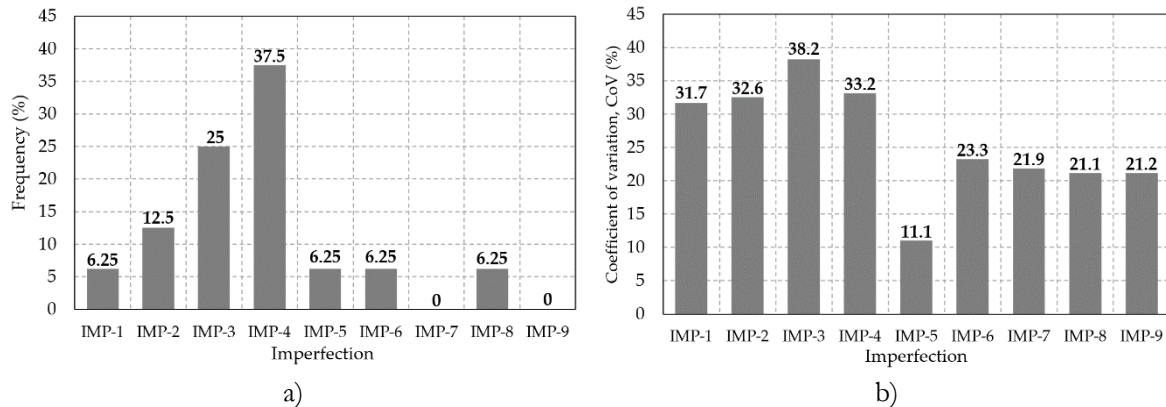


Fig. 3.31: Comparison of results: a) Frequency of imperfection leading to the lowest strength; b) CoV (%) of different imperfections around the experimental results

3.5 Summary

In this chapter, axial compression tests on 32 curved panels, both stiffened and unstiffened, were reported and the results were compared with the existing design standards and semi-empirical formulae available in the literature. Using the numerical FE models calibrated against the experimental tests, a series of material and geometrical non-linear analyses were performed to assess the imperfection sensitivity of curved panels and the influence of various imperfection shapes on their ultimate resistance. In particular, it was shown that:

- An unstable post-buckling path, governed by geometrical nonlinearities, characterizes the behavior of curved panels, with a dominant global buckling in case of unstiffened panels, whereas, in the case of stiffened panels, local buckling of both the stiffeners and the curved subpanel prevails;
- The methods proposed by Tran *et al.* [59] and in the OUTBURST research project [85] seem to be the most suitable for the estimation of the ultimate resistance of the stiffened curved panels (*i.e.* with the mean difference of 9% and 6%, respectively, and $\text{CoV} \approx 16\%$ with respect to the experimental results); however, the method from the OUTBURST research project is used further in the thesis since it allows for higher local curvatures ($Z_{\text{loc}} \leq 100$);
- The use of the design standard (*i.e.* EN 1993-1-5 and DNV-RP-C202) almost in all cases leads to an underestimation of the ultimate resistance, with the mean difference of 30% ($\text{CoV} \approx 28\%$) and 50% ($\text{CoV} \approx 37\%$), respectively;
- The imperfection sensitivity decreases with the number of stiffeners, regardless of the curvature parameter, reducing the relevance of the imperfection shape adopted;
- The equivalent geometric imperfections recommended by EN 1993-1-5 for flat plates lead to conservative results in the case of highly curved panels (*e.g.* average error $\Delta_{\text{max}} = 50\%$ for R2.5);

- The modeling of the imperfection in the form of the global eigenmode leads to the results closest to the experimental ones (mean error 7%, CoV \approx 11%), whereas the imperfection in the form of one of the first four eigenmodes leads to the safest approach in more than 80% of cases;

Finally, due to the complexity of the problem and the unpredictability of the imperfection distribution, the actual pattern needs to be standardized. Therefore, a further experimental study is necessary, with a clear definition of fabrication tolerances for curved panels that should be included in design codes in a way it was done for flat plates.

4. Elastic buckling behavior of curved panels under shear

4.1 Overview

Shear load, besides the compression load that was tackled in [chapter 3](#), is another dominant loading condition in box-girder bridge decks, close to the intermediate support, where the curved panel is integrated into the lower flange of the cross-section. However, based on the literature review presented in [section 2.4](#), it was concluded that very few studies on the curved panels under shear had been reported in the literature so far, without a clear design method for the assessment of the ultimate shear load. Hence, the thesis aims to propose a methodology, allowing the computation of the ultimate shear resistance of unstiffened simply supported curved panels under shear, thus addressing most practical cases of bridges, but also offshore and aeronautical applications.

Since the objective is to propose a design methodology that is conceptually similar to the existing one for flat plates under shear (see [2.5.2](#)), it is necessary first to calculate the critical shear load for a curved panel. Therefore, this section is dedicated to the elastic buckling behavior of curved panels only, with the ultimate goal to propose a simple expression for prediction of shear buckling coefficient k_s , thus accomplishing Task 3.1 of the thesis defined in [section 1.2](#). Subsequently, Task 3.2 is tackled in [chapter 5](#), in which the expressions for the ultimate shear load are proposed.

The numerical study, presented in this chapter, is divided into three sections. First, in [section 4.2](#), the numerical model used in the parametric study is described, whereas, the most relevant findings are discussed in [section 4.3](#). Finally, in [section 4.4](#), a new formula is proposed to estimate the critical shear stress of unstiffened curved panels, valid for three different types of edge constraints, various curvatures ($1 < Z \leq 100$) and various aspect ratios ($\alpha \leq 5.0$).

4.2 Numerical finite element model

4.2.1 Section overview

This section depicts the numerical models and numerical analyses carried out using the FEM software ABAQUS [142]. To define the critical buckling load, only the linear bifurcation analysis (LBA) is performed for each model, using the Subspace algorithm available in the software. Since the critical load is defined as the minimum load at which the buckling of panel occurs, in all LBAs carried out in this study, only the 1st eigenmode is considered.

In [4.2.2](#), the most relevant features of the numerical model (*e.g.* geometry, material properties, boundary and loading conditions, FE mesh size, etc.) are described in detail, whereas some of the assumptions used in the study presented in [section 3.4](#) are only briefly addressed. The validation of the numerical model is carried out in [4.2.3](#), using the available theoretical results as the comparator. Finally, some additional considerations regarding the curvature parameter Z are presented in [4.2.4](#), proving that this parameter is suitable to characterize the geometry of cylindrically curved panels.

4.2.2 Definition of the model

4.2.2.1 Geometry and material properties

In line with the assumption that the geometry of cylindrically curved panels is fully described only by the aspect ratio α (see Eq.(2.1)) and the curvature parameter Z , being a function of width b , thickness t and radius R (see Eq.(2.2)), the width and the thickness in this study are kept constant and equal to $b = 1000$ mm and $t = 10$ mm, respectively. Hence, to vary the curvature parameter and the aspect ratio between the desired ranges, the radius of curvature and the length of the panels are varied according to [Table 4.1](#), thus addressing all the cases with the radius-to-thickness ratio higher than $R/t > 100$.

Table 4.1: Geometry of the curved panels considered in this study

Width, b	Length, a	Thickness, t	Radius, R	Aspect ratio, α	Curvature, Z
1000 mm	200 – 5000 mm	10 mm	≥ 1000 mm	0.2 – 5.0	0 - 100

The geometry of panels is discretized by a mesh of finite elements, whose coordinates of the nodes are previously calculated and introduced in each model using a sub-routine.

Regarding the material model of structural steel applied in the models, only the nominal elastic properties relevant for the LBA are considered, such as Poisson's ratio equal to $\nu = 0.3$ and the modulus of elasticity equal to $E = 210$ GPa.

4.2.2.2 Loads and boundary condition

The loads and boundary conditions are defined using a cylindrical coordinate system (see Fig. 4.1a), with the origin at the point O that lays on the revolution axis. Similar to the numerical model used in section 3.4, the displacement field is defined by u_z , u_φ and u_r , which are the displacements in axial z -direction, the circumferential displacements, and the radial displacements, respectively.

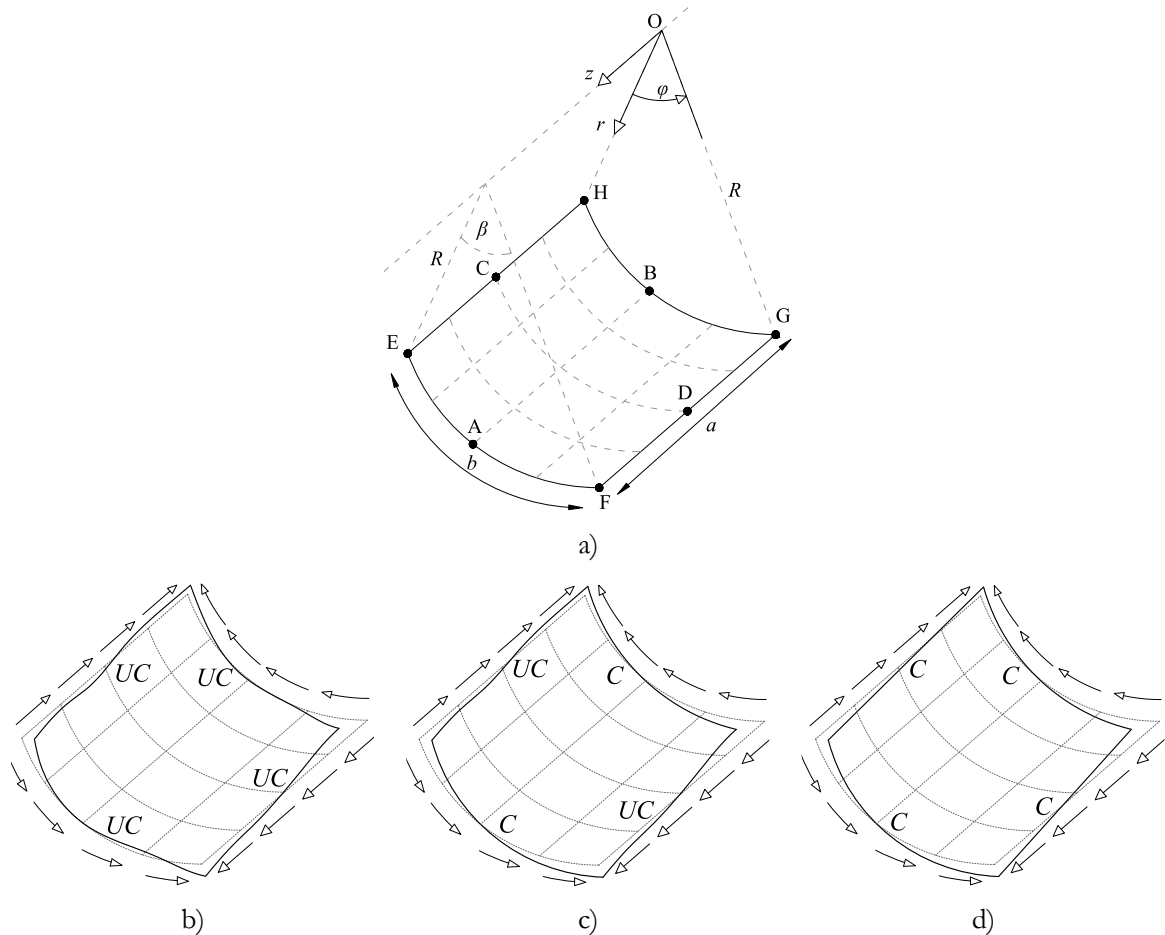


Fig. 4.1: Boundary conditions: a) coordinate system, b) BC1; c) BC2 and d) BC3

Regarding the boundary conditions, only simply supported panels are considered in this study. It is important to stress that in reality the boundary conditions of a panel are rarely simply supported, but rather somewhere in between the simply supported and the clamped condition. This is due to the surrounding supports, which have a certain torsional rigidity that make the boundary conditions of a panel elastically rotation-restrained. Therefore, the higher the torsional rigidity of support the higher the level of the edge constraint [147]. However, since the principal goal of this study is to propose a formula that returns lower bound of the shear buckling load, as it is commonly done in the design practice (*e.g.* European standard for flat plates), where a certain level of safety needs to be guaranteed, only simply supported curved panels are studied.

To ensure the desired boundary condition, the following restraints are introduced in the shell model (see Fig. 4.1): all edges restrained in the radial direction (*i.e.* $u_r = 0$); the axial displacements

prevented in points A, B, C and D (*i.e.* $u_z = 0$) and the circumferential displacements prevented point A (*i.e.* $u_\varphi = 0$).

In addition, three different boundary conditions are considered, based on the edge in-plane constraints (C – *constrained* or UC – *unconstrained* edge), encountered also in several studies (*e.g.* [55], [71]) on curved panels subjected to pure compression:

- **BC1:** all edges are free to deflect (UC) (Fig. 4.1b);
- **BC2:** curved edges EF and GH are forced to remain straight (C), while the longitudinal edges FG and EH are free to deflect (UC) (Fig. 4.1c);
- **BC3:** all edges are forced to remain straight (C) (Fig. 4.1d);

One may agree that the exact level of in-plane constraint, in reality, is difficult to determine. Hence, these three simplified cases aim to cover the possible range of behaviors, where BC1 and BC3 correspond to lower and upper bounds, and BC2 is an intermediate case. For instance, boundary condition BC2 simulates approximately the boundary conditions of a cylindrically curved bottom flange in a box-girder bridge, where rigid diaphragms prevent the curved edges to deflect freely (C), whereas the flexible webs allow the longitudinal edges to wave (UC).

To force an edge to remain straight (as required in the case of the boundary condition BC2 and BC3), it is necessary to define the kinematical equations, which dictate displacements of the nodes along the edges in a kinematically consistent manner once the edge starts to displace. These kinematical equations are introduced along the considered edge by means of keyword **EQUATION*, where the displacement of each node N is defined by translational and rotational component of the corresponding master node that governs constraint behavior. The edge constraints used in the numerical model are summarized in Table 4.2.

Table 4.2: In-plane edge constraints applied in the model for BC2 and BC3

Boundary type	Edge	Master node	Equation
BC2	EF	A	$u_3^N = u_3^A + d \cdot u_4^A$
	GH	B	$u_3^N = u_3^B + d \cdot u_4^B$
BC3	EF	A	$u_3^N = u_3^A + d \cdot u_4^A$
	GH	B	$u_3^N = u_3^B + d \cdot u_4^B$
	FG	D	$u_2^N = u_2^D + d \cdot u_4^D$
	EH	C	$u_2^N = u_2^C + d \cdot u_4^C$

In these expressions, u_2 , u_3 , and u_4 correspond to the circumferential displacement (u_φ), axial displacement (u_z) and the rotation around the radial axis, respectively, since ABAQUS uses a convention in which the radial, circumferential and longitudinal axes are interpreted as the 1-, 2-, and 3-axes, respectively. The scalar d represents the distance between a node N and the corresponding master point.

Since the translational component of the master nodes A and B (*i.e.* u_3^A and u_3^B) is prevented in the longitudinal direction due to requirements for the simply supported conditions, the axial displacement of a node N is defined only by the rotational component. This further means that the edges EF and GH may only rotate around points A and B (see Fig. 4.1c and Fig. 4.1d).

Finally, regarding the loading conditions applied in the numerical model, the shell edge load is uniformly distributed along all the edges in the middle surface of the panels.

4.2.2.3 Type and size of FE

To choose an appropriate type and dimension of the shell finite element for the discretization of the numerical models, a mesh sensitivity study is first carried out. Namely, the convergence of the shear buckling coefficient k_τ is monitored for three different curvatures, varying the size of elements and comparing several types of shell FE, commonly encountered in the literature for studies on thin shell-like structures. Since the elements are assumed to be squared, their number in the circumferential direction n_C , for a given width of $b = 1000$ mm, remains constant, whereas, in the longitudinal direction, the number of elements n_L depends on the aspect ratio. The results of the convergence study are summarized in Table 4.3.

Table 4.3: Mesh convergence study (shear buckling coefficient - k_τ)

Curvature	FE type	33.3x33.3mm ²	25x25mm ²	20x20mm ²	10x10mm ²
		($n_C = 30$)	($n_C = 40$)	($n_C = 50$)	($n_C = 100$)
$Z = 0$	S4	9.38	9.33	9.31	9.28
	S4R	9.36	9.32	9.30	9.27
	S8R5/S9R5	9.31	9.30	9.30	9.28
$Z = 50$	S4	19.11	18.95	18.87	18.76
	S4R	18.99	18.87	18.81	18.73
	S8R5/S9R5	18.81	18.76	18.78	18.72
$Z = 100$	S4	27.79	27.50	27.36	27.17
	S4R	27.62	27.40	27.30	27.16
	S8R5/S9R5	27.22	27.20	27.19	27.15

Based on these results, it is concluded that the size of an element of 25×25 mm² is sufficient to achieve numerical convergence, regardless of the FE type, which means that further increase of the number of elements practically does not affect the results. However, it is decided again to discretize the numerical models by four-node shell elements (S4R) since it is concluded that considerable CPU time saving could be achieved.

4.2.3 Validation of the model

Owing to the lack of a general analytical expression that allows the calculation of the shear buckling coefficient of the curved panels for various aspect ratios and curvature parameters, the numerical results are validated against the available theoretical results for flat panels, implemented in EN 1993-1-5 [11]. Thus, the validation is done by comparing the numerical results of the shear buckling coefficient ($k_{\tau,num}$) for flat unstiffened panel ($Z = 0$) with the theoretical results ($k_{\tau,theory}$), derived from Eq.(2.101). The results are presented in Table 4.4, from where it may be concluded

that the agreement is excellent, with the maximum difference of $\Delta_{\max} = 3.3\%$. Therefore, for the purpose of this study, in which only LBA analyses are carried out, it is possible to consider the present numerical model validated.

Table 4.4: Validation of numerical models – flat panel

$\alpha = a/b$	0.4	0.6	1.0	1.5	2.0	2.5	3.0	3.5	4.0	4.5	5.0
$k_{\tau,\text{num}}$	37.68	18.95	9.33	7.07	6.55	6.04	5.84	5.74	5.63	5.59	5.53
$k_{\tau,\text{theory}}$	37.38	18.83	9.34	7.12	6.34	5.98	5.78	5.67	5.59	5.54	5.50
Δ (%)	0.83	0.61	-0.16	-0.63	3.31	0.94	1.02	1.25	0.68	0.86	0.61

4.2.4 Justification of the curvature parameter as a key parameter

The non-dimensional curvature parameter Z , defined by Eq.(2.2), is a very convenient parameter for the characterization of the geometry of cylindrically curved panels, as it merges into one all the other relevant parameters (*i.e.* R , t , and b). As stated in Martins *et al.* [55], numerous authors questioned and confirmed the suitability of curvature parameter as a key parameter for assessment of the buckling behavior of curved panels when subjected to uniform compression. This means that two panels with the same curvature parameter, despite having different widths, thicknesses and/or radii, should always yield the same critical load.

To the best of the author's knowledge, such suitability of curvature parameter has never been validated in the case of critical shear load of curved panels. Hence, in this study, additional 1600 LBAs are carried out, aiming to verify whether the critical shear load (*i.e.* shear buckling coefficient) may be determined based only on the curvature parameter. In Table 4.5, the ranges of parameters for the presented study are summarized, whereas the mesh size and the boundary conditions (BC1) are kept the same in all analyses.

Table 4.5: Ranges of parameters for a study on the Z parameter justification

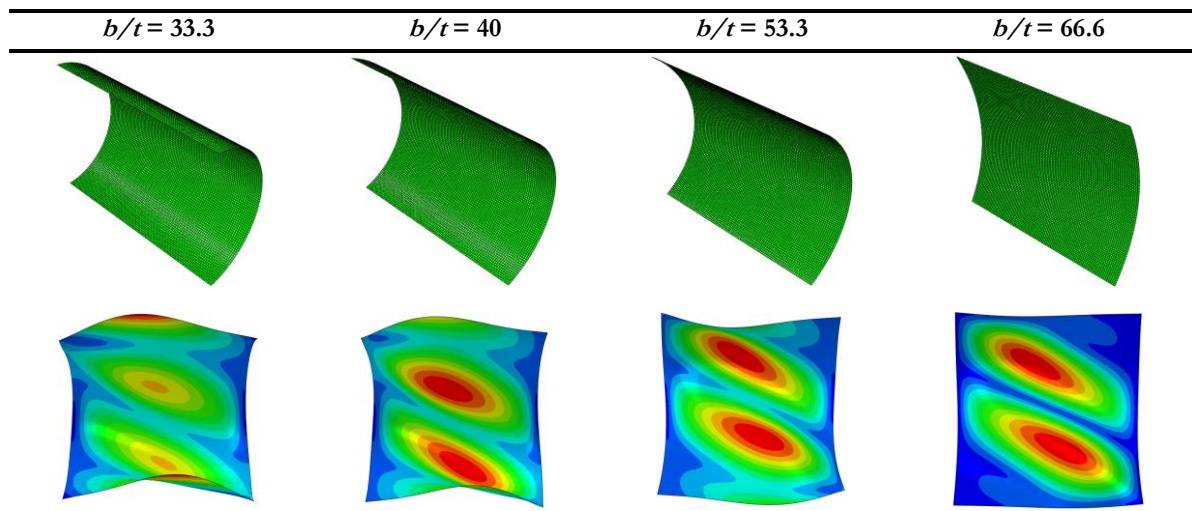
Width, b [mm]	Thickness, t [mm]	Aspect ratio, α	Curvature, Z
500 – 1000 (step 100)	5 – 15 (step 2.5)	0.5 – 3.0 (step 0.5)	0 – 100 (step 25)
1000 – 2000 (step 500)		3.0 – 5.0 (step 1)	

In each model, for a certain combination of width b and thickness t from the table, the desired curvature is obtained by varying the radius of curvature R . The results are compared against the reference values ($k_{\tau,\text{ref}}$), which are assumed to be the shear buckling coefficients of the panels with the width equal to $b = 1000$ mm, for each curvature parameter. In Table 4.6, some results of the study are presented, highlighting the most relevant findings.

Table 4.6: Justification for the use of Z as a key parameter - $k_t/k_{t,\text{ref}}$ (%)

$Z = 0$	$b = 500$ mm	$b = 600$ mm	$b = 800$ mm	$b = 1000$ mm	$b = 1500$ mm	$b = 2000$ mm
$t = 5.0$ mm	0.0	0.2	0.4	0.5	0.8	0.8
$t = 10.0$ mm	-1.2	-0.8	-0.2	0.0	0.4	0.5
$t = 12.5$ mm	-1.9	-1.3	-0.6	-0.2	0.2	0.4
$t = 15.0$ mm	-2.8	-1.9	-1.1	-0.5	0.0	0.3
$Z = 50$	$b = 500$ mm	$b = 600$ mm	$b = 800$ mm	$b = 1000$ mm	$b = 1500$ mm	$b = 2000$ mm
$t = 5.0$ mm	0.0	0.2	0.5	0.6	0.7	0.7
$t = 10.0$ mm	-2.1	-1.3	-0.4	0.0	0.4	0.6
$t = 12.5$ mm	-3.6	-2.3	-1.0	-0.4	0.2	0.5
$t = 15.0$ mm	-5.5	-3.6	-1.8	-0.9	0.0	0.3
$Z = 100$	$b = 500$ mm	$b = 600$ mm	$b = 800$ mm	$b = 1000$ mm	$b = 1500$ mm	$b = 2000$ mm
$t = 5.0$ mm	0.0	0.6	1.1	1.4	1.7	1.8
$t = 10.0$ mm	-6.2	-3.5	-1.1	0.0	1.0	1.4
$t = 12.5$ mm	-11.9	-7.0	-2.8	-1.1	0.6	1.1
$t = 15.0$ mm	-20.1	-11.9	-5.1	-2.4	0.0	0.8

Based on these presented results, it may be noticed that for low values of the b/t ratio (*i.e.* *stocky panels*), marked in bold in Table 4.6, and for increasing curvature parameter, the panels start to change qualitatively its behavior. This alteration of behavior is illustrated in Fig. 4.2, in which b/t ratio is varied ($t = 15$ mm), while keeping the same curvature parameter $Z = 100$.

**Fig. 4.2:** Different buckling behavior of a panel with $Z = 100$

From the figure, it may be observed that in case of panels with a reduced b/t ratio, the cylinder-type behavior with torsional effect starts to prevail, rather than a pure shear behavior of an isolated curved panel. Consequently, the shear buckling coefficient of these panels differs from the expected reference buckling coefficient for a given curvature parameter ($k_{t,\text{ref}}$), with an error that exceeds 5% and goes up to 20% in case of very curved stocky panels.

This further means that there are panels for which the shear buckling coefficient cannot be obtained based only on the curvature parameter, as it is assumed in the NASA curves, but additional information on the b/t ratio is required. The reason for this is that the NASA curves were mainly developed for the design of aircraft, where the b/t ratio of panels is considerably higher, and therefore, the problem of stocky panels with high curvatures was never encountered.

Therefore, it is intended in this study to define the lower bound limit for the b/t ratio, below which the curvature parameter is no longer a suitable parameter for the prediction of the shear buckling coefficient. This is achieved by using Eq.(4.1), derived from Eq.(2.2)

$$\left(\frac{b}{t}\right)_{\min} \geq \sqrt{Z\left(\frac{R}{t}\right)_{\min}} \quad (4.1)$$

where $(R/t)_{\min}$ is the minimum value of R/t ratio, taken as the one below which the error between the buckling coefficient of the considered panel (k_{τ}) and the buckling coefficient of the reference panel ($k_{\tau,\text{ref}}$) exceeds $\Delta = 5\%$. The value of $(R/t)_{\min}$ depends not only on the curvature parameter Z , but also on the aspect ratio α of the panel, as shown in Table 4.7.

Table 4.7: Minimum R/t ratio for a suitable Z parameter

$(R/t)_{\min}$	$\alpha \geq 3.0$	$\alpha = 2.0$	$\alpha = 1.0$	$\alpha = 0.5$
$Z = 0$	136	178	278	544
$Z = 25$	17	22	16.5	34.5
$Z = 50$	31.5	33	15	18.5
$Z = 75$	45.5	48	16	14.5
$Z = 100$	56	56	20.5	17

Based on the results presented in Table 4.7, the minimum values of the b/t ratio (Eq.(4.1)) are plotted in Fig. 4.3, for the aspect ratios higher than $\alpha \geq 1$. It may be noticed, for instance, that a panel with a curvature parameter equal to $Z = 60$, needs to have the b/t ratio equal or higher than $b/t \geq 30$ for the aspect ratio $\alpha = 1.0$, and $b/t \geq 46$ for $\alpha = 2.0$, in order to avoid the inconsistency in results encountered in the case of stocky panels.

However, since the objective is to define the minimum b/t ratio that would cover all the cases of curved panels, regardless of the aspect ratio, the limit (red dashed line) is conservatively adopted as an upper bound of the presented curves, which may be approximated by Eq.(4.2).

$$\left(\frac{b}{t}\right)_{\min} = \left(\frac{Z}{20}\right)^2 + \frac{Z}{2.6} + 14.5 \quad (4.2)$$

This criterion needs to be satisfied in order to avoid the aforementioned cylinder-type behavior, which further allows for a simple calculation of the shear buckling coefficient based only on the curvature parameter. Therefore, for any b/t ratio above these limits, the curvature Z may be considered a suitable key parameter for the characterization of the geometry of cylindrically curved panels, whereas for the values below the limits this statement cannot be granted.

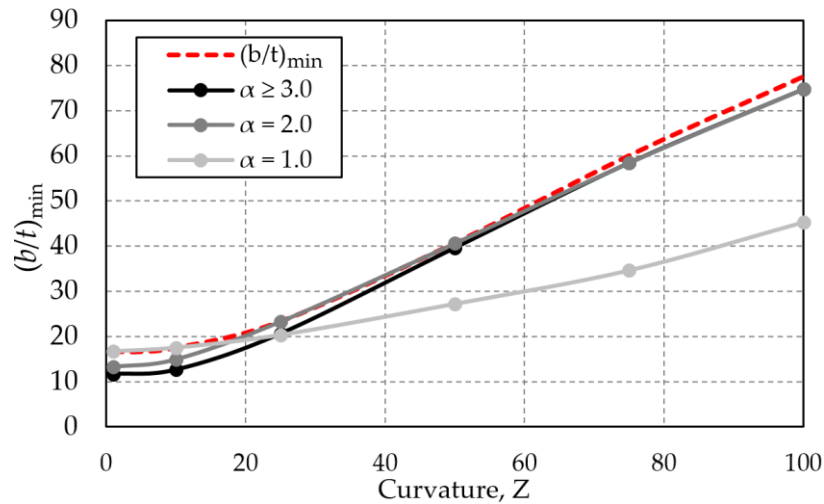


Fig. 4.3: Minimum values of b/t ratio for a suitable Z parameter

Finally, in Fig. 4.4, the b/t ratio is plotted against the curvature parameter Z for numerous real examples of the steel curved panels used in different engineering applications, addressed in chapter 2 (see Fig. 2.6). Additionally, the newly developed limitation for b/t ratio, given by Eq.(4.2), is also plotted.

It may be noticed that only a few cases of bridges with the curvature parameter $Z < 1$ have the b/t ratio below the limit. However, these panels are considered flat panels according to EN 1993-1-5 [11], and therefore, they are not of interest in this study. For panels with curvature $Z \geq 1$, none of the examined panels has the b/t ratio below the proposed limit. This approves that the Z parameter may be comfortably used for the prediction of the shear buckling coefficient for all the curved panels with the geometry that falls in the domain of the practical design interest, in the same way it is used in case of the panels subjected to in-plane compression.

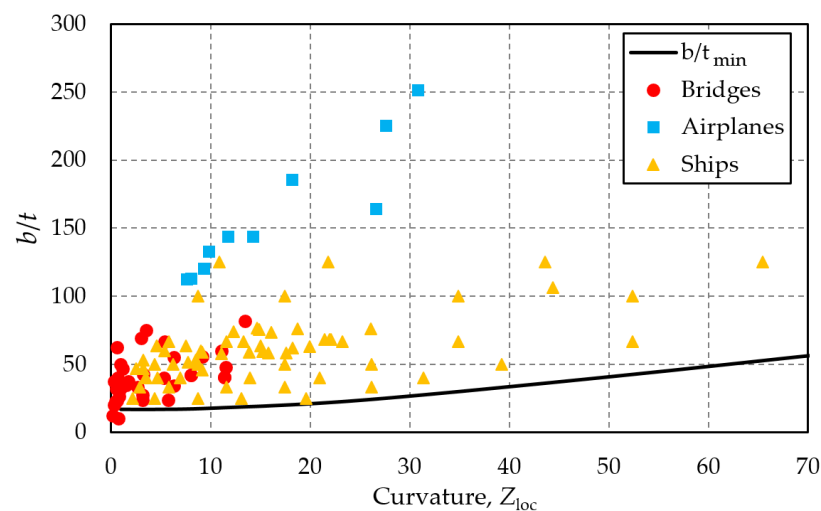


Fig. 4.4: Ranges of the b/t ratio and the Z_{loc} parameter of practical interest (see Fig. 2.6)

4.3 Parametric study

4.3.1 Section overview

This section is devoted to a numerical parametric study, carried out to characterize the buckling behavior of unstiffened simply supported curved panels under pure in-plane shear. First, the parameters varied in the study are summarized in 4.3.2, whereas the influence of aspect ratio, curvature parameter and the boundary conditions on the buckling behavior is presented in 4.3.3.

4.3.2 Ranges of parameters

The parametric study considers three boundary conditions – BC1, BC2, and BC3, presented in Fig. 4.1. For each of them, 101 different curvatures (*i.e.* $Z = 0 - 100$ with step 1) and 49 aspect ratios (*i.e.* $\alpha = 0.2 - 5.0$ with step 0.1) are varied, comprising in total 14 847 linear buckling analysis, summarized in Table 4.1.

The width and thickness are kept constant since it was proven in 4.2.4 that the curvature parameter might be reliably used for the definition of the panel's geometry, provided that the previously set criterion, given by Eq.(4.2), is satisfied. In the presented study, the b/t ratio is equal to $b/t = 100$, which satisfies the criterion for the entire range of curvature parameters.

4.3.3 Elastic buckling behavior of curved panels

4.3.3.1 Influence of aspect ratio

The dependence of the shear buckling behavior on the aspect ratio ($\alpha = a/b$) is not a novelty and it was addressed in almost all relevant references dealing with this topic, presented in section 2.4. In fact, the expression for the calculation of the shear buckling coefficient prescribed by EN 1993-1-5 for flat plates reproduced in Eq.(2.101), directly depends on the aspect ratio. As for the cylindrically curved panels, the aforementioned analytical solutions (*i.e.* NACA monographs), also allow the computation of the shear buckling coefficient as a function of various aspect ratios (see Fig. 2.20 and Fig. 2.21).

In Fig. 4.5, the numerical results are presented to emphasize the influence of the aspect ratio on the shear buckling coefficient for various curvatures and boundary conditions. It may be noticed that a very good agreement is achieved between the analytical solutions (red line) and the numerical results for the flat plate ($Z = 0$), as already shown in 4.2.3. However, for increased curvatures, Eq.(2.101) is no longer suitable for the prediction of the shear buckling coefficient, as it returns very conservative results.

Here, it is necessary to point out that the buckling behavior of cylindrically curved panels is a complex problem that cannot be considered as a function of only one variable. Namely, the form of the first eigenmode is quite difficult to anticipate since it is determined by the combination of aspect ratio and curvature parameter, and not only by one of them. In addition, the complexity of the problem increases by the inclusion of different boundary conditions since two panels with the same geometry and with different boundary conditions may also experience different buckling behavior.

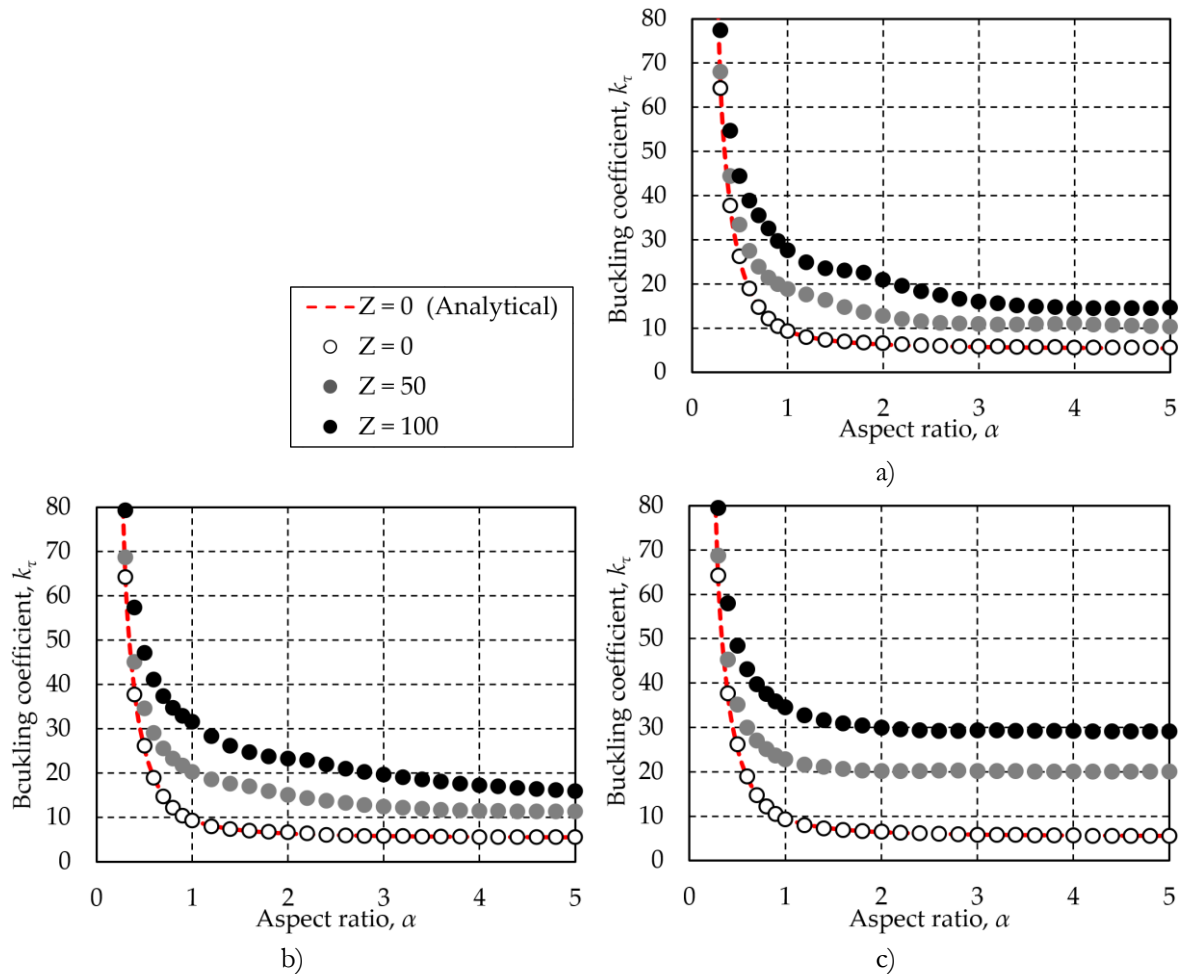


Fig. 4.5: Influence of α on the shear buckling coefficient for: a) BC1; b) BC2; c) BC3

Nevertheless, from Fig. 4.5, it is noticed that for all three boundary conditions, the critical shear stress decreases with the increment of the aspect ratio and this trend is always the same, regardless of the curvature parameter, which was also confirmed in Refs. [109], [127]. Furthermore, for high values of aspect ratio, the minimum elastic buckling coefficient stabilizes and the influence of aspect ratio becomes practically negligible.

This further means that the dependence between shear buckling coefficient and aspect ratio, for a certain curvature parameter, may be described by a parabolic function, with a format similar to Eq.(2.101). A minor deviation from this trend is noticed only in several points in the intermediate range of aspect ratio ($\alpha = 1.0 - 2.5$), for higher values of the curvature parameter (see Fig. 4.5). This may be explained by the sudden modification of the buckling pattern that is noticed to occur in that range, as it was noticed also in [127]. Namely, with a minor change of the aspect ratio, the first buckling mode may shift randomly from a symmetric to an antisymmetric buckling mode and vice versa, leading also to a sudden jump (or drop) in the shear buckling coefficient.

In Fig. 4.6, these changes in the buckling form with a change of the aspect ratios are presented for the boundary conditions BC1, BC2, and BC3, whereas the curvature parameter is kept constant and equal to $Z = 100$.

Based on this example, it may be noticed that a minor change in the aspect ratio (*i.e.* from $\alpha = 1.6$ to $\alpha = 1.8$) may cause a drastic change in the buckling pattern, depending on the boundary condition. Namely, in the case of BC1, the buckling mode shifts from the antisymmetric to symmetric; in the case of BC3, it jumps from symmetric to antisymmetric, whereas in the case of BC2, no change in the buckling mode occurs for this combination of α and Z . Therefore, two consecutive values of shear buckling coefficients in Fig. 4.5 may show a certain discrepancy from the uniformly declining trend, especially in the case of more flexible BC1, which seems to be more susceptible to these changes. Nevertheless, these deviations of the shear buckling coefficient are almost negligible and thus, they are not explicitly considered in section 4.4, where the expression for k_τ is proposed.

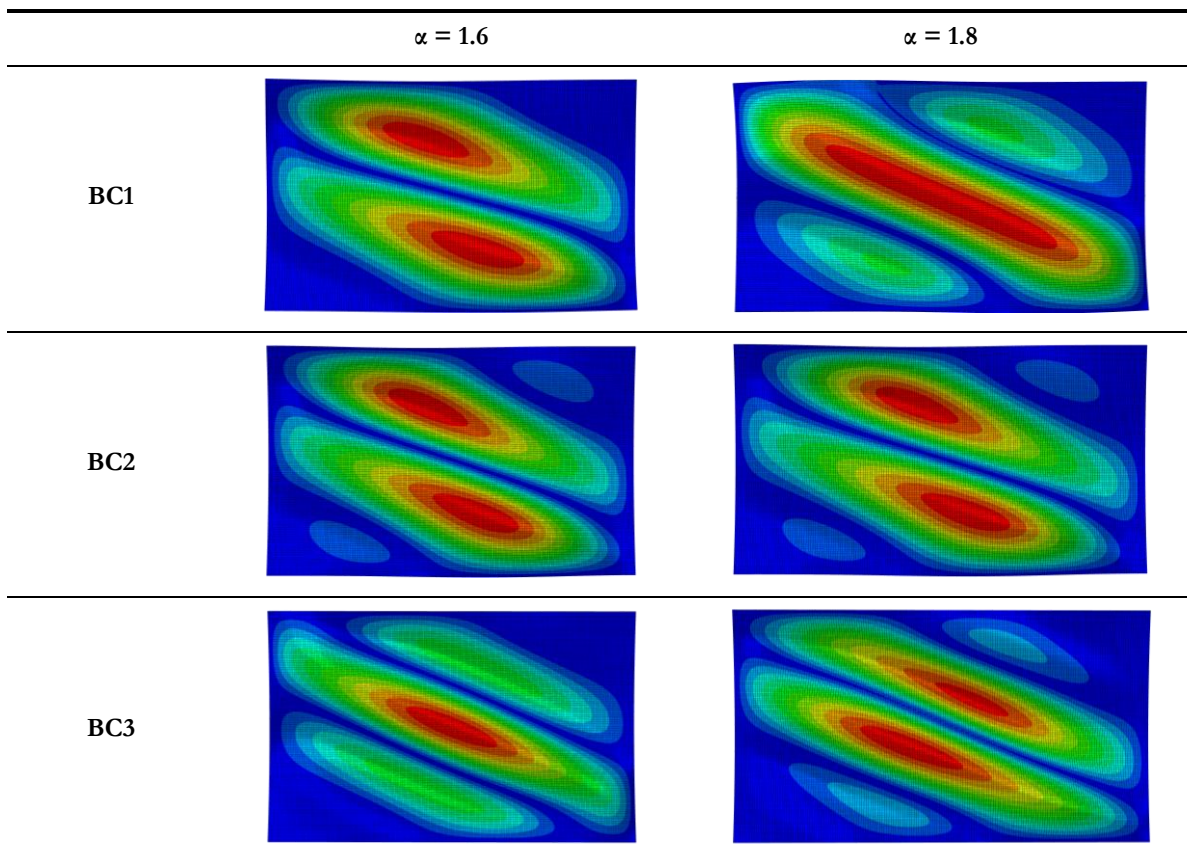


Fig. 4.6: Influence of α on the buckling mode for various boundary conditions ($Z = 100$)

4.3.3.2 Influence of the curvature parameter

The influence of the curvature parameter on the shear buckling behavior of curved panels was discovered in the very first studies dealing with this problem, summarized in 2.4.2. To analyze the $Z - k_\tau$ relation, the shear buckling coefficients obtained numerically are plotted in Fig. 4.7 against the curvature parameter, for the boundary condition type BC2 and various aspect ratios. It is important to stress that such an interpretation of the results was not possible before, owing to the various limitations found in literature (see Table 2.3).

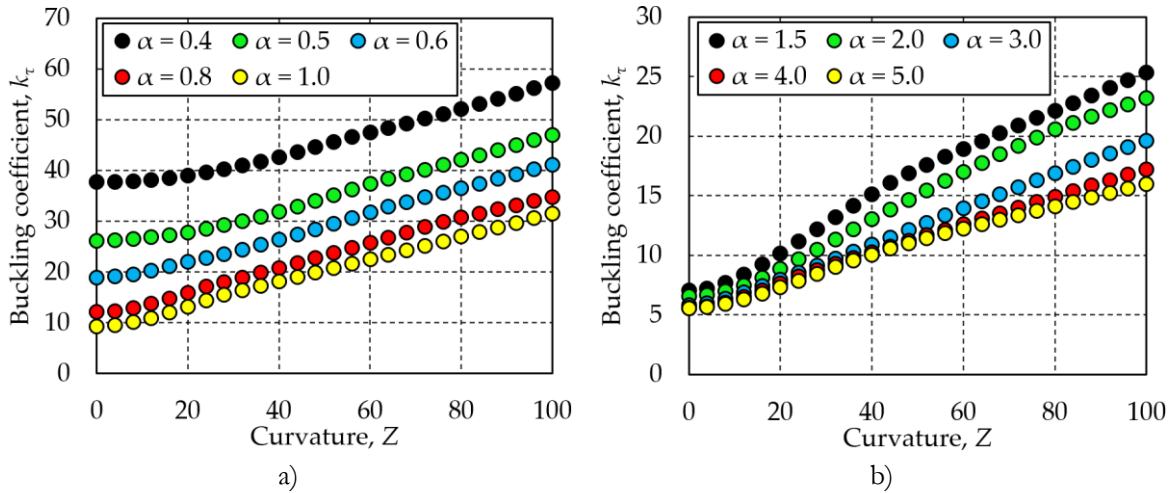


Fig. 4.7: Influence of curvature on the shear buckling coefficient: a) $\alpha \leq 1.0$; b) $\alpha > 1.0$

It may be observed from these graphs that the increase of the curvature parameter leads to an increase of the critical buckling stress. This is explained by the fact that panels with a higher curvature have also a higher second moment of area (*i.e.* initial stiffness) thus, yielding higher critical stress. Moreover, it may be noticed that this increasing trend is the same, regardless of the aspect ratio.

Furthermore, from [Fig. 4.7b](#), it may be noticed that for the entire spectrum of curvatures the influence of the aspect ratio starts to decrease for the panels with the aspect ratio higher than $\alpha \geq 3.0$. To understand to what extent its influence decreases, the shear buckling coefficients are presented in [Table 4.8](#) for various aspect ratios (*i.e.* $\alpha = 3.0$, $\alpha = 4.0$ and $\alpha = 5.0$) and various curvature parameters. In addition, the differences between the aspect ratio $\alpha = 4.0$ and $\alpha = 3.0$ (*i.e.* $\Delta \alpha_4 - \alpha_3$), as well as between $\alpha = 4.0$ and $\alpha = 5.0$ (*i.e.* $\Delta \alpha_4 - \alpha_5$) are calculated.

Table 4.8: Buckling coefficient k_τ for panels with $\alpha \geq 3.0$

	$Z = 0$	$Z = 20$	$Z = 40$	$Z = 60$	$Z = 80$	$Z = 100$
$\alpha = 3$	5.844	7.972	10.895	13.946	16.883	19.634
$\alpha = 4$	5.628	7.636	10.284	12.610	14.933	17.222
$\alpha = 5$	5.534	7.302	10.070	12.247	14.127	15.972
$\Delta \alpha_4 - \alpha_3$ (%)	-3.69	-4.21	-5.62	-9.58	-11.55	-12.28
$\Delta \alpha_4 - \alpha_5$ (%)	1.71	4.57	2.12	2.96	5.70	7.83

The results from the table indicate that the influence of the aspect ratio indeed drops gradually for $\alpha \geq 3.0$. Namely, the difference between the aspect ratio $\alpha = 4.0$ and $\alpha = 3.0$ is slightly higher only for higher curvature parameters, whereas the difference between the aspect ratio $\alpha = 4.0$ and $\alpha = 5.0$ is practically negligible for the whole spectrum of Z .

A further increase of the aspect ratio above $\alpha \geq 5.0$ would be redundant since it leads to very long panels, rarely met in the practical applications. Moreover, based on the trend presented in [Table 4.8](#), one may deduce that the behavior of such panels would be very similar to the panels with the aspect ratio equal to $\alpha = 5.0$. For instance, the shear buckling coefficient for an infinitely long flat panel (*i.e.* $Z = 0$ and $\alpha \rightarrow \infty$) asymptotically reaches the lowest theoretical value of

$k_r = 5.34$ (see Eq.(2.101)). This leads to a negligible difference of $\Delta = 3.5\%$ when compared to the buckling coefficient of a flat panel with the aspect ratio $\alpha = 5.0$ ($k_r = 5.53$). Therefore, the panels with the aspect ratio higher than $\alpha \geq 5.0$ are not considered in this study.

Finally, the influence of the curvature parameter on the eigenmode shape is illustrated in Fig. 4.8, considering panels with two different aspect ratios (*i.e.* $\alpha = 1.0$ and $\alpha = 5.0$) and the boundary condition BC2.

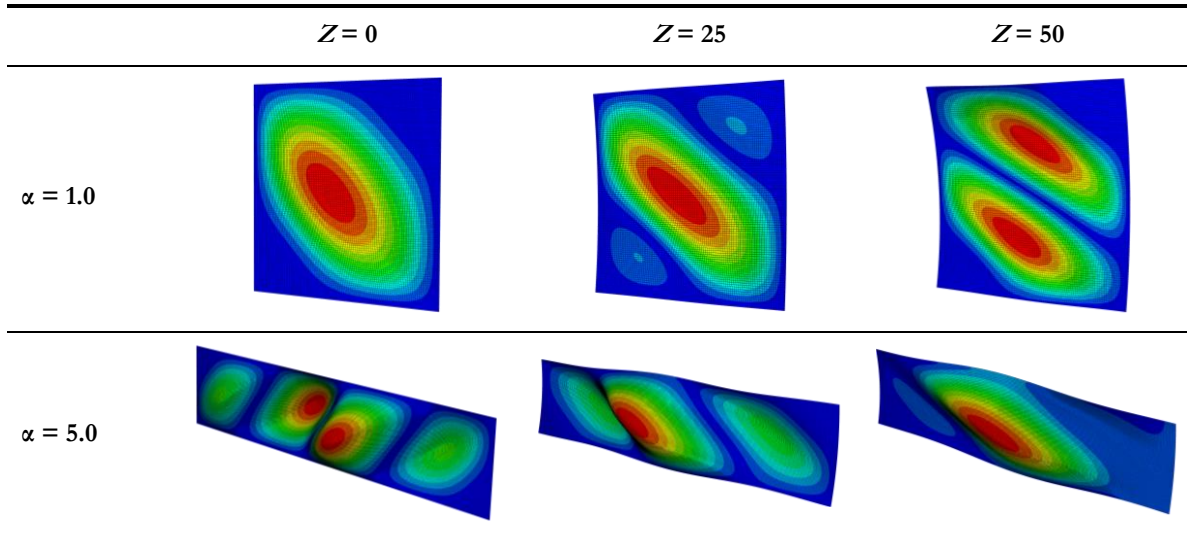


Fig. 4.8: Influence of curvature on the shear buckling mode

It may be noticed that the pattern of the 1st buckling mode varies with the curvature parameter without a clear trend, shifting occasionally from symmetric to antisymmetric shape, depending on the given combination of Z and α .

4.3.3.3 Influence of boundary conditions

The influence of the various boundary conditions on the shear buckling behavior was very scarcely investigated in the past. Namely, the analytical solutions available in the literature (*e.g.* NACA monographs [119]-[120], Domb&Leigh [41], Machaly *et al.* [126]) allow the calculation of the shear buckling coefficient for simply supported panels, without a clear specification of the in-plane edge constraints.

Therefore, the comparison of the three boundary conditions, introduced earlier in this chapter (see Fig. 4.1) is carried out for panels with various aspect ratios and curvature parameters. The most relevant results are summarized in Fig. 4.9, emphasizing the importance of the edge constraints on the critical shear load.

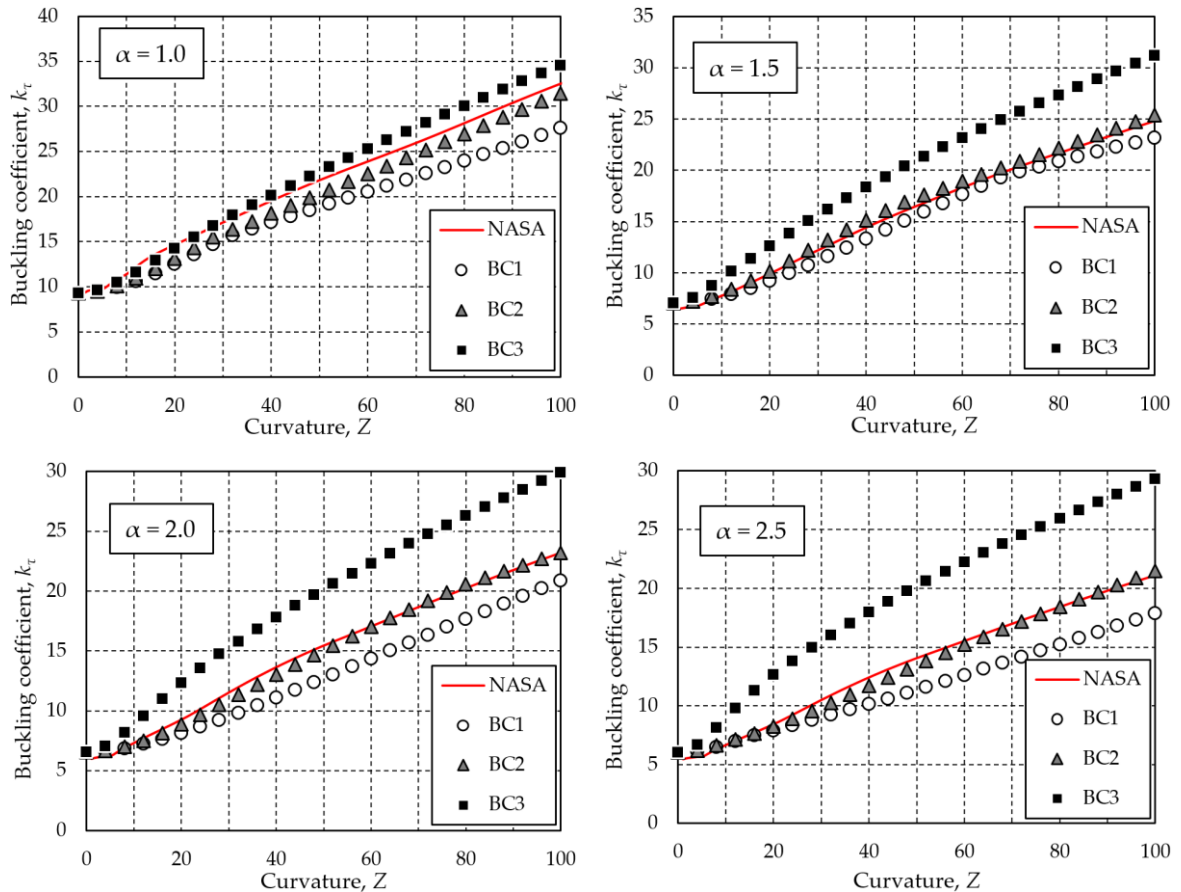


Fig. 4.9: Influence of boundary conditions - FEM vs theoretical results (NACA curves)

It may be noticed that the level of in-plane constraint has a major influence on the shear buckling coefficient. Namely, the case where the most of the DOFs are restrained (BC3), as the most rigid one, expectedly gives the highest values of the buckling load, whereas the panels with boundary condition BC1 yield the lowest buckling load. Finally, the boundary condition BC2 is an intermediate case, limited by BC1 and BC3.

Moreover, in Fig. 4.9, the comparison between the theoretical (NACA curves) and FEM results is made. It may be concluded that in the NACA monographs, the shear buckling coefficient corresponds best to boundary condition BC2, which means that the tested curved panels are most likely partially constrained. However, in some cases (*e.g.* $\alpha = 1.0$), the values of the shear buckling coefficient from the NACA curves are even higher than those obtained numerically. Therefore, since in design practice the edges are commonly assumed to be unconstrained (*i.e.* BC1 boundary condition), the use of the NACA monographs could lead to an overestimation of the buckling load, and thus an unsafe design.

In Table 4.9, the values of the shear buckling coefficients from Fig. 4.9 are presented for two aspect ratios ($\alpha = 1.0$ and $\alpha = 4.0$) and several curvature parameters. To examine the influence of the three boundary conditions, the difference between the BC2 and BC1 (*i.e.* $\Delta BC2 - BC1$), as well as between BC2 and BC3 (*i.e.* $\Delta BC2 - BC3$) are calculated.

Table 4.9: Influence of boundary conditions on shear buckling coefficient k_τ

$\alpha = 1.0$	$Z = 0$	$Z = 20$	$Z = 50$	$Z = 100$
BC1	9.33	12.51	18.84	27.58
BC2	9.33	13.15	20.31	31.46
BC3	9.33	14.25	22.78	34.55
Δ BC2-BC1 (%)	0.0	5.1	7.8	14.1
Δ BC2-BC3 (%)	0.0	-7.7	-10.8	-8.9
$\alpha = 4.0$	$Z = 0$	$Z = 20$	$Z = 50$	$Z = 100$
BC1	5.63	7.31	11.03	14.54
BC2	5.63	7.64	11.45	17.22
BC3	5.63	12.36	20.05	29.18
Δ BC2-BC1 (%)	0.0	4.4	3.8	18.4
Δ BC2-BC3 (%)	0.0	-38.2	-42.9	-41.0

The results of this comparative analysis indicate that the difference between the buckling coefficients for the three boundary conditions increases with the curvature, however, the difference does not increase uniformly (*e.g.* for $\alpha = 4.0$, the difference Δ BC2-BC1 for $Z = 20$, $Z = 50$ and $Z = 100$ is equal to 4.4%, 3.8%, and 18.4%, respectively). This is due to aforementioned complexity of the problem, where the buckling pattern and thus the buckling load that panel yields cannot be considered only as a function of the curvature Z , but also of the aspect ratio. According to [Table 4.9](#), it may be concluded that the difference between the buckling coefficients generally increases as the aspect ratio increases, which means that for the shorter panel, the role of the constraints loses its relevance.

Finally, the influence of the boundary condition on the buckling shape is demonstrated in [Fig. 4.10](#).

Based on this example, it may be noticed that the flat panels ($Z \rightarrow 0$) are insensitive to the differences between boundary conditions BC1, BC2, and BC3, which consequently explains the same buckling coefficients obtained in [Table 4.9](#). The difference in results, however, is noticeable only for higher values of curvatures since more energy is required for the onset of buckling. This is particularly emphasized in the case of fully constrained edges (BC3), where the buckling shapes are substantially different from the other two boundaries, manifested by a different number of the buckling waves.

Consequently, in [section 4.4](#), the formulae are proposed for all three cases of boundary conditions, allowing for various levels of in-plane constraint, having apparently a huge impact on the buckling behavior of the curved panels.

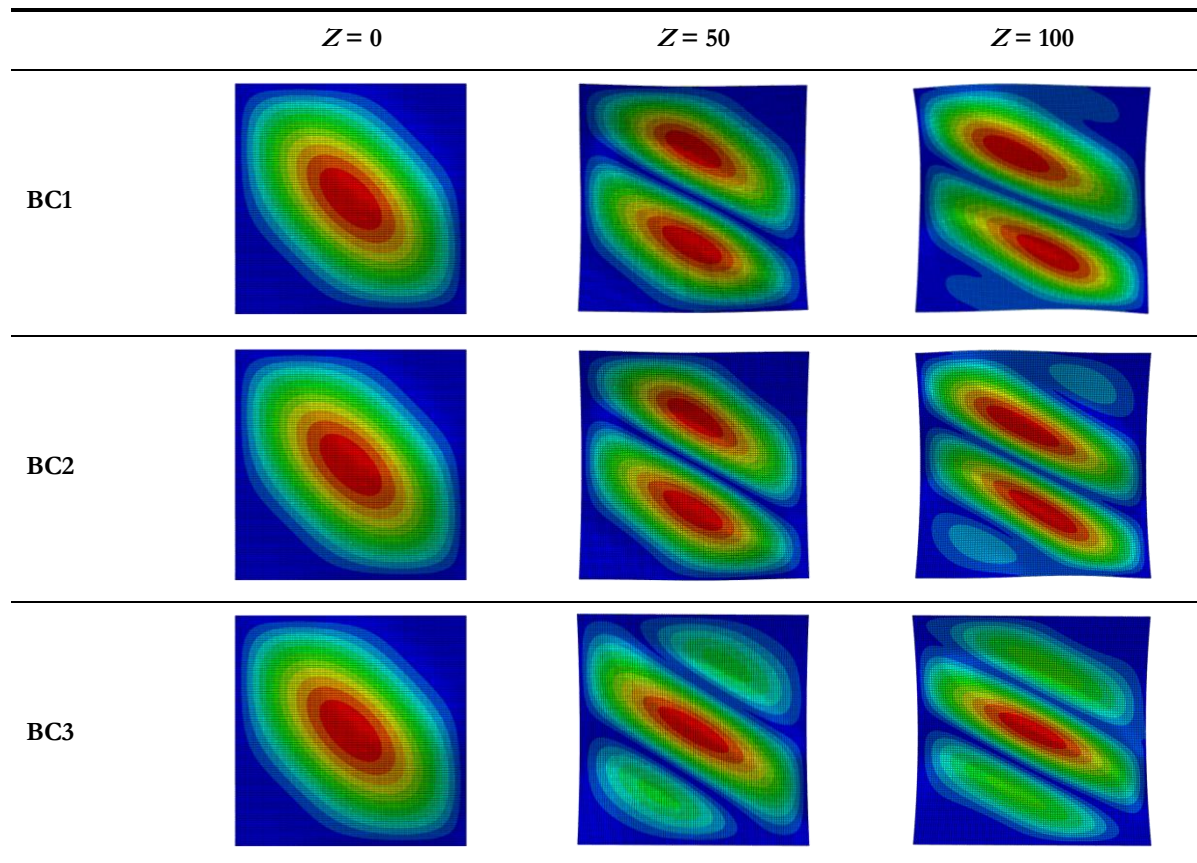


Fig. 4.10: Influence of boundary conditions on the eigenmode form ($\alpha = 1.0$)

4.4 Proposal of design rules for the buckling coefficient

4.4.1 Section overview

In this section, a new set of formulae for the prediction of the shear buckling coefficient for unstiffened simply supported curved is proposed, based on the above presented results from the parametric study. The calibration methodology used to derive the formulae is briefly described in 4.4.2, whereas in 4.4.4, the proposed formulae are statistically validated.

4.4.2 Calibration method

The principal goal is to propose the formulae with a similar mathematical framework from the European standard for flat plates (EN 1993-1-5), extrapolating them to cylindrically curved panels by adding the effect of the curvature parameter Z . This extension of the formulae is done by calibration of numerical results of k_s , within the ranges of curvature and aspect ratios from the parametric study (see Table 4.1).

To achieve that, the main challenge is to define a suitable function of two variables, $k_s = f(Z, \alpha)$, which returns the value of the shear buckling coefficient for any combination of aspect ratio and curvature parameter from the considered ranges, as presented in Fig. 4.11.

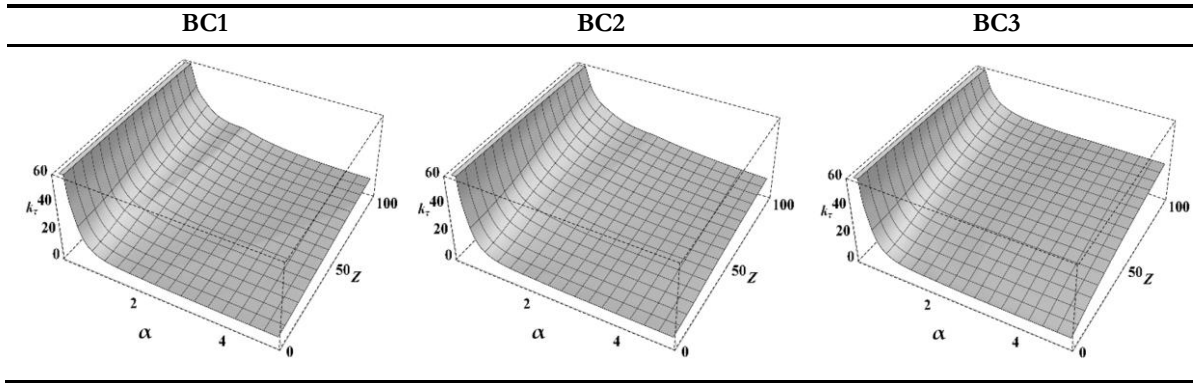


Fig. 4.11: Shear buckling coefficient as a function of the curvature and aspect ratio

The starting point is to use Eq.(2.101) from Annex A.3 of EN 1993-1-5, which reproduces the shear buckling coefficient k_τ for a flat plate ($Z = 0$), simply supported on four edges, without in-plane constraints (*i.e.* case BC1). Subsequently, the set of proposed formulae is divided in three main branches, based on the boundary conditions (BC1, BC2, and BC3), whereas each of these three branches are divided into two sub-categories of panels: *i*) short ($\alpha \leq 1.0$) and *ii*) long panels ($\alpha > 1.0$), in the same way as it is done in EN 1993-1-5.

4.4.3 Proposed formulas

The proposed formula for both the short ($\alpha \leq 1.0$) and the long panels ($\alpha > 1.0$) keeps the same parabolic format as Eq.(2.101), regardless of the boundary conditions, written in a general form by Eq.(4.3), where the parameters A_k and B_k , which are both functions of the Z parameter, are calculated according to Table 4.10, for various boundary conditions and aspect ratios

$$k_\tau = A_k + B_k \left(\frac{1}{\alpha} \right)^2 \quad (4.3)$$

Table 4.10: A_k and B_k parameters for computation of the shear buckling coefficient - k_τ ^{1,2}

	$\alpha \leq 1.0$	$\alpha > 1.0$
BC1	$A_k = 0.214Z + 2.88$ $B_k = 5.343 - \frac{Z}{175.6}$	$A_k = 0.096Z + 5.15$ $B_k = 0.135Z + 3.18$
BC2	$A_k = 0.247Z + 2.732$ $B_k = 5.34 - \frac{Z}{150.4}$	$A_k = 0.124Z + 4.94$ $B_k = 0.137Z + 3.756$
BC3	$A_k = 0.2734Z + 2.794$ $B_k = 5.33 - \frac{Z}{127.2}$	$A_k = -\left(\frac{Z}{28.86} \right)^2 + 0.349Z + 5.424$ $B_k = \left(\frac{Z}{37.735} \right)^2 - 0.0452Z + 2.422$

¹ The formulae are applicable for the curvature parameters in the range $1 < Z \leq 100$, whereas for $Z \leq 1$, Eq.(2.101) from Annex A.3 of EN 1993-1-5 should be used.

² The formulae are applicable only if the b/t ratio satisfies the criterion given by Eq.(4.2).

4.4.4 Validation

The validation of the proposed formulae is carried out by comparing the shear buckling coefficients obtained numerically ($k_{\tau, \text{num}}$) with the values obtained by using the proposed formulae ($k_{\tau, \text{prop}}$). In total, 14847 numerical models are used for the global statistical evaluation, which are divided into three groups (4949 each) based on the boundary conditions.

Statistical evaluation is made based on the $\bar{k}_{\tau, \text{prop}}/\bar{k}_{\tau, \text{num}}$ ratio, where both $\bar{k}_{\tau, \text{prop}}$ and $\bar{k}_{\tau, \text{num}}$ are first normalized against the maximum value. Besides the mean value (μ) of this ratio and the maximum relative error, the coefficient of variation (CoV) is additionally calculated for each of the three boundary conditions, assessing the difference (%) between the proposed formulae and the numerical results. In Fig. 4.12 and Table 4.11, the most relevant results of the statistical assessment of the proposed formulae are summarized.

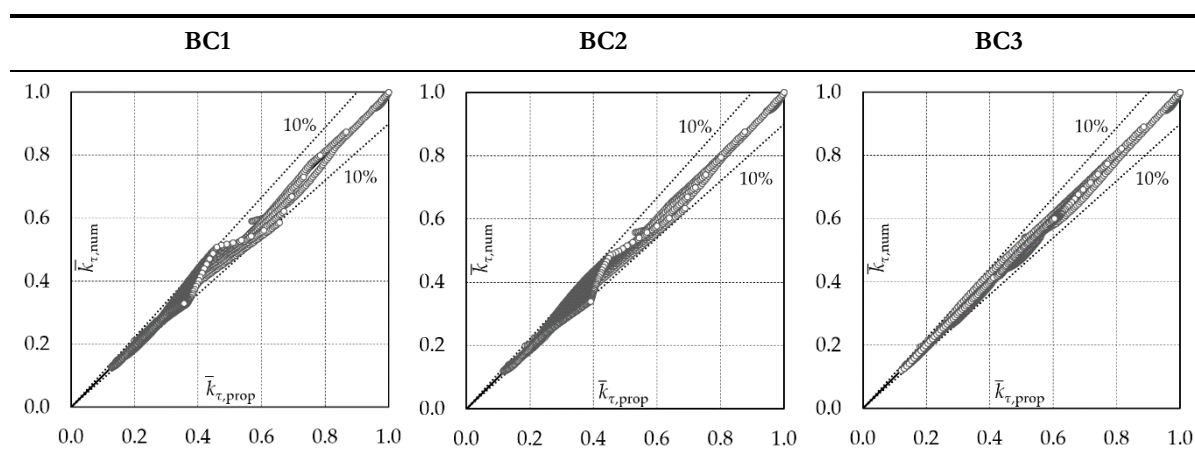


Fig. 4.12: Correlation between $\bar{k}_{\tau, \text{prop}}$ and $\bar{k}_{\tau, \text{num}}$

Table 4.11: Statistical assessment based on the ratio $\bar{k}_{\tau, \text{prop}}/\bar{k}_{\tau, \text{num}}$

Boundary condition	Number of analysis	Mean (μ)	CoV (%)	Max. error (%)
BC1	4949	1.023	3.82	-12.05
BC2	4949	1.021	4.48	13.00
BC3	4949	1.004	1.78	-6.26

Although the maximum errors for cases BC1 and BC2 are higher than 10%, the mean value of $\bar{k}_{\tau, \text{prop}}/\bar{k}_{\tau, \text{num}}$ is almost equal to 1.0, and the CoV is lower than 5% in all three cases. This shows that the proposed formulae may be reliably used for an accurate prediction of the shear buckling coefficient, both for long and short curved panels and for all three boundary conditions.

4.5 Summary

This chapter was dedicated to the buckling behavior of simply supported cylindrically curved panels subjected to pure shear stresses. The influence of several parameters on the elastic critical behavior, namely 1st buckling mode, was numerically investigated, such as curvature parameter $Z \leq 100$, aspect ratio from $\alpha = 0.2$ to $\alpha = 5.0$ and three boundary conditions: BC1 (all edges free-

to-wave), BC2 (two edges constrained and two free-to-wave) and BC3 (all edges constrained). In specific, it was concluded that:

- Cylindrically curved panels subjected to shear show very complex buckling behavior that depends on the combination of aspect ratio and curvature parameter and not only on one of them. Principally, the shorter and the more curved the panel is, the higher is the critical load;
- For very long panels, the aspect ratio has only minor influence on the critical load since for $\alpha > 4.0$ it asymptotically reaches the lowest theoretical values;
- Curvature parameter Z may be comfortably used as the key parameter for the determination of the shear buckling coefficient for all the curved panels encountered in the real applications of bridges, ship hulls, and airplanes. Only in the case of highly curved stocky panels, the behavior of panels qualitatively changes and the buckling coefficient cannot be considered only as a function of Z parameter;
- In contrast to flat plates, the buckling modes and the elastic critical stress of cylindrically curved panels under shear highly depends on the boundary conditions studied in this chapter. Moreover, the effect of the edge constraints is particularly emphasized for highly curved and long panels;
- The NACA charts give the shear buckling coefficients that correspond best to the boundary condition BC2, which in most cases is the realistic assumption, being an intermediate case. However, for the panels with the unconstrained edges (BC1), as well as the ones with all four edges constrained (BC3), the NACA monographs may lead respectively to an overestimation or underestimation of the shear buckling coefficient.

Finally, a set of expressions was proposed for the prediction of the shear buckling coefficient, using the same format of EN 1993-1-5 [11] for the flat plates, which may easily substitute the impractical and outdated NACA monographs. The formulae were numerically calibrated within geometrical ranges (*i.e.* $1 < Z \leq 100$ and $0.2 < \alpha \leq 5.0$) encountered in real engineering applications, for which it was shown that the Z parameter might be used as the key parameter. Moreover, for the very first time, the influence of various in-plane edge constraints was explicitly accounted for.

Having the expressions for the calculation of the elastic critical stress, the next challenge is to extend the scope of EN 1993-1-5 [11] and to allow the calculation of the ultimate resistance of cylindrically curved panels subjected to shear. This is done in the upcoming [chapter 5](#).

5. Ultimate shear load of curved panels

5.1 Overview

In this chapter, an extensive numerical study is carried out with the aim to investigate the post-buckling behavior of simply supported cylindrically curved steel panels subjected to a pure shear load. Therefore, this chapter tackles Task 3.2 of the thesis (defined in [section 1.2](#)) and presents a logical continuation of [chapter 4](#), in which Task 3.1 was accomplished, where the pre-buckling behavior of curved panels under shear was studied.

The principal objective is to assess the influence of geometrical parameters (*e.g.* curvature and aspect ratio), initial imperfections and edge constraints on the ultimate shear resistance, in a similar way it was done in [chapter 4](#) for the critical shear load.

Furthermore, to overcome the limitations found in the design standards, a new set of formulas are numerically derived for the prediction of the ultimate shear strength of unstiffened curved panels, with various edge in-plane constraints, applicable for curvatures and aspect ratios within the ranges that may be of the practical use in offshore, aeronautics and bridge applications.

The proposed design methodology is conceptually similar to the one for a flat plate (see [2.5.2](#)); however, the domain of its application is extended to a wide range of the curvature parameter. Hence, it is required first to calculate the shear buckling coefficient k_s for a curved panel, which can be obtained by using the formulas developed in [chapter 4](#) or by carrying out numerical calculations.

The chapter is divided into three sections. First, in [section 5.2](#), a detailed description of the numerical model used in the parametric study is provided. Subsequently, in [section 5.3](#), the most relevant results of the parametric study are discussed, emphasizing the way the varied parameters of the study affect the behavior of the curved panels. [Section 5.4](#) presents the newly proposed expression for the determination of the ultimate shear resistance of unstiffened curved panels, valid for three different types of edge constraints, various curvatures ($Z \leq 50$) and aspect ratios ($\alpha \leq 5.0$). Finally, in order to demonstrate how to use adequately the proposed methodology, an example is presented in [section 5.5](#).

5.2 Numerical finite element model

5.2.1 Section overview

The numerical models and numerical analyses for the presented study are carried out using the FEM software ABAQUS [142]. Since some of the modeling assumptions were already addressed before, in [section 3.4](#) and [4.2.2](#), more emphasis in [5.2.2](#) is given only to some features of the numerical model that are specific for the study carried out in this section. The validation of the numerical model is carried out in [5.2.3](#), separately for flat plate and curved panel models, using the available theoretical results as the comparator.

5.2.2 Definition of the model

5.2.2.1 Type of analysis

Following the same approach described in [section 3.4](#), two types of analyses are performed in this study: *i*) Linear elastic bifurcation analysis (LBA) and *ii*) Geometrically and materially nonlinear analysis with imperfections included (GMNIA).

The LBA is first performed for each model, with the aim to extract the eigenmodes, which are then used as the shapes of the initial geometrical imperfections in a GMNIA. In order to obtain a non-linear static equilibrium solution, the arc-length Riks' method [143] is used.

The ultimate resistance of a curved panel is determined as the maximum load factor on the load-deformation curve. However, it is necessary to observe carefully the load-displacement curves since the arc-length routine may, in some cases, decide to follow an inappropriate secondary (post-critical) equilibrium path [144]. Namely, depending on the geometrical configuration and the initial imperfections, curved panels under shear load may exhibit two distinct types of structural instability: *i*) bifurcation instability and *ii*) snap-through instability, as presented in [Fig. 5.1](#).

The bifurcation instability, which commonly occurs in the case of shallow curved panels with low curvature parameters, is recognized by a sudden change of deformation direction after the critical (bifurcation) point is exceeded. In the case of shear load, due to the development of stabilizing tension field mechanism (see [2.4.2](#)), a stable symmetric bifurcation takes place with the secondary equilibrium path that rises above the critical load. This behavior is very similar to

one of the flat plates, and commonly enables considerable exploitation of the post-buckling load reserves.

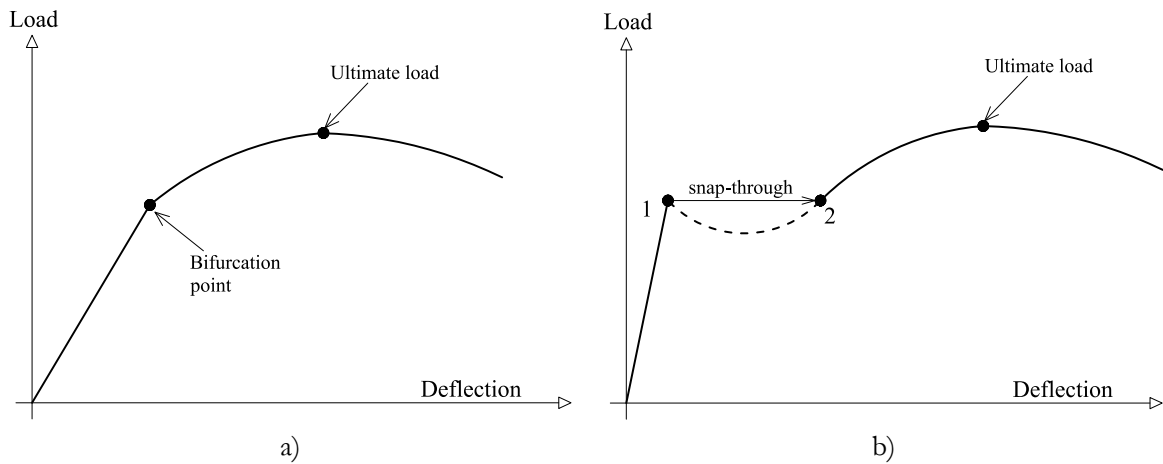


Fig. 5.1: Types of instability: a) bifurcation and b) snap-through

On the other hand, in the case of curved panels with higher curvatures, a snap-through instability occurs, characterized by a sudden increase in deformation under a constant load. Namely, once the shear load reaches a certain value (denoted by point 1 in Fig. 5.1b) the system can maintain equilibrium only if the displacement snaps suddenly from point 1 to point 2 as depicted by the solid horizontal line. In reality, the structure behaves in such a way that, once the first peak is reached, the load passes abruptly from one equilibrium state (point 1) to another equilibrium state (point 2), without any load reduction presented by the dashed line. As a result, the actual ultimate load is reached only after a new equilibrium is established, and not at the first peak point. The dashed line represents an unstable equilibrium state and, in general, it can be registered only if the system is subjected to an ideal displacement controlled condition, such as the one achieved in ABAQUS software, with a carefully defined size of the arc-length.

5.2.2.2 Geometry

The geometry of a curved panel is fully defined by the aspect ratio and the curvature parameter, defined by Eq.(2.1) and Eq.(2.2), respectively. In fact, in 4.2.4, it was shown that the non-dimensional curvature parameter Z is a suitable parameter to characterize the geometry of cylindrically curved panels under shear if the b/t ratio of the panel satisfies the criterion, given by Eq.(4.2).

However, when assessing the ultimate load of a panel, it is not sufficient to define only the curvature parameter Z and the aspect ratio α since two panels, with different b/t ratios, even if the curvature parameter and the aspect ratio are the same, may have entirely different ultimate resistances. Hence, in addition, it is necessary to specify the non-dimensional slenderness parameter $\bar{\lambda}_w$, reproduced by Eq.(2.99) since it accounts for the b/t ratio of the panel.

In this study, the thickness is kept constant ($t = 10$ mm), the non-dimensional slenderness parameter is varied in the range found in EN 1993-1-5 for the flat panels subjected to a shear load between ($\bar{\lambda}_w = 0.3 - 3.0$), whereas the width b is considered as a variable, calculated by Eq.(5.1), derived from Eq.(2.99).

$$b = 37.4 \varepsilon t \bar{\lambda}_w \sqrt{k_\tau} \quad \text{with } \varepsilon = \sqrt{\frac{235}{f_y}} \quad (5.1)$$

In this equation, the shear buckling coefficient k_τ is calculated using the formulas developed in [section 4.4](#), as a function of the curvature parameter Z and the aspect ratio α .

For this study, the aspect ratio is varied from $\alpha = 0.5$ to $\alpha = 5.0$, whereas the curvature parameter is held up to $Z \leq 50$ since it was shown in [Fig. 4.4](#) that in most of the practical cases, the local curvature does not exceed the value of $Z \leq 40$.

The geometry of panels is discretized by a mesh of FE, whose type and size are defined in the following paragraphs. The coordinates of all the nodes are previously calculated and introduced in each model using a sub-routine.

5.2.2.3 Applied initial imperfections

Owing to the lack of information on the ‘real’ material and geometrical imperfections, the initial imperfections are modeled as the equivalent imperfections, following the recommendations from Annex C.5 of EN 1993-1-5 for flat plates. According to the standard, for the panels and subpanels, the shape of the initial imperfections should have a form of a critical eigenmode, with an amplitude equal to a minimum between $a/200$ and $b/200$.

In addition, based on the results from a series of studies on the shape, the amplitude and the sign of the imperfections, carried out and presented in one of the following sections, it is concluded that the imperfection shape of the 1st buckling mode with an amplitude equal to $b/200$ leads in most cases to a safe design. Such an assumption was justified also by former authors (*e.g.* Featherstone [127], Amani *et al.* [129]) who investigated the influence of the imperfection shape on the ultimate resistance of curved panels under shear. In specific, Featherston (2003) claims that in 85% of cases, the minimum ultimate load is obtained with an imperfection in the form of either the first or the second eigenmode. Moreover, Amani *et al.* (2011) confirmed that the form of the first eigenmode often results in the most critical case, emphasizing that the shape of the imperfection has only minor influence on the ultimate load in the case of slender panels.

Finally, in all numerical models, the imperfection is assumed to be oriented radially inward, as it is shown later that such imperfection always results in lower ultimate resistance.

The implementation of the equivalent initial imperfections in ABAQUS is achieved using the keyword **IMPERFECTION*, as already presented in [3.4.2](#). Namely, the shape of the 1st buckling mode is obtained from linear bifurcation analysis (LBA), carried out on a *perfect* structure, which is then introduced in a model through a perturbation of radial translational DOF for each node using [Eq.\(3.1\)](#).

5.2.2.4 Applied material model

The material used in numerical models is steel grade S355 JR. The material is modeled as elastic-plastic, with linear strain hardening, disregarding the yield plateau. The elastic properties (*i.e.* Young’s modulus E and Poisson’s coefficient ν) used in LBA, as well as the plastic properties

(*i.e.* yield strength f_y and ultimate strength f_u) used in GMNIA that are adopted from standard EN 10025 [148] recommendations, are summarized in Table 5.1.

According to ECCS Publication no. 125 [149], the tangent modulus is adopted as $E/100$ referring to 1% linear strain hardening, which was proven to be a solid assumption in several references in the literature (*e.g.* [8], [10], [78]). Finally, the material model is presented in Fig. 5.2 and it is introduced in the FE software as true stress-true strain, as suggested by EN 1993-1-5.

Table 5.1: Material properties of steel S355 ($t = 10$ mm)

Young's modulus, E	Poisson's coefficient, ν	Yield strength, f_y	Ultimate strength, f_u
210 GPa	0.3	355 MPa	470 MPa

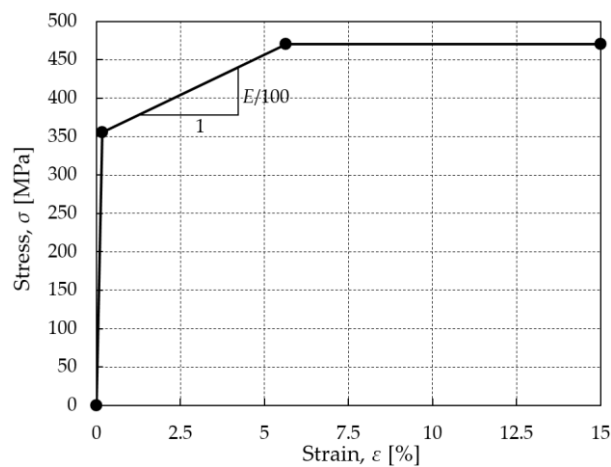


Fig. 5.2: Material behavior applied in GMNIA

5.2.2.5 Loading and support conditions

The loads and the boundary condition for this study are kept the same as in chapter 4, in which the elastic buckling behavior of curved panels under shear was investigated. Therefore, a detailed description of the three boundary conditions (BC1, BC2, and BC3) considered in the study, as well as the application of the edge shear load, may be found in 4.2.2.

5.2.2.6 Type and size of FE

A linear four-node shell element with reduced integration (S4R) is used for the model discretization since it was found a suitable FE type for curved panels under shear in chapter 4.

To define an appropriate size of the shell FE, a mesh convergence study is carried out by monitoring the convergence of the shear reduction factor χ_w , while varying the size of the FE. In contrast to the study carried out in chapter 4, in which the width b was kept constant ($b = 1000$ mm), in the study on the ultimate shear resistance, the width depends on the slenderness parameter $\bar{\lambda}_w$, and for each model is calculated by Eq.(5.1). Therefore, assuming that the FE is squared ($b_{FE} = a_{FE}$), the size of an element is defined by the number of finite elements in the circumferential direction (n_C), *i.e.* $b_{FE} = b/n_C$. The total number of elements ($n_C \times n_L$)

depends on the aspect ratio, where n_L represents the number of FE in the longitudinal direction and it may be obtained as $n_L = \alpha \times n_C$.

In the presented mesh sensitivity study, three different curvatures are considered, whereas the aspect ratio ($\alpha = 1.0$), the slenderness parameter ($\bar{\lambda}_w = 2.0$) and the boundary condition BC1 are kept constant. The results of the study are summarized in [Table 5.2](#).

Table 5.2: Mesh convergence study (shear reduction factor - χ_w)

Curvature	Slenderness	$n_C = 50$	$n_C = 60$	$n_C = 70$	$n_C = 80$	$n_C = 90$	$n_C = 100$	$n_C = 120$
$Z = 0$		0.458	0.454	0.451	0.449	0.449	0.448	0.448
$Z = 30$	$\bar{\lambda}_w = 2.0$	0.312	0.308	0.305	0.302	0.301	0.301	0.301
$Z = 50$		0.270	0.265	0.261	0.257	0.257	0.257	0.257

Based on these results, it may be concluded that 80 finite elements ($n_C = 80$) along the curved edge b are sufficient to achieve numerical convergence, which means that increasing the number of elements does not affect the shear reduction factor.

5.2.3 Validation of the model

Owing to the lack of experimental results or a general analytical expression for the calculation of the ultimate shear resistance of the curved panels, the numerical models are validated by comparing the results with: *i*) existing methods for flat panels in shear; *ii*) numerical results from Amani *et al.* [129] for curved panels.

5.2.3.1 Flat plate model

In a recent study by Zhang *et al.* [150], the authors proposed a new approach for the ultimate shear strength of a flat plate, comparing their results with the existing methods, including the European standard. Most of the methods propose a semi-empirical expression, assuming that all edges remain straight, which corresponds to the boundary condition BC3, defined earlier in the thesis. Hence, in [Fig. 5.3](#), the numerical results for the boundary condition BC3 are compared with the existing methodologies for two aspect ratios ($\alpha = 1.0$ and $\alpha = 2.0$) and for various values of double slenderness ratio λ_β , defined in [150] as $\lambda_\beta = (b/t)(f_y/E)^{1/2}$.

A large scatter in the results could be observed for both aspect ratios, which seems to be particularly noticeable for plates with increased slenderness, where the difference between some of the methods reaches 30-40%. Since the methods are based merely on the numerical results, such a significant difference might be explained only by the differences in the modeling assumptions adopted by different authors.

Nevertheless, in the case of squared panels ($\alpha = 1.0$), arguably good agreement ($\Delta_{\max} < 3\%$) is achieved between FEM results and the results obtained using the method proposed by Zhang *et al.*, whereas for the aspect ratio equal to $\alpha = 2.0$, the FEM results are close to the ones obtained by Nara *et al.*, with the maximum difference of $\Delta_{\max} < 5\%$. Therefore, it may be concluded that the numerical model gives the ultimate resistance within the expected values. However, due to

high variability in the results predicted by the various methods, the overall impression is that further validation against both numerical and experimental results would be of great benefit.

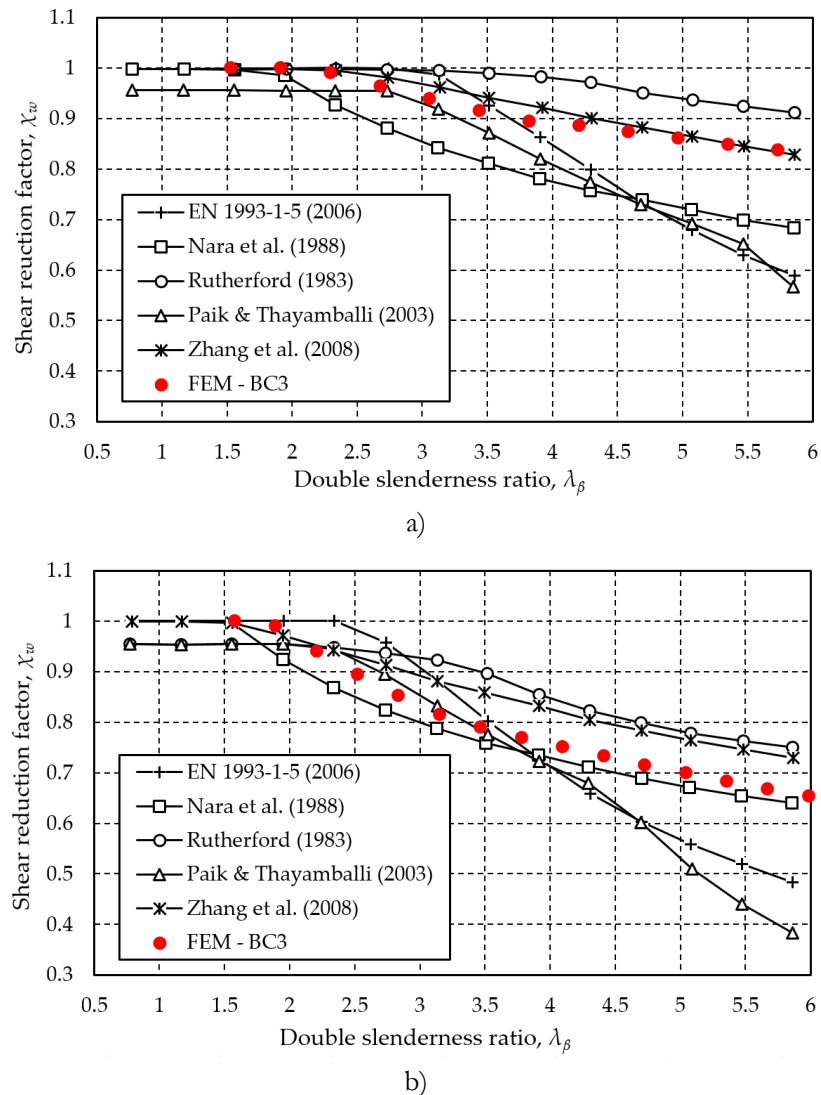


Fig. 5.3: Comparison between FEM results and various methods: a) $\alpha = 1.0$ and b) $\alpha = 2.0$

5.2.3.2 Curved panel model

The comparison of the numerical results against the results obtained from Amani *et al.* is shown in Fig. 5.4, where the force-displacement curves are plotted for a curved panel ($Z = 15$ and $\alpha = 1.0$), with various levels of the imperfection amplitudes (δ_0) and boundary conditions that correspond to the case BC1. The applied shear load τ is normalized to the yield shear load $\tau_u = f_y/\sqrt{3}$, whereas the out-of-plane (radial) displacement (u_r) measured in the middle point of the panel is normalized to the thickness of the panel, equal to $t = 3$ mm according to Amani *et al.* [129].

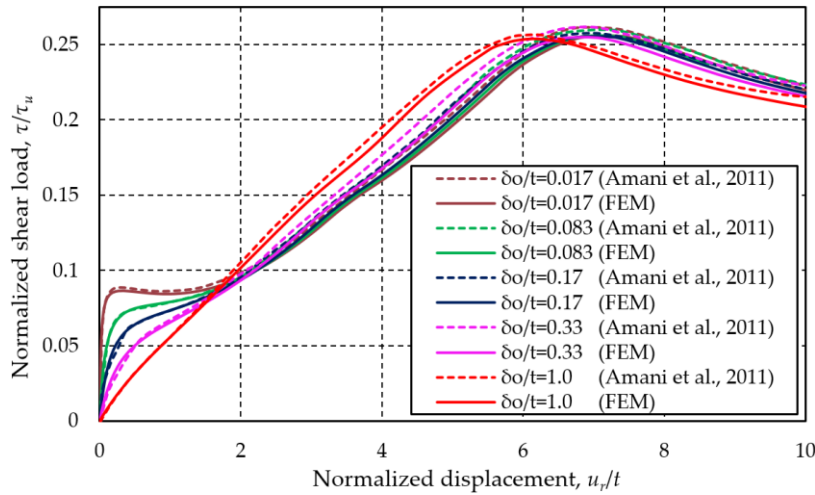


Fig. 5.4: Comparison between numerical results: FEM (solid) and Amani *et al.* (dashed)

It may be noticed that the results obtained by the numerical model correspond to the ones obtained by Amani *et al.* [129], despite several differences assumed in the numerical models. Namely, in the numerical model by Amani *et al.*, the points E, F, G, and H restrain the movements in the \bar{x} -direction, whereas in the model used for the current study, these axial displacements are restrained in points A, B, C, and D (see Fig. 4.1). In addition, the density of the mesh considered in the two numerical models is not the same. In the model by Amani *et al.*, only 30 FE are adopted in the circumferential direction ($n_c = 30$), whereas in the model used in the study a more refined mesh is considered ($n_c = 80$). This explains a certain discrepancy in results, especially in the post-buckling phase, leading to slightly higher values ($\Delta_{\max} < 3.5\%$) of the ultimate resistance in the case of Amani *et al.* Nevertheless, it may be concluded that the behavior of panels is qualitatively and quantitatively the same, which to some extent validates the numerical model used in this study.

5.3 Parametric study

5.3.1 Goal and scope

The goal of the parametric study is to characterize the post-buckling behavior of simply supported cylindrically curved panels subjected to a pure shear load. Based on the collected data from the study, a new set of formulas for the determination of the ultimate shear load is proposed in section 5.4. The parametric study comprises 3 different boundary conditions – BC1, BC2, and BC3 (see Fig. 4.1). For each of them, 9 different aspect ratios, 6 different curvatures, and 27 different slenderness parameters are varied, comprising in total 4374 LBAs and 4374 GMNIAs, summarized in Table 5.3.

Table 5.3: Scope of the parametric study

Boundary condition	Slenderness, $\bar{\lambda}_w$	Curvature, Z	Aspect ratio, α
BC1, BC2, BC3	0.3 - 3.0 (step 0.1)	0 - 50 (step 10)	(0.5 - 1.0) (step 0.25)
			(1.0 - 3.0) (step 0.5)
			(3.0 - 5.0) (step 1)

5.3.2 Buckling behavior of the panel

5.3.2.1 General considerations

One typical example of the load-displacement curve of a panel with a higher curvature parameter (*i.e.* $Z = 50$) that undergoes snap-through buckling addressed earlier in this chapter, is illustrated in Fig. 5.5.

The response of the panel may be clearly divided into several characteristic phases, addressed also in the study by Amani *et al.* [129]. After the bifurcation point (1) is reached, the membrane strength of the panel decreases due to the development of the buckling modes, resulting in an unstable equilibrium path until the minimum elastic post-buckling load is reached at point (2). This softening phase (1-2) is governed by the geometric nonlinearities and, thus, depends on the initial geometric imperfections. Namely, the higher the amplitude of the imperfections, the smoother is the post-buckling response, *i.e.* without the peak at the bifurcation point.

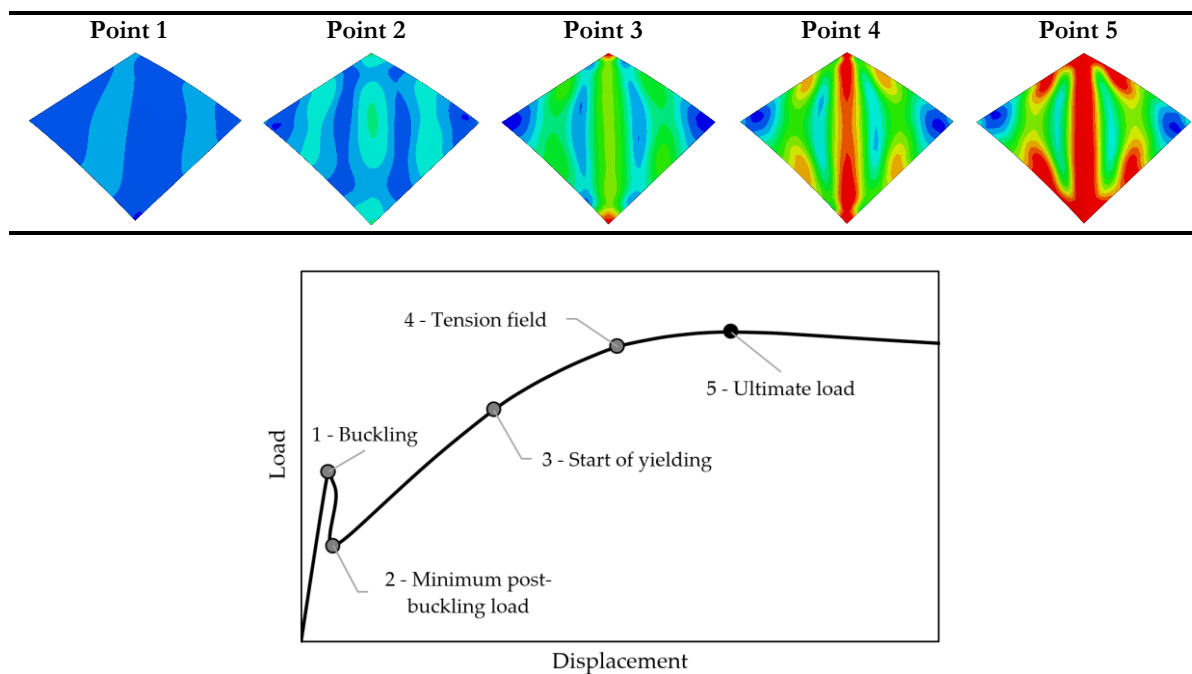


Fig. 5.5: Post-buckling behavior of a curved panel subjected to shear loading

After the minimum post-buckling load is reached at point (2), starts a post-buckling hardening phase, until the ultimate capacity is reached at point (5). Namely, as the load increases, the yielding of the material occurs first in the corners of the panel at point (3), which is quickly distributed across the diagonal of the panel, forming the *tension field* at point (4). Further increase of shear load leads to the ultimate shear resistance of the panel at point (5), after which starts another softening phase, characterized by large deformations and spread of plasticity.

The shape of the load displacement-curve presented above highly depends on the geometry of panel, boundary conditions and the initial imperfection, which is discussed in the following few paragraphs.

5.3.2.2 Influence of geometry

In the case of flat plates, the influence of geometry on the ultimate resistance is introduced in EN 1993-1-5 [11] through the slenderness parameter $\bar{\lambda}_w$, reproduced by Eq.(2.99), whereas the influence of the aspect ratio is accounted for indirectly through the shear buckling coefficient k_τ (see Eq.(2.101)).

Regarding the cylindrically curved panels, the influence of the aspect ratio and the curvature parameter on the post-buckling behavior and the ultimate resistance was acknowledged in almost all relevant historical references (e.g. [41], [126], [129], [127]).

The influence of these two parameters on the ultimate shear resistance is illustrated in Fig. 5.6, where the shear reduction factor χ_w is plotted against the b/t ratio of the panels ($t = 10$ mm), for various aspect ratios and curvature parameters, while the boundary conditions are kept the same (BC1). The shape of the initial imperfections is assumed affine to the shape of the 1st buckling mode, with an amplitude of $b/200$.

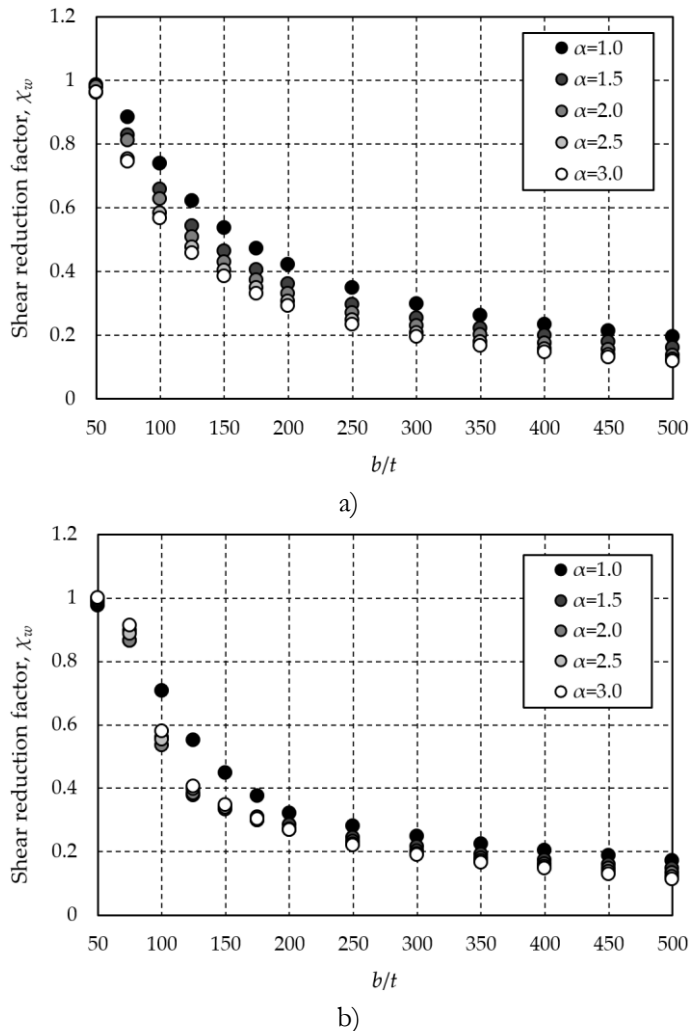


Fig. 5.6: Influence of geometry on the ultimate shear resistance for a) $Z = 0$ and b) $Z = 40$

From these graphs, several important conclusions may be drawn. First, the higher the aspect ratio is, the lower is the ultimate resistance, regardless of the slenderness (b/t) and curvature of

the panel (Z). A certain deviation is noticed in the case of panels with a high curvature parameter and intermediate slenderness ($100 < b/t < 200$) (see Fig. 5.6b). This happens due to a strong sensitivity of these panels to the shape of the initial imperfections, which is discussed later in this section.

Furthermore, in chapter 4, it was shown that for high values of aspect ratio, its influence on the shear buckling coefficient k_s becomes negligible, regardless of the curvature parameter (see Fig. 4.5). A similar trend is observed for the ultimate shear resistance of curved panels. This could be explained by the fact that for long panels, the shear load is not resisted by the entire panel but only one portion of the panel participates in shear resistance. What portion of the panel is activated in the resisting mechanism is closely related to the level of the edge constraint, which is tackled in the following subsection.

As for the influence of the curvature parameter Z , as shown in Fig. 4.7, higher curvatures result in higher critical loads since the second moment of area increases. However, an increase of the curvature parameter leads to a ‘shell-like’ behavior with a reduced post-critical strength reserve (see Fig. 5.5), resulting in a drop of the ultimate shear resistance. This declining trend is shown in Fig. 5.7, where the applied shear load is normalized to the yield shear load, whereas the circumferential displacement (u_φ) in the point C (see Fig. 4.1) is normalized with the thickness of the panel.

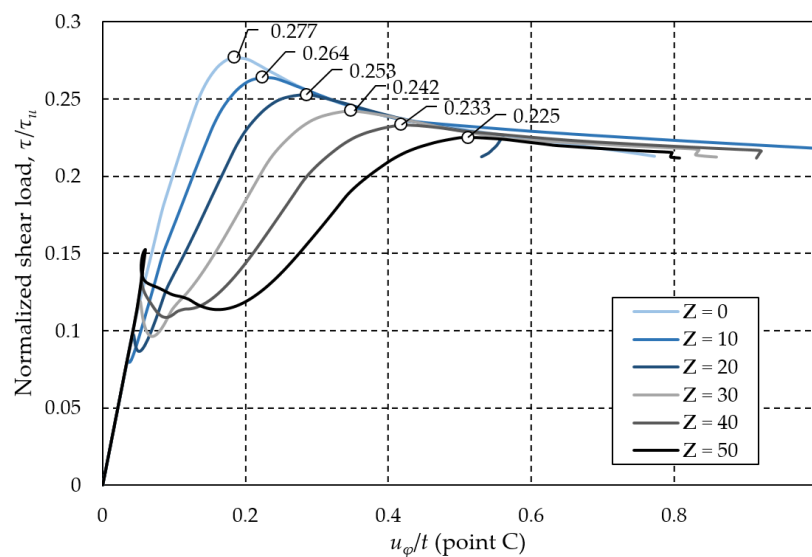


Fig. 5.7: Influence of curvature on the ultimate shear resistance for $\alpha = 1.0$ and $b/t = 300$

The figure clearly shows that the higher curvature results in a more unstable post-critical behavior, leading to increased deformations and to a drop in the ultimate resistance (23% in this case when compared to flat panel).

Finally, in the case of the stocky panels, with very low slenderness ($b/t < 50$), the ultimate resistance is insensitive to the aspect ratio and curvature parameter. These panels are under pure shear, no buckling occurs, and their ultimate resistance corresponds to the yield load.

5.3.2.3 Influence of the boundary conditions

The influence of the various in-plane edge constraints on the critical shear stress (τ_{cr}) was investigated in [chapter 4](#). It was shown that the impact of the edge constraints is particularly emphasized in the case of highly curved panels since the curvature adds nonlinearity to the pre-buckling state of the panel. On the other hand, the influence of the in-plane edge constraints on the ultimate shear resistance of curved panels has never been reported in the literature, in any topic-related reference.

The design standard for the flat panels (EN 1993-1-5 [11]) prescribes the rules for simply supported panels, however, without a clear specification of the in-plane edge constraints. Namely, the design methodology provided in the standard refers to the flat webs of the girders, surrounded by flanges and the transverse stiffeners. Prior to the publication of the standard, numerous authors investigated the influence of the flexibility of the flanges and the vertical stiffeners on the ultimate shear resistance of the web, resulting in a several tension field models, summarized by Dubas & Gehri [128]. As it is presented in this chapter, some of these conclusions could refer also to the curved panels.

For stocky panels with low slenderness, the ultimate shear load corresponds to the yield load, regardless of the boundary conditions, as shown in [Fig. 5.8](#). In the case of a panel with constraint edges (BC3), an elastic-perfectly plastic response is achieved, where the plasticity is spread all over the panel without a force reduction.

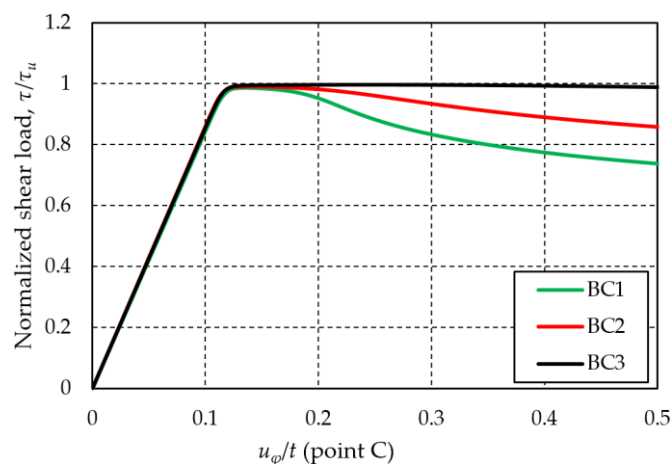


Fig. 5.8: Influence of the boundary conditions on the panels with a low slenderness

On the other hand, for very slender panels, the ultimate resistance highly depends on the level of the edge constraints. Namely, in the case of boundary conditions without any in-plane constraints (BC1), a redistribution of the shear stresses occurs and predominant membrane stresses develop in narrow strips, anchored to the corners of the panel, being the most rigid parts of the structural element (see [Fig. 5.9a](#)). Hence, in this case, the tension field cannot be developed and the exploitation of the post-critical reserves is prevented, resulting in low ultimate resistance.

Furthermore, for higher curvature parameters (see [Fig. 5.9b](#)), the predominant membrane stresses are developed at even lower values of load, which additionally decreases the ultimate resistance.

Regarding the influence of the aspect ratio, in general, the higher the aspect ratio, the more premature distribution of the membrane stress occurs (*i.e.* at a lower value of the shear load). However, as shown in Fig. 5.9c, for aspect ratios higher than $\alpha \geq 2.0$, these stresses are not concentrated in the corners, but in the zones located close to the middle of a panel, where a new local resisting mechanism develops.

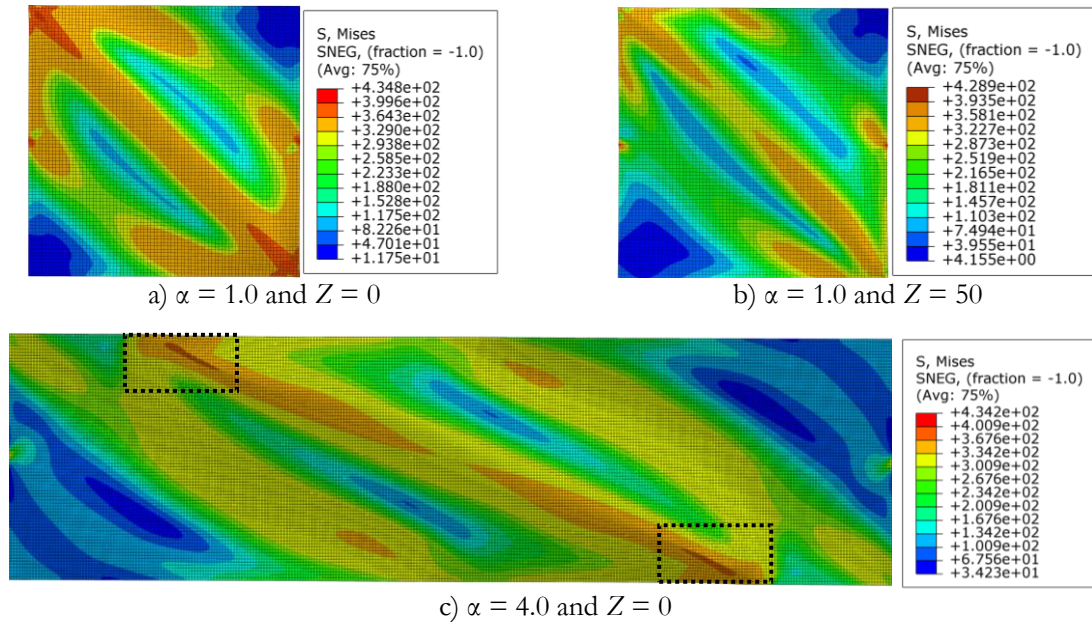


Fig. 5.9: Deformed shapes of the panels with boundary condition BC1

In the case of boundary conditions BC2 and BC3, the tension field may be developed since the edges provide sufficient rigidity to take the compressive force components that appear as a response to an increase of the tensile force component along the diagonal of the panel. Hence, considerable post-critical reserves may be mobilized, which results in a higher ultimate shear resistance than in the case of boundary condition BC1.

Depending on the level of the constraint of edges, the position, the width and the inclination angle (φ) of the tension field may vary considerably. Based on Fig. 4.1c, it may be concluded that the behavior of a panel with the boundary condition BC2 corresponds to Basler's tension field model, illustrated in Fig. 5.10.

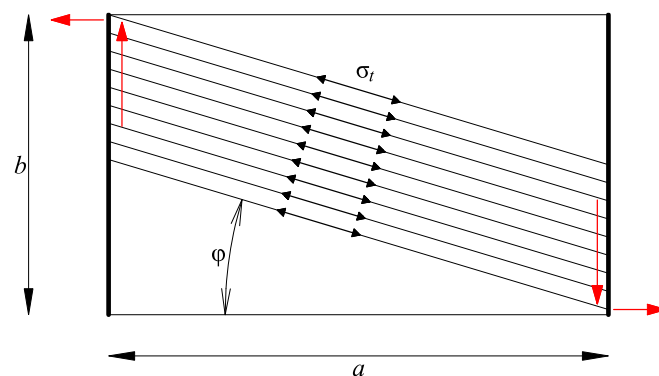


Fig. 5.10: Basler's model (adapted from [128]) – boundary condition BC2

According to Basler's model, the compressive components are received only by two curved edges, which act in this case as the transverse stiffeners of the girder, whereas the other two longitudinal edges are not a constraint since they may displace freely. This means that the shear resistance depends on the vertical reaction only since the lateral edges have no rigidity to take the horizontal reaction. Consequently, the higher is the aspect ratio (*i.e.* the distance between the 'transverse stiffeners'), the smaller is the angle of the inclination φ of the tension band and thus the smaller the ultimate resistance, followed by a considerable increase of deflection.

On the other hand, in the case of boundary condition BC3, the compressive components are taken by all four edges and the panel's behavior is similar to the behavior of a web with both transverse stiffeners and the rigid flanges. This leads to a considerably stiffer system with reduced deflections, which enables full exploitation of the post-critical reserves and thus a higher ultimate resistance.

It should be also highlighted that in contrast to BC2, in the case of BC3, the inclination angle of the tension band remains constant, regardless of the aspect ratio, as shown in Fig. 5.11 where these two boundaries are compared, for $Z = 50$. However, even in the case of BC3, the inclination angle is dictated by the curvature parameter. Namely, the angle tends to decrease with an increase of the curvature, thus jeopardizing full exploitation of the post-critical reserves. As a consequence, for a high curvature (*e.g.* $Z = 50$), the ultimate resistance decreases for the aspect ratios up to $\alpha \leq 3.0$, after which the reduction factor stabilizes and the influence of the aspect ratio becomes negligible. In the case of panels with lower curvatures ($Z < 30-40$), where the inclination angle increases, the influence of the aspect ratio on the ultimate resistance is noticeable only for the aspect ratios up to $\alpha < 2.0$.

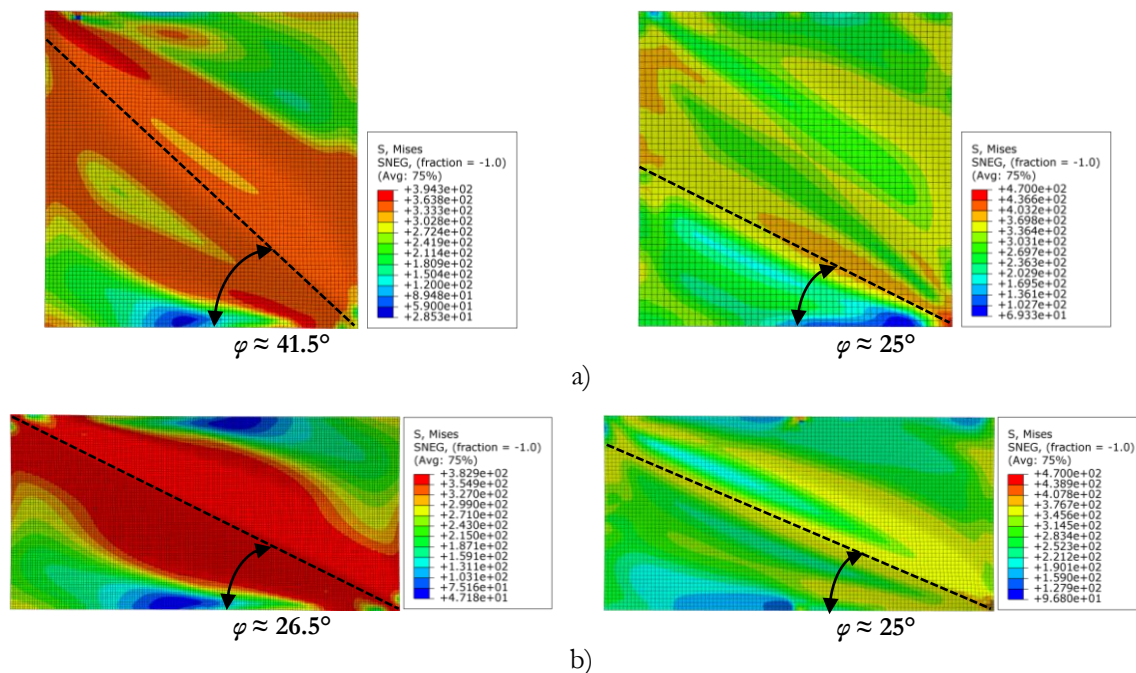


Fig. 5.11: Comparison of the deformed shapes for BC2 (left) and BC3 (right): a) $\alpha = 1.0$ and b) $\alpha = 2.0$

Finally, in Fig. 5.12, the comparison between the three boundary conditions is presented, considering both a flat ($Z = 0$) and highly curved panels ($Z = 50$), whereas the aspect ratio is kept

constant and equal to $\alpha = 2.0$. In both examples, the shear reduction factor is plotted against the relative slenderness, which is in the design standards referred to as a *buckling curve*.

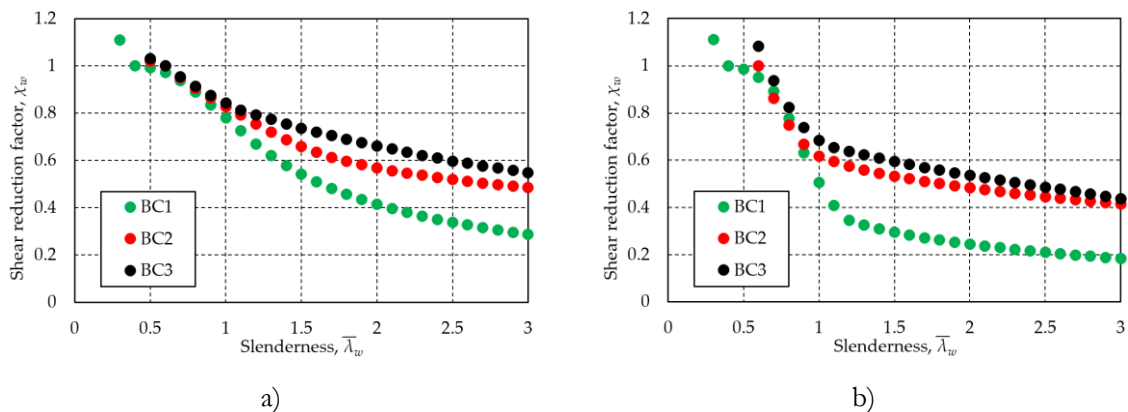


Fig. 5.12: Influence of BC on the ultimate shear resistance: a) $Z = 0$ and b) $Z = 50$

As explained earlier in this section (see Fig. 5.8), for stocky panels with low slenderness, the difference between the three boundary conditions is practically negligible. However, for higher values of slenderness, it may be noticed that an unconstrained panel (BC1) has considerably lower values of the ultimate resistance than in the case of partially constrained (BC2) or fully constrained (BC3), regardless of curvature parameter. Finally, it may be concluded that the difference between BC2 and BC3 decreases with the increase of curvature. This might be explained by the fact that in case of a fully constrained panel (BC3), the curvature prevents the full exploitation of the post-critical reserves, thus leading to the ultimate resistance closer to BC2.

Based on the presented results, one may conclude that the in-plane constraints have a substantial effect on the ultimate resistance of curved panels subjected to shear and thus cannot be neglected in the design process. Hence, in section 5.4, the formulas are proposed for each of the three cases of boundary conditions.

5.3.2.4 Influence of the initial geometric imperfections

In the following paragraphs, some additional aspects regarding the shape, the amplitude and the sign (*i.e.* direction) of the imperfections used in the numerical models are analyzed, in an attempt to discover their influence on the ultimate resistance of curved panels.

i) Influence of imperfection shape:

As specified earlier in this chapter, the shape of the initial imperfections affine to the 1st buckling mode is adopted, as the shape that in most cases leads to the lowest ultimate resistance (*e.g.* [127], [129]). However, it is essential to highlight that the shape of the first eigenmode is not similar in shape for all the curved panels subjected to shear since their behavior is often very complex, without a clear trend, which makes the prediction of the shape of buckling mode almost impossible. In chapter 4 (see Fig. 4.6), it was shown that the pattern of the first buckling mode may shift randomly from symmetric to antisymmetric shape and vice versa, depending on the combination of aspect ratio and curvature parameter and does not depend only on one of them separately.

In Fig. 5.13, the reduction factor χ_w of the unconstrained panels (*i.e.* BC1) is plotted against the slenderness parameter $\bar{\lambda}_w$, both for a shallow ($Z = 10$) and a highly curved panel ($Z = 50$), considering several aspect ratios.

Based on these graphs, it may be observed that the behavior of the shallow panels is quite similar to flat plates, with no significant influence of the aspect ratio on the ultimate resistance, for the entire range of $\bar{\lambda}_w$. However, for panels with higher curvatures (*i.e.* $Z > 20$) that show a ‘shell-like’ behavior, the dependence on the aspect ratio is much more emphasized, especially in the intermediate range of the slenderness parameter ($0.6 < \bar{\lambda}_w < 1.2$).

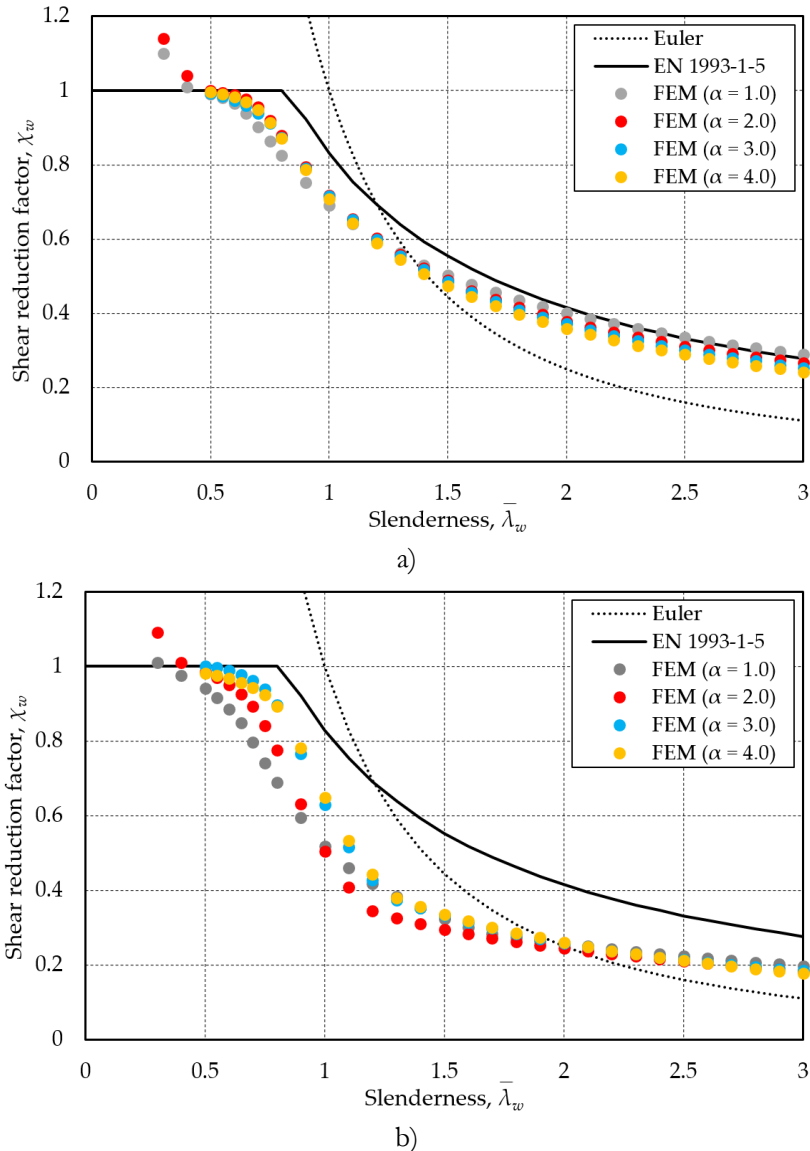


Fig. 5.13: Influence of α on the ultimate shear resistance for a) $Z = 10$ and b) $Z = 50$

It means that in this specific range of slenderness parameter, where the ultimate load is driven by the yield strength of the material, the higher aspect ratio does not necessarily result in lower ultimate resistance. The reason is that a higher aspect ratio may result in a more favorable shape of the first buckling mode (*i.e.* initial imperfection), which leads to the entirely different behavior of the panel and thus different and higher ultimate resistance.

To understand better the influence of the imperfection form on the ultimate strength in this imperfection-sensitive range of slenderness parameter ($0.6 < \bar{\lambda}_w < 1.2$), a brief sensitivity analysis is performed, where several shapes of the imperfections (*i.e.* first four buckling modes) are considered. The results of the study, in which three curvatures and two aspect ratios are considered, are presented in [Table 5.4](#) and [Table 5.5](#).

Table 5.4: Influence of imperfection shape on the shear reduction factor χ_w ($\alpha = 1.0$)

		$Z = 10$	$Z = 30$	$Z = 50$
$\bar{\lambda}_w = 0.8$	1 st mode	0.825	0.662	0.699
	2 nd mode	0.873	0.742	0.673
	3 rd mode	0.975	0.874	0.870
	4 th mode	0.958	0.906	0.821
$\bar{\lambda}_w = 1.0$	1 st mode	0.691	0.477	0.518
	2 nd mode	0.763	0.602	0.497
	3 rd mode	0.861	0.696	0.717
	4 th mode	0.831	0.763	0.651
$\bar{\lambda}_w = 1.2$	1 st mode	0.597	0.421	0.418
	2 nd mode	0.662	0.499	0.402
	3 rd mode	0.709	0.511	0.612
	4 th mode	0.67	0.573	0.475

Table 5.5: Influence of imperfection shape on the shear reduction factor χ_w ($\alpha = 2.0$)

		$Z = 10$	$Z = 30$	$Z = 50$
$\bar{\lambda}_w = 0.8$	1 st mode	0.879	0.808	0.785
	2 nd mode	0.851	0.775	0.792
	3 rd mode	0.952	0.877	0.837
	4 th mode	0.943	0.9	0.871
$\bar{\lambda}_w = 1.0$	1 st mode	0.718	0.558	0.505
	2 nd mode	0.710	0.559	0.565
	3 rd mode	0.839	0.689	0.623
	4 th mode	0.802	0.749	0.691
$\bar{\lambda}_w = 1.2$	1 st mode	0.602	0.451	0.345
	2 nd mode	0.607	0.456	0.384
	3 rd mode	0.730	0.549	0.438
	4 th mode	0.663	0.557	0.534

The results from the study indicate that the ultimate load may vary significantly depending on the imperfection shape, with the maximum difference between the lowest and the highest value of almost 60% (*e.g.* for $Z = 30$, $\bar{\lambda}_w = 1.0$, $\alpha = 1.0$). Furthermore, it may be observed that the form of the 1st buckling mode leads to the lowest resistance in most cases (12 out of 18), whereas in the remaining 6 cases, the second mode is the critical one, leading to a slightly lower ultimate resistance than the first mode ($\Delta < 5\%$ in all 6 cases). Finally, the higher modes have less influence on the ultimate load.

An example in which the second mode is critical (e.g. for $Z = 50$, $\bar{\lambda}_w = 0.8$, $\alpha = 1.0$) is presented in Fig. 5.14a, where for the sake of comparison, force-displacement curves are plotted for all four imperfection forms. Once again, the shear load is normalized to the yield shear load, whereas the circumferential displacement (u_ϕ) in the point C (see Fig. 4.1) is normalized with the thickness of the panel. In the other example, shown in Fig. 5.14b, force-displacement curves are plotted for the same curvature and slenderness; however, with the aspect ratio equal to $\alpha = 2.0$.

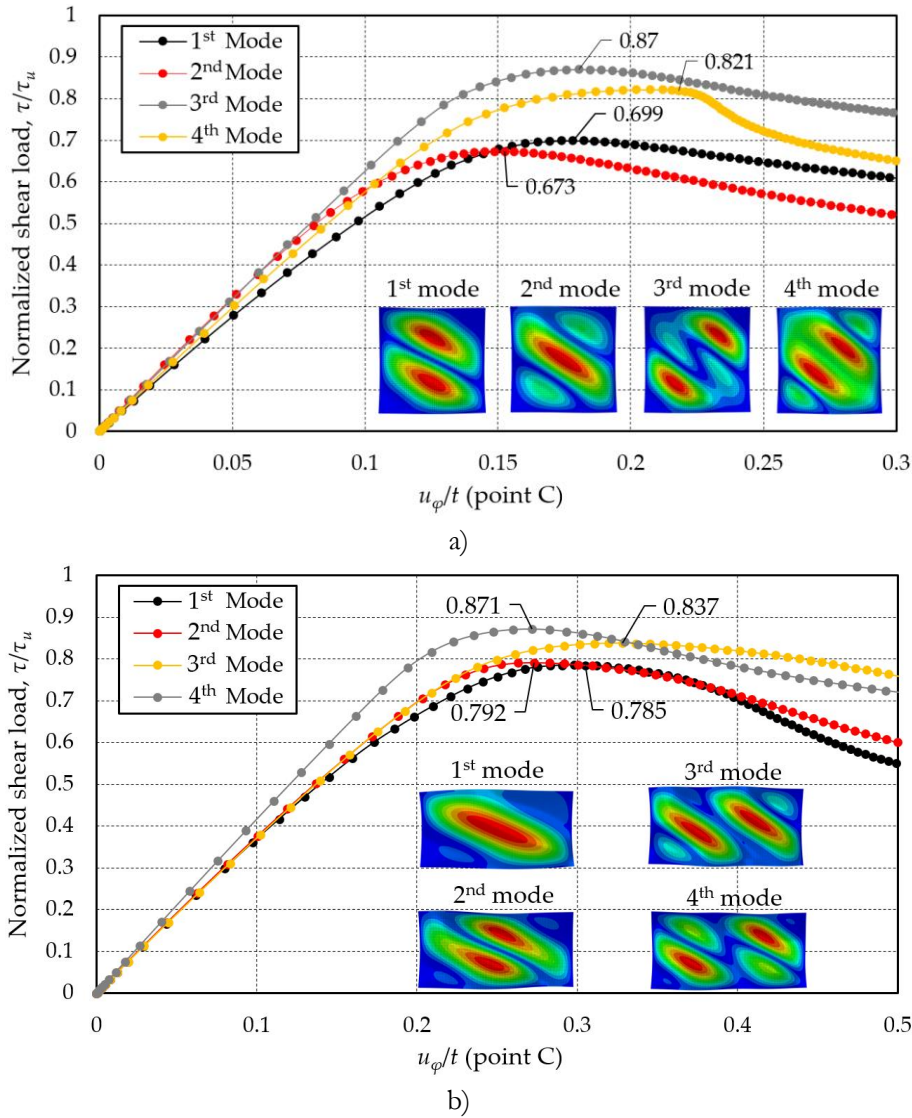


Fig. 5.14: Influence of the imperfection shape: a) $\alpha = 1.0$ and b) $\alpha = 2.0$

From these figures, it may be clearly seen how the imperfection form affects the response of panels, where the second mode leads to the lowest ultimate resistance in the first case ($\alpha = 1.0$), whereas in the second case ($\alpha = 2.0$), the first mode is the critical one. Moreover, the figures show the diversity of the imperfection shapes for the first four buckling modes, despite the same slenderness and the curvature parameter. Namely, for $\alpha = 1.0$, the first buckling mode is antisymmetric and the second mode is symmetric, while for $\alpha = 2.0$ it is opposite, resulting in a different and even higher ultimate resistance, as it was already observed and discussed in Fig. 5.13b.

Finally, for higher values of the slenderness parameter ($\bar{\lambda}_w > 1.2$), variation in the ultimate resistance with the aspect ratio is negligible since in that range the ultimate load is mainly driven by elastic behavior.

A similar study is carried out for boundary conditions BC2 and BC3, in which the influence of the imperfection form on the ultimate resistance is investigated for two different aspect ratios while keeping the curvature and the slenderness parameter constant and equal to $Z = 50$ and $\bar{\lambda}_w = 1.2$, respectively. The results are summarized in [Table 5.6](#).

Table 5.6: Influence of imperfection shape on the shear reduction factor χ_w (BC2 and BC3)

		1 st mode	2 nd mode	3 rd mode	4 th mode
BC2	$\alpha = 1.0$	0.705	0.737	0.772	0.768
	$\alpha = 2.0$	0.575	0.589	0.65	0.668
BC3	$\alpha = 1.0$	0.784	0.759	0.770	0.790
	$\alpha = 2.0$	0.599	0.614	0.622	0.619

It may be concluded that in the case of boundary conditions BC2 and BC3, the panels do not show significant imperfection sensitivity in this range. Namely, the maximum difference between the lowest and the highest ultimate load is 16% in the case of BC2 and 4% in the case of BC3. This is due to the development of the tensile band that positively affects the post-critical behavior, reducing the panel's sensitivity to imperfections, as described by Dubas & Gehri [128].

Based on the imperfection sensitivity analysis presented herein, one may conclude that the shape of the first buckling mode is a satisfactory assumption for the shape of the initial imperfections, leading in most cases to a 'safe design'. In addition, it is shown that the shape affine to the second mode may lead to a lower resistance; however, the difference between these two shapes is almost negligible ($\Delta < 5\%$), which coincides with the findings from the former references (*e.g.* [127], [129]).

Hence, due to a continuing need for generality and simplicity, the equivalent imperfection affine to the 1st buckling mode is adopted in order to derive the expressions for the ultimate shear resistance, something, which to the authors' knowledge is still not available in the literature. Nevertheless, it is a general impression that further study on the imperfection sensitivity is necessary, where not only the fictive forms of imperfections affine to the buckling modes should be considered, but also the measured realistic forms.

ii) Influence of imperfection amplitude:

Regarding the amplitude of the imperfections, as it was specified before, an amplitude equal to a minimum between $a/200$ and $b/200$ is adopted in this study, according to the prescriptions from EN 1993-1-5 [11]. In the case of both flat and curved panels subjected to the axial compression, these amplitudes give conservative results as shown in [chapter 3](#) of this thesis, and confirmed by several authors (*e.g.* [8], [78], [146]). Moreover, Rusch & Lindner [146] back-calculated an amplitude equal to $b/420$ for the Winter curve for plates under pure compression. Hence, it is also intended to compare these two amplitudes ($b/200$ and $b/420$) for curved panels

under shear and to understand to what extent they affect the ultimate resistance. The results of the comparison are presented in Fig. 5.15, for boundary condition BC1, aspect ratio $\alpha = 2.0$ and two curvature parameters. For the sake of comparison, the buckling curve ($\chi_w - \bar{\lambda}_w$) from EN 1993-1-5 is additionally plotted.

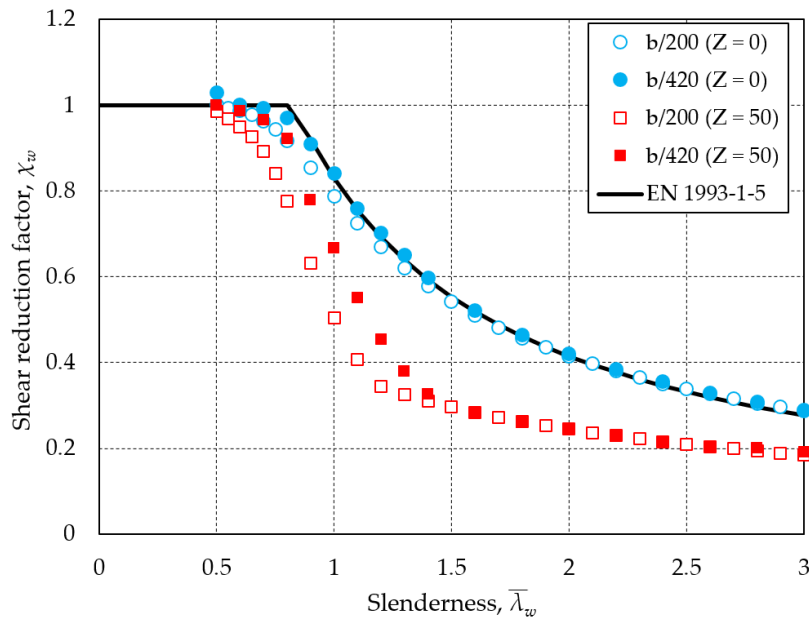


Fig. 5.15: Comparison between two imperfection amplitudes – $b/200$ and $b/420$

The figure indicates that the difference between the two amplitudes is not very significant, especially in the case of the flat panels, due to the presence of the tensile component that decreases the imperfection sensitivity, as it was pointed out several times in this chapter. A larger difference between the amplitudes is noticed only in the intermediate range of the slenderness parameter ($0.6 < \bar{\lambda}_w < 1.2$), due to the aforementioned particular sensitivity of these panels, and it is specifically emphasized for the higher values of curvatures, where the maximum difference in shear reduction factor may reach up to $\Delta_{\max} \approx 32\%$ (e.g. for $\bar{\lambda}_w = 1.0$ and $Z = 50$). For higher slenderness, once again, the difference is practically negligible regardless of the curvature parameter. It should be also mentioned that both $b/200$ and $b/420$ are considerably high values for the imperfections. Consequently, the bending and buckling displacements are combined and the panels do not exhibit a clear-cut difference between the pre-buckling and tensile field phase, which is in detail explained by Dubas & Gehri [128], and could be seen also in Fig. 5.4.

Lastly, Fig. 5.15 also shows that a quite good agreement is achieved between the curve proposed by the standard for the flat plate and the numerical results when the amplitude is equal to $b/420$, but also for the value equal to $b/200$. Nevertheless, due to the lack of more precise information for the imperfection of the curved panels subjected to a shear load, the recommended value (i.e. $b/200$) is selected in the parametric study and the formulas are built based on this assumption.

iii) Influence of imperfection sign:

Finally, the sign of the imperfections (i.e. its direction) is investigated and presented herein, being a parameter that may become relevant in case of the curved panels subjected to shear.

In general, the imperfection shape may be symmetric or antisymmetric, as shown, for instance, in Fig. 5.14. In the case of the antisymmetric shape, the ultimate resistance is insensitive to the direction of the imperfections. However, in the case of the non-flat panels with the symmetric imperfection shape, it is no longer irrelevant in what direction the buckling waves propagate and thus, the ‘positive’ (δ_0^+) and the ‘negative’ (δ_0^-) imperfections must be distinguished. The two possible imperfection signs are schematically illustrated in Fig. 5.16, with the ‘positive’ imperfection oriented radially inward, whereas the negative has the opposite orientation.

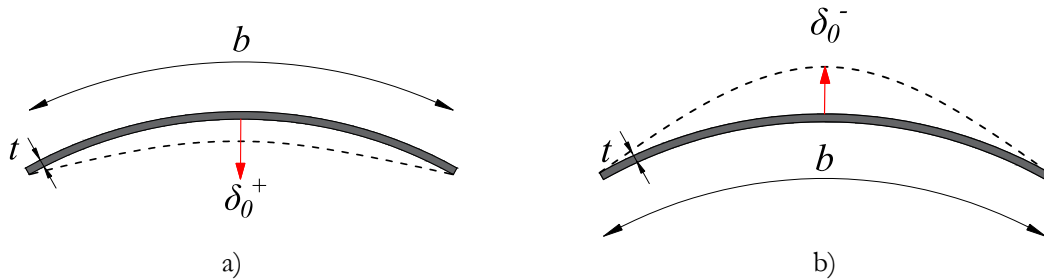


Fig. 5.16: imperfection sign: a) positive and b) negative

Subsequently, a comparison between these two imperfection signs is made, in an attempt to discover which sign is less favorable, *i.e.* leads to lower ultimate shear resistance. In Fig. 5.17, some of the most representative results are shown, using as an example a panel with an aspect ratio equal to $\alpha = 2.0$ and boundary condition BC1, while keeping the amplitude constant and equal to the previously adopted value of $b/200$.

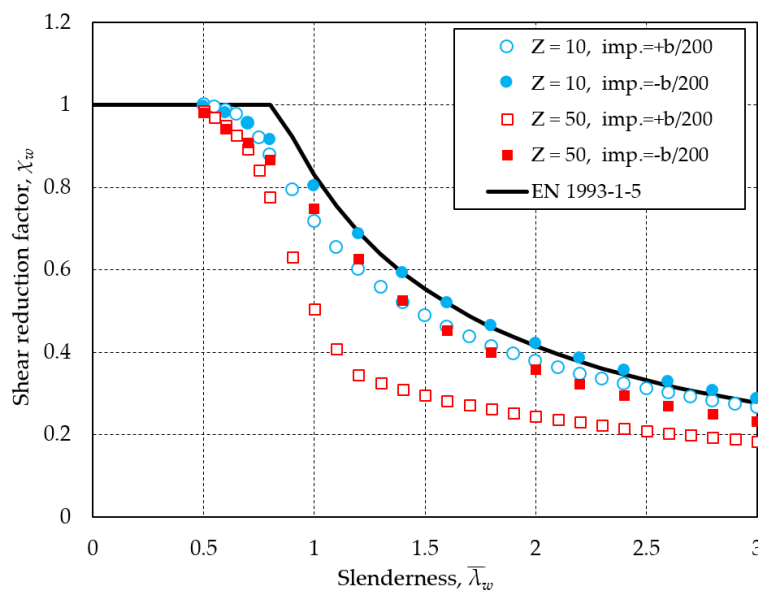


Fig. 5.17: Comparison between two imperfection signs – *positive* and *negative*

Based on the results from the comparative study, it is concluded that imperfection oriented radially inward always results in lower ultimate resistance, regardless of the curvature parameter. Moreover, the difference between the two imperfection signs seems to increase with the curvature parameter. For instance, for slenderness $\bar{\lambda}_w = 1.2$, the difference is equal to $\Delta \approx 14\%$ and $\Delta \approx 80\%$, for $Z = 10$ and $Z = 50$, respectively. Therefore, in section 5.4, where the design rules for the ultimate resistance are proposed, the positive sign of the imperfections is considered as the less favorable case.

5.4 Proposal of design rules for the ultimate resistance

5.4.1 General

The determination of the ultimate shear resistance of a flat panel (*i.e.* a web of a girder) by EN 1993-1-5 [11] is shown in 2.5.2. According to this method, in Eq.(2.96), it is required to calculate first the reduction factor χ_w , which is a function of the slenderness parameter $\bar{\lambda}_w$. Depending on the stiffness of the surrounding stiffeners, the standard provides two different buckling curves ($\chi_w - \bar{\lambda}_w$) for the flat webs, reproduced by Eq.(2.97) and Eq.(2.98), which may be used for any aspect ratio.

It is necessary to emphasize that both buckling curves in EN 1993-1-5 are obtained as lower bounds to a large set of experimental data performed on the girders [128], where χ_w is plotted against $\bar{\lambda}_w$ calculated using the theoretical values of the critical stress (see Eq.(2.99)). However, as shown in chapter 4, the real critical shear stress and thus the real slenderness parameter may highly depend on the exact level of the constraints provided by the flanges and the vertical stiffeners. Therefore, the use of the theoretical values of the critical stresses as an approximation may lead to the horizontal translation of the buckling curves and subsequently to an underestimation of the ultimate resistance.

The main advantage of the numerical simulation carried out in this study, is that the boundary conditions are well controlled so that the calculated value of the critical stress and slenderness parameter corresponds exactly to the considered panel. Hence, the principal objective of this study is to propose new formulas using a similar buckling-curve format ($\chi_w - \bar{\lambda}_w$) adopted from standard, however, for non-flat panels and with a clear specification on the in-plane edge constraints. The extension of the formulas from the standard is done by calibrating the FEM results of χ_w , covering the ranges specified in Table 5.3.

5.4.2 Calibration methodology

As shown in previous sections, the ultimate shear resistance decreases with the increase of the curvature parameter, regardless of the boundary condition and thus, a buckling curve needs to be defined separately for each curvature parameter.

In the case of the boundary condition BC1, the influence of the aspect ratio on the buckling curve is negligible (see Fig. 5.13) and thus, only one buckling curve is required for each curvature parameter, as presented in Fig. 5.18.

This further implies that the reduction factor can be determined as a function of only two variables, *i.e.* $\chi_w = f(\bar{\lambda}_w, Z)$, and not as a function of the aspect ratio. For the sake of the simplicity, the minor variations of the shear reduction factor noticed to occur in the imperfection-sensitive range of slenderness ($0.6 < \bar{\lambda}_w < 1.2$), are neglected. Conservatively, for the calibration of formulas, the values of χ_w in this range are adopted as the lowest ones from all considered aspect ratios. For instance, in the example presented in Fig. 5.13, the values obtained with $\alpha = 1.0$ are adopted.

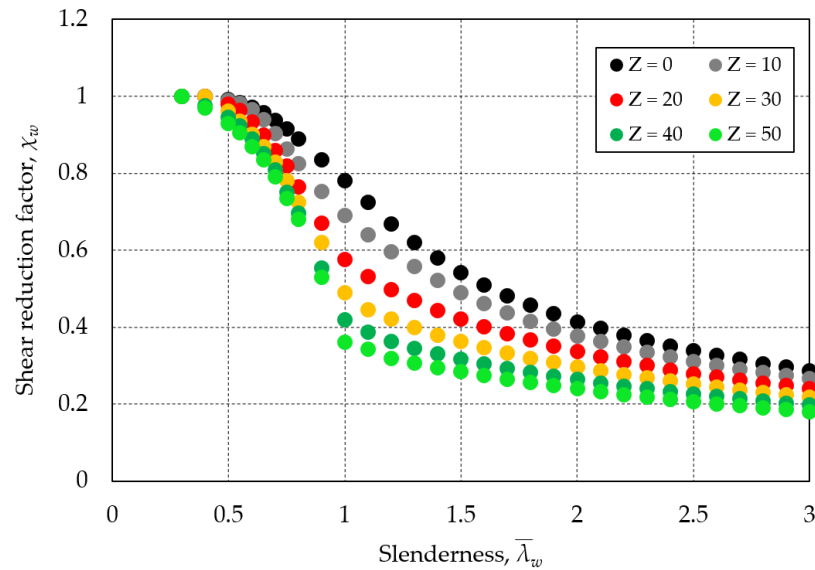


Fig. 5.18: Buckling curves for boundary condition BC1

On the other hand, in the case of the boundary conditions BC2 and BC3, where the tension field may be developed, the reduction factor χ_w additionally depends on the aspect ratio, with a noticeable influence for values up to $\alpha \leq 3.0$ and $\alpha \leq 2.0$, respectively. It implies that the reduction factor for BC2 and BC3 is defined as a function of three variables, *i.e.* $\chi_w = f(\bar{\lambda}_w, Z, \alpha)$. Therefore, for each curvature parameter, it is necessary to generate several buckling curves, which account for the various values of the aspect ratio.

An example is shown in Fig. 5.19 and Fig. 5.20, where the buckling curves for curvature equal to $Z = 50$ are plotted for boundary condition BC2 and BC3. It may be observed that for the panels with the aspect ratio higher than $\alpha > 3.0$ (*i.e.* $\alpha > 2.0$ for BC3), the buckling curve that corresponds to $\alpha = 3.0$ (*i.e.* $\alpha = 2.0$ for BC3) is adopted.

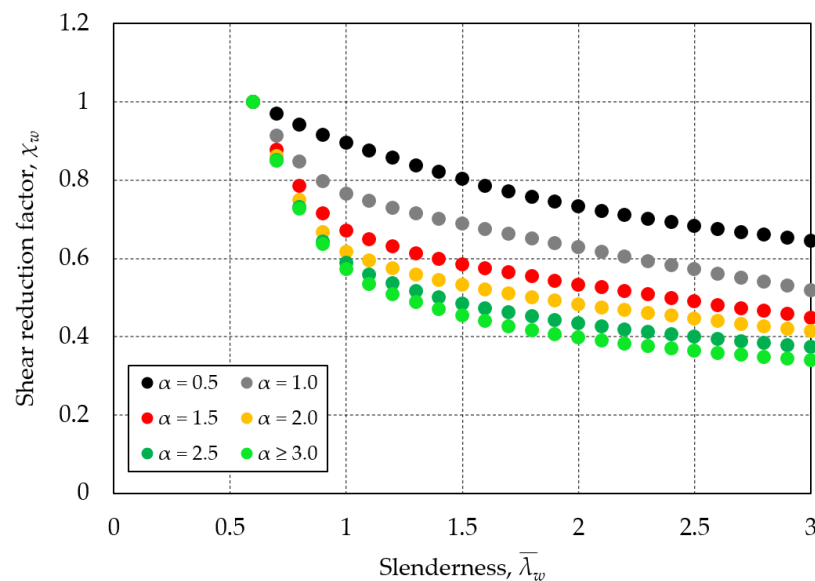


Fig. 5.19: Buckling curves for boundary condition BC2 ($Z = 50$)

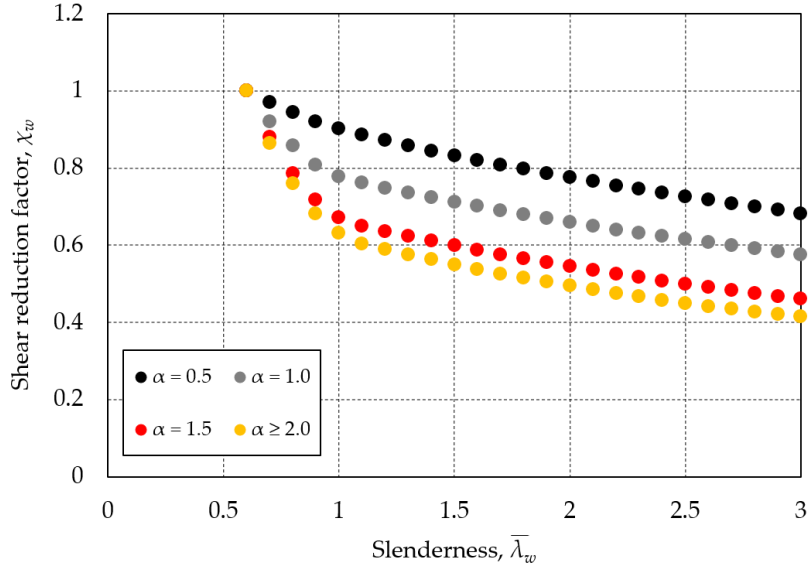


Fig. 5.20: Buckling curves for boundary condition BC3 ($Z = 50$)

Hence, the main challenge in the calibration process is to define a suitable function of two variables (BC1) or three variables (BC2 and BC3), which fits nicely to the FEM results of the shear reduction factor, for any combination of α and Z .

The starting assumption in the calibration process is to use the rational function from EN 1993-1-5 (see Eq.(2.97) and Eq.(2.98), which determines χ_w for a flat plate, simply supported on four edges, with no specification on the level of the edge in-plane constraints. Therefore, the proposed formulas are firstly divided into three main branches, based on the boundary conditions (BC1, BC2, and BC3), and subsequently, each of these three branches are split into two sub-categories of panels, in the same way as it is done in EN 1993-1-5 [11]: *i*) with low slenderness parameter ($\bar{\lambda}_w < 1.1$) and *ii*) with high slenderness parameter ($1.1 \leq \bar{\lambda}_w < 3.0$).

5.4.3 Proposed formulas

The proposed formula for the panels with high slenderness parameter ($1.1 \leq \bar{\lambda}_w < 3.0$) retained the format of a rational function from the standard, regardless of the boundary conditions. On the other hand, for the panels with low slenderness parameter ($\bar{\lambda}_w < 1.1$) a polynomial function of the second degree is found more appropriate, given in a general form by Eq.(5.2)

$$\chi_w = \begin{cases} 1.0 & \text{if } \bar{\lambda}_w \leq \bar{\lambda}_{w,0} \\ A_\chi \bar{\lambda}_w^2 + B_\chi \bar{\lambda}_w + C_\chi & \text{if } \bar{\lambda}_{w,0} < \bar{\lambda}_w < 1.1 \\ \frac{A_\chi}{B_\chi + \bar{\lambda}_w} & \text{if } 1.1 \leq \bar{\lambda}_w \leq 3.0 \end{cases} \quad (5.2)$$

where $\bar{\lambda}_{w,0}$ is the length of the initial plateau, *i.e.* for which the reduction factor is equal to $\chi_w = 1.0$, given by Eq.(5.3)

$$\bar{\lambda}_{w,0} = \begin{cases} 0.4 & , \text{ BC1 and } Z \leq 30 \\ 0.3 & , \text{ BC1 and } Z > 30 \\ 0.6 & , \text{ BC2 or BC3} \end{cases} \quad (5.3)$$

In Eq.(5.2), the parameters A_χ , B_χ and C_χ are functions of α and/or Z , which are calculated using Table 5.7 and Table 5.8 for slenderness $1.1 \leq \bar{\lambda}_w < 3.0$ and $\bar{\lambda}_w < 1.1$, respectively.

Table 5.7: A_χ and B_χ parameters ($1.1 \leq \bar{\lambda}_w < 3.0$)

BC1	$A_\chi = \frac{335.5 - Z}{380}; \quad B_\chi = \frac{3.7 + Z}{47.5}$
BC2	$A_\chi = -\left(\frac{Z}{250} - 0.43\right)\alpha^2 + \left(\frac{Z}{46.9} - 2.91\right)\alpha - \left(\frac{Z}{40.8} - 6.41\right)$ $B_\chi = -\left(\frac{Z}{100.6} - 0.33\right)\alpha^2 + \left(\frac{Z}{20.2} - 2.56\right)\alpha - \left(\frac{Z}{28.8} - 5.67\right)$
BC3	$A_\chi = \left(\frac{Z}{119.2} + 0.45\right)\alpha^2 + \left(\frac{Z}{257.7} - 4.45\right)\alpha - \left(\frac{Z}{18.3} - 10.15\right)$ $B_\chi = -\left(\frac{Z}{2000} - 0.34\right)\alpha^2 + \left(\frac{Z}{25.8} - 4.1\right)\alpha - \left(\frac{Z}{14.3} - 9.6\right)$

Table 5.8: A_χ , B_χ and C_χ parameters ($\bar{\lambda}_w < 1.1$)

BC1	$A_\chi = -\frac{Z}{57.7} - 0.48; \quad B_\chi = \frac{Z}{86} + 0.25; \quad C_\chi = -\frac{Z}{367} + 1.0$
BC2	$A_\chi = -\left(\frac{Z}{125.8} - 0.035\right)\alpha^2 + \left(\frac{Z}{27.2} - 0.03\right)\alpha - \left(\frac{Z}{73.3} - 0.04\right)$ $B_\chi = \left(\frac{Z}{65.8} - 0.03\right)\alpha^2 - \left(\frac{Z}{14.1} + 0.19\right)\alpha + \left(\frac{Z}{39.4} - 0.13\right)$ $C_\chi = -\left(\frac{Z}{160.9} - 0.004\right)\alpha^2 + \left(\frac{Z}{34.2} + 0.13\right)\alpha - \left(\frac{Z}{97.5} - 1.06\right)$
BC3	$A_\chi = -\left(\frac{Z}{125.8} + 0.005\right)\alpha^2 + \left(\frac{Z}{30} + 0.12\right)\alpha - \left(\frac{Z}{87.6} + 0.025\right)$ $B_\chi = \left(\frac{Z}{58.5} - 0.03\right)\alpha^2 - \left(\frac{Z}{14.2} + 0.275\right)\alpha + \left(\frac{Z}{41.3} - 0.08\right)$ $C_\chi = -\left(\frac{Z}{136} - 0.02\right)\alpha^2 + \left(\frac{Z}{33} + 0.12\right)\alpha - \left(\frac{Z}{96.7} - 1.05\right)$

The slenderness parameter $\bar{\lambda}_w$ is calculated by Eq.(2.99), with the shear buckling coefficient k_τ obtained using the formulas proposed in chapter 4 (see Table 4.10).

It should be highlighted that the objective is to propose a universal formula (see Eq.(5.2)) that accounts for all boundary conditions and geometries studied, which leads to a considerably more complex problem, incomparable with the problem of flat plates. Moreover, the aim is to provide expressions that reproduce the numerical results with very high accuracy (*i.e.* $\Delta_{\max} < 5\%$), which

consequently led to relatively more complex expressions for the A_χ , B_χ and C_χ parameters. However, it is emphasized that all expressions are explicit and thus very easy to implement in hand calculation.

Finally, for the practical engineering application, the expressions proposed above could be further simplified, if conservatively adopted $\alpha = 2.0$ for all the buckling curves, which in most cases gives the lowest value of the shear reduction factor. In that case, for the boundary conditions BC2 and BC3, the proposed formulas would have the forms given in [Table 5.9](#) and [Table 5.10](#), respectively.

Table 5.9: Simplified expressions for A_χ , B_χ and C_χ parameters (BC2)

$\bar{\lambda}_{w,0} < \bar{\lambda}_w < 1.1$	$A_\chi = \frac{Z}{35.6} + 0.12$; $B_\chi = -\frac{Z}{18} - 0.63$; $C_\chi = \frac{Z}{42.8} + 1.34$
$1.1 \leq \bar{\lambda}_w \leq 3.0$	$A_\chi = \frac{1155 + 1.07Z}{500}$; $B_\chi = \frac{93.5 + 1.23Z}{50}$

Table 5.10: Simplified expressions for A_χ , B_χ and C_χ parameters (BC3)

$\bar{\lambda}_{w,0} < \bar{\lambda}_w < 1.1$	$A_\chi = \frac{Z}{42.6} + 0.19$; $B_\chi = -\frac{Z}{20.7} - 0.75$; $C_\chi = \frac{Z}{48} + 1.37$
$1.1 \leq \bar{\lambda}_w \leq 3.0$	$A_\chi = \frac{228 - Z}{75}$; $B_\chi = \frac{Z + 494}{179}$

These simplified expressions are suitable for quick verification of the ultimate shear resistance of curved panels. However, the maximum difference between the FEM results and the simplified expression may reach, in some cases, the value of $\Delta_{\max} = 20\%$, thus leading to an overly conservative design. Hence, for more precise design, the expressions given in [Table 5.7](#) and [Table 5.8](#) should be used.

5.4.4 Validation

To validate the proposed formulas, the numerical results of the shear reduction factor ($\chi_{w, \text{num}}$) are compared with the corresponding values obtained by using the formulas ($\chi_{w, \text{prop}}$). In total, 4374 FE models are used for the global statistical evaluation, divided into three groups (1458 each) based on the three boundary conditions, as it was done also in [chapter 4](#). The most relevant results of the statistical assessment (*i.e.* the mean value, the coefficient of variation and the maximum relative error) of the proposed formulas are summarized in [Fig. 5.21](#) and [Table 5.11](#).

Table 5.11: Statistical assessment based on the ratio $\bar{\chi}_{w, \text{prop}}/\bar{\chi}_{w, \text{num}}$

Boundary condition	Number of analysis	Mean (μ)	CoV (%)	Max. error (%)
BC1	1458	0.996	1.76	+6.04
BC2	1458	0.999	1.64	-4.99
BC3	1458	1.006	1.66	-4.90

The statistical evaluation is made based on the $\bar{\chi}_{w,prop}/\bar{\chi}_{w,num}$ ratio, where all the values are normalized against the maximum value, separately for each of the three boundary conditions.

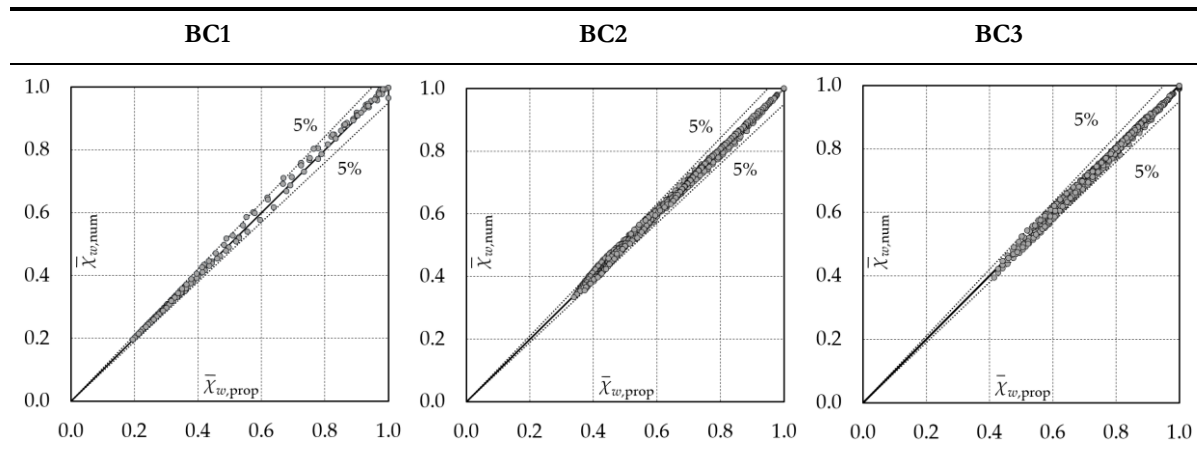


Fig. 5.21: Correlation between $\bar{\chi}_{w,prop}$ and $\bar{\chi}_{w,num}$

Based on the presented statistical evaluation, it is concluded that the proposed formulas may be reliably used for an accurate determination of the shear reduction factor, for all three boundary conditions, within the considered geometrical ranges.

5.5 Application of design rules

To determine the ultimate shear resistance V_{Rd} , several steps need to be carried out, as schematically presented in Fig. 5.22.

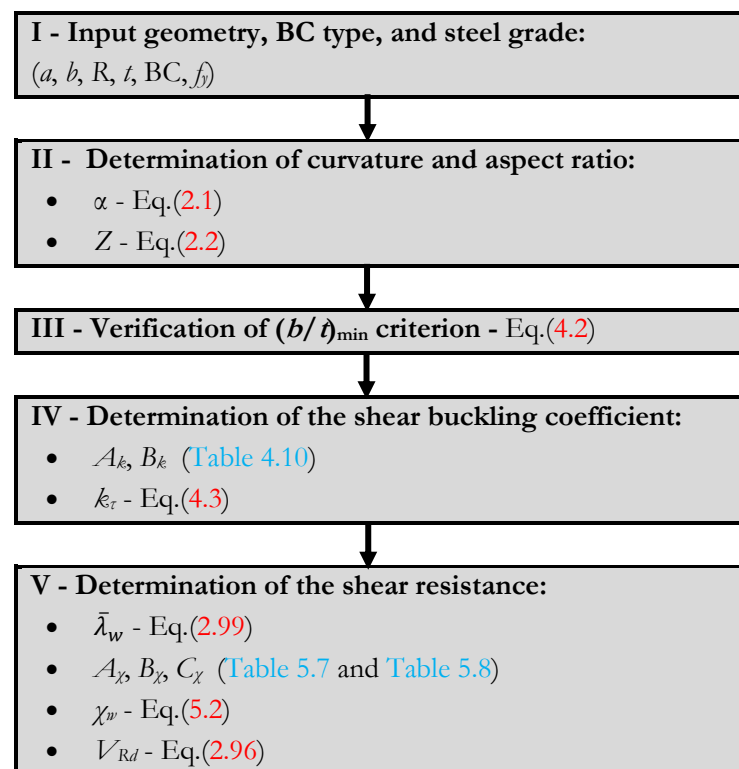


Fig. 5.22: Flowchart for determination of the ultimate shear resistance of curved panels

Following the procedure from Fig. 5.22, one example of curved panels is chosen to demonstrate the appropriate use of the proposed methodology. The results are summarized below, as follows:

I – Input data:

The geometry is adopted within the ranges encountered in real bridge applications, with the boundary condition BC2, whereas the steel S355 is assumed, as shown in Table 5.12.

Table 5.12: Definition of example

Width, b	Length, a	Radius, R	Thickness, t	Boundary	Steel
1000 mm	4000 mm	5000 mm	10 mm	BC2	S355

II – Definition of aspect ratio and curvature parameter:

$$\alpha = \frac{a}{b} = 4.0 \quad (5.4)$$

$$Z = \frac{b^2}{Rt} = 20 \quad (5.5)$$

III – Verification of criterion for minimum b/t ratio:

$$\frac{b}{t} = 100 > \left(\frac{b}{t}\right)_{\min} = \left(\frac{Z}{20}\right)^2 + \frac{Z}{2.6} + 14.5 = 23 \quad (5.6)$$

IV – Determination of the shear buckling coefficient:

$$A_k = 0.124Z + 4.94 = 7.42 \quad (5.7)$$

$$B_k = 0.137Z + 3.756 = 6.5 \quad (5.8)$$

$$k_\tau = A_k + B_k (1/\alpha)^2 = 7.83 \quad (5.9)$$

V – Determination of the ultimate shear resistance:

$$\bar{\lambda}_w = \frac{b/t}{37.4 \cdot \varepsilon \cdot \sqrt{k_\tau}} = 1.175 \quad (5.10)$$

$$A_\chi = -\left(\frac{Z}{250} - 0.43\right)\alpha^2 + \left(\frac{Z}{46.9} - 2.91\right)\alpha - \left(\frac{Z}{40.8} - 6.41\right) = 1.62 \quad (5.11)$$

$$B_\chi = -\left(\frac{Z}{100.6} - 0.33\right)\alpha^2 + \left(\frac{Z}{20.2} - 2.56\right)\alpha - \left(\frac{Z}{28.8} - 5.67\right) = 1.446 \quad (5.12)$$

$$\chi_w = \frac{A_\chi}{B_\chi + \bar{\lambda}_w} = 0.6185 \quad (5.13)$$

$$V_{Rd} = \chi_w b t f_y / \sqrt{3} = 1266 \text{ kN} \quad (5.14)$$

Since the aspect ratio is higher than $\alpha > 3.0$, in Eqs. (5.11)-(5.12), the buckling curve that corresponds to the value equal to $\alpha = 3.0$ is used, as shown in Fig. 5.23.

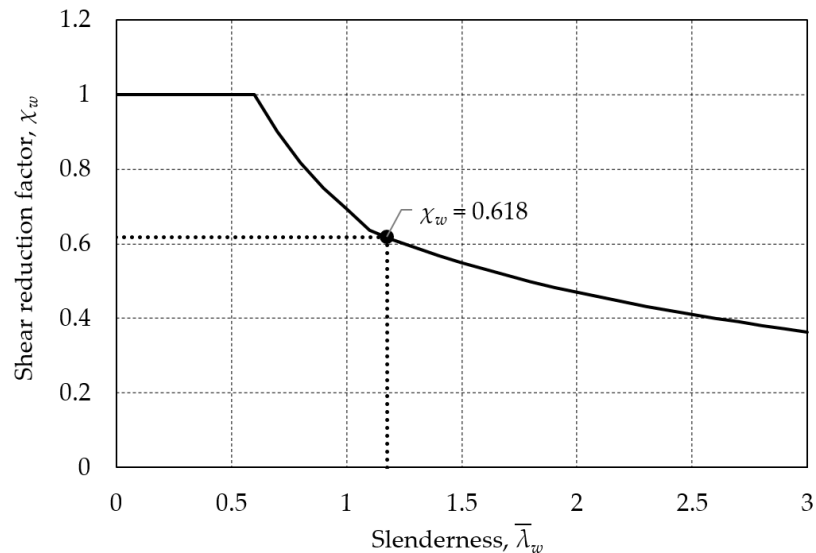


Fig. 5.23: Corresponding buckling curve for the considered study cases ($Z = 20$, $\alpha > 3.0$)

As it may be seen, using the proposed formulas given by Eq.(5.2), it is possible to plot the corresponding buckling curves for any desired combination of the curvature parameter and aspect ratio, within the domain of this study. Finally, the calculated ultimate resistance ($V_{Rd,prop} = 1266$ kN) is compared with the value obtained numerically ($V_{Rd,num} = 1246$ kN), and a very good agreement is achieved ($\Delta = +1.61\%$).

5.6 Summary

The chapter was devoted to the post-critical behavior of unstiffened simply supported curved panels when subjected to pure shear stresses and to the determination of their ultimate shear resistance. The influence of several parameters on the ultimate shear resistance was numerically investigated, such as *i*) curvature parameter ($Z \leq 50$); *ii*) aspect ratio ($\alpha = 0.5-5.0$); *iii*) three boundary conditions - BC1 (all edges free-to-wave), BC2 (two curved edges constrained and two longitudinal free-to-wave) and BC3 (all edges constrained); and *iv*) the initial imperfections (shape, amplitude, and sign).

In particular, it was shown that:

- The higher the curvature parameter and the aspect ratio, the lower is the ultimate resistance. However, the post-critical behavior depends on both geometrical parameters and not only one of them;
- For very slender panels, the ultimate resistance highly depends on the rigidity of the boundary conditions. Namely, in case of more rigid boundary conditions (*i.e.* BC2 and BC3), where the tension field may be developed, considerable post-critical reserves could be mobilized, resulting in a higher ultimate shear resistance;
- Moreover, in the case of boundary conditions BC2 and BC3, owing to the presence of the tensile band, the panels show lower sensitivity to the geometric imperfections. On the other hand, in case of BC1, panels are susceptible to the shape and the amplitude of

the imperfections, which is particularly emphasized in the case of more curved panels ($Z > 20$) for the intermediate range of the slenderness parameter ($0.6 < \bar{\lambda}_w < 1.2$);

Finally, a set of expressions was proposed, using the same buckling curve ($\chi_w - \bar{\lambda}_w$) approach from EN 1993-1-5 [11] for the flat plates, which enables an accurate estimation of the shear reduction factor for curved panels. The proposed method requires the calculation of the shear buckling coefficient first, which can be obtained using the formulas proposed in [chapter 4](#). The formulas were derived assuming the equivalent geometric imperfections recommended by EN 1993-1-5, with the shape affine to the 1st buckling mode and an amplitude equal to a minimum between $a/200$ and $b/200$, which leads to a safe design. The proposed formulae are valid for curvatures and aspect ratios within the ranges that may be of practical use in offshore, aeronautics and bridge applications.

6. Experimental study on curved bottom flanges in steel box-girder bridge decks

6.1 Overview

In this chapter, a study on the entire box-girder bridge cross-section integrating the bottom curved panel is carried out, which is one of the principal goals of this thesis, defined as Task 4 in [section 1.2](#). More specifically, the goal is to assess the M - V interaction behavior of a box girder bridge deck near the intermediate support, giving an emphasis to the zone where the curved panel in the bottom flange is subjected to both in-plane compressive and shear stresses, which was addressed in Task 2 ([chapter 3](#)) and Task 3 ([chapter 4](#) and [chapter 5](#)).

To accomplish the desired targets from Task 4 in the most elaborate way, the research strategy is to divide the study into two equally relevant steps - Task 4.1 and Task 4.2. This section deals only with the first step, in which the results from the experimental campaign on the bridge-deck specimens are in detail reported. The collected data from this section serve as the benchmark in the subsequent Task 4.2, tackled in [chapter 7](#), in which an extensive numerical study on this type of bridge decks is carried out. Together, these two steps should contribute to the development of solid knowledge on the M - V interaction behavior of this innovative cross-section type, and eventually to the proposal of new robust design rules in the final part of this thesis ([chapter 8](#)).

The experimental campaign, presented in this chapter, is carried out within the OUTBURST research project [18] and it comprises two bridge deck prototypes, tested as three-point bending tests, thus simulating the bridge behavior near the intermediate support. The prototype box-

girder bridge segments are in scale 1:3 with respect to a real study case identical, with identical geometry, however, with two different steel grades (S460 and S690). Both tests are performed in the laboratory of the Civil Engineering Department at the University of Coimbra.

The scientific significance of the presented experimental study is twofold: *i)* it gives an insight into the real behavior of the box-girder bridge deck with a curved bottom flange. Such an experimental program was not reported in the literature, least of all with the scale that is tested within the OUTBURST research project; *ii)* the reported results serve as a reliable benchmark for the future work, available for the entire scientific community. This allows for the reproduction of experimental and/or numerical results, thus extending the scope of the study presented herein.

The chapter is divided into three sections. In [section 6.2](#), all the major steps carried out prior to the tests are described in detail, starting from the real case study of the bridge until the final adoption of the test specimens. In particular, the geometry and the material properties of the specimens are specified. Subsequently, in [section 6.3](#), the layout of the experiment is represented, including the instrumentation used for data acquisition in both tests. Finally, the most relevant test results are discussed in [section 6.4](#).

6.2 Design of test specimens

6.2.1 Introduction

The design of the test specimens had to comply with several requirements and some inevitable restrictions. Firstly, since the key objective is to test a curved bottom flange as part of a bridge deck subject to longitudinal compression and shear, it is necessary to consider a bridge segment with intermediate support that could have this stress state. Secondly, the bridge deck should correspond to a realistic and potentially efficient bridge design. Therefore, the strategy is to consider a real multi-span bridge deck with a trapezoidal box-girder cross-section, and subsequently, to design a variant solution using a transversally curved bottom flange/web.

The main constraint to the experimental program was related to the limitations on the maximum width of the test specimens due to transportation restrictions. Therefore, it was necessary to design a scaled-down specimen that maintained the relevant features of the variant solution. Finally, the test specimens had to comply with the University of Coimbra laboratory specifications, in terms of geometry and load application capacity.

This section summarizes the reference case study of a bridge deck followed by the description of the test specimens. In addition, the material properties of the S460 and S690 steels are specified, obtained from tensile coupon tests. Finally, some of the main fabrication challenges for this innovative bridge type are highlighted.

6.2.2 Reference case study

The deck cross-section of the reference case study described herein is proposed by GRID International [151]. The bridge is a continuous five-span composite steel-concrete box-girder deck with standard reinforced concrete abutments and piers. It is designed to carry a roadway

with a single carriageway of two lanes. The deck comprises two lateral spans of 37.8 m and three central spans of 54 m, in a total of 237.6 m length, as shown in Fig. 6.1.

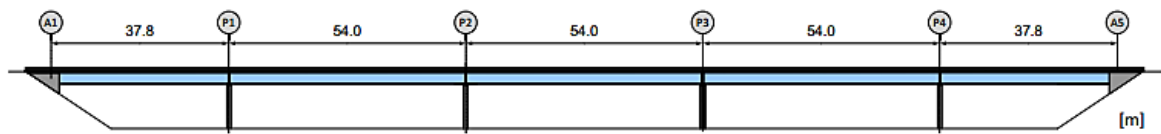


Fig. 6.1: Span layout of the reference case study - bridge elevation [151]

The deck cross-section comprises a steel-box girder with a concrete slab supporting the roadway. Both the slab and the non-structural bridge elements are symmetrical with respect to the bridge axis. The slab has a 2.5% inclination on either side of the bridge axis. The bridge deck is 10930 mm wide, carries two traffic lanes (3700 mm wide in each direction) and VRS barriers. Two pedestrian walkways 1600 mm wide, concrete stringcourse and a steel balustrade are provided on either side of the carriageway. The slab is formed by 70 mm precast planks and 180 mm cast in place concrete, allowing a fast construction.

Based on this realistic case study, the alternative solution with cylindrically curved steel panels is developed, adopting a box-girder section 2250 mm deep, as indicated in Fig. 6.2. The box girder is formed by *i*) a curved bottom soffit with a radius of 2500 mm (whose center coincides with the slab top surface) longitudinally stiffened with 250 x 25 mm flats at 950 mm centers; *ii*) webs with 46 degrees of inclination with regards to the horizontal axis; and *iii*) standard plate top flanges, 80 mm thick.

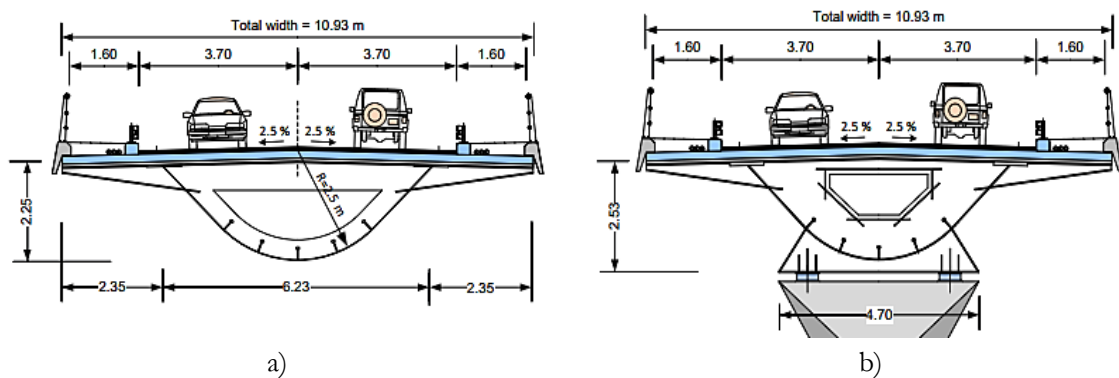


Fig. 6.2: Alternative cross-section with the curved panel at a) span and b) pier [5]

From these figures, it may be noticed that the center distance between top flanges is 6230 mm, whereas the slab cantilevers are 2350 mm long. The welded I-shape cantilever beams vary in depth from 509 mm to 130 mm at the tip, whereas the diaphragms are designed as flat plates with 450 x 16 mm dimensions. Only over the supports, a 30 mm thick closed diaphragms are adopted. To transfer the reaction forces to the piers, a 4700 mm wide support box is provided, shown in Fig. 6.2b. The reinforced concrete slab is supported by cross-beams every 2160 mm, which coincides with the position of the girder diaphragms, as presented in Fig. 6.3, where also 3400 mm wide stiffened bottom curved flange is presented.

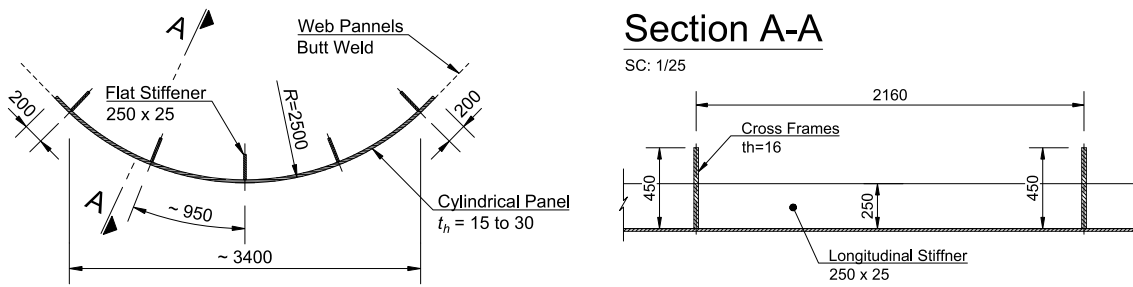


Fig. 6.3: Curved steel plate in the bottom flange (adapted from [5])

The structural steel distribution for a typical 54 m span is designed to comply with the existing standards, and it is presented in Fig. 6.4. For construction simplicity reasons, the slab is adopted with a constant thickness of 250 mm. The girder also has a constant depth of 2250 mm, whereas the thickness of the upper and lower flanges, as well as the flat web, decreases towards the mid-span of the box girder, as indicated in Fig. 6.4. The flat webs, which are longitudinally unstiffened, have the same steel distribution and the thickness as the cylindrical panel, varying between 30 mm at the supports and 15 mm at mid-span. The upper flange is 800 mm wide, with the thickness that varies between 80 mm at the support and 40 mm at mid-span. To provide full composite behavior, three rows of 175 x Ø22 mm head studs are provided (see Fig. 6.4), with spacing varying between 150 mm and 300 mm at the supports and mid-span, respectively. For more details regarding the proposed alternative solution, the reader is invited to see references [5] and [151].

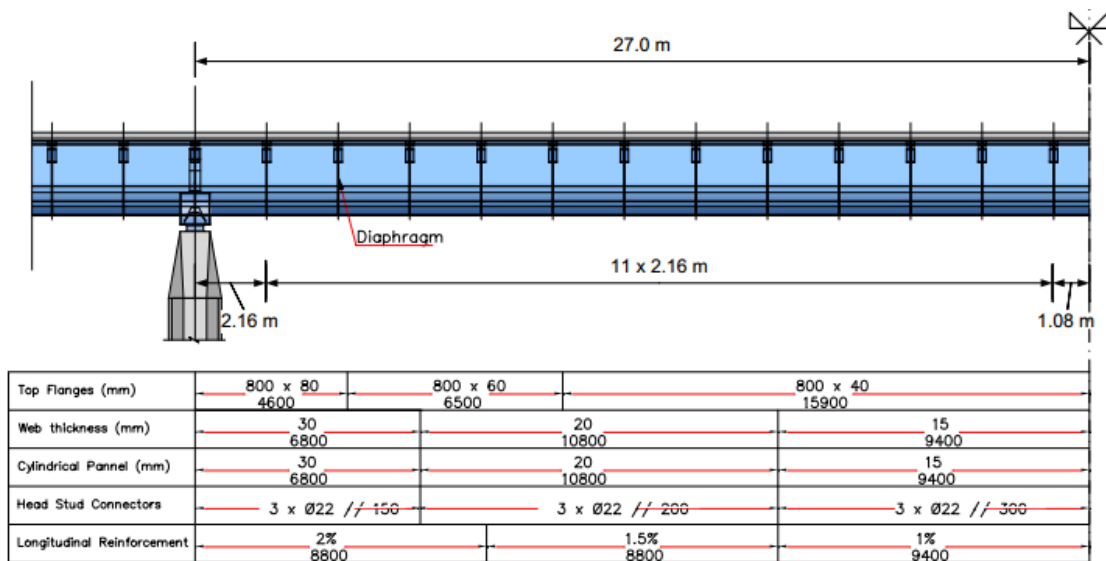


Fig. 6.4: Structural steel distribution [5]

Finally, the main geometrical parameters of the proposed solution, defined in section 2.2, such as the global and local curvature parameters, aspect ratios and plate slenderness, are summarized in Table 6.1. In addition, for the sake of comparison, the average value of these parameters is provided, based on the data collected on the real examples of bridges with curved cross-sectional panels from Table 2.2.

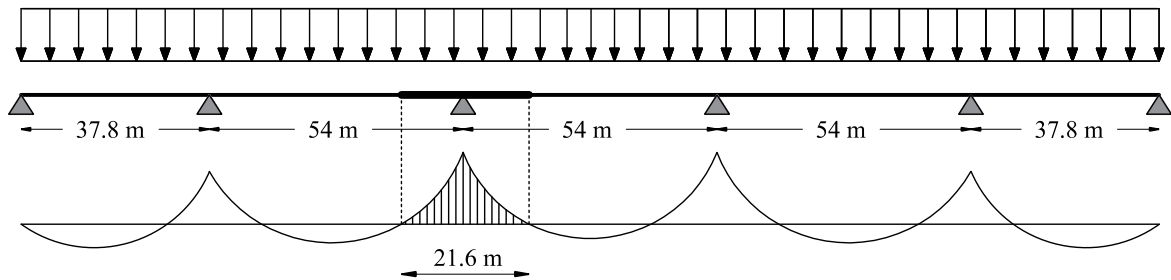
Table 6.1: Geometrical parameters of the adopted cross-section at support

	Z	α	b/t	Z_{loc}	α_{loc}	b_{loc}/t
Real examples (avg.)	100	0.7	165	3	4	28
Case study	235	0.5	140	12	2.3	32

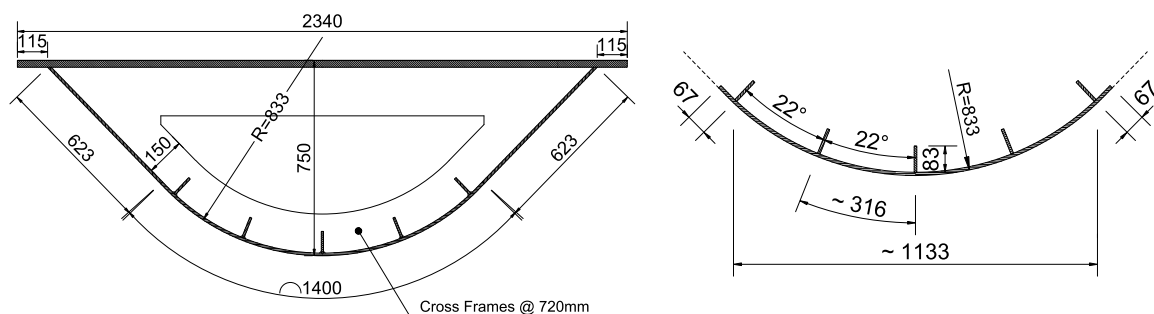
It may be observed that all parameters fall inside the ranges of typical bridge geometries. However, in order to grasp the benefits of higher curvatures, the global curvature, $Z = 235$, and the local curvature, $Z_{loc} = 12$, are on the upper bound of the existing bridge decks.

6.2.3 Geometry of test specimens

The goal of the experimental tests is to reproduce the behavior of the bridge deck in the vicinity of intermediate support with a length of approximately $0.2 \times L$ ($L \approx 54$ m) on both sides of the support, which corresponds to the distance between two zero-bending moments. This results in a bridge deck segment with a total length of approximately 21.6 m (*i.e.* $0.4 \times L$), as shown in Fig. 6.5.

**Fig. 6.5:** Length of bridge deck close to an intermediate pier

This segment is proportionally scaled-down by about a 1:3 ratio to meet the aforementioned road transportation constraint of approximately 2400 mm on the width. The new dimensions of all relevant parts of the test specimens are presented in Fig. 6.6, whereas some additional information is provided in Table 6.2.

**Fig. 6.6:** Cross-section of the tested prototypes

The figure indicates that the cross-section consists of a curved bottom panel, approximately 1400 mm wide and flat webs welded to the curved panel. To secure an adequate load application and the desired boundary conditions, the specimens are extended by $a = 720$ mm on both sides. Consequently, the total length of each specimen is equal to $L + a + a = 8640$ mm (see Table 6.2).

Table 6.2: Adopted geometry of the tested prototype in [mm]

	Symbol	R = 1:1	R = 1:3
Total length	L	21600	7200
Top flange thickness	t_f	80	25
Bottom flange thickness	t	30	10
Cross-frames distance	a	2160	720
Stiffener thickness	t_{st}	25	8
Cross-frame thickness	t_{cf}	16	5
Diaphragm thickness	t_d	30	10

Finally, it is necessary to emphasize that several simplifications are introduced in the tested deck prototype (see Fig. 6.6):

- The cross-section is considered as a homogeneous steel section, and not as a composite one, where the reinforced concrete slab above the intermediate support is replaced by an equivalent steel plate, resulting in a top flange with a constant thickness;
- The inclination of the slab of 2.5% is neglected, resulting in a flat top flange;
- The cross-section of the bridge deck that participates in load-bearing capacity consists only of the box girder part, whereas the cantilevers are omitted;

6.2.4 Fabrication challenges

The two test specimens are fabricated by MCE GmbH within the OUTBURST project [18] (see Fig. 6.7). During the fabrication, several unexpected challenges were encountered that deserve to be highlighted.


Fig. 6.7: Fabrication of test specimens by MCE GmbH

Firstly, the scaling of the specimens resulted in thin plates with relatively thick butt welds. Therefore, the welding had to be done with a particular caution since these thick welds showed a tendency to shrink in the cooling phase, causing warping and distortion of the adjacent plates. One example of this phenomenon is detected after a thorough inspection of the specimen made in S690, where the longitudinal stiffeners experienced a severe bow imperfection, with an amplitude of almost $\delta_{loc} \approx 20$ mm (*i.e.* $\delta_{loc} \approx b/4$), as shown in Fig. 6.7. Nevertheless, such huge bow imperfections are identified only in the zones of the bottom flange located far from the

intermediate support, where the failure is anticipated, thus, their influence on the behavior of the bridge prototype is insignificant.

Moreover, due to the scaling, the assembly order of the specimens required another change in the design. Namely, in the full-scale deck, the holes in the diaphragms would have been big enough to allow access to the welder inside the box-girder. However, in the downscaled specimen, these holes are too small and thus, two rectangular openings (windows) are left open on each side of the specimens. Moreover, these two windows are used also for the installation of measuring equipment inside the section. The windows are closed by welding in the laboratory of the University of Coimbra after the instrumentation is completed, as shown later in [section 6.3](#).

However, the most intricate fabrication issue turned out to be the assembly of the longitudinal stiffeners and perpendicular cross-frames. Commonly, in the case of trapezoidal box cross-sections, the assembly starts with the welding of the longitudinal stiffeners onto the bottom flat panel. Subsequently, the assembly of the cross-frame is achieved by sliding over the longitudinal stiffeners until the desired position, followed by complete welding at the end. However, in the case of a curved panel, each flat longitudinal stiffener takes a different global angle and therefore, the sliding of the cross-frame is not feasible. In this particular case, it is possible to assemble manually all parts at the desired position before welding, owing to relatively lightweight cross-frames. However, for larger-scale structures, the use of a different longitudinal stiffener would be recommendable, *e.g.* trapezoidal stiffeners with inclined side plates.

Finally, the chosen steel grades of S460 and S690 require special attention in the workshop, both in terms of quality management, certificates (workshop and welders), heating, costs, etc. Hence, although these materials are covered by existing design codes, their use is still rather limited in the bridge industry.

6.2.5 Material properties

The mechanical properties of the S460 NL and S690 QL steels are obtained by a standard tensile test, according to ISO 6892-1 [152], performed at room temperature in the strain control method A222, with a strain rate equal to 0.00025 s^{-1} .

For the tensile tests, ten specimens in total (five per steel) are cut directly from the bridge prototypes after the tests are completed. The samples are taken from the flat parts of the webs, at the far end of each of two bridge prototypes since these areas are not exposed to any external load during the experimental test. To assess the level of anisotropy of this material, the test samples are taken in two perpendicular directions, according to the scheme presented in [Fig. 6.8](#).

All specimens have the thickness equal to $t = 10 \text{ mm}$. The mechanical properties relevant to the characterization of the material are summarized in [Table 6.3](#), where the values correspond to an average obtained from five tests. The modulus of elasticity E is obtained by means of linear regression, as recommended in Annex A of ISO 6892-1 [152].

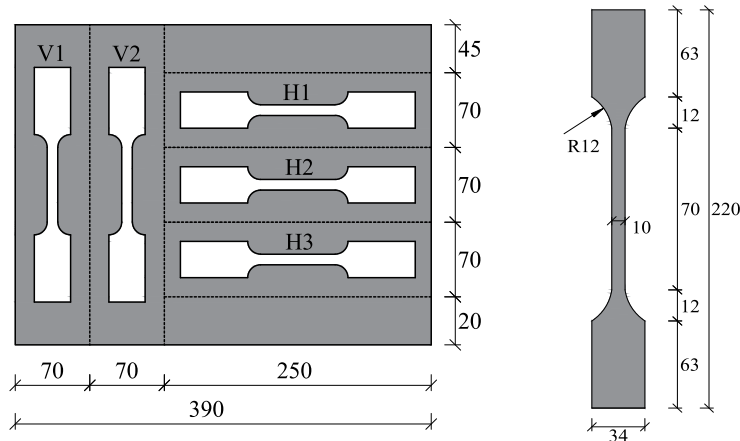
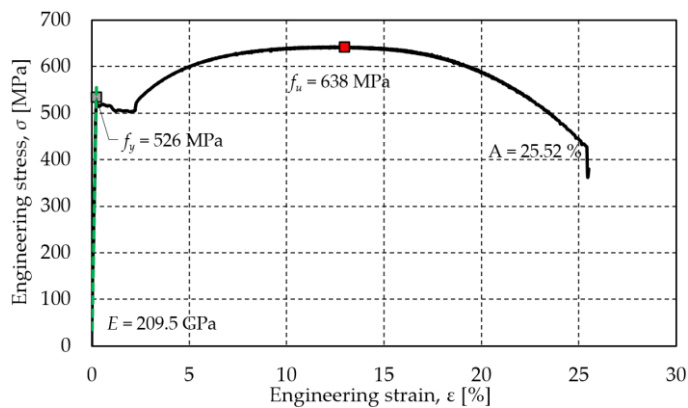


Fig. 6.8: Geometry and orientation of the tensile test specimens

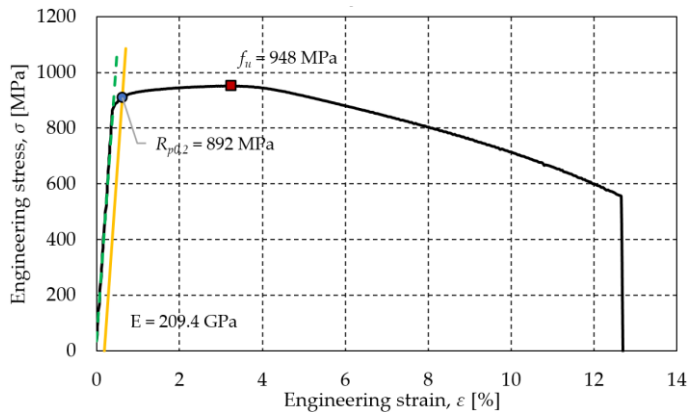
Table 6.3: Measured mechanical properties for two steels – engineering stresses

Steel	E [GPa]	f_y [MPa]	f_u [MPa]	f_u/f_y	A_t [%]
S460	209.5	526	638	1.20	26.1
S690	209.4	892	948	1.06	13.8

For each steel grade, one representative engineering stress-strain curve obtained from the tensile coupon tests is shown in Fig. 6.9. For the high-strength steel (S690) the yield strength corresponds to the proof strength ($R_{p0.2}$), shown in Fig. 6.9b.



a)



b)

Fig. 6.9: Engineering stress-strain curves: a) S460; b) S690

Based on the results of tensile coupon tests it is concluded that both materials might be considered isotropic, showing the same mechanical properties in two perpendicular directions. For both materials, the yield strength exceeded the nominal values by 14% in the case of S460 and 29% in the case of S690.

From these graphs, it may be noticed that steel S460 is characterized by discontinuous yielding, with a yield plateau between the start of yielding and the start of uniform work-hardening. On the other hand, the higher strength steel (S690) shows a less ductile behavior, with a considerably lower f_u/f_y ratio, and almost two times lower values of the percentage total elongation after fracture (A_t).

6.3 Experimental layout

6.3.1 Definition of the setup

To assess the complex behavior of a box girder bridge deck near the intermediate support, where the moment-shear ($M - V$) interaction occurs, the two bridge prototypes in a scale 1:3 are tested as three-point bending tests. The global view of the test setup is shown in Fig. 6.10.

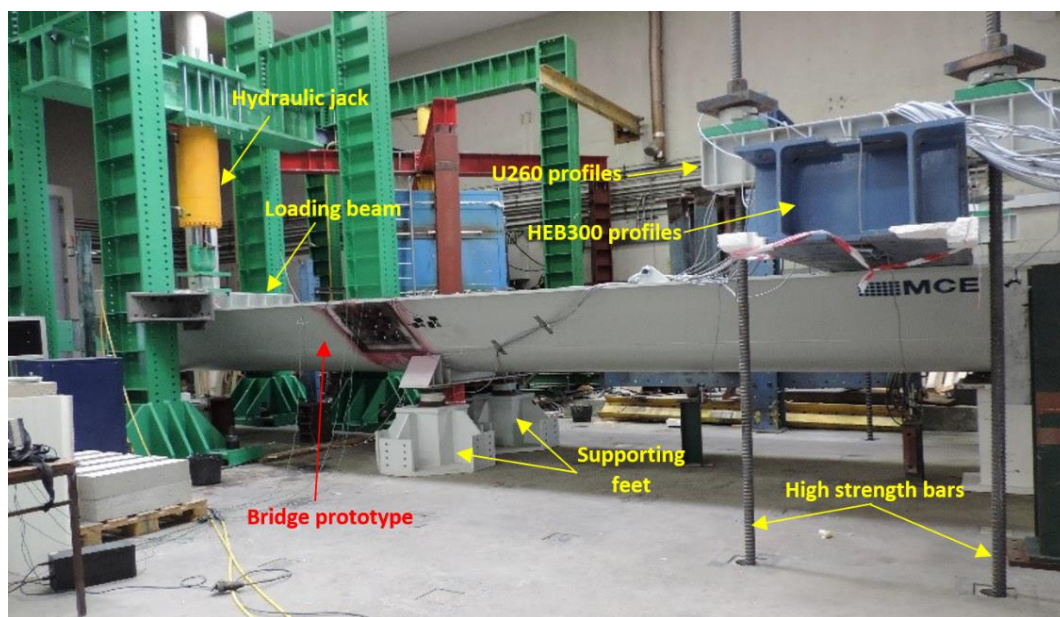


Fig. 6.10: Global view of the test setup

To achieve the desired load and boundary conditions, the following material is designed and fabricated for the experimental tests:

- 1 bridge prototype made of steel S460 and another identical in S690
- 2 supporting feet where the intermediate support is placed
- 1 loading beam (stiffened HEB300 profile), placed below the hydraulic jack
- 2 supporting beams (back-to-back U260 profiles – white colour)
- 2 supporting beams (HEB300 profiles – blue colour) supporting U260 profiles
- 4 high strength pre-stressing systems (Ø47 mm) 4.5 m long.

Besides the bridge prototypes made of steel S460 and S690, all other auxiliary elements are made of steel S355. Moreover, 4 pre-stressing HSS threadbar systems with the corresponding accessories (plates, nuts, washers) used in both tests, are adopted from a catalog [153].

Each bridge prototype is loaded by a concentrated force on one end using an Agop 6000 kN actuator, as indicated in Fig. 6.11a. The load is transferred to the bridge deck through a load beam made of a stiffened HEB300 profile. The middle support of the segment is supported by two support feet, connected together by means of bolts.

At the other end of the bridge prototype, 4 high strength bars anchored to the reaction beam in the ground, act as a counter-reaction and prevent the rotation of the bridge segment upwards. The bars are supported by two simply supported beams, made of two back-to-back UPN260 profiles (white-coloured), designed to sustain huge local transversal forces from the bars. These two beams are supported by another two welded beams made of HEB300 profiles (blue-coloured), as presented in Fig. 6.11b.



Fig. 6.11: Test setup: a) load application; b) end support - 2 back-to-back U260 beams (white) and 2 HEB300 beams (blue)

Finally, the lateral movements of the bridge prototype during the load application are prevented by two specially designed lateral constraints attached to the loading frame, with a 5 mm distance from the segment, as shown in Fig. 6.12.

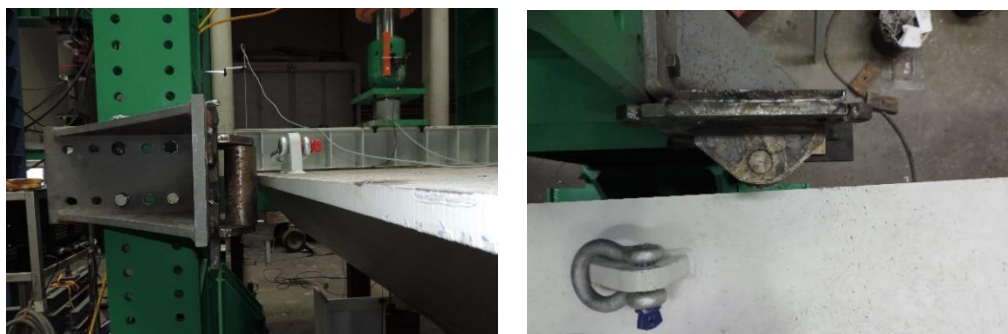


Fig. 6.12: Lateral constraints

6.3.2 Instrumentation

During the two experimental tests, the following data is acquired:

- Applied axial force and reaction (with load cells)
- Vertical, lateral and longitudinal displacements (with LVDTs)
- Strains (with strain gauges – SGs)

6.3.2.1 Linear displacement transducers (LVDTs)

In total, 10 LVDT TML are used in each test to record vertical, lateral and longitudinal displacements of the specimen, positioned according to the scheme in Fig. 6.13.

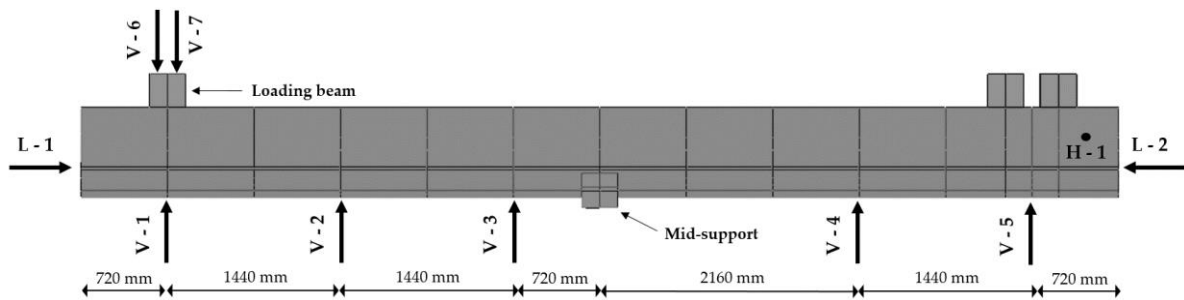


Fig. 6.13: The position of LVDTs

Out of 7 LVDTs that measure vertical displacements (*i.e.* V-1 to V-7), V-6 and V-7 are placed at two ends of the loading beam to monitor if the load is centered during the test (see Fig. 6.11a), V-1, V-2, and V-3 are placed at one side of the bridge segment that is moving downwards (see Fig. 6.14a), whereas the remaining two, V-4 and V-5, are placed at the opposite side of the mid-support (see Fig. 6.14b).



a)



b)

Fig. 6.14: LVDTs to measure vertical displacements: a) V-1, V-2, and V-3; b) V-4 and V-5

Finally, 2 LVDTs (L-1 and L-2) measured the longitudinal displacement at the two ends of the bridge specimen (see Fig. 6.15a), whereas one LVDT (H-1) is used to measure potential horizontal (in-plan) displacements (see Fig. 6.15b).



a)



b)

Fig. 6.15: LVDTs to measure: a) longitudinal (L-2) and b) horizontal (H-1) displacements

6.3.2.2 Load cells

For the load measurements, five load cells (type C6A) are used in each test. As may be seen in Fig. 6.11b, four of them (R1, R2, R3, and R4), with the capacity of 2 MN, are placed at the position of the 4 high strength bars to measure the forces in the bars. The last one, with the capacity of 5 MN, is placed at the position of the loading point (F), as shown in Fig. 6.11a.

6.3.2.3 Strain gauges

In total, 99 SGs and 103 SGs (type FLA-6-11) are used for the S460 and S690 specimens, respectively. They are located in 3 different cross-sections, 150 mm, 300 mm and 570 mm away from the intermediate support, where the failure of the prototype is anticipated, as shown in Fig. 6.16.

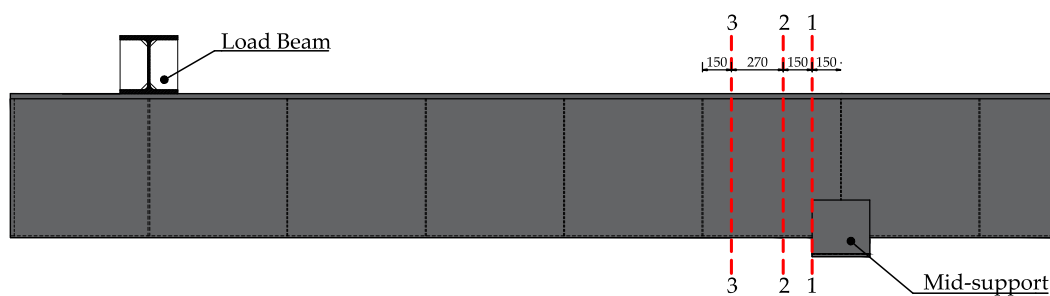


Fig. 6.16: Position of SGs close to the intermediate support

The position of all SGs in the cross-section is illustrated in Fig. 6.18. This scheme refers to the specimen S690. In the case of the specimen S460, the position of SGs is the same, however, without 4 SGs on the top flange in plane 1-1 (*i.e.* 4T and 5T). In this figure, the circular symbol refers to a single SG that measures strains only in the longitudinal direction. These individual SGs are placed only on the longitudinal stiffeners that may be considered as a linear element with the dominant strains only in the longitudinal direction. On the other hand, the rectangular symbol refers to 2 SGs placed orthogonally to each other, as shown in Fig. 6.17a. Namely, owing to the limited number of data logger channels (*i.e.* 6 x HBM MX1615 with 16 channels and 1 x HBM MX840 with 24 channels), instead of rosettes, which commonly measure strains in 3 directions (0° , 45° , and 90°), two ‘normal’ SGs are used at each point of interest. In Fig. 6.17a, it may be seen that one SG is placed to measure strains in the longitudinal direction (L) and the other one is placed in the perpendicular (or transversal) direction (T).

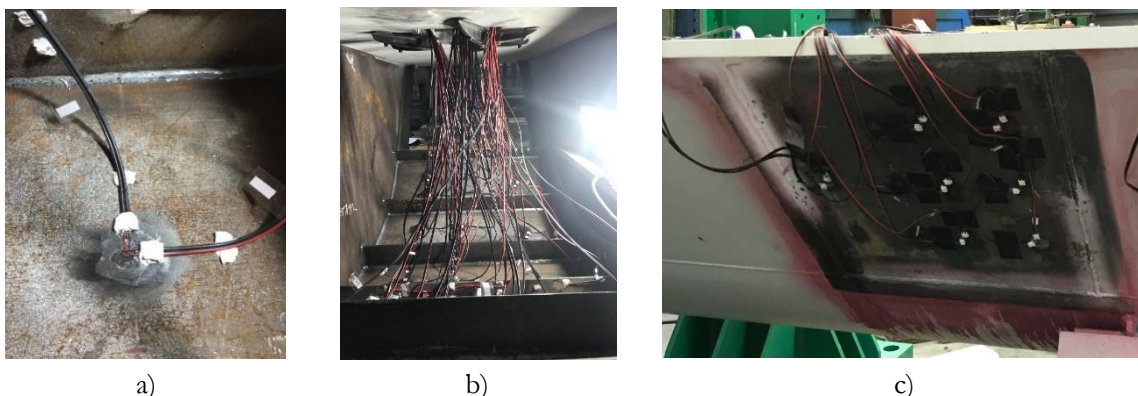






Fig. 6.17: a) Application of SGs (L and T); b) SGs on curved part (C and N); c) SGs on flat webs (F)

Designation	Position	Number of SG			Symbol
		1-1	2-2	3-3	
C	Curved bottom flange	16	16	8	 (2SG)
F	Flat webs	12	12	4	 (2SG)
T	Top flange	10	-	-	 (2SG)
N	Longitudinal stiffeners	10	10	5	 (1SG)

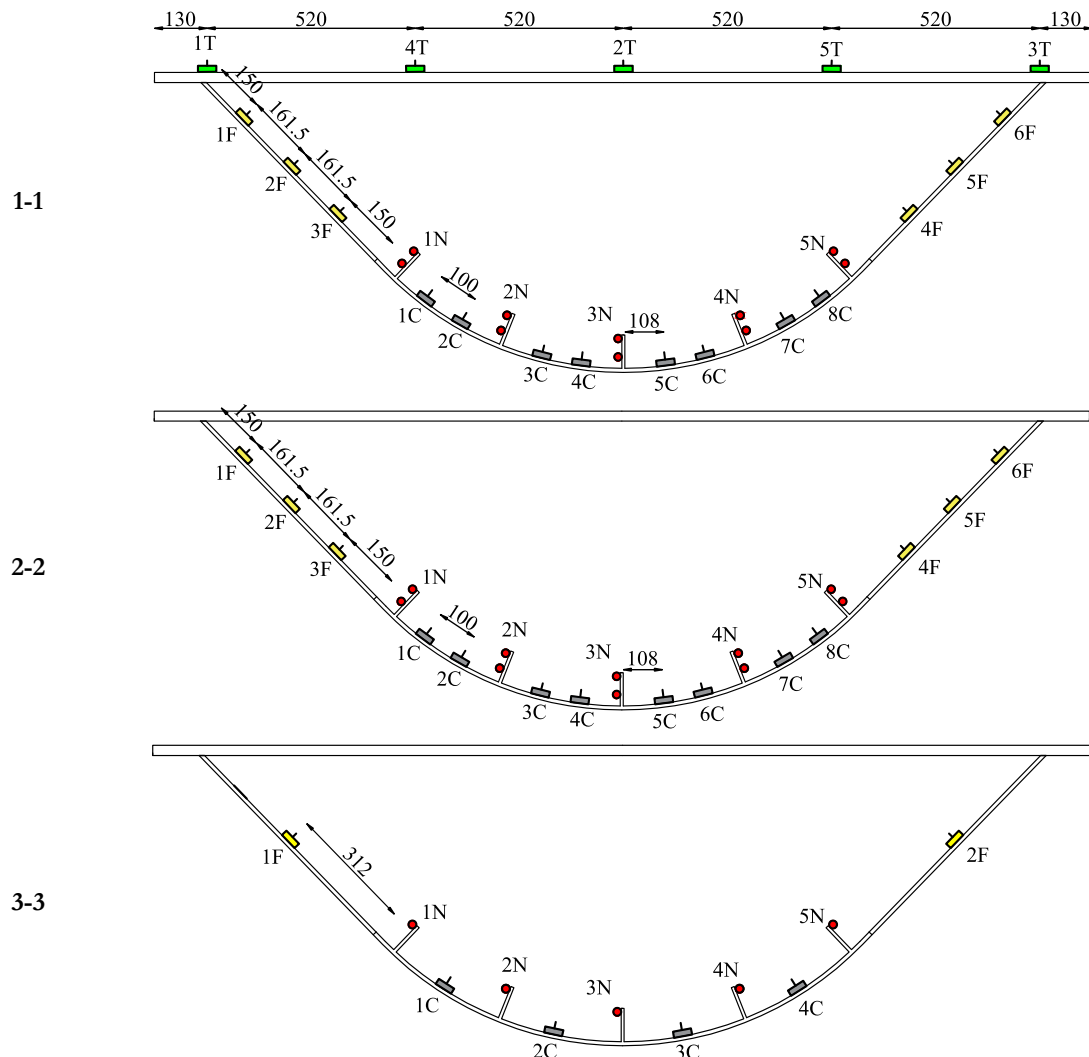


Fig. 6.18: Position of SGs in cross-sections 1-1, 2-2 and 3-3

As mentioned before, to allow the installation of SGs inside the box section, two ‘windows’ ($613 \times 613 \text{ mm}^2$) are cut off from the flat webs on both sides of the specimen, close to the intermediate support. All strain gauge cables that transmit the information to the data logger are led outside of the box through one of the holes ($200 \times 200 \text{ mm}^2$) that is deliberately left on the top flange for this reason (see Fig. 6.17b). After the instrumentation inside of the box is finished, the ‘windows’ are closed by full welds with metallic backing on three sides, and an ordinary fillet weld to the top plate. Subsequently, the SGs, which measured the strains on the flat webs (F), are attached to the outer surface of the windows, as shown in Fig. 6.17c.

6.4 Experimental results

6.4.1 Loading

As explained in [section 6.3.2](#), the load is recorded at 5 points of the test setup, presented in [Fig. 6.19](#). Besides the vertical load (F) applied on the specimen with the hydraulic jack, the reactions ($R1$, $R2$, $R3$, and $R4$) are recorded at the positions of the high strength bars, corresponding to the axial force induced in the bars.

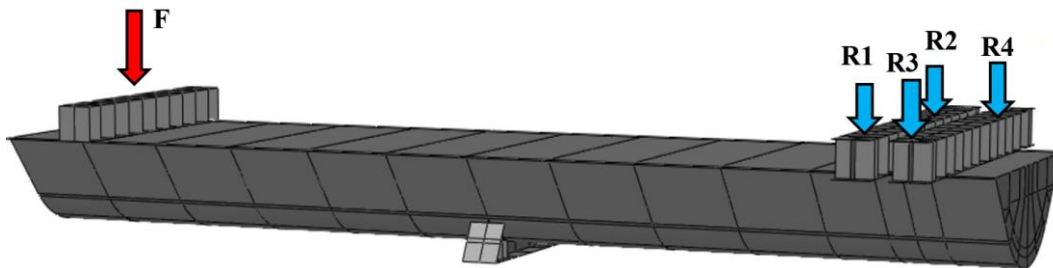


Fig. 6.19: Measurements of applied load (F) and reactions ($R1$ - $R4$)

The load application in two tests is stopped when the vertical displacement at the position of the load ($V-1$) reached the value of approximately 125 mm and 160 mm, respectively, which occurred in the descending branch of the force-displacement curves, presented in [Fig. 6.20](#).

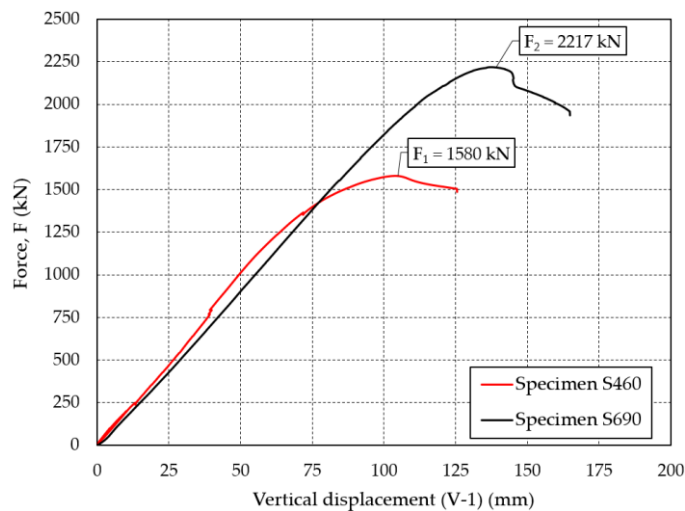


Fig. 6.20: Load (F)-displacement ($V-1$) curves

As it may be seen, the maximum load reached values of $F_1 = 1580$ kN and $F_2 = 2217$ kN, for specimen S460 and S690, respectively. Although the difference in the nominal value of the yield strength between the two steels is 50% (or in this case 70% when considering measured values of the yield strength from [Table 6.3](#)), the difference between the ultimate loads is approximately 40%. This means that in the case of the higher steel grade specimen (S690), which is more sensitive to the buckling phenomenon than specimen in S460, the local buckling occurred even before the yield strength is achieved, which caused a slight reduction of the ultimate load.

Regarding the data recorded by the four load cells at the position of the high strength bars, the load-displacement curves are presented in [Fig. 6.21](#). It may be noticed that in both tests, the

sum of these four reactions at the moment when the ultimate load is reached (*i.e.* $\Sigma R \approx 1400$ kN and $\Sigma R \approx 2060$ kN) corresponds to the applied load F , which confirms that the bridge specimens behaved statically in the desired way. The differences of $\Delta_1 = 13\%$ and $\Delta_2 = 7.5\%$ are due to the fact that the bars do not have the theoretically infinite rigidity and may be considered as springs with a certain axial rigidity. This means that a small portion of the force, responsible for the axial extension of the bars, is not measured by the load cells.

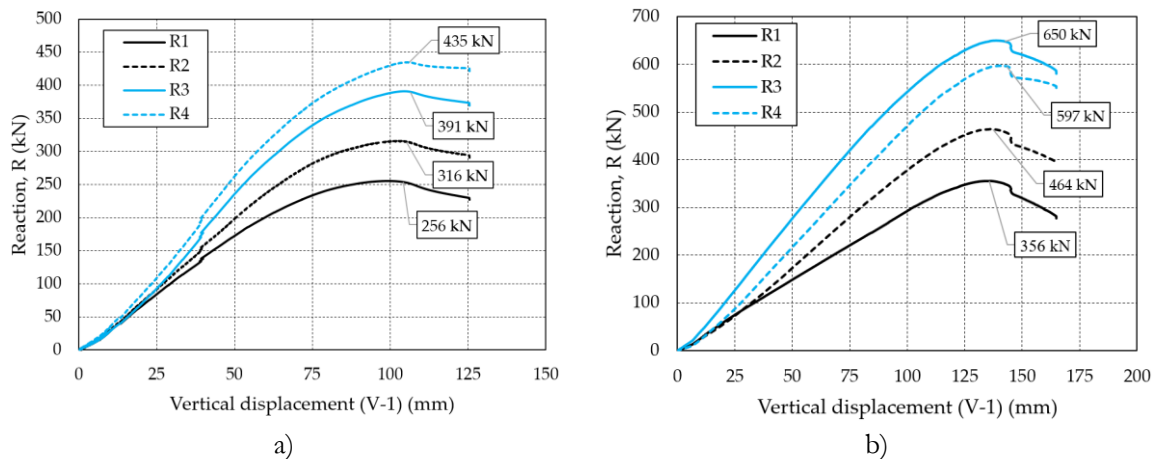


Fig. 6.21: Reactions at the end-support: a) specimen S460 and b) specimen S690

Finally, it should be emphasized that the reactions $R1$ and $R3$ are not equal respectively to reactions $R2$ and $R4$, which is in contrast to the expectations. However, the differences might be explained by the uneven pre-stressing forces that are introduced in the bars when they are anchored in the reaction beam. Moreover, the tested system is statically indeterminate, which means that not only the axial forces but also certain horizontal forces are introduced in the bars during the load application. Consequently, some of the bars are subject to bending rather than the pure axial extension, thus reducing the measured axial force.

6.4.2 Displacements

The displacements of the bridge prototypes are measured with LVDTs, as described in 6.3.2. For specimen S690, a comparison between the initial position of the prototype (before the test) and its position after the test is presented in Fig. 6.22. Using the surrounding frame as a reference, it may be noticed that the segment bent downwards at the end of the test.

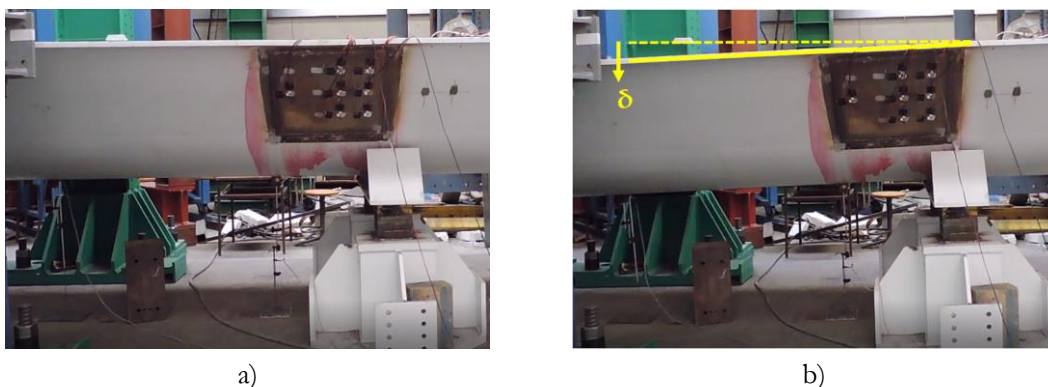


Fig. 6.22: Vertical displacement of the bridge: a) before and b) after the test

Based on the data recorded by LVDTs, the deformed shape of both specimens at the moment when the ultimate load is reached is schematically illustrated in Fig. 6.23.

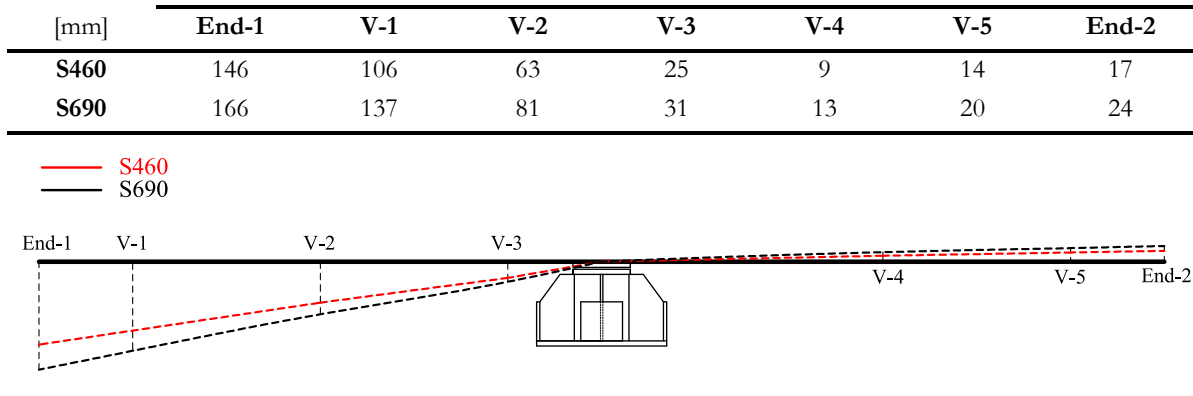


Fig. 6.23: Vertical displacements measured at the ultimate load in [mm]

Besides the vertical, the horizontal (in-plan) and the longitudinal displacements are also recorded (see L-1, L-2, and H-1 in Fig. 6.13) and their values at the ultimate load are summarized in Table 6.4.

Table 6.4: Longitudinal and horizontal displacements measured at the ultimate load

[mm]	L-1	L-2	H-1
S460	0.8	-0.7	1.6
S690	8.7	-8.4	6

It may be noticed that the horizontal displacements of the specimen S690 are considerably higher than those of the specimen S460; however, they are still negligible when compared to the vertical displacements presented before. Hence, in both cases, the desired behavior of the specimens is achieved.

6.4.3 Strains

The strains are measured at various points (see 6.3.2), mainly in the zone close to the intermediate support where the failure occurred. In Fig. 6.24 and Fig. 6.25, the development of strains with the force is presented at several relevant points of cross-section 1-1, for both specimens, whereas all the readings from all points are presented in Annex B (B.1). The notations L and T correspond to ‘longitudinal’ and ‘transversal’ (or ‘tangential’) directions (see Fig. 6.18).

From these graphs, it may be noticed that the strains in the longitudinal direction (ε_1) are significantly higher than those in the tangential direction (ε_2). Furthermore, it may be concluded that the strains in the curved part of the cross-section (C) exceeded the yield strain ($\varepsilon_u \approx 0.2\%$), indicating that bridge specimens underwent plastic deformations in the bottom part, whereas the flat webs (F) remained in the elastic domain. Finally, based on the signs of the strains ε_1 in the flat webs (*i.e.* 1F and 6F are positive, 2F, 3F, 4F and 5F are negative), it is clear that the elastic neutral axis crosses the flat webs somewhere between the strain gauges 1F and 2F. This is further discussed in 6.4.4, where the stress state in the cross-section is determined, using the measured strains.

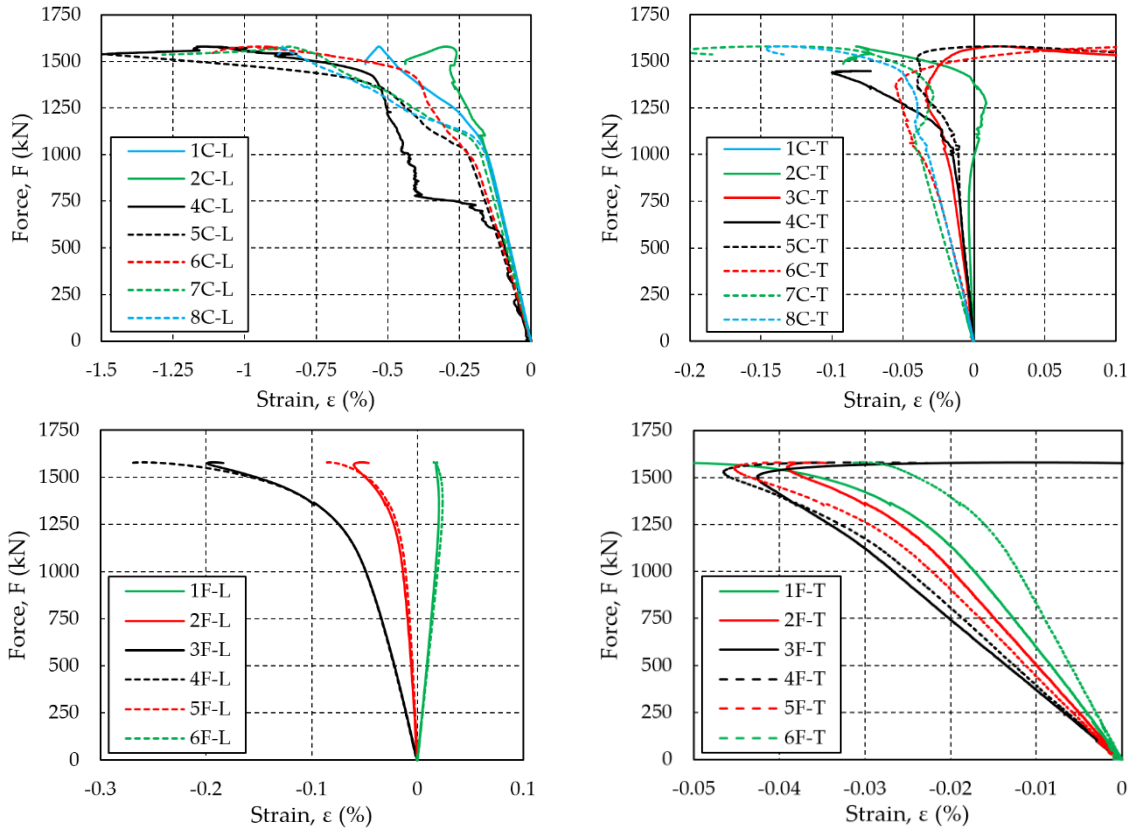


Fig. 6.24: Strains in curved (C) and flat (F) parts of cross-section 1-1 – S460

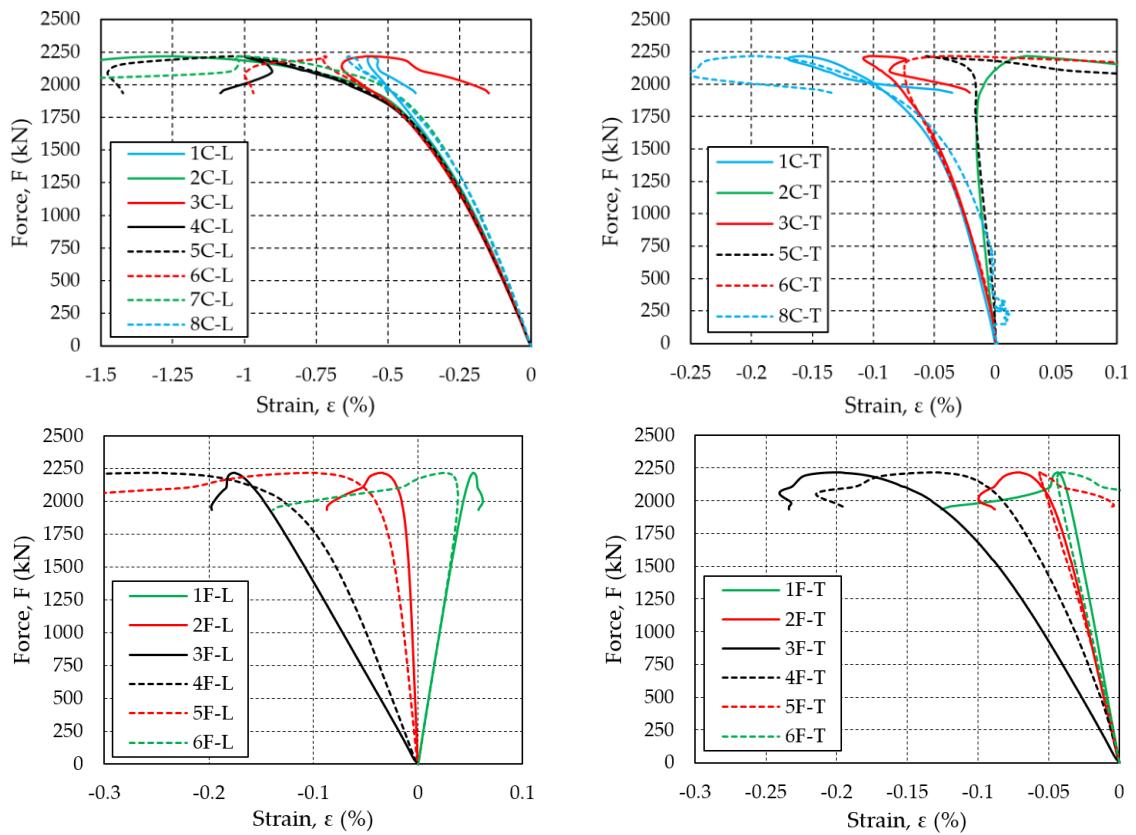


Fig. 6.25: Strains in curved (C) and flat (F) parts of cross-section 1-1 – S690

6.4.4 Stresses

6.4.4.1 General

If the bridge prototype is considered as a linear (1 - dimensional) element, having one dimension (length L) significantly larger than the other two (width b and height h), the axial stresses (σ_1) may be calculated using Hooke's law given by Eq.(6.1)

$$\sigma_1 = E\varepsilon_1 \quad (6.1)$$

On the other hand, if the panels and sub-panels of the prototype cross-sections are considered as planar (2 - dimensional) elements under a biaxial stress state, the axial in-plane stresses (σ_1 and σ_2) may be calculated using Kirchhoff - Love plate theory [154], applicable for thin isotropic plates, defined by Eq.(6.2) and Eq.(6.3) as

$$\sigma_1 = \frac{E}{1-\nu^2} [\varepsilon_1 + \nu\varepsilon_2] \quad (6.2)$$

$$\sigma_2 = E\varepsilon_2 + \nu\sigma_1 \quad (6.3)$$

where ε_2 is the strain measured in the tangential direction, *i.e.* perpendicular to the axial x -axis.

Using the strain values measured by the SGs and reported in 6.4.3, the values of axial stresses (σ_1) calculated by Hooke's law (Eq.(6.1)) and Kirchhoff - Love plate theory (Eq.(6.2)) are compared in the following paragraphs. Furthermore, these values are also compared with the axial stresses calculated by classical beam theory (LBT), obtained from Eq.(6.4)

$$\sigma_1 = \frac{M}{W_y} = \frac{Fl}{I_y} e_z \quad (6.4)$$

where W_y and I_y are section modulus and the second moment of area of the gross cross-section, F is the applied force, l is the distance between the point of load application and the considered cross-section, and e_z is the vertical coordinate of the considered point in the cross-section with respect to the elastic neutral axis.

The results of the comparison are shown in Fig. 6.26, where ' σ -Hooke', ' σ -Kirchhoff' and ' σ -LBT' correspond to the axial stresses (σ_1) calculated using Eq.(6.1), Eq.(6.2) and Eq.(6.4), respectively. In these graphs, the stress evolution is plotted against the force at point 2F/5F (see Fig. 6.18) in all three planes (1-1, 2-2 and 3-3) for both bridge specimens. Due to the symmetry of the box-girder cross-section, in the case of ' σ -Hooke' and ' σ -Kirchhoff', the stresses are obtained using the average value of the strains measured on the left side of the cross-section (*i.e.* 2F) and the corresponding ones on the right side (*i.e.* 5F).

The graphs indicate that the difference between the stresses calculated using linear (Hooke) and planar (Kirchhoff-Love) theory is noticeable only in plane 1-1 since it lays in the vicinity to the intermediate support, where a complex stress state exists with non-negligible tangential stresses. Another explanation for a larger difference between these two theories in plane 1-1 might be the imprecise readings from the SGs, *i.e.* their exact orientation and the angle between longitudinal (L) and tangential (T) strain gauge. On the other hand, in-plane 2-2, which is more

distant from the intermediate support, this difference slowly decreases, while in plane 3-3, there is practically no difference, which means that the bridge segment might be considered a linear (1 - dimensional) structure for the determination of the stress state.

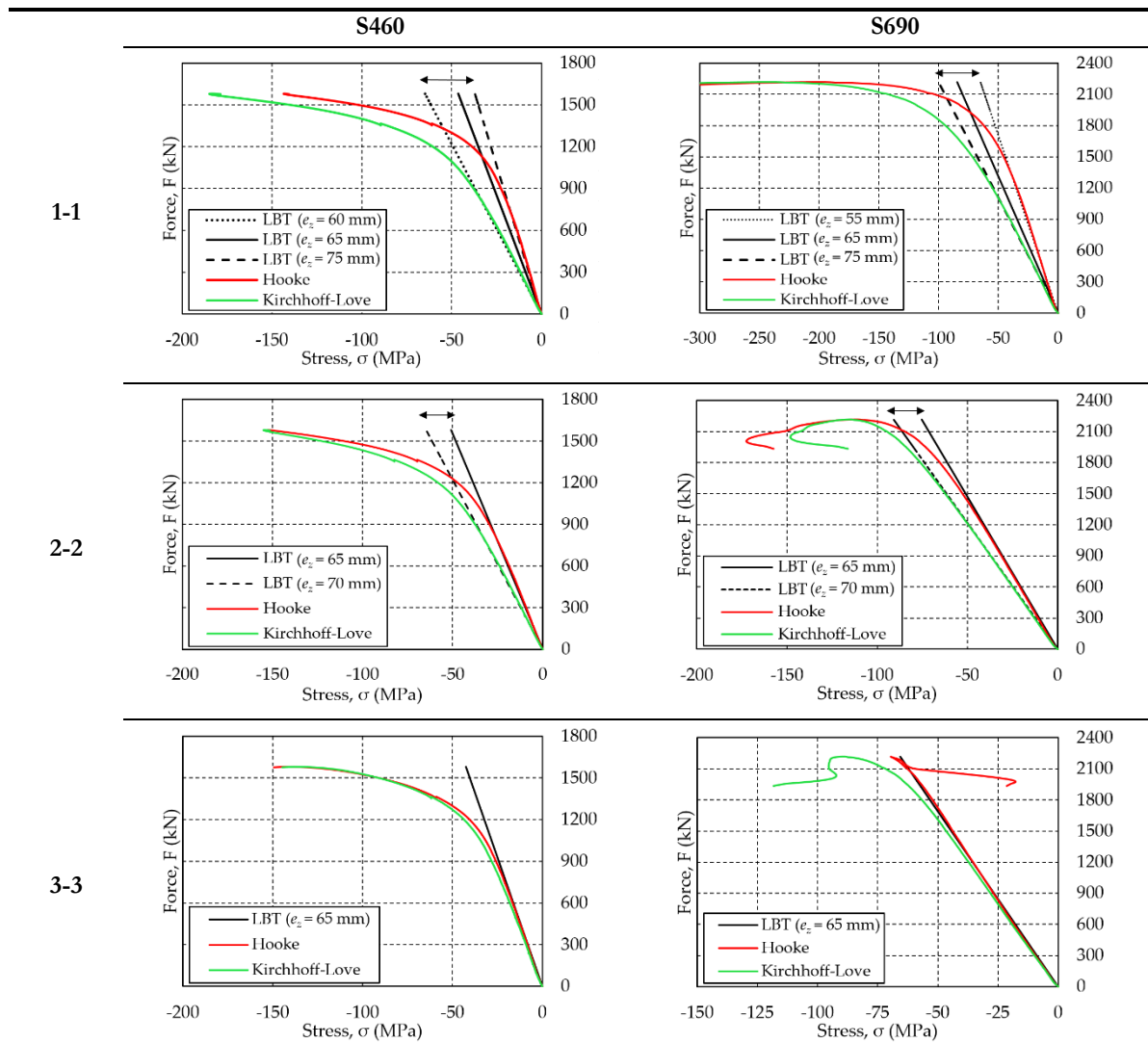


Fig. 6.26: Comparison of the experimental and analytical (LBT) results at point 2F/5F

Regarding the stresses defined by LBT (Eq.(6.4)), a good agreement with the experimental results reproduced by Eq.(6.1) (*i.e.* Hooke's theory) is achieved in planes 2-2 and 3-3, whereas a larger discrepancy is noticed in plane 1-1. These values are obtained assuming that the SGs lay exactly at $e_z = 65$ mm away from the neutral axis. However, in Fig. 6.26, it is shown that even a small variation of the SG position ($\Delta e_z = \pm 10$ mm) has a significant impact on these results.

Nevertheless, in all the points where the comparison is made, a good correspondence between the experimental and the analytical results is obtained ($\Delta < 10\%$), which gives confidence in the validity of the experimental measurements. Namely, the stresses obtained with plate theory (Kirchhoff-Love) are slightly higher than those calculated with the beam theory (LBT); however, for a quick estimation of the stresses in the cross-section of the bridge prototype, this difference may be considered negligible. Finally, the linear beam theory may be comfortably used for the

prediction of the stresses within the elastic range (*i.e.* until the extreme fiber starts to yield), whereas beyond that point, a non-linear theory must be considered.

6.4.4.2 Stresses in flat web and curved panel (F and C)

Using the strain measurements and the linear theory (Eq.(6.1)), the stress distribution along the height of the specimens is presented in Fig. 6.27 and Fig. 6.28 for various levels of the load, both for section 1-1 and 2-2. The values of the stresses are again adopted as the average of the ones on the left side of the cross-section (*e.g.* 1F, 2F, 1C, 2C etc.) and the corresponding ones on the right side (*e.g.* 6F, 5F, 8C, 7C etc.). For stresses that exceed the yield strength, for the sake of simplicity, it is assumed that the stress is equal to yield strength measured in 6.2.5.

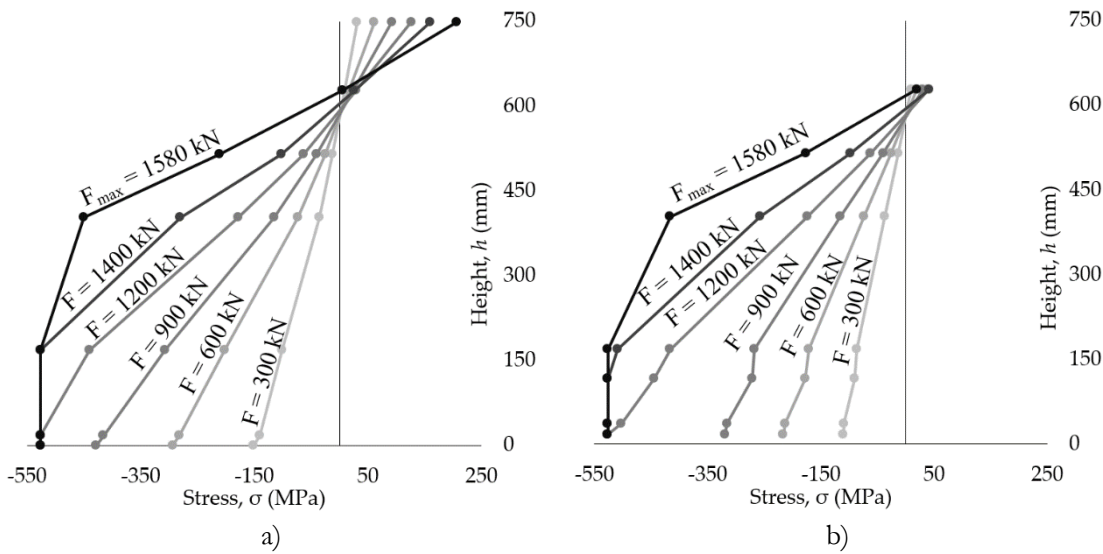


Fig. 6.27: Axial stresses in specimen S460 in cross-section: a) 1-1 and b) 2-2

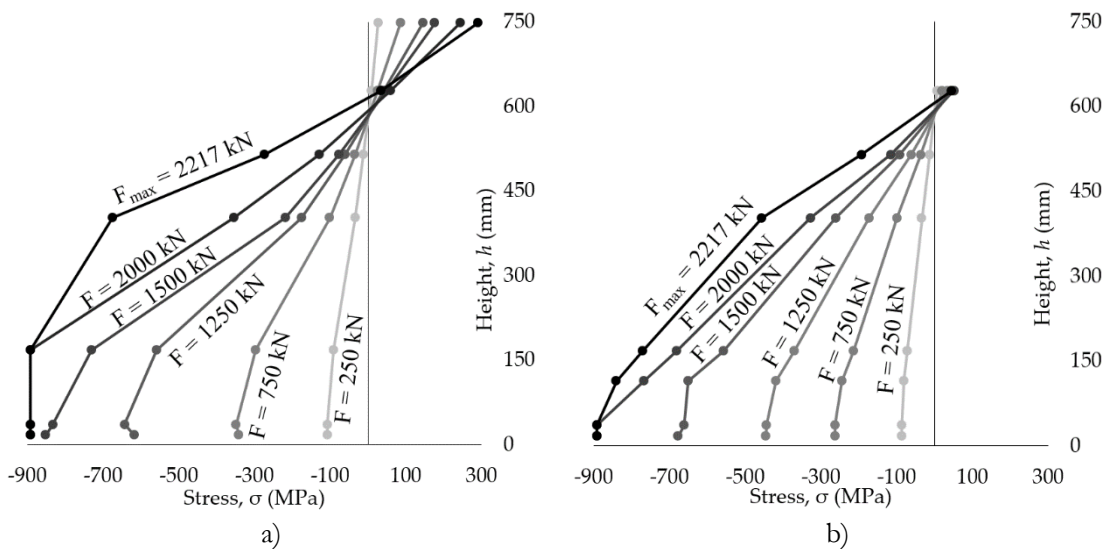


Fig. 6.28: Axial stresses in specimen S690 in cross-section: a) 1-1 and b) 2-2

In both cases, the linear stress distribution is observed for forces up to 60-70% of the maximum force, at which, the yield stress is reached at the bottom (compressed) fiber of the cross-section. Subsequently, with the additional increase of load, the yielding zone starts to spread

towards the neutral axis; however, due to local buckling, the cross-section fails before the full plastic moment is developed.

To verify this statement, the elastic bending moment M_{el} , at which the extreme fiber reaches yielding stress (see Fig. 6.29a), as well as the plastic bending moment M_{pl} (see Fig. 6.29b), are calculated for the gross cross-section, using the yield strength f_y obtained in 6.2.5. The calculated values are summarized in Table 6.5, whereas in Fig. 6.30, the development of the bending moment in the cross-section above the intermediate support, normalized to the plastic moment M_{pl} , is plotted against the rotation of the loaded cantilever of the bridge.

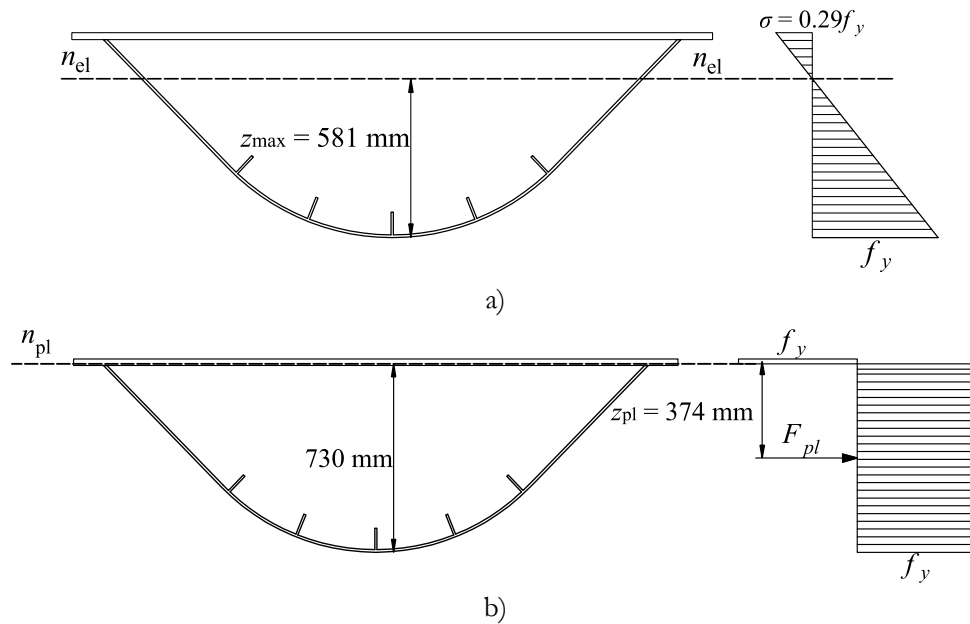


Fig. 6.29: a) Elastic bending moment M_{el} ; b) Plastic bending moment M_{pl}

Table 6.5: Elastic, plastic and measured bending moments

	M_{el} [kNm]	M_{pl} [kNm]	$M_{exp,max}$ [kNm]
Prototype S460	5103	8670	5686
Prototype S690	8654	14832	7981

The results indicate that in the case of the prototype S460, the cross-section has sufficient capacity to sustain additional load after the yielding of the extremely compressed fiber, but the plastic resistance cannot be reached. On the other hand, in the case of the prototype S690, the ultimate bending resistance (calculated with the real material properties) is reached slightly before the extreme fiber yields, which means that local buckling of the curved bottom flange occurred. It is important to emphasize that the analyzed cross-section is subject not only to bending moment but also to shear forces, thus, the value M_{exp} presented in Table 6.5, cannot be necessarily considered the bending resistance of the cross-section.

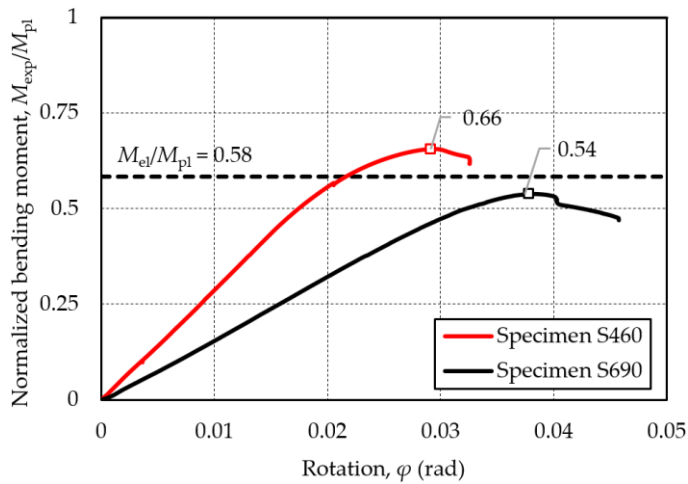


Fig. 6.30: Moment-rotation curves

Finally, based on Fig. 6.29, it may be observed that the elastic neutral axis passes through the flat webs (*i.e.* 581 mm from the bottom fiber), whereas the plastic neutral axis crosses the top flange of the section (*i.e.* 20 mm from the top fiber). However, after yielding is reached in the extreme fiber of the cross-section, the neutral axis starts to shift towards the plastic neutral axis, as shown in Fig. 6.31, where the stress distribution measured by the SGs is presented for several levels of load.

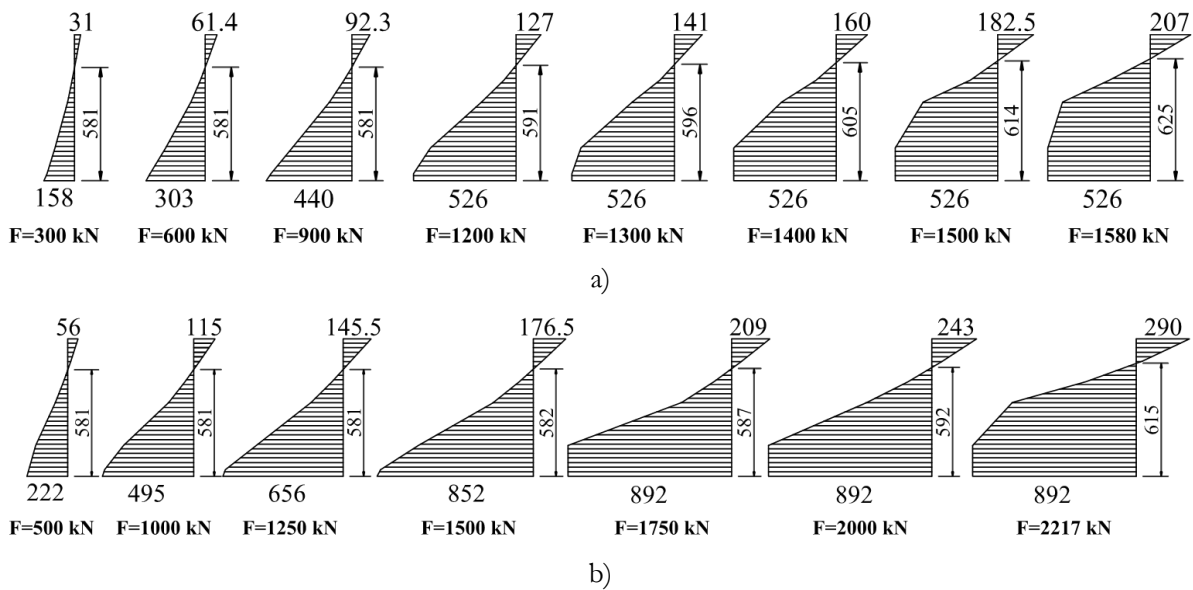


Fig. 6.31: Neutral axis shifting after yielding at section 1-1 for a) S460 and b) S690

According to these experimental results, it may be noticed that the position of the elastic neutral axis before the yield stress is reached is indeed 581 mm away from the bottom fiber, which coincides with the analytical value shown in Fig. 6.29a.

Based on the calculated plastic section modulus ($W_{pl} = M_{pl}/f_y$), which is equal to $16.63 \times 10^3 \text{ cm}^3$, and elastic section modulus ($W_{el} = I_y/\bar{z}_{\max}$) equal to $9.7 \times 10^3 \text{ cm}^3$, the shape factor f is calculated as $f = W_{pl}/W_{el} \approx 1.7$, which falls inside the usual range for box-girders (*i.e.* $f = 1.5 - 2.0$).

6.4.4.3 Stresses in the top flange (T)

Due to the shear strains, the longitudinal tensile bending stresses in wide top flanges reduce with the distance from the webs. Based on the results from the first experimental test, carried out with specimen in S460, it is noticed that this phenomenon called *shear lag effect* occurred, and thus, for the subsequent test in S690, additional SGs are placed along the top flange (*i.e.* 4T and 5T in Fig. 6.18) to obtain a more refined distribution of the tensile stresses.

In Fig. 6.32, the distribution of longitudinal tensile stresses is plotted across the width of the top flange for various values of the applied force F .

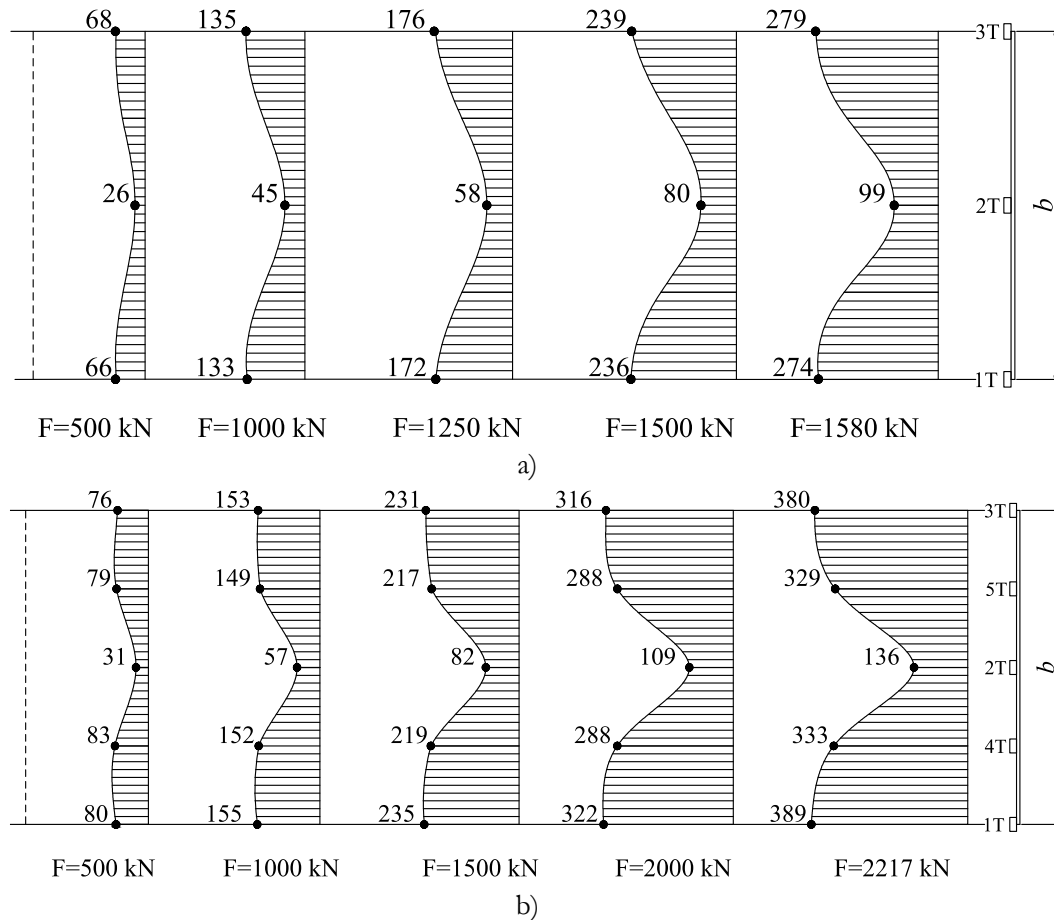


Fig. 6.32: Shear lag effect in the prototype: a) S460 and b) S690 – σ_1 [MPa]

Based on these figures, it may be observed that the stresses in the middle of the top flange are significantly lower (approximately 3 times) in comparison to the stresses in the edges of the flange. Furthermore, the shape of this distribution is not parabolic, as it is generally assumed. Therefore, since linear beam theory (LBT) does not recognize directly shear lag effect, to make axial stresses in the top flange comparable with the ones calculated by LBT, in Fig. 6.27a and Fig. 6.28a, as well as in Fig. 6.31, it is necessary to find an average value ($\sigma_{1,avg}$), using these measured values.

6.4.4.4 Stresses in longitudinal stiffeners (N)

Finally, the data from the SGs placed on the longitudinal stiffeners are also assessed for both tests. The position of SGs, as well as their notation, is shown in Fig. 6.33, where the index number refers to the number of stiffeners (1 to 5), whereas the letter indicates the position of the SG (*i.e.* T- ‘top’ and M- ‘middle’).

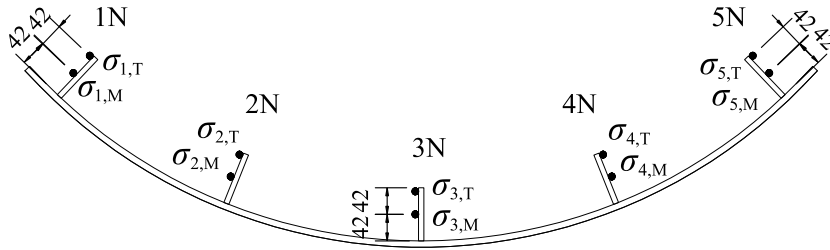


Fig. 6.33: Position and notation of SGs on the longitudinal stiffeners

Since the stiffeners are considered the linear elements, the axial stresses are determined using Hooke’s law, given by Eq.(6.1). The development of the axial compressive stresses for increasing values of the applied force F is presented for the cross-section 2-2 of prototype S690 since only in this cross-section no data losses occurred during the test in any of the strain gauges. Due to the symmetry of the cross-section, the results are presented only for three stiffeners (*i.e.* 1N, 2N, and 3N). The stresses presented in Fig. 6.34 correspond to the average of stresses obtained at two symmetrical stiffeners (*e.g.* 1N and 5N; 2N and 4N).

	F = 250 kN	F = 750 kN	F = 1500 kN	F = 1750 kN	F = 2000 kN	F = 2217 kN
1N	 20 $\sigma_{1,T}$ $\sigma_{1,M}$ 52	 80 $\sigma_{1,T}$ $\sigma_{1,M}$ 196	 115 $\sigma_{1,T}$ $\sigma_{1,M}$ 296	 133 $\sigma_{1,T}$ $\sigma_{1,M}$ 356	 154 $\sigma_{1,T}$ $\sigma_{1,M}$ 424	 213 $\sigma_{1,T}$ $\sigma_{1,M}$ 556
2N	 74 $\sigma_{2,T}$ $\sigma_{2,M}$ 76	 286 $\sigma_{2,T}$ $\sigma_{2,M}$ 300	 428 $\sigma_{2,T}$ $\sigma_{2,M}$ 460	 505 $\sigma_{2,T}$ $\sigma_{2,M}$ 548	 603 $\sigma_{2,T}$ $\sigma_{2,M}$ 648	 892 $\sigma_{2,T}$ $\sigma_{2,M}$ 892
3N	 79 $\sigma_{3,T}$ $\sigma_{3,M}$ 92	 317 $\sigma_{3,T}$ $\sigma_{3,M}$ 368	 502 $\sigma_{3,T}$ $\sigma_{3,M}$ 592	 608 $\sigma_{3,T}$ $\sigma_{3,M}$ 730	 740 $\sigma_{3,T}$ $\sigma_{3,M}$ 892	 892 $\sigma_{3,T}$ $\sigma_{3,M}$ 892

Fig. 6.34: Axial stresses in longitudinal stiffeners - prototype S690 (cross-section 2-2)

The figure shows that the stiffener in the middle (3N) reaches the yield stress when the applied load reached approximately 70-80% of the maximum load ($F \approx 1500 - 1750$ kN). The yielding of stiffeners 2N and 4N occurred only at the maximum values of load ($F \approx 2200$ kN), whereas in the edge stiffeners (1N and 5N), the stresses did not reach the yield strength f_y .

In the case of specimen S460, similar results are obtained, with the exceedance of the yield strength in the middle stiffener at around 70-80% of the maximum applied force ($F \approx 1200 - 1300$ kN), and in the stiffeners, 2N and 4N almost at the maximum applied load ($F \approx 1500$ kN).

6.4.5 Failure mode

Using the experimental results, the objective is to get an insight into the buckling behavior of the stiffened curved panels when subject to compression. Namely, in both tests, failure occurred at the curved bottom flange close to the intermediate support, as shown in Fig. 6.35.

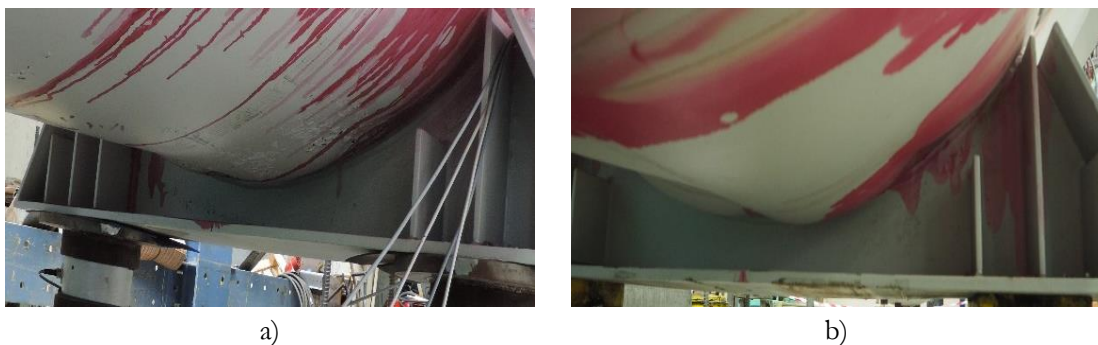


Fig. 6.35: Failure mode of the bottom curved panel: a) specimen S460; b) specimen S690

In addition, using cameras placed inside the box segment during the tests, it is possible to capture the buckling mode, which is presented in Fig. 6.36. In this figure, yellow arrows indicate the stiffeners movement direction after the buckling occurred, whereas the red arrows show the direction in which sub-panels moved.

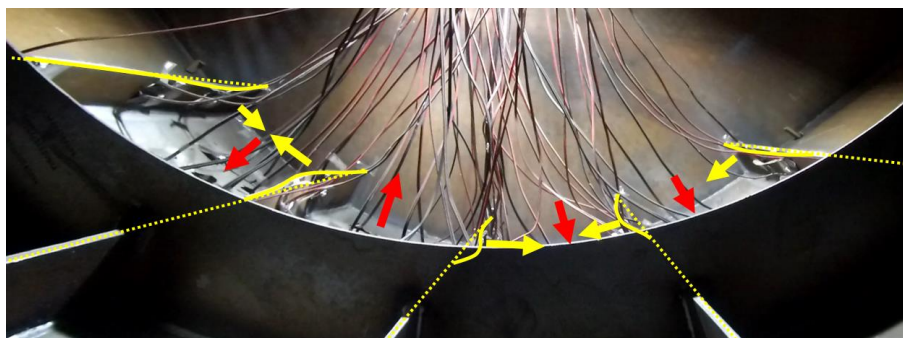


Fig. 6.36: Failure mode of the bottom curved panel inside the box-girder – specimen S460

Based on Fig. 6.36, the collapse mechanism is schematically presented in Fig. 6.37, from where it may be nicely seen that the longitudinal stiffeners and curved subpanels in-between both attained local buckling, whereas no global buckling (plate-like or column-like) of the entire stiffened curved panel is detected.

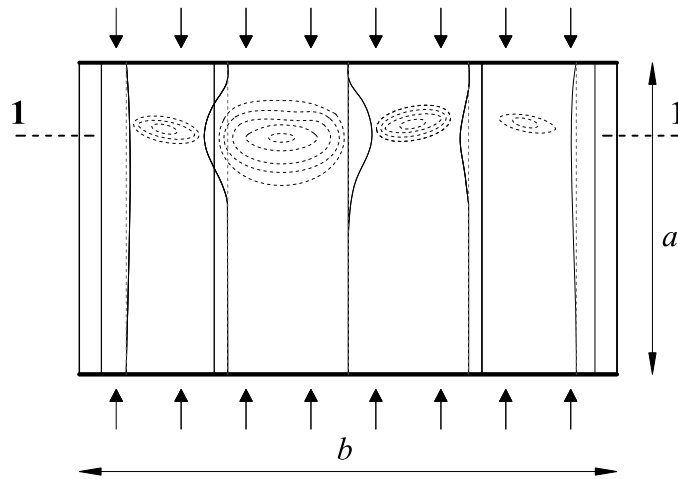


Fig. 6.37: Local buckling of the stiffened bottom curved panel

The figure shows that local buckling occurred in the vicinity of cross-section 1-1, approximately 150 mm away from the intermediate support, as anticipated in Fig. 6.16. The deformed shape of cross-section 1-1 is presented in Fig. 6.38 for four levels of applied force F , with the normalized stress distribution obtained from the SGs.

Based on these figures, it may be noticed that the yielding in the bottom flange started when the force reached approximately $0.7F_{\max}$, whereas the local buckling occurred at force close to the ultimate load. This means that the ultimate load is mainly driven by the yielding of the material, whereas the local buckling only slightly reduced the ultimate resistance of the curved stiffened bottom flange.

Almost identical collapse mechanism was obtained in the study by Piculin & Može [85], in which isolated curved stiffened panels, tested under uniform axial compression, are also derived from the bridge case study defined in 6.2.2, however, downscaled 5 times.

Moreover, in the subsequent numerical study carried out by Piculin & Može [60], the authors concluded that in the case of highly curved stiffened panels, global buckling has almost no effect on the ultimate resistance due to a high cross-section inertia, which coincides with the findings reported by Tran ([8], [59]). Thus, it may be stated that failure of highly curved panels, with the geometry encountered in bridge applications, is governed mainly by local buckling, which is confirmed by the test results from both experimental campaigns reported in this thesis (*i.e.* in chapter 3 and in this chapter), but also by the experimental results from Piculin & Može [85].

This further means that the resistance at high curvatures is not affected by the aspect ratio α of the panel since the local buckling of subpanels is independent of the panel length a . Consequently, in the case of highly curved panels, it is possible to reduce the number of cross-frames, which may significantly reduce the fabrication costs and the environmental impact, by reducing the material consumption, the amount of welding and the amount of work. Nevertheless, this assumption is to be checked and discussed in more detail in chapter 7 and 8, where the numerical study is carried out, extending the limited set of geometric parameters covered in the presented experimental study.

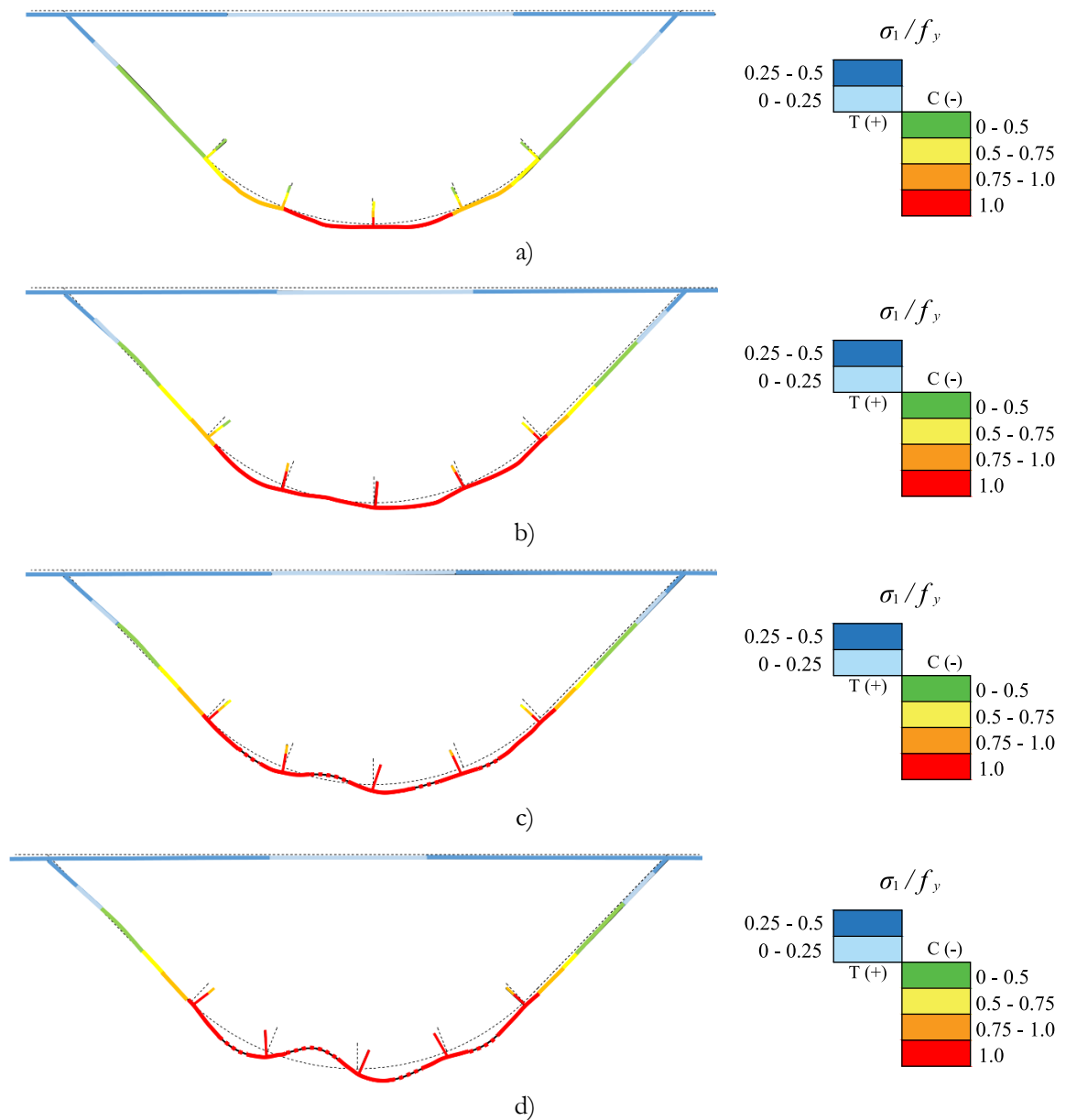


Fig. 6.38: Deformed shape of prototype S460 (cross-section 1-1) for: a) $F = 0.7F_{\max}$; b) $F = 0.9F_{\max}$; c) $F = 0.95F_{\max}$; and d) $F = F_{\max}$

6.4.6 Comparison between test results and verification procedures

Since there are still no design rules to assess the buckling behavior, as well as the bending (M_{Rd}) and shear resistance (V_{Rd}) of a box-girder cross-section with a stiffened curved bottom flange, the experimental results are verified using two different design approaches:

- i) Equivalent flat panel approach
- ii) Curved panel approach

6.4.6.1 Equivalent flat panel approach – Method 1

This approach corresponds to the design rules for trapezoidal box-girder bridge cross-section from EN 1993-1-5 [11], described in detail in 2.5.3; however, assuming an equivalent flat stiffened panel in the bottom flange instead of a curved panel, as indicated in Fig. 6.39.

As it may be noticed, the bottom flange is assumed to be the entire curved part of the cross-section, with the width $b = 1400$ mm, whereas the web is considered a 612 mm wide flat plate that connects the bottom and the top flange.

Following the steps defined in 2.5.3, to determine the bending resistance M_{Rd} , it is necessary to calculate the effective section modulus $W_{d,eff}$, which consists of the gross area of the top flange (in tension) and the effective area of the bottom flange and webs.

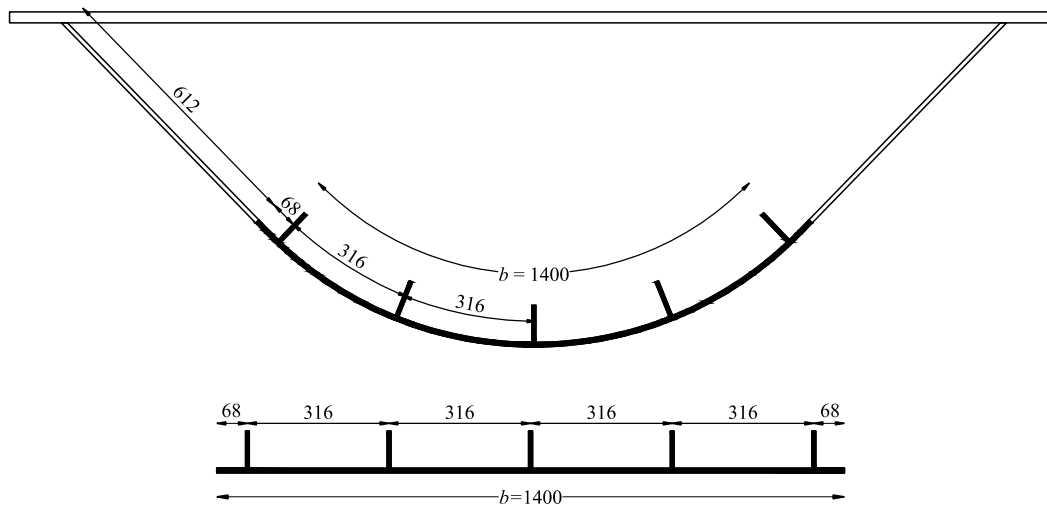


Fig. 6.39: Equivalent flat panel approach

6.4.6.2 Curved panel approach – Method 2

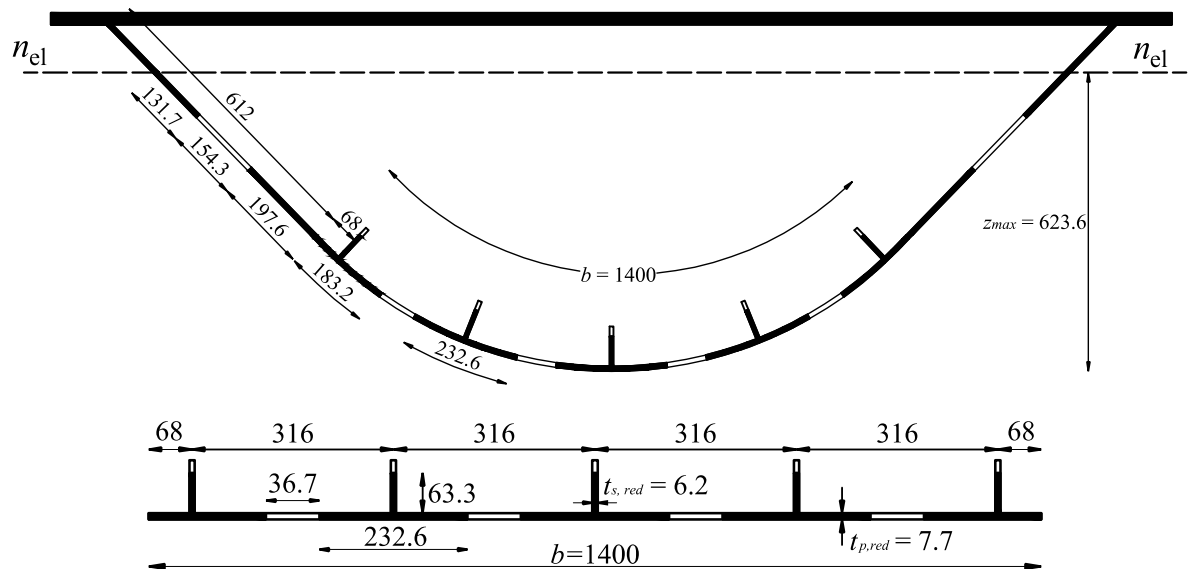
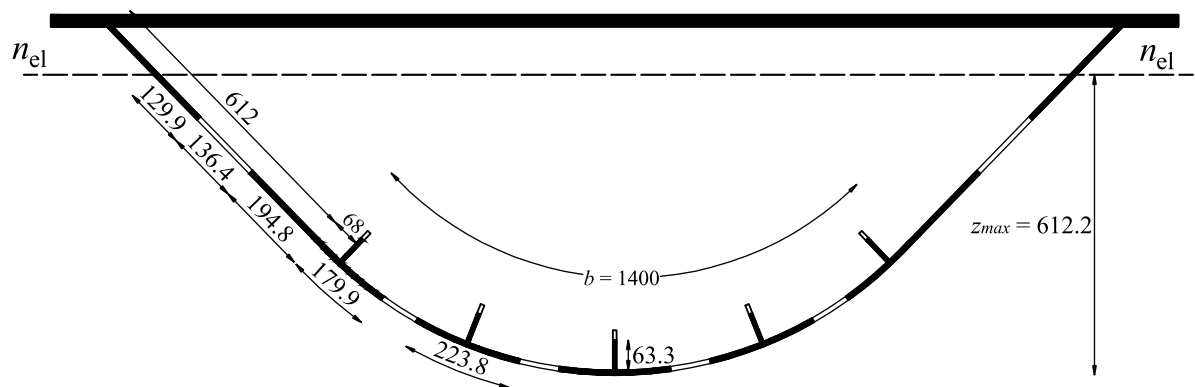
This approach is fundamentally equivalent to the previous one; however, the effect of curvature is explicitly accounted for. Namely, a simplification is adopted, according to which the entire curved panel (see Fig. 6.39) is assumed to be the bottom flange, subjected to uniform axial compression ($\psi = 1.0$). Consequently, such assumption allows the use of the same design methodology from EN 1993-1-5 [11], where instead of the procedure for flat stiffened panel, the methodology developed within the OUTBURST research project [85] could be applied since it was proven in chapter 3 the most adequate for the curved panels with $Z > 100$. All the steps for the determination of the local and global buckling of curved stiffened panels using this methodology are described in detail in 2.5.1.

6.4.6.3 Comparison of results

The effective cross-sections, obtained using these two methodologies, are presented in Fig. 6.40 and Fig. 6.41 for steel S690, whereas the corresponding bending resistances are summarized and compared in Table 6.6 for both steel grades.

Table 6.6: Comparison of bending moment capacity

	Test	Equivalent plate method		Curved panel method	
	M_{exp} [kNm]	$M_{eff,1}$ [kNm]	$M_{eff,1}/M_{exp}$	$M_{eff,2}$ [kNm]	$M_{eff,2}/M_{exp}$
Specimen S460	5686	3931	0.69	4430	0.78
Specimen S690	7981	5365	0.67	6529	0.82

**Fig. 6.40:** Effective cross-section of specimen S690 according to equivalent panel approach**Fig. 6.41:** Effective cross-section of specimen S690 according to curved panel approach

As may be seen from the results in the table, both methods give bending resistance lower than the one obtained in the experimental tests, and the ratio between M_{eff}/M_{exp} does not seem to vary significantly with the steel grade. However, the method in which the curved panel is explicitly considered (Method 2) gives results much more realistic and closer to the experimental ones, when compared to the first simplified method. It should be noted that Method 2 is also a simplified method since the whole curved panel is assumed to be under most unfavourable uniform compression, which to some extent justifies slightly conservative results when applying this method ($M_{eff}/M_{exp} \approx 0.8$).

Since the main difference between the two methods lays in the determination of the local and global buckling of the bottom curved panel, all the relevant effective width factors are compared in [Table 6.7](#).

Table 6.7: Comparison of two design approaches – bottom flange effective width factors

Specimen	Method	$\sigma_{cr,loc}$ [MPa]	ρ_{loc}	$\sigma_{cr,p}$ [MPa]	ρ	$\sigma_{cr,c}$ [MPa]	χ_c	ρ_c
S460	1	760	0.884	1824	1.0	1666	0.78	0.82
	2	1110	0.824	Z > 100 ($\rho = 1.0$)		30746	1.0	1.0
S690	1	760	0.735	1824	1.0	1666	0.72	0.77
	2	1110	0.708	Z > 100 ($\rho = 1.0$)		30746	1.0	1.0

Based on the results of this comparative study, several important conclusions should be highlighted:

- 1) The flat panel approach (Method 1) gives smaller reduction (*i.e.* higher local reduction factor ρ_{loc}) than a curved sub-panel since small local curvature have a less favorable post-buckling response, being more sensitive to local imperfections ([8],[9],[10])
- 2) On the other hand, due to a significantly higher second moment of area, the plate-type and column-type buckling stresses are much higher in the case of the curved panel than the equivalent buckling stresses of a stiffened flat plate, thus, no global buckling occurs ($\rho_c = 1.0$).
- 3) Hence, it may be concluded that the collapse of the highly curved stiffened curved panels, such as those used in the experimental test, is governed by the local buckling of sub-panels.

Nevertheless, the conclusions are made based on the data obtained from the experiments and are therefore limited to specimens similar to those used in this study. To verify the validity of the proposed procedure for an arbitrary stiffened curved panel, an extensive parametric study is carried out in [chapter 7](#).

Finally, regarding the shear resistance of the cross-section, due to the lack of design rules for this type of box-girder cross-section, the comparison is made between the experimental results and the procedure given by EN 1993-1-5 [11] for flat webs, as described in [2.5.2](#). The main results are presented in [Table 6.8](#).

Table 6.8: Comparison of shear force capacity

	Test		EN 1993-1-5	
	F_{exp} [kN]	$V_{bw,exp}$ [kN]	V_{bw} [kN]	$V_{bw,exp}/V_{bw}$
Specimen S460	1580	1098	1808	0.61
Specimen S690	2217	1541	2384	0.65

The table indicates that only around 60-65% of the shear capacity of the flat webs is exhausted in the experimental tests, which confirms that failure of two specimens is due to insufficient bending capacity, *i.e.* buckling of the bottom curved flange.

However, it is one of the main objectives of this PhD thesis to discover what part of the cross-section with the curved bottom flange actively contributes to the shear resistance, besides the flat webs. This particular problem is tackled in [chapter 8](#), where an extensive numerical study is carried out and the whole spectrum of the M - V interaction behavior (*i.e.* from pure bending to ‘almost’ pure shear) is characterized.

6.5 Summary

In this chapter, two identical prototype box-girder bridge segments, in scale 1:3 with respect to a real study case, with two different steel grades (S460 and S690) were experimentally tested. Segments were tested as three-point bending tests, with the aim to assess the complex behavior of a box girder bridge deck near the intermediate support, where the moment-shear (M - V) interaction occurs. This chapter gave a detailed description of the most relevant data, such as load measurements, displacements, strains, stresses, failure modes, etc. The main observations from the tests were:

- In both prototypes, failure occurs in the bottom (curved) flange, where both the longitudinal stiffeners and the curved panel in-between buckled close to the intermediate support;
- The collapse mechanism is governed by the local buckling of the longitudinal stiffeners and curved subpanels in-between, whereas no global buckling (plate-like or column-like) of the entire stiffened curved occurred;
- Consequently, the resistance of the highly curved stiffened panels is not affected by the aspect ratio of the panel since the local buckling of subpanels is independent of the panel length. This might be one of the substantial advantages of this type of bridge cross-section since considerable saving could be made by reduction of the transversal cross-frames and diaphragms;

Finally, the experimental results were compared with two proposed design methods: *i*) equivalent flat-panel approach and *ii*) curved panel approach and it was concluded that the latter, which was developed within the OUTBURST research project, gave a more realistic approximation of the test results.

However, the validity of this design method needs to be verified for a wider spectrum of the geometrical parameters, with the dimensions that may be encountered in real bridge applications. This is done in [chapter 7](#), where a parametric study is carried out, using a numerical FEM model calibrated against the experimental results reported in this chapter.

7. Numerical study on box-girder bridge cross-section integrating curved panels

7.1 Overview

The objective of this chapter is to analyze the $M - V$ interaction behavior of a box-girder bridge deck, with a cross-section that integrates a curved bottom flange, and thus, to accomplish Task 4.2 of the thesis, defined in [section 1.2](#). More specifically, the goal is to characterize the entire spectrum of behavior, *i.e.* from pure bending to ‘almost’ pure shear, and to assess the validity of the bending and shear resistance models, as well as the $M - V$ interaction equation, available in the literature. Therefore, a comprehensive numerical study is carried out using ABAQUS software, in which multiple geometrical parameters are varied within the common ranges found in bridge applications.

Firstly, in [section 7.2](#), a reliable FE model is built and verified against the experimental results reported in [chapter 6](#). In [section 7.3](#), some changes adopted in the numerical model prior to the parametric study are presented, and the scope of the study (*i.e.* ranges of geometrical and material parameters) is specified. Finally, in [section 7.4](#), the most relevant results of the numerical investigation are demonstrated and discussed.

The collected results from this parametric study serve as a solid benchmark in the subsequent [chapter 8](#), where the assessment of the available design resistance models is carried out and new (modified) design rules are proposed.

7.2 Calibration of the FEM numerical model

7.2.1 Section overview

This section deals with the development of the FEM numerical model and its validation against the experimental results, presented in [chapter 6](#).

The numerical model, which is set up by using the FEM software ABAQUS [142], is determined by the following input parameters: geometry, material model, boundary conditions, loads, element type, mesh size, and initial imperfections. A detailed definition of all these parameters is provided in the subsequent sections.

7.2.2 Definition of the model used for the calibration

7.2.2.1 Type of analysis

For each numerical model in this study, two types of analyses are performed: *i*) Linear elastic bifurcation analysis (LBA) and *ii*) Geometrically and materially nonlinear analysis with imperfections included (GMNIA), in the same way, it was done in previous numerical studies from this thesis (see in [3.4.2](#) and [5.2.2](#)).

Namely, the LBA is performed first to extract the eigenmodes, which are subsequently used as the shapes of the initial geometric imperfections in a GMNIA. In all simulations, the ultimate resistance is considered as the maximum load factor on the load-deformation curve, obtained by the arc-length Riks' method [143], which is particularly suitable for numerical problems where non-linear static equilibrium solutions are sought with descending load level and/or the displacement along the loading path.

7.2.2.2 Geometry

The geometry of the numerical models corresponds to the geometry of test specimens, defined in [6.2.3](#). The mathematical model consists of a bridge deck specimen, one loading beam, and two supporting beams, as shown in [Fig. 6.19](#). Each specimen contains 9 open cross frames (see [Fig. 6.6](#)) and 6 closed diaphragms, located at the two ends of the bridge segment, below the loading beam, at the intermediate support, and below each of two supporting beams.

7.2.2.3 Applied material model

The material behavior of two steel grades, assigned to the bridge deck segments in the numerical simulations are presented in [Fig. 7.1](#). Namely, the structural steel is modeled as an elastic-plastic material, defined by true stress-strain relation, obtained from engineering stress-strain relations determined by tensile coupon tests in [6.2.5](#).

As it may be noticed in two figures, the measured engineering stress-strain diagrams (grey curves), are first simplified and approximated by a polygonal (blue) curve and then transformed in the form of true (Cauchy) stress and logarithmic strains (red curve) using [Eq.\(7.1\)](#) and [Eq.\(7.2\)](#)

$$\sigma_{\text{true}} = \sigma_{\text{eng}} (1 + \varepsilon_{\text{eng}}) \quad (7.1)$$

$$\varepsilon_{\text{true}} = \ln(1 + \varepsilon_{\text{eng}}) \quad (7.2)$$

Since the tensile coupon tests are not carried out for the 25 mm thick top flange, the material is modeled as elastic-plastic, with linear strain hardening, disregarding the yield plateau. The plastic properties (*i.e.* yield strength f_y and ultimate strength f_u) are adopted based on the material specification provided by the project partner MCE GmbH [18], who produced the bridge deck specimens (see Table 7.1). It is needless to say that the axial stresses in the top flange, at the instant when the ultimate force is reached, remained in the elastic range in both tests (see Fig. 6.32). Hence, the only relevant parameter for the characterization of the material behavior for the top flange is the Young's modulus.

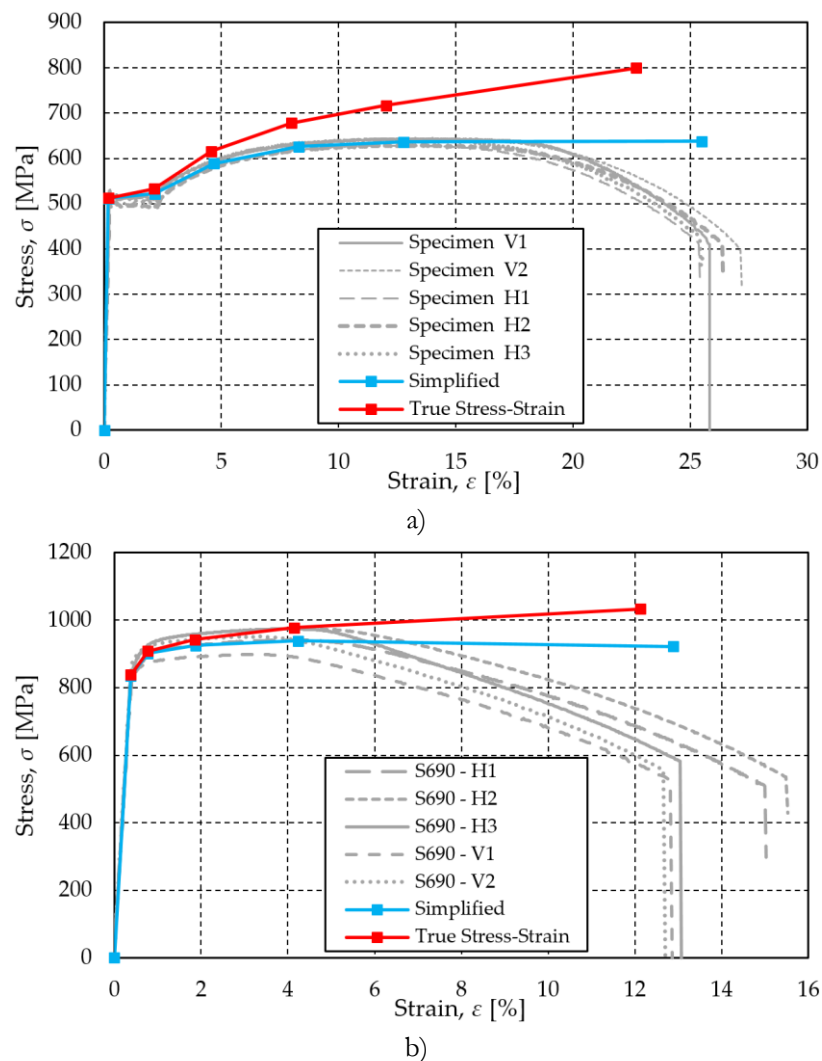


Fig. 7.1: Stress-strain relations applied in FEM: a) S460 and b) S690

Table 7.1: Mechanical properties of steels in the top flange (by MCE GmbH [18])

Steel	E [GPa]	f_y [MPa]	f_u [MPa]	f_u/f_y	A_t [%]
S460	209.5	460	628	1.36	23.5
S690	209.4	828	940	1.13	15

Finally, for all the other auxiliary elements made of steel S355 (loading and supporting beams, see Fig. 6.19), the same bi-linear elastoplastic material model used in chapter 5 is adopted, with a hardening module equal to $E/100$ (following the recommendations of Annex C of EN 1993-1-5:2006), as indicated in Fig. 5.2.

7.2.2.4 Loading and support conditions

The load and boundary conditions are modeled in such a way to simulate as closely as possible the real conditions provided in the two experimental tests, as schematically illustrated in Fig. 7.2.

Regarding the boundary conditions, all three translational DOF (*i.e.* in X, Y, and Z-direction) are prevented at the intermediate support, as indicated in the figure. On the opposite side of the load, 4 high strength pre-stressing bars are modeled as springs, with the axial stiffness, k , calculated by Eq.(7.3) as

$$k_i = \frac{R_i}{\delta_i}, \quad (i = 1, 2, 3, 4) \quad (7.3)$$

where R_i is the axial force measured in the cables using load cells and δ_i is the measured displacement of the bridge deck segment measured at the position of the bars (see section 6.4). In ABAQUS, spring is an *engineering feature* defined by a pair of reference points, whereas the distance between these two points is not pertinent since the spring stiffness is explicitly defined in the software.

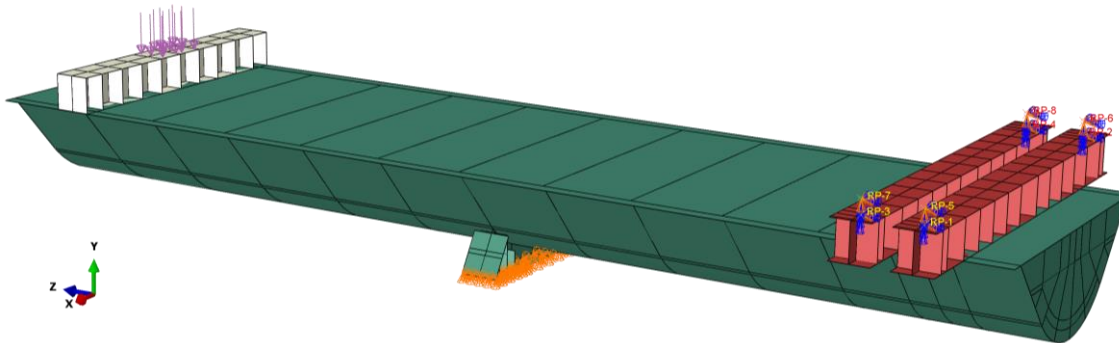


Fig. 7.2: Applied loading and support condition

According to Fig. 6.19 and Fig. 7.2, spring 1 is defined by RP-3 and RP-7, spring 2 is defined by RP-4 and RP-8, etc. Table 7.2 and Table 7.3 summarize the spring stiffnesses adopted in the FEM models, for the two specimens, separately.

Table 7.2: Stiffness of the springs adopted in the FEM model – specimen S460

Spring	Force, R_i (kN)	Displacement, δ_i (mm)	Stiffness, k_i (kN/mm)
1	256	14	18.3
2	316	14	22.6
3	391	15	26.1
4	435	15	29.0

Table 7.3: Stiffness of the springs adopted in the FEM model – specimen S690

Spring	Force, R_i (kN)	Displacement, δ_i (mm)	Stiffness, k_i (kN/mm)
1	356	19.5	18.3
2	464	19.5	23.8
3	650	21	30.2
4	597	21	28.4

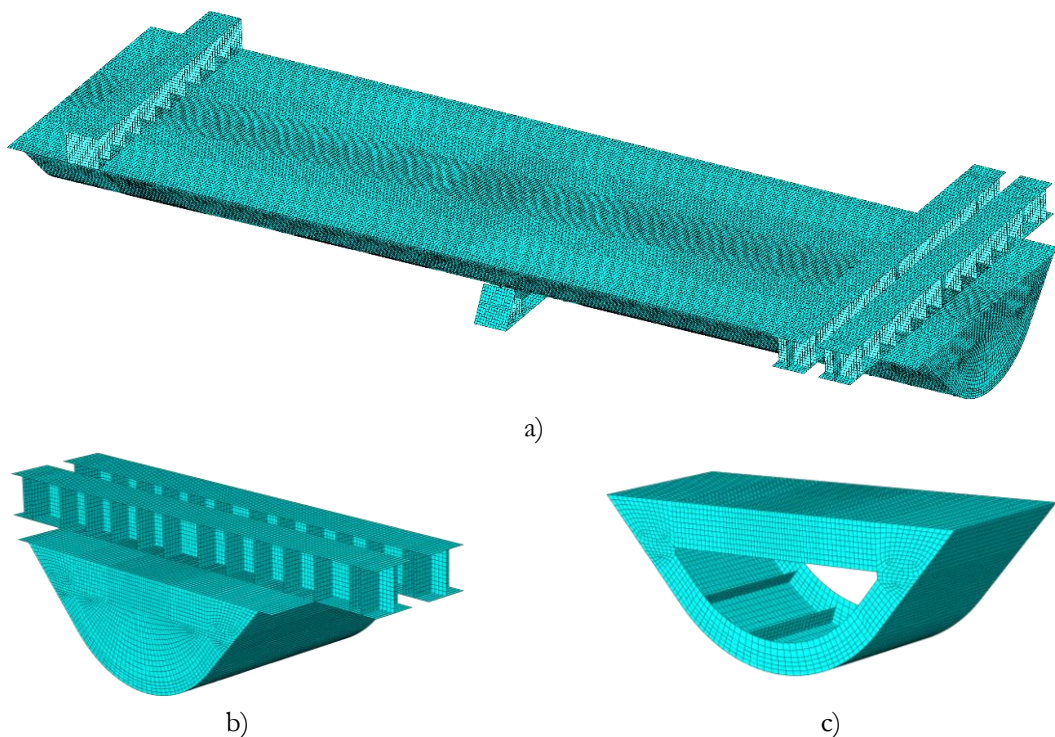
Regarding the loads, to avoid numerical singularities, instead of a concentrated force F , the uniformly distributed load is applied on a 'small area', as shown in Fig. 7.2, simulating the contact area between the loading beam and the head of the hydraulic jack. Additionally, the self-weight of the specimen is introduced in the model, assuming the standard steel density of $\rho = 7850 \text{ kg/m}^3$.

Finally, in the numerical model, *tie constraint* is used to simulate the contact between the loading (and supporting beams) and the top flange of the bridge deck.

7.2.2.5 Type and size of the FE mesh

For the model discretization, four-node shell elements with the reduced integration (S4R) are used, with a mesh size of approximately $150 \times 150 \text{ mm}^2$, comprising in total around 200 000 FE, as shown in Fig. 7.3.

Although the mesh configuration is slightly too refined, for calibration purpose, it is not necessarily intended to reduce the number of finite elements since considerably powerful computing machines are used. However, for the forthcoming parametric study, where an increased number of the numerical simulations is carried out, a convergence study is conducted to optimize the number of FE, while keeping the accuracy of the results.



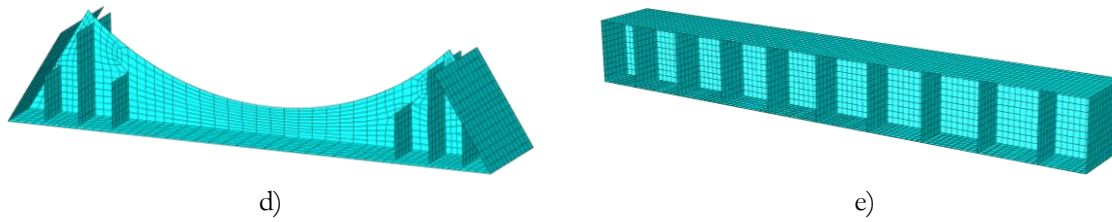


Fig. 7.3: a) FE mesh configuration used for the model calibration; b) supporting beams; c) segment between two cross-frames; d) supporting foot; e) loading beam

7.2.2.6 Initial imperfections

Owing to the lack of information on the exact shape of the initial imperfections, the recommendations for design by FEM from Annex C.5 of EN 1993-1-5 are followed. Hence, equivalent geometric imperfections are assumed, accounting for both geometric and structural imperfections (*i.e.* residual stresses). As already explained in [section 3.4](#), the initial geometric imperfections in ABAQUS are commonly introduced by a perturbation of translational degrees of freedom for each node in the finite element model. The coordinate perturbation may be defined by a linear superposition of the buckling modes (eigenmodes) of the panel, obtained from LBA performed on a *perfect* structure.

For the calibration of the FE model, two different buckling modes are simulated and combined, as presented in [Fig. 7.4](#): *i*) 1st eigenmode, causing buckling due to shear and *ii*) 14th eigenmode, corresponding to the first mode that causes buckling due bending moment (*i.e.* due to compression in the bottom curved flange).

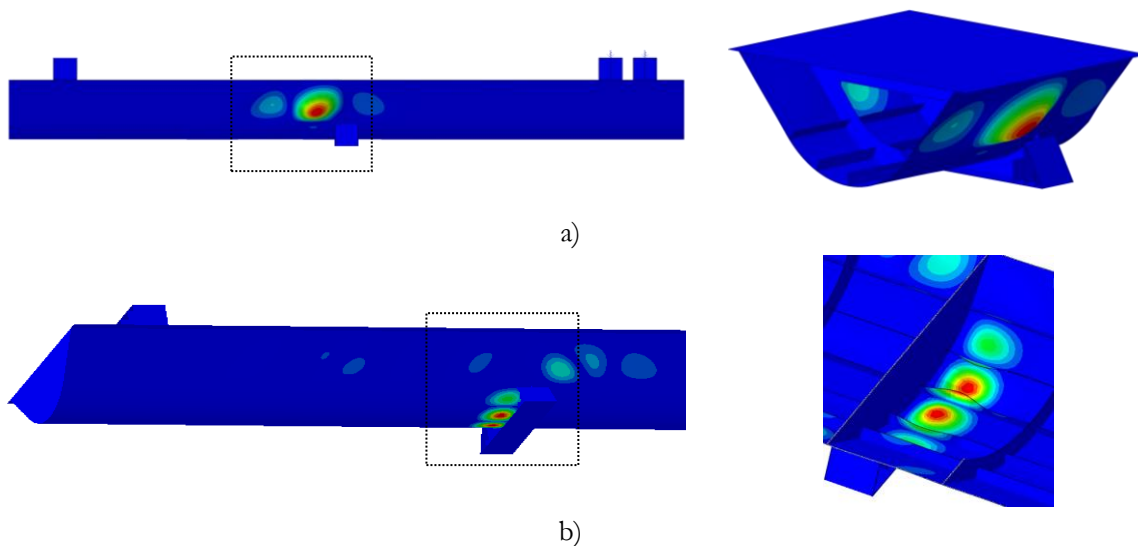


Fig. 7.4: Eigenmodes used for the calibration of the model: a) 1st mode and b) 14th mode

To achieve a good convergence, the imperfection amplitudes are varied from $h_w/100$ to $h_w/200$ for the 1st (shear-governed) eigenmode, and from $b/200$ to $b/400$ for the 14th (compression-governed) eigenmode, until results matching the experimental ones are obtained. According to [Fig. 6.6](#), h_w corresponds to the flat part of the web, being the subpanel with the largest width ($h_w \approx 623$ mm), whereas b represents the width of the bottom flange ($b = 1400$ mm).

Although the results showed that there are no large differences ($< 7\%$) between the ultimate loads using different imperfection shapes or different signs, a more comprehensive study on the imperfection sensitivity is carried out and presented in the following [section 7.3](#), with the aim to adopt one uniform imperfection for all the numerical models in the parametric study.

7.2.3 Model validation by experimental test results

The numerical model is validated using comparison with the experimental tests (see [section 6.4](#)), where the main comparators are: *i*) the collapse shape and *ii*) the force-vertical displacement curves.

In both experimental tests, the failure mode is almost identical and it occurs at the bottom (curved) flange close to the intermediate support. The failure modes are compared from outside (see [Fig. 6.35](#)) and from inside (see [Fig. 6.36](#)) with the ones obtained numerically, and a very good agreement is achieved for both bridge deck specimens, as it may be seen in [Fig. 7.5](#).

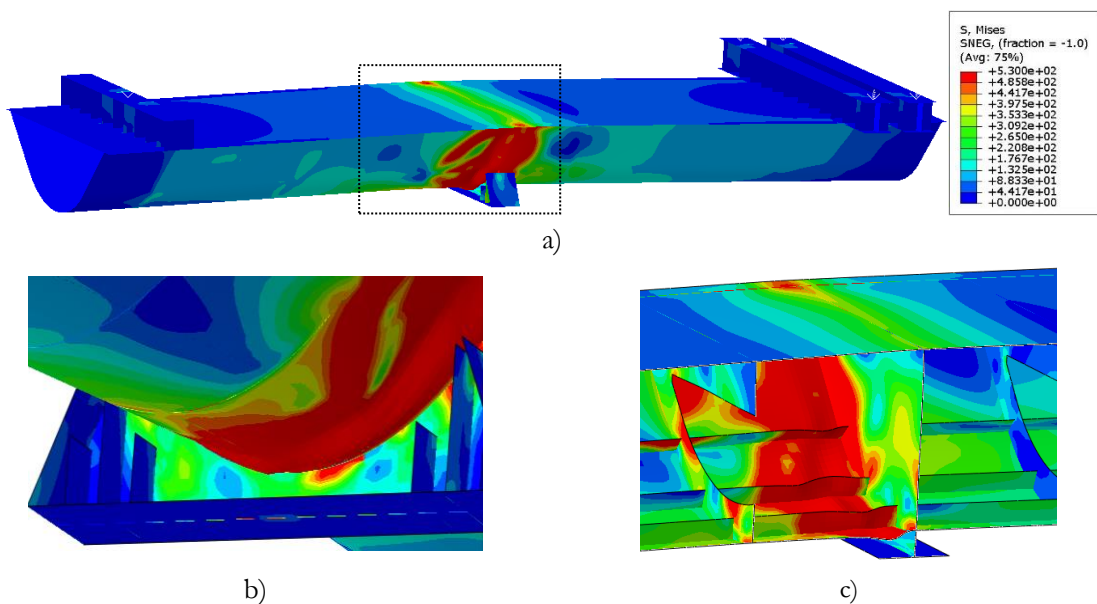


Fig. 7.5: a) Failure mode obtained by FEM; b) outside; c) inside

The force-vertical displacement curves for specimens S460 and S690 are presented in [Fig. 7.6](#). A good agreement is obtained, with differences in the ultimate strength of $\Delta S460 = 2.53\%$ and $\Delta S690 = 2.98\%$. This minor difference may be partly attributed to the inevitable load eccentricities, uneven contacts between specimens and the loading (and supporting) beam, and partly due to various simplifications made, such as the adoption of the buckling modes as the shapes of the imperfections or the approximation of the pre-stressing bars by springs.

Based on this comparative study, it may be concluded that the adopted geometry, material properties, boundary conditions, loads, size and type of FE adequately simulate the behavior of the tested specimens. Thus, the numerical model may be further utilized for the parametric study.

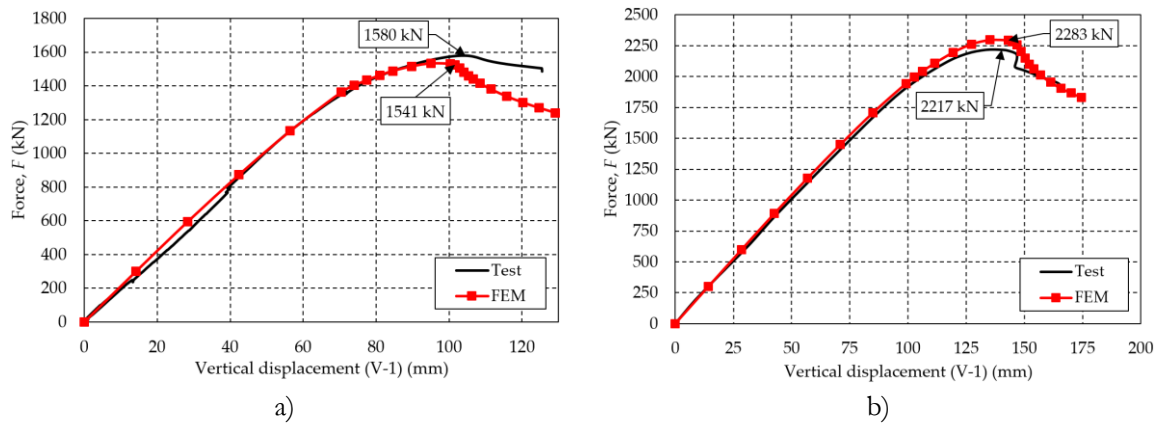


Fig. 7.6: Comparison of force-displacement curves: a) specimen S460; b) specimen S690

7.3 Parametric study

7.3.1 Section overview

The goal of the parametric study is to characterize the behavior of a box-girder bridge deck near the intermediate support, where the moment-shear ($M - V$) interaction occurs.

In the parametric study presented herein, the interaction between these two internal forces in the desired cross-section is provided by a 3-point bending layout, similar to the one used in the two experimental tests. In the mechanical model used for the validation in the previous section, the geometry of the segments (including diaphragms, cross-frames), boundaries (supporting foot, high-strength bars), and loads are explicitly modeled to simulate the conditions achieved in the experimental campaign. Since this model is found somewhat too complex and thus impractical for a broad parametric study on the $M - V$ interaction, several changes (*i.e.* simplifications) are introduced in a new model, described in this section.

Moreover, particular emphasis is given to the scope of the parametric study. Namely, the study aims to cover only the most practical ranges of parameters commonly found in bridges, which has significant importance for the validity interval of the studied $M - V$ interaction model.

7.3.2 Definition of the FE model for the parametric study

This section gives an overview of the main changes adopted in the numerical model, with respect to the model used for the calibration in [section 7.2](#).

7.3.2.1 Geometry

To reduce the CPU time of the analysis, it is necessary first to simplify the geometry of the mechanical model, which is achieved in two steps presented in [Fig. 7.7](#).

Step 1 - Removal of all the elements used in the experimental test (loading beam and supporting beams) that physically do not belong to the bridge deck specimen. Consequently, the *tie constraint* contacts between the top flange and these elements are also removed (see [Fig. 7.7a](#));

Step 2 - Replacement of the cross-frames and diaphragms by rigid bodies, which simplifies the geometry of the model, resulting in a lower number of finite elements (see Fig. 7.7b).

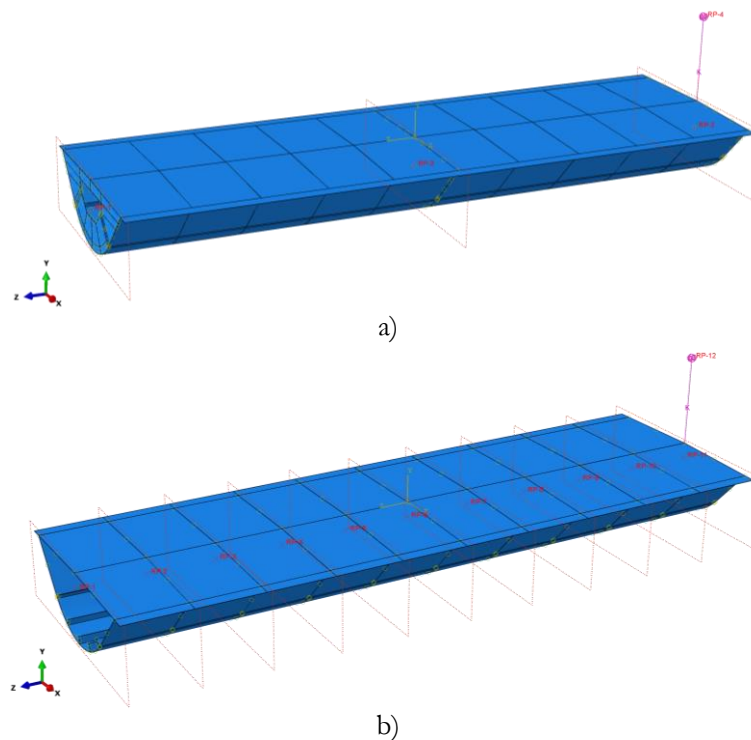


Fig. 7.7: Simplified FE model: a) Step 1; b) Step 2

It is noticed that in these figures, in the simplified model, the four springs from the initial (calibration) model are replaced by a single spring, with an adequate axial stiffness k . Furthermore, the boundary conditions and the applied concentrated force are assigned to the reference points (RP), which are tied to all points of a considered cross-section by means of a *rigid body constraint*. The force-displacement curves and failure modes of the three models (*i.e.* calibration model, simplified model 1, and simplified model 2) are compared in Fig. 7.8 for specimen S460.

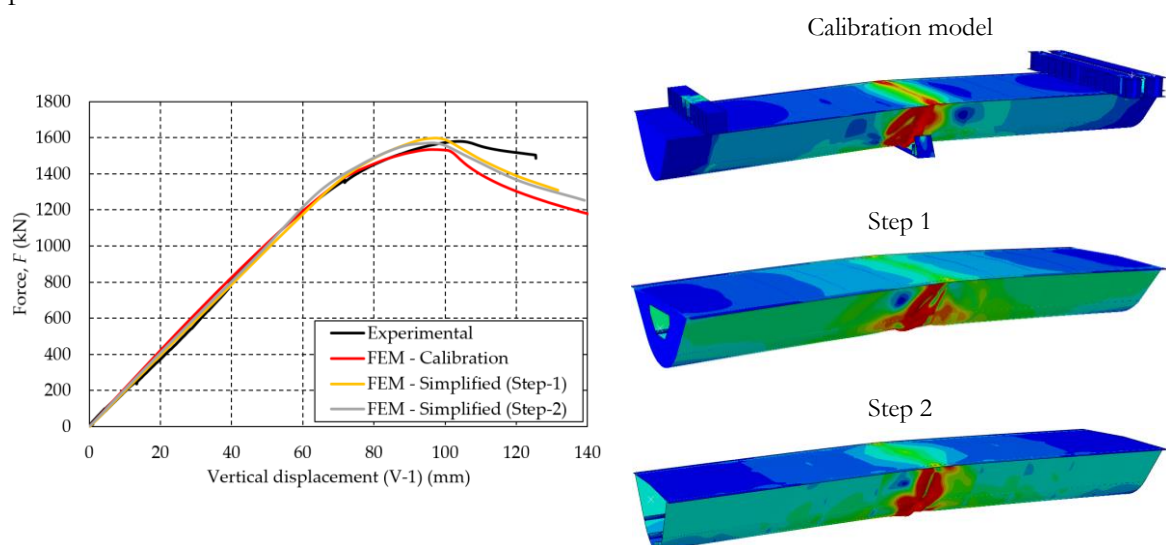


Fig. 7.8: Simplified FE model vs experimental results - comparison of results

Based on the force-displacement curves and the failure modes presented in the figure, it may be stated that the behavior of the bridge deck specimen remained almost unchanged, despite all the simplifications made, with a difference in the maximum force applied less than 3%. This means that all these simplifications may be also used in the models for the parametric study, thus reducing considerably the computation time.

7.3.2.2 Static scheme

The 3-point bending test layout, with a force on one side and support on the opposite side of the segment, was found to be a more suitable solution for the experimental investigation of the interaction behavior, due to the better control of the boundary conditions and thus more accurate anticipation of the bridge deck segment behavior. However, for the parametric study, the static scheme is slightly modified and adapted to simulate the behavior of the intermediate support. Namely, a simply-supported beam is adopted, where the concentrated force in the middle replaces the intermediate support from the test layout, as illustrated in Fig. 7.9.

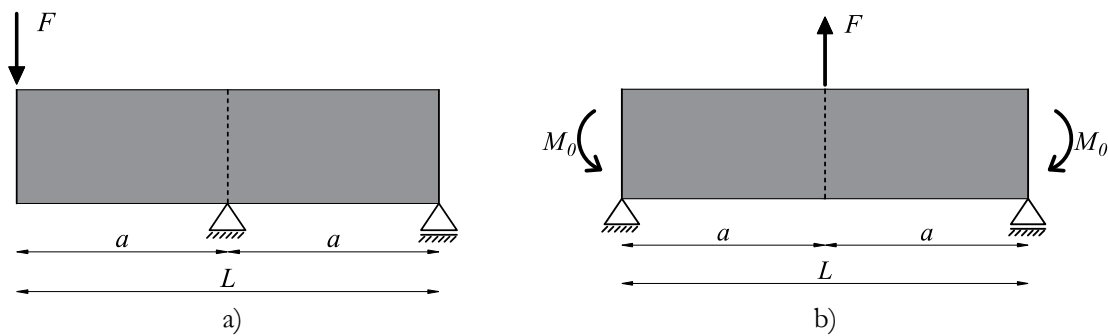


Fig. 7.9: Static scheme: a) experimental test; b) numerical parametric study

Different M/V -ratios (ψ) are achieved by applying different values of the concentrated force F and concentrated bending moment M_0 and by varying the length of the specimen L . For each model, ψ is determined at the mid cross-section, where the shear force is equal to $V = F/2$, whereas the moment is equal to $M = M_0 + F \cdot L/4$.

To ensure the desired simply-supported boundary conditions, all three translational degrees of freedom are prevented at one end of the beam, whereas on the opposite end, only vertical and out-of-plane displacements are prevented. Furthermore, the rotational degree of freedom around the axial axes of the specimen is also prevented. All the boundary conditions and concentrated loads are applied at the corresponding reference point (RP), which coincides with the center of gravity of the cross-section, as presented in Fig. 7.7.

7.3.2.3 Applied material model

For the numerical parametric study presented herein, structural steel S355 is considered, because of its widespread use in bridge construction.

The material is modeled as elastoplastic with strain-hardening according to the recommendations from C.6 of EN 1993-1-5, with Young's modulus equal to $E = 210$ GPa and Poisson's coefficient $\nu = 0.3$. The material behaves linearly elastic up to the yield stress (f_y), after

which an isotropic hardening behavior occurs with a hardening modulus equal to $E/100$ until the ultimate strength (f_u) is reached (see also Fig. 5.2). After the ultimate strength is exceeded, the material is assumed to behave perfectly plastic. The yield and ultimate strength are adopted based on the characteristic values of the material properties given in EN 10025-2 [148], as presented in Table 7.4.

Table 7.4: Characteristic values of considered material properties – steel S355 [148]

f_y [MPa]				f_u [MPa]
$t < 16$ mm	$t = 16-40$ mm	$t = 40-63$ mm	$t = 63-80$ mm	
355	345	335	325	470 MPa

7.3.2.4 FE mesh size

The specimens are discretized by S4R shell elements. Their size is defined based on a convergence study, where it is obtained that sufficiently accurate results are obtained with finite elements of 50×50 mm², as shown in Fig. 7.10.

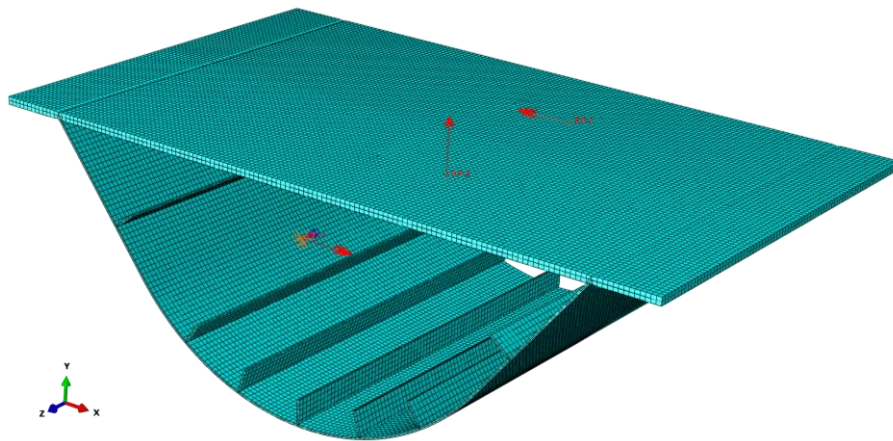


Fig. 7.10: Example of a numerical model used for the parametric study

As it may be seen, 5 finite elements are adopted across the depth of a longitudinal flat stiffener, whereas a particular effort is made to ensure an integer number of FE between stiffeners, so that the bottom node of each stiffener coincides with the corresponding node of the curved panel.

7.3.2.5 Applied initial imperfections

Finally, the initial imperfections for the parametric study are adopted based on the results from an imperfection sensitivity analysis, in which the first four eigenmodes are considered as a potential initial geometric imperfection shape, whereas the amplitudes are varied in a range between $b/400 - b/800$. Moreover, for this study, two groups of analyses are executed and investigated separately, one in which the bridge deck fails in shear (Fig. 7.11), and the other in which the specimen fails in bending, due to compressive stresses in the bottom flange (Fig. 7.12).

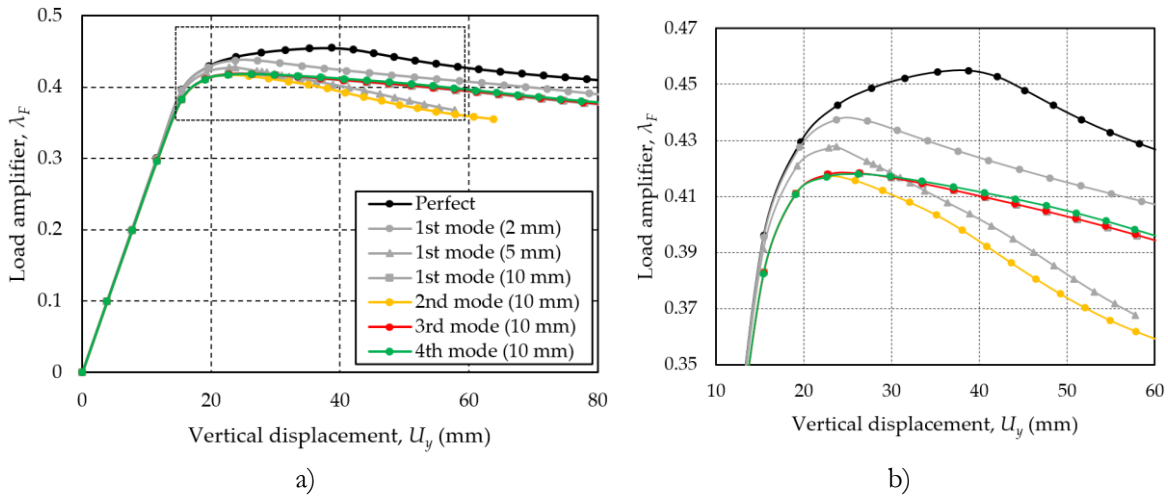


Fig. 7.11: Imperfection sensitivity analysis – shear failure: a) force-displacement curves; b) peak region of force-displacement curves

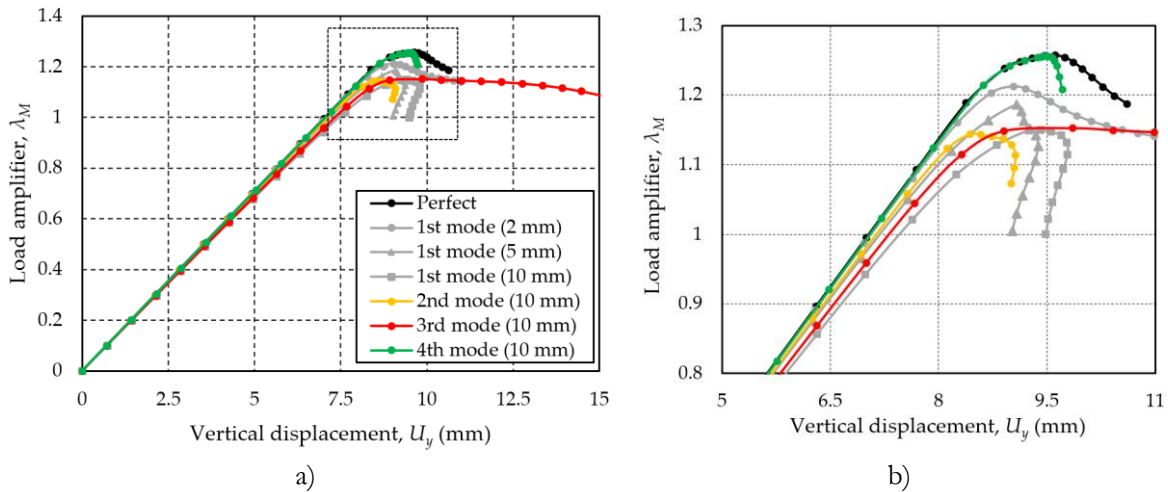


Fig. 7.12: Imperfection sensitivity analysis – bending failure: a) force-displacement curves; b) peak region of force displacement curves

In these figures, the force load amplifier λ_F and the bending moment load amplifier λ_M (*i.e.* load proportionality factors), obtained from GMNIA for arbitrary applied concentrated force F and bending moment M , are plotted against the vertical displacement (U_y) of the point laying in the middle of the bottom flange in the middle plane, *i.e.* plane where load F is applied.

Based on the presented results, one may notice that both shapes and the amplitudes considered in this study have a minor influence ($\Delta_{\max} = 8\%$) on the behavior of the specimen and its ultimate resistance. Therefore, equivalent geometric imperfections are adopted, with a shape affine to the 1st buckling mode, and an amplitude equal to $b/400$.

It is necessary to stress that for an investigation of the M - V interaction behavior, as indicated also in the study by Jäger *et al.* [139], the adoption of the 1st buckling mode is a clever approach since it contains the relevant failure mode depending on the applied internal forces, thus accounting for the change of the failure mode in the interaction domain depending on the M/V -ratio.

7.3.3 Scope of the study

The geometrical parameters varied in the parametric study are carefully chosen to fall within the limits of practical ranges in bridge application, discovered and demonstrated in [section 2.3](#). Namely, using the cross-section of the reference case study on a scale $R = 1:1$, proposed by GRID International [151] (see [6.2.2](#)), several key parameters for the definition of the curved bottom flange geometry are varied in a parametric numerical study to investigate their effect on the $M - V$ interaction behavior.

In total, 210 different bridge cross-section geometries are selected, where 5 different curvatures of the bottom curved flange (*i.e.* $Z = 0$, $Z = 50$, $Z = 100$, $Z = 200$ and $Z = 300$) and 3 aspect ratios (*i.e.* $\alpha = 0.5$, $\alpha = 1.0$ and $\alpha = 1.5$) are varied. The length of the specimen $L = 2a$ (see [Fig. 7.9](#)), defined by the aspect ratio $\alpha = a/b$, is equal to $L = 4200$ mm, $L = 8400$ mm, and $L = 12600$ mm, for the aspect ratios 0.5, 1.0 and 1.5, respectively, where the width of the bottom flange is kept constant and equal to the width of the reference case study (*i.e.* $b = 4200$ mm).

Regarding the bottom curved flange, besides the curvature parameter and the aspect ratio, several other parameters are varied, such as two different thicknesses ($t = 15$ mm and $t = 25$ mm), but also three longitudinal stiffener typologies - one flat ($b_{st}/t_{st} = 250/25$ mm) and two types of trapezoidal stiffeners, as illustrated in [Fig. 7.13](#).

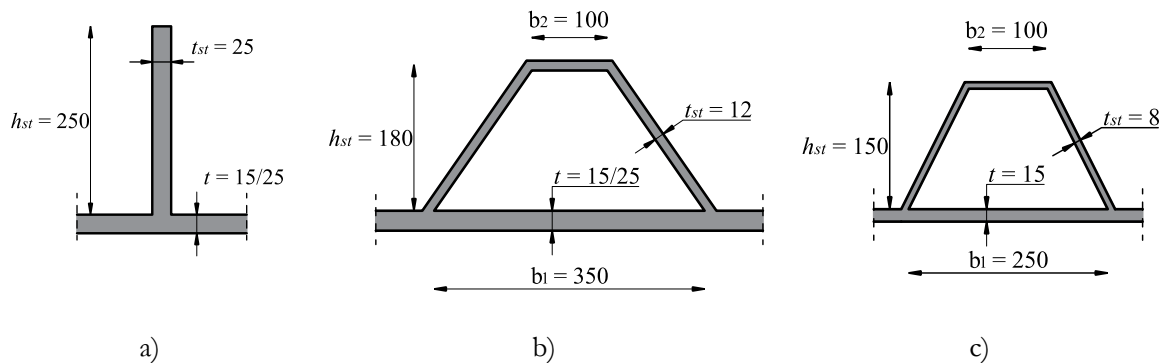


Fig. 7.13: Stiffener typologies: a) flat; b) trapezoidal– Type 1 and c) trapezoidal – Type 2

Moreover, for each of the presented typologies, two configurations of longitudinal stiffeners are considered, which is achieved by varying the number of stiffeners between $n_{st} = 3$ and $n_{st} = 5$, as presented in [Fig. 7.14](#) for extreme values of curvatures, *i.e.* $Z = 0$ and $Z = 300$.

There are four different stiffener configurations, *i.e.* with 3 and 5 flat stiffeners, and with 3 and 5 trapezoidal stiffeners, where the distances between the stiffeners (b_{loc} and b_{edge}) are kept the same for all curvature parameters. Trapezoidal stiffener Type 1 ([Fig. 7.13b](#)) is used in the configuration with 3 longitudinal stiffeners, whereas Type 2 ([Fig. 7.13c](#)) is applied in the case of 5-stiffened plates. Moreover, [Fig. 7.14a](#) shows that in the configurations with flat stiffeners and trapezoidal stiffener Type 1, two thicknesses of the bottom flange are considered ($t = 15$ mm and $t = 25$ mm), while in the case of the trapezoidal stiffener Type 2 only 15 mm thick plates are considered, comprising in total 7 different bottom flange geometries, for each curvature.

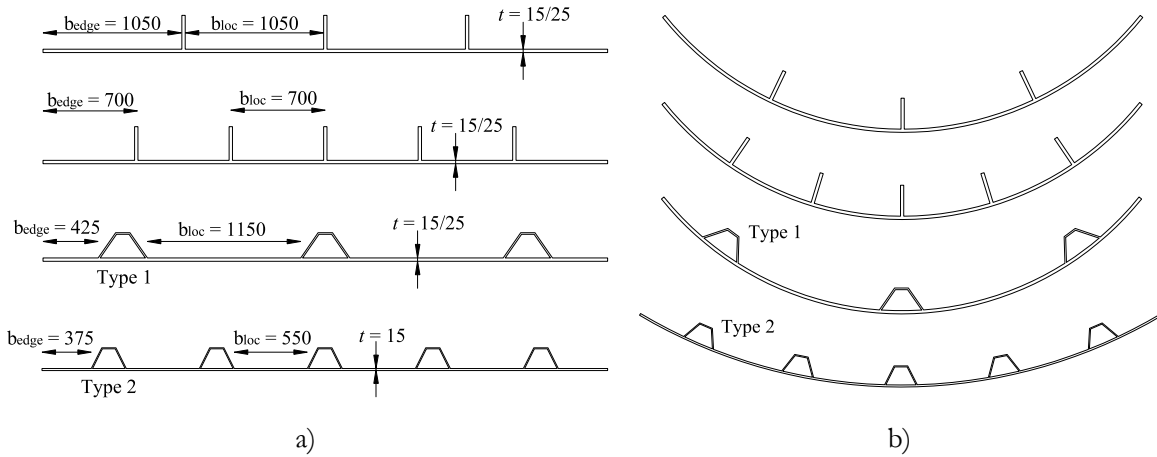


Fig. 7.14: Stiffener configurations: a) $Z = 0$; b) $Z = 300$

It is necessary to highlight that one of the goals of the study presented herein, is to assess the aforementioned two design methods, one proposed by Tran *et al.* (2014a) [59] and the other by the OUTBURST research project [85], for the calculation of the effective properties of curved panels subjected to pure compression. Since the main difference between the two methods lies in the calculation of the local buckling of the sub-panels, the b/t -ratio in this study is varied in a wide range (up to 70), which exceeds the common ranges of the slenderness found in the bridges built so far (see Fig. 2.6). Furthermore, since none of the two methods tackled explicitly the local buckling of the longitudinal stiffeners, the dimensions of the stiffeners are chosen to be class 3 (or lower), thus isolating merely the local buckling of the sub-panels, which allows for a direct comparison of these two methods.

Regarding the cross-section shape, in all studied models, the depth of the curved panel f is kept lower than the total height H of the cross-section, which corresponds to the first case in Fig. 2.5. Namely, in bridges with a curved bottom flange built so far and reported in section 2.3, the shape with $f < H$ is identified in 21 out of 22 cases. Hence, it is found justified to study this more common solution, where a clearer distinction between the bottom flange and the web can be made. Besides, all 210 FEM models may be divided into two main groups (105 models each): *i*) cross-sections with a constant height ($H = \text{const.}$) and *ii*) cross-sections with a variable height ($H = \text{var.}$), illustrated in Fig. 7.15a and Fig. 7.15b, respectively.

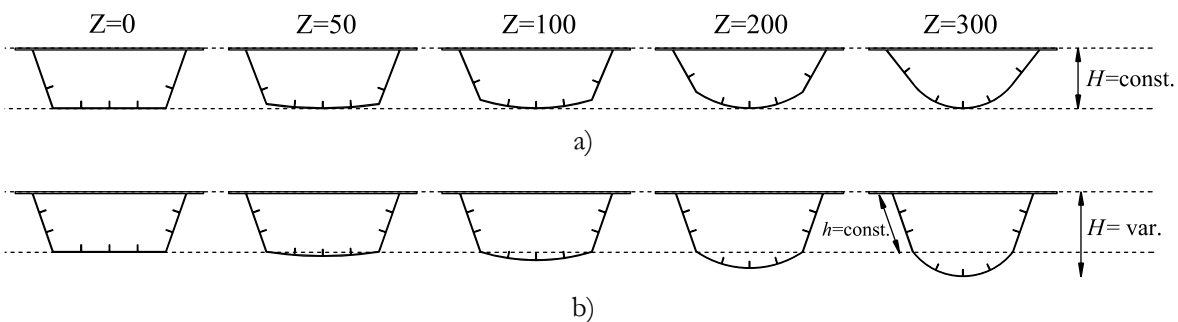


Fig. 7.15: Cross-section with: a) constant height; b) variable height H

In the first group ($H = \text{const.}$), the total height is kept constant, which results in a shorter flat web (b) with the increase of curvature. On the other hand, in the second group, the width of the flat web b is kept constant for all the cross-sections, which leads to an increased total height with the curvature. The reason for considering these two groups of cross-sections is threefold: *i*) First, it is intended to compare somehow the performance of the bridge cross-sections with a curved bottom flange with respect to the corresponding conventional (trapezoidal) cross-section with a flat bottom flange. However, as it is later discovered, for a given trapezoidal box-girder with a flat bottom flange ($Z = 0$), it is difficult (if possible at all) to define a corresponding cross-section with a curved bottom flange of equal area that may allow a straightforward comparison of their performances. Namely, in the first group ($H = \text{const.}$), the second moment of area of a cross-section with a higher curvature is considerably reduced with respect to the trapezoidal cross-section, resulting in lower bending resistance, but also a lower material consumption. On the other side, in the second group, the bending resistance increases with the curvature, but the height and the material consumption also increase. Therefore, it is decided to account for both groups of cross-sections, representing the lower and the upper bounds of a given trapezoidal cross-section. *ii*) Secondly, by varying the height of the cross-section and the depth of the curved bottom flange, various positions of the neutral axis may be achieved and thus different stress gradients in the bottom curved flange. This is particularly important since one of the objectives is to assess the simplified ‘curved panel method’, described in 6.4.6, according to which a uniform axial compression ($\psi = 1.0$) is assumed in the entire bottom flange. *iii*) Finally, by varying the ratio between the flat web and the bottom curved panel, while keeping the same height of the cross-section, or by keeping the same height of the flat part of the web only, it is aimed to distinguish and track the influence of both curved panel and flat web in the shear resistance of the cross-section.

As for the flat webs, the thickness is also varied between $t_w = 15$ mm and $t_w = 25$ mm. Namely, inspired by the real examples of bridges, in the reference case study defined by GRID International [151] the thickness of the web and the thickness of the bottom curved panel are kept the same and equal to ($t = t_w = 25$ mm), which falls within the common ranges (*i.e.* 25 - 40 mm) reported in section 2.3. However, to allow for the shear buckling of the webs, it is found that the thickness of 15 mm is sufficiently thin for the occurrence of this instability phenomenon. It is necessary to stress that in those cases where the bottom flange is $t = 25$ mm thick, both thickness $t_w = 15$ mm and $t_w = 25$ mm of the web t_w are considered, whereas in those cases where the bottom flange is $t = 15$ mm thick, only thickness $t_w = 15$ mm is studied. Furthermore, regarding the longitudinal stiffeners in the webs, the corresponding typologies used for the bottom flange are adopted (see Fig. 7.13), where the number of the stiffeners varied between $n_{\text{st,web}} = 1$ and $n_{\text{st,web}} = 2$ for $H = \text{const.}$ and $H = \text{var.}$, respectively, as illustrated in Fig. 7.15a and Fig. 7.15b. The position of the longitudinal stiffeners, both trapezoidal and flat, is summarized in Fig. 7.16, for various cross-section shapes.

Finally, since the principal focus of this study is dedicated to the bottom curved flange subjected mainly to the axial compression, the simplifications related to the top flange mentioned in section 6.2 are adopted here as well. Specifically, in all numerical simulations, a thick flat top

flange with a constant width is considered ($b_f/t_f = 7000/75$ mm), thus substituting the composite steel-concrete top flanges, while keeping the position of the neutral axis close to the top flange.

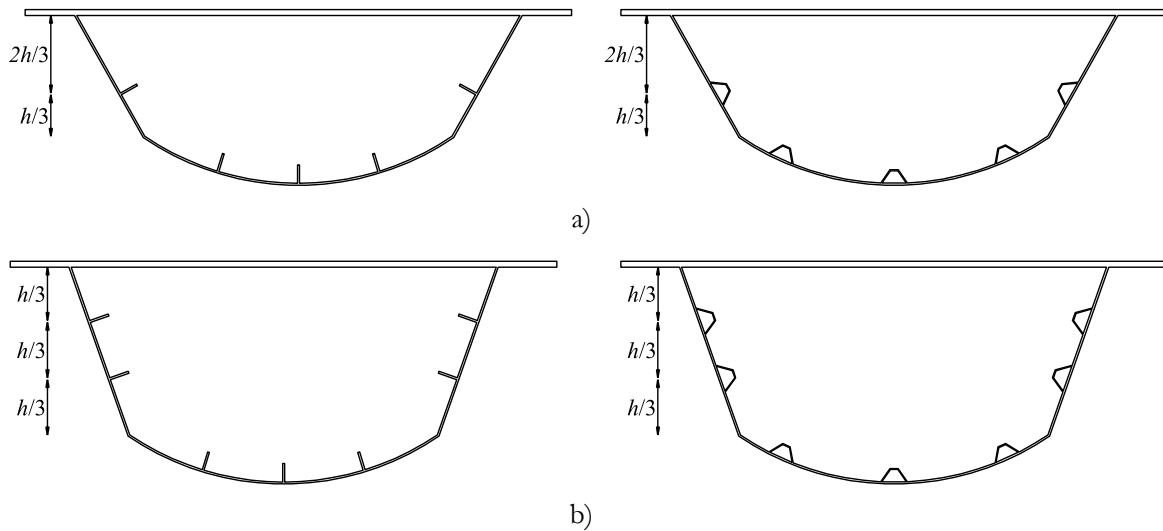


Fig. 7.16: Position of the longitudinal stiffeners on webs: a) $H = \text{const.}$ ($n_{\text{st,web}} = 1$);
b) $H = \text{var.}$ ($n_{\text{st,web}} = 2$)

7.4 Results of the parametric study

7.4.1 Section overview

For all 210 box-girder configurations described in the previous section, both the ultimate resistances and failure modes are assessed, aiming to characterize the entire spectrum of behavior, *i.e.* from pure bending to ‘almost’ pure shear. In this study, 10 different M/V -ratios (ψ) are considered (see Fig. 7.9b), whereas two extreme ratios correspond to pure bending and shear resistances, while the other eight represent intermediate points of the interaction. Hence, the total number of the executed numerical simulations is 2100.

The main output of the parametric study is numerically generated $M-V$ interaction diagrams for various box-girder bridge cross-sections with curved bottom flange, which are essential for the verification of the applicability and safety of the $M-V$ interaction criterion proposed by Jáger *et al.* [139], given by Eqs.(2.122)-(2.123), adopted in prEN 1993-1-5 [140].

7.4.2 $M-V$ interaction

For each geometry, the load-deflection ($F - \delta$) curves are first assessed, measured in the middle of the span, *i.e.* reference point RP-3 (see Fig. 7.10). In Fig. 7.17, using as an example a box-girder subjected to 3-point bending, with an aspect ratio of $\alpha = 0.5$ and a curved bottom flange 25 mm thick with three flat stiffeners and a curvature equal to $Z = 300$, the $M-V$ interaction behavior is illustrated.

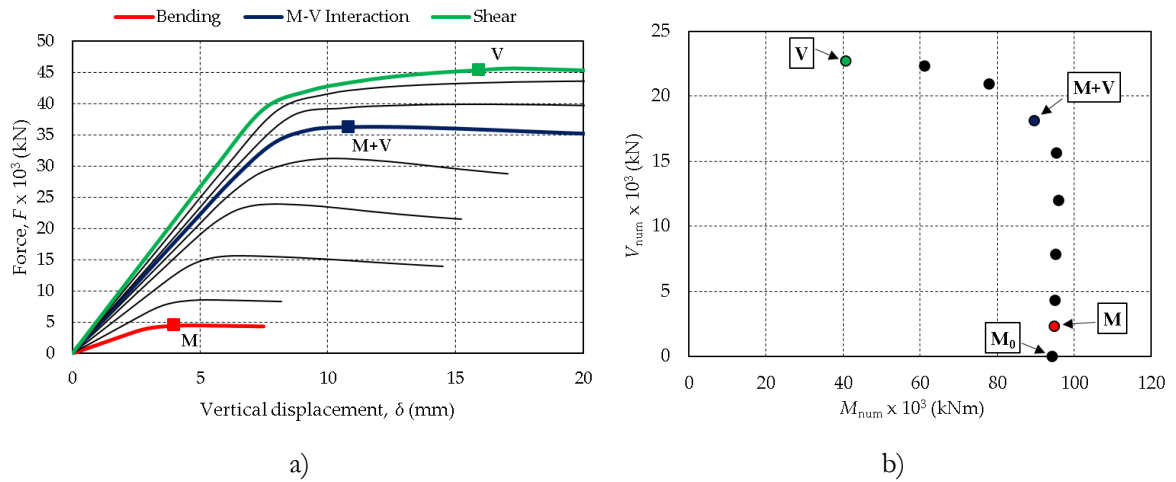


Fig. 7.17: a) Force-deflection curves and b) M - V interaction diagram for box-girder ($H = \text{const.}$; $Z = 300$; $\alpha = 0.5$; $n_{st} = 3$; $t = 25$ mm; $t_w = 25$ mm)

In Fig. 7.17a, 9 F - δ curves are plotted to show the entire spectrum of M - V interaction behavior, starting from ‘almost pure’ bending (M) up to ‘almost pure’ shear (V), including 7 intermediate curves (M+V) that correspond to different M/V ratios. Pure bending is achieved by applying only the concentrated bending moments (M_0) in reference points RP-1 and RP-2 (see Fig. 7.9b), whereas pure shear can never be achieved since the applied force F , besides shear, also includes bending moment in the girder. It is also necessary to say that long span specimens with higher aspect ratios fail only in bending, which is characterized by a low resistance and increased vertical deformation, thus the entire M - V interaction spectrum may not be achieved.

In Fig. 7.17b, the corresponding M - V interaction diagram is shown, where each of the 10 points is defined by two coordinates [M_{num} ; V_{num}], calculated by $V_{num} = F_{max}/2$, and $M_{num} = M_0 + F_{max} \cdot L/4$, where F_{max} is the maximum force read from the corresponding F - δ curve in Fig. 7.17a. As stated before, the only exception is for pure bending, where no vertical force F is applied, resulting in $V_{num} = 0$ and $M_{num} = M_0$.

For the considered case ($Z = 300$), and two more curvature parameters ($Z = 0$ and $Z = 100$), the corresponding bending failure modes (M), shear failure modes (V) and the mixed failure modes (M+V) are illustrated in Fig. 7.18. A bending dominant failure mode is characterized by the local buckling of the sub-panels in the bottom flange (and webs), whereas in the case of mixed failure modes, both local buckling of the flange due to bending and global or local buckling of the web due to shear occurred simultaneously. Finally, shear dominant failure is recognized by the development of a tension field band across the web of the cross-section.

In Fig. 7.19 and Fig. 7.20, all numerically generated M - V interaction diagrams are summarized, which are used in the subsequent chapter of the document for the assessment of the M - V interaction criterion proposed by Jáger *et al.* [139]. For a simpler interpretation of the results, the diagrams are divided into two main groups, $H = \text{const.}$ (Fig. 7.19) and $H = \text{var.}$ (Fig. 7.20), as explained in Fig. 7.15. Besides, for each of these two groups, the diagrams are further divided into seven sub-groups, based on various stiffener configurations and plate thicknesses.

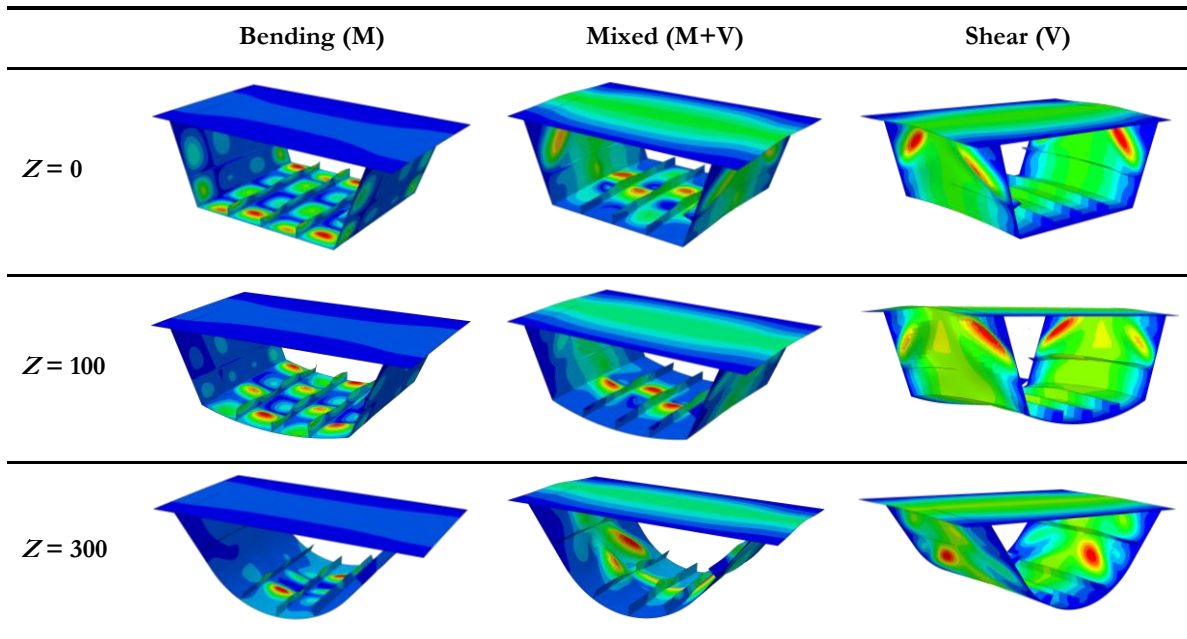


Fig. 7.18: Bending (M), mixed (M+V) and shear dominant (V) failure modes and Mises stress distributions

In these diagrams, the x -axis ($M_{\text{num}}/M_{\text{Rd,num}}$) and the y -axis ($V_{\text{num}}/V_{\text{Rd,num}}$) indicate that the numerical results are normalized against numerically determined bending and shear resistances for the given cross-section configuration. In other words, each point of an M - V interaction diagram, defined by two coordinates [M_{num} ; V_{num}] is on one side divided by the bending resistance ($M_{\text{Rd,num}}$) obtained for pure bending (case M_0 in Fig. 7.17b), and on the other side by the shear resistance ($V_{\text{Rd,num}}$) obtained for shear dominated failure (case V in Fig. 7.17b).

The reason for the normalization against the numerically determined resistances is twofold: *i*) To compare qualitatively the M - V interaction behavior for different box-girder cross-sections (*i.e.* with different curvatures), it is necessary to compare the shape of the M - V diagrams rather than their resistances. Namely, as one may expect, in the case of $H = \text{const.}$ cross-sections, the higher curvature implies the reduction of the second moment of area and thus the reduction of the cross-section resistance, whereas, in the case of $H = \text{var.}$, the second moment of area of the cross-section increases with the curvature, which leads to increased resistance. Hence, the mere quantitative comparison of the resistances would be superfluous and could fail to interpret the real difference in the behavior of different cross-sections; *ii*) Owing to the lack of the analytical bending and shear resistance models for the studied cross-sections with a curved bottom flange, the results are normalized against the numerical resistances. Consequently, the extreme two points of each diagram that correspond to pure bending (M_0) and ‘almost’ pure shear (V) are equal to 1.0. The results can not be used for a direct evaluation of the criterion proposed by Jäger *et al.* [139] since the reference resistances are taken from the FE analysis. However, in the following chapter of the thesis, new analytical models for the prediction of the bending and shear resistances are proposed and incorporated in the existing M - V interaction criterion, which will allow for the comparison between the analytical and numerical results.

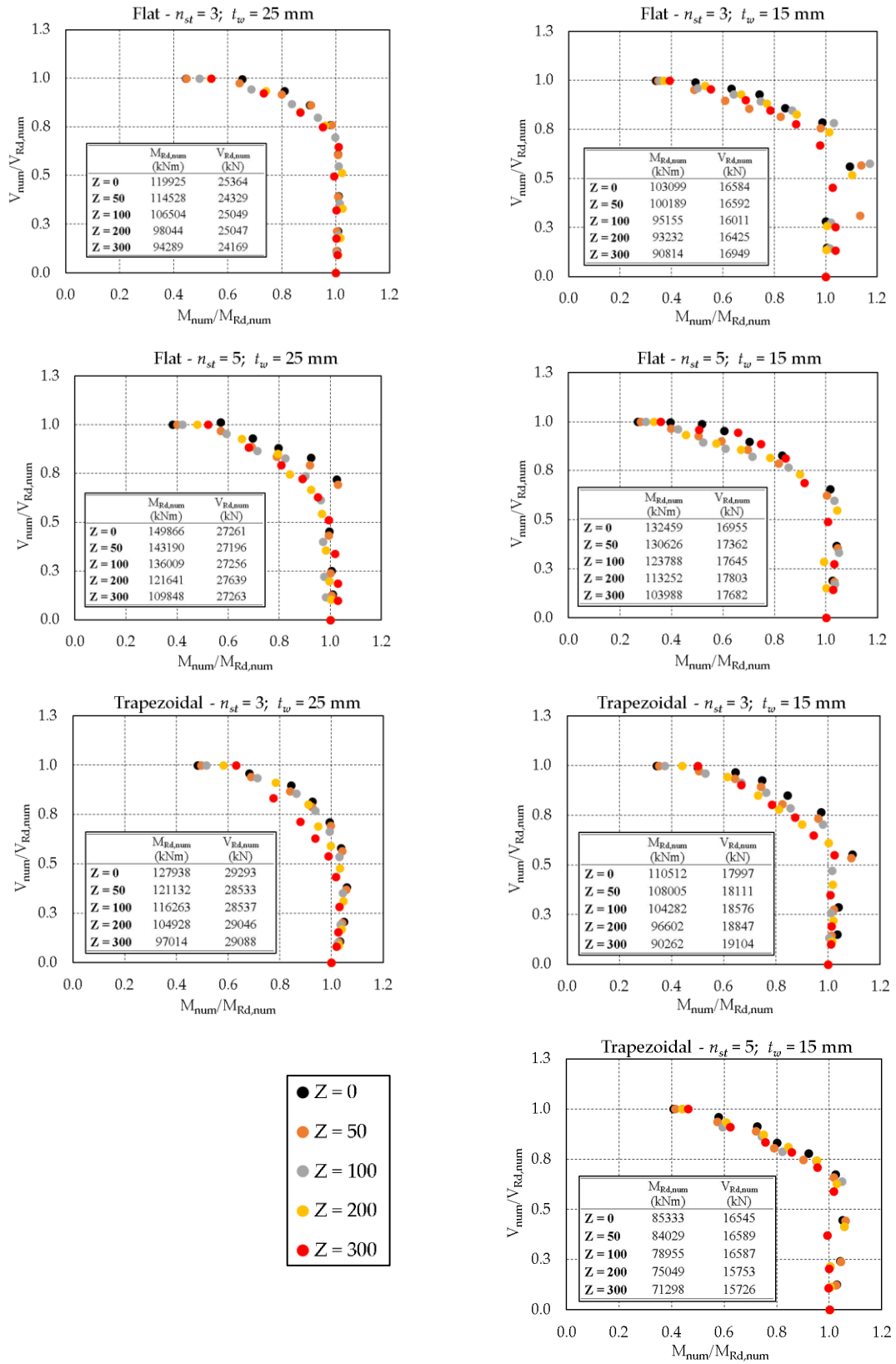


Fig. 7.19: M - V interaction diagrams for $H = \text{const.}$ and various Z parameters

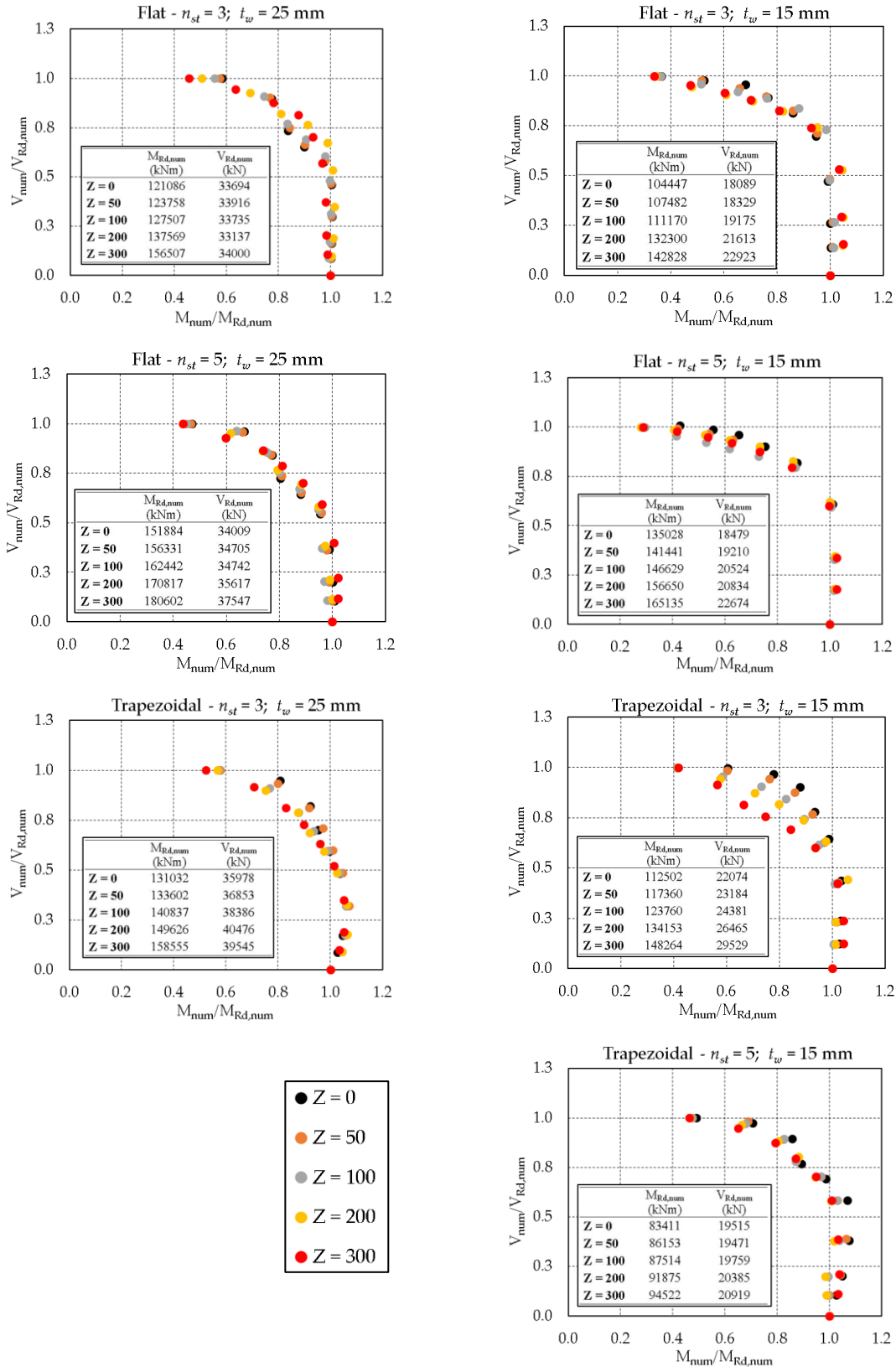


Fig. 7.20: $M-V$ interaction diagrams for $H = \text{var.}$ and various Z parameters

All the diagrams in Fig. 7.19 and Fig. 7.20, regardless of the geometry, confirm clearly that there is no need to consider interaction for small values of the shear force (approx. $V_{\text{num}}/V_{\text{Rd,num}} < 0.5$). It is interesting to note that the bending resistance increases slightly when a small shear force is applied. This increase is attributed to the more favorable moment gradient, which takes place as soon as the force F is applied, whereas the reference bending resistance (case M_0) comes from numerical simulations with uniform bending. However, for higher values of the shear force ($V_{\text{num}}/V_{\text{Rd,num}} > 0.5$), an M - V interaction takes place characterized by an obvious bending resistance reduction. At what shear utilization ($\eta_{\beta,\text{lim}} = V_{\text{num}}/V_{\text{Rd,num}}$) the interaction starts depends on the geometry of the cross-section (*i.e.* curvature, thickness, number and type of stiffeners, etc.). In general, it may be noticed from the diagrams that the interaction starts with the shear force exceeding approximately 50% of the shear resistance, which coincides with the provisions given in EN 1993-1-5, as well as with the M - V criterion proposed by Jäger *et al.* [139]. However, it may be noticed that the limiting shear utilization, at which the interaction occurs, varies between $\eta_{\beta,\text{lim}} = 0.4 - 0.7$, which may lead to slightly unsafe results on one side, and on the other side, to conservative results. Since the value of $\eta_{\beta,\text{lim}}$ directly depends on the shear resistance $V_{\text{Rd,num}}$, which in this case is estimated from the numerical simulations using the shear dominated cases, this variation may be attributed to the accuracy of such estimation. Hence, in chapter 8, only the value prescribed in the design codes of $\eta_{\beta,\text{lim}} = 0.5$ is considered.

In addition, it should be mentioned that after the shear force exceeds the limiting value ($\eta_{\beta,\text{lim}}$), the extent of the moment resistance reduction (*i.e.* the shape of the M - V interaction diagram) is not uniform and equivalent for all the cross-sections, but it highly depends on the entire set of the geometrical parameters. In an attempt to understand the influence of a single (or more) geometrical parameters on the M - V interaction behavior, the diagrams from Fig. 7.19 and Fig. 7.20 are rearranged and summarized in Annex C (C.1), so that 7 different configurations of the same curvature parameter are gathered in the same graph, separately for $H = \text{const.}$ and $H = \text{var.}$ In spite of the difficulty in finding a clear correlation between a single geometrical parameter (*e.g.* number of stiffeners, curvature, thickness, etc.) and the shape of the M - V interaction diagram since all the diagrams are rather similar, some regularities in response are noticed. Namely, the thickness (t_w) and the stiffeners configuration of the webs seem to have the greatest impact on the M - V interaction behavior. In the case of lightly stiffened slender webs (see Fig. 7.19 - right), it may be noticed that after $\eta_{\beta,\text{lim}}$ is exceeded a sudden reduction of bending moment takes place, which may be attributed to shear buckling of the web that occurs for higher shear forces. On the other hand, for the thicker and more stiffened webs (*e.g.* $H = \text{var.}$ and/or $H = \text{const.}$ with $t_w = 25$ mm), the transition zone between the bending dominated and shear dominant response is much smoother.

Finally, it must be reminded that in the case of I-girders and/or trapezoidal box-girders, there is a clear distinction between the flange and the web of a cross-section, which considerably eases the interpretation of the M - V interaction behavior and subsequently the application of the standard design rules. According to all rules that address the problem of the M - V interaction (see 2.5.3), there is no interaction if the applied bending moment is smaller than the bending resistance coming from the effective flanges alone ($M < M_f$). However, in the case of the box-girder with a curved bottom flange, it is not clear what is the ‘web’ and what is the ‘flange’ in a cross-section,

which implies that this condition at this phase cannot be applied. Therefore, owing to the complexity of the problem and in an attempt to be consistent with the existing design rules, a deeper study is carried out in the following chapter of the thesis to identify what part of the cross-section participates in the shear and what in the bending resistance.

7.5 Summary

In this chapter, a numerical parametric study was carried out, in which the $M - V$ interaction behavior of a box-girder bridge deck cross-section with a curved bottom flange was characterized. For the parametric study, a reliable FE model was built and verified against the experimental results, reported in [chapter 6](#). The reported study aimed at covering all the relevant geometrical parameters (*e.g.* curvature parameter, aspect ratio, the thickness of flange and web, stiffener type, number, and configuration, etc.) that fall within the most common ranges found in the real examples of bridges.

For all considered geometrical configurations, 10 different M/V -ratios were applied, aiming to characterize the entire spectrum of behavior, *i.e.* from pure bending to ‘almost’ pure shear. The main output of the parametric study was numerically generated $M-V$ interaction diagrams for various box-girder bridge cross-sections with curved bottom flange. These results serve as a solid benchmark in the subsequent [chapter 8](#), where the available $M-V$ interaction criterion proposed by Jáger *et al.* [139] is statistically assessed and the modified design rules are proposed.

8. Design proposals for bridge cross-sections integrating curved steel panels

8.1 Overview

According to the task flowchart in [section 1.2](#), the previous chapter tackled Task 4.2 of the thesis, where a numerical study on the M - V interaction behavior of a box-girder bridge deck with curved bottom flange is carried out, generating an extensive database of FE results in a form of M - V interaction diagrams. Using the collected data, the goal of this chapter is now to assess if the M - V interaction equation recently proposed by Jáger *et al.* [139], adopted in prEN 1993-1-5 [140], may also be safely applied in the case of box-girder bridge cross-sections with a curved bottom flange.

However, as shown in [Fig. 8.1](#) that plots the M - V interaction equation, Eqs.(2.122)-(2.123), for the application of this criterion, it is necessary first to define the effective bending resistance ($M_{eff,Rd}$) and the web shear resistance ($V_{bm,Rd}$) of the cross-section. This is found to be the main challenge and one of the main motivations for the present thesis since there are still no analytical design rules that may be used to calculate these two values for studied cross-section typology.

Hence, following closely the analytical resistance models for the trapezoidal box-girders from EN 1993-1-5, defined in [2.5.3](#), a study on a new bending resistance model is carried out first in [section 8.2](#), whereas in [section 8.3](#), a new analytical shear model is developed. Subsequently, in [section 8.4](#), based on the new (modified) resistance models, the M - V interaction equation is accordingly redefined and assessed against the FEM results obtained in [chapter 7](#). Finally, in

section 8.5, all three models (*i.e.* bending resistance model, shear resistance model, and the M - V interaction model) are statistically assessed against the numerical results by calculating the partial factor (γ_M) and thus, completing the last task of the thesis (Task 5, see section 1.2).

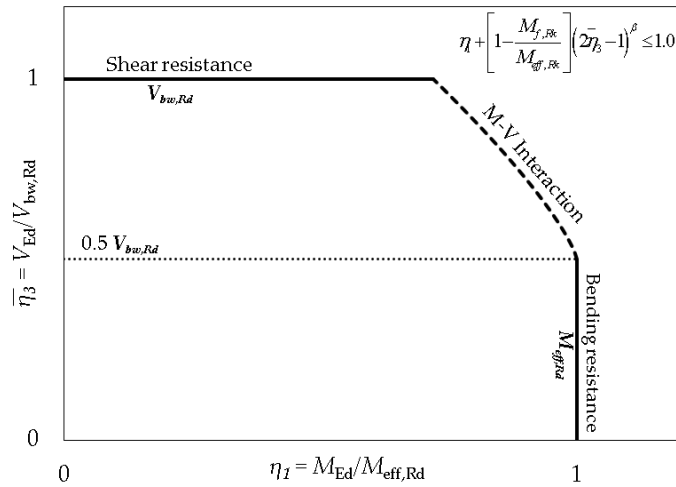


Fig. 8.1: Graphical interpretation of the M - V interaction formula by Jäger *et al.* [139]

8.2 Bending resistance model

8.2.1 Introduction

In chapter 7, the pure bending resistances are determined using the verified numerical model (case M_0 , see Fig. 7.17) for 210 different geometries of box-girder cross-sections with a curved (and flat) stiffened bottom flange. Depending on the geometry (*i.e.* stiffener configuration, aspect ratio, and curvature parameter), several typical bending failure modes are attained, as presented in Fig. 8.2. For heavily stiffened short bridge decks (Fig. 8.2a), it can be clearly seen how the bottom flange reaches yield strength over a larger area, without any evidence of buckling. For shorter spans and higher curvatures or heavily stiffened bottom flanges, commonly the local buckling of subpanels is the governing failure mode as presented in Fig. 8.2b, but also in Fig. 7.18. Finally, for longer spans and lower curvatures, the global buckling mode is obtained (Fig. 8.2c), characterized by buckling of the entire bottom flange with accompanying stiffener buckling.

For the M - V interaction check and for the development of a new bending resistance model, which is the main goal of this section, all three failure modes are accounted for. Nevertheless, one may conclude that the bottom flange, either flat or curved, is dominantly subjected to axial compression regardless of the failure mode. Consequently, the bending resistance of the box-girder cross-section directly depends on the bottom flange resistance to axial compressive stresses.

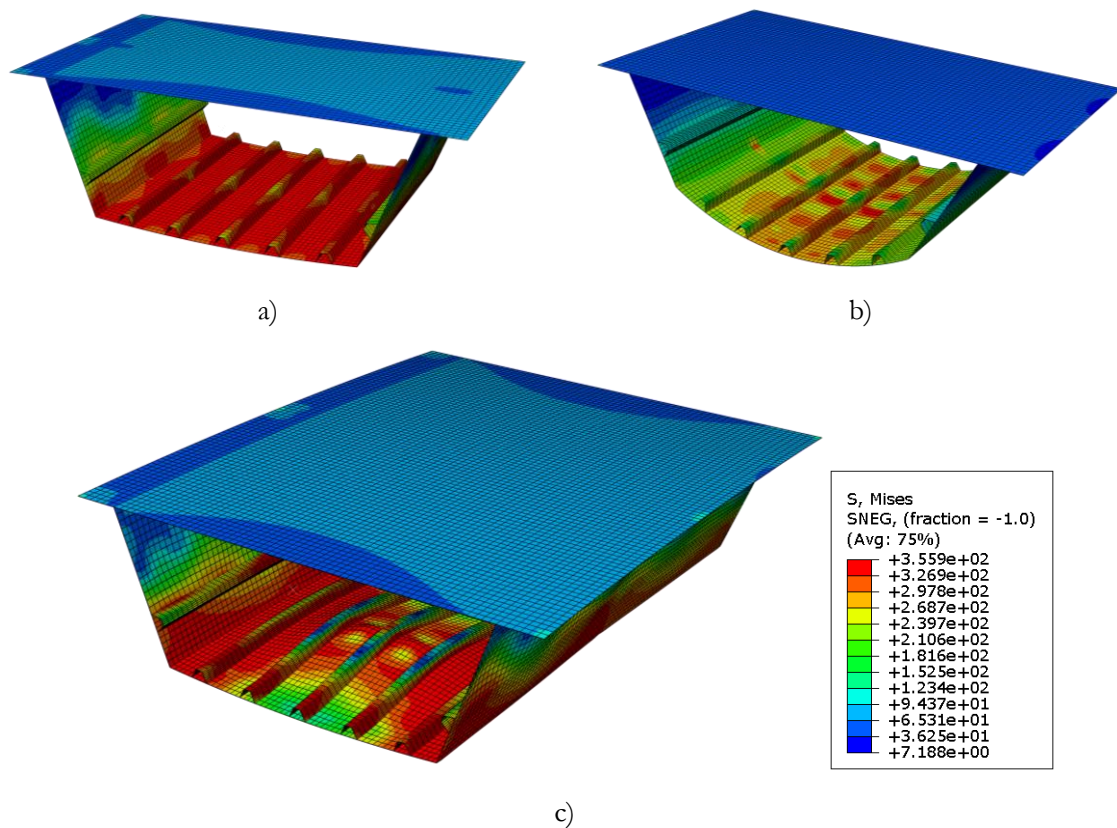


Fig. 8.2: Typical bending failure modes - FEM: a) yielding of bottom flange; b) local buckling; c) global buckling

This is completely in line with the analytical bending resistance model prescribed by EN 1993-1-5 (see 2.5.3), according to which, the bending resistance of a class 4 box-girder cross-section ($M_{eff,Rd}$) is determined in two consecutive steps:

- i) calculation of the effective cross-section of the stiffened bottom flange and
- ii) calculation of the effective cross-section of the stiffened web.

However, the use of this standard model to obtain analytically the bending resistance for the cross-sections considered in the parametric numerical study is not correct owing to two main problems. Firstly, the bottom flange of the cross-section is not flat, hence, these cases fall outside of the scope of the standard, which is limited to very low curvatures (*i.e.* $Z < 1$). Secondly, the standard method assumes that the bottom flange is subjected to a uniform axial compression, which is true in the case of a trapezoidal box-girder with a flat panel having the same constant distance from the neutral axis. On the other hand, in the case of a cross-section with a curved bottom flange, not all the parts of the panel are equally distant from the neutral axis, which means that the axial stresses are not uniformly distributed along with the panel but a stress gradient is always present. This further means that a clear distinction between the bottom flange and the webs in a cross-section with a curved bottom flange cannot be made, at least not in a way it is done for the trapezoidal box-girders.

The first of these two issues was tackled in [chapter 3](#) of the thesis. Namely, since the main difference between these bridge decks and conventional trapezoidal box-girder decks is the

presence of a transversely curved panel in the bottom flange, it is necessary to develop adequate design guidance to deal with curved panels as an individual structural element, subjected to axial compression. As shown in 3.3.3, numerous authors proposed different analytical methods to calculate the effective properties of a curved stiffened panel under uniform compression. Based on a thorough comparative study against the results from the experimental compression tests carried out in chapter 3, it was concluded that the methods proposed by Tran *et al.* [59] and in the OUTBURST research project [85] seem to be the most suitable for the estimation of the compressive resistance of the stiffened curved panels. However, the dimension ranges of the tested individual curved panels do not correspond to the realistic full-scale geometries encountered in bridge deck applications; hence, another numerical study is carried out in the forthcoming 8.2.2, where these two analytical methods are again assessed but only this time for an extended range of geometrical parameters potentially found in curved bridges.

Regarding the second problem, which disables a straightforward use of EN 1993-1-5 methodology for the calculation of the bending resistance of cross-sections with a curved panel, this topic is partly addressed in 6.4.6 of the thesis. Owing to the lack of the adequate design rules, two simplified design approaches were proposed and assessed against the experimental results on two box-girder bridge deck specimens: *i*) ‘Equivalent flat panel approach’ (Method 1) and *ii*) ‘Curved panel approach’ (Method 2).

Based on the results of the comparison, it was concluded that Method 2, in which the effect of the curvature is explicitly accounted for, gives a better estimation of the bending resistance, *i.e.* closer to the experimental results. However, since the conclusions are made based on a small data sample (*i.e.* two experimental tests), the validity of this design method needs to be verified for a wider spectrum of the geometrical parameters, with the dimensions encountered in real bridge applications. Hence, in chapter 7, using a numerical FE model validated against the experimental, a parametric study was carried out comprising 210 different geometries, and thus extrapolating the limits of the experimental campaign. Using the ‘Curved panel approach’ (Method 2), the bending resistance $M_{eff,Rd}$ is analytically calculated for all 210 geometries and statistically assessed in 8.2.3.

8.2.2 Study on the isolated bottom flange under pure compression

8.2.2.1 Scope of study

The aim of the non-linear numerical study presented herein is threefold: *i*) to determine the buckling resistance (and effective area) of the stiffened curved and non-curved panels under pure compression; *ii*) to compare the numerical resistances to the methods proposed by Tran *et al.* [59] and by OUTBURST research project [85] and *iii*) to assess the computed resistances for two different boundary conditions.

The geometry of the panels considered for this study is identical to the geometry of the bottom flanges of the box-girder cross-sections analyzed in chapter 7. Hence, this study may be understood as a supplementary sub-study, where the bottom flanges are extracted from the corresponding box-girder cross-sections and subjected to uniform compression, which is in accordance with the bending resistance design methodology proposed in this section.

The numerical FE model of isolated curved panels is obtained from the numerical model of the bridge cross-section, which was already validated against the experimental results in [section 7.2](#). Since the failure of the bridge cross-section subjected to 3-point bending is governed by the collapse response of the curved bottom flange dominantly subjected to compression, it may be considered for the actual problem that the FE model of an isolated panel is also validated to a certain extent, giving sufficiently realistic estimations of the real resistances. Therefore, all the details of the FE model (*e.g.* geometry, applied material, adopted mesh configuration) are addressed in [chapter 7](#).

In total, 60 different geometries are chosen from [7.3.3](#), where the main geometrical parameters are adopted to fall within the ranges found in real examples of bridges (*e.g.* $Z = 0-300$, $Z_{loc} < 0 - 18.75$, $\alpha = 0.5-1.5$, $b/t = 28-46$). In the case of flat stiffeners, only the thickness of $t = 25$ mm is considered, whereas, in the case of trapezoidal stiffeners, the thicknesses of 15 mm and 25 mm are considered for $n_{st} = 5$ and $n_{st} = 3$, respectively.

8.2.2.2 Imperfections

Regarding the initial geometric imperfections, as explained in [7.3.2](#), for the characterization of the M - V interaction behavior of a bridge deck cross-section, the adoption of the 1st buckling mode is a suitable solution since it contains the relevant failure mode depending on the applied M/V -ratio. Hence, in order to be consistent with the results of the corresponding bending resistance obtained in [chapter 7](#), also in this study the imperfections are modeled as equivalent geometric imperfections recommended by EN 1993-1-5, with a shape affine to the 1st eigenmode and the amplitudes defined in [Fig. 3.24](#).

It is needless to remind that the objective of this study is not to carry out another imperfection sensitivity analysis of curved panels under compression as this problem was addressed by the authors, whose design methods are under assessment in this section, and in [chapter 3](#) of the thesis. In other words, it is not attempted to define the most critical imperfection shape since that information should be already contained in the proposed design methods, being established as a lower bound of a much broader numerical study than one presented in this thesis. The purpose of this supplementary study is merely to compare the two design methods and to define, which one fits better the numerical results assuming the realistic bridge geometries. The adoption of the 1st buckling mode as the imperfection shape is justified also by the fact that both authors in their studies (Tran [\[8\]](#) and Piculin & Može [\[85\]](#)), assumed the 1st buckling mode as the imperfection shape and compared with other imperfection shapes. As discussed already in [chapter 3](#), it is to expect that the numerical models with the 1st eigenmode shape give safe results when compared to these analytical models; however, the same trend might be obtained even if the actual imperfection pattern is explicitly introduced in the model. This was confirmed by Piculin & Može [\[85\]](#), where the authors compared their experimental results of both flat and curved panels with two different numerical models: *i*) with the imperfection measured in the tests and *ii*) with the imperfection affine to the 1st eigenmode. The difference between the simplified model (ii) and the experimental results was even lower than that of the more realistic model (i), with an average difference of 3% and 8%, respectively.

8.2.2.3 Load and boundary conditions

The isolated simply-supported curved panels under uniform compression were studied in [chapter 3](#), where the numerical model was first calibrated against the experimental tests. Therefore, the same modeling technique for the application of loads and boundaries is adopted in this study (see [Fig. 3.22](#)).

However, several modifications are introduced to simulate the behavior of a bottom flange of a box-girder deck, which in reality is located between rigid (or semi-rigid) transversal cross-frames, *i.e.* diaphragms. To make the boundary conditions symmetric, the longitudinal displacements at the edge CD of panels are released (*i.e.* $u_z \neq 0$), and instead, the in-plane compressive load, q_x , is uniformly distributed as it is done on the edge AB (see [Fig. 3.22](#)). Hence, the panels are modeled as simply supported (hinged) on all four edges, but two different supporting conditions (constraints) are considered on the loaded edges AB and CD:

i) **'free'** - no constraints are accounted for, *i.e.* the rigidity of the transversal frames is neglected and the loaded edges are allowed to wave freely

ii) **'rigid'** - the nodes of the loaded panel ends (including stiffeners) are connected by rigid constraint equations, thus the edges remain straight.

The consideration of these two boundary conditions is not a novelty. On the contrary, in almost all previous investigations, addressed in [2.4.1](#), where both flat and curved panels were studied under pure compression ([\[8\]](#), [\[9\]](#), [\[10\]](#), [\[59\]](#), [\[60\]](#), [\[85\]](#)), the distinction between these conditions was emphasized. Moreover, in the most recent study on flat stiffened panels under uniform compression by Haffar *et al.* (2019) [\[155\]](#), the authors compared these two boundary conditions and showed that although both conditions are considered 'hinged' a significant difference in critical stress may be obtained (avg. 30-35%).

8.2.2.4 Model validation

Although the numerical model used in this study is almost identical to the one calibrated against the experimental tests, due to the modifications made in the supporting conditions, the model is validated with the results obtained by Tran [\[8\]](#) and Manco [\[10\]](#), who performed a similar study. Besides, the geometry of the specimens tested in [chapter 3](#) is downscaled for the tests, thus does not correspond to the real bridge cross-section geometry. To validate the model, the same conditions (geometry, imperfections, material, boundary conditions, etc.) from Tran's numerical model [\[8\]](#) are reproduced. In total, 6 models are compared, all of which have the same width and thickness of the panel ($b = 4800$ mm; $t = 12$ mm), and the same stiffener configuration (*i.e.* 8 flat stiffeners with $t_{st} = 16$ mm and $h_{st} = 150$ mm), whereas three aspect ratios ($\alpha = 0.5, 1.0$ and 1.5) and two curvatures ($Z = 0$ and $Z = 192$) are considered. The author considered the first global mode from eigenmodes with an amplitude of min ($a/400; b/400$), whereas the hinged boundary conditions are considered with 'rigid' constraint on both loaded edges. The numerical results are compared in terms of the ultimate resistance (in MN) in [Table 8.1](#).

Table 8.1: Validation of the numerical models with results from Tran [8] and Manco [10] for ‘rigid’ boundary conditions – ultimate resistance (MN)

	$Z = 0$				$Z = 192$		
	Tran [8]	Manco [10]	FEM	EC3-1-5	Tran [8]	Manco [10]	FEM
$\alpha = 0.5$	16.9	17.8	16.8	16.1	21.9	20.64	21.2
$\alpha = 1.0$	8.20	7.80	8.70	8.50	18.0	17.68	18.1
$\alpha = 1.5$	7.70	7.23	7.35	5.70	15.2	15.21	15.45

Based on the table it is possible to verify that the maximum difference between the numerical model used in this study (FEM) and the results from Tran [8] and Manco [10] is 6% and -5.6%, respectively, whereas the maximum difference between Tran [8] and Manco [10] is -6%. The differences between the three models may be explained by different software packages used, different mesh type and size considered, and different imperfection shapes adopted since the first global mode in LBA analysis is found based on the visual observation of eigenmodes. Nevertheless, the values of the maximum differences verified for all cases are low, so it is possible to consider the present numerical model validated.

As may be seen in Table 8.1, for the flat panels ($Z = 0$), the results from all three studies are compared with the values obtained using EN 1993-1-5. It is interesting to observe that the numerical results for the considered geometry may differ considerably from the design codes, and it seems that the difference is particularly high for higher aspect ratios. For the aspect ratio $\alpha = 0.5$, $\alpha = 1.0$, and $\alpha = 1.5$, the maximum differences are respectively equal to 10.56%, -8.23%, and 35.1%, whereas on average from three numerical models, the differences are respectively 6.63%, 4.7%, and 30.3%.

8.2.2.5 Discussion of results

The results from 120 numerical analyses, coming from 60 different geometries and 2 types of boundary conditions - ‘free’ and ‘rigid’ are here discussed. For each model, a nonlinear analysis with initial imperfections (GMNIA) is performed to determine the ultimate compressive resistance, defined as the maximum load on the corresponding load-displacement curve. The main objective of the study is to assess the influence of the most relevant parameters (curvature Z , aspect ratio α and boundary conditions) on the ultimate resistance of stiffened panels, but also to compare the results with two analytical models from Tran *et al.* [59] and by OUTBURST research project [85].

The results are divided into two groups based on the stiffener typology, *i.e.* flat or trapezoidal, which are presented in Fig. 8.3 and Fig. 8.4, respectively. These two groups are additionally subdivided based on the number of stiffeners, *i.e.* $n_{st} = 3$ and $n_{st} = 5$. In all graphs, the reduction factor ρ_c on the vertical axis is plotted against the curvature parameter Z . The reduction factor is obtained as the ratio between the maximum axial force obtained in numerical simulations and the plastic resistance of the panel ($N_{pl} = Af_f$). Besides the numerical results for two types of boundary conditions (free and rigid), in each graph, the results obtained analytically from two aforementioned methods are presented, as well as the results obtained from EN 1993-1-5, calculated for the corresponding flat panel ($Z = 0$).

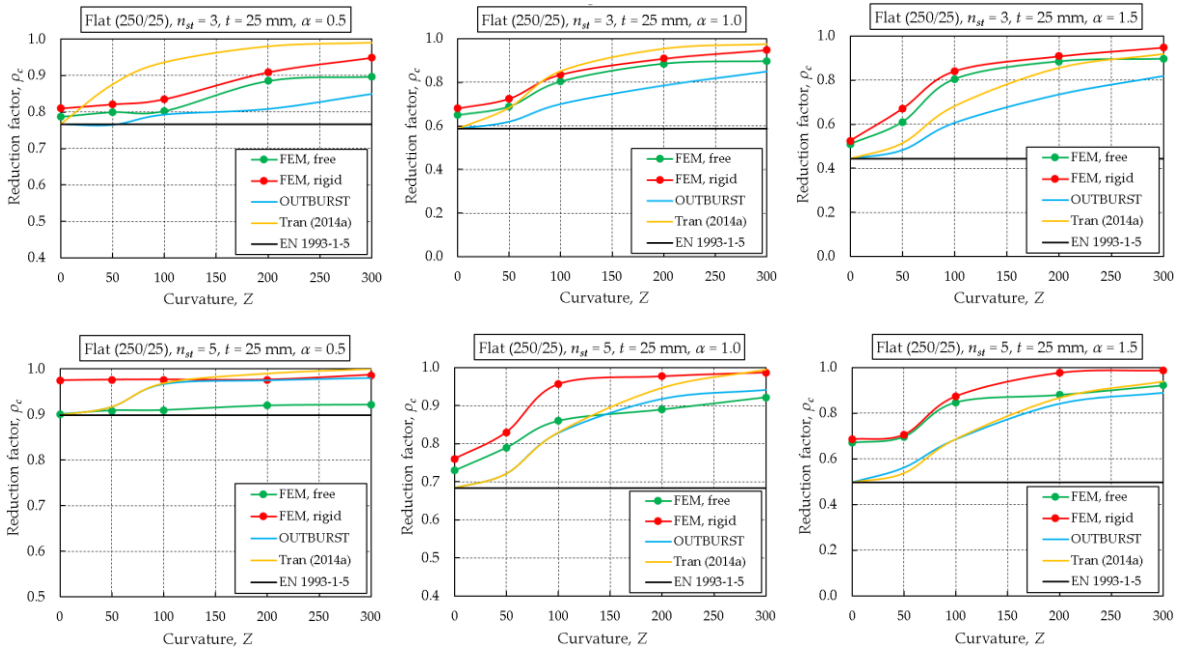


Fig. 8.3: Comparison between FEM and analytical results for panels with flat stiffeners

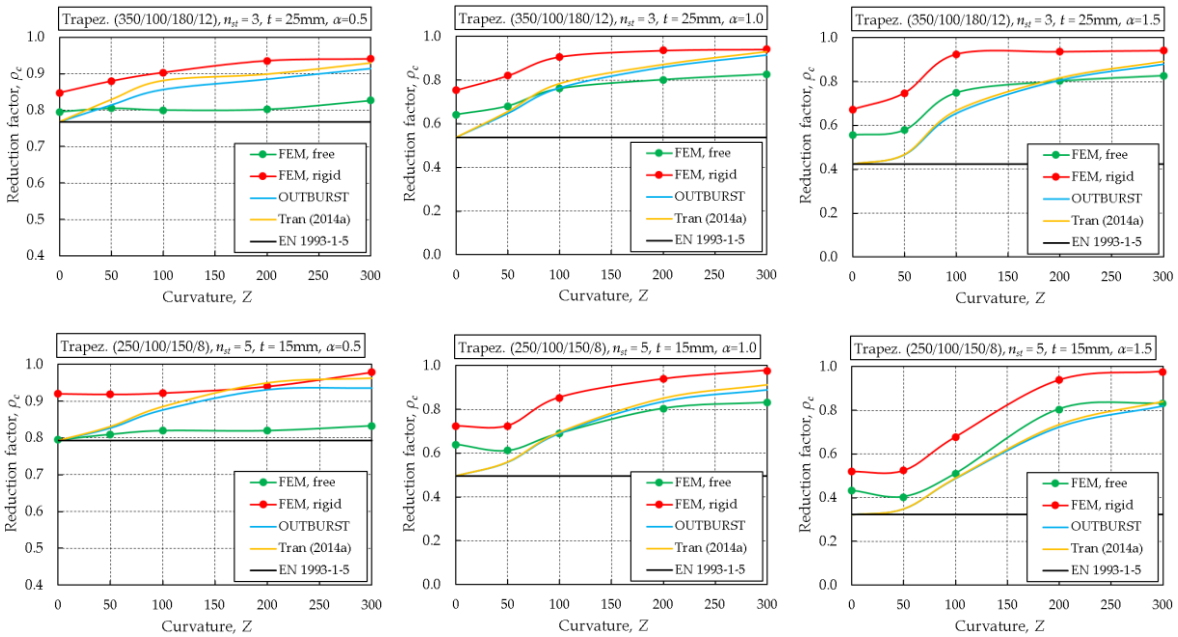


Fig. 8.4: Comparison between FEM and analytical results for panels with trapezoidal stiffeners

Based on the presented results, several conclusions may be drawn, some of which were already discussed in [chapter 3](#).

- The curvature undisputedly increases the ultimate strength of panels, which is particularly noticeable for higher aspect ratios (*i.e.* $\alpha \geq 1$);
- As expected, the ultimate resistance strongly depends on the boundary conditions, despite all of them being nominally simply-supported. For all considered panels, a higher resistance is obtained for ‘rigid’ boundary conditions (on average 11.5%).

- It is worth saying that the difference is particularly emphasized in the case of trapezoidal stiffeners (on average 17.7%), whereas, in the case of flat stiffeners, the difference between the two boundary conditions drops to 5.5%. This may be attributed to the fact that the application of rigid diaphragms at the plate ends restrains additional DOFs, thus forcing the same rotation at the plate ends, which eventually tries to deform all longitudinal stiffeners similarly. Hence, the force required for this deformation to occur is directly related to the torsional rigidity of the longitudinal stiffeners, which is known to be substantially higher for a closed trapezoidal stiffener when compared to an open flat stiffener that possesses merely its Saint-Venant torsional stiffness. As a consequence, on one side, the rigidity of a trapezoidal stiffener against flexural-torsional buckling is higher, while on the other side, being hardly twisted, higher deformation energy is required, resulting in large strain deformations of the panels between the stiffeners and thus increased ultimate load.
- For short ($\alpha = 0.5$) heavily stiffened plates ($n_{st} = 5$), the ultimate resistance is governed by the local buckling of subpanels (see Fig. 8.2b), while the global buckling has little (if any) effect on the ultimate resistance. Hence, for these panels, an increase of curvature does not necessarily increase the panel's ultimate resistance with respect to the flat ones since the local curvatures of subpanels in bridge design rarely exceed $Z_{loc} < 15$ as shown in Fig. 2.6;
- Consequently, the favorable effect of curvature on the ultimate resistance is particularly pronounced for longer and lightly stiffened plates (flat stiffeners, or light trapezoidal stiffener – Type 2 in Fig. 7.13), where, for instance, the resistance for $Z = 300$ can be up to 2 times higher compared to $Z = 0$;
- Furthermore, owing to the high inertia of the cross-section in the case of panels with higher curvatures, no global buckling (plate-type or column-type) occurs, as shown also in experimental results (see Table 6.7). This means that failure is governed by local buckling of subpanels in combination with material yielding. Consequently, the resistance of highly curved panels converges towards a constant value regardless of the aspect ratio since the local buckling is independent of the panel length. This confirms the observations found in the literature by multiple authors [8], [10], [85];
- Finally, it is discovered that in contrast to flat plates, in the case of highly curved panels ($Z \geq 200$), due to high cross-section inertia and strong arch effect, the type and size of longitudinal stiffeners have only a negligible influence on the ultimate resistance ($\Delta_{max} < 1\%$), at least for the stiffeners class 3 considered in this study.

These findings present some of the crucial advantages of curved panels used in these innovative bridge deck cross-sections since considerable savings could be made by reduction of the number of the transversal cross-frames (*i.e.* diaphragms) but also by the reduction of the number and size of longitudinal stiffeners.

The numerical results are compared with the resistance calculated from EN 1993-1-5 [11], and the results are summarized in Fig. 8.5. Since the code is limited to flat plates only, the resistance of curved panels is calculated assuming an equivalent flat stiffened panel, as shown in Fig. 6.39.

The reason for this comparison is merely to assess the conservatism of the design code when used for the calculation of the curved panels.

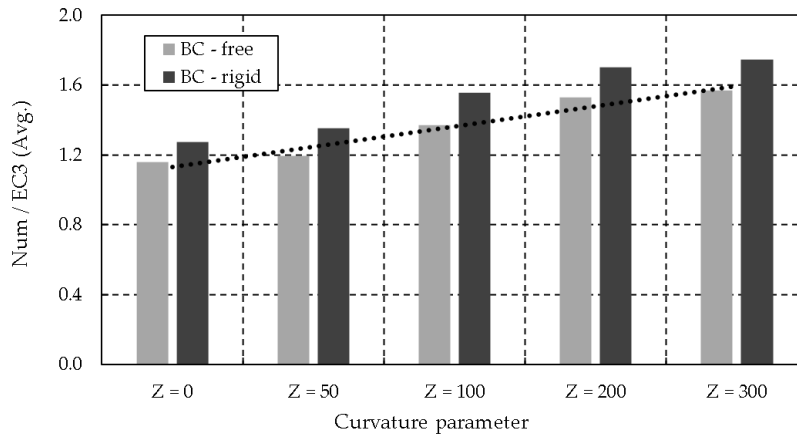


Fig. 8.5: Numerical results vs EN 1993-1-5 [11] – comparison of the ultimate resistances for various curvatures Z (avg.)

The figure indicates that the difference between the GMNIA-based resistances and the EC3-based resistances increases with the curvature from approximately 21.7% for $Z = 0$ (considering both ‘free’ and ‘rigid’ BC), up to 66% for $Z = 300$, which confirms the observations stated in [chapter 3](#) of the thesis. To have a better insight on the influence of different parameters varied in the study, the mean differences between numerical results and EN 1993-1-5 [11] are provided in [Table 8.2](#) and [Table 8.3](#), separately for two types of boundary conditions.

Table 8.2: Numerical results vs EN 1993-1-5 [11] – comparison of the ultimate resistances for ‘free’ boundary condition (avg.)

	$Z=0$	$Z=50$	$Z=100$	$Z=200$	$Z=300$	Mean
$\alpha = 0.5$	1.02	1.03	1.03	1.06	1.08	1.05
$\alpha = 1.0$	1.17	1.21	1.36	1.48	1.52	1.35
$\alpha = 1.5$	1.29	1.35	1.72	2.04	2.10	1.70
Mean	1.16	1.20	1.37	1.53	1.57	1.36

Table 8.3: Numerical results vs EN 1993-1-5 [11] – comparison of the ultimate resistances for ‘rigid’ boundary condition (avg.)

	$Z=0$	$Z=50$	$Z=100$	$Z=200$	$Z=300$	Mean
$\alpha = 0.5$	1.10	1.12	1.13	1.17	1.20	1.14
$\alpha = 1.0$	1.28	1.36	1.56	1.65	1.70	1.51
$\alpha = 1.5$	1.44	1.58	1.99	2.29	2.35	1.93
Mean	1.28	1.35	1.56	1.70	1.75	1.53

It is interesting to observe that the difference in the case of a flat panel ($Z = 0$) for ‘free’ and ‘rigid’ supports is respectively 16% and 28%, hence significant. The difference of 28% is justified by the fact that the code does not account for the additional restraints applied in the model on the loaded edges; however, in the bridge design, these boundary conditions (*i.e.* ‘rigid’) are much closer to the realistic ones, which means that the design code, in this case, is over-conservative.

As for the ‘free’ supported plates, which should completely correspond to the ones in the code, the difference is noticeable only for higher aspect ratios (*e.g.* 29% for $\alpha = 1.5$). A relatively poor agreement in results is due to several inaccuracies:

(i) In the case of plates with trapezoidal stiffeners, the design standard does not account for the positive effect of the torsional rigidity, which leads to an underestimation of the resistance. This may be confirmed by comparing the mean differences for ‘free’ supported plates, but separately with flat and trapezoidal stiffeners, which is respectively equal to 11.7% and 19.8%.

(ii) On the other hand, in the case of long flat plates, either with flat or light trapezoidal stiffeners, the global plate-type buckling prevails, with significant participation of the interaction parameter ξ , defined by Eq.(2.30). This leads to another two groups of uncertainties that have been recently rigorously studied:

(ii-a) First, the buckling curve from EN 1993-1-5 (Winter’s curve) used for plate buckling of plates subjected to direct stresses has been criticized lately by numerous authors (Haffar *et al.* [155], Schillo *et al.* [156], Martin *et al.* [157], Sinur [158]), to name a few. In all of the mentioned studies, the authors claim that a set of formulae given in Annex A of EN 1993-1-5 for the calculation of the critical stresses of stiffened plates do not precisely consider all the possible parameters, such as more realistic boundary conditions (edge constraints found in bridges) and torsional rigidity of stiffeners. Consequently, an underestimation of the critical stresses was reported (*e.g.* up to 31.4% according to Haffar *et al.* [155]). Besides the over conservative critical stress formulae, the authors also agreed that the critical stress-resistance relation ($\lambda - \rho$) is too optimistic.

(ii-b) In addition to the plate-type buckling formulae, the interaction formula given by Eq.(2.29) was also questioned in recent years. Tran [8] even proposed a modified formula, given by Eq.(2.74), which fits better the results obtained in a large numerical study.

Although the flat stiffened plates are not the topic of this thesis, it is important to highlight these inconsistencies between the standard and the numerical results found by different authors since the two methods for curved panels, that are under scrutiny in this study, are based on the same design philosophy from the standard EN 1993-1-5 (see 2.5.1.3).

Finally, in Fig. 8.6, the FEM results are compared with both analytical methods, *i.e.* by Tran *et al.* [59] and by OUTBURST research project [85], where the mean differences between the ultimate resistances are presented separately for two end supports (‘free’ and ‘rigid’) and various curvature parameters ($Z > 0$).

Based on these two graphs, it may be stated that the two methods give virtually identical results. Namely, in contrast to Fig. 8.5, in both cases, a descending trend is noticed with the increase of curvature. This may be attributed to the aforementioned dominant local buckling of the subpanels with almost no effect of the global buckling. As shown before in Table 6.7, in the case of curved panels with a strong arch effect, the critical stresses for column-type buckling ($\sigma_{cr,c}$), although physically impossible, is much higher than that of the plate-type behavior ($\sigma_{cr,p}$), resulting in the interpolation parameter ξ equal to 0 for all considered cases (see Eq.(2.30)). Hence, the effectiveness of a stiffened panel is obtained only from the column buckling reduction

factor (χ_c), whereas the plate post-buckling resistance is neglected. This further means that the uncertainties and inaccuracies found in formulae from Annex A of EN 1993-1-5 and in the interpolation formulae, addressed in the previous few paragraphs, are avoided in the calculation of the ultimate resistance of curved panels. Therefore, the higher the curvature, the more the difference between the FEM results and analytical results relies merely on the quality of the methods for the assessment of the local buckling phenomenon of curved subpanels, which are quite accurate for both Tran's and OUTBURST methods (*i.e.* -6% and -2% for 'free' supports, and 4% and 8% for 'rigid' support).

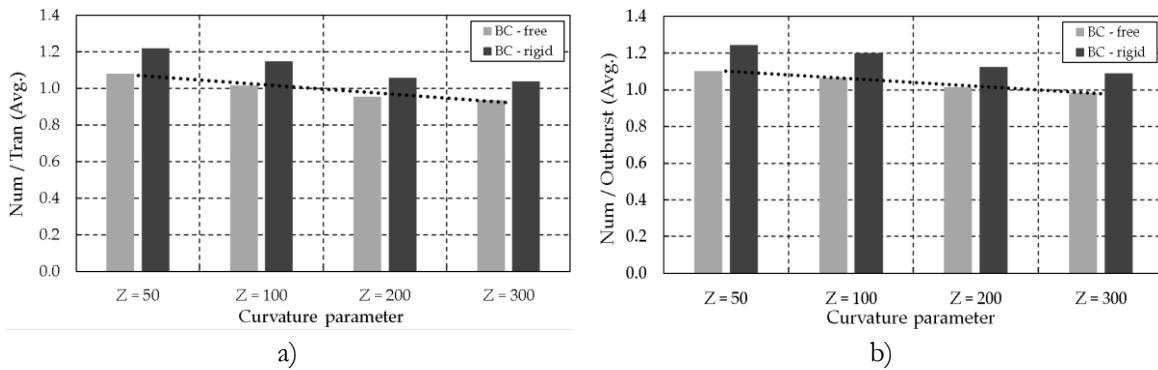


Fig. 8.6: Comparison of the ultimate resistances for various curvatures (avg.): a) FEM vs Tran *et al.* [59] and b) FEM vs OUTBURST [85]

To choose a more suitable method, these two design proposals are compared against each other in Fig. 8.7 for the entire scope of 60 different geometries studied.

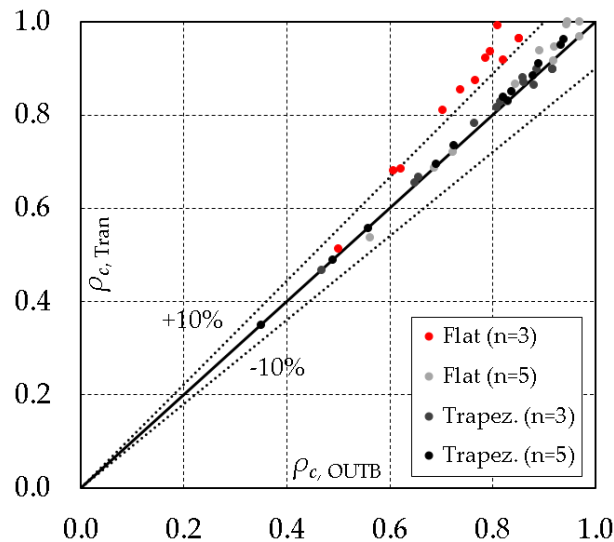


Fig. 8.7: Comparison of methods by Tran *et al.* [59] and OUTBURST [85]

Based on Fig. 8.7, it may be concluded that the difference between the two methods for the considered range of geometrical parameters is arguably small (in average 4.6%), with the highest difference of 14% for lightly stiffened panels, with 3 flat stiffeners (points in red in Fig. 8.7). A slightly higher disagreement in results may be attributed to different approaches that these two methods assume for the assessment of the local buckling of the subpanels. Namely, in Tran's proposal, the local buckling is determined for a corresponding flat plate, neglecting the local

curvature, whereas the method proposed within OUTBURST research project [85], the effect of local curvature is explicitly accounted for, by applying the expressions developed by Martins *et al.* [78] for unstiffened curved panels. Therefore, the flat panel approach (used by Tran) gives optimistically higher local reduction factor (ρ_{oc}) than a corresponding curved sub-panel with $Z_{loc} = 18.75$ since small local curvature has a less favorable post-buckling response, being more sensitive to local imperfections ([8],[9],[10]). In other cases, with 5 stiffeners and/or trapezoidal stiffeners considered in this study, the subpanels have considerably low local curvature ($Z_{loc} < 8$), thus the effect of curvature is practically lost, leading to a negligible difference between the two methods (in average 2%).

In addition, in Fig. 8.8 and Fig. 8.9, as well as in Table 8.4, the two methods are statistically compared against the FEM results for various categories of models, divided into groups based on the support conditions, type of stiffeners, curvature parameter, and the aspect ratio. In general, the results show that the method proposed by Tran is slightly less conservative for the studied range of parameters; however, the method seems to give overly optimistic resistance of panels (max. error 15%).

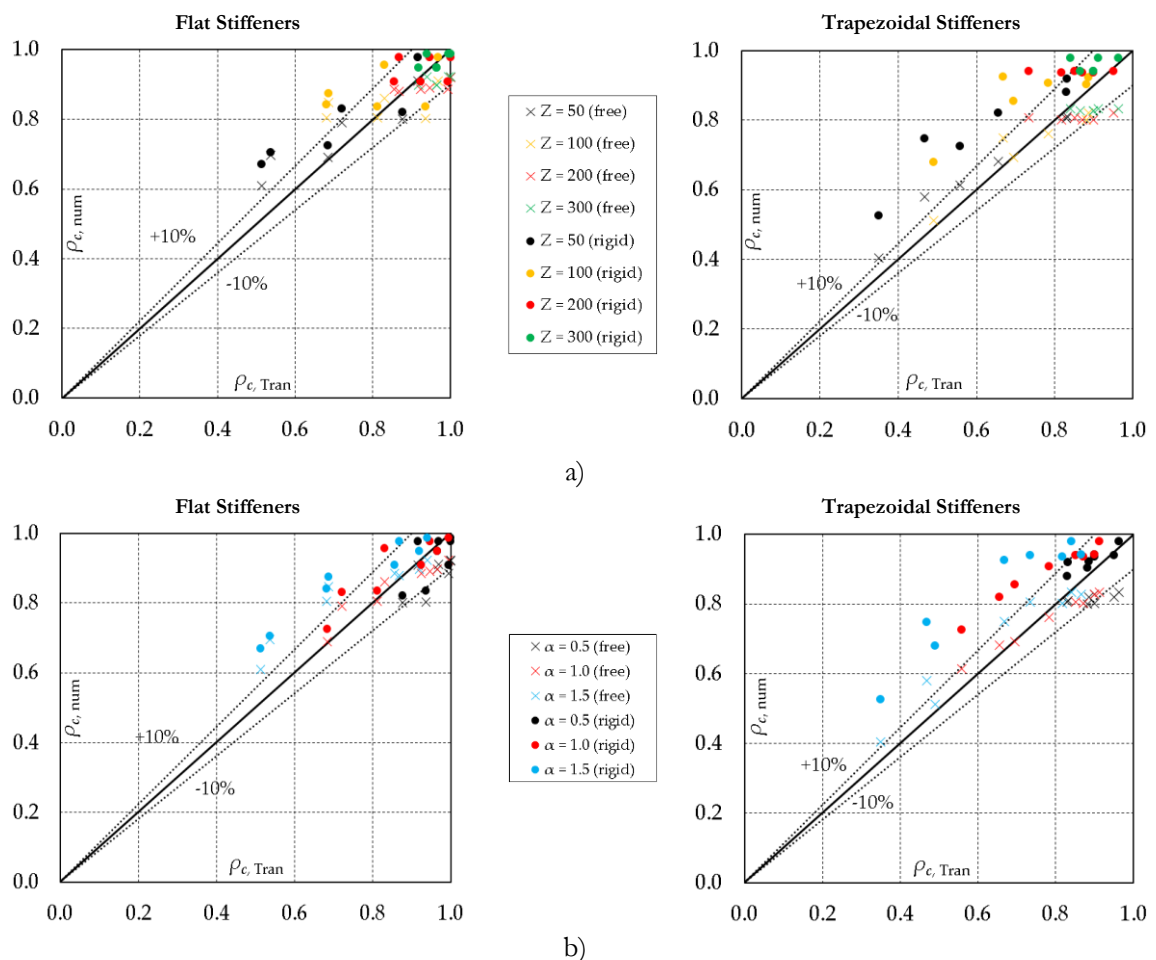


Fig. 8.8: FEM vs Tran *et al.* [59] in a function of a) Z parameter and b) aspect ratio

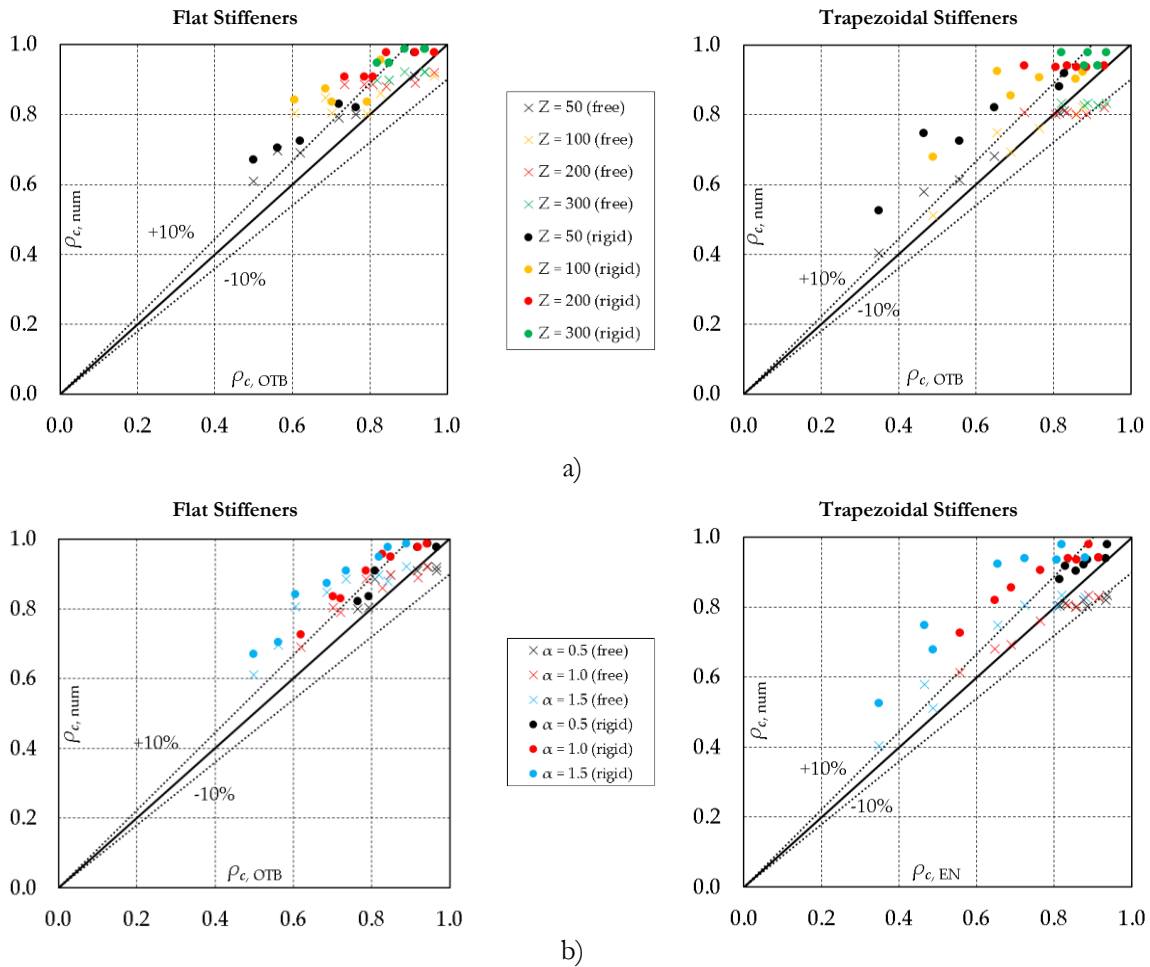


Fig. 8.9: FEM vs OUTBURST [85] in a function of a) Z parameter; b) aspect ratio

Regarding the type of stiffeners, as indicated in Table 8.4, a better agreement between the results is achieved for flat stiffeners than the trapezoidal ones since both methods fail to account adequately for the torsional rigidity of trapezoidal stiffeners. The same may be stated for the results of a comparison between the two boundary conditions. Namely, both methods are inspired by the EC3 formalism, hence not accounting for ‘rigid’ constraints on the loaded edges, which explains an underestimation of the results by 12% and 16%, respectively, for two methods.

Table 8.4: Comparison between methods by Tran *et al.* [59] and OUTBURST [85] with respect to the FEM results

	Flat stiffener		Trapezoidal stiffener		‘Free’ Support		‘Rigid’ Support	
	Tran	Outburst	Tran	Outburst	Tran	Outburst	Tran	Outburst
St. Dev.	0.12	0.11	0.16	0.16	0.11	0.11	0.15	0.14
Mean	1.04	1.07	1.08	1.09	1.0	1.04	1.12	1.16
CoV (%)	11.5	10.3	15.0	14.8	10.5	10.3	13.5	11.6

Finally, the figures show that the highest difference between the FEM results and both analytical methods is obtained for longer ($\alpha \geq 1$) and less curved panels ($Z \leq 100$), *i.e.* for the panels that dominantly exhibit global buckling mode (see Fig. 8.2c). Since both methods use the

conservative formulae for plate-type buckling and interpolation equation from the standard, it may partly explain the underestimated values of the panels' resistance.

To sum up, based on the comparative study presented herein, one may agree that the choice on the 'better' method between the two is not straightforward since Tran's proposal seems to be at times too optimistic, whereas the method developed within the OUTBURST research project for certain configurations give too safe results. In the case of the bridge deck design, where the recent trend is to use curved panels with higher curvatures for aesthetical reasons, due to relatively small aspect ratios and heavily stiffened bottom flanges, it may be claimed that both methods would give the same or almost identical results. This is due to the aforementioned strong arch effect that prevents the global buckling to occur, thus both methods converge to the same simplified method, in which it is required to determine the effective area merely due to the local buckling of subpanels. In such case, the accuracy of both methods is significantly increased since multiple uncertainties discovered in EN 1993-1-5 are avoided (*i.e.* difficulty in definition of the critical stress in terms of the edges constraints and rigidity of longitudinal stiffeners, the applicability of the Winter's curve, adequacy of the interpolation equation, etc.). Therefore, in the case of bridge decks, where the local curvature parameter of the bottom curved flange rarely exceeds $Z_{loc} < 15-20$ (see Fig. 2.6), technically, both methods may be equally applied.

Without any particular preference, the author of the thesis decided to use the method developed within the OUTBURST research project for the determination of the bending resistance in the following section, despite being slightly more conservative and more complicated. The only reason is that the method explicitly accounts for the unfavorable post-critical behavior of the curved panels with small-to-intermediate values of the local curvature parameter.

8.2.3 Bending resistance – FEM vs Analytical model

Using Eq.(2.116), the bending resistance is calculated analytically for all 210 geometries of box-girder cross-sections with a curved (and flat) stiffened bottom flange, shown in section 7.3. The results are subsequently compared with the corresponding bending resistance (case M_o , see Fig. 7.17), obtained from computer simulations in section 7.4.

As stated before, for the calculation of the bending resistance of a class 4 box-girder cross-section ($M_{eff,Rd}$), the *Curved panel approach* (*i.e.* Method 2 in 6.4.6) is used, being the method that explicitly accounts for the effect of curvature in the bottom flange. Similar to the method for trapezoidal box-girders, given by the actual design code, the determination of the effective cross-section modulus (W_{eff}) is done in two steps, described in detail in 2.5.3.

- I - calculation of the effective cross-section of the stiffened bottom flange
- II - calculation of the effective cross-section of the stiffened web

For the application of this bending analytical model, it is necessary first to specify clearly what is the bottom flange and what is the web in these non-trapezoidal cross-sections. Therefore, using the analogy with the method used for the trapezoidal cross-sections from EN 1993-1-5 [11], a simplification is adopted, according to which the entire curved panel is assumed to be the bottom flange, subjected to uniform axial compression ($\psi = 1.0$), as shown in Fig. 6.39 and in Fig. 8.10.

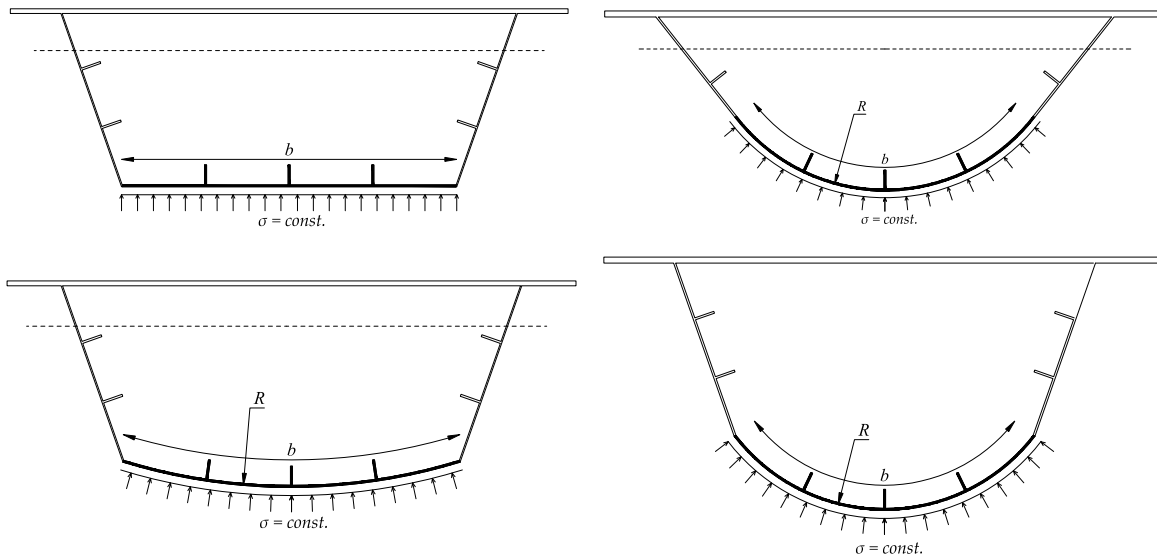


Fig. 8.10: Definition of the ‘bottom flange’ (in black) in box-girders with curved bottom flange for various Z parameters

Namely, such simplification, although conservative, is very suitable for widespread engineering practice since it corresponds to what is currently done in EN 1993-1-5 [11]. In this thesis, the OUTBURST design method reported by Piculin & Može [85] is considered, whose all required steps for the determination of the local and global buckling of curved stiffened panels are described in detail in 2.5.1.

Once the effective area of the bottom flange is determined, a new position of the neutral axis is found and the rules in Annex A from EN 1993-1-5 [11] for the determination of the effective area of stiffened flat webs in bending are applied, in accordance with Fig. 2.28 and Table 2.10. The web is the part of the cross-section between the top flange and the bottom curved flange, defined in Fig. 8.10.

An example with all the required steps for the determination of the bending resistance of a cross-section with a curved bottom flange is shown later in Annex D (D.2). In Fig. 8.11, the normalized bending resistances, obtained numerically (\bar{M}_{num}) and analytically (\bar{M}_{analy}) (as characteristic values, without partial factors) are compared for various Z parameters and aspect ratios, illustrating also the mean values of the $\bar{M}_{\text{num}}/\bar{M}_{\text{analy}}$ ratio for different categories.

Fig. 8.11 shows that the numerical results give considerably higher bending resistance for all 210 studied geometries. It may be stated that the difference of approximately 40% is constant, regardless of the curvature parameter and the type of cross-section (*i.e.* $H = \text{const.}$ and $H = \text{variable}$), whereas the influence of the aspect ratio on this difference is much more pronounced. A similar trend was noticed and discussed in 8.2.2 (see Fig. 8.9b), where the isolated panels under pure compression are studied. It was concluded that the difference between the FEM and analytical results is particularly high for longer ($\alpha \geq 1$) and less curved panels ($Z \leq 100$), where the global buckling mode of the bottom flange may occur (see Fig. 8.2c), requiring the use of conservative formulae for the estimation of the critical plate-type stress and interpolation equation from the standard.

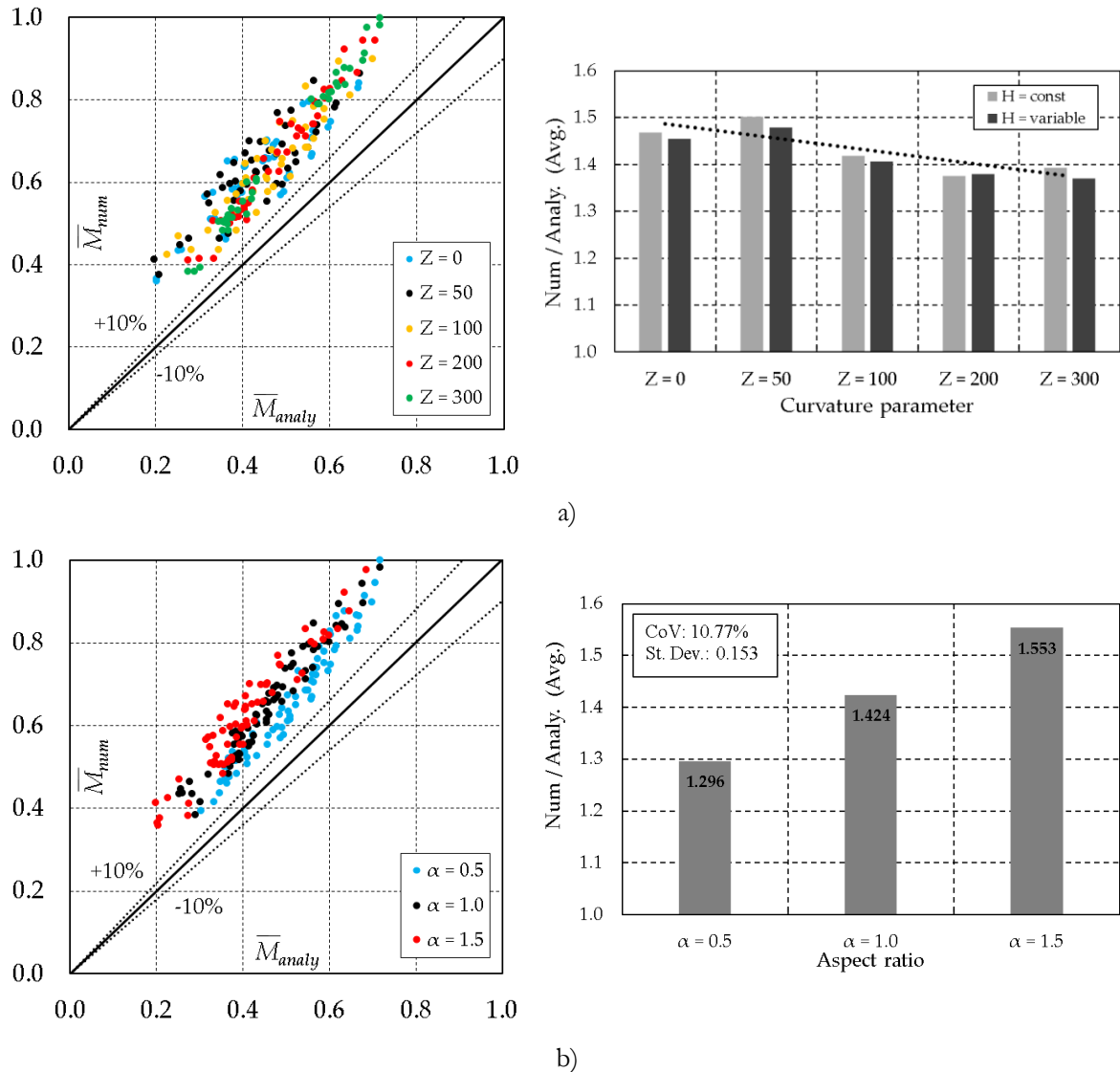


Fig. 8.11: Comparison of FEM results with the analytical model: a) for various Z parameters and b) various aspect ratios

These results for the $\bar{M}_{num}/\bar{M}_{analy}$ ratio, regardless of the curvature parameter, are mainly attributed to two inaccuracies: (i) the analytical method does not account for the additional restraints on the loaded edges, applied in the FE model to simulate the rigid transversal frames (diaphragms) that undoubtedly exist in a real bridge deck; and (ii) the analytical model assumes the most unfavorable uniform axial stress gradient across the height of the curved bottom flange.

The first of these two inaccuracies was discussed in 8.2.2, but merely on the level of the isolated bottom flanges under axial compression that are analyzed for two types of boundary conditions - ‘free’ and ‘rigid’. The difference between the GMNIA-based resistances and the EC3-based resistances in the case of flat plates ($Z = 0$) with ‘rigid’ supports reached a significant 28% (see Table 8.3). On the other hand, the difference between the FEM results and the analytical method used for curved panels ($Z > 0$) showed a decreasing trend with the curvature (see Fig. 8.6), owing to the local buckling phenomenon that prevails due to a strong arch effect, which consequently reduces the number of inaccuracies in the analytical model and reduces the

difference. Therefore, in the case of the whole box-girder cross-section subjected to bending, the difference between the numerical and analytical results also seem to show a slightly descending trend (see Fig. 8.11 - right). However, the consistency of a high $\bar{M}_{\text{num}}/\bar{M}_{\text{analy}}$ ratio is kept due to the second inaccuracy specified above, *i.e.* the higher the curvature of the bottom flange, the more conservative becomes the assumption of a bottom flange subjected to a uniform compression ($\psi = 1.0$). In fact, the conservatism of this assumption is two-fold: (i) firstly, the effective area of the bottom flange (A_{eff}) is smaller than the one obtained in the computer simulations; and (ii) secondly, this conservative estimation of the effective bottom flange is indirectly reflected on the estimation on the effective area of the webs too. Namely, the more non-effective the bottom flange, the higher the new position of the neutral axis and subsequently the less favorable the stress gradient along with the web height. This means that the webs in the analytical model are calculated for a more severe axial stress distribution, which additionally underestimates the bending resistance. And last but not the least, although the conservatism of the design standard was multiple times emphasized, the method for the calculation of the effective area of webs under variable axial stresses, given in Annex A of EN 1993-1-5 was never assessed in this thesis. However, the recent work by Haffar *et al.* [155] reveals that the method for the determination of the plate-type critical stress from Annex A of EN 1993-1-5 is particularly conservative in the case of non-orthotropic flat plates (*i.e.* with $n_{st} < 3$). This might partly justify the difference obtained between \bar{M}_{num} and \bar{M}_{analy} since for all cross-sections considered in the presented parametric study, the number of stiffeners on the flat webs was either equal to $n_{st} = 1$ or $n_{st} = 2$. Furthermore, the webs and the longitudinal stiffeners are restrained by ‘rigid’ support, which may only enlarge the $\bar{M}_{\text{num}}/\bar{M}_{\text{analy}}$ ratio.

In conclusion, despite the significant difference between the FEM and analytical results, the proposed bending resistance model is simple to apply from the engineering standpoint, and it even returns slightly less conservative results than the model from EN 1993-1-5 used for the trapezoidal box-girders with a flat bottom flange (40% vs 48%). However, since the proposed model is based on the same conservative formulae from EN 1993-1-5, a better estimation of the bending resistance of box-girders with curved panels may be achieved whenever the formulae in the design code account for several relevant parameters (*e.g.* level of edge constraint, the torsional rigidity of the stiffeners, lightly stiffened plates ($n_{st} < 3$), etc.). The proposed model is further statistically evaluated in section 8.5, where the partial factor (γ_M) is calculated.

8.3 Shear resistance model

8.3.1 Introduction

To complete the assessment of the safety and applicability of the M - V interaction equation proposed by Jäger *et al.* [139] in the case of box-girder bridge cross-sections with a curved bottom flange, besides the moment resistance ($M_{\text{eff,R}}$) tackled in section 8.2, it is necessary to determine also the shear resistance ($V_{\text{bw,R}}$), which is the topic of this section.

In chapter 7, the shear resistances are determined using the verified numerical model (case V , see Fig. 7.17) for 210 different geometries of box-girder cross-sections with a curved (and flat) stiffened bottom flange. Depending on the web stiffener configuration and the slenderness of

the web sub-panels, two distinct shear failure modes are attained: (1) global buckling and (2) local sub-panel buckling, as presented in Fig. 8.12a and Fig. 8.12b, respectively. In fact, the geometry of the webs is deliberately chosen in such a way to allow for the two typical situations covered by the Eurocode-based shear buckling resistance model, described in 2.5.2. In the presented example, two failure modes are achieved by varying merely the thickness of the web t_w . Namely, for thinner webs with relatively high sub-panel slenderness (*i.e.* $h_w/t_w > 72\varepsilon/\eta$ according to EN 1993-1-5), local buckling occurs, whereas for thicker and lightly stiffened webs, the global shear failure becomes dominant.

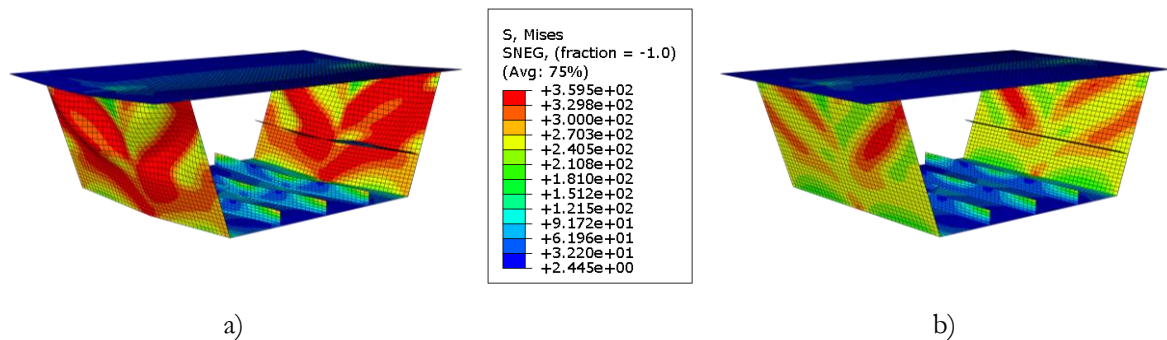


Fig. 8.12: Typical shear failure modes - FEM: a) global buckling and b) local buckling

Similarly to the bending resistance model, the principal objective is to use the existing rules from EN 1993-1-5 for flat stiffened webs and to extend and adapt them to allow for the determination of the shear resistance of this non-conventional box-girder cross-section. However, unlike the bending resistance model, where the behavior of the curved bottom flange under axial compression was studied and reported by numerous authors in the literature, to the best of the author's knowledge, no study has ever dealt with the shear resistance of the bridge deck cross-sectional geometries studied in this thesis. Therefore, to define a new analytical shear resistance model, it is necessary to carry out several intermediate steps that are systematically presented in 8.3.2 to 8.3.5. Furthermore, for the development of a new shear resistance model, which is the main goal of this section, both failure modes are accounted for.

8.3.2 Comparison of EN 1993-1-5 and FEM results

Owing to the lack of the adequate design rules for the studied box-girder cross-section typology, the starting point is to compare the FEM-based shear resistance (V_{num}) presented in section 7.4 and the shear resistance calculated from EN 1993-1-5 [11] (*i.e.* V_{EC3}). Such comparison is demonstrated already in 6.4.6 (see Table 6.8), where the EC3-based results are compared with the experimental ones; however, it was concluded that the results were not representative since both test specimens failed dominantly in bending. This limitation is overcome in the parametric numerical study, where, by controlling the M/V ratio in the cross-section, it is possible to attain a shear failure mode and the corresponding shear resistance.

The procedure from the standard for the calculation of the shear resistance of a stiffened web is described in detail in 2.5.2. However, for the comparison presented herein, it is necessary to emphasize the assumptions adopted:

(1) Due to the presence of transversal stiffeners (diaphragms), the shear resistance is calculated by Eq.(2.96) assuming the *rigid* end posts, hence the required shear reduction factor is obtained by Eq.(2.98);

(2) Only the contribution from the web ($V_{bw,R}$) is considered, while, due to the uncertainty, the contribution from the top and bottom flanges ($V_{bf,R}$) is omitted;

(3) Since the design standard is limited to flat plates, the shear resistance is calculated only for a flat part of the web with the height marked as $h_{w,flat}$ in Fig. 8.13, *i.e.* the part between the top flange and the bottom flange, as defined in Fig. 8.10.

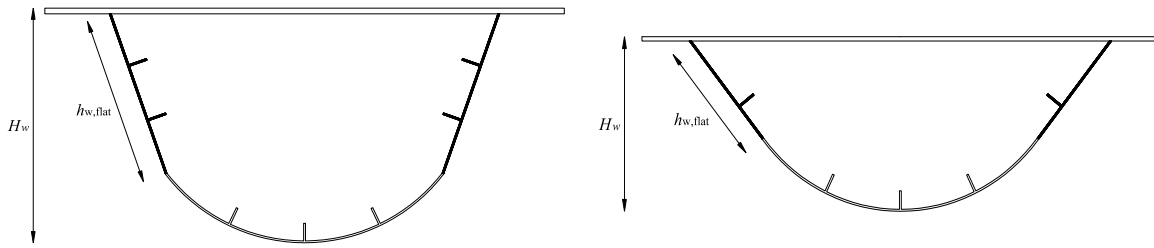


Fig. 8.13: Definition of the ‘flat web’ (in black) in box-girders with a curved bottom flange

(4) In the current study, only webs with 1 or 2 longitudinal stiffeners and an aspect ratio of less than $\alpha < 3.0$ are studied, hence the Eq.(2.102) from Annex A.3 of EN 1993-1-5 for the definition of the shear buckling coefficient k_τ is required. However, this expression was originally proposed by Beg [159] in a slightly different form, given by Eq.(8.1):

$$k_{\tau,Beg} = 4.1 + \frac{6.3 + 0.05 \frac{10.92 I_{sl}}{t_w^3 h_w}}{\alpha^2} + 1.44 \sqrt[3]{\frac{10.92 I_{sl}}{t_w^3 h_w}} \quad (8.1)$$

By comparing Eq.(2.102) and Eq.(8.1), it may be noticed that the expressions are practically identical, except that the standard prescribes the stiffener’s second moment of area to be one-third of its actual value (*i.e.* $I_{sl}/3$) in the shear buckling coefficient. As stated in [139], the reason for the 1/3 stiffness reduction in EN 1993-1-5 is due to a smaller post-buckling reserve of longitudinally stiffened panels compared to unstiffened panels. However, in studies by Jáger *et al.* [139], as well as in the recent experimental and numerical studies by Pavlovčič *et al.* [160][161], Eq.(2.102) from EN 1993-1-5 was questioned and it was concluded that the standard gives conservative results even if no reduction of the second moment of area is applied. Therefore, in this study, the FEM-based shear resistances are compared with the standard-based results for both reduced bending stiffness $I_{sl}/3$ and full bending stiffness ‘ I_{sl} -full’, using respectively Eq.(2.102) and Eq.(8.1) for the determination of the shear buckling coefficient.

In Fig. 8.14 and Table 8.5, the GMNIA-based shear resistances (V_{num}) are compared with the characteristic values calculated from EN 1993-1-5 (V_{EC3}) for all cases from the parametric study where the dominant shear failure was possible to attain. As stated before, in many cases of bridge decks, especially with a higher aspect ratio ($\alpha > 1.0$), the bending failure mode is dominant,

regardless of the M/V ratio applied in the model. These cases are excluded from the current study in order to eliminate any biased conclusion.

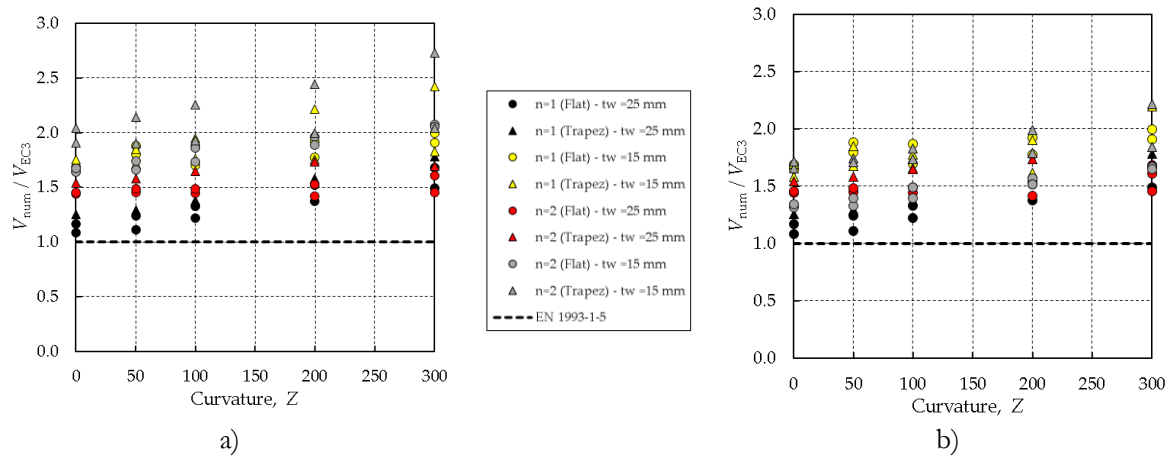


Fig. 8.14: Comparison of the shear resistances calculated by FEM and EC3 considering:
a) $I_{sl}/3$ and b) I_{sl} - full

Table 8.5: Statistical assessment of the V_{num}/V_{EC3} ratio for various Z parameters

V_{num}/V_{EC3}	$Z = 0$		$Z = 50$		$Z = 100$		$Z = 200$		$Z = 300$	
	$I_{sl}/3$	I_{sl}	$I_{sl}/3$	I_{sl}	$I_{sl}/3$	I_{sl}	$I_{sl}/3$	I_{sl}	$I_{sl}/3$	I_{sl}
St. Dev.	0.27	0.21	0.29	0.22	0.29	0.23	0.30	0.24	0.35	0.28
Mean	1.57	1.47	1.63	1.54	1.68	1.57	1.79	1.66	1.91	1.77
CoV (%)	17.2	14.3	17.7	15.9	17.0	12.9	17.0	11.7	18.4	13.2

Based on the presented results several relevant conclusions may be drawn. First, the procedure given in the design standard, indeed underestimates the shear resistance, which coincides with the findings from all recent studies dealing with this problem (*e.g.* Jäger *et al.* [131][139], Sinur *et al.* [162][163]). There are several possible explanations for this: (i) the aforementioned consideration of 1/3 of the stiffener's second moment of area; (ii) the neglect of the torsional rigidity of the closed longitudinal stiffeners; and (iii) the omission of the flange contribution in hand calculation.

Regarding the reduction of stiffness, it may be observed from Fig. 8.14b that even if the full second moment of area (I_{sl}) is considered, the results are safe; however, the difference drops significantly, from 57% to 47% in the case of trapezoidal box-girders ($Z = 0$), and from 91% to 77% in case of the most curved girders ($Z = 300$). Jäger *et al.* [131][139] in their study also found the reduction of stiffness unjustified, hence suggesting the use of the full second moment of area.

As for the second source for a high V_{num}/V_{EC3} ratio, it may be noticed in Fig. 8.14 that the results for trapezoidal longitudinal stiffeners (triangular symbols) are the most conservative due to the omission of the beneficial torsional rigidity in the hand calculation. For instance, in the case of trapezoidal bridge deck cross-section with flat bottom flanges ($Z = 0$), the mean difference between V_{num} and V_{EC3} for girders with flat web stiffeners and trapezoidal ones is 47% and 69%, respectively. These values decrease to 39% and 57% if the full flexural rigidity of the stiffeners is considered; either way, the standard undoubtedly underestimates the torsional rigidity

in the case of closed stiffeners. Similar results were found also by former authors, Sinur *et al.* [163] and Jáger *et al.* [139], where the latter obtained the difference of almost 87% between the numerical and analytical results for certain configurations of closed stiffeners. Moreover, the authors particularly criticized the inadequacy of the formulae given by EN 1993-1-5 for the determination of the shear buckling coefficient in the case of webs with less than $n_{st} < 3$ stiffeners, which is the case for all the webs in this study. In fact, the standard overestimates the effect of local shear buckling, not accounting for the tendency of the rigid edge constraint to deform all longitudinal stiffeners in the similar way, which in the case of rigid and hardly twisted closed stiffeners may result in large strain deformations of the subpanels and consequently increased bearing capacity.

Concerning the last possible reason for large V_{num}/V_{EC3} ratios obtained, the contribution from the flanges ($V_{bf,R}$) is not considered due to twofold uncertainty. First, the contribution from the bottom flange is not accounted for in this comparison since it is still unclear what exactly is the bottom flange for the studied box-girders and what is the actual contribution of the curved panel in shear bearing capacity. The participation of the curved bottom panel in the shear resistance is yet to be revealed in 8.3.3. Secondly, the contribution of the top flange is also not considered since the studies by Sinur *et al.* [163] and Jáger *et al.* [139] showed that the consideration of the flange contribution is too optimistic for heavy flanges, which applies also to this study, where the top flange is intentionally adopted as overly thick to replace the composite steel-concrete top flanges and to keep the position of the neutral axis close to the top flange. Therefore, although the numerical model undoubtedly accounts for at least minor flange contribution, owing to the unsafety of the EC3-like model, this component is neglected in hand calculation.

Finally, regardless of the cross-section geometry, type, and flexural stiffness of the longitudinal stiffeners, it may be seen from Fig. 8.14 and Table 8.5 that the standard model for the calculation of the shear resistance is not adequate for cross-sections with increased curvatures. In fact, the V_{num}/V_{EC3} ratio is gradually increasing for the elevated curvatures, reaching an average difference of 91% for $Z = 300$. This indicates that merely consideration of the flat part of the web (with height $h_{w,flat}$ in Fig. 8.13) is not sufficient and that a part of the bottom curved panel also contributes to the shear resistance. To what extent the bottom flange participates in the shear resistance is discussed in 8.3.3.

8.3.3 Study on the shear participation of the curved bottom flange

Based on the results from the previous section, where the shear resistance from computer simulations was compared with the resistance of the flat part of the web using the method from EN 1993-1-5, it is noticed that the curved bottom flange also contributes to the development of shear stresses. To confirm this statement, the distribution of the shear stresses at the moment of failure, obtained in FEM simulations, is plotted in Fig. 8.15 and Fig. 8.16 for cross-sections with various curvatures of bottom flange, respectively for $H=const.$ and $H=var.$ (see Fig. 7.15). These two examples illustrate how the part of the cross-section receiving the shear stresses gradually increases with the curvature.

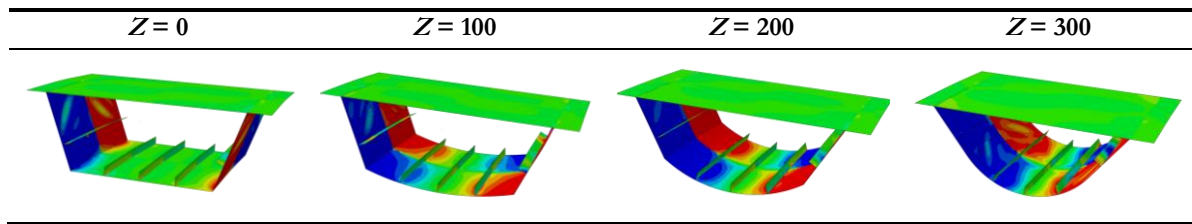


Fig. 8.15: Shear stress distribution in cross-sections with $H=const.$ (FEM)

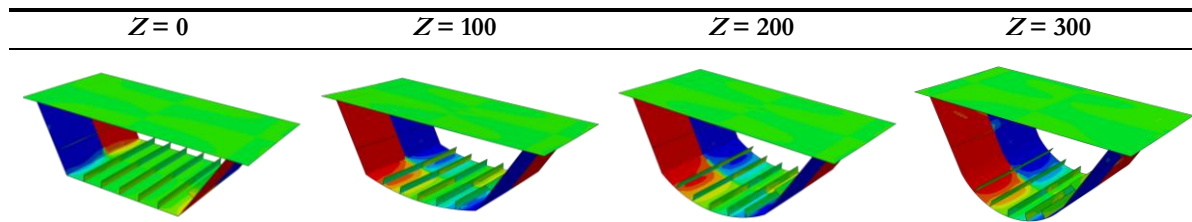


Fig. 8.16: Shear stress distribution in cross-sections with $H=var.$ (FEM)

To understand to what extent the curved parts are activated, in Fig. 8.17, the area of the cross-section that participates in shear resistance, obtained from FEM results as $A_{w,Z} = V_{num}/f_{yw}$, is normalized with the shear area of a corresponding trapezoidal box-girder ($A_{w(Z=0)}$) and plotted against the curvature parameter Z , separately for cross-sections with constant and variable height. The results are categorically divided into 7 groups, based on the geometry of the cross-section, where n_w and n_f in the legend refer to the number of stiffeners on the web and flange, respectively.

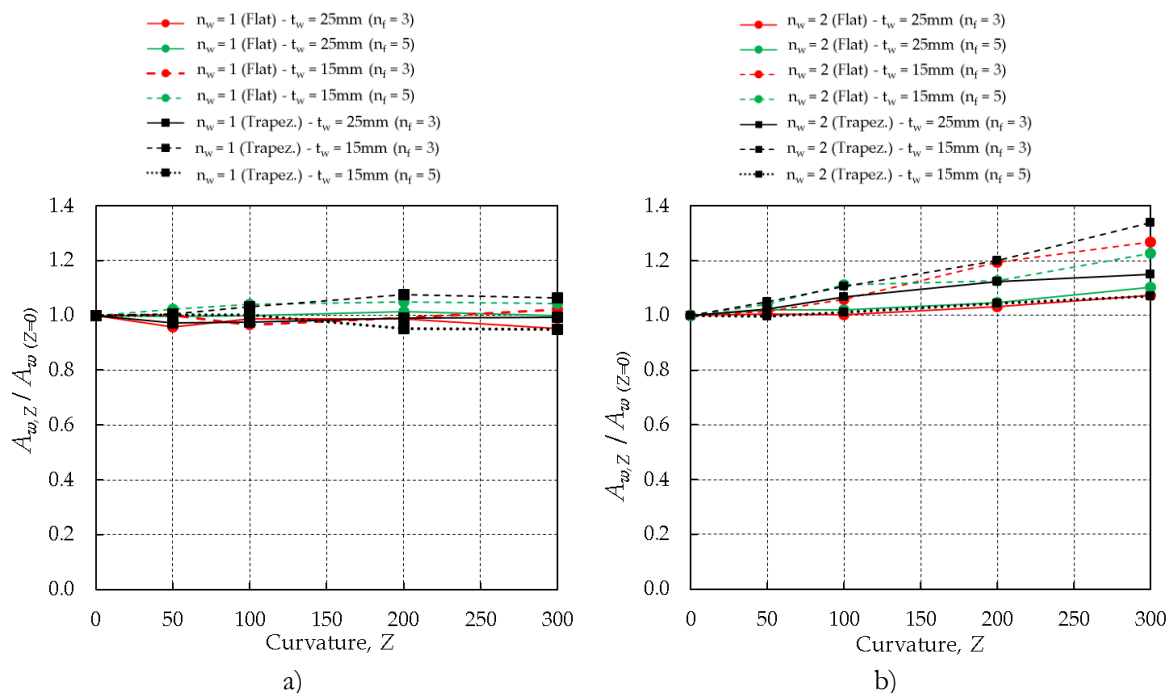


Fig. 8.17: The ratio between the area participating in shear resistance in a cross-section with curved bottom flange ($Z > 0$) and cross-section with flat bottom flange ($Z = 0$) for:
a) $H=const$ and b) $H=variable$

Fig. 8.17a shows that in the case of a cross-section with constant height, the area of the cross-section that participates in the shear resistance also remains constant and equal to the reference case (*i.e.* $Z = 0$), with a max difference of 6.7%. Since in this group of cross-sections the total

height remains the same, while the flat part of the web reduces with the increase of curvature, it may be deduced that the shear resistance directly depends on the total height H_w of the cross-section and not only on the height of the flat part $h_{w,flat}$ (see Fig. 8.13). This may be also understood from the results in Fig. 8.17b, where the cross-sections with variable height are studied. Namely, unlike the cross-sections with $H = \text{const.}$, in sections with $H = \text{var.}$, the flat part remains constant, while the total height increases with the curvature, which directly increases the shear resistance of the cross-section.

This confirms the assumption that the total shear resistance of a cross-section, besides the flat part of the web with depth $h_{w,flat}$, should be increased for an extra portion of the bottom curved flange, with the length marked as L_w in the remaining of the document.

To define the length L_w , the starting point is to use the analogy with the known expression for the plastic shear resistance (V_{pl}) of a thin-walled circular cross-section, shown in Fig. 8.18a.

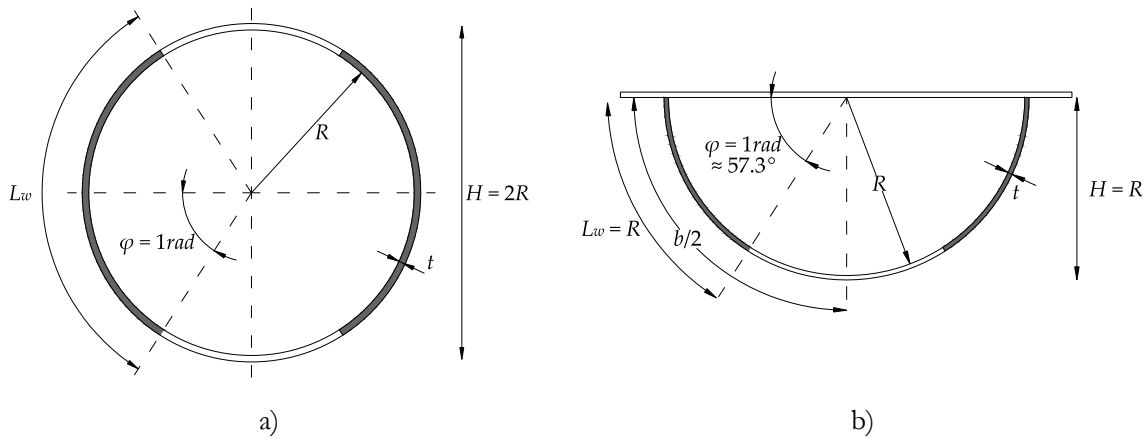


Fig. 8.18: Notations and the shear area A_w for a) circular and b) half-circular cross-section

Using the notations from Fig. 8.18a, the shear area A_w of a circular cross-section is calculated by Eq.(8.2) as:

$$A_w = 2L_w t \quad (8.2)$$

In the literature, the shear area of a thin-walled circular cross-section is often given by Eq.(8.3) as:

$$A_w = \frac{2}{\pi} A \approx 0.64A \quad (8.3)$$

where A is the total area of the tubular cross-section, obtained as $A = 2R\pi t$, with t being the thickness and R the radius of the cross-section. After substituting the expression for the area (A) in Eq.(8.3), the expression for the shear area may be transformed into Eq.(8.4) as:

$$A_w = \frac{2}{\pi} (2R\pi t) = 2 \cdot (2R) \cdot t \quad (8.4)$$

Finally, combining Eq.(8.2) and Eq.(8.4), the length L_w of the circular cross-section that participates in the plastic shear resistance is expressed by Eq.(8.5) as:

$$L_w = 2R \quad \rightarrow \quad L_w = H \quad (8.5)$$

where H is the height of the cross-section, equal to $H=2R$ (see Fig. 8.18a). This confirms once again that the height of a cross-section dictates the shear area, *i.e.* the length of the cross-section that participates in the shear resistance.

Analogously, for a half-circle cross-section, the length L_w is equal to $L_w = R$, thus corresponding to the length of an arc with the central angle equal to $\varphi = 1$ rad (*i.e.* $\approx 57.3^\circ$), as indicated in Fig. 8.18b. Assuming a half-circle cross-section as an extreme shape of a box-girder bridge deck, with the total width b , it may be deduced that the length L_w is equal to $L_w \approx 0.64 \cdot (b/2) \approx 2/\pi \cdot (b/2)$, as shown in Fig. 8.18b. The ratio between the length L_w and the half-width $b/2$ is named ‘shear participation’ in the thesis, denoted by $\xi_s = L_w / (b/2)$ ($0 < \xi_s < 1$), which in the case of a half-circular cross-section is equal to $\xi_s = 2/\pi$.

The validity of this statement is verified numerically by integrating the shear stresses (τ) from a 3-point bending model, similar to the models used in the parametric study; however, with a half-circular cross-section shape. The width of $b = 4200$ mm is equal to the width of the bottom flange in all cases from the parametric study, whereas the thickness of $t = 25$ mm is adopted as sufficiently thick to avoid shear buckling, thus allowing for the determination of the shear plastic resistance and comparison with Eq.(8.3). For the considered b/t ratio, and the radius, which in the case of a half-circle is equal to $R = b/\pi$ (≈ 1336.9 mm in this case), the curvature parameter is equal to $Z = 528$. The distribution of the shear stresses at the moment of shear-dominated failure is presented in Fig. 8.19.

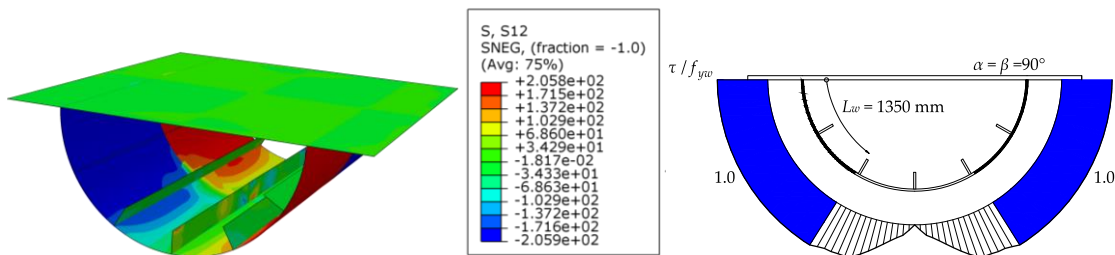


Fig. 8.19: Shear stress distribution at reaching the plastic resistance (V_{pl})

As it may be observed from the figure, the shear stress reached yield shear stress ($f_{yw} = f_y/\sqrt{3}$) along the arc approximately $L_w \approx 1350$ mm long, which confirms that the shear participation in a half-circular shaped cross-section is equal to $\xi_s = 2/\pi$.

Using as a reference this extreme cylindrical cross-section shape, the objective is to determine now the shear participation for more realistic bridge deck cross-sections, *i.e.* with the shapes studied in the parametric study in 7.3.3. Therefore, another numerical study is carried out, to understand to what extent the angles α and β , shown in Fig. 8.20, may influence the parameter ξ_s . The study comprises 66 different geometries of bridge decks, some of which have already been addressed in the parametric study. The angle α describes the inclination of the curved bottom flange with respect to an imaginary horizontal line, measured from the contact point between the flat web and bottom flange. For the two extreme cases, *i.e.* a trapezoidal box-girder with a flat bottom flange and aforementioned half-circular cross-section, this angle is equal to $\alpha = 0^\circ$ and $\alpha = 90^\circ$, respectively, whereas, for any other intermediate case, the angle α is defined by Z -parameter. On the other hand, the angle β is the angle between the top flange and the flat web,

hence represents the inclination of the flat web. In this study, four different values of angle β are considered (45° , 60° , 75° , and 90°), where the angle $\beta = 90^\circ$ corresponds to the half-circular cross-section. The range for the β angle is adopted based on the common web inclinations, identified in the real bridge examples, mentioned in [chapter 2](#).

The curvature parameter in this study is varied between $Z = 0$ and $Z = Z_{\max}$, where the latter is defined as the curvature for which the inclination of the bottom flange and flat web coincide (*i.e.* $\alpha = \beta$). This means that the angle β dictates the maximum value of the angle α (*i.e.* $\alpha \leq \beta$) and subsequently, the maximum value of the curvature parameter Z_{\max} . For instance, in the case of $\beta = 90^\circ$, the maximum value of the angle is also $\alpha = 90^\circ$, which corresponds to a half-circular section, leading to $Z_{\max} = 528$, for the values of the width $b = 4200$ mm and the thickness $t = 25$ mm, considered in this study.

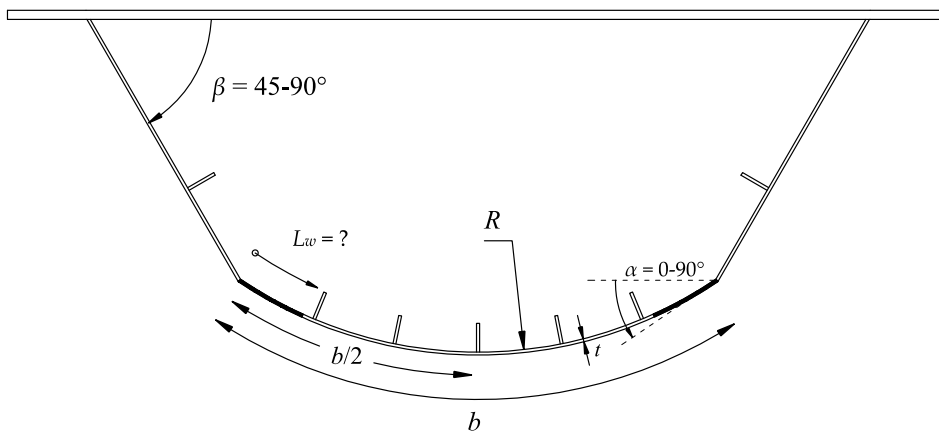


Fig. 8.20: Definition of relevant geometric parameters for the study on the shear participation of the curved bottom flange ξ_s

Similar to the example of a half-circular cross-section presented in [Fig. 8.19](#), for each of 66 studied geometries, either with $H=\text{const.}$ or $H=\text{var.}$, the distribution of the shear stresses at the moment of shear-dominated failure is assessed and the corresponding length L_w is derived as the length of the arc where the shear stress reaches the yield shear stress. An example with $\beta = 60^\circ$ is illustrated in [Fig. 8.21](#), where the shear distribution and the length L_w are presented for 4 different curvature parameters, including the maximum curvature of $Z_{\max} = 352$ in this case, obtained for $\alpha_{\max} = \beta = 60^\circ$.

The results indicate that there is a gradual growth of the length L_w with the curvature Z . In fact, in the case of a flat bottom flange ([Fig. 8.21a](#)), the shear is resisted only by the webs, resulting in the shear participation of the bottom flange equal to $\xi_s = 0$. For the remaining three curvatures, *i.e.* $Z = 100$, $Z = 200$, and $Z = 352$, the length L_w is approximately equal to 258 mm, 570 mm, and 926 mm, respectively, which leads to the shear participations of $\xi_s = 0.12$, $\xi_s = 0.27$, and $\xi_s = 0.44$.

Following the same logic, the contribution of the bottom flange in the shear plastic resistance is obtained for all the studied cases and the results are summarized in [Fig. 8.22](#), where ξ_s is plotted against the angle α for 4 different angles β .

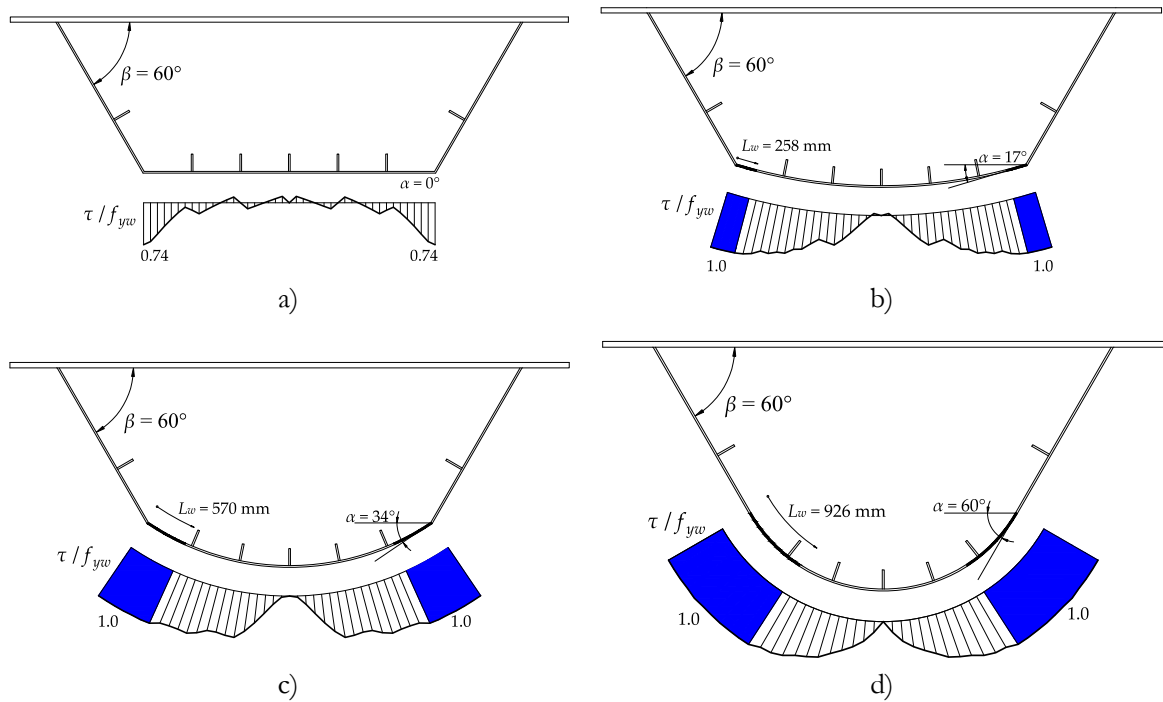


Fig. 8.21: Shear stress distribution in the bottom flange at reaching the plastic resistance (V_{pl}) for $H=\text{var.}$ and curvatures: a) $Z = 0$; b) $Z = 100$; c) $Z = 200$ and d) $Z = Z_{\max} = 352$

The results show that the angle β has almost no influence on the shear participation, whereas the angle α directly affects the parameter ξ_s and this regularity is the same for both groups of the cross-sections (*i.e.* with $H = \text{const.}$ and $H = \text{var.}$). Furthermore, the results show that $\alpha - \xi_s$ correlation may be approximated by a linear function, with $\xi_s = 0$ for $\alpha = 0^\circ$ (*i.e.* trapezoidal box-girder) and $\xi_s = 2/\pi$ for $\alpha = 90^\circ$ (*i.e.* half-circular cross-section).

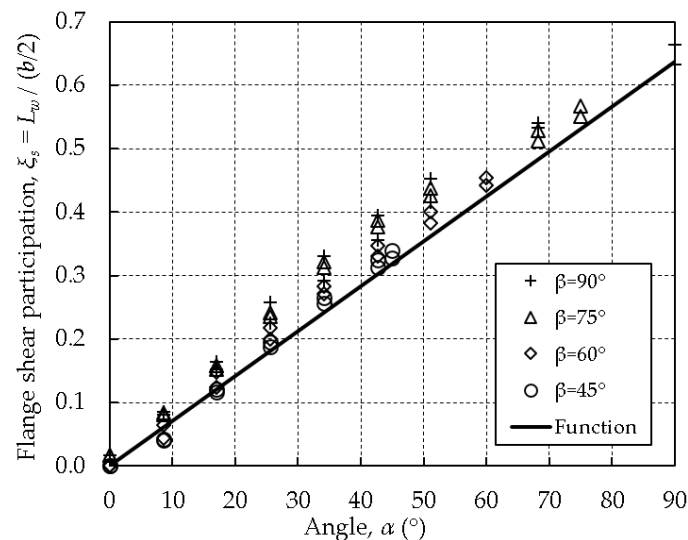


Fig. 8.22: Bottom flange shear participation as a function of α and β angles

Hence, the length L_w might be now calculated in a function of α by Eq.(8.6) as:

$$L_w = \frac{b}{\pi} \left(\frac{\alpha}{90} \right) \tag{8.6}$$

Since the angle α is equal to the central angle of an arc with the length $b/2$ (see Fig. 8.20), and thus may be expressed in radians as $\alpha = (b/2)/R$ or in degrees as $\alpha = (b/R) \cdot (90/\pi)$, the length L_w may be rewritten by Eq.(8.7), where Z is the curvature parameter, and t is the thickness of the bottom flange.

$$L_w = \frac{1}{R} \left(\frac{b}{\pi} \right)^2 = \frac{Z \cdot t}{\pi^2} \quad (8.7)$$

Finally, now that the length L_w is defined, it is possible to calculate shear plastic resistance V_{pl} , using Eq.(8.8) as:

$$V_{pl,Rk} = \frac{(h_{w,flat} \cdot t_w + L_w \cdot t) f_y}{\sqrt{3}} \quad (8.8)$$

where $h_{w,flat}$ is the length of the flat part of the web, defined in Fig. 8.13, t and t_w are thicknesses of the bottom flange and flat web, respectively, and L_w is the part of the bottom flange that participates in the shear plastic resistance, calculated by Eq.(8.7).

8.3.4 Proposal of a new shear resistance model

Once the plastic shear resistance ($V_{pl,Rk}$) is determined, the objective is to propose a design method for the prediction of the shear resistance ($V_{bw,Rk}$), allowing for the shear buckling phenomenon as well. As specified before, the initial idea is to use the same $\bar{\lambda}_w - \chi_w$ design methodology from the standard; however, modified to account for the contribution of the curved panel in the shear resistance. In Fig. 8.14 and Table 8.5, the analytical method from EN 1993-1-5 applied only to the flat part of the web is compared with the numerical results, and it is concluded that merely consideration of the flat part of the web (with height $h_{w,flat}$ in Fig. 8.13) is not sufficient for the shear resistance estimation. Namely, even for the trapezoidal box-girders with a flat bottom flange ($Z = 0$), the V_{num}/V_{EC3} ratio is found considerably high (*i.e.* mean difference of 57% for $I_{sl}/3$ and 47% for full stiffener inertia I_{sl}). However, the V_{num}/V_{EC3} ratio tends to increase with the increase of the bottom panel curvature, reaching, for instance, the mean difference of 91% for $Z = 300$, with the max difference of 150%.

Therefore, the objective of this study is not to propose a completely new analytical method, but to slightly adjust the one from the standard, making it applicable for the cases of bridge decks with a curved bottom flange, with a V_{num}/V_{EC3} ratio within an acceptable margin, *i.e.* at least close to the one for the non-curved girders.

The design methodology from the standard for the calculation of the web contribution to the shear buckling resistance is described in detail in 2.5.2. The method is based on the $\bar{\lambda}_w - \chi_w$ correlation, defined by Eq.(2.98) for the rigid end-posts. Therefore, to assess the applicability of this method for the studied cross-sections, for each model it is necessary first to determine numerically the values of slenderness parameter ($\bar{\lambda}_{w,num}$) and the reduction factor ($\chi_{w,num}$) and to compare with the formula given by Eq.(2.98), as presented in Fig. 8.23. Using Eq.(8.8) for the plastic shear resistance $V_{pl,Rk}$ derived in 8.3.3, the slenderness ($\bar{\lambda}_{w,num}$) and the reduction factor ($\chi_{w,num}$) are calculated by Eq.(8.9) and Eq.(8.10) as:

$$\bar{\lambda}_{w,num} = \sqrt{\frac{f_y/\sqrt{3}}{\tau_{cr}}} = \sqrt{\frac{V_{pl}}{V_{cr}}} \quad (8.9)$$

$$\chi_{w,num} = \frac{V_{num}}{V_{pl}} \quad (8.10)$$

where V_{cr} is the critical shear force, *i.e.* the force at which the 1st shear eigenmode occurs, obtained directly from linear bifurcation analysis (LBA), whereas V_{num} is the ultimate shear resistance obtained from GMNIA analysis, as described in section 7.4 (see Fig. 7.17).

The numerical results in Fig. 8.23 indicate that the shear buckling curve from EN 1993-1-5 is a lower bound curve of the buckling resistance for any considered bridge deck geometry. This justifies the initial intention of using the method from EN 1993-1-5 for determination of the shear buckling resistance also in the case of cross-sections with a curved bottom flange. However, although the results look virtually safe for the entire scope of the study, in the cases where the webs have higher slenderness (approx. $\bar{\lambda}_{w,num} > 1.0$, see the grey range in Fig. 8.23), the reduction factor χ_w may be overestimated, leading to unsafe results. The reason for this discrepancy is the difference between analytically (EC3-based) and numerically (FEM-based) derived relative slendernesses. Namely, according to the analytical design method, the slenderness parameter is obtained using the critical shear stress calculation from Annex A of EN1993-1-5, which is applicable only for the flat plates (*i.e.* flat webs). On the other hand, in numerical simulations, the critical stresses are calculated for the entire cross-section (and not only flat part of the web), which leads to more realistic reduced critical shear stress and thus increased relative slenderness parameter.

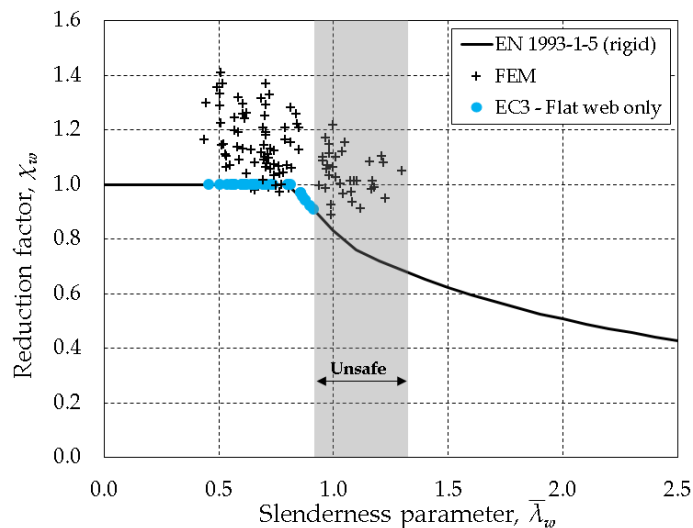


Fig. 8.23: Verification of the FEM results against the EC3-based method with respect to the $\bar{\lambda}_w$ - χ_w correlation

For all numerical models considered in the study, the slenderness is calculated using the EC3-like methodology (applied on the flat webs), as well as the corresponding reduction factor, using Eq.(2.98), and the results are presented in Fig. 8.23 with blue dots. As it may be noticed, for those cases from the ‘grey area’ ($\bar{\lambda}_{w,num} > 1.0$), the use of the EC3-based method may considerably reduce the slenderness parameter and subsequently overestimate the reduction factor (*i.e.* $\chi_{w,EC3} > \chi_{w,num}$).

To overcome this safety deficiency, while attempting at the same time to keep the design code mathematical formalism, a slightly modified shear resistant model is proposed, named ‘Extended web method’. In fact, according to this analytical model, the same rules for the web contribution to shear buckling resistance from EN 1993-1-5 are applied; however, the height of the flat web, for which the resistance is calculated, is elongated from $h_{w,flat}$ to h_w . As it may be seen in Fig. 8.24, the latter is obtained as the projection of the cross-section total depth H_w , which remains the same in the extended model, onto the plane of the flat part of the web (*i.e.* $h_w = H_w / \sin\beta$). Since it was proven multiple times that the shear resistance dominantly depends on the total height of the cross-section H_w , this simplified extended model (see Fig. 8.24b) may be considered reasonably accurate.

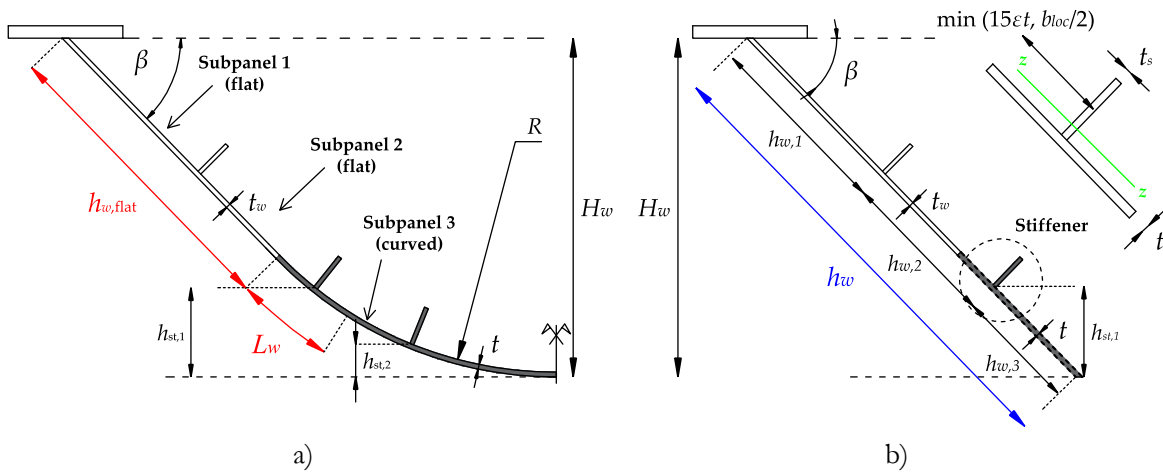


Fig. 8.24: Proposed shear resistance model: a) real web geometry; b) extended flat web

Using the notations from Fig. 8.24, the characteristic shear buckling resistance of the web panel alone (without flange contributions) may be calculated by Eq.(8.11) as:

$$V_{bw,Rk} = \frac{\chi_w [h_{w,flat} t_w + (h_w - h_{w,flat}) t] f_y}{\sqrt{3}} \leq V_{pl,Rk} \quad (8.11)$$

where $V_{pl,Rk}$ is the characteristic plastic shear resistance, given by Eq.(8.8), whereas χ_w is the shear reduction factor obtained from Eq.(2.98) of EN 1993-1-5, assuming a rigid end post.

For the calculation of the reduction factor, as we know, it is necessary to calculate first the slenderness parameter $\bar{\lambda}_w$, defined by Eq.(2.99). As explained in 2.5.2 (see Eq.(2.100)) the slenderness is calculated for the entire stiffened web, with corresponding elastic buckling coefficient k_{τ} , and for the entire width h_w ; however, it should not be lower than the slenderness of each subpanel, considered as an unstiffened panel (flat or curved) with the corresponding $k_{\tau,i}$ and local width $b_{loc,i}$. For the actual case, Eq.(2.100) may be adapted by Eq.(8.12) as:

$$\bar{\lambda}_w = \max \left(\frac{h_w / t_w}{37.4 \cdot \varepsilon \cdot \sqrt{k_{\tau}}}; \frac{b_{loc,i} / t_i}{37.4 \cdot \varepsilon \cdot \sqrt{k_{\tau,i}}} \right) \quad (8.12)$$

To explain how the critical stress (and slenderness) are calculated, a more general example is considered, *i.e.* the one from Fig. 8.24. Before any calculation, it is necessary to define the number and position of the longitudinal stiffeners considered in the extended web model, for which the following guidelines may be applied:

- (1) All longitudinal stiffeners on the flat part of the web are kept in the extended web model and their position remains unchanged;
- (2) Only those stiffeners on the curved bottom flange that are found in the zone that participates in the shear resistance (*i.e.* inside the length L_m , see Fig. 8.24a) are kept in the extended web model and their positions, defined by $h_{st,i}$, remain unchanged with respect to the bottom (dashed) line;
- (3) The stiffeners outside of the arc length L_m may be excluded from the model since in this zone the shear stresses become less relevant, as shown in Fig. 8.21. Therefore, the consideration of all bottom flange stiffeners in the extended web model would only artificially enhance the critical stress of the web, which would eventually lead to unrealistically stocky webs and unsafe (high) reduction factors.

As may be seen in the example shown in Fig. 8.24, the extended web has two longitudinal stiffeners (one on the flat part of the web and the other on the curved within the length L_m), thus the extended web consists of three subpanels. This means that besides the global critical stress and slenderness of the entire 2-stiffened web, for each of three subpanels another local critical stress and slenderness need to be determined as follows:

i) Global critical stress and slenderness – Whole web:

The expressions for the hand calculation of the shear buckling coefficient k_τ are provided in Annex A.3 of EN 1993-1-5, given by Eqs.(2.102)-(2.104), depending on the number of the stiffeners and the aspect ratio $\alpha_w = a/h_w$. The slenderness is then obtained using the first part of Eq.(8.12).

ii) Local critical stress and slenderness – Subpanel 1:

As illustrated in Fig. 8.24, the first subpanel is a flat panel between the top flange and the first stiffener, with the aspect ratio equal to $\alpha_{w,1} = a/h_{w,1}$. Hence, for the calculation of the shear buckling coefficient ($k_{\tau,1}$), Eq.(2.101) from Annex A of EN 1993-1-5 for unstiffened flat plates should be used. Subsequently, the local slenderness parameter is obtained using the second part of Eq.(8.12), where the local width is equal to $b_{loc,1} = h_{w,1}$, while the thickness is equal to the thickness of the flat web, *i.e.* $t_1 = t_w$.

iii) Local critical stress and slenderness – Subpanel 2:

According to the example in Fig. 8.24, the second subpanel is also flat panel between the first and the second stiffener, with the aspect ratio equal to $\alpha_{w,2} = a/h_{w,2}$. The subpanel is considered flat with the thickness t_w , although it also includes a small curved part with the thickness t . This is merely due to the safety reasons since in the bridge decks the web thickness is rarely (if ever) higher than the thickness of the bottom flange (*i.e.* $t_w \leq t$). The hand calculation of both local critical stress ($k_{\tau,2}$) and slenderness parameter is completely the same as in the case of Subpanel 1; however, in Eq.(8.12), the local width is replaced by $b_{loc,2} = h_{w,2}$, while the thickness remains the same and equal to $t_2 = t_w$.

iv) Local critical stress and slenderness – Subpanel 3:

Finally, the subpanel 3 in the considered example is curved in the real geometry with the width $b_{loc,3}$ (Fig. 8.24a), whereas in the extended web model, the subpanel is substituted by a flat one with the width $b_{w,3}$. Since the buckling behavior of an unstiffened curved panel under shear is somewhat different from the behavior of a flat panel (as shown in chapter 4), for the safety requirements, it is necessary to calculate the critical stress of both curved ($k_{\tau,3,C}$) and flat panel ($k_{\tau,3,F}$), as follows:

- The shear buckling coefficient ($k_{\tau,3,C}$) of an unstiffened curved subpanel, with the aspect ratio $\alpha_{w,3} = a/b_{loc,3}$ and the local curvature $Z_{loc} = b_{loc,3}^2/Rt$, may be calculated using Eq.(4.3) developed in chapter 4, assuming the boundary condition BC2 due to the presence of the rigid diaphragms on both curved edges.

- On the other hand, the shear buckling coefficient ($k_{\tau,3,F}$) of the corresponding flat subpanel is calculated by Eq.(2.101), in the same way, it is done for subpanels 1 and 2. Namely, the panel is assumed to be simply supported by a longitudinal stiffener on one side and by fictive support along the other longitudinal edge, whereas the local width and the thickness of the panel are equal to $b_{loc,3} = b_{w,3}$ and $t_3 = t$, respectively.

Subsequently, for the determination of the relative slenderness of the subpanel 3, in Eq.(8.12), the lower of the two critical stresses is to be considered, *i.e.* $k_{\tau,3} = \min(k_{\tau,3,C}; k_{\tau,3,F})$.

Finally, using the proposed analytical model, the $\bar{\lambda}_w - \chi_w$ correlation is recalculated for all the cases from the parametric study, and similar to Fig. 8.23, the results are compared with the numerical ones in Fig. 8.25.

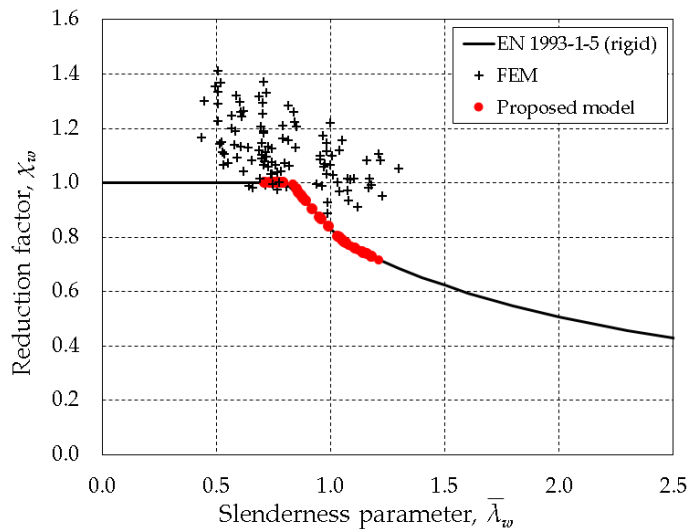


Fig. 8.25: Verification of the FEM results against the EC3-based extended web method with respect to the $\bar{\lambda}_w - \chi_w$ correlation

By comparing the analytical results (red dots) in Fig. 8.25 with the results from Fig. 8.23 (blue dots), in which only the flat web is considered, it may be noticed that the web extension shifts the results rightwards on the $\bar{\lambda}_w - \chi_w$ curve due to increased slenderness parameter $\bar{\lambda}_w$. Therefore, it may be concluded that the application of the proposed extended web method leads to a safe

design for the entire scope of the studied bridge deck configurations since the method allows for a more realistic assessment of the relative slenderness, *i.e.* closer to the ones obtained in the computer simulations ($\bar{\lambda}_{w,num}$).

8.3.5 Shear resistance – FEM vs Analytical model

Using Eq.(8.11), the shear buckling resistance is calculated analytically for all box-girder cross-section geometries, studied in section 7.3, and the results are subsequently compared with the corresponding shear resistance (case V , see Fig. 7.17), obtained from computer simulations in section 7.4. An example with all required steps for the determination of the shear resistance of a cross-section with a curved bottom flange is shown in Annex D (D.3).

In Fig. 8.26, the GMNIA-based shear resistances (V_{num}) are compared with the values calculated using the proposed analytical method (V_{analy}) for all cases from the parametric study where the dominant shear failure is possible to attain. The comparison is made using the characteristic values, *i.e.* without consideration of the partial factors. As stated before, in the case of bridge decks with a higher aspect ratio ($\alpha > 1.0$), the bending failure mode is dominant, regardless of the M/V ratio applied in the model. Hence, these cases are eliminated from this comparative study to avoid biased conclusions. For the sake of complicity, the comparison for the trapezoidal box-girders ($Z = 0$) is repeated, although these results are presented in Fig. 8.14.

As it may be noticed, the proposed extended web approach applied in cases with curvatures higher than $Z > 0$ is safe, presenting a lower bound of all numerical results. In fact, only in two cases with very high curvatures ($Z = 200$ and $Z = 300$) and with 1 flat web stiffener, the method overestimates the numerical results for 2% and 6%, respectively. However, more importantly, the method succeeds in reducing the considerably high V_{num}/V_{EC3} ratios obtained in Fig. 8.14, especially in the case of high bottom flange curvatures (*e.g.* $V_{num}/V_{EC3} = 2.0$ - 2.5 for $Z = 300$). As it may be noticed in Table 8.6, where the V_{num}/V_{analy} is statistically assessed, in contrast to a rising trend of the V_{num}/V_{EC3} ratio, the use of the proposed method leads to a constant or even slightly declining trend of the V_{num}/V_{analy} ratio with the increase of curvature.

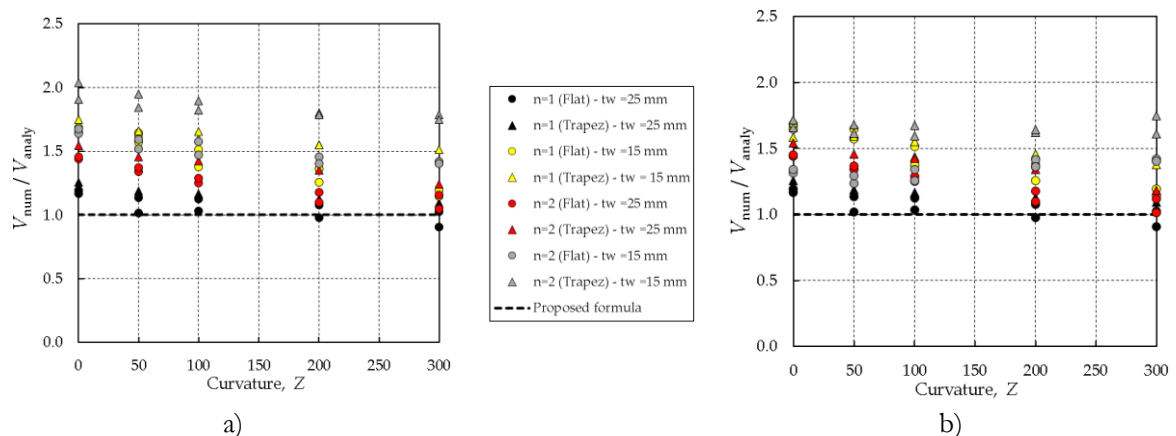
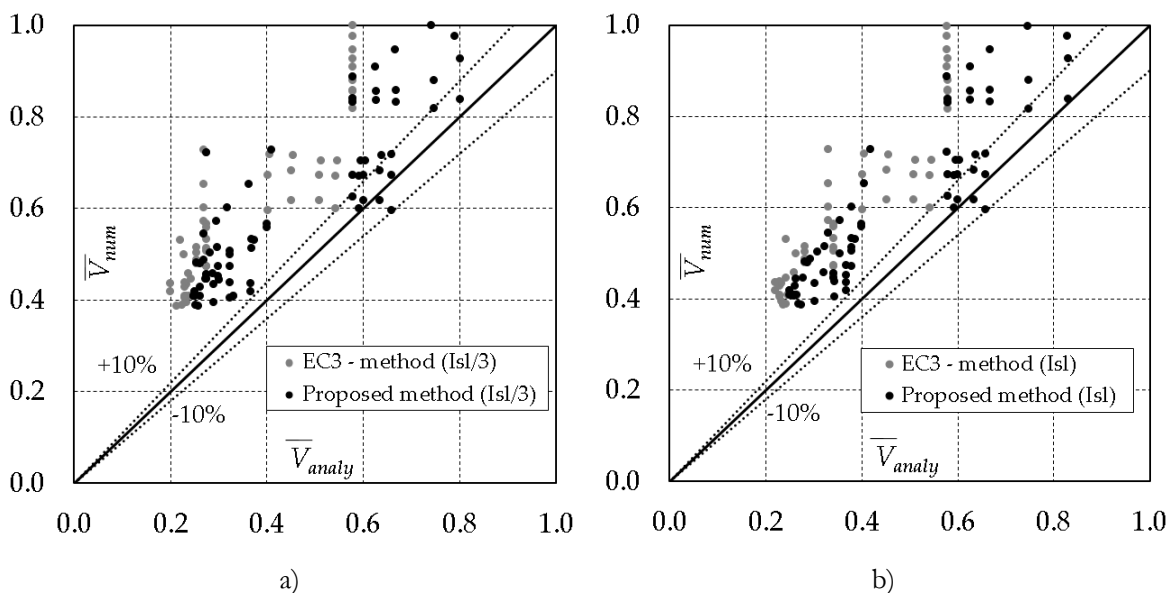


Fig. 8.26: Comparison of the shear resistances calculated by FEM and by new analytical method considering: a) $I_{sl}/3$ and b) I_{sl} - full

Table 8.6: Statistical assessment of the V_{num}/V_{analy} ratio for various Z parameters

V_{num}/V_{analy}	$Z = 0$		$Z = 50$		$Z = 100$		$Z = 200$		$Z = 300$	
	$I_{sl}/3$	I_{sl}	$I_{sl}/3$	I_{sl}	$I_{sl}/3$	I_{sl}	$I_{sl}/3$	I_{sl}	$I_{sl}/3$	I_{sl}
St. Dev.	0.27	0.21	0.26	0.22	0.26	0.18	0.26	0.20	0.27	0.24
Mean	1.57	1.47	1.50	1.41	1.44	1.35	1.36	1.30	1.29	1.26
CoV (%)	17.2	14.3	17.7	15.3	17.8	13.6	18.9	15.5	20.6	19.2

The results from the table indicate that the proposed analytical model, although still quite conservative for all curvature parameters, tends to decrease the difference with respect to the FEM results found in Table 8.5. This is illustrated in Fig. 8.27, where the shear resistances obtained numerically (\bar{V}_{num}) and analytically (\bar{V}_{analy}) are normalized against the maximum values. The proposed method seems to be particularly advantageous for very high curvatures, where, for instance, the mean difference of 91% for $Z = 300$ (see Table 8.5) dropped to satisfactory 29%. However, since the proposed method is an extension of EN 1993-1-5 approach, whose adequacy was questioned and criticized in one of the previous sections, this significant safety margin remains, regardless of the cross-section geometry configuration.


Fig. 8.27: Comparison of the EC3-method and the proposed method against the FEM results considering: a) $I_{sl}/3$ and b) I_{sl} - full

In an attempt to reduce further the V_{num}/V_{analy} ratio, as shown before, the full stiffener flexural stiffness is considered by using Eq.(8.1), and the results are summarized in Fig. 8.26 and Table 8.6. As it may be noticed, the application of the full stiffener inertia virtually reduces the difference for all curvature parameters. Namely, the consideration of the full inertia is particularly emphasized in the case of thin webs prone to buckling, where the full inertia of the stiffeners may partly compensate for the deficiency of the overly conservative standard approach for the calculation of the global shear buckling. Hence, the positive effect is even more pronounced for 2-stiffened webs. However, in some cases, especially where the buckling of the web does not occur, there is no difference if 1/3 of the inertia is considered of the full inertia, as shown in Fig. 8.28.

In conclusion, despite the difference between the FEM and analytical results, it may be stated that the proposed shear resistance model is as simple to apply as the method from the design standard; however, producing more accurate results than the model from EN 1993-1-5 used for the trapezoidal box-girders with a flat bottom flange. Nevertheless, since the proposed model implements the same conservative formulae from EN 1993-1-5, a better estimation of the shear resistance of box-girders with curved panels may be achieved once the formulae from the standard are adequately revised to account for several relevant parameters (*e.g.* level of edge constraint, the torsional rigidity of the stiffeners, lightly stiffened plates ($n_{st} < 3$), etc.).

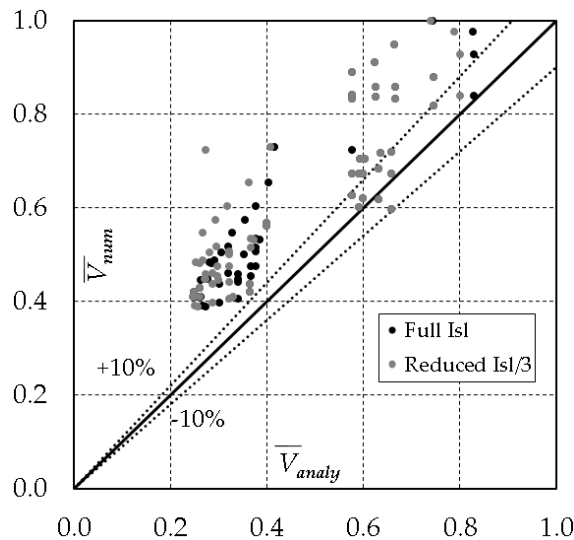


Fig. 8.28: Comparison of the proposed method against the FEM results considering full (I_{st}) and reduced ($I_{st}/3$) longitudinal stiffener inertia

Furthermore, the consideration of the full stiffener inertia in the shear buckling coefficient may be applied for girders with stiffened webs, and the proposed shear analytical method would still return safe solutions, at least for the ranges of parameters studied in this thesis. However, this problem requires further investigation since, for instance, in the mentioned work by Jáger *et al.* [139], the authors claim that the full stiffener inertia may lead to an overestimation of the shear buckling resistance for certain I-girder typologies.

The proposed shear resistance model is further statistically evaluated in section 8.5, where the partial factor (γ_M) is calculated.

8.4 Assessment of the M-V interaction equation

In this section, the applicability of the M - V interaction equation, developed by Jáger *et al.* [139] (Eqs.(2.122)-(2.123)) is assessed against the collected numerical results in chapter 7. As specified before, the main challenge for a direct application of this criterion in the case of the box-girder bridge deck cross-sections with the curved bottom flange is the lack of the adequate analytical models for determination of the bending ($M_{eff,Rk}$) and the shear resistance ($V_{bw,Rk}$). However, these obstacles are tackled in section 8.2 and section 8.3, where the new analytical resistance models for bending and shear, respectively, are developed and statistically assessed against the numerical

results. Therefore, by implementing the new (modified) resistance models in the M - V interaction equation by Jáger *et al.* [139], a straightforward safety assessment of this criterion may be conducted against the FEM results.

The M - V interaction formula given by Eq.(2.122), is commonly found in the literature in a slightly shorter format, given by Eq.(8.13), as illustrated in Fig. 8.1.

$$\eta_1 + \left[1 - \frac{M_{f,Rk}}{M_{eff,Rk}} \right] (2\bar{\eta}_3 - 1)^\beta \leq 1.0 \quad \text{with} \quad \beta = \left(\frac{M_{f,Rd}}{M_{el,eff,Rd}} + 0.2 \right)^{15} + 1 \quad (8.13)$$

where η_1 is the ratio between the applied (M) and the effective resistant bending moment ($M_{eff,Rk}$) calculated using the method proposed in section 8.2; whereas $\bar{\eta}_3$ is the ratio between the applied (V) and the shear buckling resistance of the web panel alone ($V_{bm,Rk}$) calculated by the method proposed in section 8.3. It should be noticed that for the comparison between the FEM results and proposed analytical methods, no partial factors are considered, thus, according to EN designation, the resistances obtained are the characteristic (R_k) and not the design values (R_d).

Before the comparison is made, it is also important to clarify how the bending resistance of the section considering the effective area of the flanges alone ($M_{f,Rk}$) is obtained. Namely, to maintain consistency with the developed bending and shear resistance models, the same assumption is retained, according to which the ‘bottom flange’ is considered the entire curved stiffened panel (see Fig. 8.10). Therefore, the effective area of the bottom flange, required for the calculation of $M_{f,Rk}$ is obtained using the method proposed by the OUTBURST research project [85] for a stiffened curved panel under uniform compression, whereas the top flange, being in tension, is considered fully effective. In Fig. 8.29, the ranges of M_f/M_{eff} ratio are plotted for each curvature parameter. As it may be noticed, M_f/M_{eff} ratio increases with the increased curvature owing to the reduction of the non-flange parts (*i.e.* webs) of the cross-section, particularly in the case with the constant height ($H = \text{const}$).

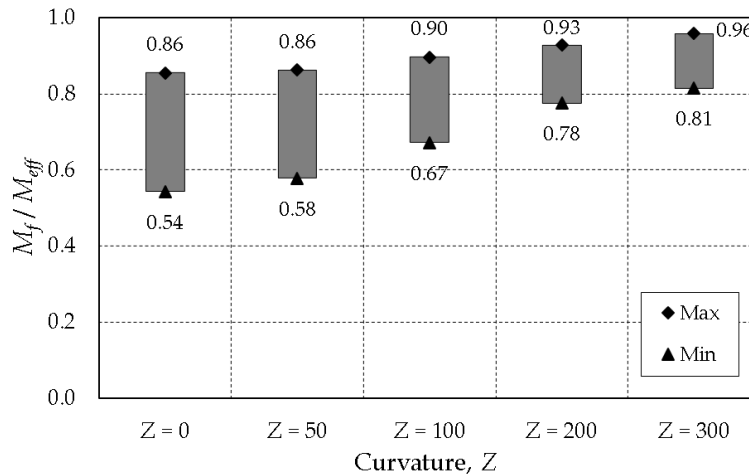


Fig. 8.29: M_f/M_{eff} ratios considered in the study

In Fig. 8.30, the 3D plot of all the numerical results is shown, together with the adjusted interaction equation (Eq.(8.13)), considering both the full I_{sl} (red dots) and the reduced inertia $I_{sl}/3$ (black dots) of the stiffener in the shear buckling coefficient. The horizontal and the vertical

axes represent the ratio of the FEM-based results and the corresponding bending ($\eta_1 = M_{num}/M_{eff,Rk}$) and shear resistance of the web panel alone ($\bar{\eta}_3 = V_{num}/V_{bw,Rk}$).

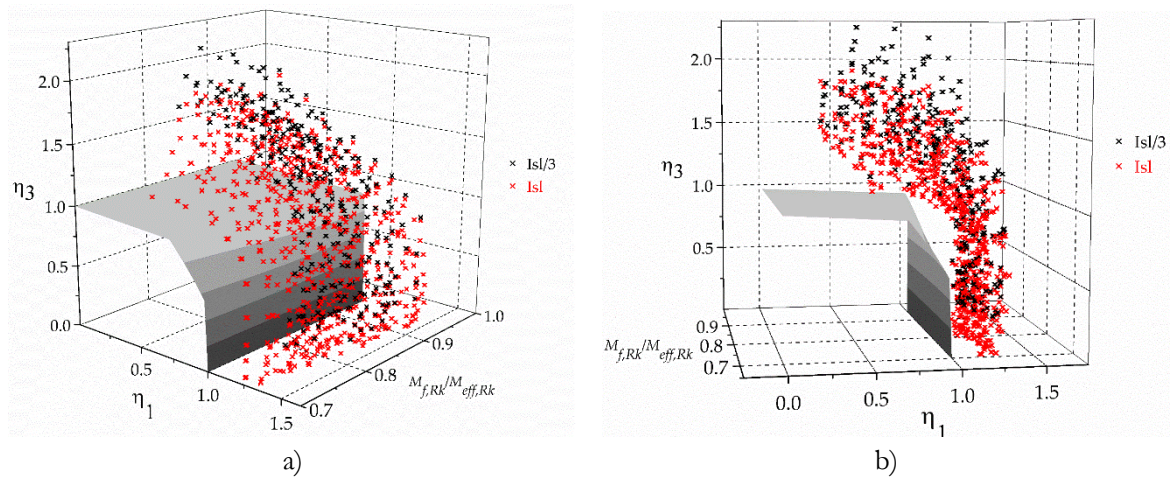


Fig. 8.30: Comparison between the FEM results and M-V interaction formula Eq.(8.13) for both I_{sl} (red) and $I_{sl}/3$ (black): a) front view; b) back view

The third axis represents the $M_{f,Rk}/M_{eff,Rk}$ ratio, which may have a significant influence on the shape of the M - V interaction diagram, as shown in an example in Fig. 8.31. In this example, 5 bridge deck cross-sections are considered, with the same geometrical parameters ($H = var.$, $t_w = 15mm$, $n_{st} = 5$), where 5 different $M_{f,Rk}/M_{eff,Rk}$ ratios are obtained by varying the curvature parameter. To show the difference between the reduced and full stiffener inertia, in each graph, the results are plotted for both $I_{sl}/3$ (black) and I_{sl} (red).

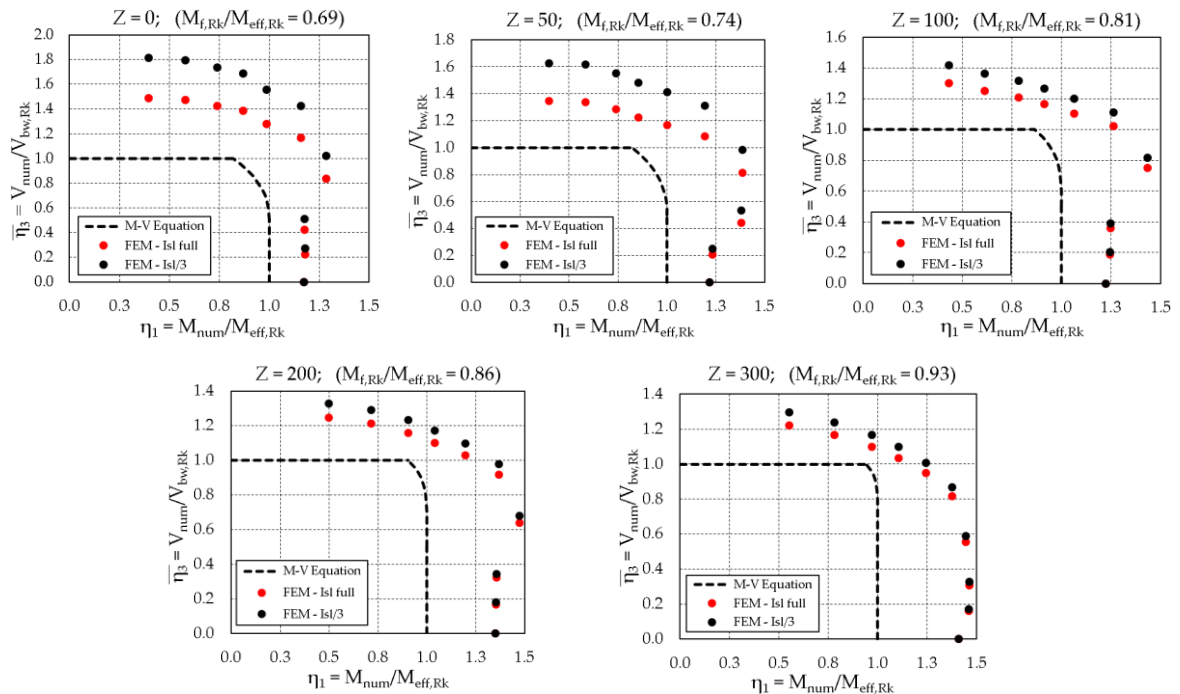


Fig. 8.31: FEM results vs M-V interaction formula for various $M_{f,Rk}/M_{eff,Rk}$ ratios

The graphs indicate that all the points are above the M - V interaction equation, which means that the use of Eq.(8.13) leads to a safe design for the studied geometries of bridge decks. Similar conclusions were found by Jäger *et al.* [139]. Namely, the authors claim that in the case of I-

girders with heavy flanges, commonly used in bridges ($M_{f,Rk}/M_{eff,Rk} > 0.88$), the modified equation leads to considerably safe results (avg. error up to 50% for $I_{sl}/3$ and up to 35% for I_{sl}), principally due to the conservatism of the shear resistance model from EN 1993-1-5.

The numerical results from Fig. 8.30 are statistically evaluated using the $M-V$ interaction formula. The statistical assessment is based on the distance between the numerically computed resistances and its central projection to the used $M-V$ interaction curve (*i.e.* surface). The statistical evaluation is summarized in Table 8.7, whereas the results are graphically interpreted in Fig. 8.32, separately for the reduced ($I_{sl}/3$) or the full (I_{sl}) second moment of area of the longitudinal stiffeners.

Table 8.7: Statistical assessment of the numerical results with respect to the M-V interaction formula Eq.(8.13) for both I_{sl} and $I_{sl}/3$ and various Z parameters

	$Z = 0$		$Z = 50$		$Z = 100$		$Z = 200$		$Z = 300$	
	$I_{sl}/3$	I_{sl}	$I_{sl}/3$	I_{sl}	$I_{sl}/3$	I_{sl}	$I_{sl}/3$	I_{sl}	$I_{sl}/3$	I_{sl}
SD (%)	25.8	19.8	20.9	14.6	18.8	13.3	15.6	12.5	15.1	14.0
Mean	1.454	1.400	1.419	1.354	1.372	1.329	1.367	1.340	1.363	1.351
CoV (%)	17.7	14.1	14.7	10.8	13.7	10.0	11.4	9.3	11.1	10.4
Max	2.243	1.886	2.145	1.846	2.086	1.839	1.984	1.805	1.966	1.924
Min	1.171	1.165	1.093	1.083	1.080	1.076	1.075	1.069	1.011	1.010

Based on the results of the statistical evaluation, several conclusions should be highlighted. First, none of the intermediate points are under the interaction equation, when only the web contribution to the shear resistance is considered ($V_{bw,Rk}$). Namely, the minimum differences obtained vary between approx. 17% and 1.0% on the safe side, from $Z = 0$ to $Z = 300$, respectively, which confirms that the $M-V$ interaction equation may be safely applied across the entire range of parameters covered in this thesis ($M_{f,Rk}/M_{eff,Rk} \approx 0.7-1.0$). Secondly, once again a non-negligible level of conservatism may be noticed, which comes from the conservatism of both bending and shear resistance models, discussed in detail in sections 8.2 and 8.3, respectively. According to Table 8.7, the average differences vary between 45% for trapezoidal box-girders ($Z = 0$) to around 35% for the most curved girders ($Z = 300$). The descending trend is not surprising, given the declining trends obtained both in the case of the bending resistance model (see Fig. 8.11) and shear resistance model (see Fig. 8.26). Namely, based on Table 8.6, where the shear model is statistically evaluated, the mean difference decreased even more rapidly with the increase of curvature (*i.e.* from 57% for $Z = 0$ to 29% for $Z = 300$). However, the less emphasized difference obtained in the bending model (*i.e.* from 46% for $Z = 0$ to 38% for $Z = 300$), virtually flattens the average differences obtained from the statistical assessment of the overall $M-V$ interaction equation, presented in Table 8.7. Finally, the design solution in which the full inertia of the longitudinal stiffeners is considered in the assessment of the shear resistance proves once again to be safe and less conservative than the standardized one. In addition, as may be seen in Fig. 8.32, this solution shows an arguably smaller scatter of results, manifested by a reduced coefficient of variation, shown in Table 8.7.

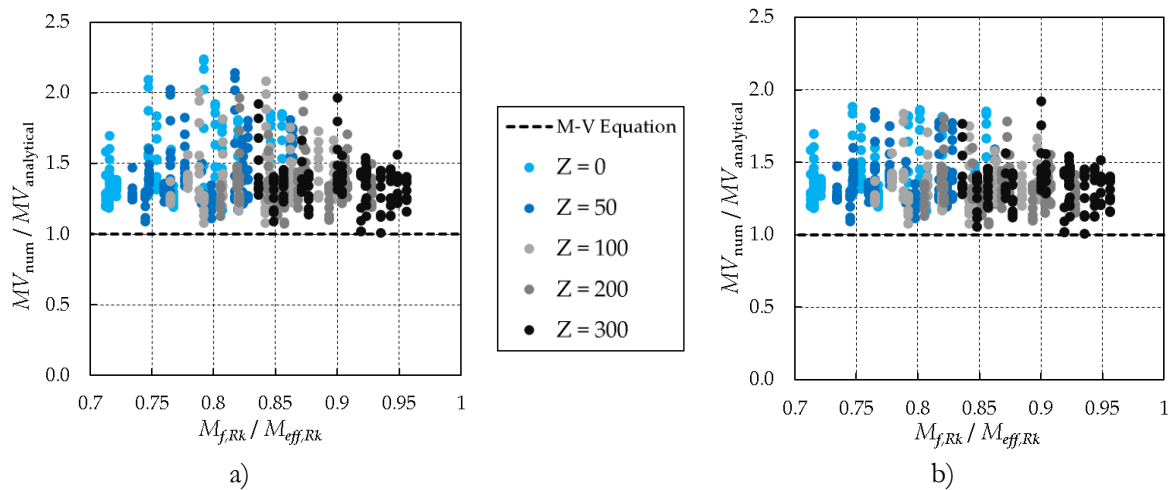


Fig. 8.32: FEM results vs M-V interaction formula for various $M_{f,Rk}/M_{eff,Rk}$ ratios:
a) $I_{sl}/3$ and b) I_{sl} - full

In the following section, besides the bending and shear resistance models, the partial factor (γ_M) is calculated also for the M - V interaction equation, thus enhancing the statistical evaluation presented in this section.

8.5 Statistical evaluation of resistance models – Determination of the partial factor γ_M

8.5.1 Introduction

To verify the structural safety of a structure, the Eurocodes use the semi-probabilistic approach, according to which each parameter (loading and resistance) has an average value (μ) (considered in the deterministic approach), but also a distribution function (for example, normal or log-normal), most often characterized by a variance (V) or a deviation (σ). The intersection of these distributions, which constitutes the probability of failure, is evaluated by means of two partial factors (γ_E and γ_M), corresponding to two independent sides - the Action and Resistance side.

In what concerns the steel structures, the Eurocodes recognize three characteristic failure modes: Mode 0 (deformation by yielding before failure - *e.g.* cross-section strength), Mode 1 (stability failure induced by imperfections and yielding - *e.g.* buckling strength of an element) and Mode 2 (fracture failure after yielding - *e.g.* strength of connections). Depending on the failure mode and the type of structure, EN 1993-1-5 and EN 1993-2 [164] recommend different partial factors for strength formulae, summarized in Table 8.8 for buildings and bridges.

Table 8.8: Recommended values for γ_M – EN 1993-1-5 and EN 1993-2

Structure type	Failure mode		
	Mode 0 ($\gamma_{M,0}$)	Mode 1 ($\gamma_{M,1}$)	Mode 2 ($\gamma_{M,2}$)
Buildings	1.00	1.00	1.25
Bridges	1.00	1.10	1.25

The objective of this section is to determine the appropriate values of γ_M for the strength formulae (*i.e.* resistance models) proposed in the previous three sections. Namely, the statistical evaluation is carried out separately for the bending resistance (M_{eff} , see Eq.(2.116)), shear resistance (V_{bs} , see Eq.(8.11)) and M - V interaction resistance models (Eq.(8.13)) and subsequently compared with the recommended values from Table 8.8 by the standard.

8.5.2 EN 1990 - methodology used for evaluation of γ_M

The partial factor γ_M is calculated on the basis of the procedure given in Annex D of EN 1990 [165] – ‘Design assisted by testing’. Although this procedure is primarily based on the evaluation of physical (experimental) tests carried out in the laboratory, it remains valid also for the evaluation of ‘numerical experiments’ (*i.e.* FEM-based result), carried out using computer simulations. This is particularly convenient when a large pool of ‘experimental’ results is required, in an attempt to account for a broad range of geometrical and material parameters, which would lead to unacceptably demanding laboratory test campaigns, such as the testing of over 200 bridge deck geometries studied in this thesis. Needless to say, to carry out an extensive campaign of numerical experiments for the reliability analysis, it is of the utmost importance to validate first the numerical model against real (physical) tests, which is done in the presented case in section 7.2.

In the following paragraphs, the main steps of this methodology are briefly described, whereas some specific remarks and simplifications are highlighted. Although in Annex D of EN 1990 [165] the procedure is divided into seven main steps, the 4-step approach from SAFEBRICITILE project [166] is used in this study, adopted also in Annex E of prEN 1993-1-1 [167].

- **STEP 1:**

In the first step, a theoretical resistance (strength) function is defined by Eq.(8.14)

$$r_t = g_r(\underline{X}) = g_r(X_1, X_2, \dots, X_j, \dots, X_k) \quad (8.14)$$

where \underline{X} represents the set of selected basic independent variables X_j , influencing the resistance of the relevant limit state. In this case, the safety coefficients γ_M are separately evaluated for three different resistance functions r_{tM} , r_{tV} and r_{tMV} , given by Eq.(2.116), Eq.(8.11) and Eq.(8.13), corresponding to the bending, shear, and M - V interaction resistance model, respectively.

For each considered geometry i in the parametric study, the theoretical resistances (*i.e.* resistance functions) ($r_{t,i}$) are compared with the ‘experimental’ values ($r_{e,i}$), obtained from advanced numerical simulations as specified before.

The biggest challenge of the first step is to choose appropriately the most relevant independent basic variables X_j and to collect the necessary statistical database (mean values, standard deviation, and/or the coefficient of variation) for each of them from the previous knowledge (*i.e.* literature). Namely, in the case of a simple resistance function that may be expressed as a product of several variables (*e.g.* axial resistance of a steel section), the choice of the independent variables is rather straightforward. However, for the three resistance functions under the current study, the degree of difficulty to separate individual variables tends to increase considerably since the strength

formulae are much more complex and several variables are often interrelated. For instance, to calculate the bending resistance of a box-girder cross-section with class 4, it is necessary to determine the effective section modulus W_{eff} . Although it seems like a parameter that depends only on the geometrical variables (*e.g.* thickness, width, thickness and height of the stiffeners, etc.), it also depends on the material properties (*e.g.* yield strength, modulus of elasticity) at various levels: *i*) for the computation of the critical stresses; *ii*) for the definition of the local buckling of sub-panels, through the parameter ε (see Eq.(2.26)); *iii*) through the slenderness parameter λ for both plate-type and column-type behavior (see Eq.(2.23)), etc. The level of complexity further increases in the assessment of the M-V interaction resistance function.

Finally, it should be highlighted that the required statistical data for all the mentioned variables is not always available in the literature. For instance, the statistical parameters for the main material properties (f_y, f_u, E) are well-reported and may be found in some of the actual standards (*e.g.* EN 10025-2 [148]) or the literature [166]. On the other hand, the standard deviation and/or variance of the geometrical parameters are covered by European Standard for execution and fabrication EN 1090-2 [168]. However, only the database for the most general geometrical parameters is available, such as the thickness t , the width b , and the length a of a steel plate, whereas, the specific data for the presented case (*e.g.* the radius of curvature R of the bottom flange, the local subpanel geometry b_m , etc.) are still not standardized.

Therefore, owing to an increased level of uncertainty for the presented study, based on the choice of the basic variables, for which the database exists in the standardized form, four different scenarios are considered for the statistical assessment, summarized in Table 8.9. In this table, f_y and E are the yield strength and the modulus of elasticity, t , b , and a are the thickness, the width, and the length of the bottom flange panel, whereas t_w and h_w are the thickness and the height of the webs, respectively.

Table 8.9: Scenarios for the statistical assessment based on the choice of the basic variables

Scenario	Material variables		Geometrical variables				
	f_y	E	t	b	a	t_w	h_w
1 – ‘None’	-	-	-	-	-	-	-
2 – ‘ f_y only’	X_1	-	-	-	-	-	-
3 – ‘Mat + Geom’	$\max(X_1; X_2)$		$\max(X_3; X_4; X_5; X_6; X_7)$				
4 – ‘All’	X_1	X_2	X_3	X_4	X_5	X_6	X_7

According to the first scenario, all the variables are assumed as deterministic quantities with no variability. Tran [8] also considered this scenario for the assessment of the partial factor of the proposed formula. In the second scenario, only the variation of the yield strength is considered, being the basic variable with the highest impact on all three resistance functions under evaluation. In the third scenario, studied by Tankova *et al.* [169], only one material and one geometrical variable are combined, however, the ones with the highest coefficient of variations, V_{mat} and V_{geom} , respectively. Finally, in the last scenario, both the material and the geometrical parameters are considered as random variables, despite their mutual dependence and even overlapping in some cases. The second, third, and fourth scenarios were considered in the SAFEBRICKTILE project [166], where the latter two were assessed as slightly too conservative.

Nevertheless, the advantage of considering these 4 scenarios is that a certain sensitivity of the partial factor may be assessed, depending on the number of random variables. The distributions of the basic variables considered in these four scenarios are given in Table 8.10.

Table 8.10: Recommended distributions for material and geometrical variables [166]

Basic variable	Symbol	$X_{\text{mean}}/X_{\text{nom}}$ (Mean/Nominal)	V_{X_i} (CoV)
Material	f_y	1.2	5.0%
	E	1.0	3.0%
Geometry	t	1.0	2.5%
	b	1.0	0.9%
	a	1.0	0.9%
	t_w	1.0	2.5%
	h_w	1.0	0.9%

- **STEP 2:**

In the second step, the results from each of n ‘numerical experiments’ (*i.e.* FEM-based result) ($r_{e,i}$) are compared with the theoretical values (*i.e.* resistances obtained using proposed analytical formulae) ($r_{t,i}$). This comparison is carried out in several consecutive sub-steps defined in Annex D of EN 1990 [165]. First, it is necessary to determine the so-called ‘mean value correction factor’ (b), which represents the inclination of the regression line through the origin for considered scatter of n ($r_{t,i}; r_{e,i}$) points, as schematically presented in Fig. 8.33.

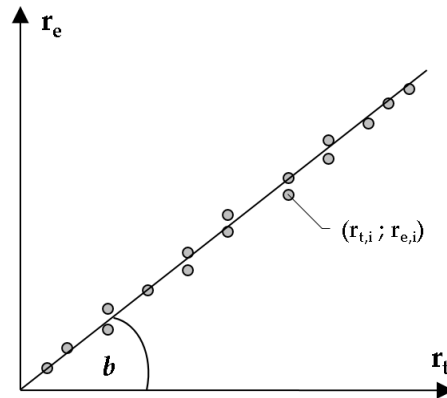


Fig. 8.33: Schematic illustration of $r_t - r_e$ diagram

The correction factor b may be calculated through least-square approximation, by Eq.(8.15):

$$b = \frac{\sum_{i=1}^n r_{t,i} \cdot r_{e,i}}{\sum_{i=1}^n (r_{t,i})^2} \quad (8.15)$$

Once the mean value of the correction factor b is calculated, it is necessary to determine the error term δ_i for each pair of ($r_{t,i}; r_{e,i}$) using Eq.(8.16) and subsequently the coefficient of variation of error term V_δ by equation Eq.(8.17).

$$\delta_i = \frac{r_{e,i}}{b \cdot r_{t,i}} \quad (8.16)$$

$$V_\delta = \sqrt{\exp(S_\Delta^2) - 1} \quad (8.17)$$

where

$$S_\Delta^2 = \frac{1}{n-1} \sum_{i=1}^n (\Delta_i - \bar{\Delta})^2 \quad (8.18)$$

$$\bar{\Delta} = \frac{1}{n} \sum_{i=1}^n \Delta_i \quad (8.19)$$

$$\Delta_i = \ln(\delta_i) \quad (8.20)$$

In theory, the coefficient of variation V_δ should be sufficient to represent the variation of the theoretical resistance model r_t . However, since in reality the number of tests is often limited and thus insufficient to cover all the variation in the model, the total coefficient of variation V_r needs to be increased by the variation of the basic input variables V_n (*i.e.* $V_r^2 = V_\delta^2 + V_n^2$). The calculation of V_n is addressed in the following step.

- **STEP 3:**

In the first two steps, the statistical evaluation refers merely to the differences between n ‘experimental’ results (commonly expressed in terms of strength) and the same strength obtained by the resistance function. However, in this step, the sensitivity of the resistance function itself to the variability of the basic input variables X_j is addressed, by introducing the coefficient of variation (*i.e.* error propagation) term V_n .

The calculation of the coefficient of variation of the basic input variables V_n depends primarily on the complexity of the theoretical strength formula, which is in detail explained in Annex D of EN 1990 [165] and further elaborated in SAFEFRICITILE project [166]. Namely, the standard recognizes two types of resistance functions – *i*) simple product functions (*e.g.* $r_t = X_1 \times X_2 \dots X_i$) and *ii*) more complicated resistance functions (*e.g.* $r_t = g_n(X_1, X_2 \dots X_i)$). For these two common formats of resistance functions, V_n may be calculated by Eq.(8.21) and Eq.(8.22), respectively.

$$V_n^2 = \sum V_{X_j}^2 \quad (8.21)$$

$$V_{r,t,i}^2 = \frac{1}{r_{t,i}(X_m)^2} \sum_{j=1}^k \left(\frac{\partial r_{t,i}(X_j)}{\partial X_j} \sigma_j \right)^2 \quad (8.22)$$

However, as discussed before (see STEP 1), the resistance functions under investigation in this thesis cannot be written as a simple product of independent variables, nor they have a closed analytical format for which derivative of an independent variable ($\partial r_{t,i}(X_j)/\partial X_j$) can be found. Hence, in this study, an alternative approach is implemented, according to which four simplified scenarios are considered, based on the selection of the basic input variables (see Table 8.9). Subsequently, using the distributions (*i.e.* CoV) of the basic variables considered in these four scenarios that are available in the literature (see Table 8.10), $V_{r,t}$ is then determined by Eq.(8.21),

which was found acceptably correct in aforementioned studies [166],[169]. Therefore, the value of $V_{r,t}$ for studied four scenarios is respectively $V_{r,t,1} = 0$, $V_{r,t,2} = 0.05$, $V_{r,t,3} = 0.056$ and $V_{r,t,4} = 0.07$.

It should be stated that none of these four scenarios is generally ‘more correct’ since in all cases an averaging effect is taken into account; however, the principal reason for considering all four cases is to assess the sensitivity of the partial factor γ_M to the number and the variability of the basic input variables.

- **STEP 4:**

Finally, in the last step, the partial factor (γ_M) is calculated. In general, according to Annex D of EN 1990 [165], the partial factor is determined as the ratio between the characteristic (r_k) and the design value of the strength (r_d) by Eq.(8.23) as:

$$\gamma_M = \frac{r_k}{r_d} \quad (8.23)$$

where the ‘characteristic value’ is defined as a value with a specified (non-) exceedance probability that commonly corresponds to the 5% fractile (or 95% exceedance probability), whereas the ‘design value’ is a value with a non-exceedance probability corresponding to the value of $\alpha_R \times \beta$ given (commonly equal to $0.8 \times 3.8 = 3.04$ for the reference period of 50 years).

However, as explained in [166], in the case of the design checks of steel structures, and specifically in the case where the strength is predominantly a function of the yield stress f_y , the nominal values are often close to the design point. Therefore, the ‘characteristic value’ is seldomly used in the design of steel structures, but instead, the ‘nominal value’ is considered, which results in a slightly modified expression for the determination of the partial factor given by Eq.(8.24) as:

$$\gamma_M = \frac{1}{n} \sum \gamma_{M,i} = \frac{1}{n} \sum \frac{r_{nom,i}}{r_{d,i}} \quad (8.24)$$

where $r_{nom,i}$ is the resistance function evaluated with nominal values of the input parameters ($r_{nom} = g_r(\underline{X}_{nom})$) for each specimen i , whereas $r_{d,i}$ is the resistance function evaluated with mean values of the input parameters for each specimen i , using Eq.(8.25).

$$\begin{aligned} r_{d,i} &= br_{i,i}(\underline{X}_m) \exp\left(-k_{d,\infty} \frac{Q_{rt}^2}{Q_i} - k_{d,n} \frac{Q_\delta^2}{Q_i} - 0.5Q_i^2\right) \quad , \quad n \leq 100 \\ r_{d,i} &= br_{i,i}(\underline{X}_m) \exp(-k_{d,\infty} Q_i - 0.5Q_i^2) \quad , \quad n > 100 \end{aligned} \quad (8.25)$$

In these expressions, $g_r(\underline{X}_m)$ represents the value of the resistance function evaluated with the mean values of basic input variables, $k_{d,n}$ and $k_{d,\infty}$, are the design fractile factors, respectively for n and infinite single test results, whose values are given in Table D.1 and Table D.2 of Annex D of EN 1990 [165]. Finally, the log-normal variation coefficients (Q_δ , $Q_{r,t}$, Q) are calculated from Eqs.(8.26)-(8.28) as follows:

$$Q_\delta = \sqrt{\ln(V_\delta^2 + 1)} \quad (8.26)$$

$$Q_{r,t} = \sqrt{\ln(V_{r,t}^2 + 1)} \quad (8.27)$$

$$Q = \sqrt{\ln(V_r^2 + 1)} = \sqrt{\ln(V_\delta^2 + V_{r,t}^2 + 1)} \quad (8.28)$$

It should be highlighted once again that r_d is calculated individually for each experimental results, comprising a total of n values or $r_{d,i}$.

8.5.3 Calculated γ_M factors

Finally, the proposed rules for the bending resistance (M_{eff} , see Eq.(2.116)), shear resistance (V_{br} , see Eq.(8.11)) and M-V interaction resistance (Eq.(8.13)) are statistically evaluated based on partial factor γ_M . The procedure and the main assumptions for the determination of the partial factor are described in 8.5.2. The results of the statistical assessment are thus presented separately for these three subsets (bending, shear, and M-V interaction), and compared with the value of the corresponding partial factor, recommended by EN1993-2 (see Table 8.8).

8.5.3.1 Bending

The calculated partial factors for the bending resistance model are presented in Fig. 8.34. The figure illustrates the variation of the partial factor for various curvature parameters and different scenarios considered for the assessment of the partial factor (see Table 8.9). As the total number of ‘experimental’ tests in pure bending for all curvatures is 210, the partial factor for each curvature consists of $n = 42$ results.

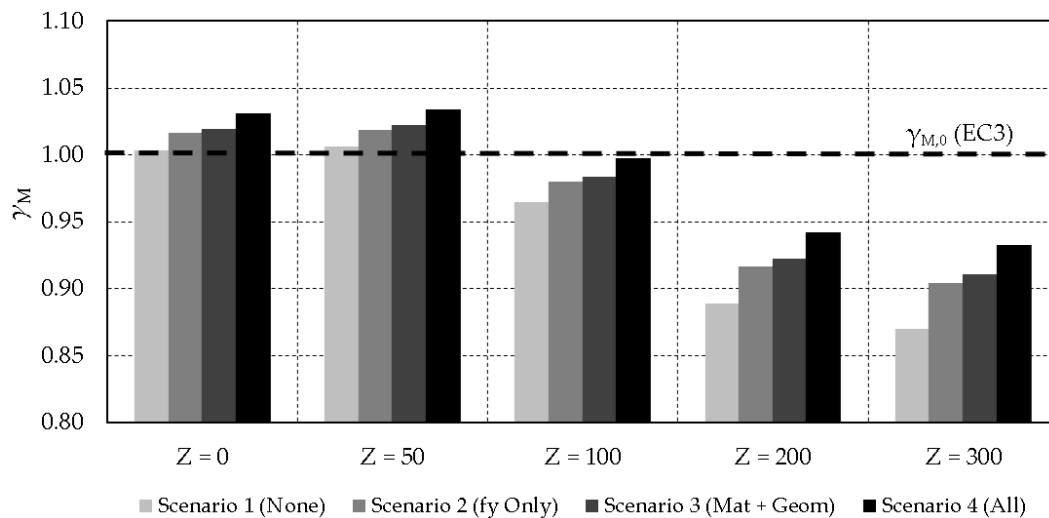


Fig. 8.34: All results organized by curvature parameter for four different distributions of the basic variables ($V_{r,t,1} = 0$, $V_{r,t,2} = 0.05$, $V_{r,t,3} = 0.056$ and $V_{r,t,4} = 0.07$)

The calculated partial factors are close to the value of $\gamma_{M,0} = 1.0$ recommended by the design standard. Namely, the partial factor shows a declining trend with the increase of curvature, from $\gamma_{M,0} = 1.03$ for $Z = 0$ to $\gamma_{M,0} = 0.91$ for $Z = 300$. Slightly lower values of γ_M may be justified by the aforementioned conservatism of the proposed methodology in the case of highly curved cross-sections (see 8.2.3). On the other hand, the variation of the partial factor with respect to the number of basic variables is not significant, regardless of the curvature parameter. Namely, the difference is more pronounced only in the first scenario, in which all the variables are assumed as deterministic quantities with no variability, which may be considered an extreme case. The

difference between the other three scenarios is less pronounced, with the highest partial factors, as expected, obtained for the scenario where the variability of all the basic variables is accounted for.

The exact values of all γ_M are summarized in Table 8.11, where it may be also seen the mean value and the CoV for each of four scenarios calculated using a larger sample of $n = 210$ results (*i.e.* for the entire scope of curvatures). The results show that the mean value varies in a very narrow range between 0.96 and 1.0, with acceptably low coefficient of variation between 6.6% and 4.8%, respectively.

Table 8.11: Partial factors γ_M for bending resistance model

	Scenario 1 (None)	Scenario 2 (f_y Only)	Scenario 3 (Mat + Geom)	Scenario 4 (All)
Z = 0	1.003	1.016	1.019	1.031
Z = 50	1.006	1.019	1.022	1.034
Z = 100	0.965	0.980	0.984	0.997
Z = 200	0.889	0.917	0.923	0.942
Z = 300	0.870	0.905	0.911	0.933
Mean	0.962	0.978	0.982	0.995
CoV (%)	6.6	5.5	5.4	4.8

In conclusion, although the partial factors obtained are slightly lower than those currently recommended by EN 1993-2 for cross-section resistance verifications, the author suggests to keep $\gamma_{M,0} = 1.0$.

8.5.3.2 Shear

The calculated partial factors for the shear resistance model are presented in Fig. 8.35. The figure illustrates the variation of the partial factor $\gamma_{M,1}$ for the aforementioned four scenarios considered for the assessment of the partial factor (see Table 8.9) and separately for reduced ($I_{st}/3$) and full (I_{st} – full) stiffener inertia. For the statistical assessment of the proposed design formula, only those experimental results with dominant shear failure are considered (around $n = 115$) since for larger aspect ratios, as stated before, ‘pure’ shear failure could not be attained.

The results indicate that the consideration of the reduced stiffener inertia ($I_{st}/3$), which is in line with EN 1993-1-5 design formula, give the partial factor equal or slightly higher than the value recommended by EN 1993-2 of $\gamma_{M,1} = 1.1$. On the other hand, the consideration of the full inertia leads to somewhat less conservative results and thus lower partial factors, which vary between $\gamma_{M,1} = 1.05$, and $\gamma_{M,1} = 1.07$ depending on the adopted distribution of the random variables. Once again, the proposed formula shows insignificant sensitivity to the number and variance of the basic input data. Consequently, it may be stated that the design code partial factor of $\gamma_{M,1} = 1.1$ is appropriate for the determination of the shear resistance.

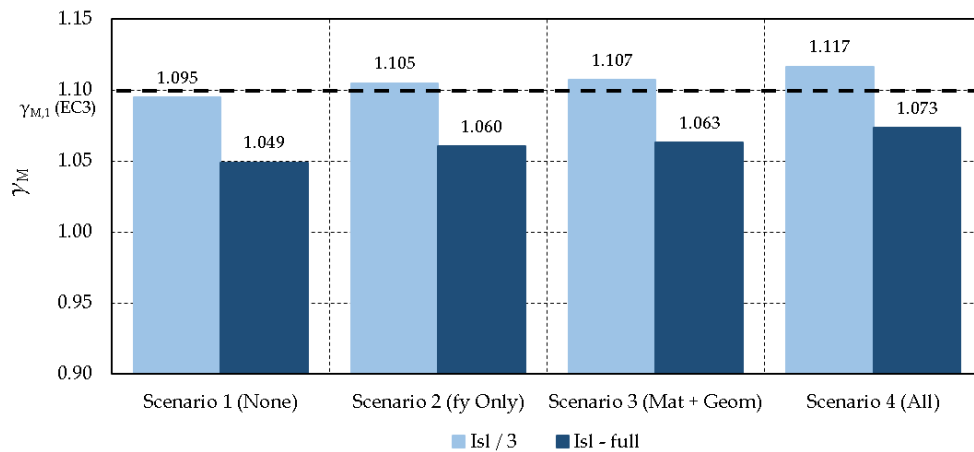


Fig. 8.35: All results organized by four different distributions of the basic variables – for reduced ($I_{sl}/3$) and full ($I_{sl} - \text{full}$) stiffener inertia

8.5.3.3 M-V interaction

Finally, the equivalent partial factor is calculated for the M-V interaction equation, and the results are represented in Fig. 8.36 and Fig. 8.37, for reduced and full stiffener inertia, respectively. Similar to Fig. 8.34, the variation of the equivalent partial factor for various curvature parameters is illustrated, separately for four scenarios assumed in the assessment of the partial factor are (see Table 8.9). The equivalent partial factor for each curvature is calculated using $n = 420$ ‘experimental’ results, whereas for the overall mean value and CoV, presented in Table 8.12 and Table 8.13, a total of $n = 2100$ results are considered.

In general, the results indicate that the equivalent partial factor varies approximately between $\gamma_M = 0.95$ and $\gamma_M = 1.05$, depending on the considered subset. In fact, in Fig. 8.36, where the reduced inertia of stiffeners is assumed, the results resemble the ones obtained for pure bending (see Fig. 8.34); however, slightly magnified partial factors are obtained due to the interaction with the shear, which tends to increase the equivalent partial factor, as indicated in Fig. 8.35. Once again, it may be noticed that the equivalent partial factor shows a declining trend with the increase of curvature, *i.e.* from $\gamma_M = 1.06$ for $Z = 0$ to $\gamma_M = 0.97$ for $Z = 300$.

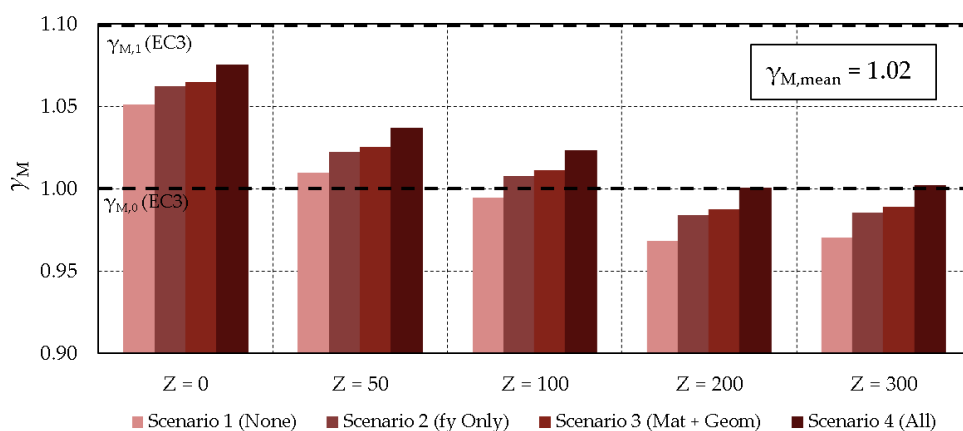


Fig. 8.36: All results organized by curvature parameter for four different distributions of the basic variables, considering reduced stiffener inertia $I_{sl}/3$

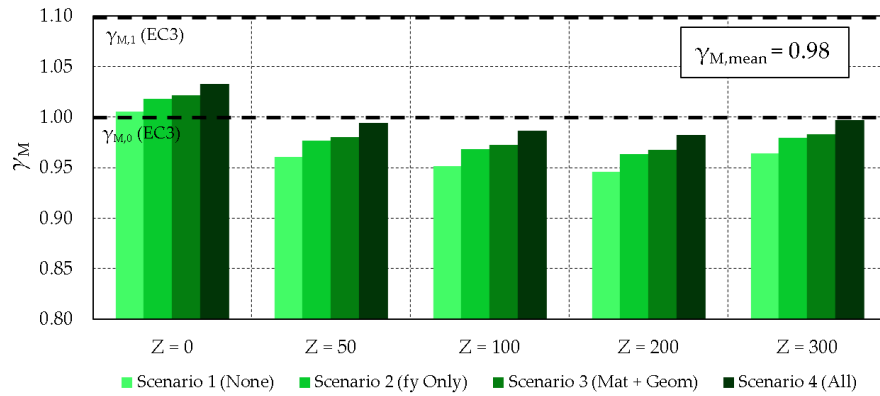


Fig. 8.37: All results organized by curvature parameter for four different distributions of the basic variables, considering full stiffener inertia I_{st} -full

Furthermore, the consideration of full inertia, yields slightly lower values of the equivalent partial factor ($\gamma_M = 0.98$ on average) with respect to the reduced stiffener inertia ($\gamma_M = 1.02$ on average), and also the lower coefficient of variations as shown in Table 8.12 and Table 8.13. Finally, the adoption of the second, third, or the fourth scenario for the distribution of basic variables, leads to virtually similar results, whereas the consideration of the first scenario results in an underestimation of the equivalent partial factor.

Table 8.12: Equivalent partial factors γ_M for M-V resistance model – $I_{st}/3$

	Scenario 1 (None)	Scenario 2 (f_y Only)	Scenario 3 (Mat + Geom)	Scenario 4 (All)
Z = 0	1.051	1.062	1.065	1.075
Z = 50	1.010	1.022	1.025	1.037
Z = 100	0.994	1.008	1.011	1.023
Z = 200	0.968	0.984	0.987	1.001
Z = 300	0.970	0.985	0.989	1.002
Mean	1.003	1.016	1.019	1.031
CoV (%)	3.4	3.2	3.1	3.0

Table 8.13: Equivalent partial factors γ_M for M-V resistance model – I_{st} full

	Scenario 1 (None)	Scenario 2 (f_y Only)	Scenario 3 (Mat + Geom)	Scenario 4 (All)
Z = 0	1.005	1.018	1.021	1.033
Z = 50	0.961	0.977	0.980	0.994
Z = 100	0.952	0.968	0.972	0.987
Z = 200	0.946	0.963	0.967	0.982
Z = 300	0.964	0.979	0.983	0.997
Mean	0.968	0.983	0.987	1.000
CoV (%)	2.4	2.2	2.2	2.0

In conclusion, it is recommended to keep the values $\gamma_{M,0} = 1.0$ and $\gamma_{M,1} = 1.1$.

8.6 Summary

In this chapter, the final task (Task 5) was accomplished, in which the applicability of the M - V interaction equation, proposed by Jáger *et al.* [139] and adopted in prEN 1993-1-5 [140], was assessed in the case of box-girder bridge cross-sections with a curved bottom flange.

First, it was necessary to define analytical models for the prediction of the bending ($M_{eff,Rk}$) and the shear resistance ($V_{bw,Rk}$) for these innovative bridge deck cross-sections, which were then directly implemented in the M - V interaction equation by Jáger *et al.* [139]. Both resistance models were adapted to have an EC3-like format and were statistically assessed against the numerical results collected in chapter 7 of the thesis.

Subsequently, the safety assessment of the M - V equation was conducted against the FEM results. The results showed that the M - V interaction equation might be safely applied across the entire range of parameters covered in this thesis ($M_{f,Rk}/M_{eff,Rk} \approx 0.7$ – 1.0), with the minimum differences between numerical and analytical results of approx. 17% and 1.0% on the safe side, from $Z = 0$ to $Z = 300$, respectively. The average differences of around 45% for trapezoidal box-girders ($Z = 0$) and 35% for the most curved girders ($Z = 300$) were explained by the conservatism of both bending resistance model and shear resistance model, discussed in detail in sections 8.2 and 8.3, respectively.

Moreover, the design solution, in which the full inertia of the longitudinal stiffeners was assumed for the determination of the shear resistance, was also studied in this chapter, and it was concluded that such a solution led to safe but less conservative results when compared to the standardized reduced stiffness ($I_d/3$).

Finally, all three models (*i.e.* bending resistance model, shear resistance model, and the M - V interaction model) were statistically assessed against the numerical results by calculating the partial factor (γ_M). The partial factors obtained were slightly lower than those recommended by EN 1993-2. Nevertheless, there are still insufficient real experimental results that could justify the reduction of the partial factor, hence, it was recommended to keep $\gamma_{M,0} = 1.0$ and $\gamma_{M,1} = 1.1$ for the bending and shear resistance models, in the design of box-girder bridges, regardless of the curvature parameter.

9. Summary and future prospects

9.1 Conclusions

For a better systematical review on the main conclusions of the work, the thesis is, for this purpose, thematically divided into three main clusters, based on the specific targeted goals, defined on the basis of the knowledge deficiencies identified in *Literature review*, as follows:

i) Individual curved panels subjected to axial compression

The topic represents the key aspect in the stability of thin-walled structures, and thus, has been widely investigated (mainly analytically and numerically) in the past. However, the main contribution of this thesis, which differentiates this study from the majority of former ones, is the experimental campaign carried out in the scope of the ULTIMATEPANEL project, thus narrowing the deficiencies discovered in the literature. In total, 32 axial compression tests were reported, both on stiffened and unstiffened curved panels, and the results were used for the evaluation of the existing design standards and semi-empirical formulae available in the literature. In particular, it was shown that:

- An unstable post-buckling path, governed by geometrical nonlinearities, characterizes the behavior of curved panels, with a dominant global buckling in case of unstiffened panels, whereas, in the case of stiffened panels, local buckling prevails;
- The methods by Tran *et al.* [59] and OUTBURST research project [85] gave a reasonably good approximation of the ultimate compressive resistance (with the mean difference of

9% and 6%, respectively, with respect to the experimental results); however, the method from the OUTBURST research project was used further in the thesis since it allows for higher local curvatures up to $Z_{loc} \leq 100$;

- The use of the available standards (EN 1993-1-5 and DNV-RP-C202) almost in all cases leads to an underestimation of the ultimate resistance, with the mean difference of 30% (CoV \approx 28%) and 50% (CoV \approx 37%), respectively;

Moreover, using the FEM models validated against the experimental tests, a numerical study was performed to assess the sensitivity of curved panels to imperfections. The following conclusions should be mentioned:

- The imperfection sensitivity decreases with the number of stiffeners, regardless of the curvature parameter, reducing the relevance of the imperfection shape adopted;
- The equivalent geometric imperfections recommended by EN 1993-1-5 for flat plates lead to conservative results (50% on average) for highly curved panels;
- The imperfections in the form of the global eigenmode lead to the results closest to the experimental ones (mean difference 7%), whereas the imperfections in the form of one of the first four eigenmodes lead to the safest approach in more than 80% of cases;

In addition, since the dimensions of the tested curved panels do not correspond to the realistic full-scale geometries encountered in bridge deck applications, another numerical study was carried, with an extended pool of the geometrical parameters. In specific, the aim of the study was: *i*) to determine the buckling resistance of the stiffened curved and non-curved panels in compression; *ii*) to compare the numerical resistances to the methods proposed by Tran *et al.* [59] and OUTBURST research project [85] and *iii*) to assess the difference between two boundary conditions - ‘free’ and ‘rigid’ (both nominally simply-supported). The following conclusions were observed:

- The ultimate resistance strongly depends on the boundary conditions, despite all of them being nominally simply-supported. For all considered panels, a higher resistance is obtained for ‘rigid’ boundary conditions (in average 11.5%), with the difference particularly emphasized in the case of trapezoidal stiffeners (in average 17.7%), attributed to torsional rigidity, which is known to be substantially higher when compared to an open flat stiffener;
- For short heavily stiffened plates, the ultimate resistance is governed by the local buckling of subpanels, while the global buckling has a minor effect. Hence, for these panels, an increase of curvature does not increase dramatically the ultimate resistance with respect to the flat ones since the local curvatures of subpanels in bridge design rarely exceeds $Z_{loc} < 15$;
- Consequently, the favorable effect of curvature on the ultimate resistance is particularly pronounced for longer and lightly stiffened plates, where, the resistance may be up to 2 times higher compared to corresponding flat plate;
- Furthermore, owing to high cross-section second moment of area in the case of very curved panels, no global buckling (plate-type or column-type) occurs, meaning that failure is governed by local buckling of subpanels in combination with material yielding.

Therefore, the resistance of highly curved panels converges towards a constant value regardless of the aspect ratio since the local buckling is independent of the panel length;

- Besides, in contrast to flat plates, in the case of highly curved panels, due to high cross-section inertia and strong arch effect, the type and size of longitudinal stiffeners have only a negligible influence on the ultimate resistance, at least for the stiffeners class 3 considered in this thesis;
- These findings present some of the substantial advantages of curved panels with respect to the flat ones since considerable savings could be made by reduction of the number of the transversal cross-frames (diaphragms) and by the reduction of the number and size of longitudinal stiffeners;
- Finally, for the considered geometrical configurations, the difference between the methods by Tran *et al.* [59] and the OUTBURST research project [85] is arguably small (on average 4.6%), with the maximum difference of 14%. Namely, Tran's method seems to be at times too optimistic, whereas the latter is too conservative for certain configurations. Nevertheless, the method developed withing the Outburst project was recommended since it explicitly accounts for the unfavourable post-critical behavior of the curved panels with small-to-intermediate values of local curvature parameter, found in bridges.

ii) **Individual curved panels subjected to in-plane shear**

Since very few studies had tackled this problem and no clear design method for the assessment of the ultimate shear had ever been reported, an extensive numerical program was carried out to overcome this deficiency. The design rules developed are conceptually similar to the codified ones for flat plates, hence, it was necessary first to propose a formula for the determination of the critical shear load for a curved panel. Therefore, a supplementary numerical study was carried out, where the influence of several parameters on the elastic critical behavior, namely 1st buckling mode, was investigated, such as curvature parameter $Z \leq 100$, aspect ratio ($\alpha = 0.2$ to $\alpha = 5.0$ and three boundary conditions (nominally simply-supported but with different levels of edge constraints). The following conclusions were highlighted:

- In general, the shorter and the more curved the panel is, the higher is the critical load. For very long panels ($\alpha > 4.0$), the aspect ratio has only minor influence on the critical load;
- In contrast to flat plates, the elastic critical stress of cylindrically curved panels under shear highly depends on the edge constraints studied in the thesis. Moreover, the effect of the constraints is particularly emphasized for highly curved and long panels;
- The NACA charts give the shear buckling coefficients that correspond best to the boundary condition BC2, which in most cases is the realistic assumption, being an intermediate case. However, the NACA monographs may lead to an overestimation or underestimation of the critical load for boundary conditions BC1 and BC3, respectively;
- Finally, a set of formulae was proposed for the prediction of the shear buckling coefficient that may substitute the use of impractical and outdated NACA monographs. The validity of formulae was verified within geometrical ranges (*i.e.* $1 < Z \leq 100$ and $0.2 < \alpha \leq 5.0$)

encountered in real engineering applications, and, for the very first time, the influence of various in-plane edge constraints was explicitly accounted for.

Subsequently, another extensive numerical study is carried out with the aim to *i*) investigate the post-buckling behavior of simply supported cylindrically curved steel panels and *ii*) propose expression for the determination of the ultimate shear resistance of unstiffened curved panels, valid for three different types of edge constraints, various curvatures ($Z \leq 50$) and aspect ratios ($\alpha \leq 5.0$). The most relevant findings from this study were:

- The post-critical behavior depends on both the curvature parameter and the aspect ratio and not only one of them; however, the higher the curvature parameter and the aspect ratio, the lower is the ultimate resistance;
- For slender panels, the ultimate resistance highly depends on the rigidity of the boundary conditions. Namely, in the case of rigid boundary conditions (BC2 or BC3), where the tension field may be developed, considerable post-critical reserves may be mobilized, resulting in a higher ultimate resistance;
- Finally, a set of expressions was proposed for simple estimation of the shear reduction factor for curved panels. The formulas were derived assuming the equivalent geometric imperfections recommended by EN 1993-1-5, which leads to a safe design. The proposed rules are valid for geometries that may be of practical use in offshore, aeronautics, and bridge applications.

iii) Curved panels integrated into box-girder bridge cross-sections subjected to bending and shear (M-V interaction)

Finally, in the scope of the European OUTBURST research project, the study on the entire box-girder bridge cross-sections integrating a curved panel in the bottom flange was carried out, to characterize the entire spectrum of behavior, *i.e.* from pure bending to ‘almost’ pure shear, and to assess the validity of the developed bending and shear resistance models, as well as the $M - V$ interaction equation, available in the literature. The study was accomplished in four steps:

(i) First, the **experimental campaign** was carried out, comprising two bridge deck prototypes, tested as three-point bending tests to achieve $M-V$ interaction near the intermediate support. Such an experimental program had not been reported in the literature, hence the scientific relevance of the reported experimental study is twofold: *i*) it gives an insight into the real behavior of the box-girder bridge deck with a curved bottom flange and *ii*) the reported results are available for the entire scientific community, allowing for the reproduction of experimental and/or numerical results, thus extending the scope of this thesis. In addition, the experimental results were compared with the *Curved panel approach* developed within the OUTBURST project, and satisfactory results were obtained.

(ii) Subsequently, a **numerical parametric study** was carried out, using a numerical FE model calibrated against the experimental results. In total, 210 different bridge cross-section geometries were considered, where the main geometrical parameters (*e.g.* curvature parameter, aspect ratio, the thickness of flange and web, stiffener type, number, and configuration, etc.) were varied within the common ranges encountered in the real examples of bridges. For each geometry, 10

different M/V -ratios were applied, characterizing the entire spectrum of $M-V$ interaction behavior and generating 210 interaction diagrams as the main output of the parametric study.

(iii) In the third step, **a new bending and shear resistance models were developed**. Both models correspond to the design rules for trapezoidal box-girder bridge cross-section from EN 1993-1-5; however, adjusted to account for the presence of the curved bottom flange, as the only difference with respect to the conventional trapezoidal cross-section shape. An example with all the required steps for the determination of the bending and shear resistance of a cross-section with a curved bottom flange is shown in Annex D.

Regarding the bending resistance model, the following conclusions were found:

- The numerical results give higher bending resistance for all 210 studied geometries (approximately 40% in average), which may be attributed to two main inaccuracies: (i) Analytical method does not account for additional restraints on the loaded edges, coming from rigid transversal frames (diaphragms), and (ii) The analytical model assumes the most unfavourable uniform axial stress gradient across the height of the curved bottom flange;
- The difference between the FEM and analytical results is particularly high for longer ($\alpha \geq 1$) and less curved panels ($Z \leq 100$), where the global buckling mode of the bottom flange may occur, requiring the use of conservative formulae for the estimation of the critical plate-type stress and interpolation equation from the standard;
- Finally, since the proposed model is based on the same conservative formulae from the actual design code, a better estimation of the bending resistance of box-girders with curved panels may be achieved once the formulae from the design code are revised to account for several relevant parameters (edge constraints, stiffeners torsional rigidity, etc.).

Relatively to the developed shear resistance model, named ‘extended web method’ in the thesis, the following findings were observed:

- The proposed extended web approach is safe, presenting a lower bound of all numerical results, except for two cases where the numerical results were overestimated for 2% and 6%;
- Moreover, being an extension of EN 1993-1-5 approach, whose conservatism was appointed by multiple authors, it is in most cases overly safe; however, it tends to decrease the difference with respect to the FEM results to satisfactory 29% with the increase of curvature parameter;
- In an attempt to reduce further the $V_{\text{num}}/V_{\text{analy}}$ ratio, the full stiffener flexural stiffness was also considered, and it was concluded that the proposed shear analytical method would still return safe solutions, at least for the ranges of parameters studied in this thesis. In fact, the consideration of the full inertia is particularly emphasized in the case of thin webs prone to buckling, where the full inertia of the stiffeners may partly compensate for an overly conservative standard approach for the calculation of the global shear buckling.

By implementing the developed bending and shear resistance models in the M - V interaction equation by Jäger *et al.* [139], the safety assessment of this criterion was conducted by comparing the analytical with the FEM results. In specific, the following conclusions were drawn:

- The M - V interaction equation may be safely applied across the entire range of parameters covered in this thesis ($M_{f,Rk}/M_{eff,Rk} \approx 0.7$ – 1.0), with the minimum differences between numerical and analytical results of approx. 17% and 1.0% on the safe side, from $Z = 0$ to $Z = 300$, respectively;
- The average differences of around 45% for trapezoidal box-girders ($Z = 0$) and 35% for the most curved girders ($Z = 300$) are explained by the conservatism of both bending resistance model and shear resistance model;
- Moreover, the design solution in which the full inertia of the longitudinal stiffeners is assumed for the determination of the shear resistance leads to safe and even less conservative results when compared to the standardized reduced stiffness ($I_d/3$).

(*ii*) Finally, a **statistical evaluation of the proposed rules** was carried out against the FEM results for all three resistance functions (*i.e.* bending, shear, and the M - V interaction model) by calculating the corresponding partial factors (γ_M). The partial factors obtained are slightly lower than that recommended by EN 1993-2, hence, it was suggested to keep $\gamma_{M,0} = 1.0$ and $\gamma_{M,1} = 1.1$, in the design of box-girder bridges, also in the case with the curved bottom flange.

9.2 Outlook on future research

Most of the targeted objectives set at the outset of the thesis were successfully accomplished. However, many relevant questions emerged along the way that ought to be addressed in the future. In this section, some aspects worth of further investigation are summarized:

More experimental results. Although two independent experimental campaigns were carried out in this thesis in [chapter 3](#) and [chapter 6](#), which lends a certain credibility to the results of the subsequent numerical investigations presented, more tests should be performed, both on isolated cylindrically curved panels and structures incorporating cylindrically curved steel panels (*e.g.* box-girder bridge segments), with the geometries other than those examined in this work. The collection of more experimental results should always be an absolute priority for multiple reasons: *i*) to obtain a realistic insight into the behavior of the curved panels; *ii*) to enhance the validity of the developed rules; *iii*) to record and create a plausible and standardized database of the initial imperfections for the curved panels and *iv*) to collect data on the material and geometrical properties to generate distributions of potential basic variables for future safety level assessments and calibration of new design rules.

Further studies on the curved panels under shear. A comprehensive numerical study on curved panels under shear was performed in [chapter 4](#) and [chapter 5](#) and the design rules were developed, yet, the study has its limitations. First of all, only the unstiffened curved panels were studied, which means that the rules developed have restricted field of application in real stiffened structures (*i.e.* bridges). Namely, the rules may be used for the verification of the shear resistance on a local level (*i.e.* curved subpanels between the longitudinal stiffeners) or the assessment of global shear resistance for lightly stiffened curved panels. Consequently, it is required to study

the influence of the longitudinal stiffeners as well and to extend the rules developed in this thesis. Secondly, the design rules developed in the thesis are purely empirical, coming from a FEM study, whereas no experimental evidence was provided to increase their validity. Hence, the work would contribute from an experimental study on curved panels under shear, similar to the one under axial compression performed in the scope of the ULTIMATEPANEL research project.

Curved steel panels under combined non-uniform compression and shear. As it was revealed in the thesis, a curved panel, being the bottom flange of a box-girder bridge cross-section is in reality subjected to a complex stress state of combined non-uniform compression and shear, which was not explicitly accounted for in the developed analytical models. To the best of the author's knowledge, no interaction formula in the literature deals with curved panels under such loading. The starting point for this study might be the interaction formula from the offshore design standards (DNV-RP-C202), used for the assessment of the ultimate strength of full revolution cylinders, based on the theoretical grounds established by Timoshenko & Gere in 1963 [121]. The development of an appropriate interaction formula may allow also for the safety verification of some extreme cases of the box-girder bridges, *e.g.* cross-sections with the depth of the curved part equal to the total height ($f = H$), as indicated in Fig. 2.5.

High strength steels (HSS). In all numerical parametric studies presented herein, the structural steel S355 was considered, being representative of common mild steel used in bridge construction. However, due to technological improvements and increasing structural and architectural demands, the use of high-strength steel is becoming nowadays more common, especially in bridge designs. This requires an adjustment of actual stability design rules, accounting for specific aspects related to the use of HSS, such as enhanced material properties, more favourable residual stress distributions, different plastic behavior, etc.

9.3 Publications

In this section, the author publications disseminated within the course of this thesis are summarized:

9.3.1 International journal papers (ISI)

- J.P. Martins, F. Ljubinkovic, L. Simões da Silva, H. Gervásio, (2018) *Behavior of thin walled curved steel plates under generalised in-plane stresses: A review*, Journal of Constructional Steel Research, Vol. 140: 191-207.
<https://doi.org/10.1016/j.jcsr.2017.10.018>
- F. Ljubinkovic, J.P. Martins, H. Gervásio, L. Simões da Silva, (2019) *Eigenvalue analysis of cylindrically curved steel panels under pure shear*, Thin-Walled Structures, Vol. 141: 447-459.
<https://doi.org/10.1016/j.tws.2019.04.025>
- F. Ljubinkovic, J.P. Martins, H. Gervásio, L. Simões da Silva, (2019) *Ultimate load of cylindrically curved steel panels under pure shear*, Thin-Walled Structures, Vol. 142: 171-188.
<https://doi.org/10.1016/j.tws.2019.04.022>

- F. Ljubinkovic, J.P. Martins, H. Gervásio L. Simões da Silva, J.O. Pedro, (2019) *Experimental behavior of curved bottom flanges in steel box-girder bridge decks*, Journal of Constructional Steel Research, Vol. 160: 169-188.
<https://doi.org/10.1016/j.jcsr.2019.05.031>
- F. Ljubinkovic, J.P. Martins, H. Gervásio L. Simões da Silva, C. Leitão, (2020) *Experimental and numerical investigation on cylindrically curved steel panels under uniform compression*, Thin-Walled Structures, Vol. 149: 106527.
<https://doi.org/10.1016/j.tws.2019.106527>
- C. Hendy, M. Cai, J.P. Martins, F. Ljubinkovic, L. Simões da Silva, (2020) *New design rules for plate girders curved in plan*, Bridge Engineering (2020). ISSN 1478-4637 | E-ISSN 1751-7664.
<https://doi.org/10.1680/jbren.19.00057>
- F. Ljubinkovic, J.P. Martins, H. Gervásio, L. Simões da Silva, (2020) *Steel box-girder bridge decks with curved bottom flange – Numerical studies*, Steel Construction, Vol. 13, Issue 3: 238-244.
<https://doi.org/10.1002/stco.202000007>
- F. Ljubinkovic, J.P. Martins, H. Gervásio, L. Simões da Silva, (2021) *Resistance of curved steel cross-sections for bridge deck applications: Design proposals*, Journal of Constructional Steel Research, Vol. 182 (3): 106679.
<https://doi.org/10.1016/j.jcsr.2021.106679>

9.3.2 International conference proceedings

- F. Ljubinkovic, J.P. Martins, L. Simões da Silva, (2017) *Cylindrically curved steel panels in bridge design: Buckling and post-buckling behavior under shear stresses*. Special Issue: Proceedings of Eurosteel 2017, Vol. 1, Issue 2-3: 888-897; September 2017, Copenhagen, Denmark.
<https://doi.org/10.1002/cepa.129>
- F. Ljubinkovic, J.P. Martins, H. Gervásio, L. Simões da Silva, C. Leitão, (2017) *Experimental analysis of unstiffened cylindrically curved panels*. Special issue: XI Conference on Steel and Composite Construction, Vol. 1, Issue 4: 448-457; December 2017, Coimbra, Portugal.
<https://doi.org/10.1002/cepa.544>
- F. Ljubinkovic, J.P. Martins, H. Gervásio, L. Simões da Silva, (2018) *Experimental investigation on the bridge segments with transversally curved bottom flange*. IOP Conference Series: Materials Science and Engineering, Vol. 419, Issue 1: 012042; 9th International Symposium on Steel Bridges; September 2018, Prague, Czech Republic.
<https://doi.org/10.1088/1757-899X/419/1/012042>

- F. Ljubinkovic, J.P. Martins, H. Gervásio, L. Simões da Silva, C. Leitão, (2019) *Experimental and numerical analysis of cylindrically curved panels under uniform compression*. 9th International Conference on Steel and Aluminium Structures (ICSAS19); July 2019, Bradford, United Kingdom.
- F. Ljubinkovic, J.P. Martins, H. Gervásio, L. Simões da Silva, (2019) *Ultimate shear resistance of cylindrically curved steel panels*. The International Colloquium On Stability And Ductility Of Steel Structures (SDSS19); 11-13 September 2019, Prague, Czech Republic.
- F. Ljubinkovic, J.P. Martins, H. Gervásio, L. Simões da Silva, C. Leitão, (2017) *Experimental and numerical investigation on the steel box-girder bridge decks with curved bottom flange*. Special issue: XII Conference on Steel and Composite Construction, Vol. 3, Issue 5-6: 118-127; December 2019, Coimbra, Portugal.
<https://doi.org/10.1002/cepa.1187>

9.3.3 OUTBURST Project dissemination

9.3.3.1 Official meetings and workshops

Within the scope of the European OUTBURST Project, the author participated in the following official meetings and workshops:

- 1st OUTBURST Meeting: 25-26 August 2016, Hotel HolidayInn, Lisbon, Portugal;
- 3rd OUTBURST Meeting: 2-3 October 2017, Univerza v Ljubljana, Fakulteta za gradbeništvo in geodezijo, Ljubljana, Slovenia;
- 4th OUTBURST Meeting: 1-2 February 2018, Universidade de Coimbra, Departamento de Engenharia Civil, Coimbra, Portugal;
- 5th OUTBURST Meeting: 27-28 September 2018, Universität Stuttgart, Institut für Konstruktion und Entwurf, Stuttgart, Germany;
- 6th OUTBURST Meeting: 7 February 2019, Euston Tower, London, United Kingdom;
- OUTBURST Workshop - *Optimization of steel plated bridges*, 28 June 2019, Universität Stuttgart, Institut für Konstruktion und Entwurf, Stuttgart, Germany;

9.3.3.2 Project deliverables and official reports

Within the scope of the European OUTBURST Project, the author participated in the production of the following official project reports and deliverables:

- F. Ljubinkovic, J.P. Martins, H. Gervásio, L. Simões da Silva, (2019) *Life cycle assessment of curved bridges*. RFCS Research Project OUTBURST (RFCS-2015-709782): Deliverable 3.1;
- F. Ljubinkovic, J.P. Martins, H. Gervásio, L. Simões da Silva, (2018) *Assessment of the public perception on bridge aesthetics*. RFCS Research Project OUTBURST (RFCS-2015-709782): Deliverable 3.2;
- F. Ljubinkovic, J.P. Martins, L. Simões da Silva, (2018) *Experimental results of tests on prototype bridge segments*. RFCS Research Project OUTBURST (RFCS-2015-709782): Deliverable 7.2;

- J.P. Martins, F. Ljubinkovic, L. Simões da Silva, (2019) *Report on calibration of numerical models with experimental results from WP7*. RFCS Research Project OUTBURST (RFCS-2015-709782): Deliverable 8.1;
- J.P. Martins, F. Ljubinkovic, L. Simões da Silva, (2019) *Report on numerical parametric study and analysis of results*. RFCS Research Project OUTBURST (RFCS-2015-709782): Deliverable 8.2;
- F. Ljubinkovic, J.P. Martins, H. Gervásio, L. Simões da Silva, (2019) *Numerical simulations on box-girder bridge cross-section integrating curved steel panels*. RFCS Research Project OUTBURST (RFCS-2015-709782): Deliverable 11.1;
- F. Ljubinkovic, J.P. Martins, H. Gervásio, L. Simões da Silva, C. Hendy, C. Minjie, J.O. Pedro, A. Biscaya, A. Reis, S. Piculin, P. Može, V. Pourostad, U. Kuhlmann (2019) *Design rules for bridge cross-sections integrating curved or nonrectangular steel panels*. RFCS Research Project OUTBURST (RFCS-2015-709782): Deliverable 11.2;
- L. Simões da Silva, J.P. Martins, F. Ljubinkovic, S. Piculin, P. Može, U. Kuhlmann, V. Pourostad, C. Hendy (2019) *Design guidelines*. RFCS Research Project OUTBURST (RFCS-2015-709782): Deliverable 12.1;
- J.O. Pedro, A. Biscaya, A. Reis, C. Hendy, C. Minjie, K.A. Santiago, F. Saba, F. Ljubinkovic, J.P. Martins, L. Simões da Silva, S. Piculin, P. Može, U. Kuhlmann, V. Pourostad (2019) *Design examples and case studies*. RFCS Research Project OUTBURST (RFCS-2015-709782): Deliverable 12.2;
- L. Simões da Silva, J.P. Martins, F. Ljubinkovic, P. Može, S. Piculin, U. Kuhlmann, V. Pourostad, A. Reis, J.O. Pedro, G. Dorrer, J. Eitelberger, M. Pircher, C. Hendy, F. Saba (2017) *Design rules for bridge cross-sections integrating curved or nonrectangular steel panels*. RFCS Research Project OUTBURST (RFCS-2015-709782): 1st Periodic Technical Report;
- L. Simões da Silva, J.P. Martins, F. Ljubinkovic, P. Može, S. Piculin, U. Kuhlmann, V. Pourostad, A. Reis, J.O. Pedro, G. Dorrer, J. Eitelberger, M. Pircher, C. Hendy, C. Minjie (2019) *Design rules for bridge cross-sections integrating curved or nonrectangular steel panels*. RFCS Research Project OUTBURST (RFCS-2015-709782): 2nd Periodic Technical Report;

9.3.4 Other publications and thesis-related presentations

- **TWG 8.3 Meeting Presentation**

- F. Ljubinkovic, J.P. Martins, H. Gervásio, L. Simões da Silva (2020), *Design of box-girder bridge cross-sections with curved bottom flange*, 20th Official Meeting of Working Group “EN 1993-1-5” & 31st Official Meeting of ECCS-TWG 8.3, September 29th, Web Meeting;

- F. Ljubinkovic, J.P. Martins, L. Simões da Silva, P. Može, S. Piculin, J.O. Pedro (2021), *Report on investigation of buckling behaviour of cylindrically curved panels*, 21st Official Meeting of Working Group “EN 1993-1-5” & 32nd Official Meeting of ECCS-TWG 8.3, February 12th, Web Meeting;

Bibliography

- [1] Unknown author, *Dangsan Bridge*, Seoul, South Korea. [Online] Available from: <https://structurae.net/en/structures/westgate-bridge>. [Accessed 6th September 2019].
- [2] Unknown author, *Westgate Bridge*, Gloucester, UK. [Online] Available from: <https://structurae.net/structures/dangsan-railway-bridge>. [Accessed 6th September 2019].
- [3] K. Hoppner, *Gateshead Millennium Bridge*, Newcastle, UK. [Online] Available from: [https://commons.wikimedia.org/wiki/File:Gateshead_Millennium_Bridge,_30_November_2008_\(3\).jpg](https://commons.wikimedia.org/wiki/File:Gateshead_Millennium_Bridge,_30_November_2008_(3).jpg). [Accessed 5th September 2019].
- [4] Unknown author, *Peace Bridge*, Londonderry, UK. [Online] Available from: <http://www.flying-media.co.uk/wp-content/uploads/2015/01/P1020767.jpg>. [Accessed 6th September 2019].
- [5] A. Reis, J.O. Pedro, A.B. Graça, C. Hendy, P. Romoli, L. Simões da Silva, and J.P. Martins, (2017) *Report on the characterization of relevant parameters of curved plated bridge structures and identification of bridge cases where they can be found*. RFCS Research Project OUTBURST (RFCS-2015-709782): Deliverable 2.1.
- [6] J. Strasky, P. Novotny, D. Arco, and I. Raventós, (2018) *Construction of “Lo Passador”: A self-anchored suspension bridge at the Ebro River Delta, Spain*, IABSE, Structural Engineering International, 24:1, 114-117.
- [7] Unknown author, *Renault Bridge, Boulogne-Billancourt, France*. [Online] Available from: https://files.structurae.net/files/photos/f000147/pers_nuit03.jpg. [Accessed 5th September 2019].
- [8] K. Tran, (2012) *Étude de la résistance et de la stabilité des tôles courbes cylindriques en acier. Application aux ouvrages d’art*. PhD thesis. Université Paris-Est, Paris. (in French).
- [9] J.P. Martins, (2014) *Behavior of cylindrical curved steel panels under in-plane stresses*. PhD thesis. University of Coimbra, Coimbra.
- [10] T. Manco, (2018) *Behavior of unstiffened and stiffened curved steel panels under in-plane and out-of-plane actions*. PhD thesis. University of Coimbra, Coimbra.
- [11] CEN, EN 1993-1-5:2006 - Eurocode 3: Design of steel structures, *Part 1-5: Plated Structural Elements*. European Committee for Standardisation, Brussels; 2006.

- [12] CEN, EN 1993-1-6:2007 – Eurocode 3: Design of steel structures, *Part 1-6: Strength and Stability of Shell Structures*. European Committee for Standardisation, Brussels; 2007.
- [13] DNVGL, (2017) RP-C202 - *Buckling Strength of Shells*. Recommended Practice, DNVGL.
- [14] DNVGL, (2018) DNVGL-CG-0128. *Buckling Class Guideline*, DNVGL, Norway.
- [15] ABS, (2018) *Guide for Buckling and Ultimate Strength Assessment for Offshore Structures*. American Bureau of Shipping.
- [16] J.P. Park, J.K. Paik, and J.K. Seo, (2018) *Numerical investigation and development of design formula for cylindrically curved plates on ships and offshore structures*. *Thin-walled Structures* 132 (8), 93-110.
- [17] J.P. Martins, F. Ljubinkovic, L. Simões da Silva, and H. Gervásio, (2018) *Behavior of thin walled curved steel plates under generalised in-plane stresses: A review*. *Journal of Constructional Steel Research*, Vol. 140; 191-207.
- [18] OUTBURST (2016-2019), *Optimal and aesthetic design of curved steel bridges*. Fund for Coal and Steel Grant Agreement No. RFCS-2015-709782.
- [19] ULTIMATEPANEL (2016-2019), *Curved thin panels for structural application*. Portuguese Foundation for Science and Technology. Referência: PTDC/ ECM-EST/1494/2014.
- [20] S. Batdorf, (1947) *A simplified method of elastic-stability analysis for thin cylindrical shells*. National Advisory Committee for Aeronautics, Report No. 874.
- [21] C. Baudin, *Pont Charles de Gaulle - Paris (75)*, technical brochure. [Online] Available from: <http://www.baudinchateauf.com/realisation/pont-charles-de-gaulle-a-paris-75/> [Accessed 13th September 2019].
- [22] Triede, *Footbridge over Tâmega River (1997)*. [Online] Available from: <https://www.triede.pt/en/works/ponte-pedonal-chaves-portugal>. [Accessed 13th September 2019].
- [23] M. Prieto, O. Gutiérrez, G. Carreras, and J. García, (2007) *Escaleritas Viaduct in Las Palmas de Gran Canaria*, *Hormigón y Acero*, nº 244, 2nd Semester.
- [24] J. Pablo, P. Arias, G. Miguel, and M. Sacristán, (2007) *Puente Atirantado Puerta de las Rozas sobre la A-6, Madrid*, *Hormigón y Acero - Realizaciones 1998-2008* [in Spanish].
- [25] M. Campos and G. Mo, (2010) *Santiago Calatrava - Outstanding Projects (2001-2010)*, [PowerPoint presentation].
- [26] J. Pablo, G. Miguel, and M. Motesinos, (2007) *Puente atirantado de acceso al parque científico y tecnológico de Cantabria, Santander*, *Hormigón y Acero - Realizaciones 1998-2008* [in Spanish].
- [27] F. Mato and A. Ruiz, (2007) *Puente Arco sobre el Río Deba*, *Hormigón y Acero - Realizaciones 1998-2008* [in Spanish].
- [28] J. Manterola, M. Gil, and J. Rojas, (2011) *Spatial Arch Bridges Over the Galindo and Bidasoa Rivers*. IABSE, *Structural Engineering International*, nº 1/2011.
- [29] J. Manterola, (2008) *Pasarela de Peatones - Zaragoza EXPO 2008* [PowerPoint presentation].
- [30] L. Viñuela and J. Salcedo, (2009) *L'Assut de l'Or Bridge (Serrería Bridge)*, Valencia, Spain, *Hormigón y Acero*, Volume 60, no. 254, 7-28.

-
- [31] S. Calatrava, (2008) *Bridge of Strings*, [Online] Available from: <https://calatrava.com/projects/bridge-of-strings-light-rail-trainjerusalem.html>; [Accessed 13th September 2019].
- [32] ArchDaily, (2009) *Knokke Footbridge*, [Online] Available from: <http://www.archdaily.com/39664/knokke-footbridge-ney-partners/>; [Accessed 13th September 2019].
- [33] L. Hauge, M. Carter, and T. Vejrum, (2012) *Stonecutters Bridge*, Hong Kong: design of steel deck, ICE, Bridge Engineering, Volume 165, Issue BE1, 53-58.
- [34] Wikiwand, (2010) *Pont Confluences*, [Online] Available from: http://www.wikiwand.com/fr/Pont_Confluences [in French]; [Accessed 13th September 2019].
- [35] Sobrino, (2016) *King-Post Truss Bridge over the Ter River in Girona, Spain*, IABSE, Structural Engineering International, no. 3/2016.
- [36] G. Mo, K. Overton, and I. Fernando, (2018) *Norgessporten road bridge, the gateway to Norway*. Conference paper: 9th International Symposium on Steel Bridges, Prague, Czech Republic.
- [37] V. Buyck, (2017) *New Wear Crossing*, Sunderland, Victor Buyck Steel Construction Brochure.
- [38] J. Radić, Z. Šavor, G. H. Kovačević, and N. Mujkanović, (2015) *Main design of the Mainland – Čiovo Island Bridge*, [Online] Available from: <https://www.researchgate.net/publication/290105639>, [Accessed 10th September 2020].
- [39] Neill & Partners, (2016-2019) *Boekeloose Bridge*, [Online] Available from: <http://www.ney.be/project/boekeloose-bridge.html>; [Accessed 13th September 2019].
- [40] Pergenova, (2020) *The Genao San Giorgio Bridge*, [Online] Available from: <https://www.pergenova.com/en/index.html>; [Accessed 10th September 2020].
- [41] M.M. Domb, and R.L. Leigh, (2002) *Refined design curves for shear buckling of curved panels using nonlinear finite element analysis*. 43rd AIAA/ASME/AHS/ASC Structures, Structural Dynamics and Materials Conference, Denver, U.S.A, Paper #2002-1257.
- [42] H.Z. Park, S.R. Cho, J.M. Cheong, and D.B. Lee, (2005) *Ultimate strength analysis of curved stiffened shell of container bilge strakes*. Proc. The Annual Autumn Meeting, Society of Naval Architects of Korea, Yong-In, pp. 189–195.
- [43] Y.W. Kwon, Y.I. Park, J.K. Paik, and J.M. Lee, (2004) *Buckling and ultimate strength characteristics for ship curved plate structures*. Proc. The Annual Autumn Meeting, Society of Naval Architects of Korea, Sancheong, pp. 351–356.
- [44] Y. Maeno, H. Yamaguchi, Y. Fujii, and T. Yao, (2004) *Buckling/plastic collapse behavior strength of bilge circle and its contribution to the ultimate longitudinal strength of ship's hull girder*. Proc. ISOPE IV, 296–302.
- [45] Lloyd's Register of Shipping, (2015) [Online] Available from: <https://www.lr.org/en/marine-shipping/>; [Accessed 13th September 2019].
- [46] S. Redshaw, (1934) *The Elastic Instability of a Thin Curved Panel Subjected to an Axial Thrust, Its Axial and Circumferential Edges Being Simply Supported*. British Aeronautical Research Committee. Report and Memorandum No. 1565.
- [47] S. Timoshenko, (1936) *Theory of Elastic Stability*. New York, McGraw-Hill.
-

- [48] K. Marguerre, (1937) *The apparent width of the plate in compression*. NACA, Technical Memorandum No. 883.
- [49] G. Gerard, and H. Becker, (1957) *Handbook of structural stability: Part III – Buckling of curved plates and shells*. NACA, Technical Note 3783.
- [50] A.S. Volmir, (1963) *Stability of elastic systems*. Fizmatig, Moscow. Trans. National Aeronautics and Space Administration. Technical Memorandum number: AD628508.
- [51] E. Stowell, (1943) *Critical compressive stress for curved sheet supported along all edges and elastically restrained against rotation along the unloaded edges*. NACA: 99–109.
- [52] S. Batdorf, and M. Schildrout, (1948) *Critical axial compressive stress of a curved rectangular panel with a central chordwise stiffener*. NACA. Technical note No. 1661.
- [53] M. Schildrout, and M. Stein, (1949) *Critical axial compressive stress of a curved rectangular panel with a central longitudinal stiffener*. NACA. Technical note No. 1879.
- [54] M.M. Domb, and R.L. Leigh, (2001) *Refined design curves for compressive buckling of curved panels using nonlinear finite element analysis*. 42nd AIAA / ASME / AHS / ASC Structures, Structural Dynamics and Materials Conference, Seattle, U.S.A. Paper 1348.
- [55] J.P. Martins, L. Simões da Silva, and A. Reis, (2013) *Eigenvalue analysis of cylindrically curved panels under compressive stresses – Extension of rules from EN1993-1-5*. Thin-Walled Structures, No. 68; 183–194.
- [56] J.P. Martins, L. Simões da Silva, and N. Silvestre, (2016) *Energy-based analytical model to predict the elastic critical behavior of curved panels*. Journal of Constructional Steel Research, No. 127; 165-175.
- [57] J. Park, K. Iijima, and T. Yao, (2008) *Estimation of buckling and collapse behaviors of stiffened curved plates under compressive load*. International Society of Offshore and Polar Engineers, USA.
- [58] M. Khedmati, and P. Edalat, (2010) *A numerical investigation into the effects of parabolic curvature on the buckling strength and behavior of stiffened plates under in-plane compression*. Latin American Journal of Solids and Structures; 7(3).
- [59] K. Tran, C. Douthe, K. Sab, J. Dallot, and L. Davaine, (2014) *Buckling of stiffened curved panels under uniform axial compression*. J. Constr. Steel Res. 103:140–147.
- [60] S. Piculin, and P. Može, (2019) *Guidelines for optimum design of longitudinally stiffened curved panels*. Research Fund for Coal and Steel (RFCS) project – optimization of steel plated bridges in shape and strength (OUTBURST, RFCS-2015-709782): Deliverable 9.2.
- [61] K. Magnucki, and M. Mackiewicz, (2006) *Elastic buckling of an axially compressed cylindrical panel with edges simply supported and one edge free*. Thin-Walled Structures, 44 (4), 387-392.
- [62] R. Wilde, K. Zawodny, and K. Magnucki, (2007) *Critical state of an axially compressed cylindrical panel with three edges simply supported and one edge free*. Thin-Walled Structures, 45, 955-959.
- [63] H. Eipakchi, and M. Shariati, (2011) *Buckling analysis of a cylindrical panel under axial stress using perturbation technique*. ZAMM Journal of applied mathematics and mechanics, Vol.91, No. 2; 138–145.
- [64] A.N.P. Andico, Y.M Park, and B.H. Choi (2018) *Buckling strength increment of curved panels due to rotational stiffness of closed-section ribs under uniaxial compression*. International Journal of Steel Structures, Vol. 18, No. 4, pp 1363–1372.

-
- [65] S. Levy, (1943) *Large deflection theory of curved sheet*. National Advisory Committee for Aeronautics, Technical Notes No. 895.
- [66] A. Volmir, (1967) *A translation of flexible plates and shells*. Air Force Flight Dynamics Laboratory, Technical Report No. 66-216, Wright-Patterson Air Force Base.
- [67] O. Tamate, and H. Sekine, (1969) *Postbuckling Behavior of Thin Curved Panels under axial compression*. Japan Society of Mechanical Engineering, Vol. 12, No. 51: 415-420.
- [68] C. Chia, (1987) *Nonlinear vibration and postbuckling of unsymmetrical laminated imperfect shallow cylindrical panels with mixed boundary conditions resting on 271 elastic foundation*. International Journal of Engineering Science, Vol. 25, No. 4: 427-441.
- [69] N. Breivik, (1997) *Thermal and mechanical response of curved composite panels*. PhD Thesis, Faculty of the Virginia Polytechnic Institute and State University, Blacksburg.
- [70] E. Magnucka-Blandzi, and K. Magnucki, (2016) *Buckling and post-buckling behavior of shallow – nearly flat cylindrical panels under axial compression*. Bulletin of the Polish Academy of Sciences, Technical Sciences, Vol. 64, No. 3.
- [71] T. Manco, J.P. Martins, C. Rigueiro, and L. Simões da Silva, (2018) *Semi-analytical model for the prediction of the post-buckling behavior of unstiffened cylindrically curved steel panels under uniaxial compression*. Marine Structures 59, 387–400.
- [72] T. Manco, J.P. Martins, C. Rigueiro, and L. Simões da Silva, (2019) *Semi-analytical model for the prediction of the post-buckling behavior of stiffened cylindrically curved steel panels under uniaxial compression*. Computers & Structures, 211, 27-42.
- [73] T. Manco, J.P. Martins, C. Rigueiro, and L. Simões da Silva, (2019) *Ultimate resistance of isotropic cylindrically curved steel panels under in-plane uniaxial compression*. Journal of Constructional Steel Research, Vol. 159, 95-108.
- [74] J.S. Park, K. Iijima, and T. Yao, (2007) *Estimation of buckling and ultimate strength for curved plates with and without stiffeners under axial compressive load*. TEAM 2007, Yokohama, Japan.
- [75] K. Tran, L. Davaine, C. Douthe, and K. Sab, (2012) *Stability of curved panels under uniform axial compression*. J. Constr. Steel Res. 69; 30–38.
- [76] CEN, EN 1993-1-1:2005 - Design of steel structures: *General rules and rules for buildings*. Brussels, European Committee for Standardisation; 2005.
- [77] K. Tran, C. Douthe, K. Sab, J. Dallot, and L. Davaine, (2014) *A preliminary design formula for the strength of stiffened curved panels by design of experiment method*. Thin-Walled Structures, Vol. 79; 129-137.
- [78] J.P. Martins, L. Simões, and A. Reis, (2014) *Ultimate load of cylindrically curved panels under in plane compression and bending – extension of rules from EN1993-1-5*. Thin Walled Struct. 77, 36–47.
- [79] J.P. Martins, D. Beg, F. Sinur, L. Simões da Silva, and A. Reis, (2015) *Imperfection sensitivity of cylindrically curved steel panels*. Thin-Walled Structures, Vol. 89: 101–115.
- [80] J.H. Kim, J.S. Park, K.H. Lee, M.H. Kim, and J.M. Lee, (2014) *Computational analysis and design formula development for the design of curved plates for ships and offshore structures*. Struct. Eng. Mech. 49 (6), 705–726.
- [81] D. Faulkner, (1975) *A review of effective plating to be used in the analysis of stiffened plating in bending and compression*. J. Ship Res., 19(1), 1-17.
-

- [82] J. Seo, C. Song, J. Park, and J. Paik, (2016) *Nonlinear structural behavior and design formulae for calculating the ultimate strength of stiffened curved plates under axial compression*. *Thin Walled Structures*, Vol. 107:1-17.
- [83] N. Silvestre, A.P.C. Duarte, J.P. Martins and L. Simões da Silva, (2019) *GBT Buckling Analysis of Cylindrical Panels Under Compression*, *Structures* 17: 34-42.
- [84] A.D. Martins and N. Silvestre, (2019) *Modal analysis of the post-buckling behaviour of cylindrical steel panels under compression: Imperfection sensitivity and local interaction*, *Thin-Walled Struct.* 144, 106345.
- [85] S. Piculin, P. Može, (2020) *Experimental and numerical analysis of stiffened curved plates as bottom flanges of steel bridges*. *J. Constr. Steel Res.* Vol. 164.
- [86] S. Piculin, P. Može, (2020) *Stability behaviour of stiffened curved plates subjected to pure compression*. *Thin-Walled Struct.* (In Press), 107313.
- [87] H. Becker, (1958) *Handbook of structural stability. Part VI : Strength of stiffened curved plates and shells*. Rapport technique, New York University, Washington.
- [88] F.C. Thomas, (1974) *A Study of Rectangular Plates Subjected to Non-uniform Axial Compression*. PhD Thesis Georgia Institute of Technology, USA.
- [89] J.S. Newell, and W.H. Gale, (1932) *A Report on Aircraft Materials*. Massachusetts Institute of Technology, USA.
- [90] E.E. Sechler, (1934) *The Ultimate Compressive Strength of Thin Sheet Metal Panels*. Ph.D. thesis California Institute of Technology.
- [91] W.A. Wenzek, (1938) *The effective width of curved sheet after buckling*. NACA. Technical Memoranda No.: 880.
- [92] H.L. Cox, and W.J. Clenshaw, (1941) *Compression tests on curved plates of thin sheet duralumin*. Aeronautical Research Council. Reports and memoranda No.: 1849.
- [93] H. Crate, and L.R. Levin, (1943) *Data on buckling strength of curved sheet in compression*. NACA. Technical Report No.: L-557.
- [94] K.V. Jackson, and A.H. Hall, (1947) *Curved plates in compression*. National Research Council, AR-1.
- [95] G. Welter, (1945) *Curved aluminum-alloy sheets in compression for monocoque constructions*. *J. Aerosol Sci.* 12 (3) 357–369.
- [96] G. Welter, (1946a) *Influence of different factors on buckling loads of curved thin aluminum-alloy sheets for monocoque constructions*. *J. Aerosol Sci.* 13 (4) 204–208.
- [97] G. Welter, (1946b) *The effect of radius of curvature and preliminary artificial eccentricities on buckling loads of curved thin aluminum-alloy sheets for monocoque constructions*. *J. Aerosol Sci.* 13 (11) 593–596.
- [98] E.H. Schuette, (1948) *Buckling of curved sheet in compression and its relation to the secant modulus*. *Journal of the Aeronautic Sciences* 15 (1) 18–22.
- [99] D.J. Tenerelli, and A.M.C. Holmes, (1972) *An Experimental Buckling Study of Skin-corrugated Ring-stiffened Curved Panels*. S.E.S.A. Spring Meeting, Cleveland, Paper No. 1993^a.
- [100] H. Gall, (1930) *Compressive strength of stiffened sheets of aluminum alloy*. Ph.D. thesis; Massachusetts Institute of Technology.

-
- [101] E. Lundquist, (1933) *Comparison of three methods for calculating the compressive strength of flat and slightly curved sheet and stiffener combinations*. Tech. Rep.; National Advisory Committee for Aeronautics, TC 455.
- [102] I.J. Gerard, and B.G. Dickens, (1936) *Stressed-skin structures. Compression tests of panels with tubular stiffeners*. Aeronautical Research Council. Reports and Memoranda No.: 1830.
- [103] W. Ramberg, A.E. McPherson, and S. Levy, (1939) *Compressive Tests of a Monocoque Box*. NACA. Technical Note No.: 721.
- [104] M. Holt, (1943) *Tests of aluminum-alloy stiffened sheet specimens cut from an airplane wing*. NACA. Technical Note No.: 883.
- [105] W. Ramberg, S. Levy, and K. Fienup, (1944) *Effect of curvature on strength of axially loaded sheet-stringer panels*. Tech. Rep.; NACA-Technical note 944.
- [106] A.B.T. Soderquist, (1961) *Experimental Investigation of Stability and Post Buckling Behavior of Stiffened Curved Plates*. Institute of Aerophysics, University of Toronto.
- [107] R.C. Tennyson, (1961) *An experimental investigation of the behavior of stiffened plates in axial compression*. UTIA. Technical Note No.: 57.
- [108] T. von Kármán, E.E. Sechler, and L.H. Donnell, (1932) *The strength of thin plates in compression*. Transaction of A.S.M.E.
- [109] C.A. Featherston, and C. Ruiz, (1998) *Buckling of curved panels under combined shear and compression*. Proceedings of the Institution of Mechanical Engineers, Part C: Journal of Mechanical Engineering Science, 212 (3), 183-196.
- [110] C.A. Featherston, (2000) *The use of finite element analysis in the examination of instability in flat plates and curved panels under compression and shear*. International Journal of Non-Linear Mechanics 35, 515-529.
- [111] R. Zimmermann, and R. Rolfes, (2006) *POSICOSS – improved post buckling simulation for design of fiber composite stiffened fuselage structures*. Composite Structures, Vol. 73, pp. 171-174.
- [112] R. Degenhardt, R. Rolfes, R. Zimmermann, and K. Rohwer, (2006) *COCOMAT – improved material exploitation of composite airframe structures by accurate simulation of post buckling and collapse*. Comp. Struct., Vol. 73, pp. 175-178.
- [113] S. Cho, H. Park, H. Kim, and J. Seo, (2007) *Experimental and numerical investigations on the ultimate strength of curved stiffened plates*. In: Proceeding 10th International Symposium on Practical Design of Ships and Other Floating Structures.
- [114] D.M.A. Leggett, (1937) *The elastic stability of a long and slightly bent plate under uniform shear*. Proc. R. Soc. A162; 62–83.
- [115] A. Kromm, (1939) *The limit of stability of curved plate strip under shear and axial stresses*. NACA. Technical note No., p. 898.
- [116] W.R. Dean, (1925) *Theory of elastic stability*. Proceedings of the Royal Society 107 (744); 734–760.
- [117] S.B. Batdorf, (1947) *A simplified method of elastic stability analysis for thin cylindrical shells I – Donnell's equation*. NACA Technical Report No, p. 1341.
- [118] M. Schildcrout, and M. Stein, (1949) *Critical combinations of shear and direct axial stress for curved rectangular panels*, NACA. Technical Note No, p. 1928.
-

- [119] S.B. Batdorf, (1947) *A simplified method of elastic-stability analysis for thin cylindrical shells II – Modified equilibrium equation*, NACA Technical Report No, p. 1342.
- [120] S.B. Batdorf, M. Stein, and M. Schildcrout, (1947) *Shear stress of curved rectangular panels*. NACA Technical Report No, p. 1348.
- [121] S.P. Timoshenko, and J.M. Gere, (1963) *Theory of Elastic Stability*, 2nd Ed. Int. student Ed. McGraw-Hill Book Company.
- [122] E.H. Baker, L. Kovalevsky, and F.L. Rish, (1972) *Structural analysis of shells*. Malabar, Florida. Robert E. Krieger Pub. Company.
- [123] M.N. Bismarck-Nasr, (1995) *Buckling analysis of cylindrically curved panels based on a two-field variables variational principle*. Computers & Structures 51 (4), 453-457.
- [124] M.P. Nemeth and J.H. Starnes Jr., (1998) *The NASA monographs on shell stability design recommendations – A review and suggested improvements*. National Space Agency. Report number: TP-1998-206290.
- [125] M.M. Domb, (2002) *Nonlinear buckling predictions of curved panels under combined compression and shear loading*. In: 23rd Congress of International Council of the Aeronautical Sciences, ICAS2002, Toronto, Canada, pp. 322.1 – 322.8.
- [126] E.B. Machaly, S.S. Safar, and E.A. Abdel-Aal, (2010) *Shear strength of horizontally curved plate girder web panels with transverse stiffeners*. Journal of engineering and applied science, Vol. 57, No. 4, pp. 257-276.
- [127] M. Amani, B.L.O. Edlund, and M.M. Alinia, (2011) *Buckling and post-buckling behavior of unstiffened curved plates under uniform shear*. Thin-walled Structures 49 (8), 1017-1031.
- [128] P. Dubas, and E. Gehri, (1986) *Structural Stability, Behavior and Design of Steel Plated Structures*, Zurich, European Convention for Constructional Steelwork (ECCS), Publication number: 44.
- [129] C.A. Featherston, (2003) *Imperfection sensitivity of curved panels under combined compression and shear*, Int. J. Non-Linear Mech. 38; 225–238.
- [130] T. Höglund, (1998) *Shear buckling resistance of steel and aluminum plate girders*. Thin-walled Structures, 29, pp. 12-30.
- [131] B. Jáger, B. Kövesdi, and L. Dunai, (2017) *I-girders with unstiffened slender webs subjected by bending and shear interaction*, J. Constr. Steel Res. 131, pp. 176–188.
- [132] K.C. Rockey, (1971) *An ultimate load method for the design of plate girders*. Proc. Colloquium on Design of Plate and Box Girders for Ultimate Strength, IABSE 1971, pp. 253–268.
- [133] M.M. Alinia and S.H. Moosavi, (2009) *Stability of longitudinally stiffened web plates under interactive shear and bending force*. Thin-Walled Struct. 47, pp. 53–60.
- [134] K. Basler, (1961) *Strength of plate girders under combined bending and shear*. J. Struct. Div. ASCE 87 (7), pp. 181–197.
- [135] T. Höglund, (1994) K18 - *Design of steel structures*, Chapter K18 and K19 From the Building Handbook (in Swedish), SBI, KTH Royal Institute of Technology, Stockholm.
- [136] CEN, EN 1999-1-1:2007 - Eurocode 9: Design of aluminium structures, *Part 1–1: General Structural Rules*, European Committee for Standardisation, Brussels; 2007.
- [137] STN 73 1401, (2008) *Navrhovanie oceľových konštrukcií* (in Slovakian) (Design of Steel Structures), SÚTN Bratislava, March 2008.

-
- [138] ČSN 73 1401, (2008) *Navrhování ocelových konstrukcí* (in Czech) (Design of Steel Structures), ČSNÍ Praha, March 2008.
- [139] B. Jáger, B. Kövesdi, and L. Dunai, (2018) *Bending and shear buckling interaction behavior of I-girders with longitudinally stiffened webs*. J. Constr. Steel Res. 145, pp. 504–517.
- [140] CEN/TC250, prEN 1993-1-5:2020 - Eurocode 3: Design of steel structures, *Part 1-5: Plated Structural Elements*. European Committee for Standardisation, Brussels; 2020.
- [141] ASTM E, 8M (1991) *Standard test method for tension testing of metallic materials* (Metric). Annual Book of ASTM Standards, Philadelphia.
- [142] D. S. Simulia, (2014) *ABAQUS FEA*. Dassault Systems, Version 6.14.
- [143] E. Riks, (1979) *An incremental approach to the solution to the solution of buckling and snapping problems*. Int. J. Solids Struct, 15:524–551.
- [144] M.A. Crisfield, (1997) *Nonlinear finite element analysis of solids and structures*. Vols. 1 and 2, John Wiley & Sons, London.
- [145] W. Koiter, (1945) *On the stability of elastic equilibrium*. (Original in Dutch). PhD thesis, University of Delft. Delft. (Translation AFFDL-TR-70-25, Wright Patterson Air Force Base, 1970).
- [146] A. Rusch & J. Lindner, (2001) *Tragfähigkeit von beulgefährdeten Querschnittselementen unter Berücksichtigung von Imperfektionen*. (Original in German), Stahlbau, Vol. 70, No. 10, pp. 765.
- [147] J.K. Paik, (2018) *Ultimate limit state analysis and design of plated structures*, Second edition, John Wiley & Sons, Chichester, UK, 2018.
- [148] CEN, EN 10025-2:2004, *Technical delivery conditions for non-alloy structural steels*, Part 2. European Committee for Standardization, Brussels; 2004.
- [149] ECCS, (2008) *Buckling of shells*, European Design recommendations. Publication No. 128, 5th ed., European Convention for Constructional Steelwork, Rotter J. M., Schmidt, H. (Eds.), Brussels.
- [150] S. Zhang, P. Kumar and S.E. Rutherford, (2008) *Ultimate shear strength of plates and stiffened panels*. Journal of Ship and Offshore Structures, Vol. 3, No. 2, pp. 105–112.
- [151] A. Reis, J.O. Pedro, A.B. Graça, (2017) *Report on the comparative study 1: alternative cross-section integrating curved stiffened steel panels*. RFCS Research Project OUTBURST (RFCS-2015-709782): Deliverable 3.3.
- [152] ISO-6892-1, (2016) *Metallic materials - Tensile testing. Part 1: Method of test at room temperature*. European Committee for Standardisation, Brussels.
- [153] DYWIDAG Prestressing Steel Threadbar System (2009) [Catalogue] DYWIDAG-SYSTEMS INTERNATIONAL LTD., Northfield Road, Warwickshire, United Kingdom.
- [154] N. Yamaki, (1984) *Elastic stability of circular cylindrical shells*. North-Holland, Amsterdam.
- [155] M.Z. Haffar, B. Kövesdi, S. Ádány, (2019) *On the buckling of longitudinally stiffened plates, part 2: Eurocode-based design for plate-like behavior of plates with closed-section stiffeners*. Thin-walled Structures 145 (2019) 106395.
- [156] N. Schillo, A. Taras, M. Feldmann, (2016) *Assessment of Safety Factor for Local Buckling*, CEN/TC250/SC3/WG5 Meeting Stuttgart, 26 February 2016.
-

- [157] P.O. Martin, T.M. Nguyen, L. Davaine, (2017) *Effect the torsional stiffness of closed section stiffeners on plate buckling in Eurocode 3 Part 1-5*, Research report, ECCS-TWG8 3.
- [158] F. Sinur, (2014) *Stability of Longitudinally Stiffened Plates*, Research Report, ECCSTWG83 Meeting in Aachen – Document TWG83-2014-045.
- [159] B. Johansson, R. Maquoi, G. Sedlacek, C. Müller, D. Beg, (2007) *Commentary and Worked Examples to DIN-EN-1993-1-5 Plated Structural Elements*.
- [160] L. Pavlovčič, A. Detzel, U. Kuhlmann, D. Beg, (2007) *Shear resistance of longitudinally stiffened panels – part 1: tests and numerical analysis of imperfections*, J. Constr. Steel Res. 63 (2007) 337–350.
- [161] L. Pavlovčič, D. Beg, U. Kuhlmann, (2007) *Shear resistance of longitudinally stiffened panels – part 2: numerical parametric study*, J. Constr. Steel Res. 63 (2007) 351–364.
- [162] F. Sinur, D. Beg, (2013) *Moment-shear interaction of stiffened plate girders – tests and numerical model verification*, J. Constr. Steel Res. 85 (2013) 116–129.
- [163] F. Sinur, D. Beg, (2013) *Moment-shear interaction of stiffened plate girders – numerical study and reliability analysis*, J. Constr. Steel Res. 88 (2013) 231–243.
- [164] CEN, EN 1993-2:2006 - Eurocode 3: Design of steel structures, *Part 2: Steel Bridges*. European Committee for Standardisation, Brussels; 2006.
- [165] CEN (2002). EN 1990, Eurocode – Basis of structural design, CEN, Brussels.
- [166] L. Simões da Silva, L. Marques, T. Tankova, C. Rebelo, U. Kuhlmann, A. Kleiner, J. Spiegler, H.H. Snijder, R. Dekker, V. Dehan, C. Haremza, A. Taras, L.G. Cajot, O. Vassart, N. Popa, (2017) *SAFEBRITILE: Standardization of Safety Assessment Procedures across Brittle to Ductile Failure Modes*, 2017, RFSR-CT-2013-00023, Final Report.
- [167] CEN/TC250, prEN 1993-1-1:2018 - Eurocode 3: Design of steel structures, *Part 1-1: General rules and rules for building*. European Committee for Standardisation, Brussels; 2018.
- [168] CEN (2011). EN 1090-2:2007+A1:2011. *Execution of steel structures and aluminium structures - Part 2: Technical requirements for steel structures*. Brussels, European Committee for Standardisation.
- [169] T. Tankova, L. Simoes da Silva, L. Marques, C. Rebelo, A. Taras, (2014), *Towards a standardized procedure for the safety assessment of stability design rules*, Journal of Constructional Steel Research, 102, pp. 290-302, Elsevier, London.

Annexes

Annex A

A.1 – Strains recorded by SG in experimental tests (from section 3.3):

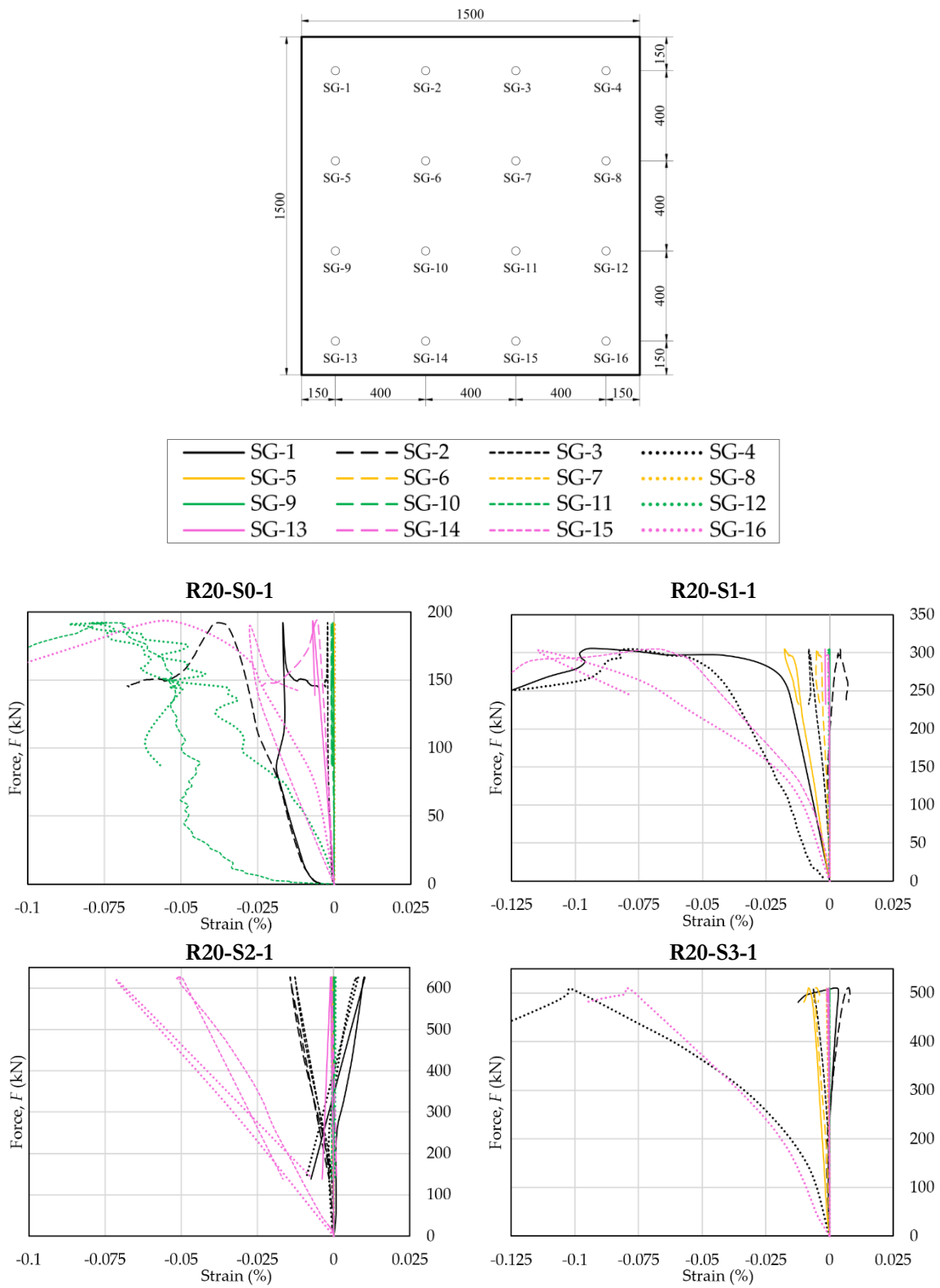


Fig. A.1: Strains measured in panels with radius $R = 20.0$ m

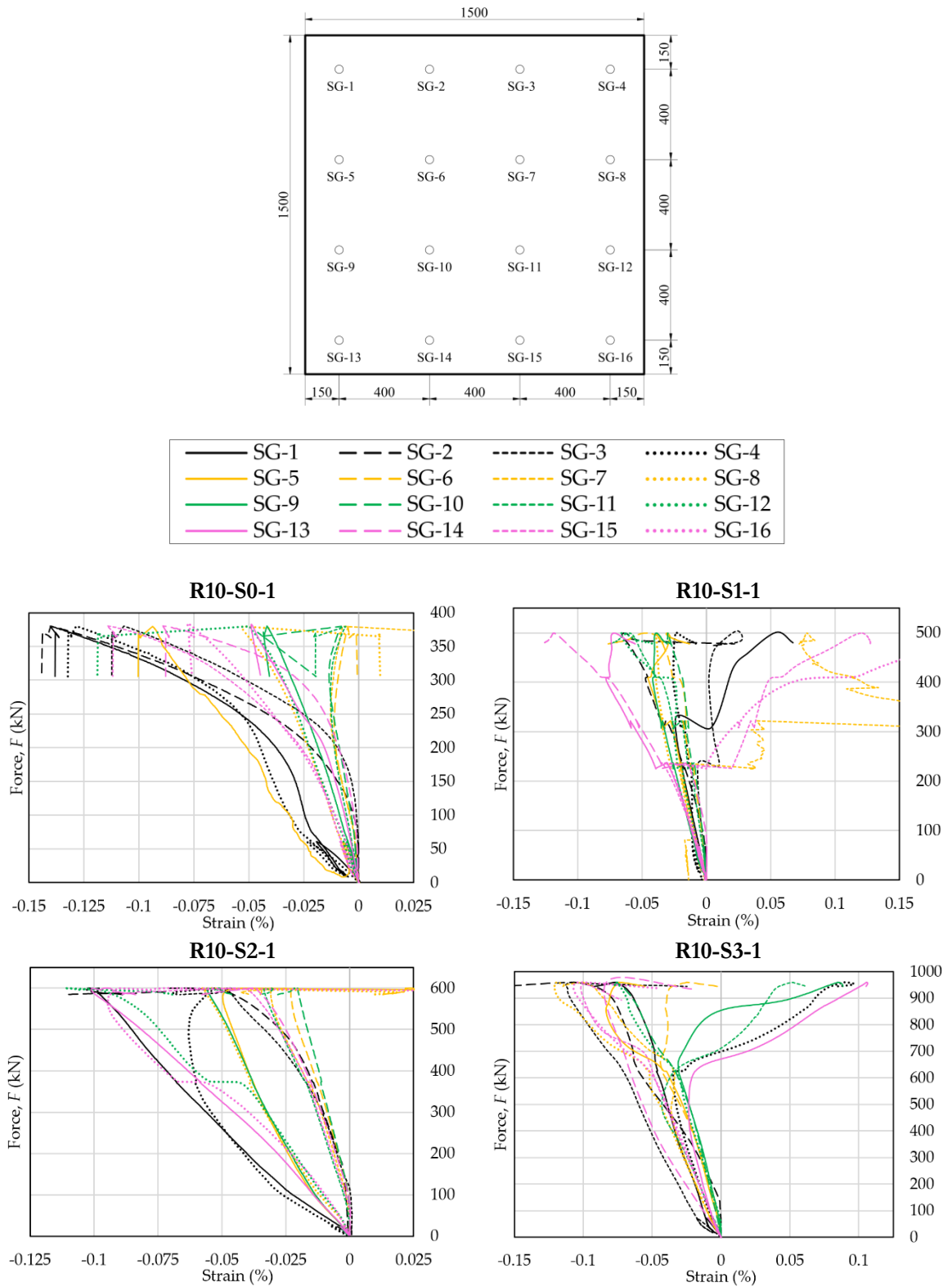


Fig. A.2: Strains measured in panels with radius $R = 10.0$ m

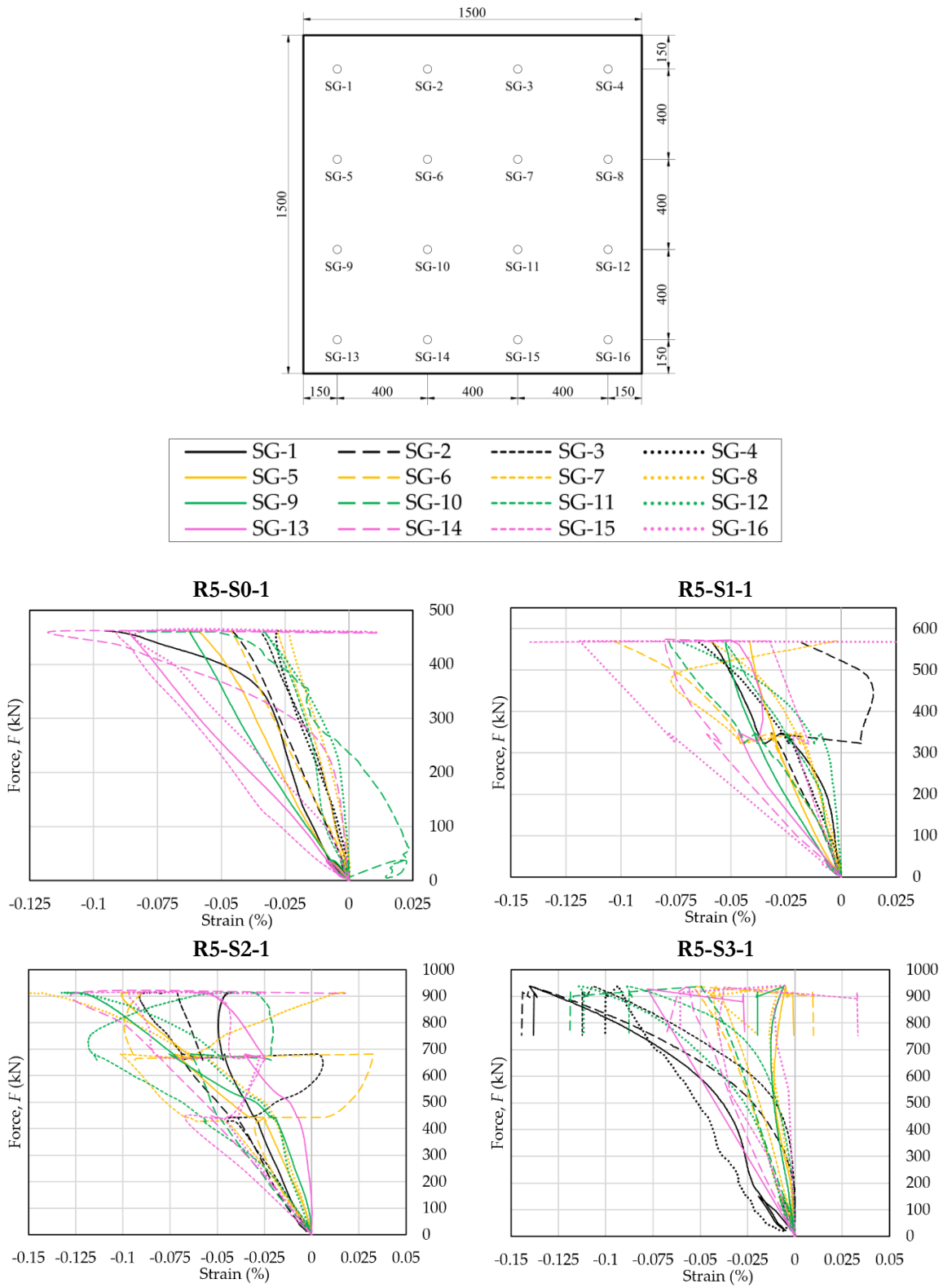


Fig. A.3: Strains measured in panels with radius $R = 5.0$ m

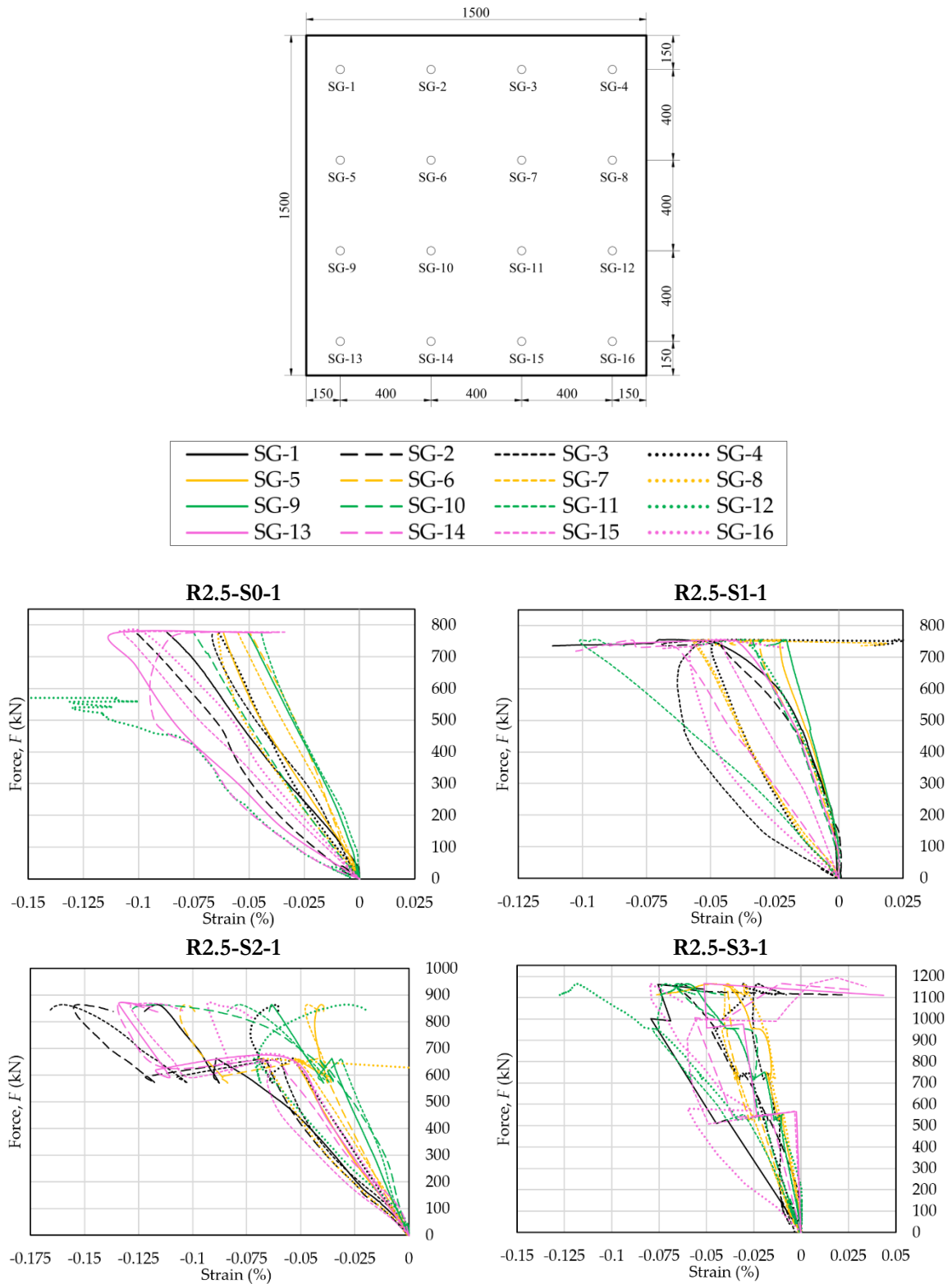


Fig. A.4: Strains measured in panels with radius $R = 2.5$ m

A.2 – Geometrical properties of stiffened test specimens used for the calculation of the ultimate strength (from section 3.3):

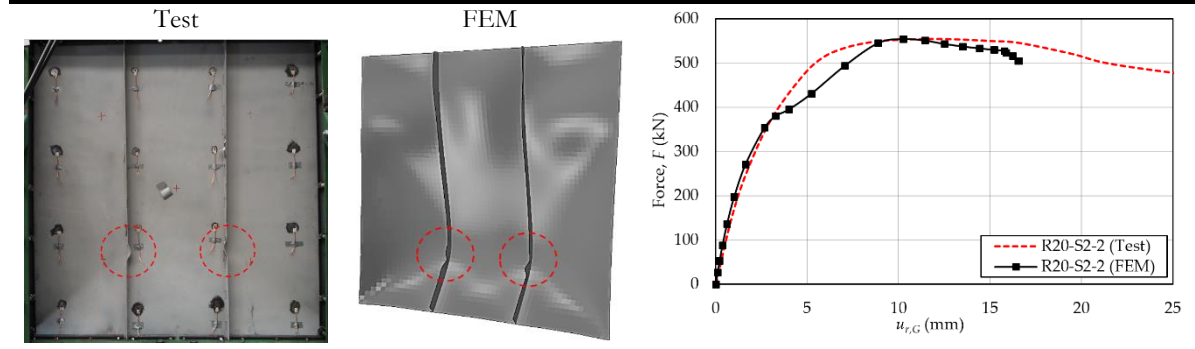
	$n_{st} = 1$	$R = 20.0$ m	$R = 10.0$ m	$R = 5.0$ m	$R = 2.5$ m
I_{sl}	$\times 10^4$ [mm ⁴]	25.15	53.13	174.49	673.38
e	$\times 10$ [mm]	2.16	1.71	1.90	3.70
$I_{sl,eff}$	$\times 10^4$ [mm ⁴]	10.39	10.51	11.20	13.29
	$n_{st} = 2$	$R = 20.0$ m	$R = 10.0$ m	$R = 5.0$ m	$R = 2.5$ m
I_{sl}	$\times 10^4$ [mm ⁴]	41.14	67.42	185.18	675.55
e	$\times 10$ [mm]	2.24	1.95	1.96	3.75
$I_{sl,eff}$	$\times 10^4$ [mm ⁴]	11.83	11.86	12.03	12.87
	$n_{st} = 3$	$R = 20.0$ m	$R = 10.0$ m	$R = 5.0$ m	$R = 2.5$ m
I_{sl}	$\times 10^4$ [mm ⁴]	57.16	83.23	200.94	693.40
e	$\times 10$ [mm]	2.24	2.03	2.03	3.81
$I_{sl,eff}$	$\times 10^4$ [mm ⁴]	12.82	12.82	12.85	13.16

***Note:** I_{sl} and e are respectively the gross second moment of area and the largest distance from the respective centroids of the plating and the stiffeners to the neutral axis of the whole cross-section used in Tran [8], Tran *et al.* [59] and OUTBURST [85];

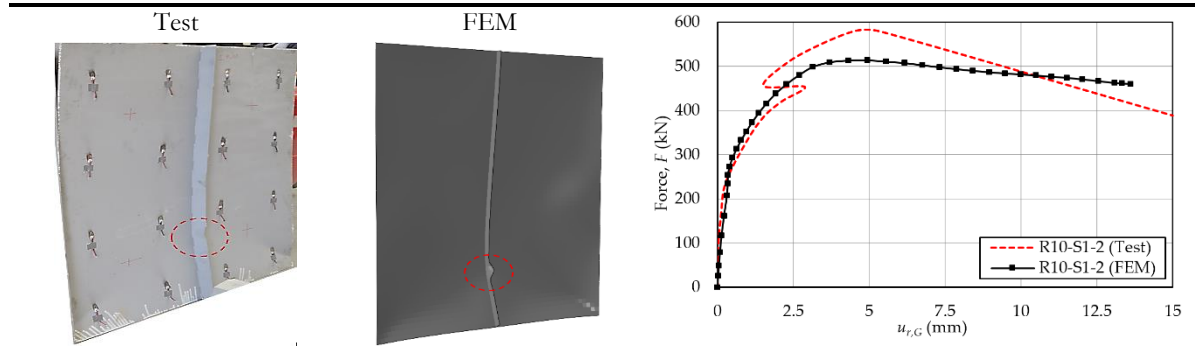
$I_{sl,eff}$ is the second moment of area of longitudinal stiffener including effective shell width used in procedure prescribed by DNV-RP-C202 [13].

A.3 – Comparison of failure modes between experimental and FEM results - backside view (from section 3.4):

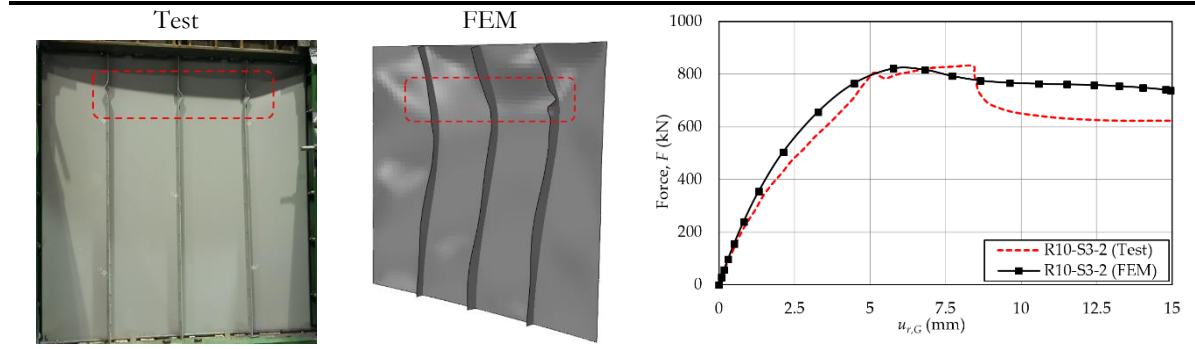
Panel: R20-S2-2



Panel: R10-S1-2

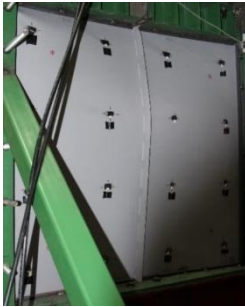


Panel: R10-S3-2

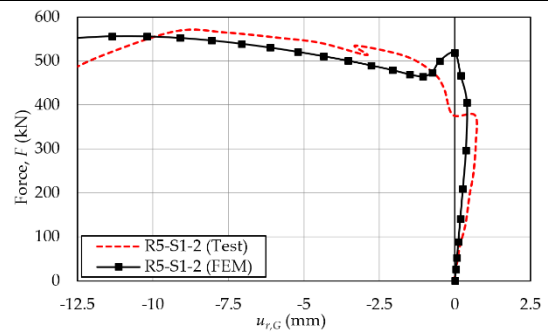
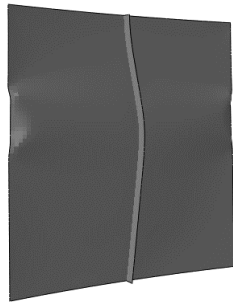


Panel: R5-S1-2

Test



FEM

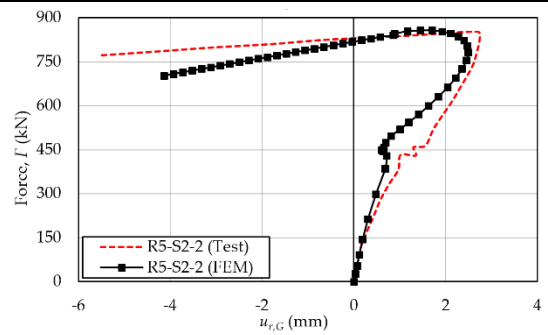


Panel: R5-S2-2

Test

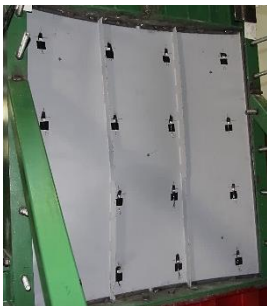


FEM

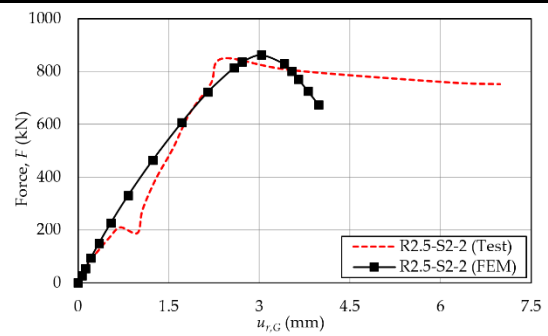
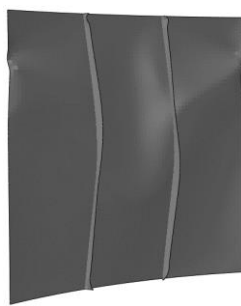


Panel: R2.5-S2-2

Test



FEM



Annex B

B.1 – Strains recorded by SG in experimental tests (from section 6.4):

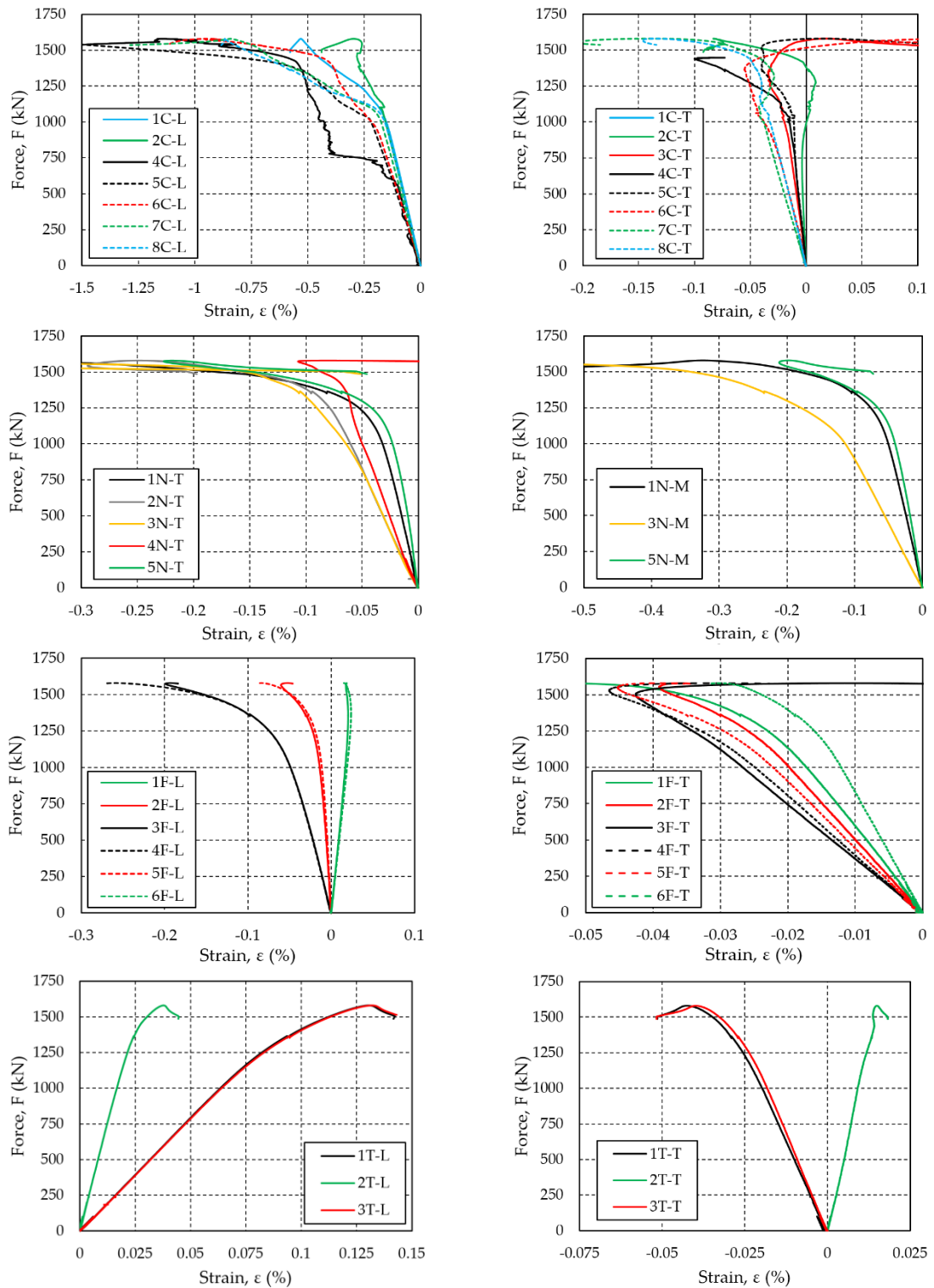
SPECIMEN S460

Fig. B.1: Strains in cross-section 1-1

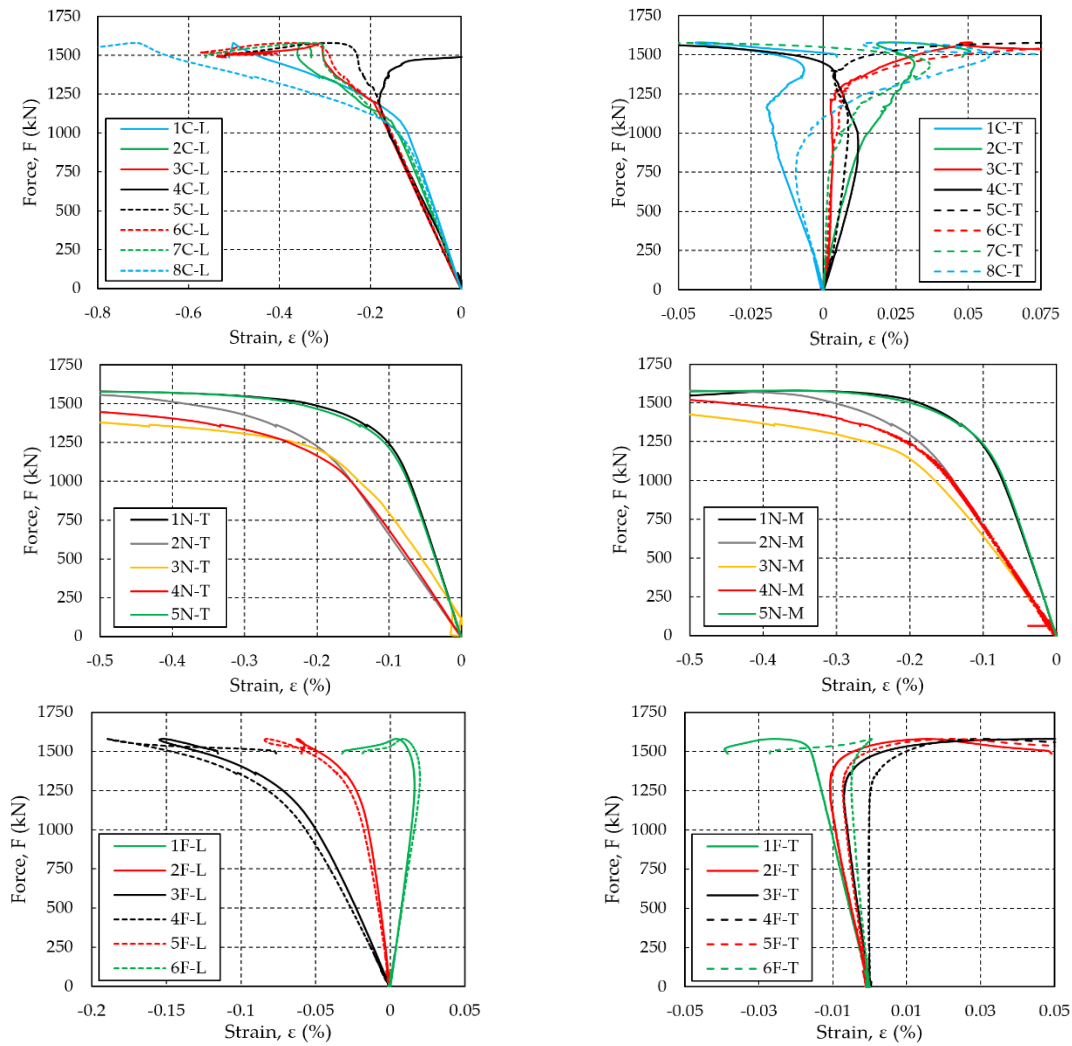


Fig. B.2: Strains in cross-section 2-2

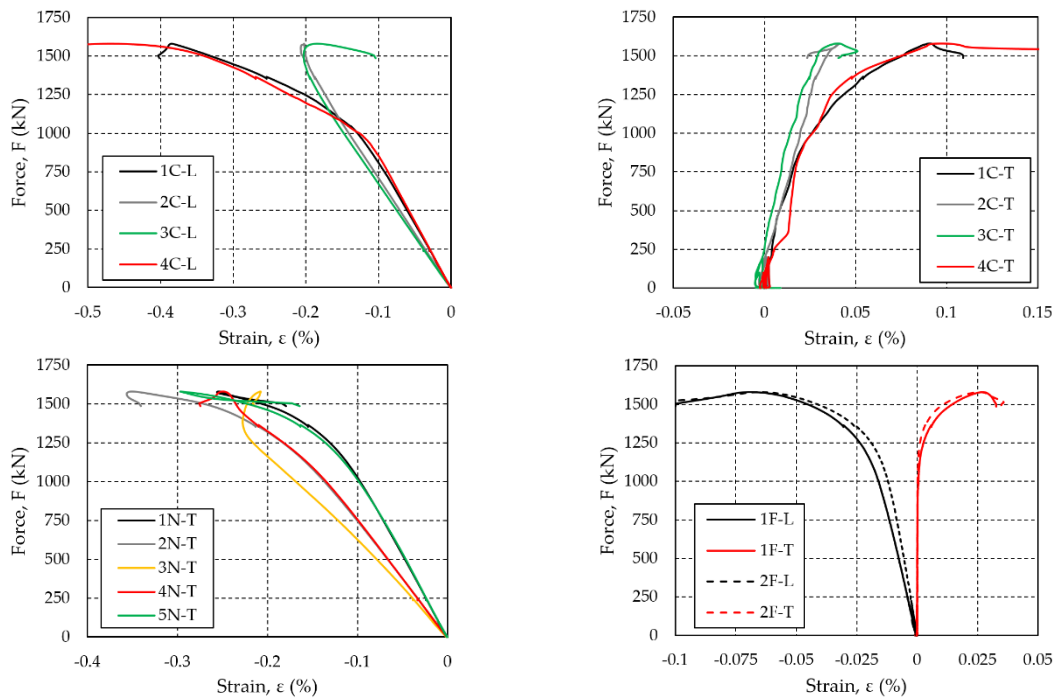


Fig. B.3: Strains in cross-section 3-3

SPECIMEN S690

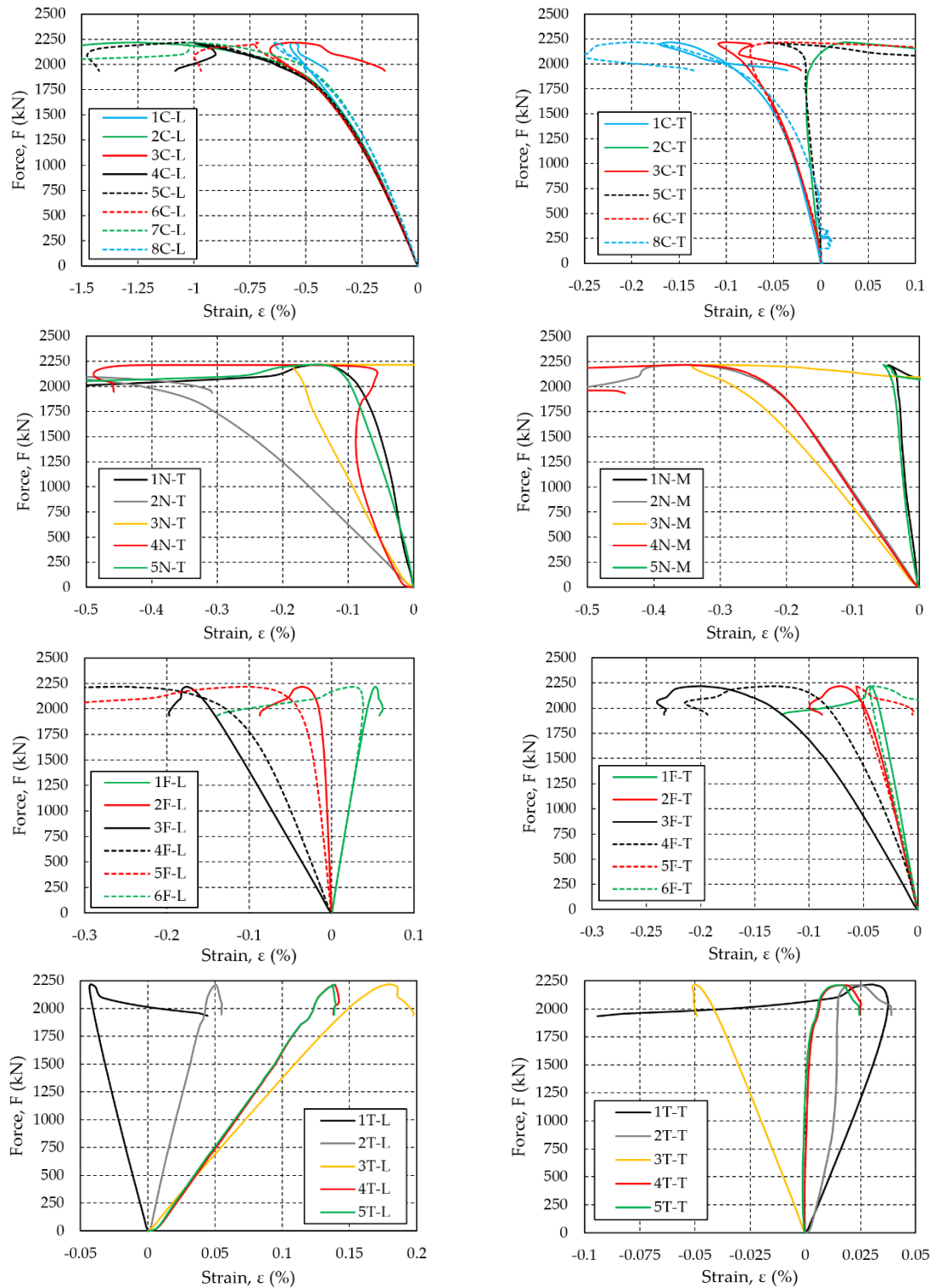


Fig. B.4: Strains in cross-section 1-1

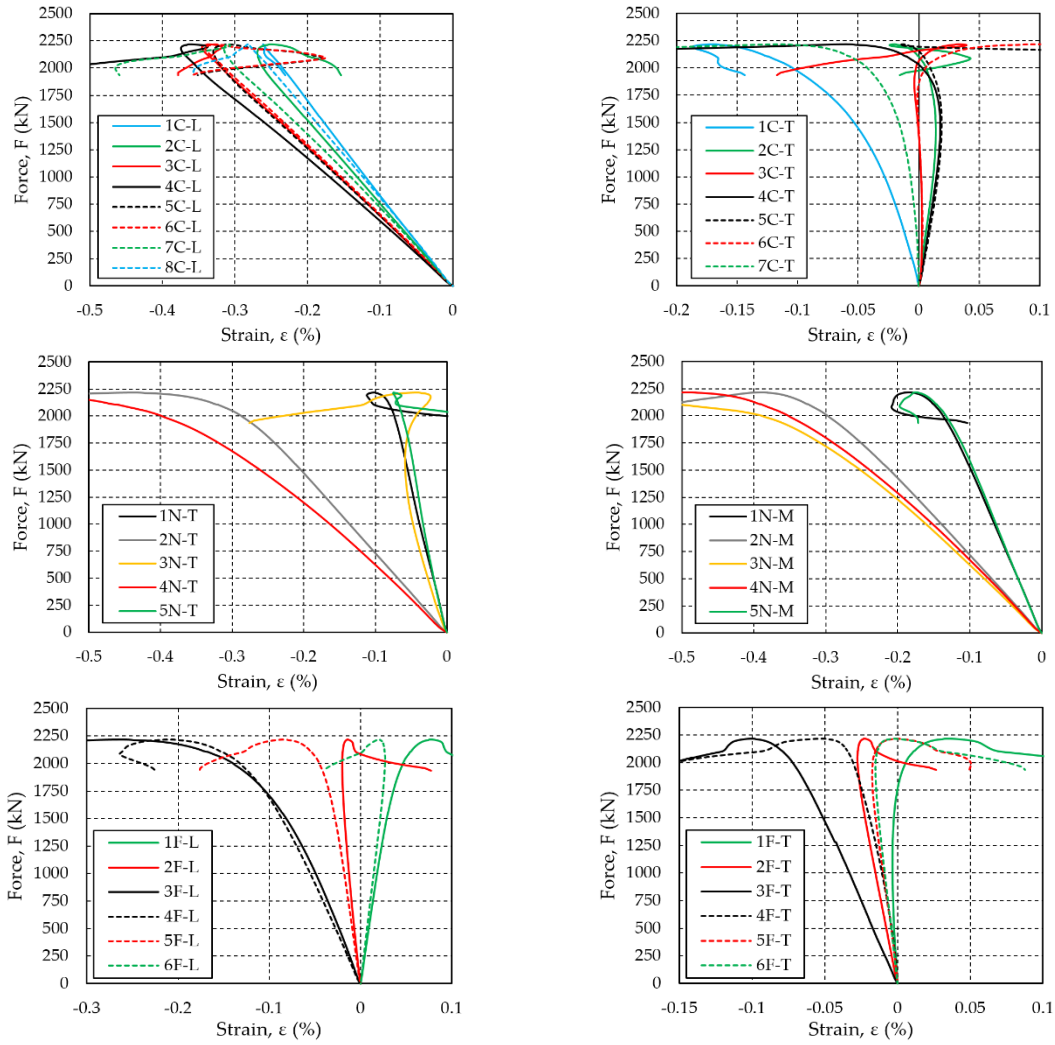


Fig. B.5: Strains in cross-section 2-2

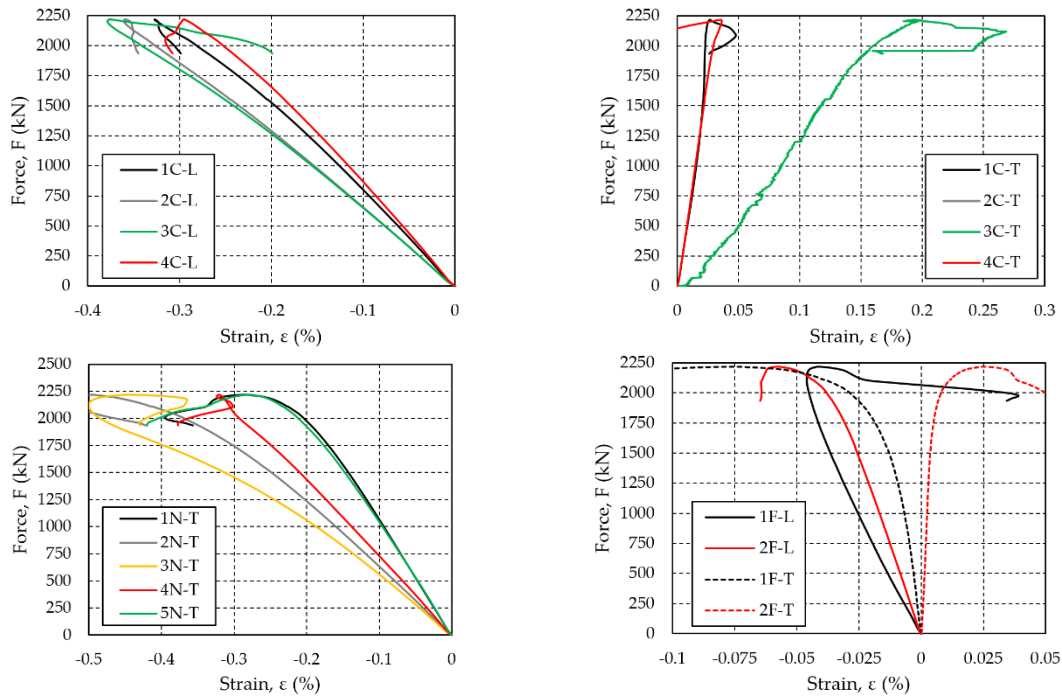
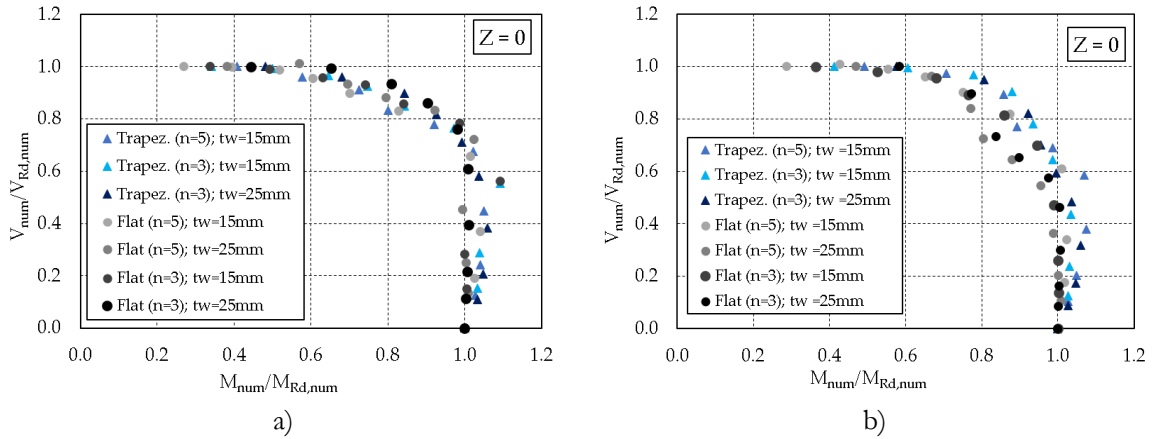
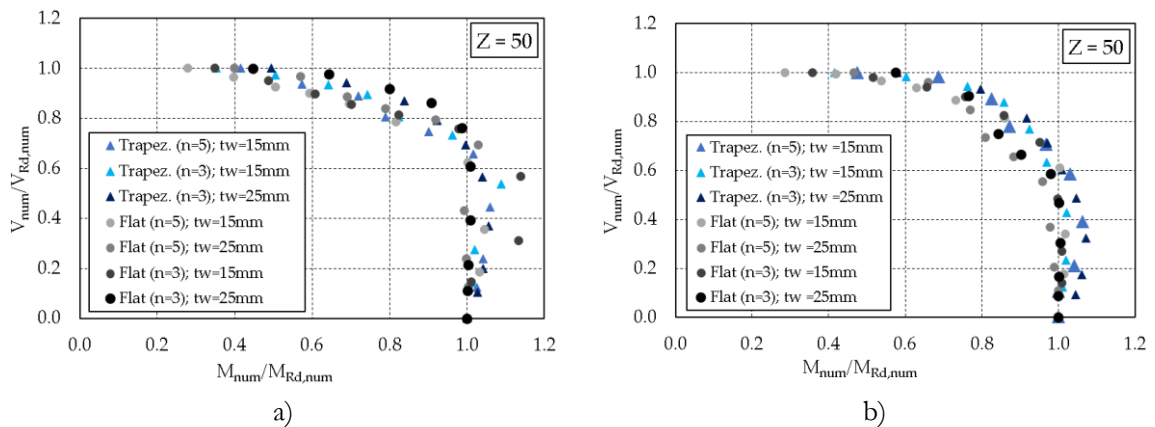
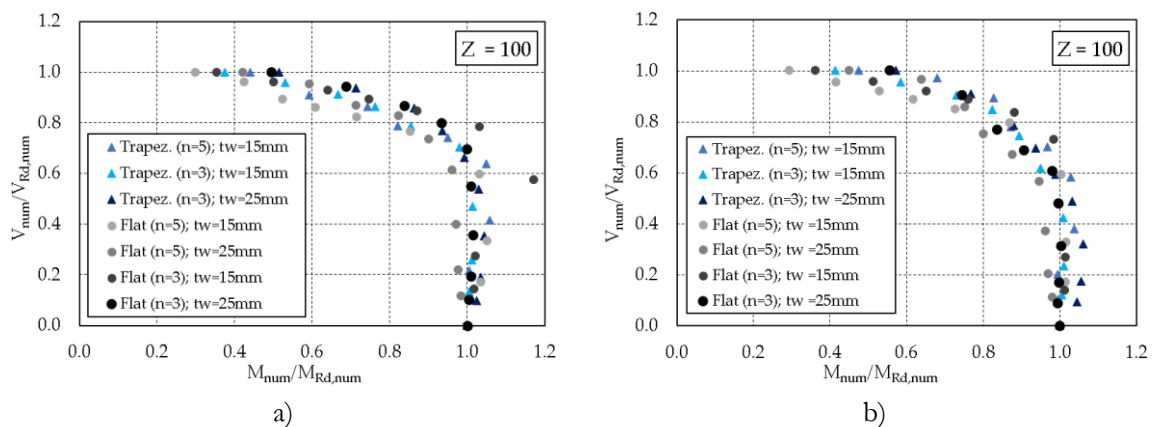


Fig. B.6: Strains in cross-section 3-3

Annex C

C.1 – M-V Interaction diagrams for various Z parameters (from 7.4.2):Fig. C.1: M - V interaction diagrams for $Z = 0$: a) $H = \text{const.}$; b) $H = \text{variable}$ Fig. C.2: M - V interaction diagrams for $Z = 50$: a) $H = \text{const.}$; b) $H = \text{variable}$ Fig. C.3: M - V interaction diagrams for $Z = 100$: a) $H = \text{const.}$; b) $H = \text{variable}$

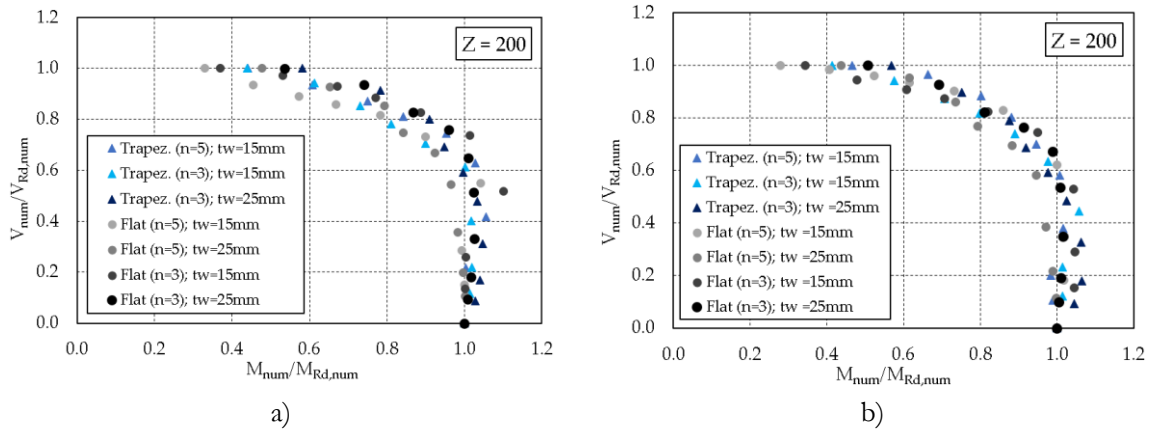


Fig. C.4: M - V interaction diagrams for $Z = 200$: a) $H = \text{const.}$; b) $H = \text{variable}$

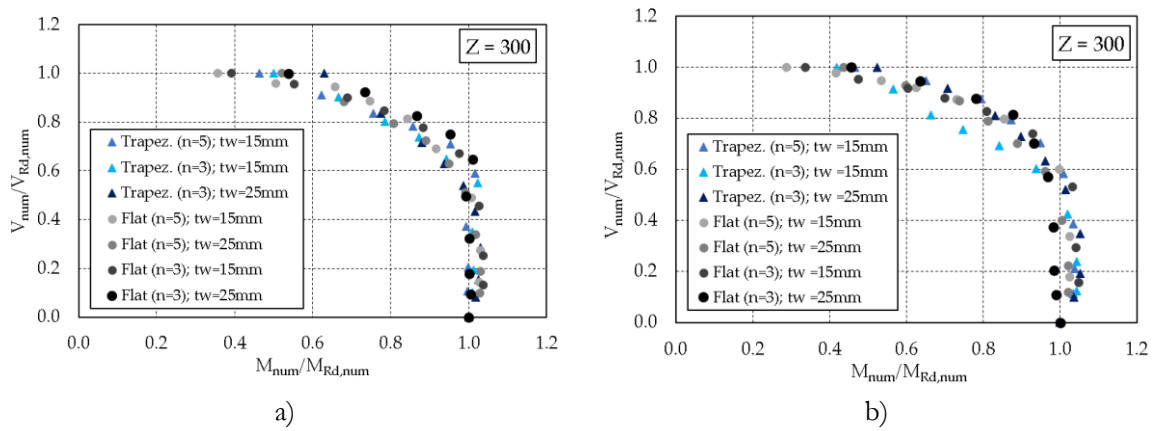


Fig. C.5: M - V interaction diagrams for $Z = 300$: a) $H = \text{const.}$; b) $H = \text{variable}$

Annex D

APPLICATION OF PROPOSED METHODOLOGY (WORKED EXAMPLE)

D.1 - Introduction

The goal of this section is to show how to calculate the bending and shear resistance of a box-girder cross-section with a curved steel panel in the bottom flange using the proposed rules in this thesis, and subsequently, how to verify if the M-V interaction criterion is satisfied. The geometry of the design example, presented in Fig. D.1 is adopted from the parametric study, carried out in section 7.3, thus allowing for direct comparison with the numerical results. The main geometrical parameters of the bottom flange are summarized in Table D.1.

Table D.1: Geometrical parameters of the design example cross-section

	Z	α	b/t	Z_{loc}	α_{loc}	b_{loc}/t
Design example	100	0.5	168	6.25	2.0	42

It may be noticed that all parameters fall inside the ranges of typical bridge geometries, reported in section 2.3. The structural steel S355 is considered, where the yield strength is adopted based on the values of the material properties given in EN 10025-2 [148], as presented in Table 7.4.

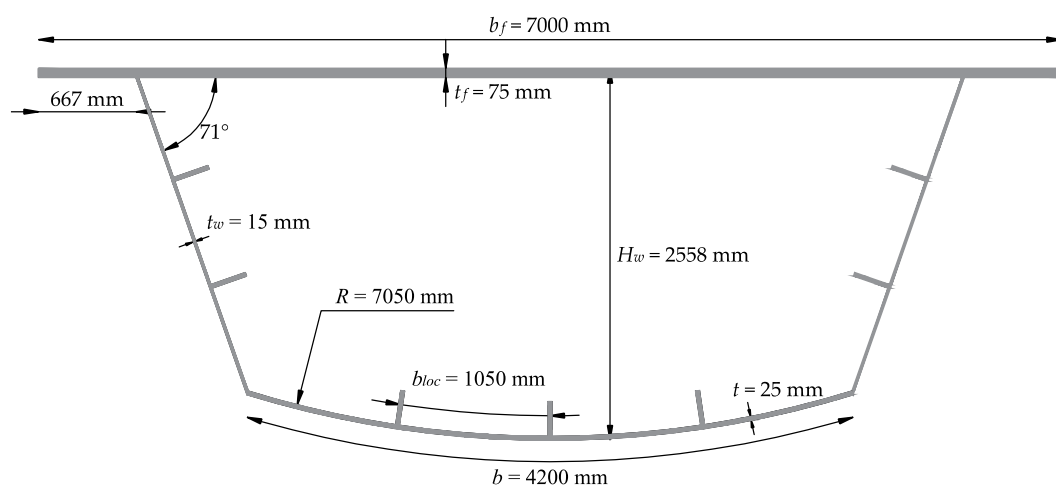


Fig. D.1: Design example – cross-section geometry

Once again, since the central focus of the thesis is the addition of the bottom curved flange in the cross-section, the simplifications related to the top flange mentioned in section 6.2 are kept also in this example.

D.2 – Bending resistance

The bending resistance of a class 4 box-girder cross-section ($M_{eff,Rd}$) is calculated using Eq.(2.116) from the design code. The effective properties of the cross-section (W_{eff}) are obtained using the *Curved panel approach* developed in this thesis (see Method 2 in 6.4.6), which is completed in two steps:

I – Effective cross-section of the stiffened bottom flange:

The curved bottom flange, for which the effective properties (A_{eff}) are calculated is presented in Fig. D.2.

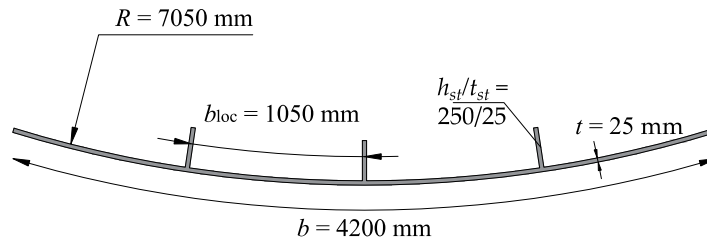


Fig. D.2: Design example – bottom flange geometry

The *Curved panel approach* assumes that the entire curved panel is subject to a uniform axial compression (see Fig. 8.10), which enables the use of the methodology developed within the OUTBURST research project [85], (see 2.5.1) as follows:

i) Local buckling - ρ_{loc}

- **Subpanel:** ($Z_{loc} = 6.25$, see Table D.1)

$$k_{\sigma,Z} = \frac{a_1 + a_2 Z_{loc} + a_3 Z_{loc}^2}{b_1 + b_2 Z_{loc} + b_3 Z_{loc}^2 + 1} = 4.5 \quad \text{see Eq.(2.11)}$$

$$\sigma_{cr} = k_{\sigma} \sigma_E = k_{\sigma,Z} \frac{\pi^2 E}{12(1-\nu^2)} \left(\frac{t}{b_{loc}} \right)^2 = 484.4 \text{ MPa} \quad \text{see Eq.(2.6)}$$

$$\bar{\lambda} = \sqrt{\frac{f_y}{\sigma_{cr}}} = 0.84 \quad \text{see Eq.(2.23)}$$

$$\rho_{loc} = \begin{cases} 1.0 & \text{if } \bar{\lambda} \leq \bar{\lambda}_{0,Z} \\ \frac{\bar{\lambda}_{0,p} - \bar{\lambda} - \rho_{0,Z} (\bar{\lambda} - \bar{\lambda}_{0,Z})}{\bar{\lambda}_{0,p} - \bar{\lambda}_{0,Z}} & \text{if } \bar{\lambda}_{0,Z} \leq \bar{\lambda} \leq \bar{\lambda}_{0,p} = 0.779 \\ \frac{\bar{\lambda} - 0.22\alpha_Z}{c_Z \bar{\lambda}^2} + S_Z & \text{if } \bar{\lambda}_{0,p} \leq \bar{\lambda} \end{cases} \quad \text{see Eq.(2.51)}$$

with α_z , c_z and S_z equal to 1.0, 1.18 and 0.0375, respectively (see Table 2.6) and

$$\bar{\lambda}_{0,Z} = 0.2 + 0.473(0.95^{Z_{loc}}) = 0.543 \quad \text{see Eq.(2.52)}$$

$$\bar{\lambda}_{0,p} = 0.5 + \sqrt{0.085 - 0.055\psi} = 0.673 \quad \text{see Eq.(2.53)}$$

Since the subpanel is considered *long* ($\alpha_{loc} > 1.0$), the local reduction coefficient is obtained as

$$\rho_{long} = C_{long} \rho = 0.75 \quad \text{see Eq.(2.55)}$$

- **Stiffener:** ($b_{st}/t_{st} = 10$; $k_{\sigma} = 0.43$)

$$\bar{\lambda} = \frac{h_{st}/t_{st}}{28.4\varepsilon\sqrt{k_{\sigma}}} = 0.65 \quad \text{with} \quad \varepsilon = \sqrt{\frac{235}{f_y}} = 0.825 \quad \text{see Eq.(2.26)}$$

$$\rho = \begin{cases} 1.0 & \text{if } \bar{\lambda} < 0.748 \\ \frac{\bar{\lambda} - 0.188}{\bar{\lambda}^2} & \text{if } \bar{\lambda} \geq 0.748 \end{cases} \rightarrow \rho_{loc} = 1.0 \quad \text{see Eq.(2.25)}$$

The effective area $A_{c,eff,loc}$ is calculated as:

$$A_{c,eff,loc} = A_{st,eff} + \sum_c \rho_{loc} b_{c,loc} t = 77812.5 \text{ mm}^2 \quad \text{see Eq.(2.28)}$$

ii) **Global buckling** - ρ_c

- **Shell-type buckling:** - ρ

$$Z_a = \frac{a^2}{Rt} \sqrt{1 - \nu^2} = 23.85 \quad \text{see Eq.(2.82)}$$

$$\gamma = \frac{1 + \frac{I_{sl,1}}{I_p}}{1 + \frac{A_{st}}{A_p}} = 57.5 \quad \text{see Eq.(2.83)}$$

with the geometrical properties of the gross cross-section of one longitudinal stiffener equal to $I_{sl,1} = 1.06 \times 10^8 \text{ mm}^4$ and $A_{st} = 6250 \text{ mm}^2$, whereas the other two parameters are $I_p = b_{loc}^3 / 12(1 - \nu^2) = 1502404 \text{ mm}^4$ and $A_p = b_{loc} t = 26250 \text{ mm}^2$.

$$k_{\sigma,Za} = \gamma \sqrt{1 + \left(\frac{4\sqrt{3}Z_a}{\pi^2 \gamma} \right)^2} = 59.9 \quad \text{see Eq.(2.81)}$$

$$\sigma_{cr,s} = k_{\sigma,Za} \frac{\pi^2 E}{12(1 - \nu^2)} \left(\frac{t}{a} \right)^2 = 1612 \text{ MPa} \quad \text{see Eq.(2.80)}$$

$$\bar{\lambda} = \sqrt{\frac{f_y}{\sigma_{cr,s}}} = 0.463 \quad \text{see Eq.(2.23)}$$

The reduction factor ρ is determined from equations for the unstiffened panels; however, considering the global curvature $Z = 100$ as:

$$\bar{\lambda}_{0,Z} = 0.2 + 0.473(0.95^Z) = 0.203 \quad \text{see Eq.(2.52)}$$

$$\bar{\lambda}_{0,p} = 0.5 + \sqrt{0.085 - 0.055\nu} = 0.673 \quad \text{see Eq.(2.53)}$$

$$\rho_{0,z} = \frac{\bar{\lambda}_{0,p} - 0.22\alpha_Z}{c_Z \bar{\lambda}_{0,p}^2} + S_Z = 0.68 \quad \text{see Eq.(2.54)}$$

with α_{\varnothing} , c_{\varnothing} and S_{\varnothing} equal to 0.545, 1.7 and -0.04, respectively (see Table 2.6).

$$\rho = \begin{cases} 1.0 & \text{if } \bar{\lambda} \leq \bar{\lambda}_{0,z} \\ \frac{\bar{\lambda}_{0,p} - \bar{\lambda} - \rho_{0,z}(\bar{\lambda} - \bar{\lambda}_{0,z})}{\bar{\lambda}_{0,p} - \bar{\lambda}_{0,z}} & \text{if } \bar{\lambda}_{0,z} \leq \bar{\lambda} \leq \bar{\lambda}_{0,p} = 0.82 \\ \frac{\bar{\lambda} - 0.22\alpha_Z}{c_Z \bar{\lambda}^2} + S_Z & \text{if } \bar{\lambda}_{0,p} \leq \bar{\lambda} \end{cases} \quad \text{see Eq.(2.51)}$$

- **Column-type buckling:** - χ_c

$$\sigma_{cr,c} = \sigma_{cr,sl} = \frac{\pi^2 EI_{sl}}{A_{sl} a^2} = 4197 \text{MPa} \quad \text{see Eq.(2.37)}$$

with A_{sl} and I_{sl} being the gross properties of the whole cross-section equal to $I_{sl} = 11.1 \times 10^8 \text{ mm}^4$ and $A_{sl} = 123750 \text{ mm}^2$.

$$\bar{\lambda}_c = \sqrt{\frac{\beta_{A,c} f_y}{\sigma_{cr,c}}} = 0.227 \quad \text{with } \beta_{A,c} = \frac{A_{c,eff,loc}}{A_{sl}} = 0.629 \quad \text{see Eq.(2.36)}$$

$$\alpha_e = \alpha + \frac{0.09}{i/e} = 0.6 \quad \text{with } i = \sqrt{\frac{I_{sl,1}}{A_{sl,1}}} = 94.5 \text{mm} \quad \text{see Eq.(2.38)}$$

where α is the imperfection factor ($\alpha = 0.49$ for open cross-section stiffeners), and e is the largest distance from the respective centroids of the plating and the stiffeners to the neutral axis of the whole cross-section $e = 115.1 \text{ mm}$.

$$\phi = 0.5 \left[1 + \alpha_e (\bar{\lambda}_c - 0.2) + \bar{\lambda}_c^2 \right] = 0.534 \quad \text{see Eq.(2.35)}$$

$$\chi_c = \frac{1}{\phi + \sqrt{\phi^2 - \bar{\lambda}_c^2}} = 0.98 \quad \text{see Eq.(2.35)}$$

- **Interpolation between shell-type and column-type buckling:** - ρ_c

$$\xi = \frac{\sigma_{cr,p}}{\sigma_{cr,c}} - 1 = -0.62 \rightarrow \xi = 0 \quad \text{see Eq.(2.30)}$$

$$\rho_c = (\rho - \chi_c)\xi(2 - \xi) + \chi_c = 0.983 \quad \text{see Eq.(2.29)}$$

iii) **Effective area of the stiffened curved plate** - $A_{c,eff}$

$$A_{c,eff} = \rho_c A_{c,eff,loc} + \Sigma b_{i,edge,eff} t = 96177 \text{mm}^2 \quad \text{see Eq.(2.27)}$$

The effective area of the bottom flange is illustrated in Fig. D.3.

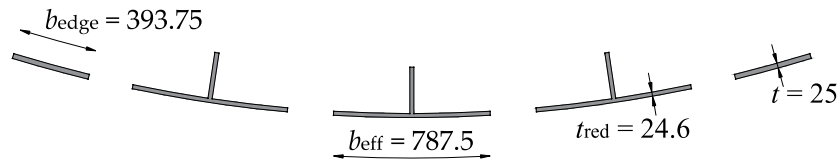


Fig. D.3: Design example – effective area of the bottom flange

II – Effective cross-section of the stiffened web:

To complete the calculation of the effective properties of the cross-section, the axial stress distribution in the web must be re-calculated, accounting for a new position of the center of gravity (*i.e.* neutral axis $n_{el,1}$) for cross-section consisting of: *i*) gross area of the top flanges; *ii*) gross area of the web and *iii*) effective area of the bottom flange calculated in the previous step. This is illustrated in Fig. D.4.

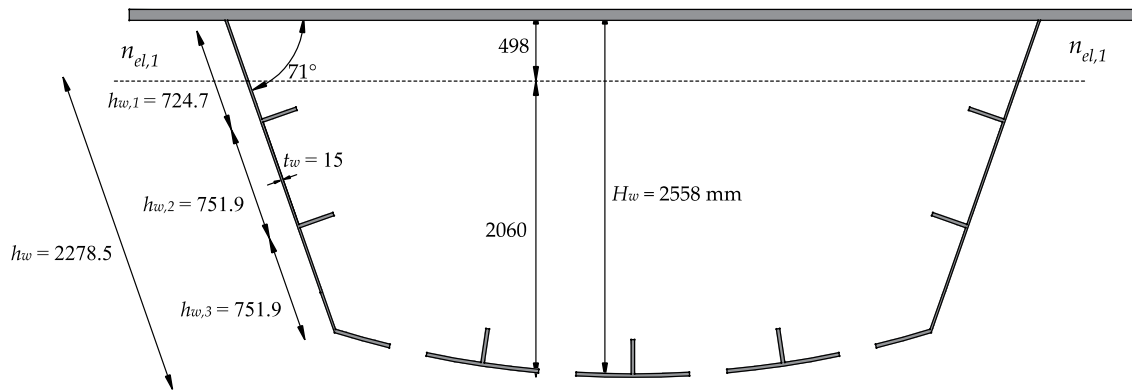


Fig. D.4: Design example – buckling of the web

Subsequently, the effective properties of a flat 2-stiffened main web, A_{eff} , subjected to bending is calculated using the procedure prescribed by EN 1993-1-5, as follows:

i) Local buckling - ρ_{oc}

The local buckling reduction factor is calculated separately for each of three subpanels (*i.e.* fields), depending on the previously calculated stress ratio ψ (see Table 2.10). In Fig. D.5, all required geometrical parameters for this calculus are summarized and some additional helpful notations are introduced.

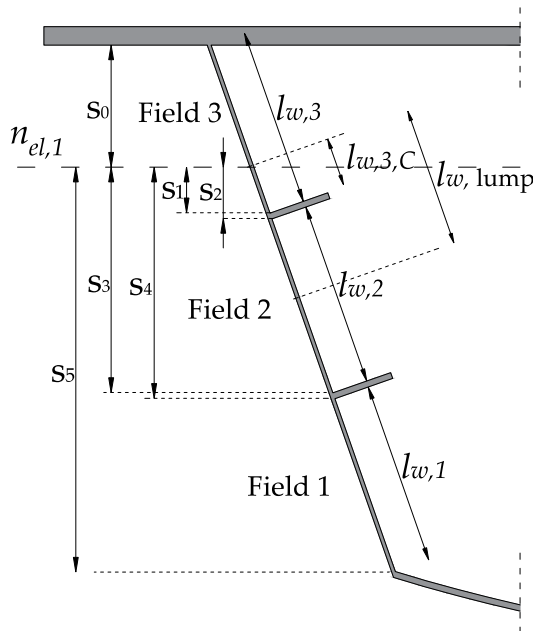
- **Field 1:** ($l_{w,1}/t_w = 50.13$; $\psi_1 > 0$)

$$\psi_1 = \frac{s_4}{s_5} = 0.589$$

$$k_\sigma = 8.2 / (1.05 + \psi) = 5.0 \quad \text{see Eq.(2.117)}$$

$$\bar{\lambda}_p = \frac{l_{w,1}/t_w}{28.4\varepsilon\sqrt{k_\sigma}} = 0.97 \quad \text{with} \quad \varepsilon = \sqrt{\frac{235}{f_y}} = 0.814 \quad \text{see Eq.(2.26)}$$

$$\rho_{loc,1} = \begin{cases} 1.0 & \text{if } \bar{\lambda} < 0.5 + \sqrt{0.085 - 0.055\psi} \\ \frac{\bar{\lambda} - 0.055(3 + \psi)}{\bar{\lambda}^2} & \text{if } \bar{\lambda} \geq 0.5 + \sqrt{0.085 - 0.055\psi} \end{cases} = 0.82 \quad \text{see Eq.(2.24)}$$



- $s_0 = 424.7$ mm
- $s_1 = 261.0$ mm
- $s_2 = 284.6$ mm
- $s_3 = 994.3$ mm
- $s_4 = 1017.9$ mm
- $s_5 = 1723.5$ mm

- $l_{w,1} = l_{w,3} = 751.9$ mm
- $l_{w,2} = l_{w,2} = 751.9$ mm
- $l_{w,3} = l_{w,1} = 724.7$ mm
- $l_{w,3,C} = 284.4$ mm
- $l_{w,lump} = 701.7$ mm

Fig. D.5: Design example – Auxiliary notations for the buckling of the web

- **Field 2:** ($l_{w,2}/t_w = 50.13$; $\psi_2 > 0$)

$$\psi_1 = \frac{s_2}{s_3} = 0.286$$

$$k_\sigma = 8.2 / (1.05 + \psi) = 6.16 \quad \text{see Eq.(2.117)}$$

$$\bar{\lambda}_p = \frac{l_{w,2}/t_w}{28.4\varepsilon\sqrt{k_\sigma}} = 0.874 \quad \text{with } \varepsilon = \sqrt{\frac{235}{f_y}} = 0.814 \quad \text{see Eq.(2.26)}$$

$$\rho_{loc,1} = \begin{cases} 1.0 & \text{if } \bar{\lambda} < 0.5 + \sqrt{0.085 - 0.055\psi} \\ \frac{\bar{\lambda} - 0.055(3 + \psi)}{\bar{\lambda}^2} & \text{if } \bar{\lambda} \geq 0.5 + \sqrt{0.085 - 0.055\psi} \end{cases} = 0.91 \quad \text{see Eq.(2.24)}$$

- **Field 3:** ($l_{w,3}/t_w = 48.3$; $\psi_3 < 0$)

$$\psi_1 = \frac{s_0}{s_1} = -1.63$$

$$k_\sigma = 5.98(1 - \psi)^2 = 41.27 \quad \text{see Eq.(2.117)}$$

$$\bar{\lambda}_p = \frac{l_{w,3}/t_w}{28.4\varepsilon\sqrt{k_\sigma}} = 0.325 \quad , \quad \varepsilon = \sqrt{\frac{235}{f_y}} = 0.814 \quad \text{see Eq.(2.26)}$$

$$\rho_{loc,1} = \begin{cases} 1.0 & \text{if } \bar{\lambda} < 0.5 + \sqrt{0.085 - 0.055\psi} \\ \frac{\bar{\lambda} - 0.055(3 + \psi)}{\bar{\lambda}^2} & \text{if } \bar{\lambda} \geq 0.5 + \sqrt{0.085 - 0.055\psi} \end{cases} = 1.0 \quad \text{see Eq.(2.24)}$$

- **Stiffener:** ($b_{st}/t_{st} = 10$; $k_{\sigma} = 0.43$)

$$\bar{\lambda}_p = \frac{h_{st}/t_{st}}{28.4\varepsilon\sqrt{k_{\sigma}}} = 0.65 \quad \text{with} \quad \varepsilon = \sqrt{\frac{235}{f_y}} = 0.814 \quad \text{see Eq.(2.26)}$$

$$\rho = \begin{cases} 1.0 & \text{if } \bar{\lambda} < 0.748 \\ \frac{\bar{\lambda} - 0.188}{\bar{\lambda}^2} & \text{if } \bar{\lambda} \geq 0.748 \end{cases} \quad \rightarrow \rho_{loc} = 1.0 \quad \text{see Eq.(2.25)}$$

Using the notation from Fig. 2.28 and Table 2.10, the calculated effective widths for three subpanels are:

$$\begin{aligned} b_{1,edge,eff} &= 280 \text{ mm} & b_{2,inf,eff} &= 393.1 \text{ mm} & b_{3,sup,eff} &= 107.3 \text{ mm} \\ b_{1,inf,eff} &= 337.5 \text{ mm} & b_{2,sup,eff} &= 289.3 \text{ mm} & b_{3,edge,eff} &= 160.9 \text{ mm} \end{aligned}$$

and the effective area $A_{c,eff,loc}$, is calculated as:

$$A_{c,eff,loc} = A_{st,eff} + \sum_c \rho_{loc} b_{c,loc} t = 30050.3 \text{ mm}^2 \quad \text{see Eq.(2.28)}$$

ii) Global buckling - ρ_c

- **Plate-type buckling:** - ρ

The stiffened web has two longitudinal stiffeners in the compression zone, hence the elastic critical plate buckling stress should be taken as the lowest of the three possible cases (see Fig. 2.24), as follows:

I) Buckling of the bottom stiffener 1:

The geometrical properties of the stiffener gross cross-section with the adjacent parts are obtained according to Fig. 2.28 and Table 2.10 as:

$$\begin{aligned} A_{sl,1} &= 17570 \text{ mm}^2 \\ I_{sl,1} &= 1.034 \times 10^8 \text{ mm}^4 \end{aligned}$$

The corresponding distances between stiffeners are:

$$\begin{aligned} b_1 &= l_{w,1} = 751.9 \text{ mm} \\ b_2 &= l_{w,2} = 751.9 \text{ mm} \\ B &= b_1 + b_2 = 1503.8 \text{ mm} \end{aligned}$$

$$a_c = 4.33 \sqrt{\frac{I_{sl,1} b_1^2 b_2^2}{t^3 B}} = 6918 \text{ mm} \quad \text{see Eq.(2.33)}$$

As $a < a_c$ ($a = 2100 \text{ mm}$), the buckling stress is obtained as follows:

$$\sigma_{cr,st} = \frac{\pi^2 EI_{sl,1}}{A_{sl,1} a^2} + \frac{Et^3 B a^2}{4\pi^2 (1-\nu^2) A_{sl,1} b_1^2 b_2^2} = 2791 \text{ MPa} \quad \text{see Eq.(2.32)}$$

Due to the stress gradient, the critical plate buckling stress is obtained by interpolation from the position of the stiffener to the most stressed edge of the plate:

$$\sigma_{cr,p,I} = \sigma_{cr,sl} \frac{s_5}{(s_3 + s_4)/2} = 4795 \text{MPa}$$

II) Buckling of the upper stiffener 2:

The geometrical properties of the stiffener gross cross-section with the adjacent parts are obtained according to Fig. 2.28 and Table 2.10 as:

$$A_{sl,2} = 14732.8 \text{ mm}^2$$

$$I_{sl,2} = 0.959 \times 10^8 \text{ mm}^4$$

The corresponding distances between stiffeners are:

$$b_1 = l_{w,2} = 751.9 \text{ mm}$$

$$b_2 = l_{w,3} = 724.7 \text{ mm}$$

$$B = b_1 + b_2 = 1476.6 \text{ mm}$$

$$a_c = 4.33 \sqrt{\frac{I_{sl,2} b_1^2 b_2^2}{t^3 B}} = 6694.5 \text{ mm} \quad \text{see Eq.(2.33)}$$

As $a < a_c$ ($a = 2100 \text{ mm}$), the buckling stress is obtained as follows:

$$\sigma_{cr,sl} = \frac{\pi^2 EI_{sl,2}}{A_{sl,2} a^2} + \frac{Et^3 B a^2}{4\pi^2 (1-\nu^2) A_{sl,2} b_1^2 b_2^2} = 3088.3 \text{MPa} \quad \text{see Eq.(2.32)}$$

Due to the stress gradient, the critical plate buckling stress is obtained by interpolation from the position of the stiffener to the most stressed edge of the plate:

$$\sigma_{cr,p,II} = \sigma_{cr,sl} \frac{s_5}{(s_1 + s_2)/2} = 19958 \text{MPa}$$

III) Buckling of both stiffener 1 and 2:

The geometrical properties of the *lumped stiffener* are obtained as :

$$A_{sl,lump} = A_{sl,1} + A_{sl,2} = 32302.6 \text{ mm}^2$$

$$I_{sl,lump} = I_{sl,1} + I_{sl,2} = 1.99 \times 10^8 \text{ mm}^4$$

Based on the position of the lumped stiffener ($l_{w,lump} = 701.7 \text{ mm}$ from the neutral axis, see Fig. D.5), the corresponding distances are:

$$b_{1,lump} = 1118.7 \text{ mm}$$

$$b_{2,lump} = 1159.8 \text{ mm}$$

$$B_{lump} = b_{1,lump} + b_{2,lump} = 2278.5 \text{ mm}$$

$$a_c = 4.33 \sqrt{\frac{I_{sl,lump} b_{1,lump}^2 b_{2,lump}^2}{t^3 B_{lump}}} = 11129 \text{ mm} \quad \text{see Eq.(2.33)}$$

As $a < a_c$ ($a = 2100 \text{ mm}$), the buckling stress is obtained as follows:

$$\sigma_{cr,lump} = \frac{\pi^2 EI_{sl,lump}}{A_{sl,lump} a^2} + \frac{Et^3 B_{lump} a^2}{4\pi^2 (1-\nu^2) A_{sl,lump} b_{1,lump}^2 b_{2,lump}^2} = 2904 \text{MPa} \quad \text{see Eq.(2.32)}$$

Due to the stress gradient, the critical plate buckling stress is obtained by interpolation from the position of the lumped stiffener (defined by $l_{w,lump} = 701.7$ mm from the neutral axis, see Fig. D.5) to the most stressed edge of the plate:

$$\sigma_{cr,p,I+II} = \sigma_{cr,sl,lump} \frac{h_w / (1-\psi_{web})}{l_{w,lump}} = 7534 \text{MPa}$$

with the stress gradient of the web equal to $\psi_{web} = -s_0/s_5 = -0.252$.

$$\sigma_{cr,p} = \min[\sigma_{cr,p,I}, \sigma_{cr,p,II}, \sigma_{cr,p,I+II}] = 4795 \text{MPa}$$

$$\beta_{A,c} = \frac{A_{c,eff,loc}}{A_c} = \frac{A_{c,eff,loc}}{A_{sl,1} + A_{sl,2}} = 0.934 \quad \text{see Eq.(2.31)}$$

$$\bar{\lambda}_p = \sqrt{\frac{\beta_{A,c} f_y}{\sigma_{cr,p}}} = 0.263 \quad \text{see Eq.(2.31)}$$

$$\rho = \begin{cases} 1.0 & \text{if } \bar{\lambda} < 0.5 + \sqrt{0.085 - 0.055\psi} \\ \frac{\bar{\lambda} - 0.055(3 + \psi)}{\bar{\lambda}^2} & \text{if } \bar{\lambda} \geq 0.5 + \sqrt{0.085 - 0.055\psi} \end{cases} = 1.0 \quad \text{see Eq.(2.24)}$$

where ψ is the stress gradient of the whole web $\psi_{web} = -s_0/s_5 = -0.252$.

- **Column-type buckling:** - χ_c

The critical stress is determined for the stiffener closest to the most compressed edge with the gross material properties $I_{sl,1} = 1.034 \times 10^8 \text{ mm}^4$ and $A_{sl,1} = 17570 \text{ mm}^2$.

$$\sigma_{cr,sl} = \frac{\pi^2 EI_{sl,1}}{A_{sl,1} a^2} = 2767.4 \text{MPa} \quad \text{see Eq.(2.37)}$$

Similar to the plate-type buckling, the critical column buckling stress is obtained by interpolation from the position of the stiffener to the most stressed edge of the web as:

$$\sigma_{cr,c} = \sigma_{cr,sl} \frac{s_5}{(s_3 + s_4) / 2} = 4755 \text{MPa}$$

$$\beta_{A,c} = \frac{A_{sl,1,eff}}{A_{sl,1}} = 0.912 \quad \text{see Eq.(2.36)}$$

where $A_{sl,1,eff} = 16028 \text{ mm}^2$ and $A_{sl,1} = 17570 \text{ mm}^2$ are respectively the effective and the gross cross-sectional area of the stiffener with the adjacent parts of the plate sheet, determined in accordance with Fig. 2.28 and Table 2.10.

$$\bar{\lambda}_c = \sqrt{\frac{\beta_{A,c} f_y}{\sigma_{cr,c}}} = 0.261 \quad \text{see Eq.(2.36)}$$

D.3 – Shear resistance

The shear resistance of a box-girder cross-section ($V_{bw,Rd}$) is calculated using the *Extended web method* developed in this thesis (see 8.3.4), defined by Eq.(8.11). The geometry of the extended web with required notations is illustrated in Fig. D.7.

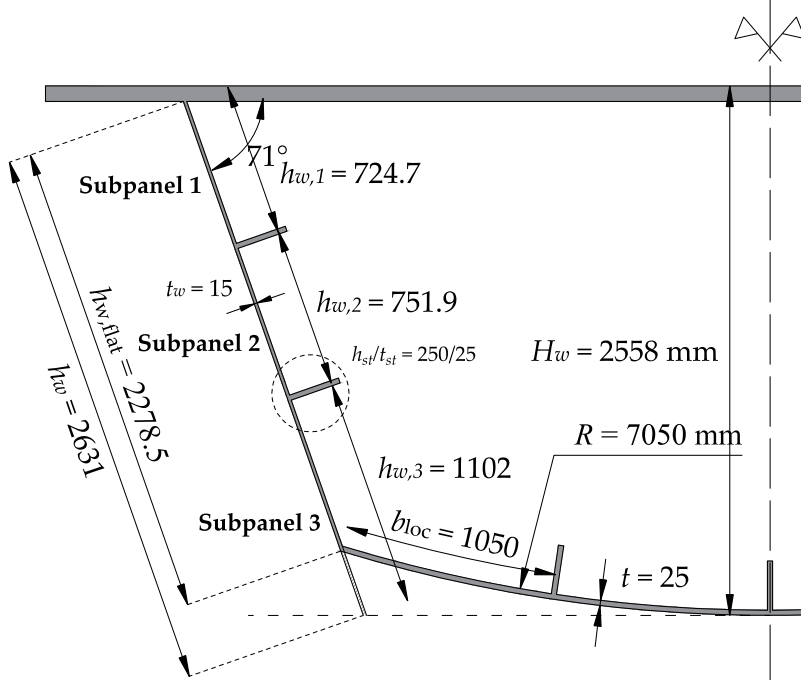


Fig. D.7: Design example – extended web geometry

First, the shear plastic resistance V_{pl} is calculated as:

$$V_{pl,Rd} = \frac{(h_{w,flat} \cdot t_w + L_w \cdot t) f_y}{\sqrt{3} \gamma_{M,1}} = 7548 kN \quad \text{see Eq.(8.8)}$$

where the partial factor is taken as $\gamma_{M,1} = 1.1$, whereas the part of the bottom flange that participates in the shear plastic resistance (L_w) is calculated as:

$$L_w = \frac{1}{R} \left(\frac{b}{\pi} \right)^2 = \frac{Z \cdot t}{\pi^2} = 253.3 \text{ mm} \quad \text{see Eq.(8.7)}$$

As $b_{loc} = 1050 \text{ mm} > L_w = 253.3 \text{ mm}$ (see Fig. D.7), the stiffeners on the bottom flange fall outside of the arc length L_w , which means that they may be excluded from the extended web model. Consequently, the main (extended) web is considered as 2-stiffened with a total height of $h_w = 2631 \text{ mm}$.

For the calculation of the reduction factor, it is necessary to calculate first the slenderness parameter $\bar{\lambda}_w$, defined by Eq.(8.12). The slenderness is calculated for the entire 2-stiffened web, with corresponding elastic buckling coefficient k_e and for the width of the extended web h_w ; however, it should not be lower than the slenderness of each of three subpanels, considered as an unstiffened panel with the corresponding $k_{e,i}$ and local width $b_{loc,i}$, indicated in Fig. D.7.

I – Global shear buckling:

The web consists of two flat stiffeners, both of which with the geometry indicated in Fig. D.8. The mechanical properties of each stiffener are as follows (all calculations done): $A_{sl,1} = 1.21 \times 10^4 \text{ mm}^2$ and $I_{sl,1} = 0.858 \times 10^8 \text{ mm}^4$. Hence, the total second moment of area is $I_{sl} = I_{sl,1} + I_{sl,2} = 2I_{sl,1} = 1.716 \times 10^8 \text{ mm}^4$.

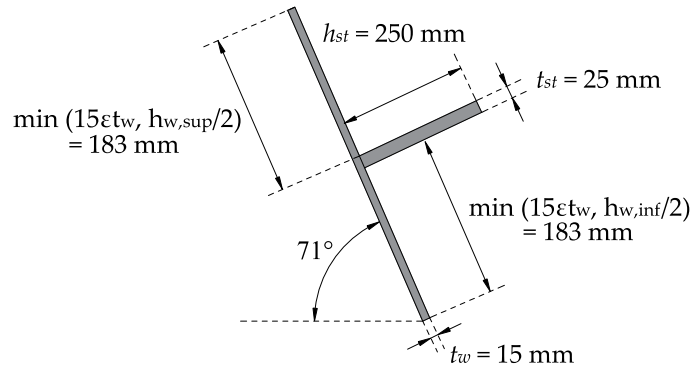


Fig. D.8: Design example – web stiffener geometry

Since the aspect ratio of the whole extended web (α_w) is equal to $a/h_w = 2100/2631 = 0.8 < 3$, the shear buckling coefficient k_τ is obtained from Annex A.3 of EN 1993-1-5 as:

$$k_\tau = 4.1 + \frac{6.3 + 0.18 \frac{I_{sl}}{t_w^3 h_w}}{\alpha_w^2} + 2.2 \sqrt[3]{\frac{I_{sl}}{t_w^3 h_w}} = 25.33 \quad \text{see Eq.(2.102)}$$

$$\bar{\lambda}_w = \frac{h_w / t_w}{37.4 \cdot \varepsilon \cdot \sqrt{k_\tau}} = 1.144 \quad \text{see Eq.(8.12)}$$

II – Local shear buckling:

- **Subpanel 1:**

The subpanel 1 is a flat panel between the top flange and the first stiffener, with the aspect ratio equal to $\alpha_{w,1} = a/h_{w,1} = 2100/751.9 = 2.8 > 1$. Hence, the shear buckling coefficient ($k_{\tau,1}$), and the local slenderness parameter ($\bar{\lambda}_{w,1}$) are obtained as follows:

$$k_{\tau,1} = \begin{cases} 4.0 + 5.34 \left(\frac{1}{\alpha_{w,1}} \right)^2 & \text{if } \alpha_{w,1} < 1.0 \\ 5.34 + 4.0 \left(\frac{1}{\alpha_{w,1}} \right)^2 & \text{if } \alpha_{w,1} \geq 1.0 \end{cases} = 5.82 \quad \text{see Eq.(2.101)}$$

$$\bar{\lambda}_{w,1} = \frac{h_{w,1} / t_w}{37.4 \cdot \varepsilon \cdot \sqrt{k_{\tau,1}}} = 0.658 \quad \text{see Eq.(8.12)}$$

- **Subpanel 2:**

The subpanel 2 is a flat panel between the two longitudinal stiffeners, with the aspect ratio equal to $\alpha_{w,2} = a/b_{w,2} = 2100/724.7 = 2.9 > 1$. Hence, the shear buckling coefficient ($k_{\tau,2}$), and the local slenderness parameter ($\bar{\lambda}_{w,2}$) are obtained as follows:

$$k_{\tau,2} = \begin{cases} 4.0 + 5.34 \left(\frac{1}{\alpha_{w,2}} \right)^2 & \text{if } \alpha_{w,2} < 1.0 \\ 5.34 + 4.0 \left(\frac{1}{\alpha_{w,2}} \right)^2 & \text{if } \alpha_{w,2} \geq 1.0 \end{cases} = 5.85 \quad \text{see Eq.(2.101)}$$

$$\bar{\lambda}_{w,2} = \frac{h_{w,2} / t_w}{37.4 \cdot \varepsilon \cdot \sqrt{k_{\tau,2}}} = 0.681 \quad \text{see Eq.(8.12)}$$

- **Subpanel 3:**

Despite small participation of curved bottom part in the shear resistance ($L_w = 253.3$ mm), the subpanel 3 is considered flat, with the aspect ratio equal to $\alpha_{w,3} = a/b_{w,3} = 2100/1102 = 1.9 > 1$. Hence, the shear buckling coefficient ($k_{\tau,3}$), and the local slenderness parameter ($\bar{\lambda}_{w,3}$) are obtained as follows:

$$k_{\tau,3} = \begin{cases} 4.0 + 5.34 \left(\frac{1}{\alpha_{w,3}} \right)^2 & \text{if } \alpha_{w,3} < 1.0 \\ 5.34 + 4.0 \left(\frac{1}{\alpha_{w,3}} \right)^2 & \text{if } \alpha_{w,3} \geq 1.0 \end{cases} = 6.44 \quad \text{see Eq.(2.101)}$$

$$\bar{\lambda}_{w,3} = \frac{h_{w,3} / t_w}{37.4 \cdot \varepsilon \cdot \sqrt{k_{\tau,3}}} = 0.951 \quad \text{see Eq.(8.12)}$$

Finally, the web slenderness that should be used for the reduction factor calculation is equal $\bar{\lambda}_w = \max(1.144 ; 0.658 ; 0.681 ; 0.951) = 1.144$.

According to clause 5.1(2) in EN 1993-1-5, the shear in the main stiffened web should be considered if the following criterion is satisfied:

$$\frac{h_w}{t_w} \geq \frac{31}{\eta} \varepsilon \sqrt{k_{\tau}} \quad , \text{ which is the case in this example } (175.24 \geq 105.8), \text{ with } \eta = 1.2.$$

Assuming a rigid end post, the reduction factor for $\bar{\lambda}_w = 1.144 > 1.08$ is obtained from EN 1993-1-5 as:

$$\chi_w = \frac{1.37}{0.7 + \bar{\lambda}_w} = 0.743 \quad \text{see Eq.(2.98)}$$

Using the values from Fig. D.7, the shear buckling resistance of a single web in box-girder cross-section (without flange contributions) is calculated as:

$$V_{bw,Rd} = \frac{\chi_w \left[h_{w,flat} t_w + (h_w - h_{w,flat}) t \right] f_y}{\sqrt{3} \gamma_{M,1}} = 5943 \text{ kN} \quad \text{see Eq. (8.11)}$$

with $\gamma_{M,1} = 1.1$. This value should be lower than the calculated plastic resistance, which is the case in this example ($V_{bw,Rd} = 5943 \text{ kN} < V_{pl,Rd} = 7548 \text{ kN}$). Finally, the corresponding shear resistance obtained by numerical simulations is equal to $V_{num} = 8376 \text{ kN}$, which is around 40% higher.

D.4 – M-V Interaction

For the sake of this example, it is assumed that the box-girder cross-section is well designed against the design values of applied force (M_{Ed} and V_{Ed}), with the following utilization factors:

$$\eta_1 = \frac{M_{Ed}}{M_{eff,Rd}} = 0.9$$

$$\bar{\eta}_3 = \frac{V_{Ed}}{V_{bw,Rd}} = 0.9$$

For this cross-section, the bending moment resistance of the flanges only is equal to $M_{f,Rd} = 77720 \text{ kNm}$, obtained considering the effective area of the bottom flange (see Fig. D.3) and the fully effective top flange.

Interaction between bending and shear should be considered if the following two conditions are satisfied:

$$\eta_1 > \frac{M_{f,Rd}}{M_{eff,Rd}} = \frac{77720}{91935} = 0.845 \quad , \text{ which is satisfied } (0.9 > 0.845)$$

$$\bar{\eta}_3 > 0.5 \quad , \text{ which is satisfied } (0.9 > 0.5)$$

Hence, the M - V interaction is verified as follows:

$$\beta = \left(\frac{M_{f,Rd}}{M_{eff,Rd}} + 0.2 \right)^{15} + 1 = 2.946 \quad \text{Eq. (8.13)}$$

$$\eta_1 + \left[1 - \frac{M_{f,Rd}}{M_{eff,Rd}} \right] (2\bar{\eta}_3 - 1)^\beta = 0.98 \leq 1.0 \quad \text{Eq. (8.13)}$$

Hence, for these utilization factors, the resistance of the considered cross-section to the interaction between bending and shear is verified. The results are illustrated in Fig. D.9, where the corresponding M - V interaction diagram for this cross-section is shown, as well as the FEM results obtained in section 7.4.

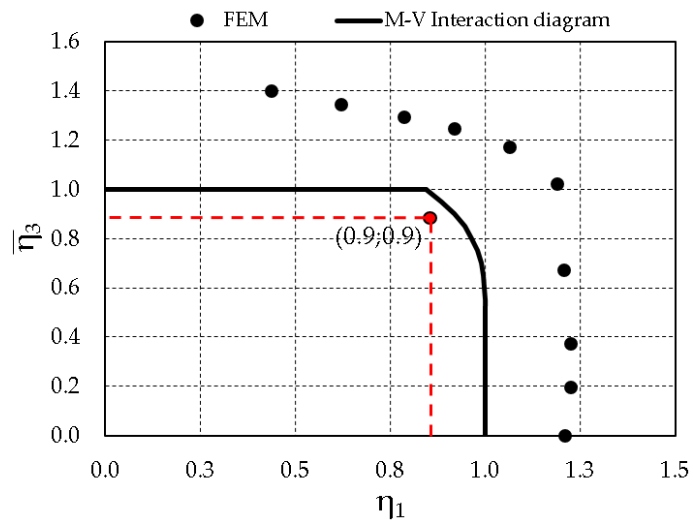


Fig. D.9: Design example – M-V interaction verification